



Rayleigh–Taylor and Richtmyer–Meshkov instability induced flow, turbulence, and mixing. II



Ye Zhou

Lawrence Livermore National Laboratory, Livermore, CA 94550, USA

ARTICLE INFO

Article history:

Available online 27 September 2017

Editor: R. Redmer

Keywords:

Rayleigh–Taylor instability
 Richtmyer–Meshkov instability
 Kelvin–Helmholtz instability
 Shock waves
 Transition
 Turbulence
 Mixing
 Astrophysical fluid dynamics
 SuperNovae
 Inertial confinement fusion (ICF)
 High energy density physics (HEDP)
 Direct numerical simulations (DNS)
 Large-eddy simulations (LES)

ABSTRACT

Rayleigh–Taylor (RT) and Richtmyer–Meshkov (RM) instabilities are well-known pathways towards turbulent mixing layers, in many cases characterized by significant mass and species exchange across the mixing layers (Zhou, 2017. *Physics Reports*, 720–722, 1–136). Mathematically, the pathway to turbulent mixing requires that the initial interface be multimodal, to permit cross-mode coupling leading to turbulence. Practically speaking, it is difficult to experimentally produce a non-multi-mode initial interface. Numerous methods and approaches have been developed to describe the late, multimodal, turbulent stages of RT and RM mixing layers. This paper first presents the initial condition dependence of RT mixing layers, and introduces parameters that are used to evaluate the level of “mixedness” and “mixed mass” within the layers, as well as the dependence on density differences, as well as the characteristic anisotropy of this acceleration-driven flow, emphasizing some of the key differences between the two-dimensional and three-dimensional RT mixing layers. Next, the RM mixing layers are discussed, and differences with the RT mixing layer are elucidated, including the RM mixing layers dependence on the Mach number of the initiating shock. Another key feature of the RM induced flows is its response to a reshock event, as frequently seen in shock-tube experiments as well as inertial confinement events. A number of approaches to modeling the evolution of these mixing layers are then described, in order of increasing complexity. These include simple buoyancy–drag models, Reynolds-averaged Navier–Stokes models of increased complexity, including $K-\varepsilon$, $K-L$, and $K-L-a$ models, up to full Reynolds-stress models with more than one length-scale. Multifield models and multiphase models have also been implemented. Additional complexities to these flows are examined as well as modifications to the models to understand the effects of these complexities. These complexities include the presence of magnetic fields, compressibility, rotation, stratification and additional instabilities. The complications induced by the presence of converging geometries are also considered. Finally, the unique problems of astrophysical and high-energy-density applications, and efforts to model these are discussed.

© 2017 Elsevier B.V. All rights reserved.

Contents

9. RT multimode flows.....	2
9.1. Initial condition effects.....	2
9.2. Mixedness and normalized mixed mass.....	7
9.3. Atwood number effects.....	12
9.4. Anisotropy	16
9.5. 2D vs 3D RTI induced flows	22

E-mail address: yezhou@llnl.gov.

10.	RM multimode flows	25
10.1.	Initial condition effects	25
10.2.	Mixedness and normalized mixed mass	31
10.3.	Atwood number dependence	32
10.4.	Mach number effects	34
10.5.	Anisotropy	36
10.6.	2D vs 3D RMI induced flows	41
11.	RM Reshock	41
11.1.	Physics of noted interest	41
11.2.	Initial condition	46
11.2.1.	Initial conditions at the time of 1st shock	46
11.2.2.	Initial conditions at the time of reshock	50
11.3.	Mixedness and normalized mixed mass	51
11.4.	Anisotropy	54
11.5.	Atwood number effects	57
11.6.	Mach number effect	59
11.7.	Models for reshocked RMI	60
11.7.1.	Single-mode	60
11.7.2.	Multi-mode	61
12.	Mix models	63
12.1.	Remarks on the initial conditions	64
12.2.	The buoyancy-drag models	65
12.3.	Two-equation models	67
12.3.1.	K-L model	67
12.3.2.	K- ε model	70
12.4.	Two-scale models	72
12.5.	Three- and four-equation models	72
12.5.1.	Original Besnard, Harlow, Rauenzhan (BHR) model	72
12.5.2.	BHR-CEA, BHR1, K-L-a	73
12.5.3.	BHR2	73
12.6.	Reynolds stress models	76
12.6.1.	Reynolds stress and ε model by Grégoire, Souffland, and Gauthier	76
12.6.2.	GSG-R, GSGf, and GSG+ models	79
12.6.3.	BHR3	79
12.6.4.	BHR two-length scale model (TLSM)	81
12.6.5.	Nikiforov model	83
12.7.	Multi-fluids	83
13.	Coupled fields and multiple instabilities	86
13.1.	Compressibility	87
13.2.	Stratification	92
13.3.	Rotation	94
13.4.	Magnetic field	99
13.5.	Multiple hydro instabilities	104
13.5.1.	RTI and RMI	104
13.5.2.	RTI and/or RMI with KHI	106
14.	Converging geometries	113
14.1.	Order of increasing convergence effects	113
14.2.	Cylindrical geometry	115
14.3.	Spherical geometry	119
15.	Astrophysical fluid dynamics and high energy density physics experiments	119
16.	Conclusion	135
	Acknowledgments	136
	References	137

9. RT multimode flows

9.1. Initial condition effects

As alluded to in Part I (Zhou, 2017), initial conditions (ICs), i.e., the initial perturbations on the inertial confinement fusion (ICF) (Lindl, 1995, 1998; Atzeni and Meyer-ter-Vehn, 2004; Betti and Hurricane, 2016) target surface, are important, as they can affect the yield of the reaction (Lindl and Mead, 1975; Hammer et al., 1999). The initial perturbations on the exterior shell of the ICF targets have been measured (Milovich et al., 2004; Dimonte, 2004).

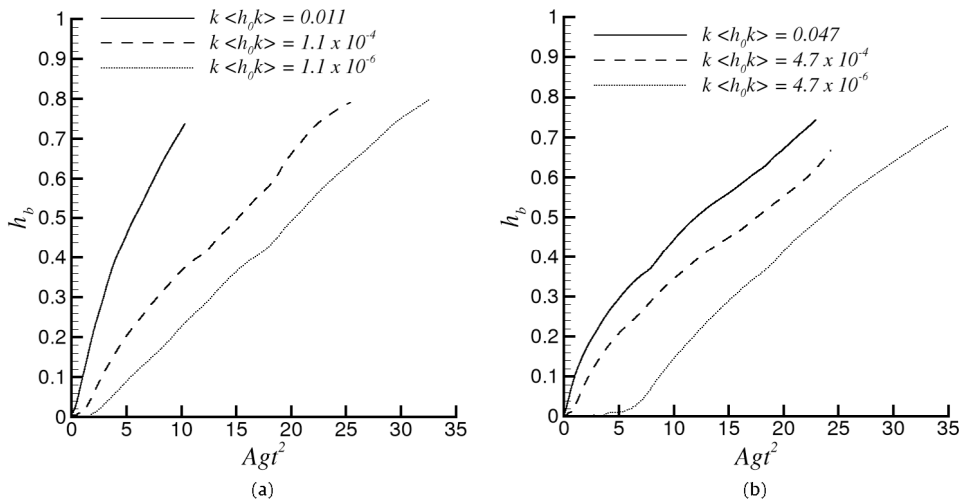


Fig. 9.1. Effect of $k \langle h_0k \rangle$: (a) Evolution of bubble amplitude, h_b for three cases with long wavelengths present in the initial conditions; (b) Evolution of bubble amplitude, h_b for mode-coupling cases.

Source: Fig. 13 of Ramaprabhu et al. (2005), *J. Fluid Mech.* with permission.

Much attention has been paid to whether the late-time flow properties depend on the specific form of the initial conditions (see, for example Dimonte, 2004; Miles et al., 2004a; Lim et al., 2010; Kuchibhatla and Ranjan, 2013). Rozanov et al. (2015) noticed that their two-dimensional (2D) and three-dimensional (3D) numerical data gave close results and argued that this may relate to their initial perturbations which promote the formation of many 2D structures in the flow. Dimonte (2004) used a model based on the Birkhoff (1955) approach to derive a logarithmic dependence of the dimensionless RT bubble growth parameter, α_b , on initial conditions. Ramaprabhu et al. (2005) and Youngs (2013) studied the effect of initial conditions on the growth rate of Rayleigh–Taylor instability (RTI) (Rayleigh, 1883; Taylor, 1950) using RTI-3D, a third-order 3D accurate finite-volume code (Andrews, 1995) and TURMOIL, a Lagrange-remap hydrocode (Youngs, 1991, 2009), respectively.

Two distinctive types of the initial conditions have been considered and were already recognized by Sharp and Wheeler (1961) and relevant to the earlier work by Inogamov (1978) and Birkhoff (1955). First, the long-wavelength perturbations are included in the initial spectral content whose amplitudes govern their late-time self-similar growth (Youngs, 2013). As an example, Inogamov (1978) argued that random perturbations with amplitude/wavelength=a constant and wavelengths up to the size of the domain would give self-similar mixing at an enhanced rate. In terms of a power spectrum, $P(k)$, for the initial perturbations, this is equivalent to $P(k) \sim k^{-3}$ where the standard deviation of the initial perturbation is given by $\sigma^2 = \int P(k)dk$. Youngs (2003, 2013), and Ramaprabhu et al. (2005) have used such initial perturbations. Second, in the opposite limit, low-wavenumber modes have negligible energy compared with the high-wavenumber content. Long-wavelengths in the flow is generated instead largely by the nonlinear coupling of modes (Haan, 1989; Dimonte et al., 2004). It seems reasonable to assume that loss of memory of the initial conditions will then occur, implying self-similar mixing (Youngs, 2013).

Ramaprabhu et al. (2005) reported that with long wavelengths present in the initial conditions, α_b was found to increase logarithmically with the initial amplitudes (Fig. 9.1a). On the other hand, in the mode-coupling dominated limit, no such dependence on initial amplitudes is observed, and α_b takes a universal lower-bound value of $\sim 0.03 \pm 0.003$ (Fig. 9.1b). This may explain the low values of α_b reported by most numerical simulations that are initialized with annular spectra of short-wavelength modes and hence evolve purely through mode-coupling. Moreover, Ramaprabhu et al. found α_b measurements in RTI computations in the mode-coupling regime to not depend on h_0k .

Olson and Jacobs (2009) performed experiments investigating the RTI of a miscible fluid combination with Atwood number $A \approx 0.2$. Taking advantage of the apparatus developed by Waddell et al. (2001) and Niederhaus and Jacobs (2003), a complex initial condition was imposed by vertical oscillation of the fluid container prior to the acceleration phase. The initial perturbations resulting from this technique can be classified as either ordered or disordered. Fig. 9.2 shows measured values of α of individual experiments plotted against the dimensionless product h_0k . The lack of a distinct trend indicates that α is not sensitive to h_0k , confirming the findings of Ramaprabhu et al. who found α_b measurements in the mode-coupling regime to not depend on h_0k .

Performing a further numerical study, Banerjee and Andrews (2009) concluded that the overall growth of the RTI mixing is strongly dependent on initial conditions. Zhang and Tan (2009) reached the same conclusion but using a high-order spectral element code, and an initial interface perturbation consisted of a random combination of Fourier modes. (Note, however, this statement is not illustrated in the paper. For example, Fig. 5b of Zhang and Tan shows no dependence on initial conditions.)

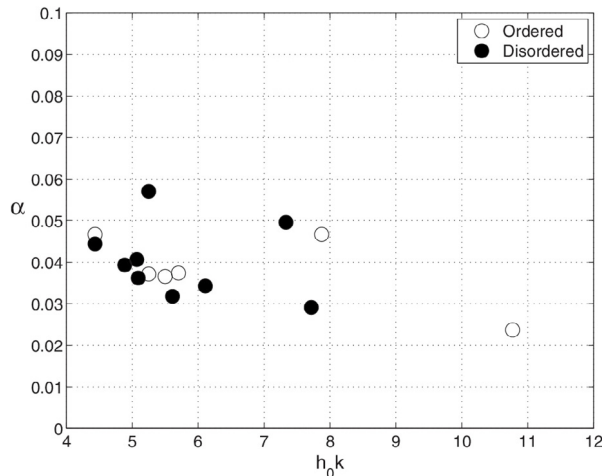


Fig. 9.2. Plot showing the variation of α with the product of the initial amplitude, h_0 , and the wave number, k . Each point represents a single experiment. Ordered and disordered perturbations are distinguished from one another in the plot by empty and filled markers, respectively.
Source: Adapted from Fig. 13 of Olson and Jacobs (2009), *Phys. Fluids*, with the permission of AIP Publishing.

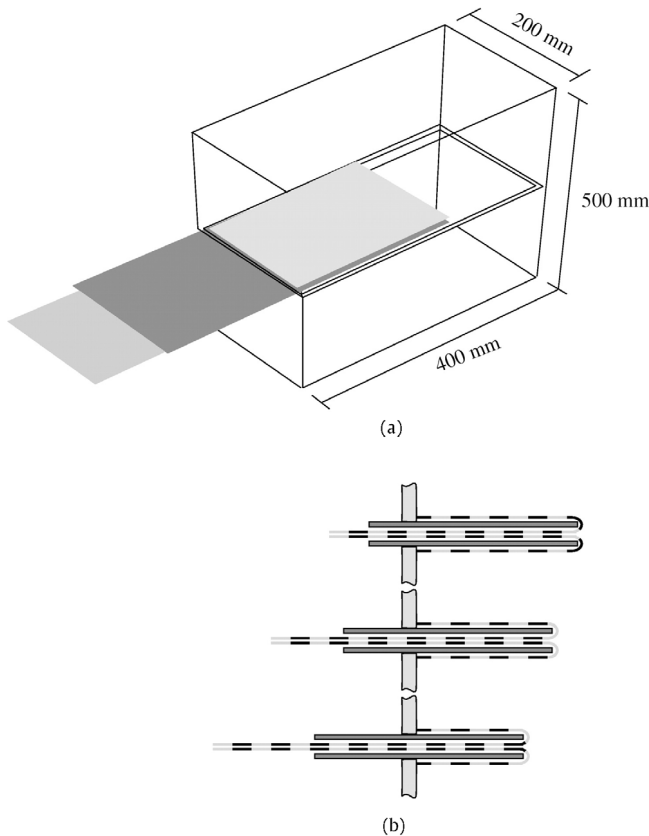


Fig. 9.3a. (a) Sketch of experimental apparatus. The hollow stainless-steel barrier is shown as dark gray and the nylon fabric as light gray. The experiments were carried out in a Perspex tank 500 mm deep, 400 mm long, and 200 mm wide. The tank has a removable aluminum sheet 1.5 mm in thickness separating heavy and light fluids (Linden and Redondo, 1991). (b) Illustration of process by which fabric (dashed) is removed through the gap between the plates (Andrews and Dalziel, 2010).

Source: Fig. 1 of Dalziel et al. (1999), *J. Fluid Mech.* with permission.

Other measurements, such as the energy-containing and dissipation scales have a relatively weak dependence on the initial perturbation (Vladimirova and Chertkov, 2009).

While the early time behavior may suggest different growth rates, Livescu et al. (2011) found an asymptotic value result, $\alpha_b \approx 0.025$, from several direct numerical simulations (DNS) with top-hat initial perturbation spectra and different spectrum

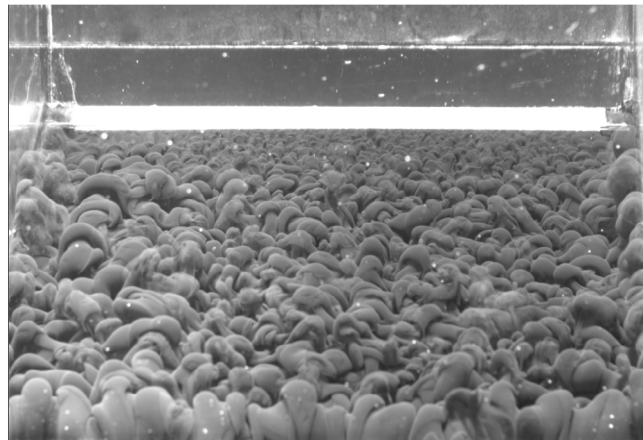


Fig. 9.3b. Early three-dimensional development of RTI as the composite barrier (white band near the top of the picture) is withdrawn.
Source: Photograph courtesy of Dr. A.G.W. Lawrie, University of Bristol, UK.

widths and/or amplitudes. On the other hand, they reported that simulations initialized with a k^{-3} perturbation spectrum reproduced the higher $\alpha_b \approx 0.065$ seen in many experiments.

The importance of the initial condition has been manifested differently. Dalziel et al. (1999) measured the velocity field generated by the removal of a thin barrier initially separating two fluids of different densities (Fig. 9.3a), which then interpenetrated and evolved into a turbulent mixing layer. Fig. 9.3b shows that the developing flow has a clear three-dimensional character growing from high wavenumbers even from the earliest times (Andrews and Dalziel, 2010). Using a measured velocity field for the start of the experiments to initialize the simulations, Dalziel et al. showed substantially improved agreement with experiment when compared with simulations using idealized initial conditions (Fig. 9.4). In a related development, Ramaprabhu and Andrews (2004b) found that numerical simulations of RTI mixing show reasonable agreement with experimental measurements of the self-similar growth rate, α , when the computations were initialized with experimental data.

Liu et al. (2006) presented a set of 3D RT multimode mixing simulations to model the experimental data of Banerjee and Andrews (2006) based on improved physics and on an improved tracking algorithm in the front tracking code. In a follow-up work, Glimm et al. (2013) used estimates of experimental initial conditions to match observed values of α_b in the range 0.05–0.85. Nevmerzhitskiy et al. (2014) also carried out interesting experiments in this matter, comparing results from relatively small natural initial perturbation versus those from both natural and specified one.

Mueschke et al. (2006) quantified the initial multimode interfacial streamwise velocity and spanwise density perturbations present at the onset of a small Atwood-number, incompressible, miscible RTI driven mixing layer using high-resolution thermocouples and planar laser-induced fluorescence (PLIF). It was shown that the measured initial conditions describe an initially anisotropic state. The evolution of various velocity and density statistics, together with velocity and density spectra, were measured. The statistics were used to investigate the early-time evolution and the onset of strongly nonlinear, transitional dynamics within the mixing layer. The early-time evolution of the density and vertical velocity variance spectra indicated that velocity fluctuations are the dominant mechanism driving the instability. A DNS was subsequently carried out using the initial conditions, geometry, and physical parameters to approximate those of this experiment (Mueschke and Schilling, 2009a,b; Schilling and Mueschke, 2010). The DNS was validated by comparing quantities from the simulation to experimental measurements (Mueschke and Schilling, 2009a). Large-scale quantities such as the bubble front penetration h_b and the mixing layer growth parameter α_b , higher-order statistics such as velocity variances and the molecular mixing parameter, and vertical velocity and density variance spectra were in favorable agreement with the experimental data. The DNS slightly underestimated the growth of the bubble front but predicts $\alpha_b = 0.07$ at the latest time, in excellent agreement with the measurement.

Soulard et al. (2015) focused on whether a loss of memory of initial conditions occurs at large scales. The large-scale properties of a self-similar RT turbulent flow is defined in an unbounded domain and assumed to have a finite initial energy. Noting that the RTI mixing zone width is typically larger than the integral scale of turbulence by a factor two to three (Soulard and Griffond, 2012; Vladimirova and Chertkov, 2009), the nondimensionalized wave number characterizing the energy containing range is much larger than 1. Soulard et al. (2015) adopted the same strategy in their previous work of unstable stratified homogeneous turbulence (Soulard et al., 2014; Griffond et al., 2014, 2015) using eddy-damped quasi-normal Markovianized (EDQNM) closure (Orszag, 1970, 1977; Lesieur, 1990; Schilling and Zhou, 2002). The non-linear contribution from the growing linear homogeneous mode of the instability is dominant, and that non-linear transfers at large scales are driven by distant triadic interactions (see related discussions for homogeneous, isotropic turbulence, Domaradzki and

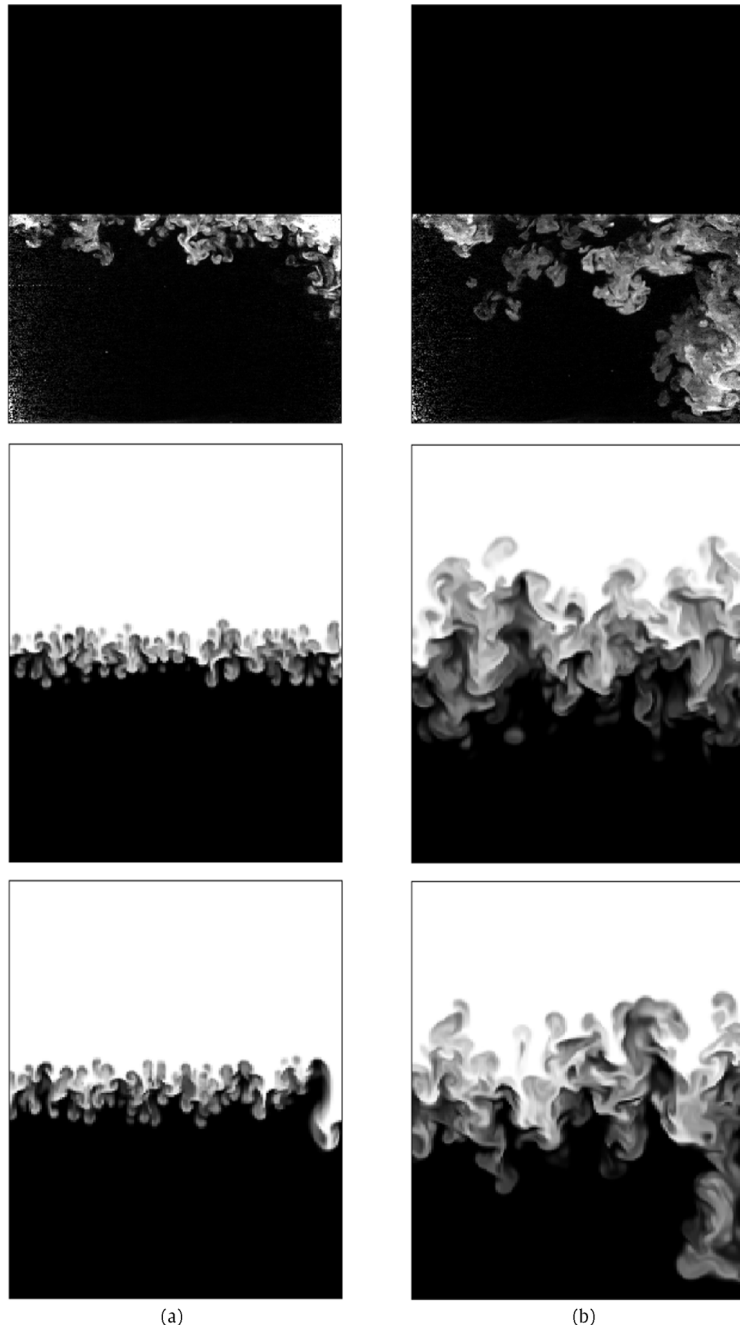


Fig. 9.4. Comparison between a typical RTI experiment (top) and simulations using idealized initial conditions (middle) and initial conditions measured from experiments (bottom). The flows are shown for (a) $\tau = 1$ ($t = 5$ s), (b) $\tau = 2$ ($t = 10$ s), (c) $\tau = 3$ ($t = 15$ s), and (d) $\tau = 4$ ($t = 20$ s). Note that only the flow in the lower half of the tank is shown in the experiment.

Source: Fig. 6 of [Dalziel et al. \(1999\)](#), *J. Fluid Mech.* with permission.

[Rogallo, 1990](#); [Ohkitani and Kida, 1992](#); [Yeung and Brasseur, 1991](#); [Zhou, 1993a,b](#); [Zhou and Speziale, 1998](#); [Zhou et al., 1996](#)). This modeled evolution shows that the large scales undergo an evolution dominated by non-linear backscattering processes. As a result, a loss of memory of initial conditions occurs at large scales, and there is no equivalent of the permanence of large eddies for RT turbulence as previously asserted by [Poujade and Peybernes \(2010\)](#).

The results discussed in this subsection also raise the possibility of design and active control of RT transition to turbulence, based on the choice of the shape and size of the initial perturbation spectrum ([Banerjee and Andrews, 2009](#)).

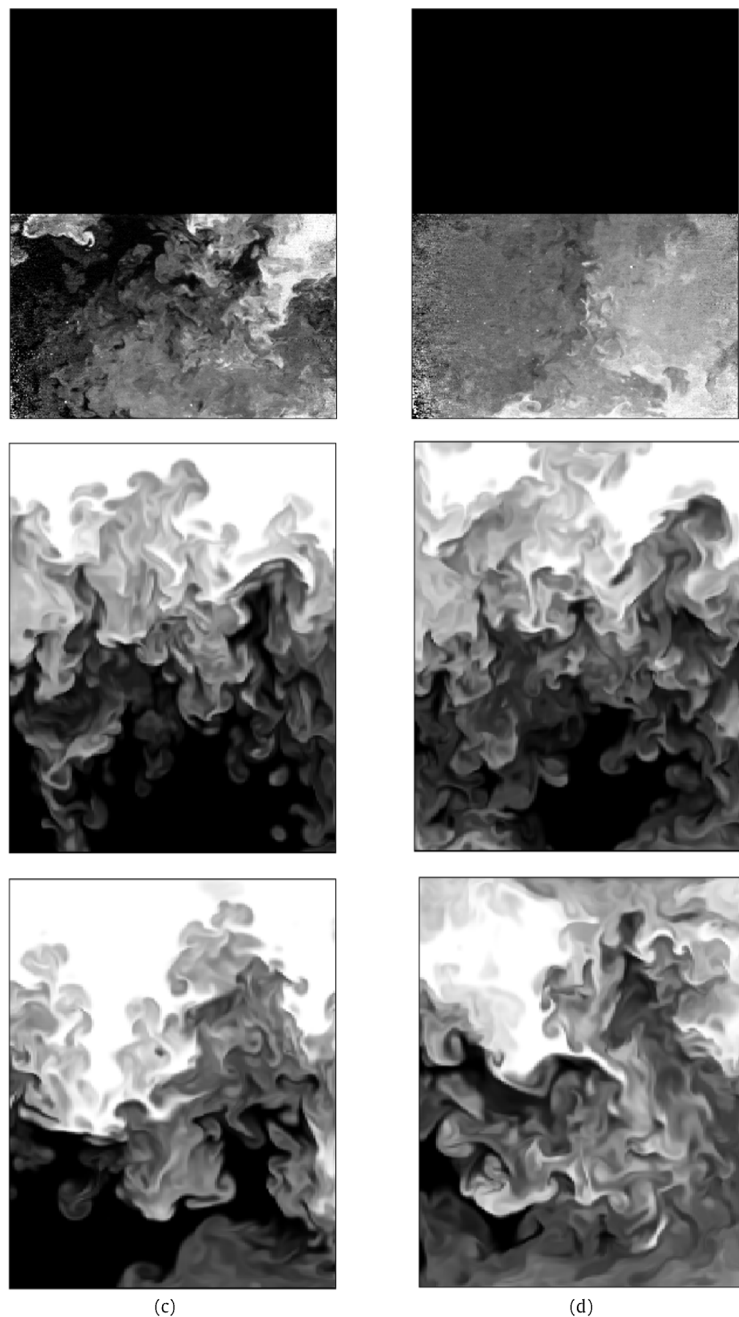


Fig. 9.4. (continued)

Source: Fig. 6 of [Dalziel et al. \(1999\)](#), *J. Fluid Mech.* with permission.

9.2. Mixedness and normalized mixed mass

It is useful to have an estimate of the fine scale mixing process. For instance, there are measurements of concentration fluctuation spectra, concentration probability density functions (PDFs), and fractal index in the experiments of Linden et al. (1994) and Dalziel et al. (1999). Measured concentration PDFs are also given in Wilson and Andrews (2002).

As noted in Wilson and Andrews (2002), the molecular mix fraction was first introduced by Dankwerts (1952) as a measure of the intensity of segregation. Youngs (1991, 1994), Linden et al. (1994) and Dalziel et al. (1999) define the ratio

$$\Theta \equiv \frac{\int_{-\infty}^{\infty} \langle X(1-X) \rangle dz}{\int_{-\infty}^{\infty} \langle X \rangle \langle 1-X \rangle dz} \quad (9.1)$$

where the mole fraction of heavy fluid is

$$X = \frac{\rho - \rho_1}{\rho_2 - \rho_1}, \quad (9.2)$$

and z is the direction of the acceleration. The quantities ρ_2 and ρ_1 are the density of the heavy and light fluids, respectively. For a “slow” reaction between components of fluids 1 and 2, the quantity Θ gives the total reaction rate divided by the reaction rate if there were no concentration fluctuation in each horizontal plane (Youngs, 2003).¹

If the mole fraction of a stoichiometric mixture is 1/2, the mole fraction of the reaction product for a fast reaction (assuming that either reactant 1 or 2 is fully depleted) is

$$X_P(X) = \begin{cases} 2X & \text{if } X \leq 1/2 \\ 2(1-X) & \text{if } X > 1/2 \end{cases} = 2 \min(X, 1-X). \quad (9.3)$$

The height of the mixing region is defined as the product thickness that would result if the entrained fluids were perfectly homogenized in x and y , i.e.

$$h \equiv \int_{-\infty}^{\infty} X_P(\langle X \rangle) dz. \quad (9.4)$$

Thus, h is an entrainment length, derived from the volumes of pure fluids entering the mixing region (Cook et al., 2004; Cabot and Cook, 2006).

The parameter Ξ measures the total product formed in the RT mixing layer relative to the product that would be formed if all the entrained fluid were completely mixed in each plane. The value of Ξ is limited by the amount of lean reactant (light fluid) in the mixture (Cook and Dimotakis, 2001; Cook and Zhou, 2002)

$$\Xi \equiv \frac{\int_{-\infty}^{\infty} \langle X_P \rangle dz}{h}. \quad (9.5)$$

Youngs (2003) noted that Ξ gives the equivalent result for a fast reaction for which either the reactant in fluid 1 or fluid 2 is fully depleted.

The mixedness parameters $\Theta, \Xi = 1$ correspond to completely mixed fluid (no horizontal variation), whereas $\Theta, \Xi = 0$ correspond to complete segregation (immiscible case). As illustrated in Fig. 9.5, initially, the layer is diffuse with small amplitude perturbations; hence, the mixedness parameters start out near unity. As the perturbations grow, they entrain fluid at a rate proportional to their wavelengths (longer wavelengths result in bigger “gulps” of pure fluid). At early times, the rate of entrainment exceeds the rate of mixing, and the mixedness parameters decrease. This is a consequence of the fact that, early on, the surface area across which the fluids can diffuse is relatively small. However, later on the interface begins to wrinkle due to baroclinic vorticity (mushroom caps) and Kelvin–Helmholtz (KH) (Kelvin, 1871; von Helmholtz, 1868) instabilities in the shearing regions along the mushroom necks; the interfacial surface area then rapidly increases, the mixing rate overtakes the entrainment rate, and the curve reverses direction (Cook and Zhou, 2002).

Cook et al. (2004) demonstrated that these two mixedness parameters give very similar measures of the state of mixing within the layer (Fig. 9.5). The mixedness curves appear to asymptote to a value somewhere around $(\Theta, \Xi) \approx (0.78, 0.79)$ for a moderate Atwood number ($A = 0.5$), $Sc = 1$ RT mixing layer. The value of $\Theta \sim 0.78$ of agrees with the DNS results of Livescu et al. (2010) on a $1024^2 \times 4032$ mesh for a flow with a much smaller Atwood number ($A = 0.04$, similar to that of Banerjee et al., 2010b).

Banerjee and Andrews (2009) reported that this global mixing parameter remained insensitive to variations in ICs and was found to asymptote to a value of 0.8. Ramaprabhu et al. (2005) reported late-time values Θ in a study where implicit large-eddy simulation (ILES) (Boris et al., 1992; Grinstein et al., 2007; Drikakis, 2003; Drikakis et al., 2005) was used to examine the influence of initial conditions on molecular mixing. As shown in Fig. 9.6, Θ appears weakly sensitive to $k\langle h_{0k} \rangle$. The large-amplitude cases (with $N_{\min} = 1$) register a slightly lower value, approaching 0.6. The authors reasoned that this could be due to large scale vortical motion that transports unmixed lighter fluid into regions of heavier fluid and vice versa (i.e. entrainment without molecular mixing). The simulations by Youngs (2003) in which long wavelengths were included also exhibit reduced molecular mixing ($\Theta \sim 0.68 – 0.74$). To delineate the sensitivity to initial perturbations, Youngs (2013) carried out ILES to study two distinctive setting. In the cases where mixing evolves from ‘small random perturbations,’ a mixedness value of $\Theta \approx 0.80$ was once again obtained. In the other cases, more typical of that observed in experiments, random long wavelength perturbations (k^{-3} spectrum) are added to give self-similar mixing at an enhanced rate. The mixedness Θ is reduced to ~ 0.68 at a late time when the long wavelength perturbations are added.

¹ It should be noted that the symbol θ has been used extensively as a measure of mixedness (see for example, Linden et al., 1994; Dalziel et al., 1999; Youngs, 1991, 1994; Wilson and Andrews, 2002; Mueschke and Schilling, 2009a; Banerjee et al., 2010b; Lee et al., 2008). Banerjee and Mutnuri (2012) illustrated (in their Table 2) that the values of so-called local mix parameter θ are very close to the global mixedness, Θ , defined in Eq. (9.1). Therefore, the notation Θ is used in this review article to reserve symbol θ exclusively for the similarity scaling of the RMI late-time evolution (Section 6, Part I).

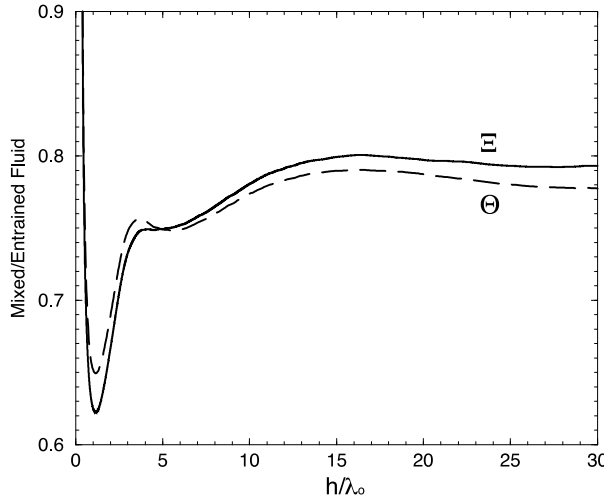


Fig. 9.5. The ratio of mixed to entrained fluid for the mixing region using data obtained from large-eddy simulations. Here, Θ , $\Xi = 1$ corresponds to completely mixed fluid (no horizontal variation), whereas Θ , $\Xi = 0$ corresponds to complete segregation (immiscible case).
Source: Fig. 12 of Cook et al. (2004), *J. Fluid Mech.* with permission.

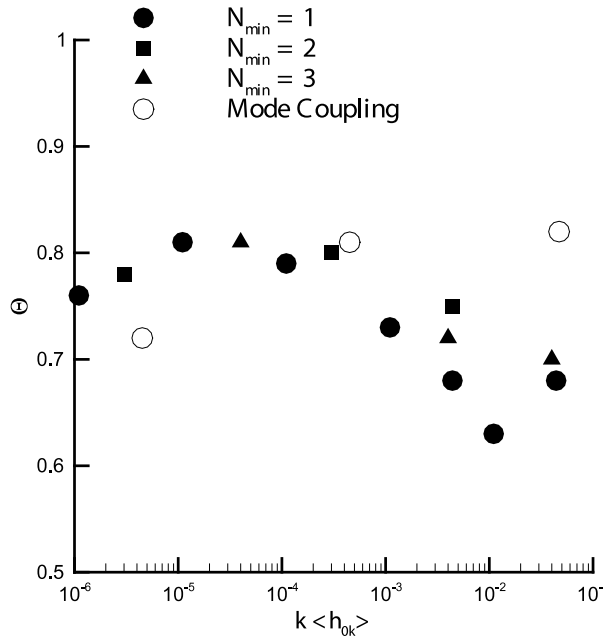


Fig. 9.6. Mixedness parameter Θ vs. $k\langle h_{0k} \rangle$.
Source: Fig. 19 of Ramaprabhu et al. (2005), *J. Fluid Mech.* with permission.

Experimentally, Kraft et al. (2009) obtained a late-time value of $\Theta \sim 0.7$ in a gas channel experiment ($Sc = 0.7$). Here, the Schmidt number (Sc) is given by $Sc = \nu/D$ where ν is the kinematic viscosity and D is the Fickian diffusivity. Banerjee et al. (2010b) measured the parameters Ξ and Θ at various downstream centerline locations of the gas channel ($Sc \sim 1$, $A = 0.03\text{--}0.6$), as a function of non-dimensionalized time (Fig. 9.7a). It is observed that both Ξ and Θ are approximately equal (~ 0.72) (Fig. 18 of Banerjee et al., 2010b), a result consistent with numerical simulations mentioned above. Fig. 9.7b (Fig. 17 of Banerjee et al., 2010b) shows the molecular mix parameter across the RT mixing layer and inspection reveals that Θ remains reasonably constant (~ 0.7) across this $Sc \sim 1$ RT mixing layer, in agreement with earlier results (Wilson and Andrews, 2002; Ramaprabhu and Andrews, 2004a) from the small-Atwood-number water channel.

The water channel experiment of Mueschke et al. (2006) resulted in lower values of Θ than that of Wilson and Andrews (2002) and Ramaprabhu and Andrews (2004a) ($\Theta \approx 0.8$). This deviation was attributed to a difference in the size of their

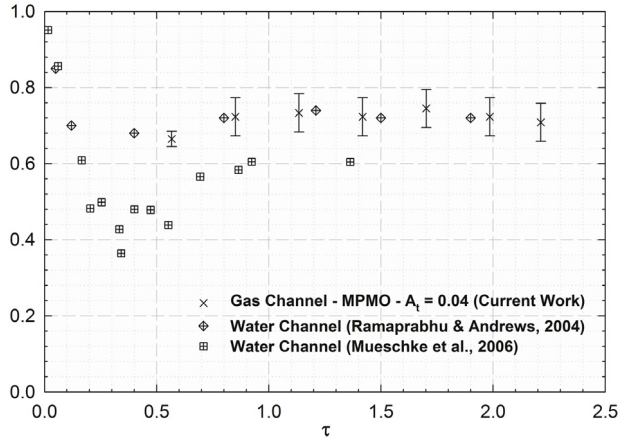


Fig. 9.7a. Comparison of the evolution of the molecular mix parameter Θ measured by Banerjee et al. at the centerline with Ramaprabhu and Andrews (2004a) and Mueschke et al. (2006) as a function of non-dimensional time.

Source: From Fig. 18 of Banerjee et al. (2010b), *J. Fluid Mech.* with permission.

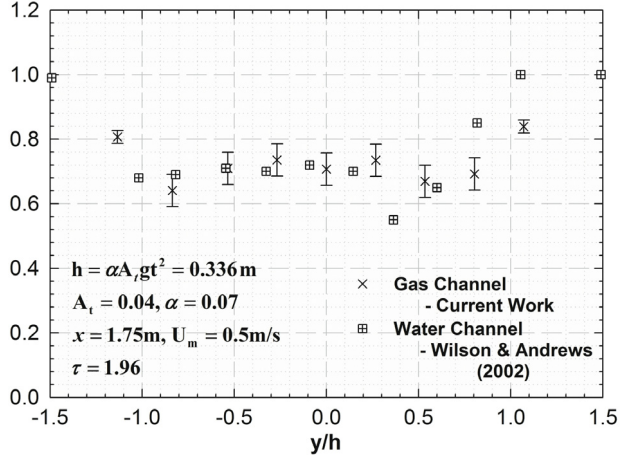


Fig. 9.7b. Comparison of molecular mix parameters across the RT mixing layer at $\tau = 1.986$ ($A = 0.04$, $x = 1.75 \text{ m}$ from the splitter plate) with Wilson and Andrews (2002).

Source: From Fig. 17 of Banerjee et al. (2010b), *J. Fluid Mech.* with permission.

thermocouple probes and to the noise elimination techniques used in their work (Mueschke and Andrews, 2006a). While the molecular mixing parameter Θ is also slightly underestimated by the DNS (Mueschke and Schilling, 2009a) during the nonlinear and weakly turbulent growth phases, the late-time value $\Theta \approx 0.55$ compares favorably with the value ($\Theta \approx 0.6$) measured in the experiment. The Texas A&M University water tunnel facility for RTI experiments is shown in Fig. 9.8.

As recalled in Banerjee et al. (2010b), the brine/water experiments of Dalziel et al. (1999) ($Sc \sim 600$) resulted in a late-time value of $\Theta \sim 0.6\text{--}0.7$. Banerjee and Mutnuri (2012) carried out an experimental study of mixing induced by RTI at $A \sim 7.5 \times 10^{-4}$ and $Sc \sim 10^3$ with a transient experimental facility developed on the working principles of the draw-tank facility at Cambridge (Dalziel et al., 1999). Fig. 9.9 shows images at different times of the RT mixing layer evolution, which was run to observe a higher ($2\times$) Reynolds number regime. At $Sc \sim 10^3$, Mueschke et al. (2009) and Banerjee and Mutnuri (2012) found that the molecular mixing parameters (Θ, \mathcal{E}) were increasing at the end of the experiment and the asymptotic value of Reynolds number could not be reached due to limitations in test-sections dimensions. Experiments at higher Reynolds number coupled with detailed diagnostics that are described above is needed to check to confirm that the same asymptotic value is reached.²

² It appears that the Reynolds number of the flows considered by Mueschke et al. (2009) was not high enough for the “mixing transition” (Dimotakis, 2000) and “minimum state” (Zhou, 2007; Zhou et al., 2003a,b) to be reached. See Part I for relevant discussion. Indeed, Youngs (2017) remarked that for water channel experiments, $Sc \sim 1000$, a significantly higher Reynolds number, probably of order 10^4 is needed to reach the plateau level. This high Sc case is not achieved in the experiments and beyond current DNS capability.



Fig. 9.8. The Texas A&M University water tunnel RT experiment. The experimental configuration was described by Snider and Andrews (1994), Wilson et al. (1999), and Andrews and Dalziel (2010).

Source: Photograph courtesy of Dr. M.J. Andrews and Dr. A. Banerjee.

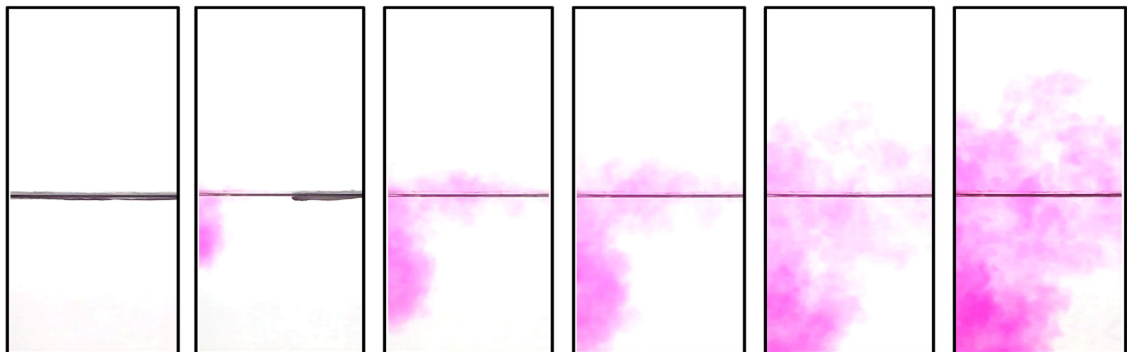


Fig. 9.9. Evolution of mixing layer using a reactive scalar at time $t = 0, 1.5, 3.9, 5.8, 11.18, 14.5$ s arranged sequentially from left to right. Phenolphthalein is added to the bottom stream for reactive scalar experiments, and changes to pink as the two layers molecularly mix. The top layer is saltwater ($\text{pH}_1 = 11.5$) while the bottom layer is freshwater ($\text{pH}_2 = 7.05$).

Source: Fig. 5 of Banerjee and Mutnuri (2012), *Experiments in Fluids*, with permission.

Gréa (2013) reported that the rapid distortion theory (RDT) (Batchelor and Proudman, 1954; Townsend, 1976; Hunt and Carruthers, 1990) procedure resulted in an RTI growth rate expression, α , which can be completely determined by the mixedness, Θ , and a dimensionality parameter introduced by the author. Soulard et al. (2016) presented an alternative algebraic relationship between α and Θ . The authors also derived a formula relating the mixedness to the second order moments of the concentration and velocity fields.

The actual amount of mixed mass could be viewed as a more direct marker of the evolution of the mixing layers due to hydrodynamic instabilities. The importance of the mixed mass is evident from recent measurements (Ma et al., 2013; Smalyuk et al., 2014) using the high-energy-density-physics platform. To frame the characterization based on how much the heavy fluids is mixed into the light fluids, the mixed mass \mathcal{M} measurement can be defined as (Zhou et al., 2016)

$$\mathcal{M} = \int 4\rho Y_1 Y_2 dV \quad (9.6)$$

where Y_1 and Y_2 are the mass fractions and ρ is the mixture density.

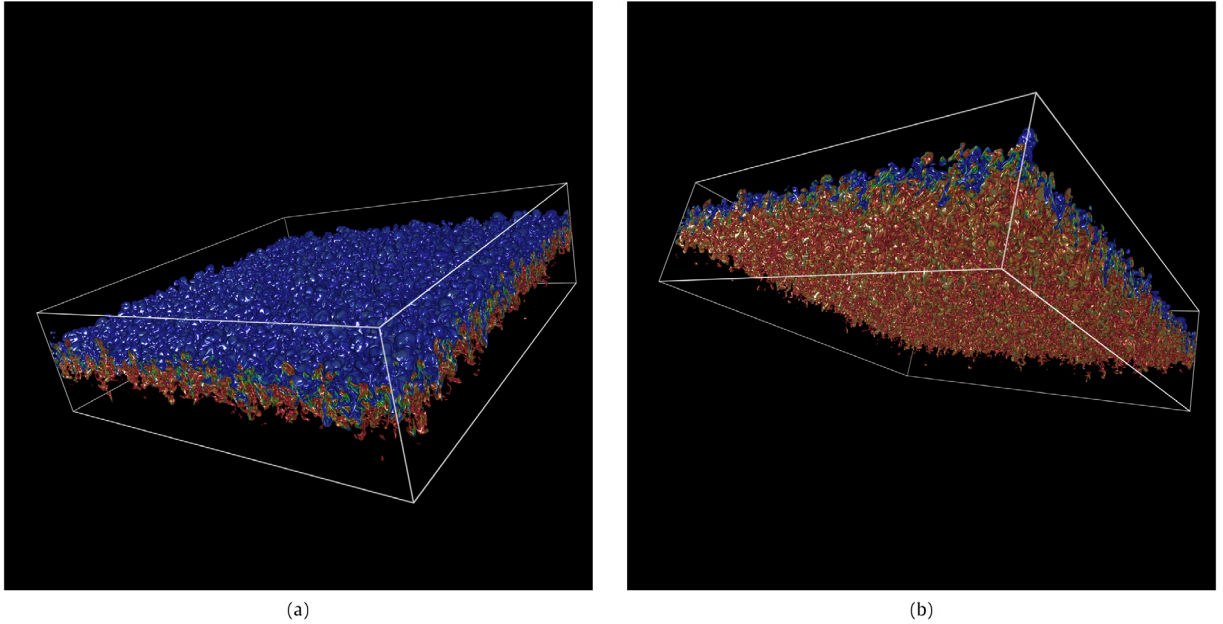


Fig. 9.10. Three-dimensional visualization of the density field at early time, viewed from (a) top and (b) bottom, showing the asymmetry of the Rayleigh–Taylor mixing layer at $A = 0.75$, with the development of bubbles on the heavy fluid side and spikes on the light fluid side. From the $4096^2 \times 4032$ simulation. Source: Adapted from Fig. 2 of [Livescu \(2013\)](#), *Phil. Trans. Roy. Soc. A*, with permission.

An especially attractive feature of the mixed mass \mathcal{M} is that it is a conserved quantity. The transport equation for the mass fraction of species m , Y_m , is given by

$$\frac{\partial \rho Y_m}{\partial t} + \frac{\partial \rho u_j Y_m}{\partial x_j} = \frac{\partial}{\partial x_j} \left(\rho D \frac{\partial Y_m}{\partial x_j} \right) (m = 1, 2), \quad (9.7)$$

where D is the Fickian diffusivity, hence

$$\frac{d}{dt} \int \rho Y_1 Y_2 dV = 2 \int \rho D \frac{\partial Y_1}{\partial x_j} \frac{\partial Y_2}{\partial x_j} dV \quad (9.8)$$

for a volume V that encloses the mixing region. Therefore the mixed mass defined in this way can only increase through diffusive processes, either physical or numerical.

The main thesis of [Zhou et al. \(2016\)](#) is that the amount of mixed mass can be viewed as a more direct marker than the mixed width of the mixing zone. The normalized mixed mass is given by

$$\Psi \equiv \frac{\int \rho Y_1 Y_2 dV}{\int \langle \rho \rangle \langle Y_1 \rangle \langle Y_2 \rangle dV}. \quad (9.9)$$

The transition from the mixed width based mixedness parameters to the normalized mixed mass is nontrivial, as the nonlinearity has risen from quadratic to cubic. With the density incorporated, Eq. (9.9) now describes the time evolution of how effectively the mass of the materials has been mixed within the mixing layer. The application of Eq. (9.9) can be found in the next subsection to depict the influence of the Atwood number for RTI as well as in Sections 10 and 11 for single and reshocked RM ([Richtmyer, 1960](#); [Meshkov, 1969](#)) instability induced flows.

9.3. Atwood number effects

The role of the Atwood number is an important issue regarding the stabilization of ablative Rayleigh–Taylor instability (ARTI) in laser-driven targets (see for instance, [Glendinning et al., 1997](#); [Ye et al., 2002](#)). This effect is also relevant to several industrial applications such as the liquid atomization, where the spike behaviors of RT instability are of great interest ([Li and Umemura, 2014](#)).

Fig. 9.10 is a visualization of the spike/bubble asymmetry when the density disparity is sufficiently large. Adopted from [Livescu \(2013\)](#), it is a density profile image of the fluids generated using the dataset from a very high resolution ($4096^2 \times 4032$) direct numerical simulation where the Atwood number is 0.75.

Fig. 9.11 shows the temporal evolution of the RTI mixed mass (Eq. (9.6)) for these three Atwood numbers (solid lines) as well as the corresponding results for the mixed width (dashed lines) multiplied by arbitrary constants ([Zhou et al., 2016](#)).

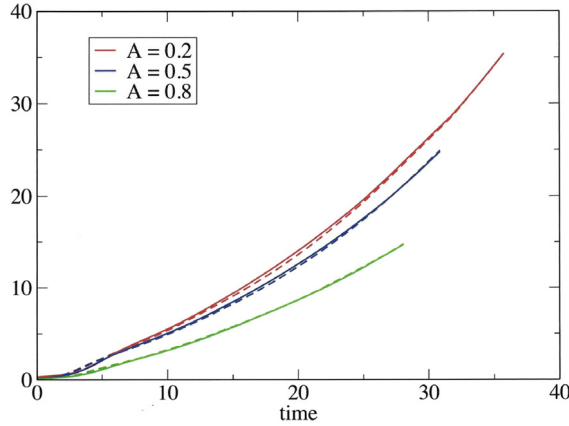


Fig. 9.11. Temporal evolution of the RTI mixed mass for these three Atwood numbers (solid lines). Also, the corresponding results for the mixed width (dashed lines), but multiplied by arbitrary constants.

Source: Fig. 1 of Zhou et al. (2016), *Phys. Plasma*.

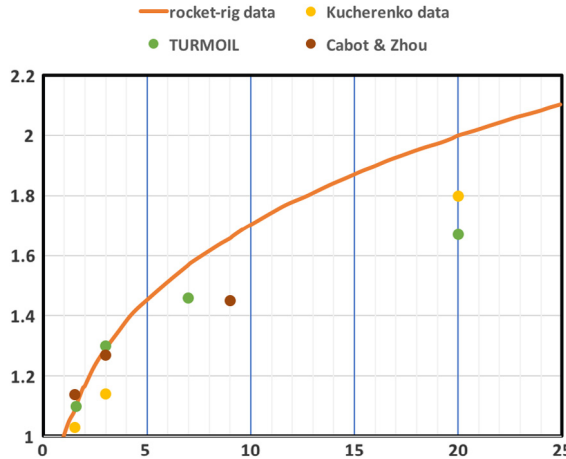


Fig. 9.12. Plot of spike/bubble mix width ratio, h_s (1%) / h_b (2%), versus ρ_1/ρ_2 . Fig. 5 of Youngs (2013), *Phil. Trans. Roy. Soc. A* with permission; additional data from DNS discussed in Cabot and Zhou (2013) added.³

Clearly, the mixed mass measurements closely track the scaling of the mixed width for all Atwood numbers cases. The $A = 0.5$ ($\rho_2/\rho_1 = 3$) simulation used 3072^3 grid points (Cabot and Cook, 2006), while the $A = 0.2$ ($\rho_2/\rho_1 = 3/2$) case used 2048^3 grid points and the $A = 0.8$ ($\rho_2/\rho_1 = 9$) simulation used $2048^2 \times 2304$ grid points (Cabot and Zhou, 2013).

For the Rocket-Rig experiments, results are given for the spike/bubble mix width ratio (h_s/h_b) and the computer simulation results have generally quoted h_s/h_b . The results of Rocket-rig resulted in a reasonable fit of $h_s/h_b = (\rho_1/\rho_2)^{0.231}$ (Youngs, 1989, 2013). For a wide range of density ratios, Youngs (2013) compared the ILES results of h_s/h_b with available experimental data from the rocket-rig (Youngs, 1989) and Kucherenko et al. (1991). Youngs (2013) stressed that this ratio is difficult to estimate both experimentally and computationally. The results of Kucherenko et al. (1991) were based on X-ray measurements of the mean volume fraction profile, while the curve for the rocket-rig experiments was based on visual estimates of the spike and bubble positions. Using the same criteria for the DNS dataset of Cabot and Zhou (2013) and Zhou et al. (2016), the values of h_s/h_b are 1.14, 1.27, and 1.45 for the heavy-to-light fluid density ratios of 1.5, 3, and 9, respectively (Fig. 9.12). It is apparent that the value of this measurement, h_s/h_b , increases along with increased density disparity.

Burton (2011) computed the bubble and spike heights, h_b and h_s , at very high Atwood numbers $0.75 \leq A \leq 0.96$, using his nonlinear large-eddy simulation (nLES) method (Burton, 2008) in part to assess the degree to which the simulations reached late time self similarity. Fig. 9.13 shows the variation of h_s/h_b with density ratio and reaches an approximate plateau value, $h_s/h_b = 1.71$, at $A = 0.9$, consistent with Fig. 9.12. Burton stated that all h_s/h_b values begin to fall off gradually at the end of the plateau in part reflecting the early appearance of boundary effects on mixing layer growth. Livescu et al. (2011) and

³ Simulations performed using the Miranda code (Cook and Cabot, 2004).

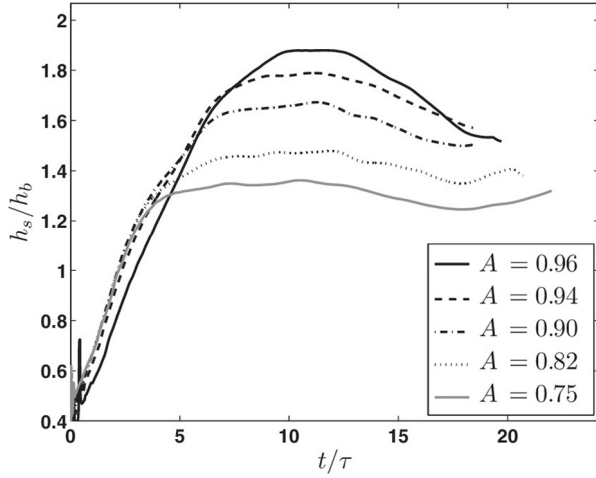


Fig. 9.13. Evolution of the ratio of integrated spike to bubble heights for various Atwood numbers at $A \geq 0.75$.
Source: Fig. 17 of Burton (2011), *Phys. Fluids*, with permission.

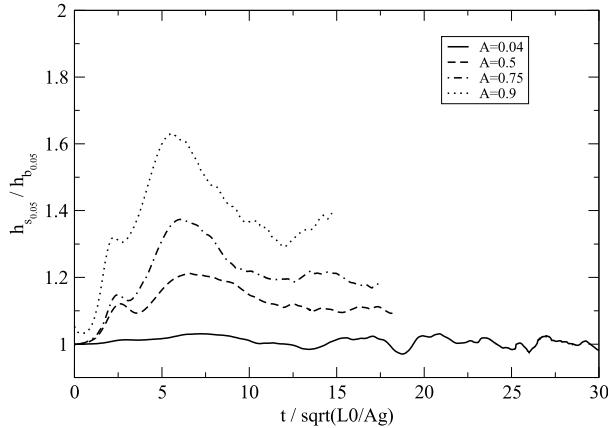


Fig. 9.14. Time evolution of the ratio of integrated spike to bubble heights for various Atwood numbers. L_0 is based on the initial perturbation spectrum and is $2\pi/30$ for all cases. Δg is constant for all cases and is 7.6172.
Source: Figure courtesy Dr. D. Livescu, Los Alamos National Laboratory.

Livescu and Wei (2012) performed a suite of DNS simulations with Atwood number ranging from 0.04 to 0.9 (grid size of $1024^2 \times 4032$) [higher resolution for the $A = 0.75$ case with a grid size of $4096^2 \times 4032$]. Fig. 9.14 illustrates the results for the spike/bubble mix width ratio versus various density ratio. Fig. 9.14 also demonstrates the influence of the boundary effects for the high Atwood number runs at late-times, suggesting that significantly larger simulations are needed. Nevertheless, evidence once again strongly indicates that as the density ratio gets larger, the h_s/h_b spike/bubble asymmetry increases.

If the RTI flows have achieved a self-similar state, the spike/bubble width is given by

$$h_i = \alpha_i \Delta g (t + t_{i,0})^2,$$

where $i = b, s$ denotes the bubble and the spike (Section 6, Part I, Zhou, 2017), and the time origins are denoted as $t_{i,0}$ (Clark and Zhou, 2003; Cabot and Cook, 2006). The spike/bubble width ratio (h_s/h_b) and its corresponding growth rate asymmetry (α_s/α_b) become interchangeable if and when a second requirement, $t \gg t_{i,0}$ is also satisfied.

Two experimental papers have reported the spike/bubble growth rate ratio α_s/α_b , and in both cases, higher α_s/α_b ratio than h_s/h_b ratio have been obtained. Dimonte and Schneider (2000) found greater asymmetry based on measuring α separately for bubbles and spikes, $\alpha_s/\alpha_b = (\rho_1/\rho_2)^{0.33 \pm 0.05}$. Youngs (2013) noted that the results of Dimonte and Schneider (2000), at high Atwood number, does appear to disagree with his ILES simulations. Including the uncertainties due to choosing the correct normalization factor for the volume fraction calculations, Akula and Ranjan (2016) performed an experiment at a moderately high Atwood number ($A = 0.73 \pm 0.02$) and determined that $\alpha_s/\alpha_b = 1.95$ or 1.93, depending on whether the virtual origin method (Snider and Andrews, 1994; Bell and Mehta, 1990) or the Ristorcelli and Clark (2004)

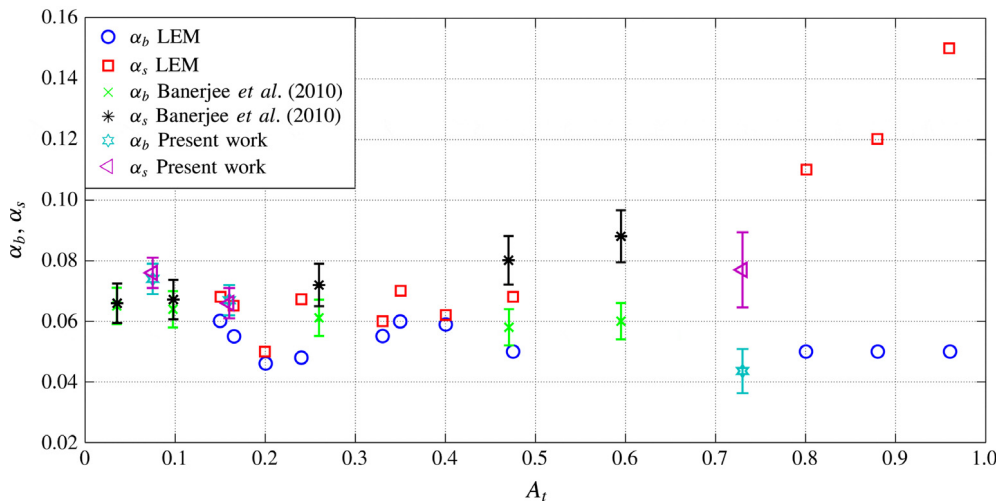


Fig. 9.15. Comparisons of α_b and α_s obtained by Akula and Ranjan (marked as present work), Banerjee et al. (2010b), and the LEM data of Dimonte and Schneider (1996).

Source: Fig. 5 of Akula and Ranjan (2016), *J. Fluid Mech.* with permission.

method is used.⁴ Akula and Ranjan reported their measured asymmetry, $h_s/h_b \approx 1.6 \pm 0.07$, which is different from the α_s/α_b mentioned above.

Hence, care must be taken when quoting the RTI experimental results. For the Rocket-rig experiment, results are given for h_s/h_b , not α_s/α_b as suggested in the caption of Fig. 2 in Zhang et al. (2016). Also, the linear electric motor (LEM) results are quoted in α_s/α_b , not h_s/h_b , as indicated in Eq. (31) of Burton (2011).

Fig. 9.15 provides the comparisons of α_b and α_s obtained by the LEM data of Dimonte and Schneider (1996) and the gas channel facilities of Banerjee et al. (2010b) and Akula and Ranjan (2016). For the spikes, the growth rate parameter $\alpha_s \sim \alpha_b$ out to $A \sim 0.5$ and then it increases dramatically. The values of the bubble growth rate α_b , on the other hand, are relatively insensitive to A . Youngs (2013) also found that his implicit large-eddy simulation (ILES) indicated that α_b should vary little with density ratio (Fig. 9.16). His ILES results were obtained from very high resolution simulations, typically using $2000 \times 1000 \times 1000$ size meshes, and he determined that the results used are mesh-converged to the point that the effect of the unresolved scales is negligible. The volume fraction contours from the ILES of Kokkinakis et al. (2015) are shown in Fig. 9.17a and b for density ratios 3:1 and 20:1 respectively.

Figs. 9.18a, 9.18b and 9.18c illustrate that \mathcal{E} , Θ , and Ψ follow similar evolutions for all Atwood numbers under consideration (Zhou et al., 2016). Despite of fairly significant span of the Atwood numbers, the mixed width based mixedness parameters, \mathcal{E} and Θ , are essentially the same with their late-time values around 0.80 and 0.78, respectively. Furthermore, Shimony et al. (2017) reported 3D RTI simulations at Atwood numbers between 0.2 and 0.9 that produced compact values of Θ at 0.80–0.77. Yet, the normalized mixed mass, Ψ , is shown to be effective in providing information on how efficiently the mixed mass is generated for a given mixed width. While the values of \mathcal{E} , Θ and Ψ are essentially undistinguishable at around 0.78 for the $A = 0.2$ case, values of Ψ curves are progressively lower, at 0.76 for $A = 0.5$ and 0.69 for $A = 0.8$ cases. It is evident; therefore, that the relative mixing measured by the mixed mass becomes less efficient as the Atwood number increases.

Burton (2011) collected the similar time evolution of the mixedness factor Θ at the five Atwood numbers. The $A = 0.75$ case reaches an approximate plateau first of $\Theta = 0.8$, a value somewhat lower than observed for the $A = 0.5$ case. He also noted that for the higher Atwood-number runs, there is a slower rise to the peak value, suggesting that these flows take longer times to achieve a self-similar state where the mixing and entrainment processes come into approximate equilibrium. Successively larger Atwood numbers also produce successively lower values of these peaks, indicating that entrainment of pure fluid becomes more significant as the Atwood number increases (Burton, 2011).

⁴ Akula and Ranjan (2016) remarked that for an Atwood number of 0.73, the Dimonte and Schneider (2000) correlation predicts a value 1.84 ± 0.16 . Recently, Shimony et al. (2017) presented the values of α_s/α_b as a function of the Atwood number from their 2D and 3D simulations and a logarithmic fit to the linear electric motor experimental results (Dimonte, 1999; Dimonte and Schneider, 2000). The authors utilized the LEEOR code, a multi-material finite volume arbitrary Lagrangian Eulerian (ALE) code with interface tracking capability, in its two versions: LEEOR2D (Freed et al., 1991) and LEEOR3D (Hecht et al., 1995) for the 2D and the 3D simulations, respectively.

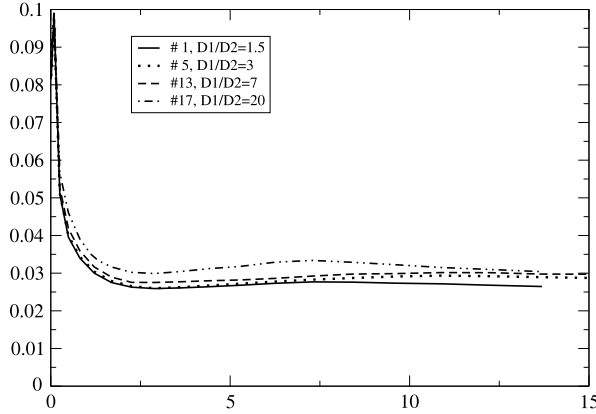
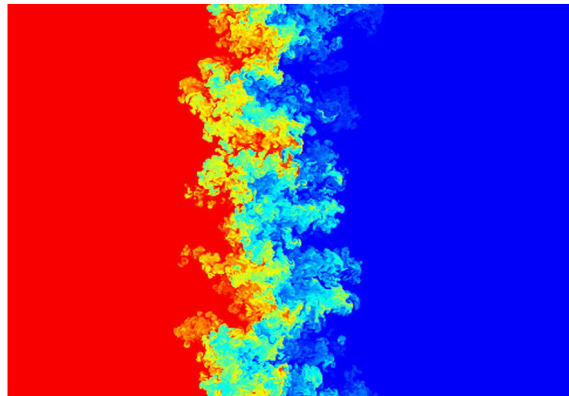
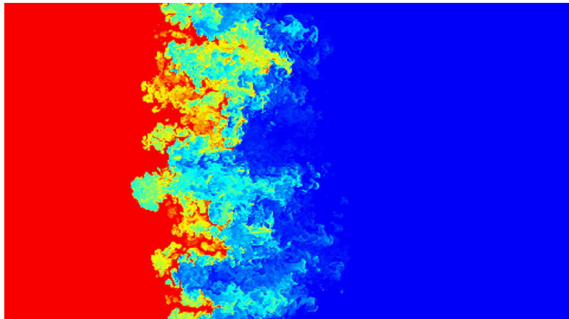


Fig. 9.16. Variation of α_b versus $X = Agt^2$ at the four density ratios considered.
Source: Adapted from Fig. 2b of [Youngs \(2013\)](#), *Phil. Trans. Roy. Soc. A* with permission.



(a)



(b)

Fig. 9.17. ILES contours of volume fraction for density ratio (a) 3:1 and (b) 20:1.
Source: Figs. 4 and 5 of [Kokkinakis et al. \(2015\)](#), *International Journal of Heat and Fluid Flow*.

9.4. Anisotropy

In all realistic flows, a description of turbulence cannot be purely isotropic and must contain some anisotropic elements. For instance, [Schneider and Gauthier \(2016a, b\)](#) displayed the visualizations of the vorticity norm from a RTI flow for two vorticity norm values. The vorticity norm $|\omega| = (\omega_i \omega_i)^{1/2}$ is equal to a certain threshold ([da Silva et al., 2011](#)). For the low value, $|\omega| = 3$, the large structures, with the torus shape corresponding to mushroom-like structures, appear clearly on

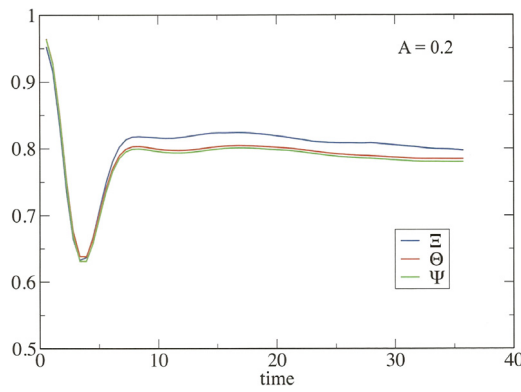


Fig. 9.18a. Temporal evolution of the mixedness parameters and normalized RTI mixed mass for Atwood numbers 0.2.
Source: Fig. 2a of Zhou et al. (2016), *Phys. Plasma*.

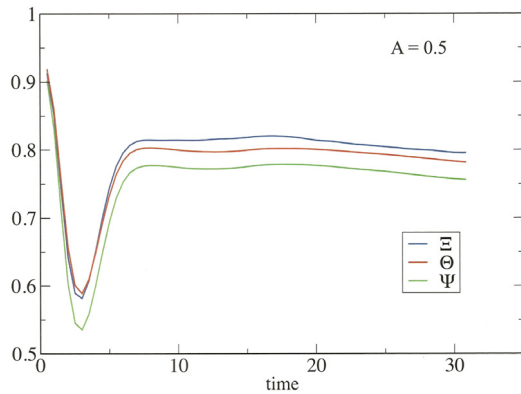


Fig. 9.18b. Temporal evolution of the mixedness parameters and normalized RTI mixed mass for Atwood numbers 0.5.
Source: Fig. 2b of Zhou et al. (2016), *Phys. Plasma*.

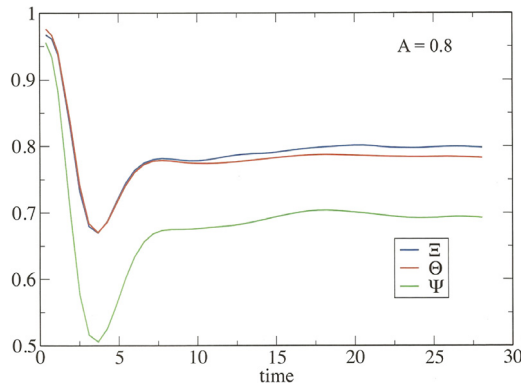


Fig. 9.18c. Temporal evolution of the mixedness parameters and normalized RTI mixed mass for Atwood number 0.8.
Source: Fig. 2c of Zhou et al. (2016) *Phys. Plasma*.

the boundaries (Fig. 9.19a). On the other hand, for the larger value of the vorticity norm, $|\omega| = 20$, the RT patterns on the boundaries disappear, and isosurfaces become lighter and tend to be oblong or take the form of short filaments attached to the mixture dominated either by the heavy (red) or by the light fluid (blue). At this level, turbulence is expected to be more isotropic and more universal (Fig. 9.19b). But the problem is that once we take anisotropy into account, we face a drastic increase in the complexity of the theory (Biferale and Procaccia, 2005).

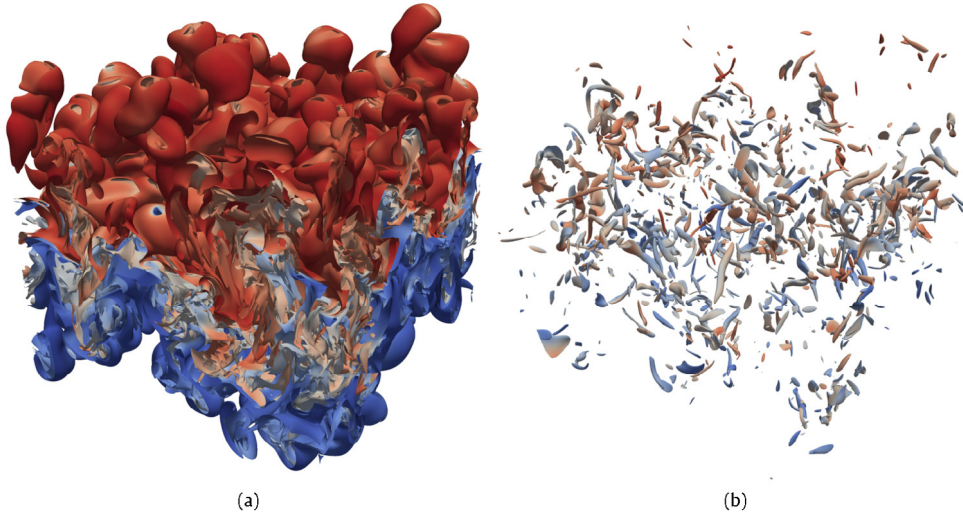


Fig. 9.19. Vorticity isosurface, top view. (a) Left: $|\omega| = 3$. (b) Right: $|\omega| = 20$, colored by the concentration. Final time of the RTI Boussinesq (1877) simulation.

Source: Fig. 7 of Schneider and Gauthier (2016b), *Fluid Dynamics Research*, with permission.

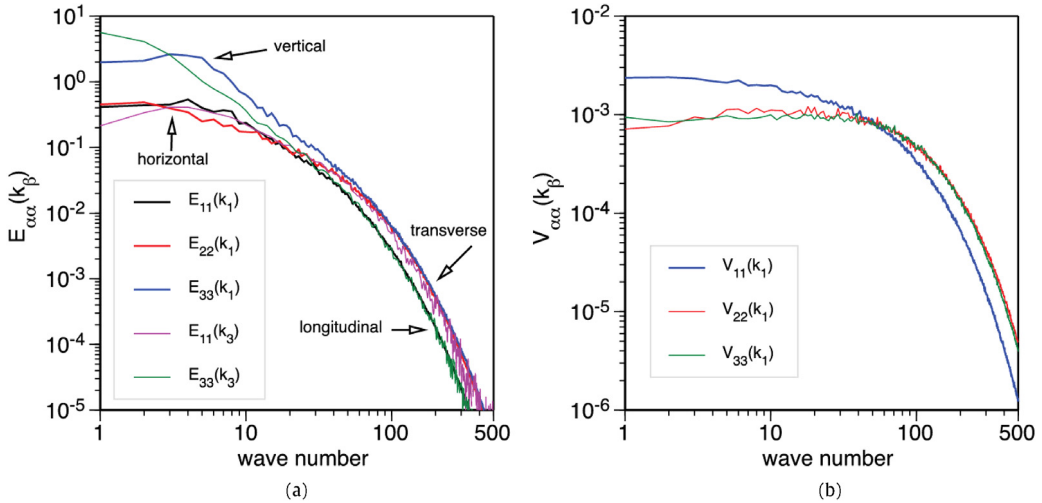


Fig. 9.20. One-dimensional spectra of (a) velocity and (b) vorticity in the $A = 0.5$ case. Vertical spectra (in k_3) for velocity components were constructed using Fourier transforms of vertical autocorrelation functions. Statistically equivalent terms have been averaged together.

Source: Fig. 7 of Cabot and Zhou (2013), *Phys. Fluids*.

Here we examine the degree to which turbulence becomes anisotropic under the effects of RT acceleration. Both physical- and spectral-space quantities containing length scale information are considered. To investigate anisotropy properties at different scale sizes, Fig. 9.20a, b shows the radial spectra $E_{\alpha\alpha}(k)$ and $V_{\alpha\alpha}(k)$ of the component energy and vorticity variances, respectively, in the $A = 0.5$ case. Although the vertical pseudo-spectra are noisy at high wave numbers, the results suggest that both longitudinal and transverse spectra for all velocity components collapse isotropically at small scales. This result is consistent with the classical phenomenology of Kolmogorov (1941), which predicts a recovery of isotropy at sufficiently small scales of the turbulent flows (see also Frisch, 1995).

In contrast, at the large spatial scales (low wave number modes) the anisotropy remains quite pronounced (see also, Zingale et al., 2005). Differences in the 1D horizontal vorticity spectra can be ascribed to different mixtures of longitudinal and transverse velocity derivative components. The $V_{22}(k_1)$ and $V_{11}(k_1)$ spectra are nearly equal while the $V_{33}(k_1)$ spectrum differs with more power at low wave numbers. It is clear that the anisotropy characteristics of $E_{\alpha\alpha}(k)$ and $V_{\alpha\alpha}(k)$ differ significantly.

In general, the large turbulent scales are highly anisotropic due to buoyancy forces in the direction of gravity, but the flow becomes much more isotropic at small scales in the core of the mixing layer (Table 9.1). As a result, the velocity displays a

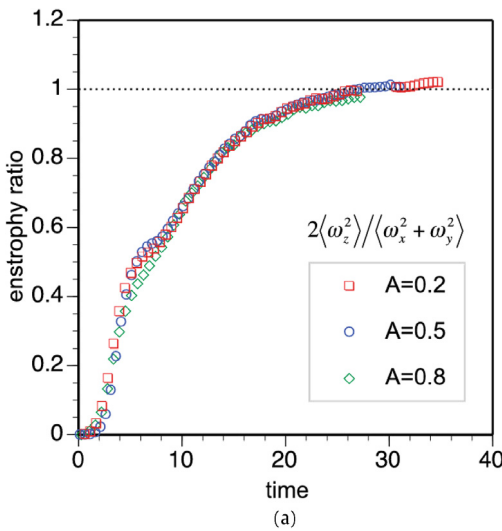


Fig. 9.20c. Isotropy of the vorticity field is shown as a function of time, measured by the ratio of vertical to horizontal enstrophy components averaged over a vertical extent of $h/3$ in the middle of the mixing layer. (The gap in the $A = 0.2$ data resulted from data lost in a catastrophic file system failure.)
Source: Fig. 2(a) of Cabot and Zhou (2013), *Phys. Fluids*.

Table 9.1

Turbulence statistics for the $A = 0.5$ case at $t = 25$ for different spatial averaging domains.

Source: Table II of Cabot and Zhou (2013), *Phys. Fluids*.

Average	$\langle u_1^2 \rangle$	$\langle u_2^2 \rangle$	$\langle u_{1,1}^2 \rangle$	$\langle u_{3,3}^2 \rangle$	$\langle \varepsilon_1 \rangle$	$\langle \varepsilon_3 \rangle$	η	$\lambda_{1,1}$	$\lambda_{3,3}$	$Re_{\lambda,1}$	$Re_{\lambda,3}$
Midplane	0.875	3.051	3.007	3.030	0.110	0.136	0.0340	0.539	1.003	65	224
Mid-slab	0.873	3.037	2.966	2.985	0.109	0.134	0.0341	0.543	1.009	65	225
Global								0.572	1.041		

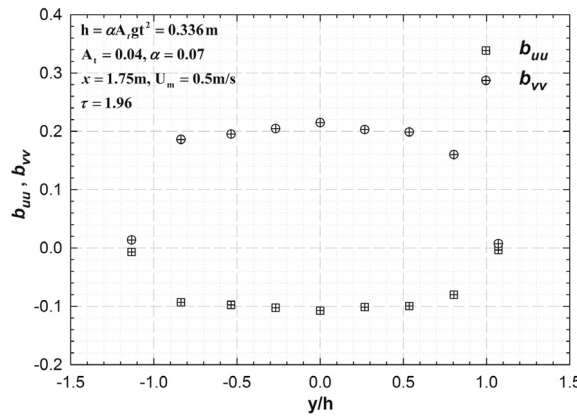


Fig. 9.21. Profiles of the anisotropic tensor (b_{uu} & b_{vv}) across the RT mixing layer at $x = 1.75$ m ($\tau = 1.986$) for an experiment at $A = 0.04$.
Source: Fig. 27 of Banerjee et al. (2010b), *J. Fluid Mech.* with permission.

high degree of anisotropy while its derivatives behave much more isotropically. In particular, the values of the Reynolds number based on the Taylor microscale are significantly anisotropic in the horizontal and vertical directions, which are approximately 60 and 220, respectively.

At late time, Cabot and Zhou showed that the small-scale motions in the flow are approaching isotropy as measured by the ratio of vertical to horizontal enstrophy (vorticity squared) components in the middle of the mixing layer, shown in Fig. 9.20c. The $A = 0.8$ case lags slightly behind the lower Atwood number cases at late times, indicating that small-scale anisotropy may be more persistent for very high density ratios. This should be obvious because gravity, the source of anisotropy, enters always as a product with the Atwood number (Mikaelian, 2014).

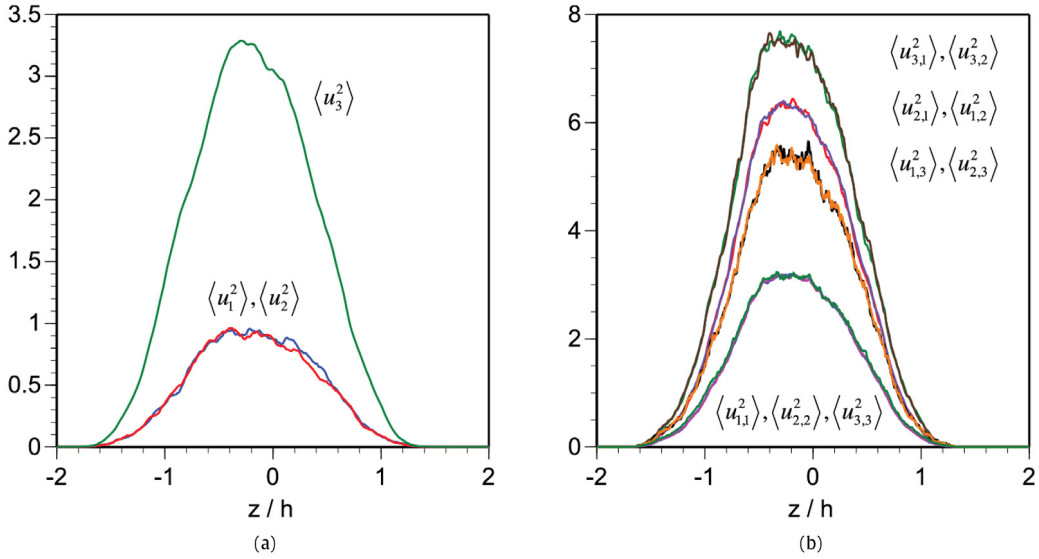


Fig. 9.22. Vertical profiles (horizontal averages) of fluctuation intensity for (a) velocity components and (b) velocity derivative components are shown at time $t = 25$ in the $A = 0.5$ case, demonstrating statistical equivalences and the degree of anisotropy.

Source: Fig. 3 of Cabot and Zhou (2013), *Physics of Fluids*.

The deviatoric part of the Reynolds stress tensor normalized by the kinetic energy term, a measure of the large-scale anisotropy,

$$b_{ij} = \langle u_i u_j \rangle / \langle u_n u_n \rangle - (1/3) \delta_{ij} \quad (9.10)$$

is very important, especially in terms of its second and third principal invariants (Lumley and Newman, 1977). Here, the Einstein summation convention is used. The tensor b_{ij} is bounded, i.e., $-1/3 \leq b_{ij} \leq 2/3$. The values of $b_{ii} = 0$ for all i corresponds to the isotropic turbulence limit, whereas the values of $b_{ii} = +2/3$ and $b_{ii} = -1/3$ correspond to having either all of the turbulent kinetic energy (one-dimensional flow) or no energy at all, respectively (Lumley, 1979; Pope, 2000).

Banerjee et al. (2010b) measured the anisotropy tensor across the RT mixing layer at a downstream location from the splitter plate at a late time. As shown in Fig. 9.21, most of the turbulent transport appears in the vertical direction. The velocity fluctuation statistics are fairly constant across the RT mixing layer, and this is consistent with the finding of Ramaprabhu and Andrews (2004a). Near the edges of the RT mixing layer, it appears that $b_{ii} \rightarrow 0$, suggesting isotropy. The profiles of these components and peak values are similar to the recent experimental paper on the gas channel (Akula and Ranjan, 2016) and small Atwood number numerical simulations (Livescu et al., 2009; Mueschke and Schilling, 2009a,b). Using direct numerical simulations, Cabot and Zhou (2013) also showed that the velocity components display a high degree of anisotropy (Fig. 9.22). Other papers have shown similar results for $\langle u_j^2 \rangle$ e.g. ILES results at various A are given in Youngs (2013).

Using two large DNS datasets, Livescu et al. (2009, 2010) found that b_{33} appears to become almost constant across the layer, with an asymptotic value around 0.3, corresponding to almost 65% energy in the vertical component, along the direction of the acceleration (Fig. 9.23a). Value of $b_{33} \approx 0.3$ is in good agreement with a DNS study of Ristorcelli and Clark (2004), where the late-time data was taken at the centerline of the single-fluid Boussinesq (1877) RTI mixing layer ($Sc = 1, Re \leq 3000, A = 0.01$).

Livescu et al. (2009) considered the scale dependence of the normal stresses anisotropy and found the normal stresses remain anisotropic at both the largest and smallest scales. At the smallest scales, $b_{33}(k) \approx 0.15$, corresponding to $\approx 50\%$ energy in the vertical component (Fig. 9.23b). The buoyancy production appears to remain important at small scales due to the cancellation between nonlinear transfer and viscous dissipation.

Burlot et al. (2015) reported the asymptotic result of $b_{33} \approx 0.35$ from their DNS and the eddy-damped-quasi-normal Markovian (EDQNM) approximation (Orszag, 1970, 1977; Lesieur, 1990). The linear approximation of the RDT breaks down at $t^* = 2$ (Fig. 9.24), but develops from the initial zero value to the asymptotic $2/3$ value computed analytically. Furthermore, Gréa et al. (2016a) investigated the sensitivity of the anisotropy measurement of a parameter of the initial energy and buoyancy spectra, which characterizes different distribution of energy at large scales. The level of anisotropy changes only very slightly.

Finally, Vladimirova and Chertkov (2009), Boffetta et al. (2009), and Schneider and Gauthier (2016a) considered the anisotropy in Rayleigh–Taylor Boussinesq turbulence. For the large-scales, the anisotropy defined as the ratio between the two rms velocity components is approximately 1.8.

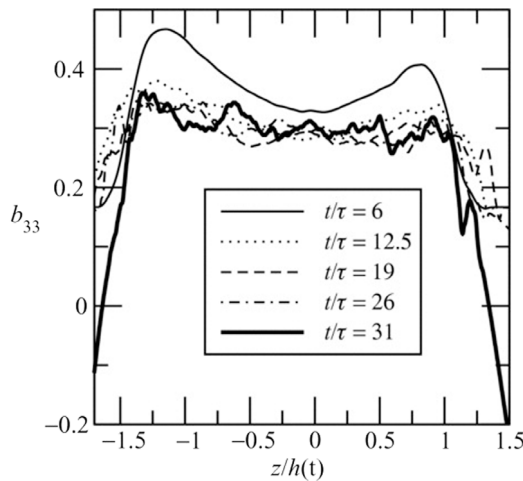


Fig. 9.23a. Vertical variation of b_{33} at different time.
Source: Fig. 13 of Livescu et al. (2009), *Journal of Turbulence* with permission.

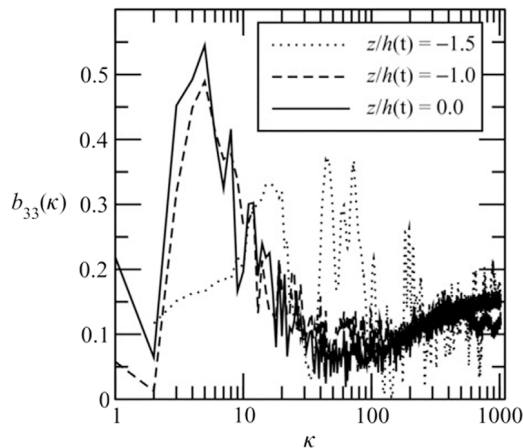


Fig. 9.23b. Wave number dependence of b_{33} (k) at different z locations.
Source: Fig. 14 of Livescu et al. (2009), *Journal of Turbulence* with permission.

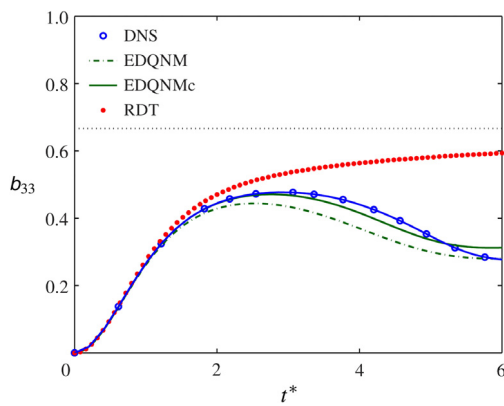


Fig. 9.24. Evolution of b_{33} computed using linear RDT, EDQNM closure, and DNS.
Source: Fig. 9 of Burlot et al. (2015), *J. Fluid Mech.* with permission.

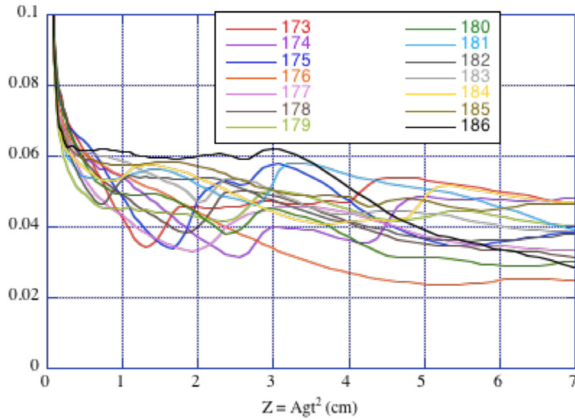


Fig. 9.25. Evolution of spatially-averaged bubble-growth parameter α_b for 14 of the 104 statistically independent realizations. Source: Fig. 4 of Clark (2003), *Phys. Fluids*, with the permission of AIP Publishing; additional realizations courtesy of Dr. T.T. Clark, Los Alamos National Laboratory (now with University of New Mexico).

9.5. 2D vs 3D RTI induced flows

Due to the time consuming nature of fully 3D simulations of the RT instability, it is desirable to run computations in 2D where possible, and several previous studies have done so (for discussions within astrophysical fluid dynamics, see for example, Couch and Ott, 2015; Müller, 2015). However, 2D turbulence is surprisingly complex, even without considering the acceleration in RTI or the shock wave in RMI, as there is no vortex stretching, the kinetic energy is inverse cascaded producing a $k^{-5/3}$ spectrum, the enstrophy is forward cascaded producing a k^{-3} spectrum (Batchelor, 1969; Kraichnan, 1967; Leith, 1968) and the small-scale motion is slow. Indeed, it requires a large $32\,768^2$ resolution to see the dual cascade (Boffetta, 2007). Yet, it is not entirely clear how to transfer the knowledge gained from a series of 2D simulations through to the 3D case.

For two-dimensional RTI flows, Zhou (2013) showed that the buoyancy force balances the inertial force at all scales below the integral length scale and thus validates the basic force-balance assumption of the Bolgiano–Obukhov scenario (Bolgiano, 1959) in 2D RT turbulence. The kinetic energy is injected by the buoyancy forces at an intermediate forcing length-scale, and the resulting kinetic energy would undergo an inverse cascade to the larger scales. The mean thermal energy as well as the mean enstrophy from the temperature/density fluctuations would forward cascade from the large to small scales. In 2D or quasi-2D simulations of an RT instability, where the homogeneous direction is substantially smaller than the extent in the direction of acceleration, a Bolgiano-type scaling has been found (see for example, Celani et al., 2006; Boffetta et al., 2012; Zhou, 2013).

The assumption that the two-dimensional problem is simpler and easier to run than the 3D case at first appears quite attractive. Variability within individual simulations is high, unfortunately; hence for these 2D simulations multiple individual realizations were employed to improve statistical convergence. For the purpose of simulating an ensemble of statistically independent mixing layers, Clark (2003) used a lattice Boltzmann method (Chen and Doolen, 1998; He et al., 1999a,b; Wei et al., 2017). This study indicated that as many as one hundred and four independent realizations are needed at 1000^2 grid resolution. In spite of a restrictive class of initial perturbations, Clark (2003) observed large variations in the value of the dimensionless growth parameter α_b among the realizations and in time within individual realizations (Fig. 9.25). Fig. 9.26a, b (adopted from Clark's Figs. 3 & 5) offered a nice comparison of α_b vs. α_s .

With ILES numerical scheme, Youngs (1991) carried out three- and two-dimensional simulations of the mixing of miscible fluids by RTI. He reported that at early time, the width of the mixing zone grows about 50% more rapidly in 3D than in 2D, consistent with the conclusions from a single-mode calculation (Tryggvason and Unverdi, 1990; Youngs, 1992). At a late stage when fully developed turbulence is approached, however, the 3D growth rate slows down and gives a value of α_b similar to that for the 2-D calculations reported here. Kuchugov et al. (2014) also studied the results of the numerical simulations of RTI in both 2D and 3D geometries. In particular, the authors attempted to differentiate the evolutions of integral characteristics between random density perturbations from that of an isolated single-mode perturbation of the interface. Consistent with that of Youngs (1991), Kuchugov et al. (2014) concluded that for the multi-mode perturbations, 3D perturbations grow somewhat faster in the first stage, however, in the second stage, the growth rate of the width of the mixing zone is nearly the same for both versions.

Young et al. (2001) performed direct numerical simulations in both two and three dimensions, where the spectral resolutions are 256 by 512 and $256^2 \times 512$, respectively. The working fluid is assumed incompressible under the Boussinesq approximation and the interface is perturbed with a spatially randomized disturbance. They focused on the comparison between two-dimensional and three-dimensional energetics and plotted the ratio of kinetic energy to potential energy

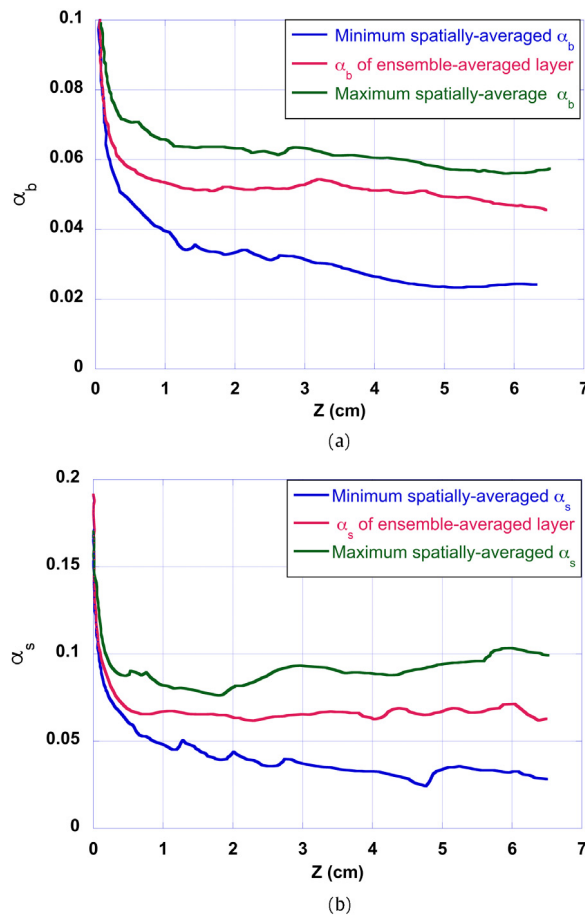


Fig. 9.26. Evolution of (a) bubble- and (b) spike-growth parameters showing extrema within the ensemble of simulations as well as the value for the ensemble-averaged layer.

Source: Figs. 3 & 5, [Clark \(2003\)](#), *Phys. Fluids*, with the permission of AIP Publishing.

available to the flow as a function of time. For early time, the growth is exponential and is similar for both two and three dimensions, after this period, two-dimensional motions are much more efficient in extracting potential energy than three-dimensional motions. The authors reported that the two-dimensional mixing zone grows more slowly than its three-dimensional counterpart.

[Cabot \(2006\)](#) revisited this issue, using datasets from very large 2D and 3D large-eddy simulations of planar, miscible RTI flow with broadband initial perturbations on uniform Cartesian 1152^2 and 1152^3 grids. While the extent of the mixing regions is roughly comparable at $t = 25$, the difference in structure between 2D and 3D RTI flow is clearly seen (Fig. 9.27). At this stage, the 2D flow exhibits large chaotic columns and whirls largely composed of pure fluid, and appears more stirred than mixed. The 3D mixing region is fully turbulent and exhibits fine-scale structure and large patches of mixed fluid, which appear light gray in the image. Two different types of initial 2D perturbations were chosen corresponding to those used in previous numerical studies: (i) In case “2Db”, initial perturbations are computed from a one-dimensional horizontal spectrum with a Gaussian bump at high frequencies. These perturbations have the same spectral shape and amplitude used in the two-dimensional perturbations for the 3D simulation, but with a different set of random phases. (ii) In case “2Ds”, initial planes of density are extracted from slices of the initial density field for the 3D simulation. He shows the temporal evolution of the ratio between the kinetic and potential energies. After the early time period, two-dimensional motions are much more efficient in extracting potential energy than three-dimensional motions. Indeed, [Cabot \(2006\)](#) found 2D mixing layer growth rates are higher than their 3D counterparts (Fig. 9.28). This finding could be interpreted from the perspective of the energy transfer process. Here, after a transient period, an inverse energy cascade is established and the energy is accumulated at the large-scales. This 2D phenomenon differs fundamentally from that in 3D turbulence where the energy is directly transferred to the small-scales, where dissipative actions take place.

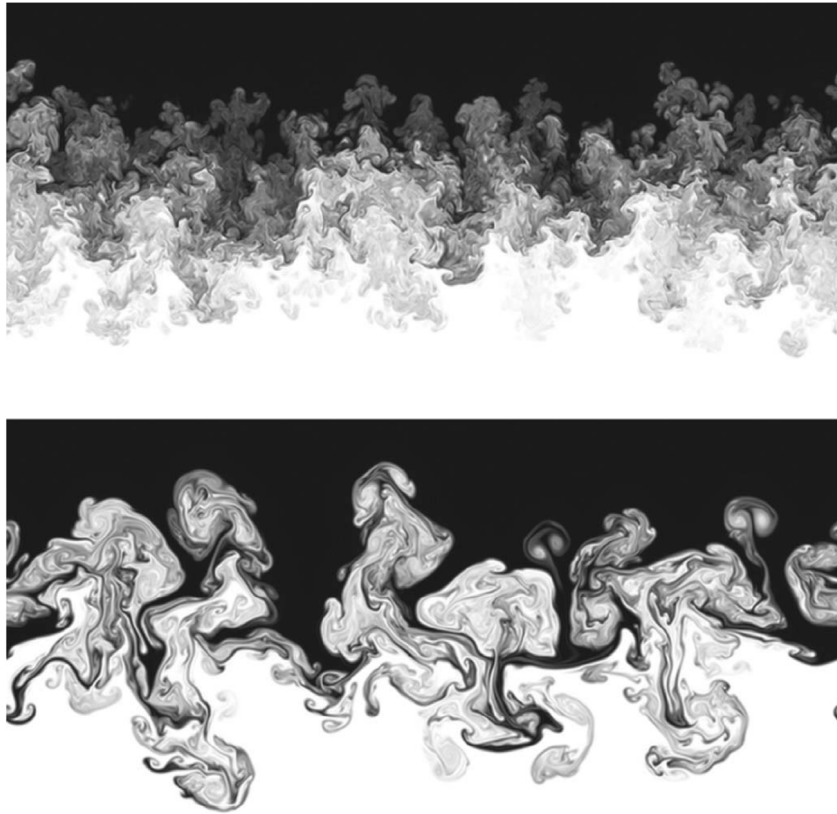


Fig. 9.27. Vertical slice of density from the 3D simulation (top) compared with the density field from a 2D simulation (bottom), both at $t = 25$. Black is heavy fluid, and white is light fluid.

Source: Fig. 2 of Cabot (2006), *Phys. Fluids*, with the permission of AIP Publishing.

The measure of enstrophy used here with variable density is $\Omega \equiv \omega^2/2\rho$ (where ω is the vorticity), which is governed by (Cabot, 2006; Tennekes and Lumley, 1972),

$$\frac{\partial \Omega}{\partial t} + \nabla \cdot (\Omega \mathbf{u}) = \rho^{-1} [\boldsymbol{\omega} \boldsymbol{\omega} : \mathbf{S} + \boldsymbol{\omega} \cdot \mathcal{B} + \boldsymbol{\omega} \cdot (\nabla \times \rho^{-1} \nabla \cdot \boldsymbol{\sigma})] \quad (9.11)$$

where the velocity strain tensor is

$$S_{ij} \equiv \frac{1}{2} \left(\frac{\partial u_i}{\partial x_j} + \frac{\partial u_j}{\partial x_i} \right) \quad (9.12)$$

and the baroclinic vector, \mathcal{B} , is

$$\mathcal{B} = \rho^{-2} \nabla \rho \times \nabla p, \quad (9.13)$$

and σ_{ij} is the viscous stress tensor.

The terms on the right-hand side of Eq. (9.11) are the production from vortex stretching, production from baroclinicity, and viscous dissipation and redistribution, respectively. Only the baroclinic production operates in the 2D flow, and a substantially lower amount of enstrophy is generated than in 3D (Fig. 9.29). Cabot (2006) also noted that during the initial stages, baroclinicity is seen to be the dominant mechanism for generating enstrophy, but at late times in the 3D flow the vortex-stretching term becomes the dominant mechanism. The vortex stretching term vanishes in 2D flow, but in 3D turbulent flow, it is the mechanism that acts to transfer large-scale energy and enstrophy to small scales.

The 2D flow, unlike the 3D flow, does not become well mixed at late times, as is made evident by direct measures of mixedness, \mathcal{E} (Fig. 9.30). This indicates that a substantial amount of pure fluid is being stirred, rather than mixed, in the 2D simulations (Cabot, 2006). Moreover, Shimony et al. (2017) found similar trend with the mixedness factor Θ at the five Atwood numbers ($0.2 \leq A \leq 0.9$), extracted from all of the 2D and 3D simulations.

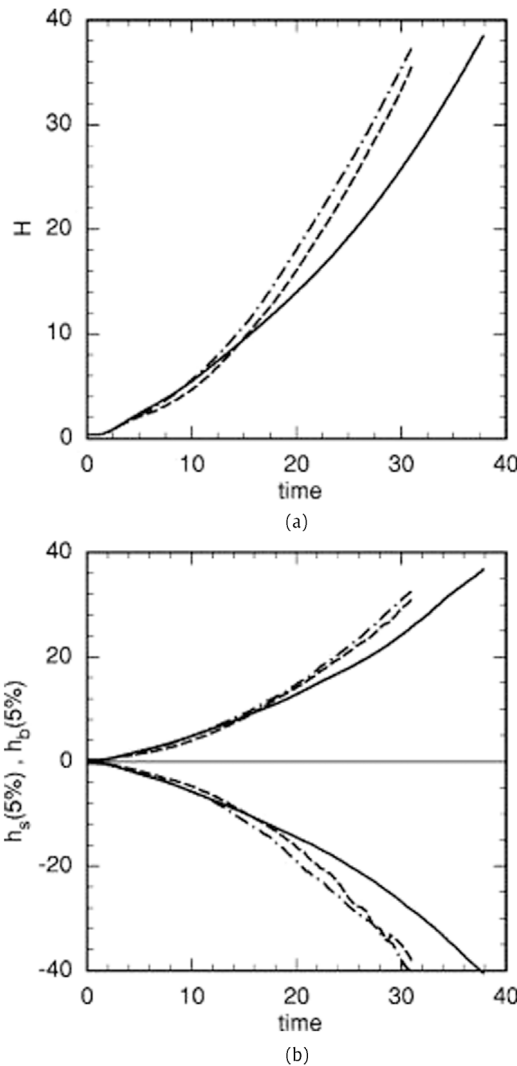


Fig. 9.28. (a) Integral product height and (b) 5% threshold values of mean density for the 3D (solid lines), 2Db (dashed lines), and 2Ds (dot-dashed lines) simulations.

Source: Fig. 3 of Cabot (2006), *Phys. Fluids*, with the permission of AIP Publishing.

10. RM multimode flows

10.1. Initial condition effects

In ICF and astrophysical applications, the Richtmyer–Meshkov (RM) instability encompasses multiple modes generated by random perturbations on the interface and these modes subsequently grow at different rates. Youngs (2013) pointed out that the influence of initial conditions (ICs) is likely to be significant in most applications. This issue is linked to the question of persistence memory of the initial conditions for the nonlinear and turbulent phases (for example Asida et al., 2005; Budzinski et al., 1994; Gowardhan et al., 2011; Kuranz et al., 2009; Neuvazhaev et al., 2004; Ukai et al., 2011; Vandenboomgaerde et al., 2014; Subramaniam et al., 2017). The ICs, as well as the initial baroclinic energy deposition, could be critical in determining whether an RMI induced mixing layer ultimately evolves into a fully developed turbulent flow.

Analytically, Saffman and Meiron (1989) formulated the problem of calculating the kinetic energy created by impulsive acceleration of an incompressible continuously stratified flow. Solutions were obtained for small density perturbations and a particular profile for various Atwood numbers and length scales (see also, Mikaelian, 1991; Pham and Meiron, 1993). In addition to the kinetic energy, Mikaelian (1991) gave expressions for density-gradient stabilization of the RMI, illustrating how the RM growth rate is reduced at diffuse interfaces.

As very well summarized in Brouillette (2002) and Ranjan et al. (2011), the change in the initial interface shape could result in a different instability phenomenon. With differing angles between the density and pressure gradients, different

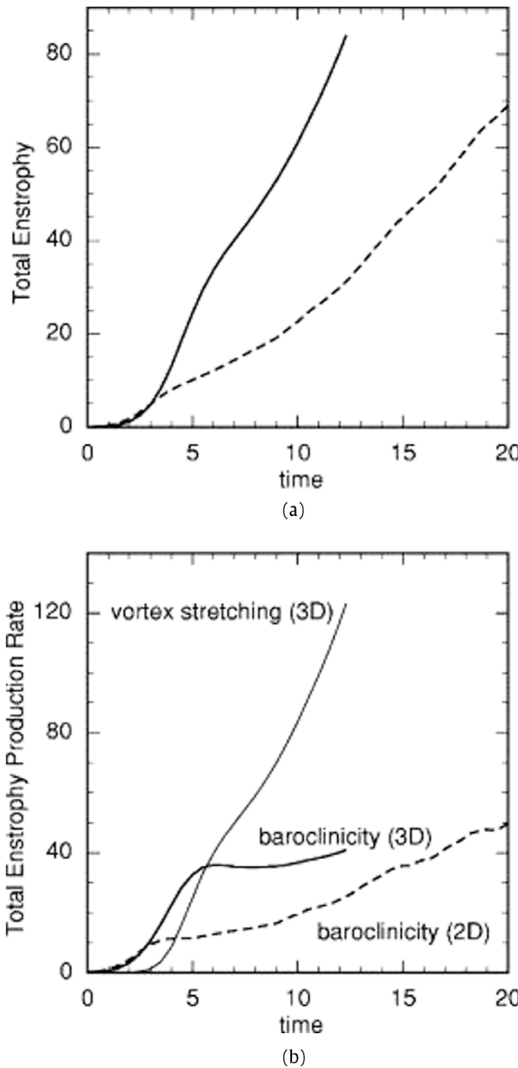


Fig. 9.29. (a) Global enstrophy and (b) global enstrophy production rates from vortex stretching and baroclinicity from 3D DNS solid lines and 2D DNS dashed lines, normalized per plane.

Source: Fig 8 of Cabot (2006), *Phys. Fluids*, with the permission of AIP Publishing.

wave pattern in the flow field as well as different amounts of vorticity will be produced during the interaction. Fan et al. (2012) studied five typical two-dimensional interfaces numerically: the diamond, ellipse, rectangle, and two kinds of triangle. The authors quantitatively estimated the intensity of vorticity produced by these five initial configurations and compared the simulated results with those estimated from relevant circulation models (Picone and Boris, 1998; Samtaney and Zabusky, 1993, 1994, 2000; Yang et al., 1994).

Mikaelian (2005a) gave analytic expressions for the growth of interfaces starting with different shapes and having continuous or discontinuous first derivatives. He pointed out that jetting occurs in the latter type, proposed using the RMI as a method to measure strength in metals, and suggested that ejecta are a form of RMI jetting. This approach was later applied to analyze high-explosive-driven experiments by Buttler et al. (2012).

By experimental and numerical means, Bates et al. (2007) studied the interaction of a shock wave with a rectangular block of sulfur hexafluoride (SF_6), occupying part of the test section of a shock tube. Ng et al. (2011) carried out quantitative analysis of the time-evolution of this flow interface and the dynamics during its transition towards fully turbulent state using the classical fractal theory. Wang et al. (2010) performed their LES on the evolution of such a rectangular block of SF_6 after the passage of a shock wave and compared the results with the experimental images. Using a two-velocity two-temperature continuum model, Zyryanov et al. (2017) considered the development of RMI resulted from the transmission of a shock wave through a cylindrical structure of heavy gas. Bai et al. (2010), Li et al. (2010) and Zou et al. (2010) studied the interaction of

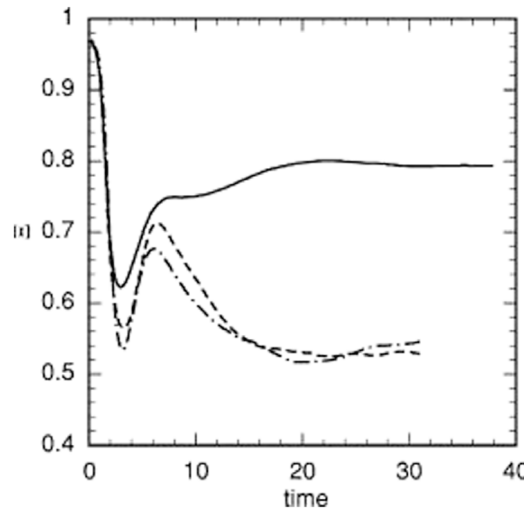


Fig. 9.30. Mixedness measure for 3D (solid line), 2Db (dashed line), and 2Ds (dot-dashed line) simulations. The standard deviation is about 7% at late times for the 2D runs.

Source: Fig. 5 of Cabot (2006), *Phys. Fluids*, with the permission of AIP Publishing.

shock waves with an elliptical gas cylinder experimentally and numerically. Zou et al. (2014) further extended this line of investigation to the evolution of double shock-accelerated elliptic cylinders. This setting allows the authors to investigate not only the flow morphology, but also the interactions between the cylinders.

McFarland et al. (2011, 2013) carried out a computational study of the RMI for an inclined interface. The simulations were performed in support of planned experiments in a shock tube facility. Through examination of a nonlinear (30 inclination angle) and a linear (80 inclination angle) initial perturbation case, the difference between these regimes was determined to be the presence or absence of the strong secondary compressible effects for the nonlinear and linear cases, respectively. Jourdan et al. (2004) and Houas et al. (2003, 2012) developed a variable inclination shock tube for the generation of shock waves of Mach numbers ranging from 1.05 to 4, moving horizontally, vertically from up to down or the opposite, or with any inclination angle. Also, Wang et al. (2012) performed experimental and numerical RMI studies of inclined air/SF₆ interface instability at Mach numbers of 1.23 and 1.41.

In a series of shock tube experiments conducted at Atomic Weapons Establishment (AWE), United Kingdom, the modification of the initial interface geometry led to two experiments with the chevron (Smith et al., 2001) and inverse chevron (Holder and Barton, 2004) profiled configurations. These profiles were achieved with the use of a fine wire grid to support the membrane initially used to separate the gases. Holder et al. (2003a) also discussed a similar experiment that used an enlarged double bump to circumvent problems with reproducibility. Bakhrakh et al. (1995) and Bashurov et al. (1997) carried out experimental and numerical studies for two types of initial interface perturbations, a “step” or a “saw”-shaped. Luo et al. (2016) and Zhai et al. (2016) reported their shock tube RMI experiments of a ‘V’ shaped air/SF₆ gaseous interface. The authors generated five ‘V’ shaped interfaces with different vertex angles (60°, 90°, 120°, 140° and 160°) where the ratio of the initial interface amplitude to the wavelength varies to inspect the effects of initial condition on the flow characteristics. Li et al. (2016) compared their numerical simulations with experimental measurements and considered the process of transition to turbulence at the material interface.

Using a shock accelerated heavy-gas cylinder,⁵ Jacobs et al. (1993, 1995) determined that the gas curtain evolution indicated three distinct flow patterns. Rightley et al. (1997, 1999) carried out experiments with single row varicose mode superimposed on a large-wavelength mode, and a multi-mode nozzle with two dominant wavelengths. Numerically, Mikaelian (1996a) simulated gas curtain experiments which evolve into (a) sinuous, (b) upstream-mushroom, and (c) downstream mushroom configurations with a single mode as performed by Budzinski et al. (1994) (see Fig. 10.1). Baltrusaitis et al. (1996) and Grove et al. (1993) conducted computational studies of gas-curtain instability. Mikaelian also proposed and simulated possible reshock experiments which evolve into more complex structures. Such structures were indeed observed in subsequent reshock experiments by Balakumar et al. (2008b). The physics of reshocked RMI is extremely important and will be the subject of a whole follow up section.

On a slightly different matter, Tritschler et al. (2014a) found that the cross-section of the heavy-gas cylinder in the experiment is not perfectly circular after inspecting Fig. 2 of Tomkins et al. (2008) carefully. Stressing that the initial deviation

⁵ Jacobs (1993) observed that the vorticity deposited on the boundary of the SF₆ cylinder by the interaction with the shock wave, separates from the heavy gas to form a pair of vortices, which subsequently wrap the SF₆ around them. He pointed out that this process is rather different from what is observed in the light gas experiments, which showed a small amount of helium to remain with the vorticity, eventually becoming part of the vortex cores. See also, Vorobieff et al. (1998, 2003) and Kumar et al. (2005).

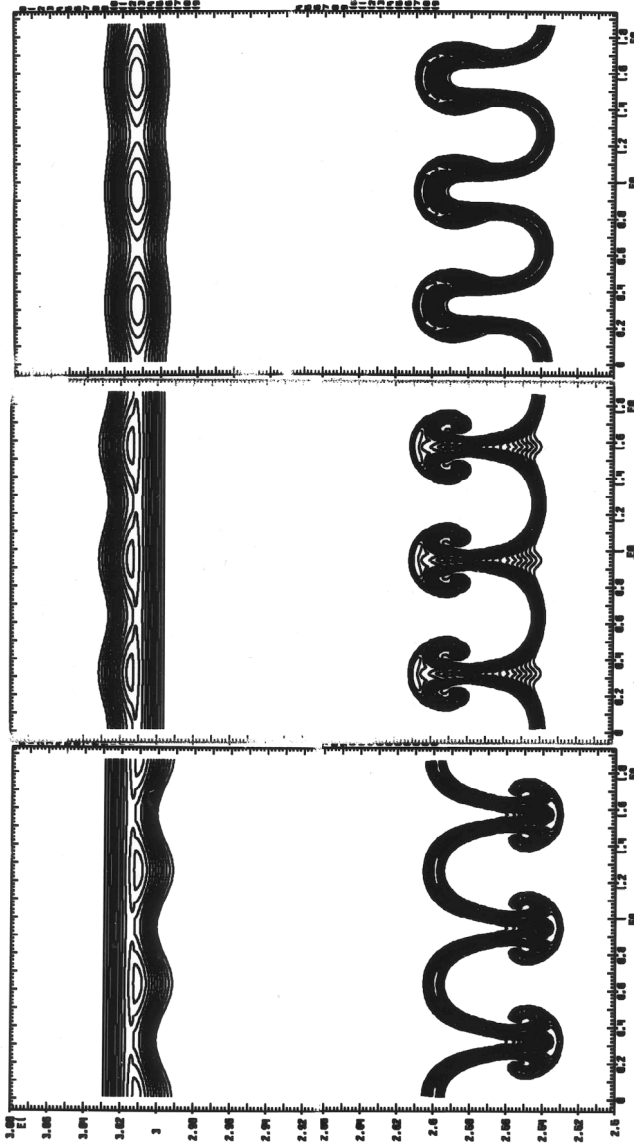


Fig. 10.1. Initial (left column) and final (right column) configurations in air/SF₆ gas-curtain simulations.
Source: Fig. 13 of Mikaelian (1996a), *Phys. Fluids* with the permission of AIP Publishing.

of the heavy-gas region from a cylindrical shape affects the baroclinic vorticity production, Tritschler et al. (2014a) introduced an uncertainty parameter to examine the impact of this initial data uncertainty on the mixing process.

Balakumar et al. (2008a) compared the development of RM instability in a varicose IC with two sinuous ICs of different wavelengths. A stable initial configuration of vortices emerges from shocking the varicose curtain, whereas an unstable initial configuration develops from the shocking the sinuous curtain. For a varicose IC, the structure width will be dominated by the advection of material by the induced velocity field. For the second ICs case, however, the vortices may self-induce to severely alter the initial vortex configuration and in conjunction with material advection, dramatically increase the layer width. Hence, this comparison suggests that the dominant mechanisms driving the growth of the layer depend upon the stability of the vortex configuration created in the initial (post-shock) flow (see also, Prestridge et al., 2013).

Balasubramanian et al. (2013) carried out further experimental and theoretical study on the effects of initial condition parameters, namely, the amplitude and wavenumber. The images of the RMI evolution after incident planar shock (*Mach* = 1.21) were captured using high resolution simultaneous planar laser induced fluorescence (PLIF) and particle image velocimetry (PIV) diagnostics. Here, the single and multi-mode membrane-free initial conditions are shown for the light-heavy-light gas curtain experiments in Fig. 10.2a. For an air-SF₆-air configuration (*A* = 0.57), Fig. 10.2b demonstrated

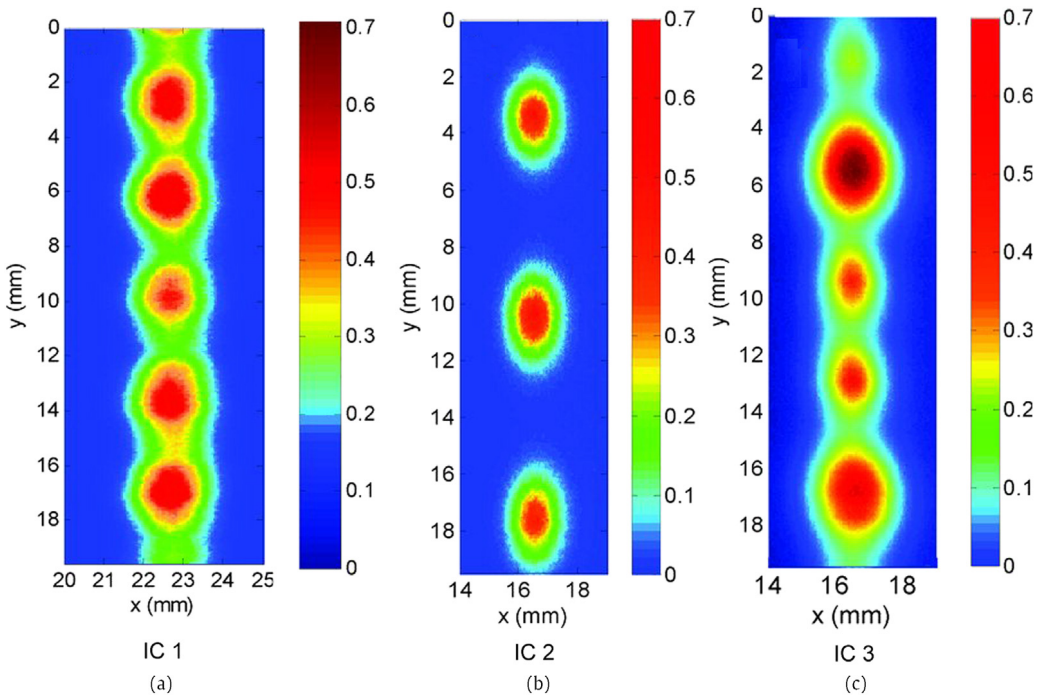


Fig. 10.2a. Initial condition concentration contour plots: (a) single mode short wavelength (3.6 mm) initial condition (IC 1), (b) single mode long wavelength (7.2 mm) initial condition (IC 2), and (c) multi-mode initial condition (IC 3). The intensity bar shows the volume fraction of SF₆.
Source: Fig. 3 of Balasubramanian et al. (2013), *J. of Turbulence* with permission.

that there is a correlation between initial condition parameters and small-scale mixing at late times, suggesting an initial condition dependence on RMI mixing. In other words, this work shows that single-mode and multi-mode RMI are different. Single-mode RMI depends on initial amplitude and wavelength. Multi-mode RMI depends weakly on IC, but is not completely independent of it.

Dell et al. (2015) focused on the early time dynamics of the RMI by analyzing the linear phase of the RMI evolution immediately after the shock passage. The amplitude of the initial single mode sinusoidal perturbation of the interface was varied from 0% to 100% of its wavelength. The growth-rate is found to be a non-monotonic function of the initial single mode sinusoidal perturbation. Therefore, the amount of energy that can be deposited by the shock at the interface is constrained. In a related work, Pandian et al. (2017) considered the influence of the relative phase and the interference of waves constituting a multiwave initial perturbation on a strong-shock-driven RM unstable interface.

To accurately initialize the surface perturbation between two materials, Youngs (2013) proposed the summation of a number of individual wave modes in accordance with an assumed surface perturbation power spectrum (Youngs, 1991). More specifically, the interface perturbations are assumed satisfying a power spectrum of the form $P(k) \sim 1/k^2$, where the perturbations are concentrated at long wavelengths (Youngs, 2004). This model is proposed to mimic a typical surface finish found for inertial confinement fusion capsules (Barnes et al., 2002; Dahlburg et al., 1995). Holder et al. (2003a) also suggested that the interface perturbations could take a form in a power spectrum proportional to k , where the majority of the perturbations are accumulated at short wavelengths. This form has been proposed for modeling the membrane rupture interface perturbations.

Through a series of carefully designed ILES, Thornber et al. (2010) inspected the influence of different 3D multi-mode initial conditions on the rate of growth of a RMI-induced turbulent mixing layer. Two different numerical methods, CNS3D (Drikakis and Tsangaris, 1993; Drikakis, 2003; Thornber et al., 2008) and TURMOIL3D (Youngs, 1982, 1991, 2007, 2009) have been used for the simulations with grid levels up to 3×10^9 grid points. They stressed that the accurate initialization of the surface perturbation requires that the modes that form the initial perturbation be linear at initialization, so that Richtmyer's theory is applicable. For the broadband case the requirement of linearity of the highest wavenumbers leads to a complex expression for the standard deviation. But this is relatively simple for the narrowband case, where the short wavelengths present in the initial perturbation have a top hat power spectrum.

As demonstrated in Fig. 10.3, the growth of the resultant mixing layer is strongly dependent on ICs, confirming the preliminary analysis of Youngs (2004). The two curves correspond to two values of RM scaling exponents. Simulations of the narrowband initial conditions at $A = 0.5$ showed good agreement with LEM experiments, giving $\theta \approx 0.275$ (Thornber, 2016). The broadband perturbation resulted in increased growth of the mixing layer up to $\theta = 0.62$, which asymptotes towards the theoretical value of $\theta = 2/3$ (see Section 6 of Part I, Zhou, 2017). Clearly, the Atwood, Mach, and Reynolds

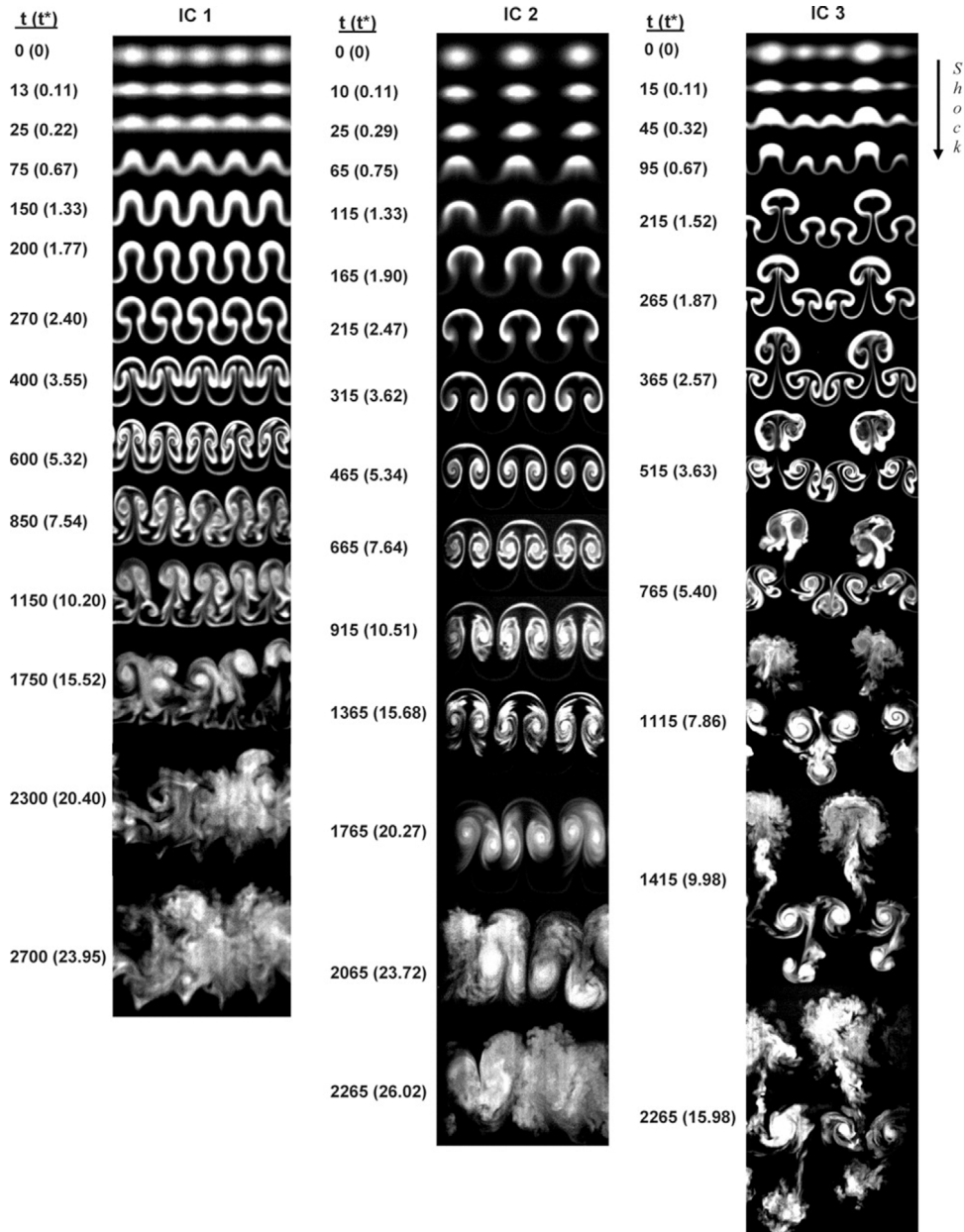


Fig. 10.2b. Time evolution of density fields for three different initial conditions. Far left: single mode short wavelength initial condition (IC 1); center: single mode long wavelength initial condition (IC 2); and far right: multi-mode initial condition (IC 3). White indicates SF₆, and black indicates air. The time $t = 0 \mu\text{s}$ corresponds to the initial condition. In all the sets of images, t is the absolute time, and t^* is the normalized time based on the initial linear growth. Source: Fig. 5 of [Balasubramanian et al. \(2013\)](#), *J. of Turbulence* with permission.

numbers may be used *a priori* to characterize RM experiments ([Motl et al., 2009](#); [Gallis et al., 2015](#)). These studies illustrated a difference between the two families of narrowband and broadband ICs; but within each family, however, the difference is not significant.

As a side comment, [Lombardini et al. \(2012\)](#) used a Gaussian profile for the initialization of their large-eddy simulation, which is between the broad and narrowband cases. The r.m.s of the multi-mode perturbation and its single-mode equivalent are equal.

Finally, the initial flows of an RMI induced flow may not be uniform. [Liu et al. \(2012a\)](#) carried out a Mach 1.27 shock tube experiment with nonuniform SF₆ flows and found that the mixing layer grows faster in the low-density areas. Large-eddy simulations of this experiments further indicated that the evolution of the flow disturbance developed slowly with a small

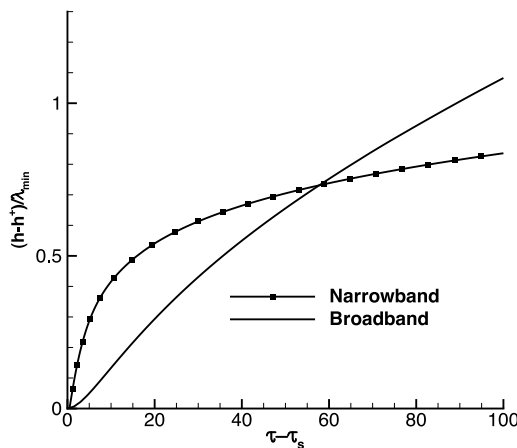


Fig. 10.3. Integral mixing width from two different initial conditions, scaled by the minimum initialized wavelength λ_{\min} plotted against dimensionless time $\tau = t \Delta u / \lambda_{\min}$. τ_s is the dimensionless time at which the shock passes through the layer.⁶
Source: Figure courtesy Dr. B. Thornber, The University of Sydney, Australia.

initial amplitude in a high-density zone. These results can be explained with a detailed analysis of vorticity and circulation of the simulated flow fields ([Xiao et al., 2016](#)).

10.2. Mixedness and normalized mixed mass

There is considerable work in estimating the fine scale mixing for RMI induced flows. Several publications are described here, and others are deferred to next two subsections to consider the influences of the Atwood and Mach numbers on the mixedness parameters.

A paper by [Oggian et al. \(2015\)](#) concerns a numerical study of the late-time behavior of a single-shocked RMI and the associated compressible turbulent mixing. The perturbation at the interface consists of a constant narrowband high wavenumber power spectrum. These authors advanced a new technique to address a limitation that numerical simulations based on the compressible flow equations tend to become less accurate at sufficiently low Mach number. Physically speaking, this approach is rather similar in spirit to that of the nonlinear perturbation models (Part I) by exploiting the fact that the RMI is a compressible flow during the early stages of the simulation and incompressible at late times. For $A = 0.5$, this hybrid compressible–incompressible solver allows numerical simulations of late-time mixing and resulted the values of the mixedness parameters converged at $\Xi \approx 0.80$ and $\Theta \approx 0.74$.

The mixedness parameters have also been obtained numerically for the broadband perturbation at Atwood number $A^+ = 0.5$ (Fig. 26 of [Thornber et al., 2010](#)). As in the case in the RTI mixing layer, the molecular mixing fraction reaches its minimum before Kelvin–Helmholtz instabilities lead to an increase of molecular mixing. As the flow evolves, it mixes them at ever smaller scales and entrains pure fluids in ever bigger parcels. The CNS3D results are almost converged at $\Xi \approx 0.38$ and $\Theta \approx 0.37$. The TURMOIL3D code predicted an even lower $\Theta \approx 0.33$. These values are much lower than the RTI cases reviewed in last section. [Thornber et al. \(2010\)](#) speculated that the decreased mixing rate occurs because the RMI induced fluids do not interact turbulently at the driving scale (which is essentially a superposition of modes), but mix at a scale that is below the driving scale, leading to a lower molecular mixing efficiency.

Using a type of broadband initial condition imposed on an interface between a helium–acetone mixture and argon ($A = 0.7$), [Weber et al. \(2012a\)](#) performed several RMI experiments in a vertical shock tube where the interface is accelerated by a $Mach = 1.6$ planar shock wave. The mixedness measurement, Ξ , was obtained for three post-shock times, starting at near 1 and ending at a value of 0.85.

More recently, [Krivets et al. \(2017\)](#) reported several experiments conducted at the University of Arizona vertical shock tube with an incident shock Mach number 1.2 between two fluids of Air and SF₆. An interface is formed in the test section of the shock tube using opposed gas flows where the heavy gas (SF₆) flows upward in the shock tube and collides with the light gas (air) flowing downward. As shown in Fig. 10.4 all of the experiments reached their terminal constant value at approximately the same time, 1 ms after shock-interface interaction. [Krivets et al. \(2017\)](#) attributed the difference in the terminal value of the mixedness, Θ , to differences in initial interface thickness and shape. The initial perturbation of experiments 4 and 5 had a significantly smaller amplitude and interface thickness than in experiments 1 through 3. This is probably the cause of experiments 4 and 5 having a lower value of mixedness. These experimentally obtained mixedness values appear to be consistent with the results from numerical simulations.

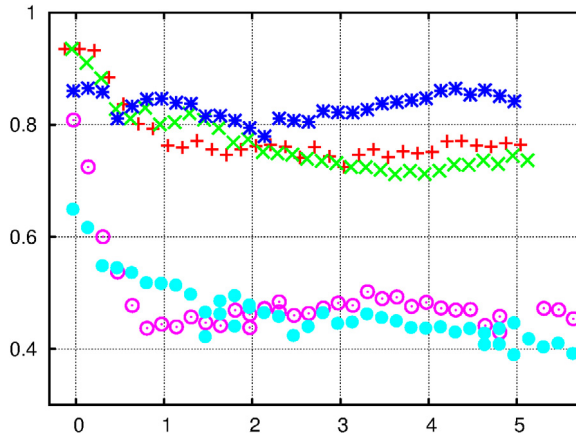


Fig. 10.4. Five experiments mixedness, Θ .
Source: Figure courtesy of Dr. V. Krivets and Dr. J.W. Jacobs, University of Arizona.

10.3. Atwood number dependence

Linear Electric Motor (LEM) was extremely helpful in studying the late time RMI scaling. LEM could achieve an impulsive acceleration (800 times earth's gravity) to approximate the RMI (see Section 6, Part I). In an important paper, [Dimonte and Schneider \(2000\)](#) measured scaling law of the RM late-time similarity in order to determine the Atwood number dependence. The variation of θ_i with a range of Atwood numbers between 0.15 and 0.96 is shown in Fig. 10.5. The bubble value of θ_b was determined to have a sample average of $\theta_b = 0.25 \pm 0.05$ in the range $A \sim 0.16\text{--}0.94$. Similarly, the spike value of θ_s was found to remain rather close to θ_b until it increases towards unity for $A > 0.8$. [Dimonte and Schneider \(2000\)](#) noted substantial scatter in θ_s for $A \sim 0.92\text{--}0.94$, which suggests that θ_s is sensitive to the experimental (initial) conditions.

[Dimonte \(1999\)](#) suggested that the trend could be expressed by $\theta_s/\theta_b = (\rho_1/\rho_2)^{0.22 \pm 0.05}$. Some extra clarification may be appropriate here. Assuming $\theta_s/\theta_b > 1$ is problematic as it implies non-self-similar behavior (all spike and no bubble eventually). An alternative interpretation of the LEM experiments is that spikes just take longer to settle down than the bubbles.⁷ As the Atwood number approaches to 1, there is little or no shear force applied to the spike side of the interaction. This means that the initial linear growth is not slowed by interaction with the second fluid and hence possibly does not form a vortex or turbulent mixing layer, growing instead directly proportional to time ([Thornber et al., 2010](#)). Indeed, essentially all the simulations have assumed $\theta_c/\theta_b = 1$, but as indicated below, it takes longer to get to self-similarity for the high Atwood case. Also, [Dimonte and Schneider \(2000\)](#) suggested that the scatter might signify a sensitivity of θ_i to initial conditions as suggested by [Youngs \(1994\)](#) and calculated by [Zhang \(1998\)](#) for the RM instability.

While the work by [Motl et al. \(2009\)](#) and [Weber et al. \(2009\)](#) considered Atwood numbers from low ($A = 0.30$) to very high ($A = 0.95$), other parameters, such as Mach number and initial amplitude, have been varied as well.

Using ILES, [Zhou et al. \(2016\)](#) investigates two specific Atwood number cases, $A = 0.5$ ($\rho_2/\rho_1 = 3$) and $A = 0.9$ ($\rho_2/\rho_1 = 20$) for the narrowband perturbation case. The corresponding incident shock wave has a Mach number of 1.843 and 1.91, respectively, where the variation in shock Mach number ensures that both cases have the same initial impulse (growth rate). Fig. 10.6a, taken from [Zhou et al. \(2016\)](#), indicates that the late-time behavior of mixed mass for $A = 0.5$ is consistent with that of RTI. Specifically, the scaling of the mixed mass is consistent with that of the mixing layer width. However, the $A = 0.9$ RMI case shows significant change in the late-time behavior. The growth rate of the mixed mass is much lower than that of the scaled width (Fig. 10.6b). The scaled width experiences sustained growth due to the high momentum of the spikes penetrating the lighter fluid. For the same time, the high Atwood number case has substantially greater anisotropy, another indicator of a slower transition towards self-similarity.

The normalized mixed mass Ψ for the RMI cases can be seen in Fig. 10.7a, b for the single shock, $A = 0.5$ and $A = 0.9$ cases, respectively. While Ψ for the $A = 0.5$ reaches its asymptotic value, Ψ for the $A = 0.9$ case still has not settled down completely, even after significant late-time computations. Apparently $A = 0.9$ case requires much longer time to decay to a constant self-similar value. This phenomenon, in turn, suggests that the flow is still undergoing an active transient period, possibly caused by physical phenomena, which do not collapse under a single scaling (elongated spikes for example). Nevertheless, the late-time values of Ψ are lower for the high Atwood number than that of lower A case (0.68 versus 0.80), consistent with the RTI flows. Again, the normalized mixed mass Ψ suggests that the higher Atwood number reduces the efficiency of generating mixed mass.

⁷ It appears that this is the view taken in the numerical simulation papers. See also, [Clark and Zhou \(2006\)](#).

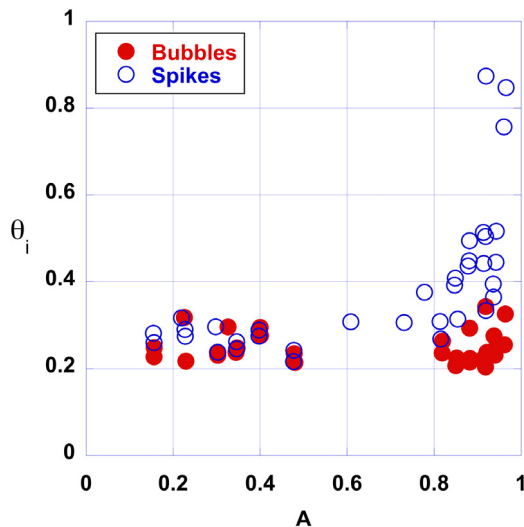


Fig. 10.5. Power-law exponents vs. Atwood number.
Source: Fig. 26 of Dimonte and Schneider (2000), *Phys. Fluids*, with the permission of AIP Publishing.

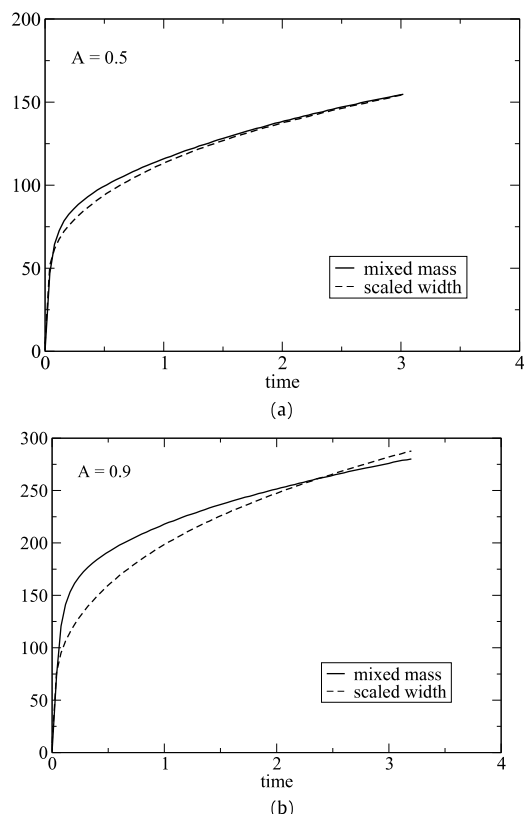


Fig. 10.6. (a), (b) Temporal evolution of the mixed mass for two single shock cases with Atwood number = 0.5 (Fig. 10.7a) and 0.9 (Fig. 10.7b). Also, the corresponding results for the mixed width (dashed lines), but multiplied by arbitrary constants.
Source: Zhou et al. (2016), Fig. 3a,b, *Phys. Plasma*.

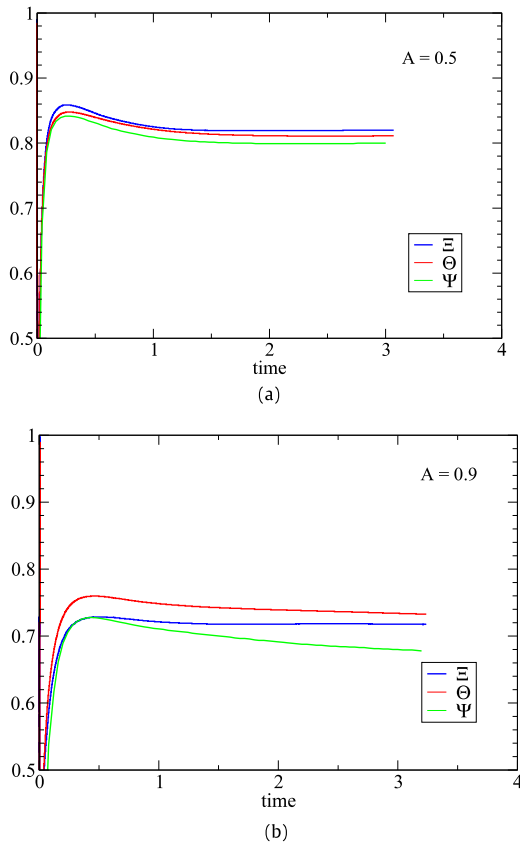


Fig. 10.7. Temporal evolution of the mixedness parameters and normalized mixed mass for the single shock case with $A = 0.5$ (a) and $A = 0.9$ (b).
Source: Zhou et al. (2016), Fig. 4a,b, *Phys. Plasma*.

Recall that for the RTI cases, Ξ and Θ have essentially the same late-time values around 0.80 and 0.78, for a wide range of Atwood numbers of 0.2, 0.5 and 0.8. However, for the RMI situations here, the values of Ξ and Θ are reduced from (0.82, 0.81) for the $A = 0.5$ case to (0.72, 0.71) for the $A = 0.9$ case, inconsistent with RTI results.

10.4. Mach number effects

It is appropriate to make some comments about expected Mach number effects. The perturbed velocity is $u' = kaA\Delta V$. Here ΔV , the velocity jump resulting from the shock wave, is either less than or comparable to the sound speed behind the shocked fluids. So unless ka is large, which is the case where shock-proximity is important (Section 2, Part I), the post-shock flow will have low Mach number and the Mach number will decrease with time. Hence the post-shock flow is usually nearly incompressible and independent of the Mach number, if suitable scaling is used.⁸

Using a technique similar to the method of Jones and Jacobs (1997), Motl et al. (2009) and Weber et al. (2009) expanded the database of Mach and Atwood numbers. These results include the first membraneless, gas-phase, interface experiments for $A > 0.5$ and $Mach > 1.5$. Images from the strongly shocked, high Atwood number experiments have provided evidence of the flattening of the bubble. Nevmerzhitskiy (2013) showed that growth of perturbations and turbulent mixing in gases is sensitive to the Mach number of the shock wave. Shi et al. (2009) also studied the mechanism of RMI flows experimentally in a vertical rectangular shock tube. The mixed zone width at the shock wave Mach number of 1.7 was not only greater than that at the other Mach numbers of 1.2 and 1.5 at the same time, but also increased with a faster rate (Fig. 7 of Shi et al., not shown).

Orlicz et al. (2013, 2015b) have obtained quantitative density and velocity fields using the LANL horizontal shock tube (see Fig. 10.8a). With varied Mach numbers, such data would allow for a more complete and detailed assessment of the different mixing states that are produced (see also their previous work, Orlicz et al., 2009). Fig. 10.8b illustrated a selection of SF₆ volume fraction maps from each Mach number experiment, with contrast customized for each image (Atwood number

⁸ See for example Fig. 10.13.

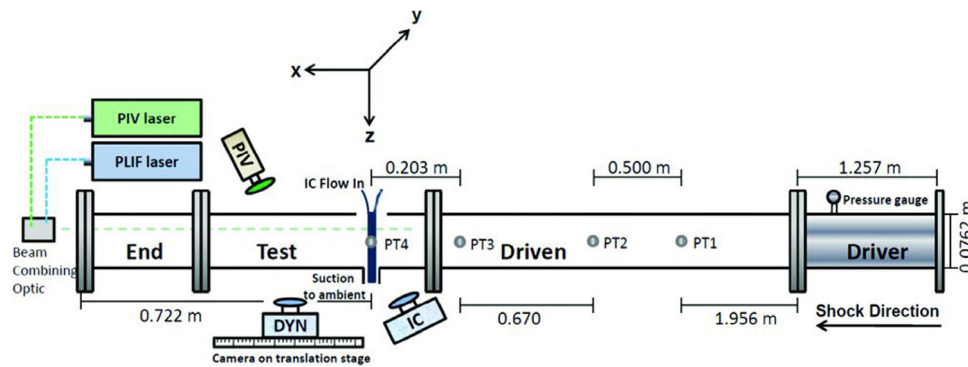


Fig. 10.8a. LANL horizontal shock tube schematic. Diaphragm is placed between Driver and Driven sections. Shock wave travels from right to left, with pressure transducers (PT) labeled 1–4. Shock speed is calculated between PT2 and PT3, and diagnostics are triggered off of PT3, while PT4 is coincident with IC location to measure time of shock interaction.

Source: Fig. 1 of Balasubramanian et al. (2013), *J. of Turbulence*, with permission.

is 0.49). The evolution of the mix width measurements⁹ for three Mach numbers are presented in Fig. 10.9 (see also Orlicz et al., 2015a).

As described in detail in Orlicz et al. (2013), the mixedness parameter Ξ is high for all cases initially, as the diffuse initial conditions are relatively uniform in the spanwise direction. As the deposited vorticity causes the instability to grow, air is entrained in the mixing layer, and thus Ξ decreases rapidly, reaching a low at $x \sim 2$ cm for each Mach number case. Small scale mixing mechanisms then begin contributing to mixing uniformity and Ξ begins increasing rapidly for each Mach number. The value of Ξ appears to be leveling off towards a higher value with an increased Mach number (Fig. 10.10a). Trends observed of Θ in the plots are similar to those of Ξ at early times, but the differences in Θ values between the Mach number cases at later times are less pronounced (Fig. 10.10b). In fact, the average values of (Ξ , Θ) over the range $x \geq 10$ cm are approximately equal to (0.82, 0.94), (0.87, 0.95) and (0.93, 0.97) for Mach 1.21, 1.36, and 1.50.

Figs. 10.11a and 10.11b shows the quantitative PLIF imaging of the turbulent mixing induced by a *Mach* = 1.6 or *Mach* = 2.2 shock wave, respectively (Weber et al., 2014a). The mixing layer is initially dominated by the growth of large-scale spikes and bubbles, but these structures eventually break apart into smaller scales, leading to scale separation as well as molecular mixing. Whereas the greater compression of the *Mach* = 2.2 flow results in a thinner mixing layer, the similarities between the two Mach number images are remarkable given the $\sim 2 \times$ difference in interface velocity, provided one scales time properly.

Weber et al. (2014a) did not observe the tendency of Ξ to increase with increased Mach number. In the *Mach* = 2.2 case, Ξ reduces more rapidly before increasing at the end, while in the *Mach* = 1.6 case, Ξ reduces steadily throughout the experiment (Weber et al., 2012a). A final value of $\Xi = 0.79$ was reached for both Mach numbers (Fig. 10.12), which is slightly lower than the asymptotic values of 0.82–0.93 in gas-curtain experiments.

The experimental results showing the relative insensitivity of Θ to the Mach number received strong support from numerical simulation of Lombardini et al. (2012). As illustrated in Fig. 10.13, the simulated Θ values are essentially independent of Mach number ($\Theta \approx 0.85$). Using DNS, Tritschler et al. (2014c) found that the growth of integral scale, mixing zone width as well as the decay rates of turbulence kinetic energy and enstrophy to be independent of the shock Mach number.

Reese et al. (2014) developed a novel technique to obtain simultaneous concentration and velocity field measurements in a RMI mixing layer after acceleration by a *Mach* 2.2 shock wave. The authors calculated the Taylor microscale by computing the curvature of the autocorrelation curve of the scalar field at $r = 0$ by fitting a parabola to the central seven points. Weber et al. (2014a) experimentally deduced several important length scales, the mixing zone width, the Taylor microscale, and the Kolmogorov length scale. For both the *Mach* = 1.6 and *Mach* = 2.2 flows, the separation of scales appears not to depend on the shock Mach number (not shown). Tritschler et al. (2014c) also numerically computed these measurements. However, increased separation of scales has been found with increasing shock Mach number (Fig. 10.14). Further work is needed to clear up this issue.

⁹ Orlicz et al. (2013) and Lombardini et al. (2012) discussed the issue of scaling the mixing layer width amongst experiments. Jacobs and Krivets (2005) and Orlicz et al. (2009) carried out their nondimensionalization based on Richtmyer's linear formulation. Orlicz et al. (2013), however, prefer to scale the time axis with the velocity jump as it is the only parameter that changes with Mach number. The reader is referred to the original publications for these scaled results.

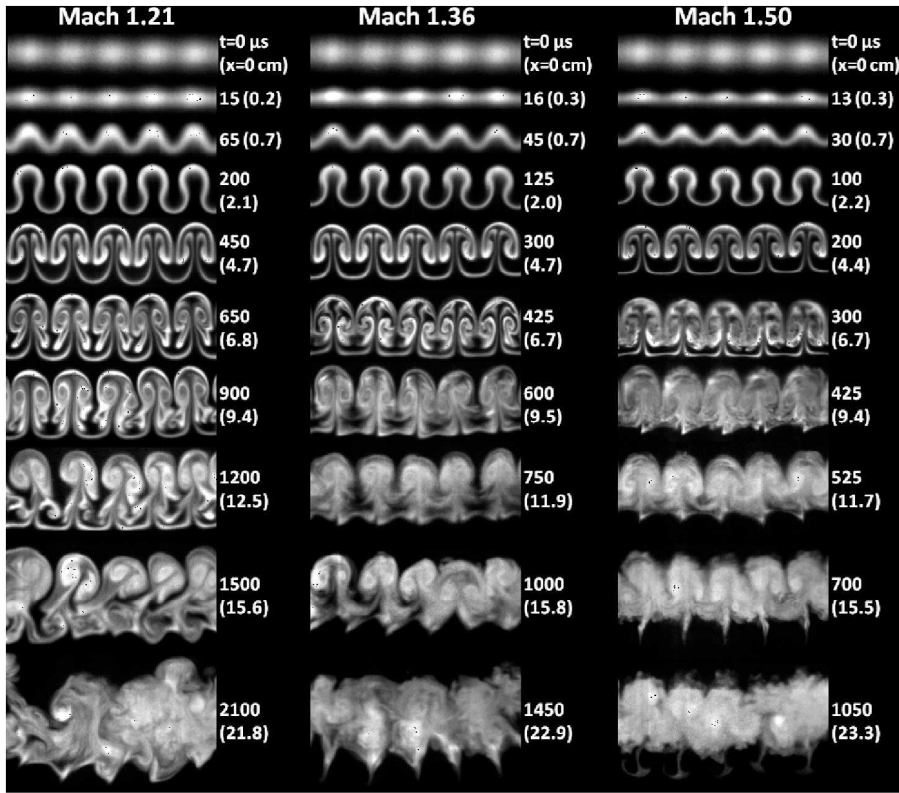


Fig. 10.8b. A selection of SF_6 volume fraction maps from each Mach number experiment. Images in each row were acquired at roughly the same location as indicated in the figure, with time t and distance traveled (x).
Source: Fig. 1 of Orlicz et al. (2015b), Springer with permission.

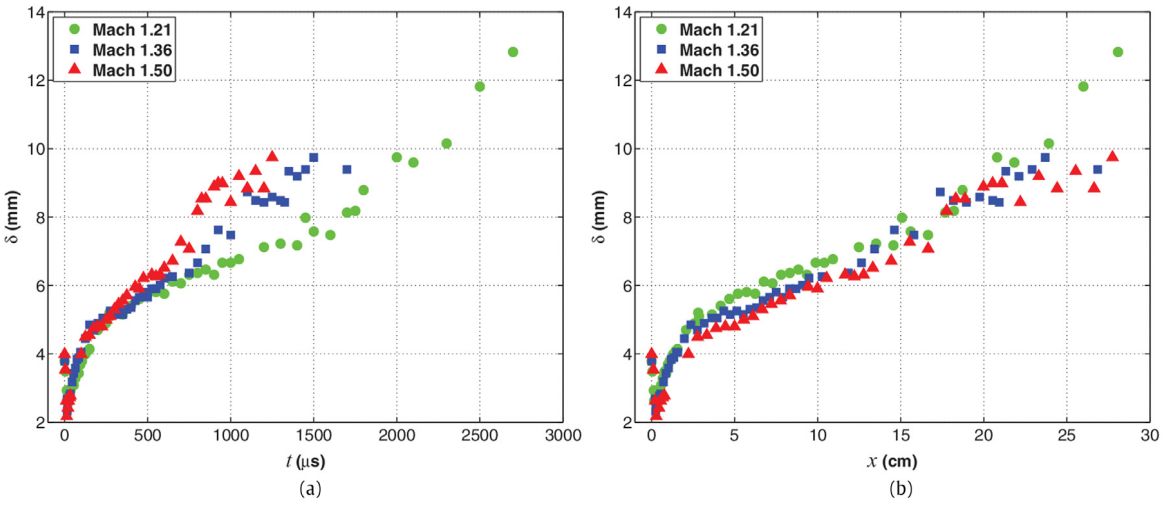


Fig. 10.9. (a) Mixing layer width vs. time. (b) Mixing layer width vs. distance traveled shows the same growth rate for each Mach number, but with a vertical offset separating the experiments until $x \approx 15$.

Source: Fig. 17 of Orlicz et al. (2013), Phys. Fluids, with the permission of AIP Publishing.

10.5. Anisotropy

Lombardini et al. (2012) carried out a study of 2D, multimode LES where a heavy-light SF_6 -air ($A = 0.67$) perturbed interface is impacted by a single shock. Fig. 10.15 shows an anisotropy measure of the velocity power spectra at three

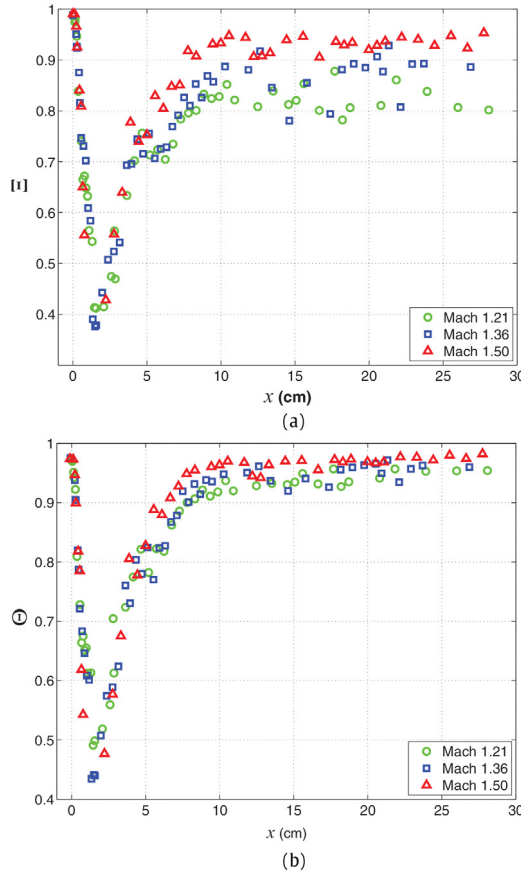


Fig. 10.10. (a), (b) Evolution of mixedness parameters (E , Θ) with distance traveled.
Source: Figs. 23 and 24 of [Orlicz et al. \(2013\)](#), *Phys. Fluids*, with the permission of AIP Publishing.

different times. Only partial isotropization of the flow (in the sense of turbulent kinetic energy and dissipation) is observed during the late-time evolution of the mixing zone.

Yet, [Thornber et al. \(2010\)](#) found that the anisotropy appears to persist to the late time at the ILES RMI flows for both the $A^+ = 0.5$ and 0.9 narrowband simulations (Fig. 10.16) where x is in the direction of shock propagation. The ratio of the component turbulent kinetic energy (TKE) in the parallel and perpendicular directions tends towards a constant value. The ratio of kinetic energies in the high Atwood case appears to be leveling off more slowly than that in the lower A setting. This is expected as the rate of growth of Kelvin–Helmholtz unstable modes is lower when the two fluids have different densities, leading to a slower transfer of fluctuating kinetic energy.

More recently, [Oggian et al. \(2015\)](#) also found that turbulent kinetic energy spectra indicated an anisotropic evolution even at late times. These calculations were performed using a hybrid compressible–incompressible CFD method ([Oggian et al., 2014](#)) for a multi-mode perturbation at the interface between two fluids of density corresponding to an Atwood number of 0.5 . The case considered consists of a shock wave with Mach number of 1.84 .

[Liu and Xiao \(2016\)](#) defined a measurement, f_i^A , an averaged fraction function for the square of various components of the energy flux. Using DNS, they found that during the whole period, the third term (direction of the shock wave) dominates the other components.

However, it does also look like the initial perturbation has a significant impact on the isotropy. Recently, [Orlicz et al. \(2015a\)](#) carried out simultaneous particle image velocimetry (PIV) and quantitative planar laser induced fluorescence (PLIF) measurements to study the evolution of a shocked heavy gas curtain. The authors measured two-dimensional velocity and density fluctuations for three different incident Mach numbers (1.21 , 1.36 , and 1.50) and a fixed initial perturbation. Fig. 10.17 shows the probability density functions (PDFs) for velocity fluctuations computed using the ensemble phase averaging for each Mach number. While there is anisotropy in the streamwise and spanwise components at the earliest times shown, the profiles of the two components are nearly identical indicating that the flow is developing isotropy at the latest times.

Prestridge stressed that initial conditions, shock Mach number, whether there is reshock or not, and time are all factors. The initial conditions strongly affect the time for transition to anisotropy, but also the incident Mach number affects

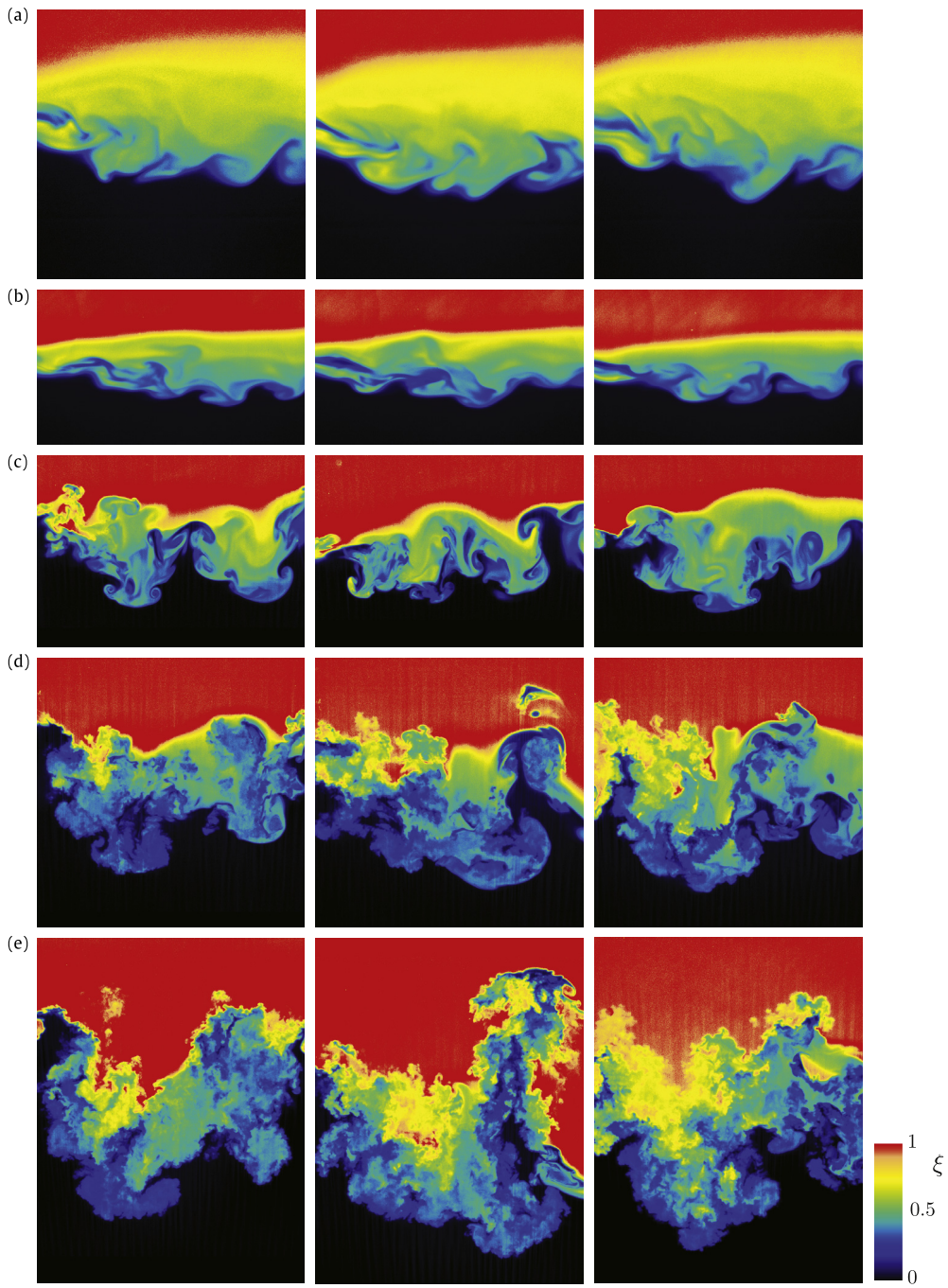


Fig. 10.11a. Selected images from Mach= 1.6 experimental sequence. First row: initial condition images. Second row: PS1, 0.14 ms after shock interaction. Third row: PS2, 0.88 ms after shock interaction. Fourth row: PS3, 2.16 ms after shock interaction. Fifth row: PS4, 3.84 ms after shock interaction. The width of each image is 14.0 cm.

Source: Fig. 3 of [Weber et al. \(2014a\)](#), *J. Fluid Mech.* with permission.

the mixing as well, in ways that are difficult to scale. The 2-D versus 3-D nature of the initial conditions is very important, as well.¹⁰ Youngs pointed out that as RM slows down with time, the width doubling time gets longer and longer and is

¹⁰ K.P. Prestridge (private communication, 2017). She pointed out one could certainly create an RM experiment that is anisotropic after reshock, e.g. with a high amplitude, single-mode, 2-D perturbation.

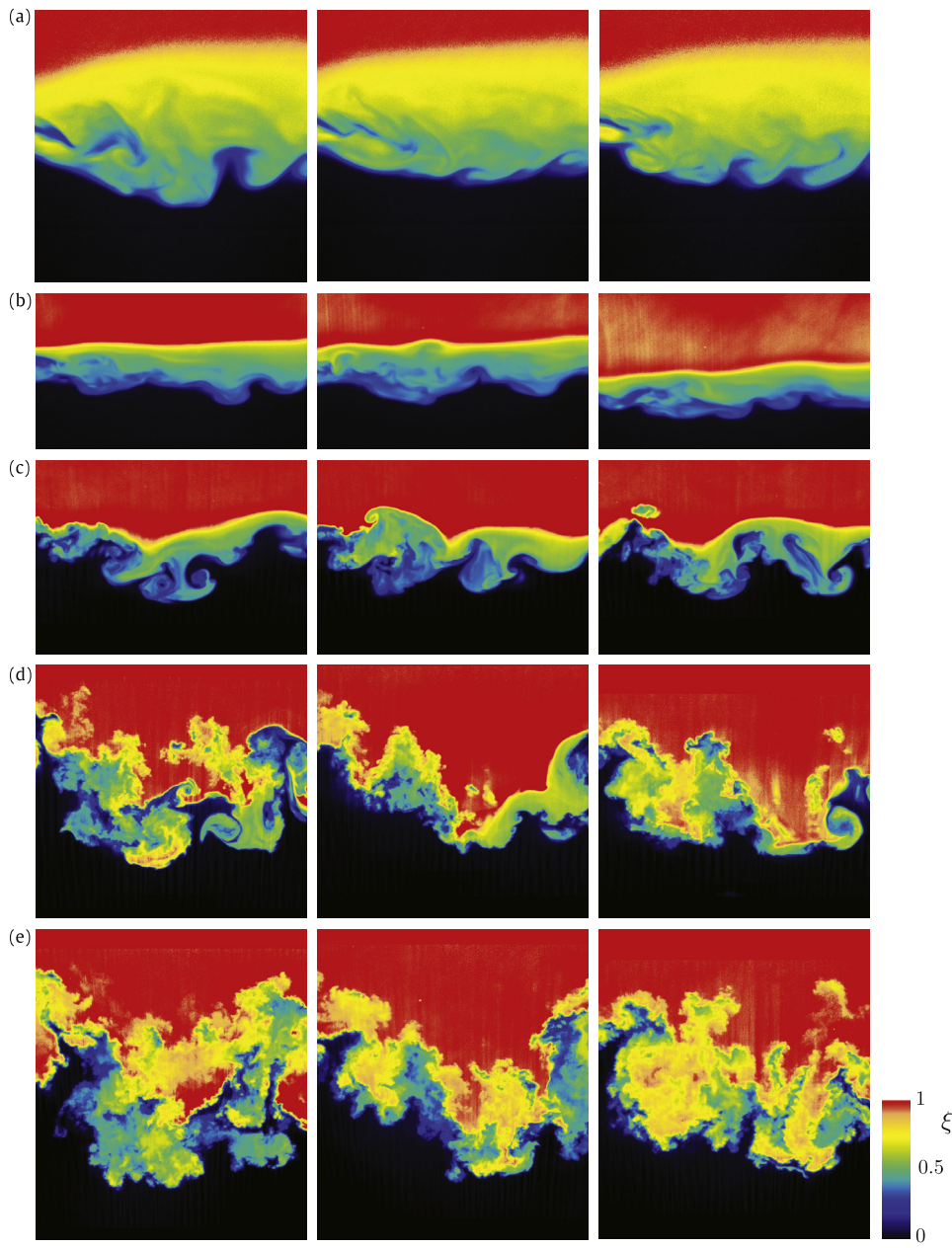


Fig. 10.11b. Selected images from Mach = 2.2 experimental sequence. First row: initial condition images. Second row: PS1, 0.10 ms after shock interaction. Third row: PS2, 0.44 ms after shock interaction. Fourth row: PS3, 1.12 ms after shock interaction. Fifth row: PS4, 2.05 ms after shock interaction. The width of each image is 14.0 cm.

Source: Fig. 4 of [Weber et al. \(2014a\)](#), *J. Fluid Mech.* with permission.

very difficult to run simulations far enough to get self-similarity – even more difficult to run experiments far enough. The differences in results can be attributed to the influence of initial conditions and to the difficulty in achieving sufficient time to establish self-similarity.¹¹

¹¹ D.L. Youngs (private communication, 2017). He doubted that Mach number effects are important.

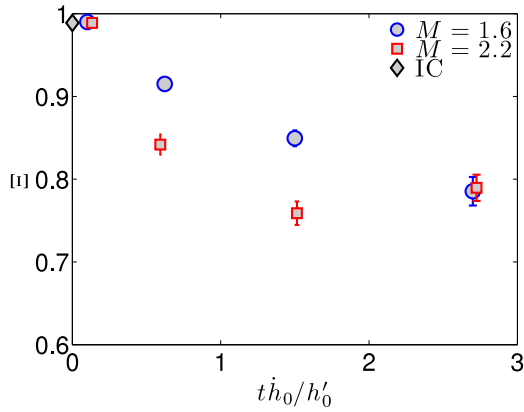


Fig. 10.12. Mixedness parameter vs. Mach numbers.
Source: Fig. 8, [Weber et al. \(2014a\)](#), *J. Fluid Mech.* with permission.

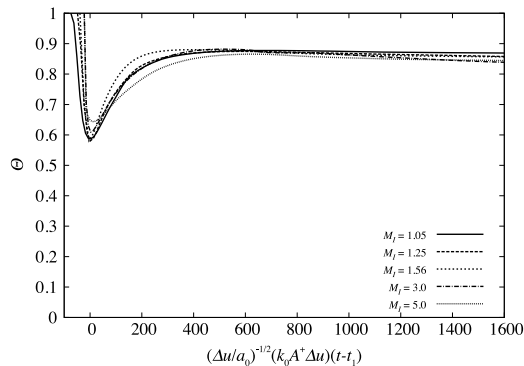


Fig. 10.13. Mixedness parameter, Θ , computed from LES of several Mach numbers.
Source: Fig. 17 of [Lombardini et al. \(2012\)](#), *J. Fluid Mech.* with permission.

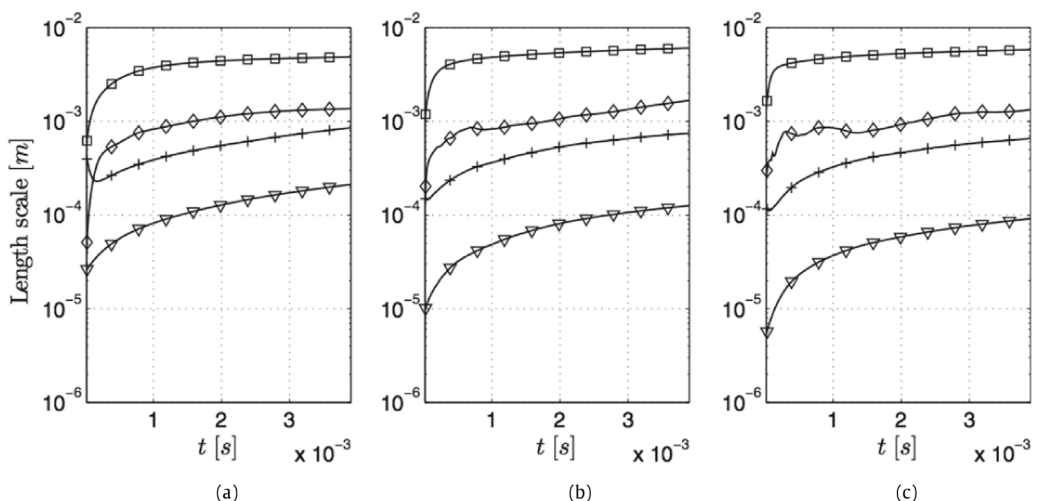


Fig. 10.14. Summary of length scales for Mach = 1.05 (a), Mach = 1.2 (b), and Mach = 1.5 (c). The solid lines with symbols represent the mixing zone width δ_x (squares), the integral length scale (diamonds), the Taylor microscale λ_T (plus), and the Kolmogorov length scale η (triangles).
Source: Fig. 8 of [Tritschler et al. \(2014c\)](#), *Phys. Rev. E*, with permission.

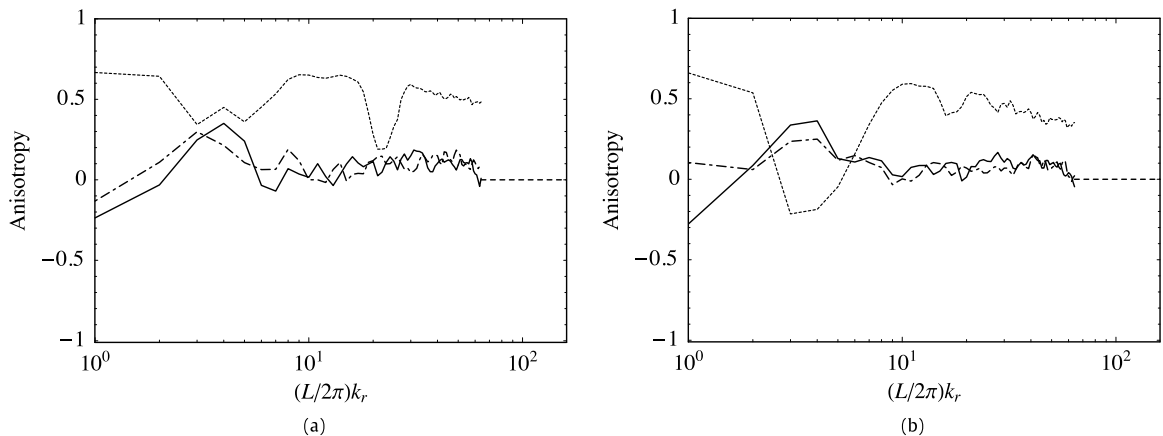


Fig. 10.15. Anisotropy measure of the velocity power spectra, at three different times, 10 (dotted line), 800 (dash-dotted line) and 1600 (solid line). Mach numbers = 1.05 (a) and 3.0 (b).

Source: Fig. 13 of Lombardini et al. (2012), *J. Fluid Mech.* with permission.

10.6. 2D vs 3D RMI induced flows

Several previous RMI studies have been performed in 2D (see for example Baltrusaitis et al., 1996; Dimonte and Ramaprabhu, 2010; Glendinning et al., 2003; Latini et al., 2007a,b; Marocchino et al., 2010; Mügler and Gauthier, 2000; Palekar et al., 2007; Piriz et al., 2008; Schilling et al., 2007; Welser-Sherrill et al., 2013).

Comparison of 2D and 3D RMI results illustrates the difference in 2D vs. 3D dynamics (Cohen et al., 2002). Fig. 10.18 shows a rendering of the entropy field for a 1024^2 two-dimensional simulation and for a vertical slice of the 1024^3 3D simulations. The contrast is evident: a predominantly fine-scale structure in the slice of the three-dimensional simulation (left panel) versus predominance of sizable structures with sharp edges in the two-dimensional results (right panel). Indeed, the 2D simulations are characterized by coalescence into structures comparable to or larger than the initial short-wavelength scale, while the 3D simulations evolve towards fine scales (Fig. 10.19); this is as one would expect from the predominance of inverse and forward cascades, respectively¹² (Kolmogorov, 1941; Batchelor, 1969; Kraichnan, 1967, 1971; Leith, 1968; Kraichnan and Montgomery, 1980).

Recently, the physics of the 2D inhomogeneous RM mixing layer has been explored through detailed simulations with carefully chosen and justified grid resolutions (Thornber and Zhou, 2015). For the broadband case, it becomes clear that the 2D flow is not going to converge to the 3D equivalent at late times, having a growth rate of $\theta = 0.625 \pm 0.005$. At the highest resolutions, the overall mix in the layer is decreasing in time towards $\mathcal{E}, \Theta \approx 0.3$. Some key differences are found such as faster growth rates and lower mix rates compared to 3D in the narrowband case. In this case, it is shown that the growth rate $\theta = 0.48$ in 2D, which is substantially higher than the 3D equivalent. The narrowband cases converge towards values of $\mathcal{E} \approx 0.64$ and $\Theta \approx 0.63$ and compared to the 3D values of $\mathcal{E} \approx 0.84$ and $\Theta \approx 0.84$. Mix in 2D is substantially lower than the 3D case as also observed in the RTI (Youngs, 1994; Cabot, 2006).

In addition, for the broadband case, the 2D simulations remain anisotropic ($TKX/TKY \sim 1.37$) while the narrowband case returns rapidly to isotropy. The spectra are very different, the 2D simulations showing a classical forward and inverse cascade in agreement with 2D homogeneous decaying turbulence (HDT) simulations.

11. RM Reshock

11.1. Physics of noted interest

Reshock occurs frequently at the ICF and astrophysical applications and there are intense efforts in experimental investigation of RMI with reshock in a laboratory setting. In many applications, multiple shockwaves pass through the mixing layer, for instance due to reflections from the center of a spherical capsule, thereby causing further enhanced mixing and destruction of the ordered velocity field. The reshocked mixing layer width deviates significantly from the singly shocked case, and the growth rate rises substantially (see for example Andronov et al., 1976, 1982; Bonazza and Sturtevant, 1996; Houas and Chemouni, 1996; Jourdan and Houas, 1996; Nikiforov et al., 1995; Erez et al., 2000).

Reshock deposits additional energy into a mixing zone formed by RM instability. It is likely that, at the time of reshock, the dominant scale will be comparable to the width of the mixing zone and this suggests that the initial post-reshock growth

¹² We see that the high- k value is negative for the former case and positive for the latter, consistent with the dominance of inverse cascade dynamics in two dimensions and forward cascade in three dimensions.

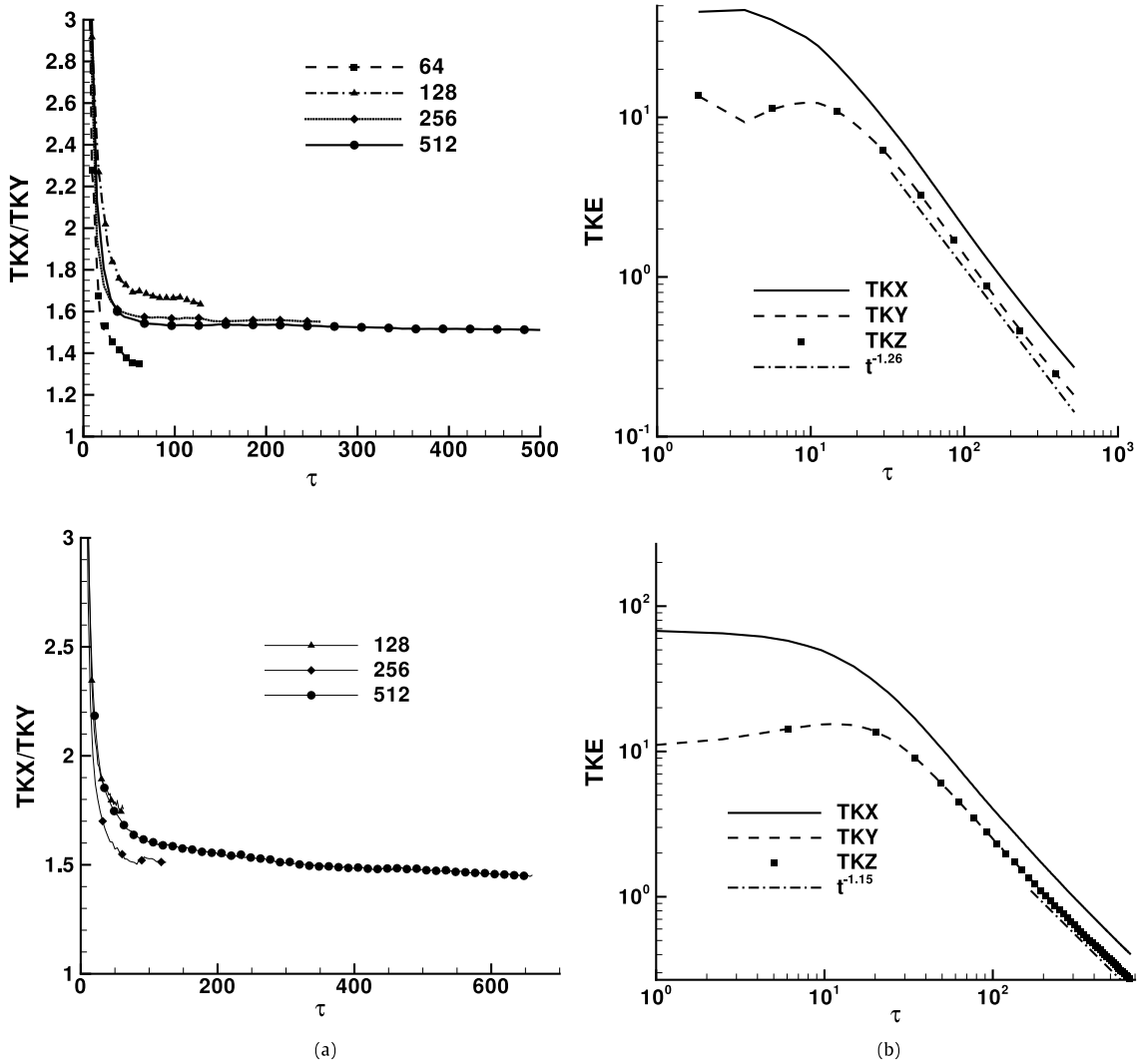


Fig. 10.16. Plots of x -, y - and z -directions total kinetic energy for the 512 cross-section $A^+ = 0.5$ and 0.9 narrowband simulation. Source: Figs. 10 and 18, [Thornber et al. \(2010\)](#), *J. Fluid Mech.* with permission.

should be approximated by the RM formula (Richtmyer, 1960; Mikaelian, 1989) with a high value of ka_0 thus giving a initial growth rate of

$$h = C_M A^+ \Delta V, \quad (11.1)$$

where the Atwood number takes its post-reshock value, ΔV is the velocity jump resulting from reshock, and C_M is a coefficient.

For the multimode case, as time proceeds, the mixing layer should then evolve towards a self-similar state with

$$h \sim t^\theta \quad (11.2)$$

as for the first shock, but possibly with a different value of θ . Non-linear models for representing this behavior are reviewed in Section 11.7.

Reshock experiments provide estimates of the coefficient C_M but as a rule do not reach the self-similar state for reshock RM. However, numerical simulations have been run to a later stage and have given estimates of reshock θ and properties of the self-similar state.

Significant advancement in the diagnostics has produced high quality data needed to understand the new physics and to provide important turbulent statistics to calibrate the mix models (see next section). For instance, [Tomkins et al. \(2013\)](#) and [Balasubramanian et al. \(2012\)](#) have measured the density self-correlation using the horizontal shock tube facility

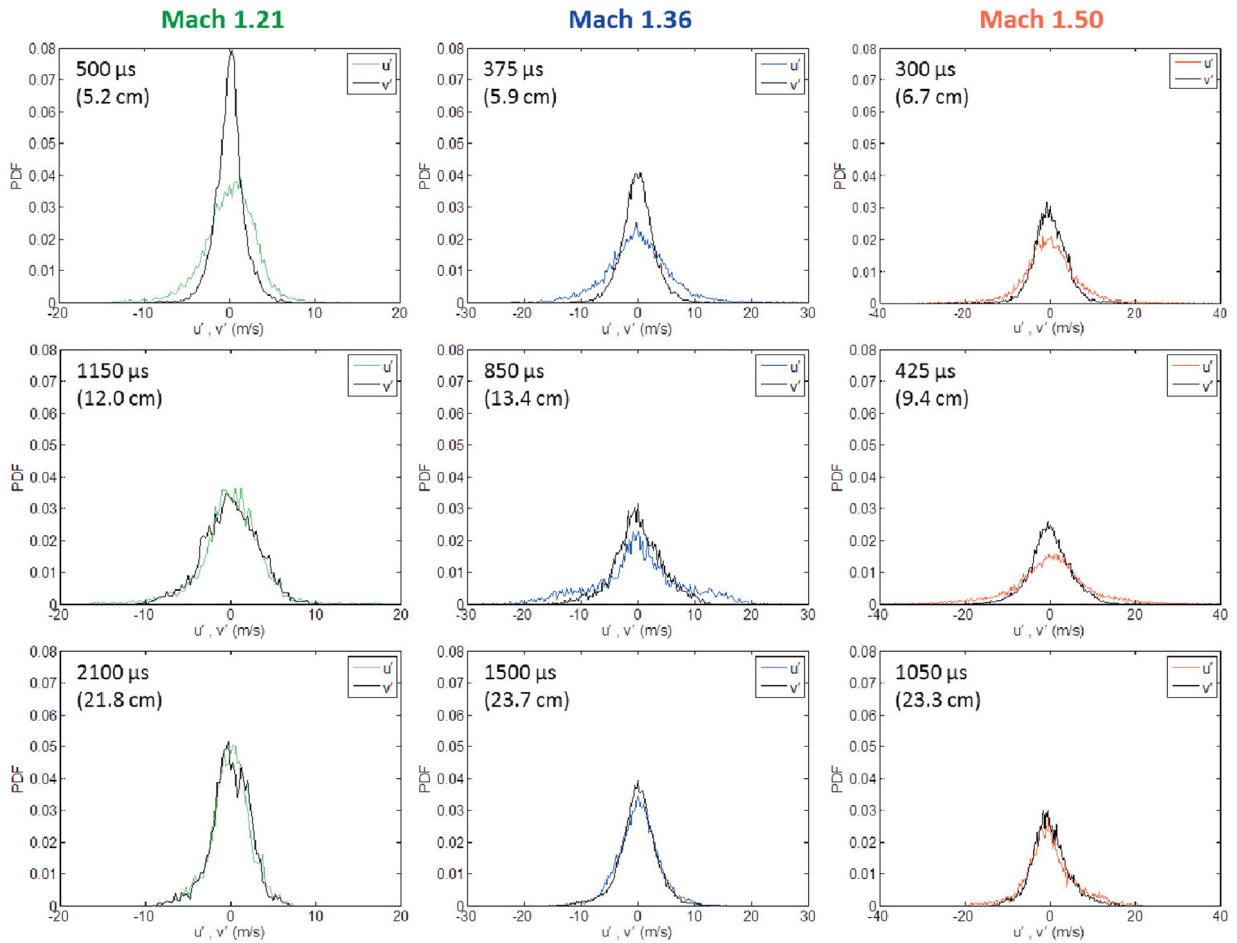


Fig. 10.17. PDFs for velocity fluctuations computed using the ensemble phase averaging for each Mach number.
Source: Fig. 5 of [Orlicz et al. \(2015a\)](#), *Phys. Fluids* with permission from AIP.

at LANL. [Balakumar et al. \(2012\)](#) have evaluated the Reynolds stress tensor and mass flux. [Balakumar et al. \(2008a, b\)](#) obtained simultaneous particle-image velocimetry–planar laser-induced fluorescence measurements in a gas curtain with and without reshock. Snapshots of the measurements obtained before and after reshock are shown in [Fig. 11.1a](#) (Figs. 12a and 12b of [Balakumar et al., 2008b](#)). Before the reshock, the highest SF₆ concentration is present in the roll-ups around the vortex cores. The ordered flow field is dramatically disturbed by the reshock wave. The change in the flow structure can be better understood by an examination of the vorticity fields. [Fig. 11.1a](#) shows a comparison of the vorticity fields before and after reshock. The presence of a row of counter-rotating vortices with bulk of the vorticity concentrated near the vortex cores is evident. Upon reshock, one would expect the baroclinic deposition of smaller scale vorticity throughout the structure, as suggested by the complex distribution of density gradients. Indeed, the ordered vorticity present gets redistributed throughout the reshocked structure and the spanwise symmetry is also not easily evident, suggesting an enhanced and evolving state of mixing after reshock.

By looking at the PIV–PLIF fields of the evolving curtain immediately after reshock, [Balakumar et al. \(2012\)](#) provided new insights on how the enhanced mixing after reshock could be understood. The experiments were conducted on a varicose SF₆ fluid layer (heavy fluid) interposed in air (light fluid) inside a LANL horizontal shock tube at an incident Mach number of 1.21 and a reflected reshock Mach number of 1.14. Unlike the pre-reshock case, which is driven by a row of approximately equispaced counter-rotating vortices, the post-reshock flow is driven by two rows of counter-rotating vortices arranged as shown in [Fig. 11.1b](#). This latter arrangement is unstable, and therefore small perturbations after reshock would result in the dislocation of the vortices. Thus, in the post-reshock case, mixing is probably driven both by vortex-induced fluid motion and by the motion of the vortices themselves, resulting in a faster transition to a turbulent state when compared to the single shocked case ([Balakumar et al., 2012](#)).

[Thornber et al. \(2011\)](#) showed the variable density turbulent kinetic energy spectra for the narrowband and broadband perturbations prior to reshock, just after reshock, and at late time. It is clear from [Fig. 11.2](#) that there is a very strong

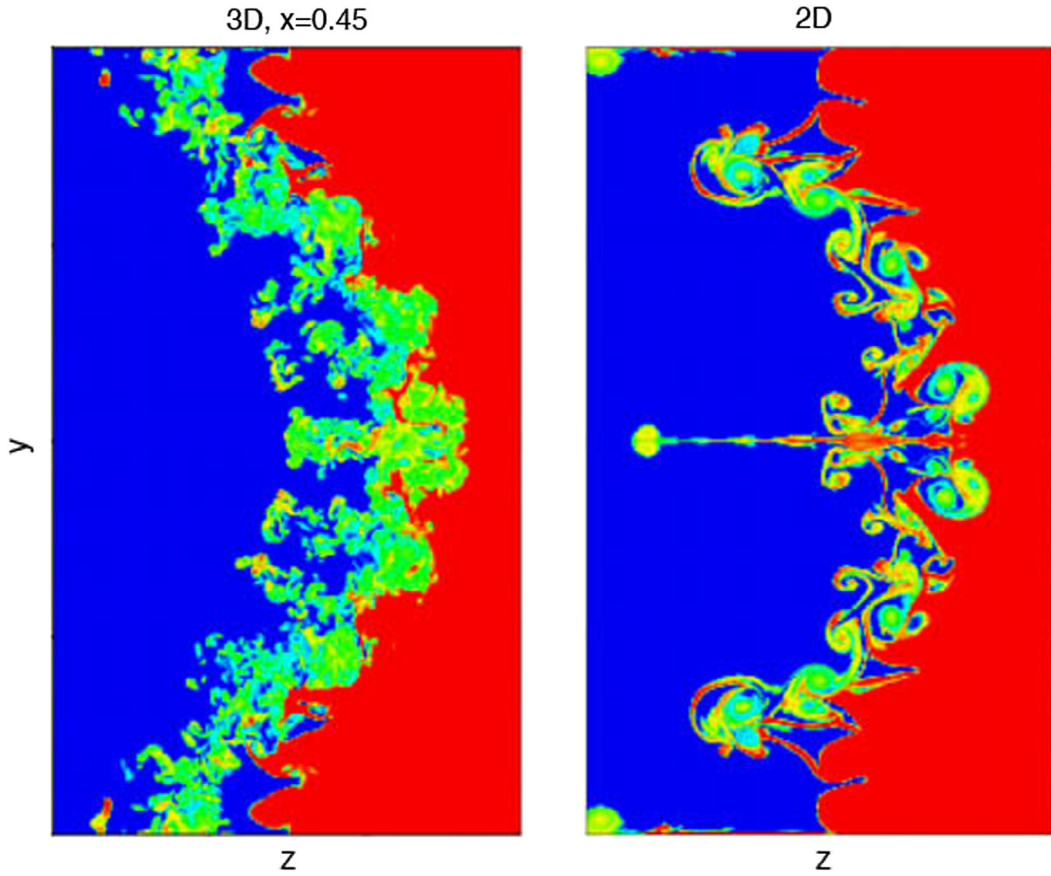


Fig. 10.18. Entropy from a slice of 3D simulation, at $t = 9$ (left) versus two-dimensional simulation (right).
Source: Fig. 11 of Cohen et al. (2002), *Phys. Fluids*.

amplification of over one order of magnitude in kinetic energy for all modes. The amplification for the narrowband case, however, is more pronounced than in the broadband case. Also, immediately following reshock (where the shock has moved fully clear of the layer) there is a Kolmogorov $k^{-5/3}$ range present in the spectrum, however at the latest time where self-similarity is achieved the spectrum has returned to a $k^{-3/2}$ scaling of Zhou (2001).

Fig. 11.3a (Fig. 14 of Tritschler et al., 2014b) shows the energy spectra before and after reshock, with a self-similar scaling of the Zhou (2001) $-3/2$ spectrum. It should be noted that the destruction of the vortical structures initiated by the reshock leads to the formation of small scales, which rapidly remove the memory of the initial condition at the large-scales (Tritschler et al., 2014b). Fig. 11.3b shows the transition process predicted by the reference grid with a resolution of 512 cells in the transverse directions.

In a seminal paper, Vetter and Sturtevant (1995) of California Institute of Technology (Caltech) performed a series of shock-tube experiments with various combinations of orientation of the high- and low-density gases (SF_6 and air), the shock direction, and the positions of the membrane and the wire mesh. This work has not only provided key data for calibrating practical models (see next section), but also offered some significant insights. It is found that the thin membrane, which forms the plane interface initially, has a non-negligible influence on the initial growth rate of the interface thickness. Furthermore, the measured growth rates after the first reflected shock are independent of membrane configuration (Fig. 11.4a) and are in good agreement with analytical predictions.

Motivated by these findings, the growth rate dependence on the strength of the reshock (e.g., Leinov et al., 2008, 2009) and the “initial condition” of the interface at the time of reshock (e.g., Balasubramanian et al., 2012; Leinov et al., 2009) has been studied intensively. Also, several works have attempted to learn more about the growth behavior of the RMI by performing experiments with well defined initial conditions without using any membranes (Jacobs et al., 2013).

The Commissariat à l'Energie Atomique experiments (Poggi, 1997; Poggi et al., 1998) can be found frequently in the experimental testing suite of the model developers. In experiments performed in the vertical shock-tube, a discontinuous heavy-light interface between hexafluoride (SF_6) and air was impulsively accelerated by an incident upward shock wave (shock strength 0.54, Mach number = 1.45) and decelerated by several reflected shock waves (from the shock tube end wall) with decreasing strength (0.38 for the first reflected shock, 0.15 for the second one). Poggi et al. (1998) obtained the Laser

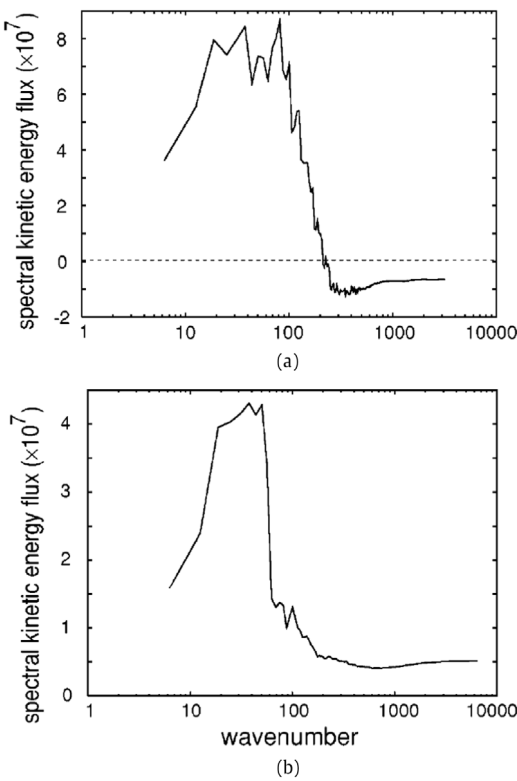


Fig. 10.19. Spectral flux in two-dimensional simulation (a) versus 3D simulation (b), both for 1024^3 resolution at t59.
Source: Fig. 13 of Cohen et al. (2002), *Phys. Fluids*.

Doppler anemometry measurements, such as the evolution of the axial velocity fluctuations of the mixing zone, before and after its interactions with reshocks. Fig. 11.4b shows the temporal evolution of the mixed widths (Müller and Gauthier, 2000) from the CEA experiments (Poggi, 1997; Poggi et al., 1998). The error bars of this visual measurement are about $\pm 10\%$.

The recent work of Griffond et al. (2017), especially that of their Figs. 3 and 5 (not shown), is a vivid reminder of the persistence of uncertainty alongside other challenges to measuring the mixing zone width experimentally. The authors performed Mach 1.2 reshocked experiments in the vertical shock tube located at ISAE, Université de Toulouse, France. The air and SF₆ gasses are initially separated by a 0.5-micron thick nitrocellulose membrane maintained parallel to the shock front by two wire grids. The Schlieren images are post-processed in two schemes to detect the boundaries of the mixing region between the two fluids and calculate the turbulence mixing layer width. The second filter performed additional step by subtracting the static uniform background color of the raw images. As described by Griffond et al., Filter 1 gives access to the core of the mixing region corresponding to the dark band visible on the images, where the nitrocellulosic membrane fragments were generated after the passage of the shock wave across the interface are concentrated. Filter 2 provides a wider mixed width that includes the white strips that can be observed near the edges of the mixing region. The choice of the detection filter thus leads to significant discrepancy in the measured mixing layer width, but trends regarding the growth of the mixing width and its dependencies are consistent between filters.

RMI in dilute gas-particle mixtures is also investigated both before and after reshock for a variety of initialization conditions in 2D (Ukai et al., 2010) and 3D (Schulz et al., 2013) simulations. Olson and Greenough (2014) compared 2D and 3D reshocked RMI flows with LES. The problem setup, including the mixture equation of state, is identical to that of Tritschler et al. (2014b). A Mach 1.5 shockwave is initialized 5 cm ahead of an interface of air and SF₆ system with multimode perturbations. The interface is initialized 40 cm from an adiabatic wall, from which the shock is reflected right before it reshocks the interface. As illustrated in Fig. 11.5a, large 2D structures nearly encompass the entire width of the image. While early time behavior is consistent with the calculations performed by Ukai et al. (2011) and nonlinear theory of Zhang and Sohn (1996), the mixed width in late time differs from that of Ukai et al., which did not find that the 2D flow grew more rapidly than 3D (Fig. 11.5b). Olson and Greenough (2014) suggested that the difference may be due to differences in initial conditions or perhaps a dependency on the simulation box size.

Using LES, Schulz et al. (2013) found that the presence of particles introduces a continuous drag on the gas-phase resulting in a delay in the time at which reshock occurs. This delay is observed to be as much as 6% and is largest for higher initial mass loadings as well as smaller particle radii. This effect results in a corresponding effect on both the final width of the mixing layer and the growth-rate of the mixing-layer after reshock.

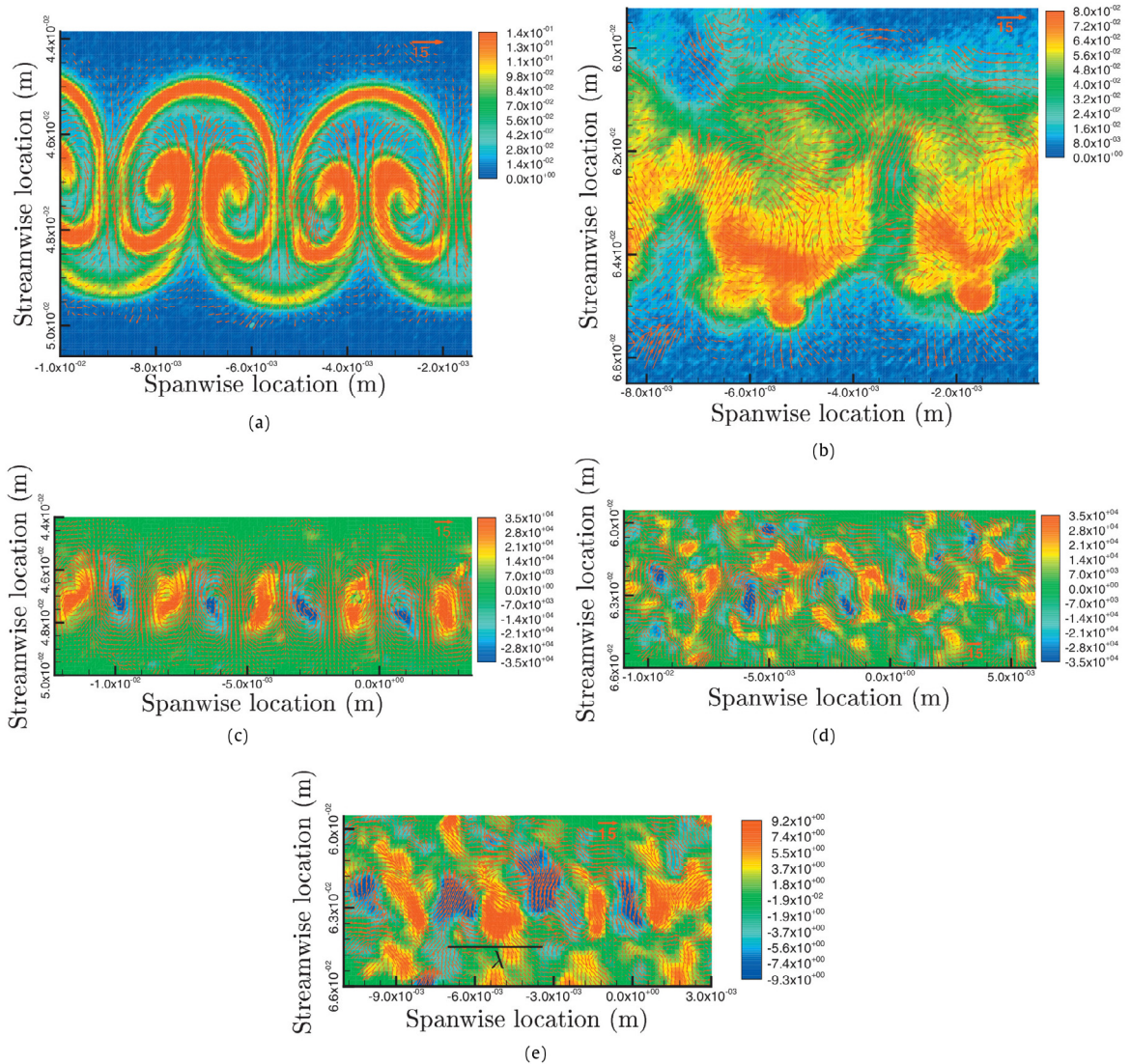


Fig. 11.1a. (a) and (b) Simultaneous PIV–PLIF snapshots showing concentration contours and fluctuating velocity vectors (a) at $t = 465 \mu s$ after first shock and (b) after reshock at $t = 665 \mu s$. (c) and (d) Fluctuating velocity vector fields superimposed on vorticity contours showing the redistribution of vorticity after reshock. The images were taken at (a) $t = 465 \mu s$ after first shock and (b) at $t = 665 \mu s$ when reshock has occurred. (e) Contour plot of the fluctuating streamwise velocity showing the presence of modes of the size of the primary wavelength at $t = 665 \mu s$. The vectors represent the fluctuating velocity. The solid line represents one primary wavelength.

Source: Fig. 12 of Balakumar et al., *Phys. Fluids*, 2008b, with the permission of AIP Publishing.

11.2. Initial condition

The question of the influence of initial conditions is more complicated for the reshock RMI. One needs to address separately two distinct cases so that the evolving mixing layer after the reshock can be evaluated. First, the initial configurations of the RMI at the time of the first shock are different, but otherwise the timing and strength of the reshock waves are the same. Second, differing states of initial conditions are generated specifically by manipulating the timing and/or the Mach numbers of the reshock.

11.2.1. Initial conditions at the time of 1st shock

In their experimental and numerical studies, McFarland et al. (2014a, b) noted that the inclined interface is membraneless, planar, and rests at an angle to the incident shock front. The advantage of this setting is a simple, easily quantified interface that can be generated with the initial vorticity deposition constant across the interface and easily predicted using the vorticity equation. Using a staggered mesh arbitrary Lagrange Eulerian (ALE) hydrodynamics code developed at LLNL, the authors

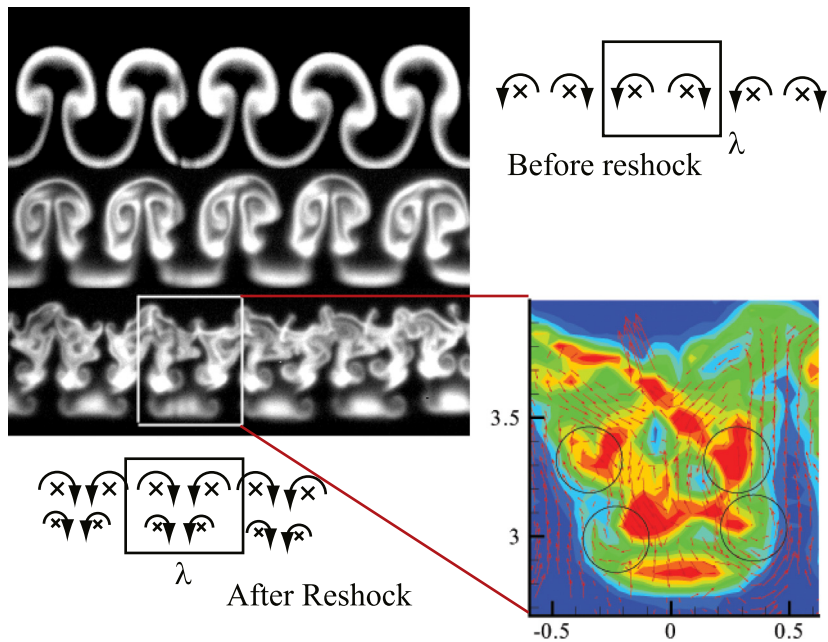


Fig. 11.1b. Simultaneous PIV–PLIF field showing multiple interacting vortices immediately after reshock.
Source: Fig. 4 of [Balakumar et al. \(2012\)](#), *J. Fluid Mech.* with permission.

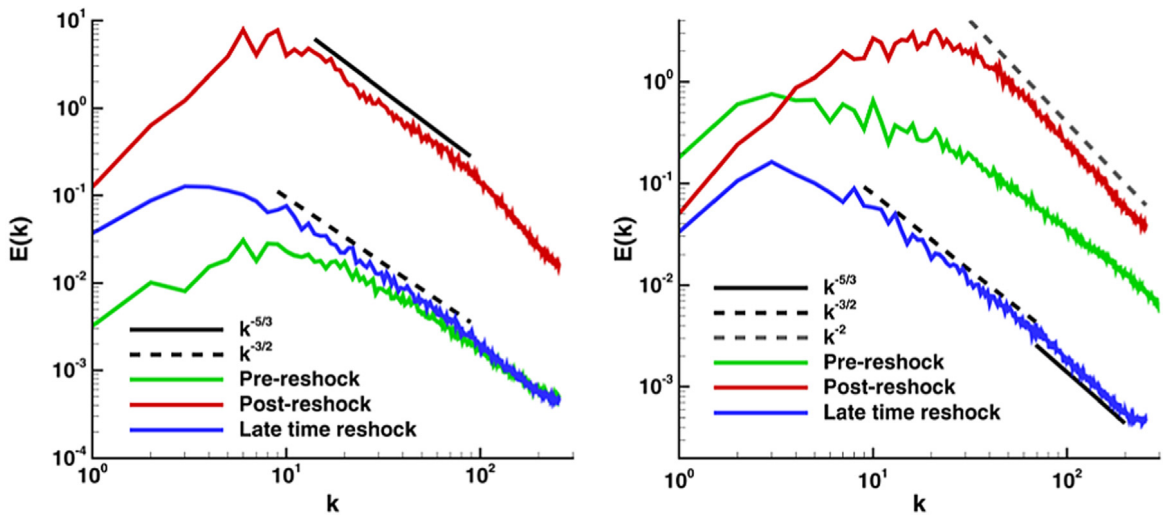


Fig. 11.2. Evolution of the kinetic energy spectra for the narrowband (left) and broadband case (right) during reshock and at late time.
Source: Fig. 15 of [Thornber et al.](#), *Phys. Fluids*, 2011, with the permission of AIP Publishing.

found that the vorticity deposited by the incident shock is initially negative but the vorticity deposited by the reshock reversed the direction of circulation to positive. The number of vortices is increased greatly in the flow field initially after the reshock, and subsequently these vortices merged and were reduced in strength at late times. [Hahn et al. \(2011\)](#) also studied the flow physics associated with the passage of a shock wave, including reshocked flow, through an inclined material interface with perturbations of two different spectra but with same variance. The case is based on the inverse chevron experiment of [Holder and Barton \(2004\)](#).

The investigation of the ICs in a planar geometry has attracted more attention because of its simplicity. [Weber et al. \(2012b\)](#) carried out the reshock experiments with six different initial amplitudes. These experiments run through relatively short time after the passage of the reshock. Consistent with the finding of [Vetter and Sturtevant \(1995\)](#), [Erez et al. \(2000\)](#)

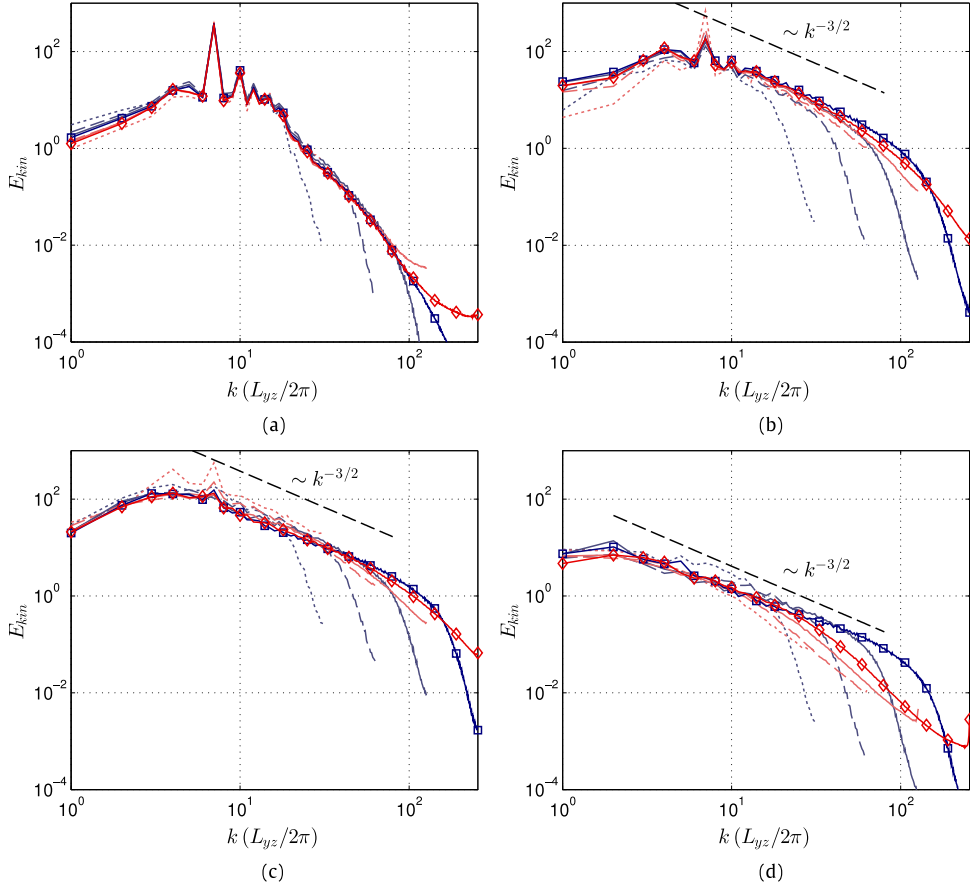


Fig. 11.3a. Spectra of TKE from Miranda (dark gray; blue online) and INCA (light gray; red online) before reshock at (a) $t = 0.5$ ms and (b) $t = 2$ ms and after reshock at (c) $t = 2.5$ ms and (d) $t = 6$ ms. The different resolutions are represented as dotted line (64), dashed line (128), solid line (256) and solid line with open squares for Miranda and open diamonds for INCA (512).

Source: Fig. 14 of Tritschler et al. (2014b), *J. Fluid Mech.* with permission.

Table 11.1

The initial amplitude and wavelength of two distinctive groups employed by Jacobs et al. (2013).

Source: Table 2, 2013, Jacobs et al., *Shock Waves*, with permission.

Group	λ_{min}	λ_{ave}	λ_{max}	a_{min}	a_{ave}	a_{max}
1	3.2	4.4	6.4	1.6	1.9	2.1
2	2.9	4.5	7.6	1.3	2.0	3.2

found that the initial membrane thickness affects the growth rate after the incident shock, but does not influence the post-reshock growth rate.

Jacobs et al. (2013) reported a reshock experiment with an air/SF₆ gas combination with a $Mach = 1.2$ incident shock wave. Initial perturbations of the interface are created by vertically oscillating the gas column within the shock tube to produce Faraday waves on the interface, resulting in a short 3D wavelength perturbation. The experiments were designed so the initial conditions were introduced into two distinct ways. Table 11.1 (reproduced from Table 2 of Jacobs et al., 2013) documented the values of experimentally measured initial amplitudes and wavelengths (obtained by finding average values for each experiment). Groups 1 and 2 correspond to the experiments in the upper and lower plots of Fig. 11.6 (Fig. 7 of Jacobs et al.), respectively. The measurements of the mixed width prior to reshock suggested two growth behaviors, both having power law growth. The differences in the growth behavior are most likely caused by differences in the initial perturbation at the arrival time of the first shock. Following reshock, significantly more consistent growth behavior is found as can be seen in the figure. In this case, both sets of experiments show linear growth with identical values of growth rate of $dh/dt = 9.26$ m/s.

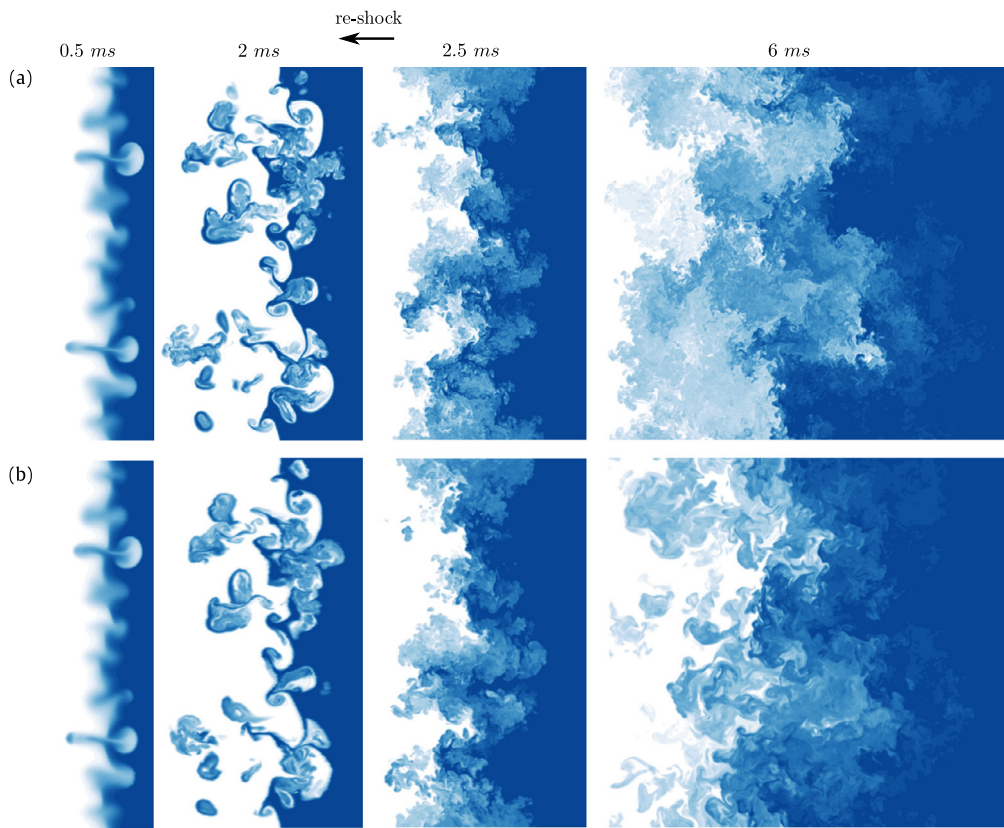


Fig. 11.3b. Color-coded plots of species mass fraction of SF₆ gas from (a) Miranda and (b) INCA at various times where data are taken from the finest grid. The contours range from 0.05 (white) to 0.75 (dark gray; blue online).

Source: Fig. 5 of Tritschler et al. (2014b), *J. Fluid Mech.* with permission.

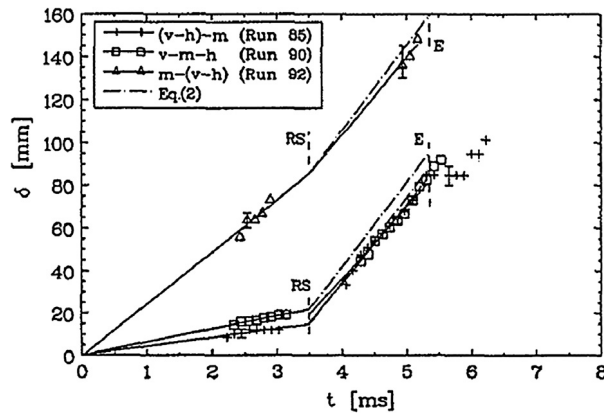


Fig. 11.4a. Time evolution of the thickness of the TMZ for the plane discontinuous interface between air and SF₆; results from high-speed motion pictures; Mach = 1.5; the legend shows the wire mesh-membrane arrangement between air and SF₆: Run 85 (v-h-m); Run 90 (v-m-h), and Run 92 (m-v-h); v-vertical wire mesh; h-horizontal wire mesh, m-membrane. (The lines are obtained by performing least - squares fit). RS: reflected shock; E: expansion.

Source: Fig. 8 of Vetter and Sturtevant (1995), *Shock Waves* with permission.

Nevertheless, Griffond et al. (2017) reported a weak dependence of the mixing zone growth rate after reshock with respect to the length of the chamber. Changing the initial condition using different mesh spacings did not change the pre and post-reshock mixing layer width, but a clear imprint of the mesh spacing is observed in the Schlieren images.

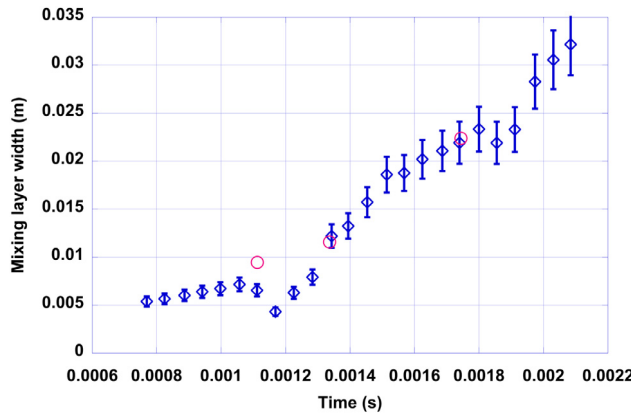


Fig. 11.4b. Evolution of the mixing-zone width vs. time from the CEA experiments (Poggi, 1997; Poggi et al., 1998). Diamonds correspond to the experimental width measured from Schlieren pictures. The error bars of this visual measurement are equal to $\pm 10\%$. The three small circles correspond to microdensitometry measurements of some Schlieren pictures.

Source: Fig. 2 of Mügler and Gauthier (2000), *Phys. Fluids*, with the permission of AIP Publishing.

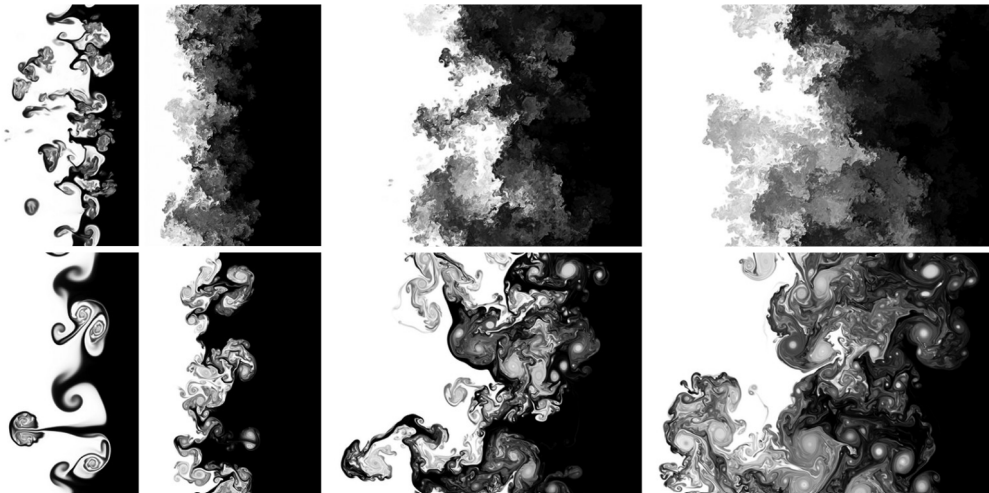


Fig. 11.5a. Contours of the mass fraction of SF_6 from white (0.0) to black (0.8) in 3D (top) and 2D (bottom) showing the qualitative difference. Temporal evolution is from left to right for times $t = 2.0, 2.5, 4.0, 6.0$ ms. Reshock occurs at $t = 2.1$ ms and first shock at $t \approx .05$ ms.

Source: Fig. 1 of Olson and Greenough (2014), *Phys. Fluids*, with the permission of AIP Publishing.

Using ILES, Nelson and Grinstein (2015) focused on the number of spectral modes over a given wave number band, applied to the two material interfaces as ICs (namely, the effect of the initial spectral density of the perturbations). When the initial spectral density of perturbations is dense, the flow is much more readily adapted to provide the needed turbulent cascade to small scales. If the initial spectral density of interface perturbations is sparse, however, additional time is needed for the turbulent cascade to populate the spectral modes needed for the establishment of an inertial range, (see also Grinstein et al., 2011).

11.2.2. Initial conditions at the time of reshock

Reilly et al. (2015) investigated the effects of both the reshock interaction time and vortex scales and distribution on the development of the inclined-interface Richtmyer–Meshkov instability. The developing interface of the inclined-interface RMI was reshocked at three different stages of development.

Balasubramanian et al. (2012) reshocked the evolving interface induced by the first incident shock ($Mach = 1.2$) at various times. With a movable wall, the amplitude and wavelength of perturbations could be changed simultaneously. A single mode, membrane-free varicose heavy gas curtain (air– SF_6 –air) was used and the density (concentration) and velocity fields were collected using planar laser-induced fluorescence (PLIF) and particle image velocimetry (PIV). These experiments provided the experimental databases for Gowardhan and Grinstein (2011) and Shankar and Lele (2014) to compare and validate their numerical simulation.

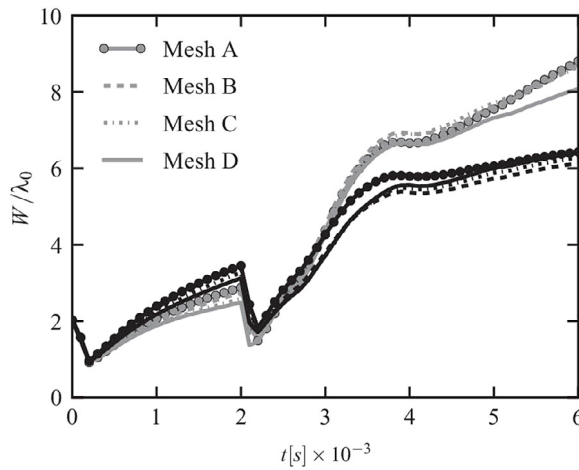


Fig. 11.5b. Mixing widths vs. time in 2D (gray) and 3D (black) for the RMI with reshock at various resolutions.
Source: Fig. 2a of [Olson and Greenough \(2014\)](#), *Phys. Fluids*, with the permission of AIP Publishing.

Table 11.2

Mixing zone widths at the various times of reshock arrival (resulted by changing the end wall distance).

Source: Table 1 of Leinov.

Endwall distance (mm)	Width of the mixing zone at the reshock arrival (mm)	Growth rate of the mixing zone following the reshock (m/s)
80	4.3 ± 0.7	23.1 ± 1.0
98	5.0 ± 0.7	23.0 ± 1.0
131	5.5 ± 0.7	21.8 ± 1.0
172	6.7 ± 0.7	23.0 ± 1.0
199	6.2 ± 0.7	24.3 ± 1.0
235	6.3 ± 0.7	23.8 ± 1.0

More specifically, [Balasubramanian et al. \(2012\)](#) carried out the experiments at the following three reshock times (denoted as t_{RS}): (a) $t_{RS} = 90 \mu\text{s}$, (b) $t_{RS} = 170 \mu\text{s}$, and (c) $t_{RS} = 385 \mu\text{s}$. The evolution of the concentration fields obtained using PLIF showed that reshocking an interface with late time (representing steeper density gradients) causes the late-time structures to mix and transition to smaller scales at a faster rate ([Fig. 11.7a](#)). This observation becomes obvious by looking at the power spectrum collected from at the center of mass of the late-time structures ([Fig. 11.7b](#), from Fig. 7 of Balasubramanian et al.) provided by these different reshock times. For a case of late reshocked interface with $t_{RS} = 385 \mu\text{s}$, the spectrum has shown more smaller scales at the expense of losing significant features at the primary wavelength. For the cases of the early reshocked interface at $t_{RS} = 90 \mu\text{s}$ and $170 \mu\text{s}$, however, the dominant wavelength is preserved with some small length-scales, and a transition to a well-mixed state is not evident.

In a comprehensive study, [Leinov et al. \(2009\)](#) investigated the evolution of the RM instability following the passage of the shock wave reflected from the test-section end wall. To make the results of the numerical simulation to agree with the experimental results, [Malamud et al. \(2014a\)](#) inspected the results of their simulations with two distinctive initial perturbation profiles ([Fig. 11.8](#)). For all end-wall positions and shock Mach numbers, it was determined that this could be achieved only when the initial perturbation was chosen to be a multi-mode one with a wide enough size. [Wang et al. \(2009\)](#) also simulated the experiments of [Leinov et al. \(2009\)](#) with two initial perturbations.

[Leinov et al. \(2009\)](#) reported that the mixing zones have reached different widths prior to the arrival of the corresponding reshocks. It is also clear that the growth rates are found to be nearly identical for all six locations of the endwall distances ([Fig. 11.9](#) and [Table 11.2](#)).

11.3. Mixedness and normalized mixed mass

It is highly desirable to understand how the reshock impacts the mixedness of the flows. In an effort to delineate the initial condition dependence, [Thornber et al. \(2011\)](#) studied the behavior of a reshocked mixing layer formed initially from a shock interacting with both broadband and narrowband perturbations. The broadband mixing layer prior to the reshock had very low values of the mixing parameters of $\Theta \approx 0.37$ and $\Xi \approx 0.38$, respectively. After reshock the mix levels increase significantly and both Θ and Ξ reached 0.7 at the end of the simulations.

Using two resolved LES with two different and independently developed numerical methods, [Tritschler et al. \(2014b\)](#) carried out a detailed investigation on the RMI with reshock evolving from a deterministic multimode planar interface. In

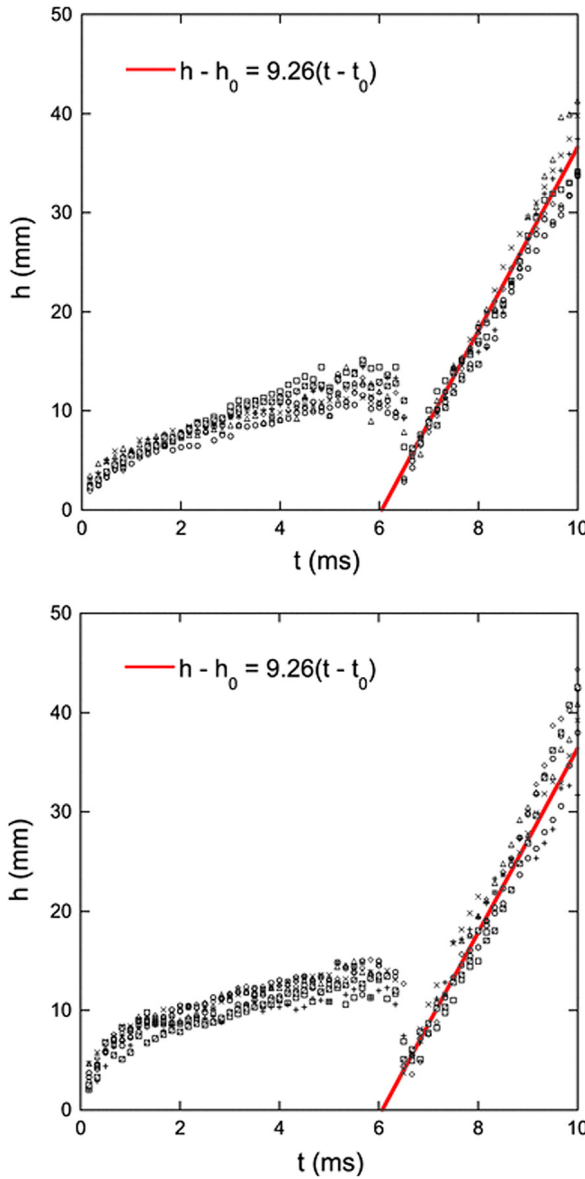


Fig. 11.6. The mixing zone growth versus the time for two different sets of initial conditions.
Source: Fig. 7 of Jacobs et al. (2013), Shock Waves, with permission.

particular, Miranda code (Cook and Cabot, 2004) includes models of physical diffusion and viscosity and uses 10th-order spatial accuracy with a fixed Eulerian mesh more suited to modeling the effects of turbulence and mixing. The instability is initiated by a shock wave with Mach number $Mach = 1.5$ and the simulation terminates at $t = 6.0$ ms, which is well beyond the occurrence of reshock at $t \approx 2$ ms. The prescribed initial conditions define a deterministic multimode interface perturbation between the gases (air and SF₆ plus acetone). As illustrated in Fig. 11.10, the mixedness parameter, Θ , starts with 1 but as bubbles of light air and spikes of heavy gas begin to interfuse, the initially mixed interface between the fluids steepens and the fluids become more segregated on the molecular level. Θ reaches its minimum at $t \approx 1.3$ ms before Kelvin-Helmholtz instabilities lead to an increase of molecular mixing. After reshock molecular mixing is strongly enhanced and reaches its maximum of 0.85 by the end of the simulation. These mixedness values are slightly higher than that found in Thornber et al. (2011).

For the narrowband simulation, the asymptotic values of the mixedness parameters are $\Theta \approx 0.78 \pm 0.02$ and $\Xi \approx 0.81 \pm 0.02$ after the reshock (Thornber et al., 2011; Zhou et al., 2016). The reshock mixed width increases significantly faster than its single shocked counterpart, even if the Atwood number $A = 0.5$ is the same (Fig. 11.11a). However, the normalized mixed mass Ψ (Fig. 11.11b) achieves a late-time value of 0.78 instead of 0.80 in the single shocked case. Note

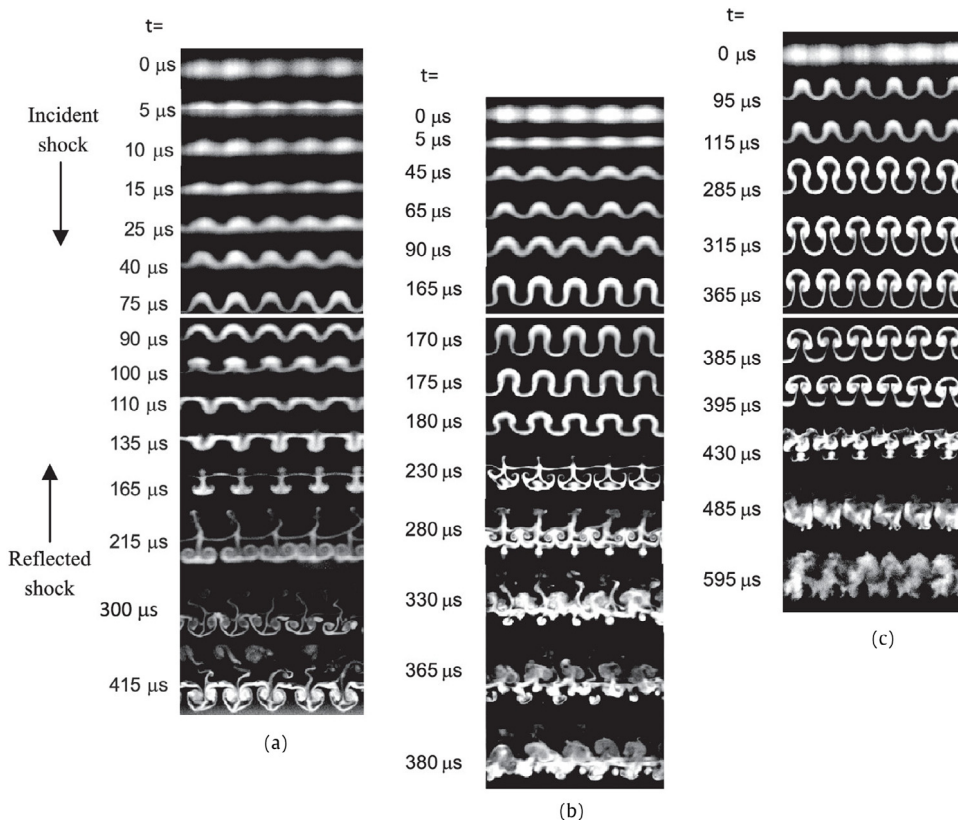


Fig. 11.7a. Three different sets of experiments, each beginning with the varicose gas curtain (top), shocked with a Mach = 1.2 shock that travels downward. Each experiment is then reshocked at a different time, as indicated below the white bar crossing the time series. Reshock occurs at time, $t = t_{RS}$ = (a) 90 μs , (b) 170 μs , and (c) 385 μs . At late times after reshock, approximately $t^* = 210 \mu s$, the large variation in mixing that occurs for each of the three cases is visible.

Source: Fig. 6 of Balasubramanian et al. (2012), *Phys. Fluids*, with the permission of AIP Publishing.

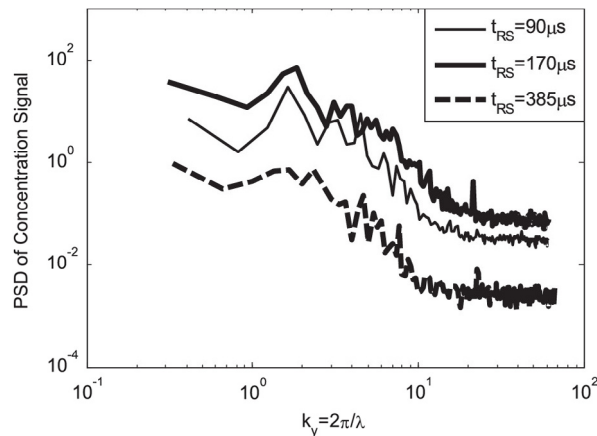


Fig. 11.7b. Power spectral density of the concentration signal for late-time flow structure after reshock at $t^* = 210 \mu s$ for three different reshock experiments (different reshock times).

Source: Fig. 7 Balasubramanian et al. (2012), *Phys. Fluids*, with the permission of AIP Publishing.

that the peak at very early times (time $\ll 1$) is caused by the inversion of the mixing layer. This result indicates that the evolution of the normalized mixed mass is dictated by the density disparity of the flows, instead of reshock (Zhou et al., 2016).

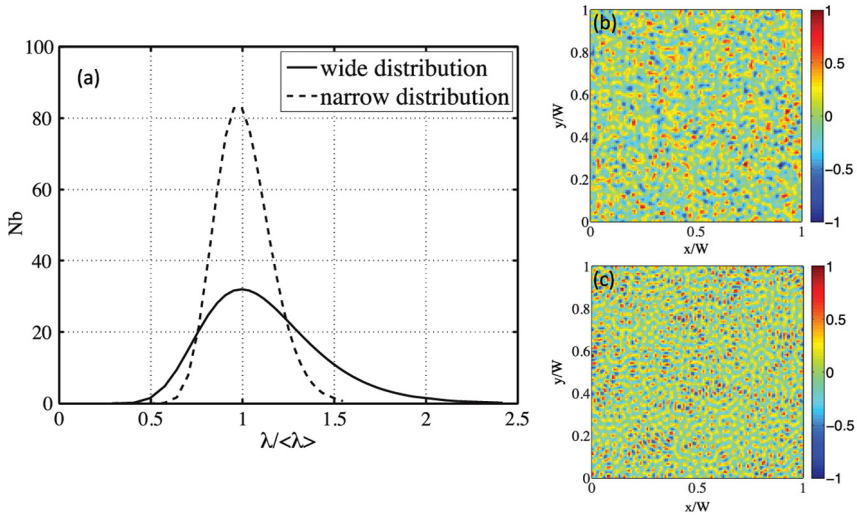


Fig. 11.8. The initial number of bubbles vs. normalized wavelength (a), and the initial interface between the air and SF₆ in arbitrary units, for the wide (b) and narrow (c) initial distributions used in the numerical simulations.

Source: Fig. 5 of Malamud et al. (2014a), *Phys. Fluids*, with the permission of AIP Publishing.

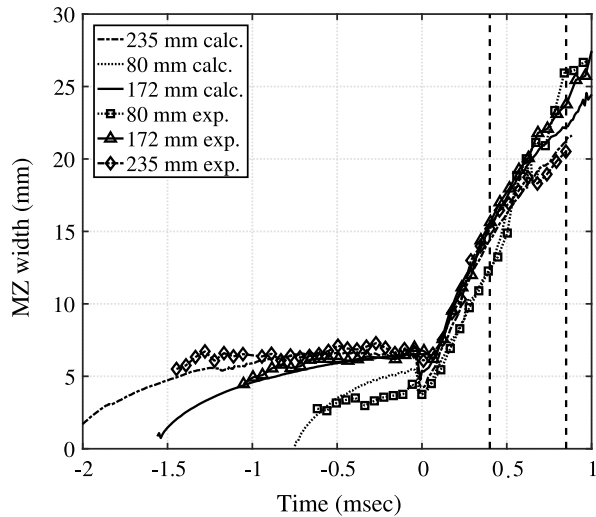


Fig. 11.9. Mixing zone width as a function of shifted time, endwall at 80, 172 and 235 mm. Experiments (-□-, -△-, -◇- respectively) and multi-mode DNS calculations (dotted, solid and dash-dot lines, respectively). Vertical dashed lines represent the rarefaction wave arrival time in the 80 and 172 mm cases.

Source: Fig. 9 of Leinov et al. (2009), *J. Fluids Mech.*, with permission.

Grinstein et al. (2013) showed instantaneous isosurfaces of the local mixedness function Θ for the planar shock-tube experiments of Vetter and Sturtevant (1995) (Fig. 11.12). The air-SF₆ interface is shocked at $t = 0$ ms, reshocked by the primary reflected shock at $t \sim 3.5$ ms, and then by the reflected rarefaction at $t \sim 5$ ms. Also, Olson and Greenough (2014) compared the values of the mixedness between two- and three-dimensional LES of the planar RMI with multimode initial conditions. As shown in Fig. 11.13, the temporal evolution of Θ in two- and three-dimensions rapidly increases immediately after the reshock, with the 3D and 2D flow approaching a value of 0.85 and 0.70 for late time, respectively. In 2D, therefore, the mixing region growth is more dominated by entrainment than it is by molecular mixing.

11.4. Anisotropy

Counter intuitively, Thornber et al. (2011) reported that anisotropy is increased, instead of decreased, after the reshock. The final stage of the RMI induced flow is the decay of all components of the turbulent kinetic energy as a power law in time,

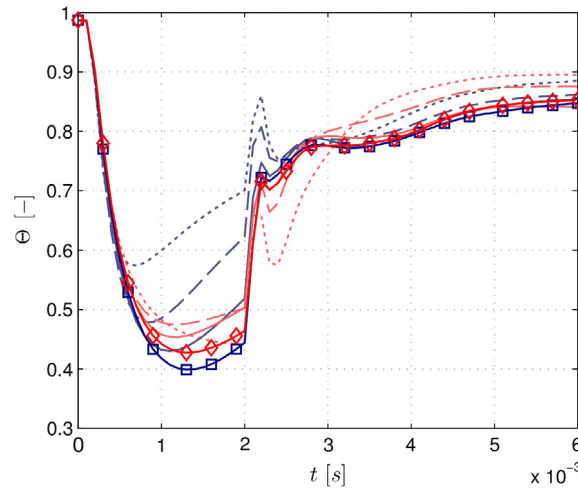


Fig. 11.10. Molecular mixing fraction, Θ . The time of reshock occurs at $t \approx 2$ ms. The highest resolution results are given by solid line with open squares for Miranda code and open diamonds for INCA code.

Source: Fig. 7 of Tritschler et al. (2014b), *J. Fluid Mech.* with permission.

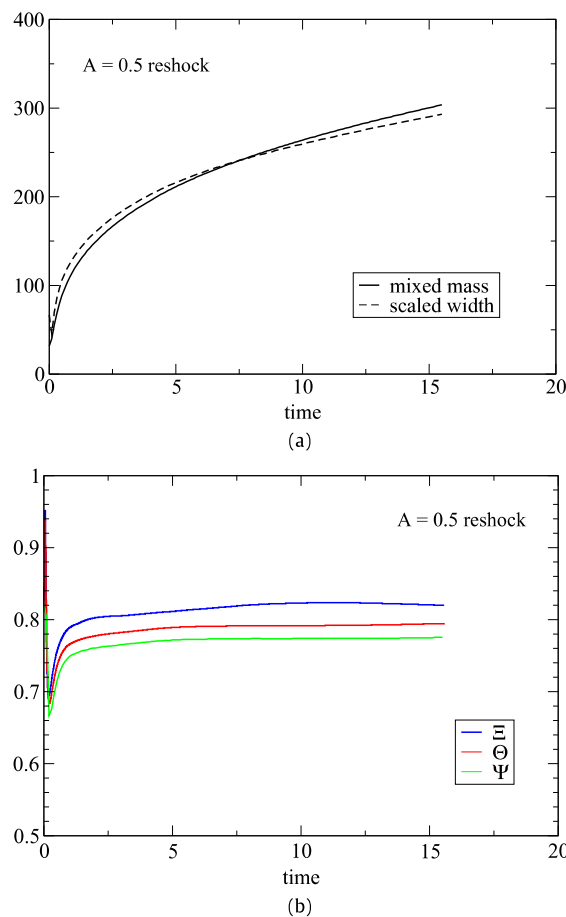


Fig. 11.11. (a) Temporal evolution of the mixed mass for the reshock case with Atwood number = 0.5. Also, the corresponding results for the mixed width (dashed lines), but multiplied by arbitrary constants. (b). Temporal evolution of the mixedness parameters and normalized mixed mass for the reshock case with $A = 0.5$ (Zhou et al., 2016, *Phys. Plasma*). All the curves plotted from the time of reshock.

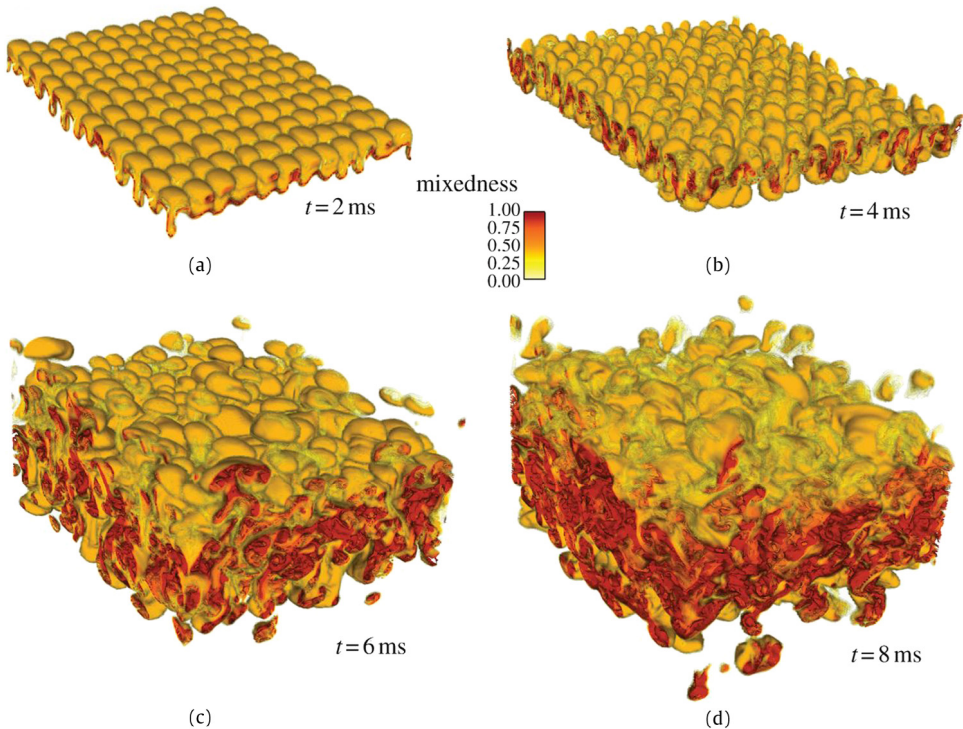


Fig. 11.12. (a–d) Instantaneous isosurfaces of the local mixedness function Θ for a planar shock-tube experiment of Vetter and Sturtevant (1995). Source: Adapted from Fig. 2 of Grinstein et al. (2013), Phil. Trans. Roy. Soc. A with permission.

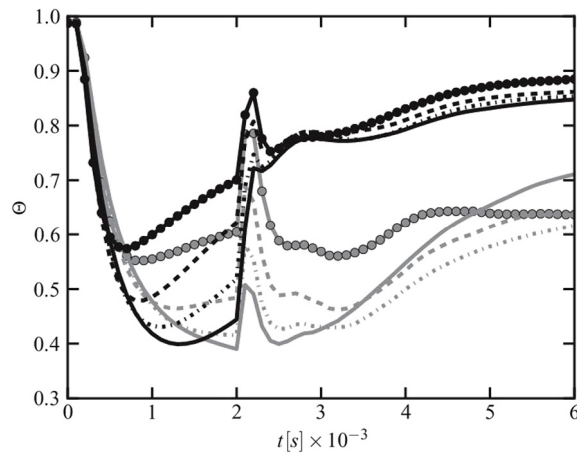


Fig. 11.13. Mixedness (Θ) parameter vs. time between 2D (gray) and 3D (black) calculations with the same legend. The late time non-monotonicity of Θ in 2D is also affected by run to run variation and shows poor grid independence. Source: Fig. 2b of Olson and Greenough (2014), Phys. Fluids, with the permission of AIP Publishing.

where the level of anisotropy (measured by TKX/TKY) remains approximately constant in time. For the narrowband case $TKX/TKY = 1.7 \pm 0.1$, and for the broadband case $TKX/TKY = 1.8 \pm 0.2$. These values are higher than the previous results for a single-shocked layer (where $TKX/TKY \approx 1.6$ and 1.5, respectively).

Tritschler et al. (2014b) also evaluated the degree of anisotropy after the reshock, but with the measure, b_{ij} , for the streamwise velocity component. The volume-averaged anisotropy in the inner mixing zone approaches an asymptotic limit of ≈ 0.04 , implying no full recovery of isotropy even after reshock (Fig. 11.14). Hence, despite reshock, the streamwise component remains the dominant velocity component throughout the simulation. The reshock resulted in a stratified anisotropy distribution around the center of the mixing zone (not shown).

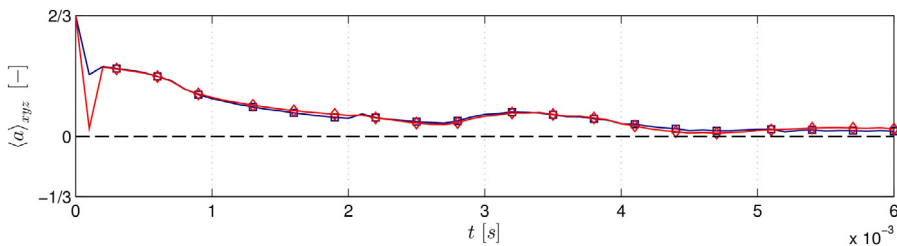


Fig. 11.14. Anisotropy (volume-averaged) of the inner mixing zone from Miranda (squares) and INCA (diamonds).
Source: Tritschler et al. (2014b), Fig. 10c, *J. Fluid Mech.* with permission.

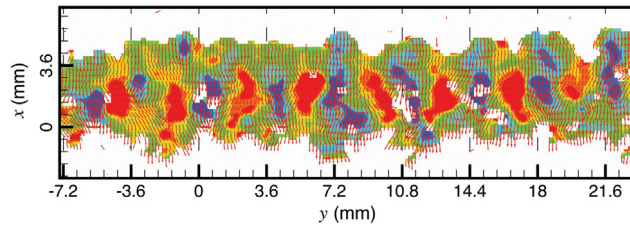


Fig. 11.15. Instantaneous streamwise velocity contours superimposed on the velocity vector field to show the presence of initial condition imprints after reshock at $t^* = 22.9$. Red and blue represent high and low streamwise velocity regions, respectively.
Source: Fig. 12 of Balakumar et al. (2012), *J. Fluid Mech.* with permission.

Ristorcelli et al. (2013) looked at the ICs dependence for fixed Mach and Atwood numbers and offered an example of how the reshock facilitates the trajectory towards isotropy. In this instance, just before reshock the value of $\langle b_{11} \rangle$ is about 0.28, which corresponds to three-times as much energy in the axial direction as compared to either of the transverse directions. At the end of the simulation after reshock, the anisotropy is much lower, $\langle b_{11} \rangle \sim 0.1$, corresponding to about 30% more energy in the axial component than in either of the transverse components.

The examination of anisotropy for the reshocked RMI flows might be further complicated by its ICs dependence, as suggested by Grinstein et al. (2011), Gowardhan and Grinstein (2011) and Thornber et al. (2012). Indeed, Balakumar et al. (2012) superimposed instantaneous streamwise velocity contours on the velocity vector field to demonstrate the presence of initial condition imprints after reshock at $t^* = 22.9$. The spanwise spacing between the contour peaks is nearly 3.6 mm, corresponding to the initial wavelength of the instability (Fig. 11.15). Fig. 11.16a displays the streamwise and spanwise velocity variances across the fluid layer after reshock. These variances are calculated as the spanwise averages of ensemble statistics (Balakumar et al., 2012). The streamwise and spanwise velocity variances are approximately equal in magnitude throughout the fluid layer (within statistical convergence errors), indicating that any propagation is less than the statistical measurement errors ($t^* = 22.9$). In addition, in an area-averaged sense, the streamwise and spanwise velocity variances appear nearly identical (Fig. 11.16b).

Once again, Youngs found that the differences in results can be attributed to the influence of initial conditions and to the difficulty in achieving sufficient time to establish self-similarity. He further noted that for the narrowband case the reshock is just an additional narrowband perturbation (albeit non-linear). Therefore, in this case the self-similar anisotropy should be expected to be the same for the single-shock and the reshock cases. For the self-similar broadband case, with initial perturbation spectrum $P(k) \sim k^m$ (see Section 11.7) it has been argued that θ should be different for the shock and re-shock cases and this is likely to correspond to different levels of anisotropy. Experiments are likely to have broadband perturbations but not necessarily of the self-similar form. This could lead to near-self similar behavior during the experiment but with further differences in the anisotropy.¹³ Broadly speaking, Grinstein et al. (2011) pointed out that the degree of anisotropy at late time could be related to the initial conditions of the fluid interface. The velocity fluctuations in the mixing zone are more isotropic when the initial interface perturbations also include short wavelengths, in which case the authors nearly recovered full isotropy. When long-wavelength perturbations are used, the mixing zone remained anisotropic except for a narrow range on the heavy-gas side.

11.5. Atwood number effects

As noted already, the RMI could occur regardless of the direction of the shock wave, from light-to-heavy or from heavy-to-light. Typically, the second shock passes from the opposite direction to the original shock. The resulting Atwood

¹³ D.L. Youngs (private communication, 2017).

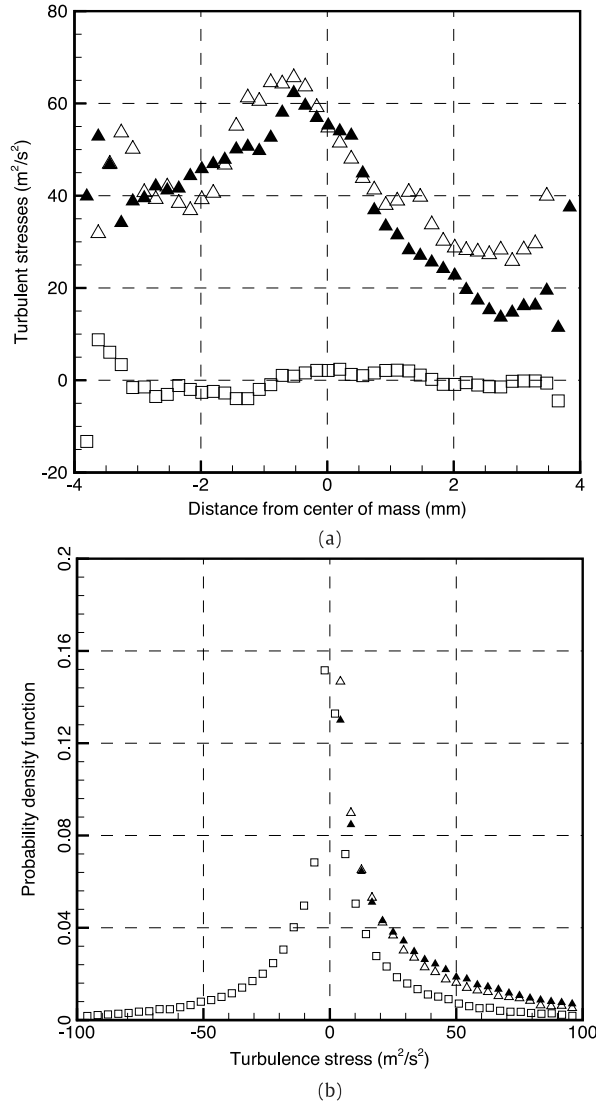


Fig. 11.16. (a) Variances of the velocity fluctuations across the fluid layer at $t^* = 22.9$. (b) Area histograms of statistics at the same time. For both panels: open triangle, $u_1'^2$; filled triangle, $u_2'^2$; open square, $u_1' u_2'$.
Source: Fig. 7 of Balakumar et al. (2012), J. Fluid Mech. with permission.

number would take either a negative or a positive value. As an example, with rather strong incident shock waves, Houas and Chemouni (1996) studied experimental measurements on reshock systems in heavy-light discontinuous interfaces separating CO₂ from different noble gases (the corresponding Atwood numbers range approximately from -0.76 to -0.14). The authors also examine the growth of the turbulent mixing zone in relation to the wall boundary layer development, behind the incident shock wave.

Brouillette and Sturtevant (1989, 1993, 1994), studied the mixing layer growth induced by successive shock waves for the heavy-light configuration air–He ($A \approx -0.76$), air–air ($A \approx 0$), as well as the light–heavy configurations air–CO₂ ($A \approx 0.20$), air–R22 ($A \approx 0.50$), and air–SF₆ ($A \approx 0.67$). The disagreements with previous experiments of Andronov et al. (1976) and Zaitsev et al. (1985) can be attributed to the existence of a wall vortex on the sidewalls (Brouillette and Bonazza, 1999) resulted by the interaction of the reflected shock with the mixing zone within the boundary layer and to the differences between the experimental setups (Lombardini et al., 2011).

For their LES, Hill et al. (2006) and Lombardini et al. (2011) used the stretched-vortex subgrid model (Misra and Pullin, 1997; Kosovic et al., 2002; Pullin, 2000) to represent the unresolvable subgrid scales. Lombardini et al. (2011) presented a systematic study of the Atwood dependence of shock-driven mixing under reshock conditions. A canonical, 3D numerical experiment reproduced interaction within a shock tube with an end wall where the incident shock Mach number is ~ 1.5 . The initial interface perturbation has a fixed dominant wavelength and a fixed amplitude-to-wavelength. The authors

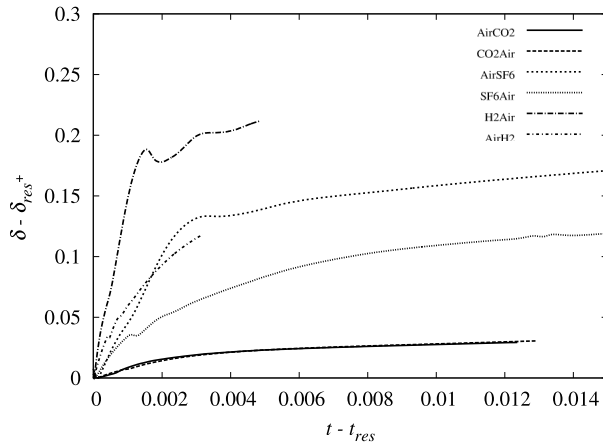


Fig. 11.17. Post-reshock mixing zone width $\delta - \delta_{res+}$ versus $t - t_{res}$ for various gas combinations. The re-shock Atwood numbers of the curves are 0.21 (Air-CO₂), 0.67 (Air-SF₆), 0.87 (H₂-Air), -0.21 (CO₂-Air), -0.67 (SF₆-Air), and -0.87 (Air-H₂).
Source: Fig. 6 of Lombardini et al. (2011), J. Fluid Mech., with permission.

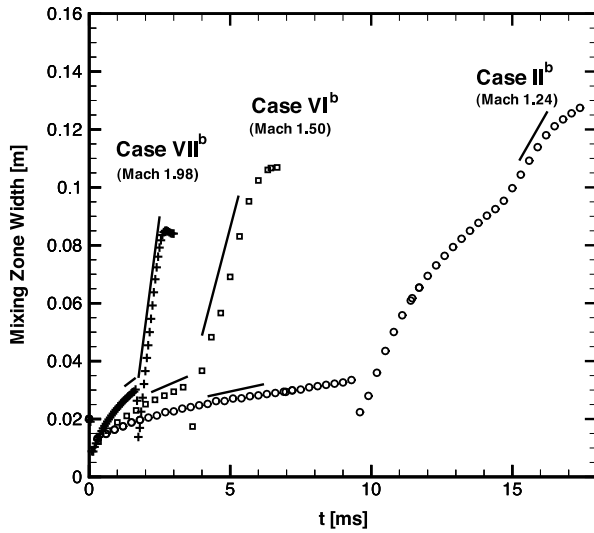


Fig. 11.18. The evolution of the mixing-layer width. The growth rates inferred from the experiments are indicated as straight lines with the appropriate slopes drawn in the approximate times over which they were observed. The incident Mach numbers of the Vetter and Sturtevant experiments are 1.24 (Case II^b), 1.50 (Case VI^b), and 1.98 (Case VII^b).
Source: Fig. 4 of Hill et al. (2006), J. Fluid Mech. with permission.

investigated the realistic gas combinations air-CO₂, CO₂-air, SF₆-air, air-SF₆, H₂-air, air-H₂, which correspond to the Atwood numbers of ± 0.21 , ± 0.67 and ± 0.87 . As illustrated in Fig. 11.17, the asymmetry of post-reshock mixing zone width becomes more and more pronounced as the Atwood number increases.

11.6. Mach number effect

In the canonical geometry of a rectangular shock-tube with a square cross-section, Hill et al. (2006) performed LES with the configuration of the gases, the geometry of the domain, and the strength of the incident shock all chosen to match those of the experiments of Vetter and Sturtevant (1995). Fig. 11.18 shows the time evolution of the mixing zone for the plane discontinuous interface between air and SF₆ for incident shock waves with Mach numbers 1.24, 1.50, and 1.98.

Leinov et al. (2009) discussed the available methods to control the reshock strength experimentally. There are essentially two approaches. Of course, varying the incident Mach number could change the strength of the reflected shock wave (Fig. 11.19 and Table 11.3). However, a comparison between such experiments is not appropriate because the perturbations would have evolved for different times prior to the reshock arrival. Instead, Leinov et al. and co-workers varied the end

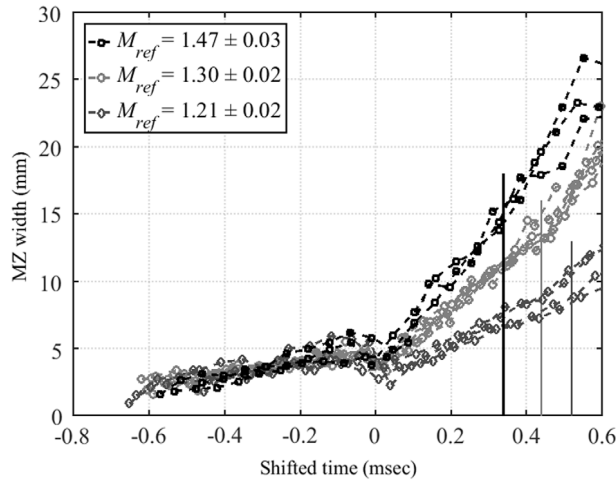


Fig. 11.19. Mixing zone width measurements as a function of shifted time for three different incident shock-wave Mach numbers (the endwall is fixed at 80 mm).

Source: Fig. 13 of Leinov et al. (2009), *J. Fluid Mech.* with permission.

Table 11.3

Reshock Mach number, overall velocity jump and mixing zone growth rates following the reshock for three experimental sets with a fixed endwall distance of 80 mm.

Source: Table 2 of Leinov et al.

Experiment	Reshock Mach number ($Mach_{ref}$)	Overall velocity jump (m/s)	Growth rate (m/s)
Set 1	1.21 ± 0.02	73.0 ± 5.0	13.1 ± 1.5
Set 2	1.30 ± 0.02	96.4 ± 5.0	23.1 ± 1.0
Set 3	1.47 ± 0.03	145.6 ± 10.0	34.6 ± 3.0

Table 11.4

Reshock Mach numbers, overall velocity jumps and the growth rates of the mixing zone following reshock for four experimental sets with different endwall rigidity. The endwall is at 80 mm. These experiments were performed with an incident Mach number of 1.2 in air.

Source: Table 3 of Leinov et al.

Endwall feature	Reshock Mach number ($Mach_{ref}$)	Overall velocity jump (m/s)	Growth rate (m/s)
Elastomeric foam	1.09 ± 0.03	36.3 ± 6.0	10.5 ± 0.8
Elastomeric foam & cardboard	1.19 ± 0.01	45.4 ± 5.0	14.3 ± 1.0
Elastomeric foam & aluminum plate	1.25 ± 0.02	73.0 ± 6.0	19.7 ± 1.0
Rigid	1.30 ± 0.02	96.4 ± 5.0	23.1 ± 1.0

wall's rigidity in order to avoid this uncertainty. With the end wall fixed at 80 mm, Table 11.4 shows the growth rates of the mixing zone following reshock for four experiments, corresponding four different reshock Mach numbers.

11.7. Models for reshocked RMI

11.7.1. Single-mode

Generalized the Richtmyer model, Brouillette and Sturtevant (1989) formulated the growth of the total width of a single-mode interface subject to $N + 1$ impulsive accelerations.

$$\left(\frac{dh}{dt} \right)_N = 2k \sum_{i=0}^N \frac{a_i^+ A_i^+ \Delta V_i}{\varphi_i} \quad (11.3)$$

where φ_i is the post-shock growth reduction factor (Duff et al., 1962), a_i^+ and A_i^+ are the post-shock amplitude and Atwood number, and k is the initial perturbation wavenumber. ΔV_i is the velocity jump of the i th reshock.

Based on the numerical studies of single-mode 2D RMI with reshock, Charakhch'yan (2001) advanced a model with the following form

$$\frac{dh_2}{dt} = \beta_c A^+ \Delta V - \frac{dh_1}{dt} \quad (11.4)$$

where (dh_1/dt) is the growth rate immediately before the reshock, A^+ is the Atwood number following the passage of the initial shock, and ΔV is the velocity jump caused by the reshock. The empirically fixed factor $\beta_c = 1.25$ (see also

Charakhch'yan, 2000). Note that (dh_2/dt) and (dh_1/dt) have opposite signs as they correspond to perturbation growths in opposite directions (Ukai et al., 2011).

Mikaelian (1985) pointed out that for a single mode in the linear regime the preshock growth rate dh^-/dt must be added to Richtmyer's growth rate $h_0 k A \Delta V$ to obtain the postshock growth rate dh^+/dt :

$$\frac{dh^+}{dt} = h_0 k A \Delta V + \left(\frac{dh^-}{dt} \right) \quad (11.5)$$

leading to an increase or decrease of the postshock growth rate, depending on the relative sign of the above two terms. In particular, if they cancel exactly, the postshock growth rate can be zero, which he termed "freeze-out" (Mikaelian, 1985).

Schilling et al. (2007) analyzed the post-reshock growth rates of 2D single-mode RMI with the ninth-order weighted essentially nonoscillatory (WENO) (Shu and Osher, 1988; Jiang and Shu, 1996; Shu, 1999; Balsara and Shu, 2000) shock-capturing method. The initial conditions and computational domain were adapted from the Mach 1.21 air (acetone)/SF₆ shock tube experiment of Collins and Jacobs (2002). For later times, the simulated data suggested that the Brouillette–Sturtevant model (1989) underestimates the growth at all times following reshock, while the Mikaelian (1989) and Charakhch'yan (2001) models overestimate the growth.

Ukai et al. (2011) performed extensive parametric studies of 2D/3D single-/multi-mode RMI to investigate the effect of the initial conditions on the late time growth patterns. The computational domain in this study was taken from that of Leinov et al. (2009). The numerical results provided support to the Charakhch'yan suggestion that the post-reshock growth rate is not a strong function of wavelength. However, the coefficients $C_C \approx 0.68$ and 1.09, instead of $C_C = 1.25$ proposed by the original Charakhch'yan model, were obtained from the 2D and 3D single-mode RMI simulations.

11.7.2. Multi-mode

For multi-mode 3D perturbation, Mikaelian's reshock model (1989) suggested the following linear correlation,

$$h = C_M A^+ \Delta V t \quad (11.6)$$

where $C_M = 0.28$ is a constant. This model was obtained by extrapolating constant-acceleration RT instability experiments (Read, 1984) applied to shock tube experiments. Here h is the total mix width from the bubble and spike sides.¹⁴

Using a post reshock Atwood number of 0.712, Leinov et al. (2009) determined the dimensionless coefficient of this model for five different experimental sets (black dots), yielding an averaged value of 0.38, and the growth coefficient range (gray area), bounded by a lower limit of 0.28 and an upper limit of 0.39 (Fig. 11.20). Ukai et al. (2011) found that the growth rates of various RMI configurations can be simply characterized by Mikaelian's reshock model with different values of coefficients obtained from a parametric study (Table 9 of Ukai et al., 2011 not shown). Jacobs et al. (2013) obtained a value of $C_M = 0.26$ with their membraneless reshock experiment. Changing the length of the shock tube (Bouzgarrou et al., 2014; Griffond et al., 2017), Bouzgarrou (2014) determined that values of C_M can be bracketed between 0.38 to 0.43. Of course, the multi-mode configuration experimental data are not appropriate for determining the parameters of Brouillette and Sturtevant (1989) and Charakhch'yan (2001) since these models were developed for a single-mode configuration.

The Mikaelian (1989) model achieved good agreement with the simulation of a reshocked multi-mode RMI flows using the same WENO scheme (Schilling and Latini, 2010), with a two-mode initial perturbation with superposed random noise to model the Mach 1.5 air/SF₆ Vetter–Sturtevant shock tube experiment (Fig. 11.21). The simulation indicates a velocity dh/dt obtained from the model is about 10% smaller than the data before reshock and around 3% smaller than the data after reshock.

Mikaelian (2011) pointed out that his 1989 reshock model should only describe the early stages of a shock or reshock. He proposed that the subsequent growth rate h begins to decay and the mix width transitions from the early $h \sim t$ behavior to $h \sim t^\theta$, with θ (θ^b or θ^s) another "constant" measured in previous RT experiments (Dimonte and Schneider, 2000). The transition from t to t^θ was argued to be a result of the mixing width forgetting the direction of the shock, i.e., turbulence becoming isotropic around $t = t^*$. The extended shock or reshock model, then, takes the form,

$$h = h_0 + 2\alpha A \Delta V t, \quad t \leq t^*, \\ h = h^* \left(1 + \frac{\dot{h}^*}{\theta h^*} (t - t^*) \right)^\theta, \quad t \geq t^* \quad (11.7)$$

where $h = h^b$ or h^s , $\alpha = \alpha^b$ or α^s , h^* and h^* are the mix width and its growth rate at $t = t^*$, ensuring continuity of both measurements. The performance of the model obviously depends on how t^* is determined. He proposed $t^* = (h_0^{b+s}/\Delta V) \beta_M$ with $\beta_M \sim 6$.

The most recent reshock RMI model is due to Mikaelian (2015), who has refined his previous procedure and suggested the following expression

$$t^* = \frac{(1 + 2\alpha \beta_M A) h_{\text{before}} - h_{\text{after}}}{2\alpha A \Delta V} \quad (11.8)$$

where the h_{before} and h_{after} are the total mixing width before and after the reshock.

¹⁴ Leinov et al. (2009) found that the growth coefficient $C_M = 0.28$ –0.39 as later studies by Dimonte and Schneider (2000) and Oron et al. (2001) revealed that there is an asymmetry between the fronts of the bubbles and spikes of the mixing zone.

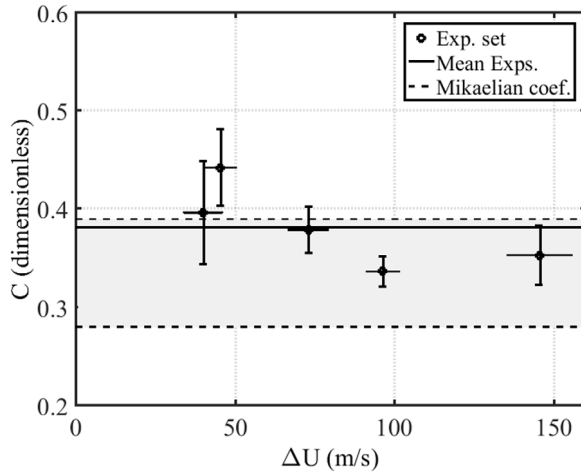


Fig. 11.20. Mixing zone growth rate dimensionless coefficients for different experimental sets (dots) and range of growth coefficient (gray area).
Source: Fig. 19 of Leinov et al. (2009), *J. Fluid Mech.* with permission.

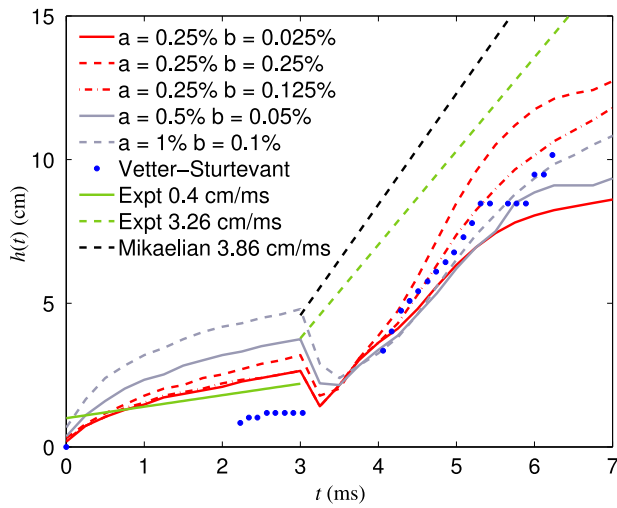


Fig. 11.21. Comparison of the mixing layer width from the simulations with the Vetter–Sturtevant (1995) experimental growth rates and data points, and with the prediction of the Mikaelian reshock model (1989). The consequences of the membrane are illustrated using different perturbation amplitudes (denoted by a and b).¹⁵

Source: Fig. 11 of Schilling and Latini (2010), *Acta Mathematica Scientia* with permission.

Fig. 11.22 (Fig. 2 of Mikaelian, 2015) shows the experimental data of Jacobs et al. (2013) and three curves computed from the updated Mikaelian (2015) reshock model. These three curves use the same five input parameters, but differing initial total mixing width, h_{before} (2.4, 3.6, and 4.8 mm). After compression, they become approximately 2, 3, and 4 mm. The intermediate curve goes nearly through the middle of the dataset and the lowest and highest curves bound the data reasonably well. Hence, the differences in the growth behavior are most likely caused by differences in the initial perturbation (Jacobs et al., 2013; Mikaelian, 2015).

It should be noted that the RM scaling parameter θ is likely to depend on the initial conditions, as can be seen in two models for reshock proposed by Thornber et al. (2011). The first is for a reshocked broadband perturbation, which is an extension of the earlier model of Youngs presented in Thornber et al. (2010), following a similar line to the analysis of Haan for the RT instability (Haan, 1989). The model predicts that for a substantially broadband perturbation, each reshock reduces the expected value of θ . For initial broadband perturbations ($P(k) \propto k^{\tilde{m}}$ spectrum), $\theta = 2/(\tilde{m} + 5)$ after the first shock (see Section 6.3). The value of second shock θ , according to Thornber et al. (2011) should vary as $\theta_{\text{reshock}} = 2/(\tilde{m} + 7)$. Given a sufficient number of reshocks, this would fall below the value of θ expected for a narrowband layer and it is then expected that the development of the layer would be independent of the initial conditions ($\theta \approx 0.26$). Given a sufficiently wide range of initial perturbations, at very late times the longest wavelengths will effectively feel a single large impulse and respond

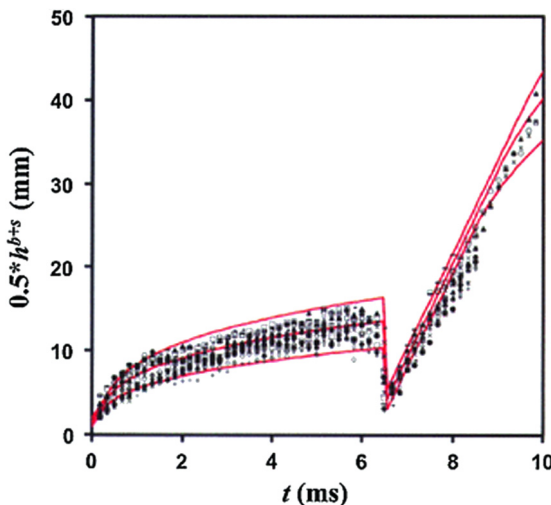


Fig. 11.22. The data of Jacobs et al. (2013) and 3 curves of the model calculated using updated Mikaelian reshock model, with the input parameters are listed in Table 1 of his paper (not shown). The 3 curves differ only in the initial values of the total mixing width: 2.4, 3.6, and 4.8 mm. and are shown as the lowest, intermediate, and highest red curves respectively. The data [and the curves] show half the total mixing width.
Source: Fig. 2 of Mikaelian (2015), Shock Waves with permission.

in a similar manner to a single shock, albeit on a very long time scale. This broadband model was compared to numerical results, showing a reasonable agreement particularly at early times.

The second model is for reshock of a self-similar mixing layer initiated from a narrowband perturbation, valid for early times. This was developed through consideration of a local Atwood number generated by a combination of a spatial mean density gradient due to mixing, and molecular mixing. This analysis demonstrated that the post-reshock growth rate is dependent on the factor $\sqrt{1 - \Theta}$, where Θ is the molecular mix prior to reshock. As this molecular mix depends on the initial conditions, there is a sustained impact of initial condition conditions on post-reshock growth. This model suggests an initial growth which is linear in time, and comparison with Mikaelian's model (1989) suggests that the coefficient C_M will include dependence on pre-reshock molecular mixing Θ . Comparison with numerical simulations indicated that the sensitivity of the free parameter in the model¹⁶ is substantially reduced compared to Mikaelian's model due to the integration of molecular mix in the growth rate formula. Also worth noting is that for narrowband perturbations it is reasonable to suppose that θ should be similar for the first shock and the reshock.

Because of the heuristic nature of their construction, the reshock models reviewed in this subsection are designed to fit, but not to predict the growth rate after the passage of the reshock.¹⁷

12. Mix models

For mixing processes of practical interest driven by density instabilities (e.g. RT and RM instabilities), excitations of spatial scales exceed the resolution possible in current and foreseeable numerical simulations. Despite the intensive efforts to develop increased computational capabilities, the mix models remain the most viable approach for the solution of practical astrophysics and ICF problems. The reason for this state of affairs becomes abundantly clear when one considers the difficulties of achieving the required high Reynolds number for RTI and RMI induced turbulent flow and of obtaining the desired turnaround time for engineering calculations. These practical problems, along with the fact that the transport models have been incorporated and integrated into most ICF or astrophysics computer codes (these are frequently referred to as hydrodynamic or hydro codes), constitute the major reasons for pursuing this approach. The Reynolds-Averaged Navier-Stokes (RANS) models that attempt to analyze and characterize these flows need to pay attention to issues of initialization of turbulence field variables, which is a serious challenge for most turbulence theories. These models implicitly assume one is starting out with fully developed turbulence (as opposed to transitioning to turbulence from a quiescent state).

Our survey of the mix modeling efforts in this section has been guided by a comprehensive consideration of existing models used for computing the turbulent mix induced by the RTI and RMI. After addressing the initialization matter, the aspects of various models will be reviewed in increasing order of complexity.

¹⁶ The free parameter C_r can be found in Eq. (18) of Thornber et al. (2011).

¹⁷ Nevertheless, Krivets et al. (2017) used Mikaelian's (2015) reshock model to extract the growth exponent θ from five vertical shock tube experiments. These experiments were performed under the same conditions, but having different initial perturbations. The values of θ are estimated varying from 0.2 to 0.6 and have been documented in Table 6.4 (Part I).

12.1. Remarks on the initial conditions

An issue arises when applying standard phenomenological models to explicitly model the mixing processes within a host hydrodynamic code: the flows must be sufficiently turbulent that the hypotheses underlying RANS turbulence models can be justified. Yet, many flows of practical interest need to be modeled over a period of time when the flow is not initially turbulent. In fact, as noted in Zhou et al. (2003a, b, 2009), the mixing problem for many applications is a transitional problem. For high energy density physics (HEDP) applications, such as experiments on lasers and Z pinches, flows start from rest at $t = 0$. Ideally, the model should mimic the linear phase of instability as well as the fully turbulent late-stage mixing. (Besnard et al., 1987, 1992).

Brown et al. (2014) summarized the “initialization” practice put in place sometime ago at Atomic Weapons Establishment (AWE), United Kingdom, to deal with this issue. At early times a buoyancy–drag mix model¹⁸ is engaged at material interfaces to calculate expected interpenetration between the light and heavy fluids. This model is a “passive” one since it does not lead to any modification of the host fluid properties. Once the passively modeled mixing region has grown sufficiently large as to be accurately represented by the host mesh, calculated fluid penetration depths are used to instantiate a smooth interpenetrating volume-fraction profile at the material interface, directly modifying the properties of the host fluid. For subsequent hydrodynamic time steps, a mix model (in the form of a multi-fluid model described in Youngs (1989, 1994), see Section 12.7) becomes engaged to model the turbulent mixing processes within the host fluids. This model is “dynamic” since it directly interacts with, and imprints upon, the fluid properties of the host code.

Rollin and Andrews (2013) developed a two-step initialization strategy for RANS-based simulations. These authors were especially concerned with the Besnard–Harlow–Rauenzhan (BHR) turbulence model developed at Los Alamos National Laboratory (LANL), (Besnard et al., 1989, 1992; Banerjee et al., 2010a; Stalsberg-Zarling and Gore, 2011; Schwarzkopf et al., 2011). In the first step, a nonlinear modal model assuming small amplitude initial perturbations, incompressible and inviscid fluids is used to track the growth of modes that exist in each initial perturbation spectrum, and modes generated by mode interactions. As reviewed in Part I, Haan (1991) has derived such a second-order mode-coupling equation. There is a significant modification though. Rollin and Andrews (2013) used Goncharov’s (2002) nonlinear solution, instead of Haan’s linear one, of the Rayleigh–Taylor instability problem in the second-order coupling term. Hence, the iterative integration of the model equations would develop solutions fully nonlinear rather than using the linear solution iteratively. It is interesting to mention in passing that the multimode model presented in Rollin and Andrews (2013) is somewhat related to a model proposed by Ofer et al. (1996), who also extended Haan’s model in order to make it applicable to the cases where nonlinear mode generation is important. In the approach taken by Ofer et al., the bubble and spike front positions and velocities, along with the simplified profiles of the mixture fraction distribution of each fluid between the bubble and spike fronts, were used with a two-fluid approximation to derive profiles for the turbulence model variables.

For the mix models developed at Commissariat à l’Energie Atomique, France (CEA), Grégoire et al. (2005) advanced a scheme linking the RMI initial conditions from an incident shock wave and perturbation interface to the initial profiles for their second-order turbulence model. Two challenges to accomplish this task were pointed out. First, one has to deal with moving boundaries between laminar regions and fully turbulent ones. Second, the energy of the perturbed motion is impulsively provided by the shock wave. As a result, the RMI-induced mixing is strongly unsteady.

In this regard, the linear interaction analysis (LIA) (Ribner, 1953, 1985) and RDT (Batchelor and Proudman, 1954; Townsend, 1976; Hunt and Carruthers, 1990) have been utilized in order to predict the initial phase of the RM instability. Griffond (2006) extended the LIA analysis from a previous application to perfect gas mixtures (Griffond, 2005) to the interaction of a shock wave with a diffuse interface of sinusoidal shape. In the continuation of weakly non-linear rapid distortion methods described in Hunt and Carruthers (1990), Gréa (2013) suggested a new simple approach to model the short-time dynamics of a strongly accelerated mixing zone. Gréa et al. (2014) studied the problem of a turbulent mixing zone, initially submitted to coupled effects of axisymmetric strain and stratification, and then subsequently accelerated. The mixing layer grows in the latter stage due to a rapid mixing induced by the RTI. Yanikin et al. (1995) proposed a “reasonable” restriction on the choice of initial conditions for their $K-\varepsilon$ model. Also, Ristorcelli and Hjelm (2010) attempted to use stochastic form of linear stability analysis to construct initial conditions.

As noted by Xiu and Karniadakis (2003), there has been an intense interest in verification and validation of large-scale simulations and in modeling uncertainty.¹⁹ Just like in the experiments, the new objective is to model the uncertainty from the beginning and not simply as an afterthought. The paper of Barmparousis and Drikakis (2017) concerned the implementation of the generalized Polynomial Chaos (gPC)²⁰ approach for parametric studies, including the quantification of uncertainty (UQ), of turbulence modeling. It was applied to RM turbulent mixing in the framework of the original

¹⁸ See next subsection.

¹⁹ See Poroseva et al. (2016) for a study of RANS simulations with DNS data for a zero-pressure gradient boundary layer over a flat plate and a fully developed channel flow.

²⁰ According to Wan & Karniadakis (2006), Polynomial chaos (PC) has been used extensively recently to model uncertainty in physical applications. It originated from homogeneous chaos first defined by Wiener (1938) as the span of Hermite polynomial functionals of a Gaussian process. Other names, such as Wiener-chaos and Hermite-chaos, are also used in literature. Ghanem and Spanos (1991) first combined Hermite-chaos with a finite element method to model uncertainty in solid mechanics (Ghanem, 1999a,b). A more general extension, termed generalized polynomial chaos (gPC), was proposed by Xiu and Karniadakis (2003) based on the correspondence between the PDFs of certain random variables and the weight functions of orthogonal polynomials of the Askey scheme.

$K-L$ turbulence, which was chosen as a prototypical example and parametric studies were performed by the authors to examine the effects of closure coefficients and initial conditions on the flow results. It was shown that the proposed method can be used to obtain a relation between the uncertain inputs and the monitored flow quantities, thus efficiently performing parametric studies.

The investigation of the uncertainty associated with the initial conditions revealed that the initial characteristic length scale L_0 has an order of magnitude higher influence to the predicted flow field compared to K_0 . This influence is clearly reflected on the reconstructed response surfaces, where a smooth dependence of the flow quantities with respect to the initial conditions is observed. The turbulent kinetic energy (TKE) within the examined interval did not affect the response of any monitored flow quantity and the growth of the instability depends almost exclusively on the level of L . The late time growth exponent increases, as expected, with respect to K_0 and L_0 , whereas the early time exponent did not present a strong correlation. From the variational analysis it was shown that the integral length of the mixing zone and total mix are approximately equally influenced from the uncertainties in the initialization process, an influence that shows a relatively small decrease towards the late times (Barmparousis and Drikakis, 2017).

12.2. The buoyancy–drag models

The buoyancy–drag model, which computes the evolution of the amplitudes of the mixing region, was the workhorse of many practical, first generation mix model calculations. Youngs (summarized in Appendix of Hansom et al., 1990), Shvarts et al. (2000), Dimonte (2000), Dimonte and Schneider (1996, 2000), Baker and Freeman (1981) and Ramshaw (1998) are examples of published papers describing the buoyancy–drag models. Briefly, the buoyancy–drag model is essentially an equation of motion that balances the inertia, buoyancy, and Newtonian drag forces (Lighthill, 1986; Clift et al., 1978; Landau and Lifshitz, 1987). The growth of the mixing region depends on the density ratio (namely, the Atwood number) and the acceleration history. By construction, this model is appropriate for the inhomogeneous and anisotropic nature of the interfaces.

The buoyancy–drag model typically takes the form that is similar to that of Oron et al. (2001),

$$(\rho_1 + C_a \cdot \rho_2) \frac{du}{dt} = (\rho_2 - \rho_1) \cdot g - \frac{C_d}{\lambda} \cdot \rho_2 \cdot u^2 \quad (12.1a)$$

where u is the velocity, g the gravitational acceleration, ρ_1 and ρ_2 the fluid densities and λ the wavelength. Here, C_a and C_d are the added mass and drag coefficients, respectively,

$$3D: C_a = 1; C_d = 2\pi,$$

$$2D: C_a = 2; C_d = 6\pi.$$

According to Oron et al. (2001), Alon et al. (1993, 1994, 1995) misinterpreted the added mass coefficient at $A = 1$ as a buoyancy coefficient for the gravitational term. Hence, different values for C_a and C_d were obtained from the Layzer equation under $A = 1$ limit.

In Hansom et al. (1990) and Linden et al. (1994) it was pointed out that Layzer's equations for bubble height, h , at $A = 1$ may be written as

$$\begin{aligned} 3D: (1 + \mathfrak{E}) \frac{du}{dt} &= (1 - \mathfrak{E}) g - \frac{2\beta_1}{\lambda} u^2 && \text{with } \mathfrak{E} = \exp(-4\beta_1 h/\lambda) \\ 2D: (2 + \mathfrak{E}) \frac{du}{dt} &= (1 - \mathfrak{E}) g - \frac{6\pi}{\lambda} u^2 && \text{with } \mathfrak{E} = \exp(-6\pi h/\lambda) \end{aligned} \quad (12.1b)$$

where for the 3D case, $\beta_1 = 3.83171$ is the first zero of the Bessel function, and $R = \lambda/2$ is the radius of a cylindrical tube. These equations have the form *mass* × acceleration = *force–drag*. Note that there is further discussion of the Layzer equation in Part I.

Eq. (12.1a) then follows by taking the non-linear limit ($\mathfrak{E} = 0$) and making modifications to allow for $A < 1$. Also, if the wavelength grows in proportion to the width of the mixing zone, i.e. $\lambda \propto h$, then the buoyancy–drag model has a solution $h \sim gt^2$ and can represent self-similar RT mixing.

Ramshaw (1998) used Lagrange's equations to derive a version of the buoyancy–drag model. However, there is a difference in the form of the model. Part of the quadratic term in Eq. (12.1a) is attributed to conservation of kinetic energy ($\sim hu^2$):

$$\frac{d}{dt} (hu^2) = 0 \implies \frac{du}{dt} = -\frac{u^2}{2h}.$$

In the non-linear limit the quadratic term has the form

$$-\left(\frac{u^2}{2h} + C_D \frac{u|u|}{h}\right).$$

In terms of bubble and spike mixing fronts and with the help of the classical work of Lamb (1932), Cheng et al. (2000) found that the added mass coefficient depends on the bubble geometry: it equals 1 for a cylindrical front bubble and 1/2 for

a spherical front bubble in three space dimensions. This work was concerned with the parameters α and θ of the late-time similarity from the perspective of the buoyancy–drag model. The main results of this work were two fold. First, it showed that α_b alone is sufficient to determine α_s except when $A = 1$, where an additional parameter is needed (see also Glimm et al., 1999; Cheng et al., 1999). Second, within the framework of a simple *ordinary differential equation* (ODE) model, the values of α determine the values of θ , in agreement with available data.

Later, Cheng et al. (2002a) obtained a closed form solution for the edges of the mixing zone of acceleration driven RT and RM mixing layers. In the RT case, for instance, the solution contains a quadrature. Terms that are $O(1)$ in t are obtained approximately from late time RT asymptotics. Moreover, for RTI in both the moderately compressible and weakly compressible regimes, Jin et al. (2005) found that the phenomenological drag coefficient, which occurs in the single mode buoyancy–drag equation, is directly related to the terminal velocities.

Layzer's equations do not require that g should be constant. Hence buoyancy–drag models are directly applicable to time-varying accelerations and can be applied to complex problems by taking the time variation of ρ_1 , ρ_2 and g from a hydrocode simulation. This is most easily implemented for a 1D Lagrangian simulation where values of ρ_1 , ρ_2 and g near the interface are readily obtained. One method of doing this is described in Hansom et al. (1990). In this case spike and bubble tips are tracked through the Lagrangian mesh and the bubble density is taken to be the mean density of the fluid between the interface and the bubble tip (similarly for the spike density). Values of the acceleration are measured at the bubble and spike tips. The effect of compression of the mixing zone needs to be taken into account. In the Hansom paper this is treated by interpreting bubble and spike velocities as being relative to the Lagrangian mesh so that, in the absence of instability, the mixing zone is compressed at the same rate as the fluid. The treatment of shocks is problematic. Layzer's equations (Eq. (12.1b)) are valid for impulsive accelerations. However, for turbulent RMI, mixing occurs both for shocks traveling from light to heavy and heavy to light. A possible way of ensuring that model gives this behavior is to use $|(\rho_1 - \rho_2)g|$ rather than $(\rho_1 - \rho_2)g$ in Eq. (12.1a) if shock acceleration is detected. Similar modifications are used in Dimonte and Tipton (2006) and Kokkinakis et al. (2015), where a buoyancy–drag source term is included in a $K-L$ model.

In the context of the buoyancy–drag dynamics, Drake (2012) demonstrated that the amount of spike penetration in core-collapse supernovae (Bethe, 1990; Janka et al., 2007; Smarr, 2009) depends on the relative amount of drag. For experiments performed on the OMEGA laser (Boehly et al., 1995, 1997) with decelerating interfaces, buoyancy–drag models have proven successful, after adjusting for compressibility effects, in explaining observations with 2D, single-mode perturbations, but provide an only partial agreement in the multimode cases (Miles et al., 2004b). Melvin et al. (2015) carry out sets of simulations in order to determine the dependence of key ICF hot spot simulation properties on the deuterium–tritium fuel adiabat. The authors used a variable acceleration buoyancy–drag model (Cheng et al., 2000, 2002b) to estimate the spike penetration into the hot spot, a process that limits alpha heating and lowers overall neutron yield.²¹ More recently, Rana et al. (2017) coupled a 1D inertial confinement fusion simulation code with a 1D buoyancy–drag model to study the performance of National Ignition Campaign design.

Under the special case of constant acceleration, Bouquet et al. (2007) found that the ODE of the buoyancy–drag model becomes autonomous, i.e., the equation no longer depends explicitly on the independent variable t . The equation admits the Lie point symmetry (Ibragimov, 1999; Olver, 1993). From this property, it can be shown that the order of the differential equation can be reduced from two to one (Bouquet et al., 1991; Leach et al., 1988).

Srebro et al. (2003) generalized the buoyancy–drag equation for the growth of a single-mode perturbation. While the previous model is valid only at very late time (the asymptotic stage), the generalized version has been extended to all instability stages. The evolution of a multimode spectrum of perturbations from short wavelength random noise is described using a single characteristic wavelength. With a self-similar parameter, Cao et al. (2011) derived analytically the solutions to the generalized Srebro et al. (2003) model, which has been modified slightly in order to describe properly the growth of bubbles and spikes separately (Cao and Chow, 2005).

Recently, Zhang et al. (2016) advanced a generalized buoyancy–drag model by incorporating conservation of mass and momentum and by utilizing a symmetry factor to highlight the property of density fields occurring in actual flows. Also, the authors assumed a parabolically-varying velocity profile and replaced the local speed of advance of the mixing fronts by a volume-averaged one. Three model parameters are determined by resorting to asymptotic solutions. The model has been validated by several experiments with a wide range of density ratios and different acceleration histories.

Finally, the Rapid Distortion Theory (RDT), in conjunction with a dynamical systems approach, also lent support to the soundness of the buoyancy–drag equation (Gréa, 2013). Restricting to the RTI induced flows, the existence of a central manifold is established and the dimension of the problem is reduced. This is associated with a Lagrangian formulation depending only on the mixing layer width and its derivative, so that the dynamics of mix zone width degenerates into a buoyancy–drag model.

Note that turbulence is not treated directly by the buoyancy–drag model (Zhou et al., 2002). Kokkinakis et al. (2015) argued that these buoyancy–drag models are of limited use as they cannot model multiple mixing interfaces, cannot be easily extended to two and three dimensions and cannot address de-mixing (reduction of total fluid masses within the mixing zone); this can occur when there is a reversal in the pressure gradient and there is not complete mixing at a molecular level within the mixing region.

²¹ See Cheng et al. (2013, 2014a, 2016) for a related ICF model.

12.3. Two-equation models

In Reynolds-averaged Navier–Stokes (RANS) modeling, an ensemble average is performed and the flow is split into a mean and a fluctuating part (Reynolds, 1895)²². Two-equation single-point RANS models are obtained from applying this procedure to the Navier–Stokes equations and truncating the number of fluctuation equations at two. The Reynolds decomposition of an arbitrary scale, f , is denoted by

$$f = \bar{f} + f' \quad (12.2a)$$

while Favre decomposition (Favre, 1965; Bilger, 1975) is denoted by

$$f = \tilde{f} + f'' \quad (12.2b)$$

where $\tilde{f} = \overline{\rho f}/\overline{\rho}$. For steady flows, the measurements defined by the ensemble and time averages are the same (so-called “ergodic hypothesis,” see, for example, Mathieu and Scott, 2000).

Closure approximations are then postulated to close the resulting second- and higher-order correlations (Speziale, 1991). Here, the mean hydrodynamics equations for a single fluid phase are augmented with evolution equations for the turbulent kinetic energy per unit mass K as well as a second governing equation which has been suggested in several forms (Wilcox, 1998). The turbulent kinetic energy, of course, is produced at the expense of internal or potential energy in order to conserve total energy. As for the second transport equation needed for the closure, the dissipation rate ε or the scale length L of the dominant eddies is most frequently utilized.

Actually, there is a variety of two equation models K - Z with $Z = K^m/L^n$ (Lauder and Spalding, 1974). The first applications of RANS modeling to RT were described in Belen'kii and Fradkin (1965), Neuvazhaev and Yakovlev (1976a, b), and Neuvazhaev (1994), but these were one-equation turbulence models with $L = \text{mixing zone width}$. Andronov et al. (1976, 1979) then went on to use a two equation model but this was a K - ν_t model,²³ not a K - ε or K - L model.

One should note the oversimplification in the traditional two-equation turbulence model for mix calculations. The two-equation model can be remarkably successful in describing fully developed turbulence, but it may be inherently challenged in dealing with the production of turbulence from interfacial instabilities. Specifically, these two-equation turbulence models are isotropic, but the turbulent flows induced by hydrodynamic instabilities are both inhomogeneous and anisotropic (Zhou et al., 2002). If RMI turbulence is regarded as the evolution of TKE deposited instantaneously by the shock then, by a simple dimensional argument (Barenblatt, 1983) one finds $h \sim t^{2/3}$. Mikaelian (1990b) pointed out that we have to appeal to the non-isotropic nature of RMI to obtain $h \sim t$ behavior. Subsequently Morgan and Greenough (2016) also stated that the assumption of homogeneous turbulence (Batchelor, 1953) that is implicitly built into the K - L model closures is particularly inaccurate for the early-time evolution.

12.3.1. K - L model

The length-scale equation is first attributed to the classical work by Rotta (1951a, b) and Wolfstein (1970) (see also Speziale, 1987, 1991). Mellor and Yamada (1982) and Mellor and Herring (1973) have discussed the application of the K - L model to either atmospheric or oceanic boundary layers. It has also been applied to the prediction of astrophysical phenomena (Scannapieco and Brüggen, 2008; Brüggen et al., 2009) and compared against measured mixing layer widths from ICF targets (Hurricane et al., 2012; Smalyuk et al., 2012, 2013).

The K - L model has an attractive feature over that of the K - ε model in the context of ICF applications. The initialization of the L profile can be related, at least theoretically, to the interface perturbation, which would be correspond directly to the surface roughness of the capsule.

Aided by the LEM experimental data of Dimonte and Schneider (2000) and the shear layer mixing data obtained by Brown and Roshko (1974), Chiravalle (2006) implemented the K - L model reported in Tipton (1999) into a Lagrangian code with a von Neumann Richtmyer artificial viscosity and calibrated the three model parameters. The predicted total mix width as a function of time was subsequently compared with the experimentally determined values obtained from the RM shock-tube experiments of Vetter and Sturtevant (1995) and Poggi et al. (1998).

The K - L turbulent mixing model (e.g. Dimonte and Tipton, 2006), brought to bear in an arbitrary Lagrangian–Eulerian simulation code ARES, takes the following form (Morgan and Greenough, 2016),

$$\begin{aligned} \frac{D\bar{\rho}}{Dt} &= -\bar{\rho} \frac{\partial \tilde{u}_i}{\partial x_i} \\ \bar{\rho} \frac{D\tilde{Y}_a}{Dt} &= \frac{\partial}{\partial x_i} \left[\left(\bar{\rho} D_a + \frac{\mu_t}{N_Y} \right) \frac{\partial \tilde{Y}_a}{\partial x_i} \right] \end{aligned}$$

²² According to a fascinating article by Launder (2015), this landmark paper was only grudgingly accepted by two very distinguished referees (Sir George Stokes and Sir Horace Lamb) and initially raised little external interest.

²³ Here ν_t denotes the turbulent viscosity. Using dimensional analysis, the K - ν_t model can be related to the K - ε model by $\nu_t \propto K^2/\varepsilon$ (Chou, 1945) and to the K - L model by $\nu_t \propto LK^{1/2}$ (Rotta, 1951a), respectively. Of course, the K - ε and K - L models are connected by $L \propto K^{3/2}/\varepsilon$ (Hanjalić and Launder, 1972; Launder and Spalding, 1974).

Table 12.1

K-L model constants (from Morgan and Greenough, 2016).

	α_b	a_t	b_t	d_t	C_C	C_L	N_Y	N_e	N_K	N_L
Standard set	0.060	1.414	1.20	3.50	1.00	1.00	1.00	1.00	1.00	0.50
Alternative set	0.025	0.290	3.50	1.00	0.33	0.28	0.14	0.14	0.14	0.07

$$\begin{aligned} \bar{\rho} \frac{D\tilde{u}_j}{Dt} &= -\frac{\partial \bar{p}}{\partial x_j} + \frac{\partial}{\partial x_i} (\bar{\sigma}_{ij} + \bar{\rho} \tau_{ij}) \\ \bar{\rho} \frac{D\tilde{e}}{Dt} &= -\bar{p} \frac{\partial \tilde{u}_i}{\partial x_i} + b_t \frac{\mu_t}{\bar{\rho}^2} \left(\frac{\partial \bar{\rho}}{\partial x_i} \frac{\partial \bar{p}}{\partial x_i} \right) + d_t \frac{\bar{\rho}}{L} K^{3/2} + \frac{\partial}{\partial x_j} \left[\tilde{u}_i \bar{\sigma}_{ij} - \bar{q}_j + \frac{\mu_t}{N_e} \frac{\partial \tilde{e}}{\partial x_j} \right] \\ \bar{\rho} \frac{DK}{Dt} &= -b_t \frac{\mu_t}{\bar{\rho}^2} \left(\frac{\partial \bar{\rho}}{\partial x_i} \frac{\partial \bar{p}}{\partial x_i} \right) + \bar{\rho} \tau_{ij} \frac{\partial \tilde{u}_i}{\partial x_j} - d_t \frac{\bar{\rho}}{L} K^{\frac{3}{2}} + \frac{\partial}{\partial x_i} \left[\left(\mu + \frac{\mu_t}{N_K} \right) \frac{\partial K}{\partial x_i} \right] \\ \bar{\rho} \frac{DL}{Dt} &= C_C \bar{\rho} L \frac{\partial \tilde{u}_i}{\partial x_i} + C_L \bar{\rho} \sqrt{2K} + \frac{\partial}{\partial x_i} \left[\frac{\mu_t}{N_L} \frac{\partial L}{\partial x_i} \right] \end{aligned} \quad (12.3)$$

where Y_a is the scalar mass fraction of the component a , D_a indicates the binary molecular diffusivity of component a , and e is the specific internal energy.

To complete above equations, the eddy viscosity, Reynolds stress tensor, strain rate tensor and viscous stress tensor are given by

$$\begin{aligned} \mu_t &= a_t \bar{\rho} L K^{1/2}, \\ \bar{\rho} \tau_{ij} &= 2\mu_t \bar{S}_{ij} - \frac{2}{3} \bar{\rho} K \delta_{ij} \\ \bar{S}_{ij} &= \frac{1}{2} \left(\frac{\partial \tilde{u}_i}{\partial x_j} + \frac{\partial \tilde{u}_j}{\partial x_i} \right) - \frac{1}{3} \frac{\partial \tilde{u}_m}{\partial x_m} \delta_{ij} \\ \bar{\sigma}_{ij} &= 2\mu \bar{S}_{ij}. \end{aligned}$$

The heat flux vector, q_j , is defined as

$$q_j = \underbrace{-\kappa \frac{\partial T}{\partial x_j}}_{\text{conduction}} - \underbrace{\sum_{l=1}^N \rho h_l D_l \frac{\partial Y_l}{\partial x_j}}_{\text{enthalpy diffusion}}$$

where T indicates temperature, κ indicates thermal conductivity, and h_l is the specific enthalpy of component l . Also, $v_t = \frac{\mu_t}{\bar{\rho}}$, $D/Dt \equiv \partial/\partial t + u_i \partial/\partial x_i$, and the standard model coefficients can be found in Table 12.1.

It should be noted that the Dimonte and Tipton (2006) has a more complex treatment for the turbulence kinetic energy source than that implied by Eq. (12.3). The 2006 paper describes a combination of the buoyancy–drag model with the standard K – L model. A key point is a better formulation of the RM source (positive whatever the shock direction).

Kokkinakis et al. (2015) tested the performance of the K – L model (Dimonte and Tipton, 2006) using the ILES results documented in Youngs (2013). The ILES data were obtained with TURMOIL, a Lagrange–Remap hydro-code, which calculates the mixing of compressible fluids by solving the Euler equations plus advection equations for fluid mass fractions. For Rayleigh–Taylor flows at initial density ratios 3:1 and 20:1, the accuracy of the models was examined against the ILES data for different interface pressures and specific heat ratios. The authors recommended two modifications in the original version (Dimonte and Tipton, 2006) of the K – L model. First of all, Kokkinakis et al. found that the correct treatment of the enthalpy flux is needed in the K – L model in order to obtain temperature profiles that agree well with ILES. Indeed, Cook (2009) suggested that when there is species diffusion between N different fluids in multi-component flows (whether turbulent or molecular), an enthalpy diffusion term should be present to account for the energy transfers associated with the compositional changes. It is interesting that the enthalpy term has nearly negligible impact on the mixing width (not shown), but has significant effect for the maximum TKE (Fig. 12.1b). Secondly, the local Atwood number and cell-center gradients are calculated using the densities at the cell face by simple averaging of the numerically reconstructed values, which are obtained from the calculation of the inviscid fluxes. A significant difference between these two treatments can be observed for the self-similar growth rate of maximum TKE (not shown). At any rate, the proposed modifications significantly improve the results of the K – L model, which are found to be in good agreement with ILES with respect to the self-similar mixing width, volume fraction and turbulent kinetic energy profiles, as well as the peak turbulent kinetic energy (TKE) growth rate (Fig. 12.1a).

Morgan and Greenough (2016) also inspected the performance of the K – L model by running a large number of two-dimensional LES realizations with multimode perturbations in the initial conditions (see Fig. 12.2a). The goal here was to simulate the experimental configuration by Tomkins et al. (2008) of a planar shockwave interacting with a cylinder of SF₆

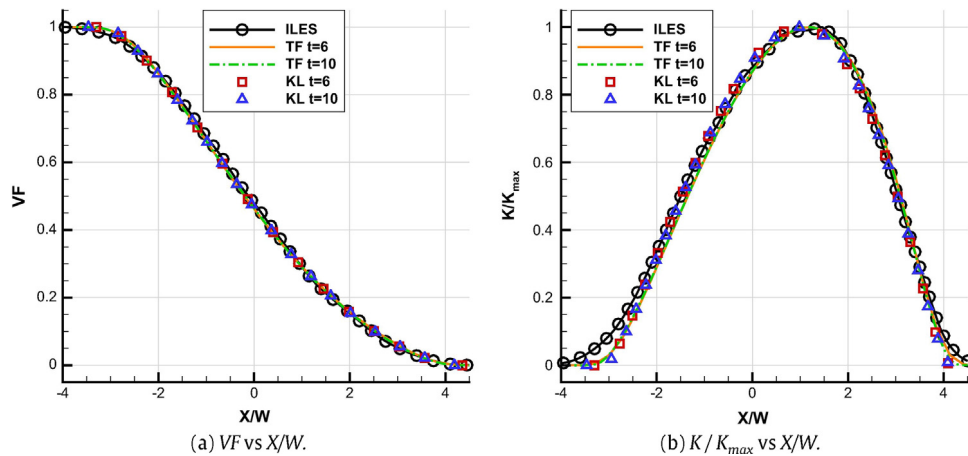


Fig. 12.1a. Volume fraction (left) and Turbulent kinetic energy (right) profiles for RTI mixing of fluids with initial density ratio 3:1.
Source: Fig. 8 of Kokkinakis et al. (2015), *International Journal of Heat and Fluid Flow*.

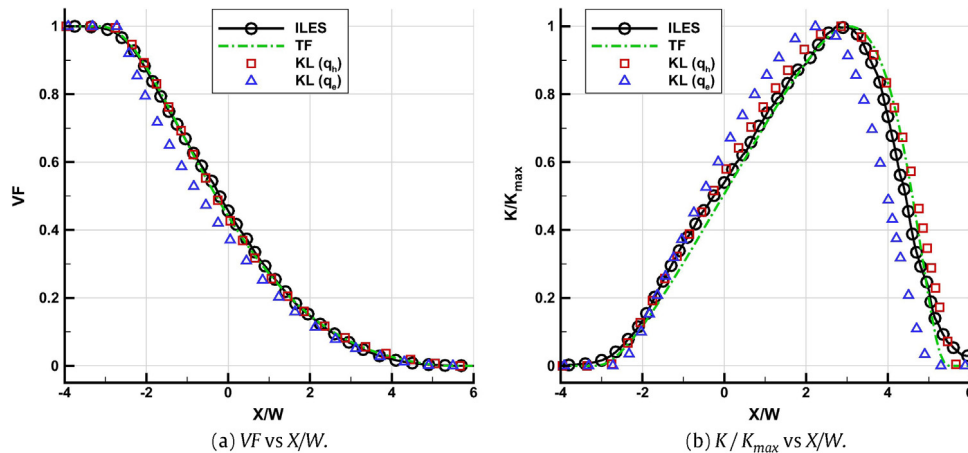


Fig. 12.1b. Volume fraction (left) and Turbulent kinetic energy (right) profiles for RTI mixing of fluids with initial density ratio 20:1. Effect of enthalpy diffusion term.
Source: Fig. 14 of Kokkinakis et al. (2015), *International Journal of Heat and Fluid Flow*.

in air (see also the high-order simulations of this experiment conducted by Shankar et al. (2011)). One of the methods used to initialize turbulence quantities in the $K-L$ RANS calculation was motivated by the approach discussed in Johnson and Schilling (2011a, b). In that work, the RANS models (derived by assuming fully developed turbulent flow), were applied to the linear phase of hydrodynamic instability-generated flows. For simulations with a discontinuous mean flow, the authors found that the growth rates obtained using two-equation RANS models tended to scale with grid resolution. The analytical solutions obtained for both the $K-\varepsilon$ and $K-L$ models in the absence of diffusion provide insight into the choice of appropriate initial conditions for RANS models, impose various constraints on the model coefficients, and can be used to verify numerical discretizations of the model equations.

It should be noted that some recent RANS models set their coefficients based on a self-similar analysis (Dimonte and Tipton, 2006; Morgan and Wickett, 2015). Dimonte and Tipton (2006) derived the coefficient based on the Rayleigh–Taylor bubble growth rate by assuming the value of $\alpha_b = 0.060$ observed experimentally for an immiscible flow. As a result, Morgan and Greenough (2016) considered the possibility of whether a new coefficient, with the lower $\alpha_b = 0.025$, the value obtained in computational studies using ideal initial conditions (see part I), would fix the issue of over-prediction of mixing observed with the standard $K-L$ prescription. The two coefficient sets are summarized in Table 12.1.

Fig. 12.2b (Fig. 22 of Morgan and Greenough, 2016) compared the magnitude of turbulence kinetic energy extracted from the LES ensemble simulations with those from the $K-L$ model predictions. It was clear that neither RANS simulation agrees with LES of the growth rate or spatial distribution of this important quantity (i.e. the TKE). In particular, the authors noted that the RANS simulations predict a more homogenized TKE field and failed to capture the peaks of TKE more localized in the vortex cores as suggested by the LES ensemble simulations.

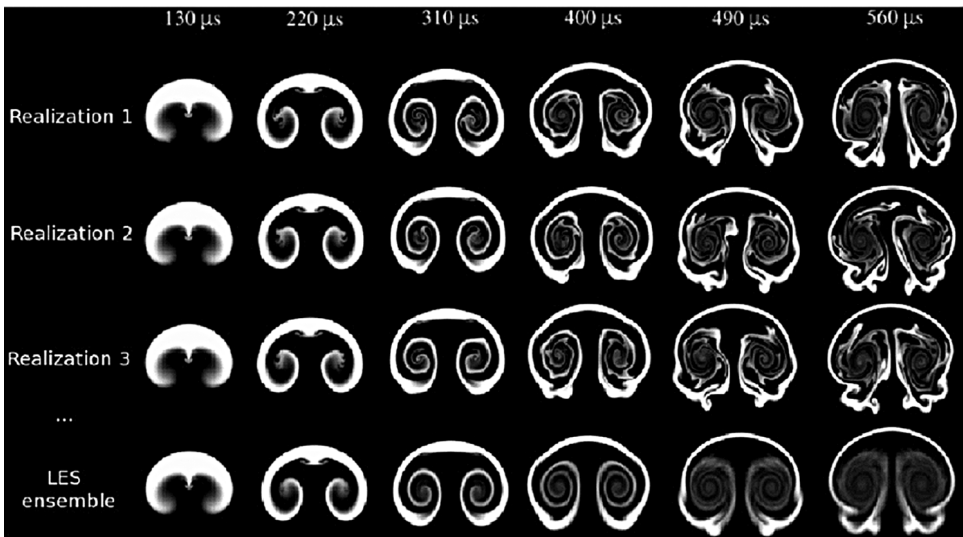


Fig. 12.2a. Effect of initial conditions: SF₆ mass fraction contours obtained from three realizations with perturbed initial conditions and ensemble-averaged contours computed from all 20 realizations. Contours plotted from $Y_{\text{SF}_6} = 0.1$ (black) to 0.6 (white).
Source: Fig. 6 of Morgan and Greenough (2016), Shock Waves, with permission.

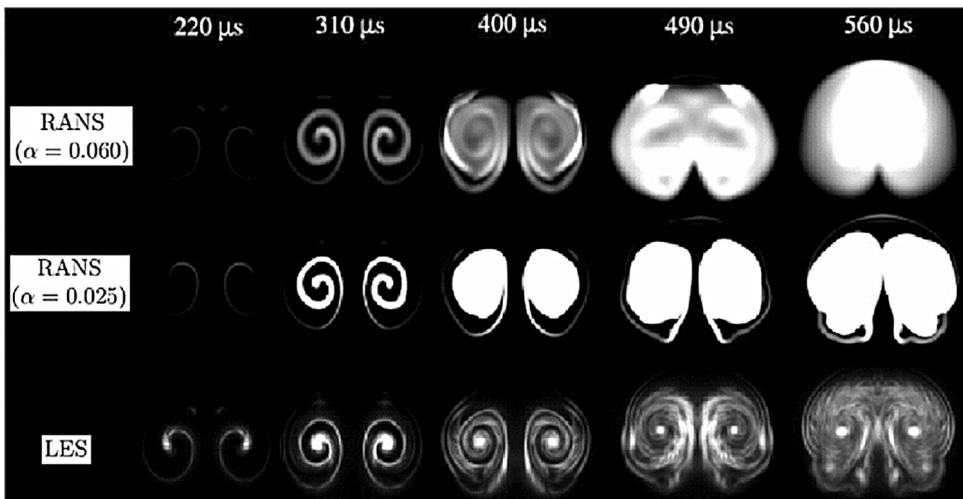


Fig. 12.2b. A comparison of turbulence kinetic energy predicted by three approaches. RANS results taken from simulations on mesh C with $L_0 = 0.01\mu\text{m}$ using standard (top) and new (middle) coefficient sets. Contours of K plotted from 0.0 (black) to $2.0 \times 10^{-7} \text{ gcm}^2/\mu\text{s}^2$ (white).
Source: Fig. 22 of Morgan and Greenough (2016), Shock Waves with permission.

While the $K-L$ mixing model uses a single velocity, which makes it numerically efficient and robust, it precludes the description of de-mixing when the acceleration reverses sign (Kokkinakis et al., 2015).

12.3.2. $K-\varepsilon$ model

In the standard $K-\varepsilon$ model – which is probably the most popular two-equation model (Speziale, 1991), the length and time scales are built up from the turbulent kinetic energy, K , and dissipation rate, ε (Jones and Launder, 1972). As noted in their paper, much of the original ideas come from the Harlow and Nakayama (1967, 1968).²⁴ The dissipation rate equation is obtained by dividing each term of the kinetic energy equation by the turbulent time scale, K/ε . The final form of the

²⁴ In an interesting memoir, Harlow (2004) recounted the research activities of T-3, a group he formed in the Theoretical Division of Los Alamos National Laboratory, as it used scientific computing to solve fluid dynamics problems.

equation is obtained by introducing appropriate dimensionless coefficients (see also Hanjalić and Launder, 1972; Launder and Spalding, 1974; Hanjalić, 1994).

Gauthier and Bonnet (1990) calibrated the $K-\varepsilon$ model with the shock tube experiments of Andronov et al. (1976) and Brouillette and Sturtevant (1989). In order for the model to be valid under strong gradients, the authors found that the classical linear closure relations must be supplemented with some algebraic relations. While other constants were chosen conventionally, two sets of constants ($C_{\varepsilon 0}$ and σ_ρ) were needed for the model to match the experimental data. A detailed study revealed that the spectrum is wider in the Andronov et al. experiment than in the Brouillette and Sturtevant case, but with the same magnitude for the small length scales.

RANS models are often applied to three-dimensional flows having a dominant direction (the direction of the mean flow gradients, taken to be the x_3 direction here), with the averaging over the perpendicular (homogeneous) x_1 and x_2 directions. The mean flow equations are coupled to modeled equations for the turbulent kinetic energy K and its dissipation rate, ε (Gauthier and Bonnet, 1990),

$$\begin{aligned} \frac{dK}{dt} &= \left(S^2 - \frac{\mathcal{N}^2}{\sigma_\rho} + \frac{2d-2}{d} \mathfrak{D}^2 \right) v_t - \frac{2}{d} \mathfrak{D} K - \varepsilon + \frac{1}{\bar{\rho}} \frac{\partial}{\partial x_3} \left[\left(\mu + \frac{\mu_t}{\sigma_K} \right) \frac{\partial K}{\partial x_3} \right] \\ \frac{d\varepsilon}{dt} &= \frac{\varepsilon}{K} \left(C_{\varepsilon 1} S^2 - C_{\varepsilon 0} \frac{\mathcal{N}^2}{\sigma_\rho} + \frac{2d-2}{d} C_{\varepsilon 3} \mathfrak{D}^2 \right) v_t - \frac{2}{d} C_{\varepsilon 3} \mathfrak{D} \varepsilon - C_{\varepsilon 2} \frac{\varepsilon^2}{K} + \frac{1}{\bar{\rho}} \frac{\partial}{\partial x_3} \left[\left(\mu + \frac{\mu_t}{\sigma_\varepsilon} \right) \frac{\partial \varepsilon}{\partial x_3} \right] \end{aligned} \quad (12.4)$$

where σ_ρ , σ_K , σ_ε and $C_{\varepsilon m}$ ($m = 0, 1, 2$, and 3) are positive dimensionless coefficients and $d = 1$ for fluctuations with the dominant velocity component.²⁵ The turbulent viscosity is given by $v_t = \frac{\mu_t}{\bar{\rho}} = C_\mu \frac{K^2}{\varepsilon}$, where $C_\mu = 0.09$ (Durbin and Petterson Reif, 2001; Chen and Jaw, 1998). The mean shear, square of the Brunt–Väisälä frequency, and dilatation are defined as

$$S \equiv \frac{\partial \tilde{u}_i}{\partial x_3}, \mathcal{N} \equiv \sqrt{-\frac{1}{\bar{\rho}^2} \frac{\partial \bar{\rho}}{\partial x_3} \frac{\partial \bar{p}}{\partial x_3}}, \mathfrak{D} \equiv \frac{\partial \tilde{u}_3}{\partial x_3}$$

with $i = 1$ or 2 (see for example Johnson and Schilling, 2011a).

Yanikin et al. (1995) applied a $K-\varepsilon$ model for computations of turbulent mixing in 2D compressible flows, including turbulent mixing at acceleration at an angle to the interface. Leith (1986) and Leith and Margolin (1990) implemented two turbulence models in a two-dimensional fluid code. In this work, a two-equation model, which describes the average mixing due to turbulence, was modified to include terms relating to compressible flows. In addition, a subgrid-scale two-equation model including stochastic backscatter (Leith, 1990; Zhou, 1991) provided realizations of random, but resolvable structures. Morán-López and Schilling (2013, 2014) developed a multicomponent $K-\varepsilon$ RANS model that includes an improved shock production closure, enthalpy diffusion, and other quantities typically neglected (molecular dissipation, diffusion, and conduction etc.), and showed that very good agreement could be obtained with the mixing layer widths before and after reshock from the shock tube experiments of Vetter and Sturtevant (1995), Poggi et al. (1998) and Leinov et al. (2009). The mixing layer widths were also compared to results from Lagrangian simulations of the Reynolds-averaged Euler equations closed using the originally formulated BHR turbulence model (Valerio et al., 1999).

On the other hand, Yang et al. (2011) focused instead on applying the $K-\varepsilon$ model to constant and variable acceleration RTI mixing. As noted in Part I, the RTI with a complex acceleration history is an interesting topic, with detailed experimental and numerical studies with consecutive periods of RT-unstable, -stable, and -unstable acceleration (Kucherenko et al., 1993, 1997a,b; Youngs, 1997; Dimonte et al., 2007; Ramaprabhu et al., 2013, 2016; Aslangil et al., 2016). The authors compared the time evolution of the mixing layer width between the $K-\varepsilon$ model to the data of Kucherenko et al. and Youngs.

Gréa (2015) applied a stability analysis of the self-similar solution to the equations for the $K-\varepsilon$ mix model in order to identify slow manifolds. By projecting the state variables on it, the dimension of the problem is reduced and the model is transformed into a set of ordinary differential equations. Even if its coefficients have been correctly calibrated for the self-similar solution, Gréa showed that the model could generate unphysical growth rates when the mixing zone enters a rapid phase and can have an important sensitivity to initial conditions. One might argue that this work has some parallel to that of Speziale and Mac Giolla Mhuiris (1989), who placed an emphasis on examining the ability of RANS models to predict equilibrium states accurately for a range of values of the parameter Ω/S (the ratio of the rotation rate to the shear rate). In particular, the $K-\varepsilon$ model was found to erroneously yield equilibrium states that were independent of Ω/S .

Before concluding this discussion on the $K-\varepsilon$ model, recall that such prescriptions trace their origin to aerodynamic applications (Speziale, 1991; Wilcox, 1998). Here, the interaction of shock waves with turbulent media could also be an important issue. Sinha et al. (2003) found that modeling shock front distortion or imposing realizability constraints (Durbin, 1996; Shih et al., 1995) were necessary, as the standard $K-\varepsilon$ model performs poorly against either direct numerical simulation (DNS) in the general case or linear interaction analysis (LIA) in the weak turbulence limit.

²⁵ $d = 3$ for isotropic velocity fluctuations.

12.4. Two-scale models

A two-scale model might be appropriate for describing the mixing zone evolution. The results from the DNS suggest that there are two regions containing different physical processes: (1) the regional interfaces (bubble and spike fronts) where fluid interpenetration is occurring, and the medium is inhomogeneous and anisotropic; and (2) the interior of the turbulent region, where it is assumed that the medium is homogeneous and isotropic at high Reynolds number (this assumption is for modeling purposes and is not necessarily correct for low Reynolds number).

[Grégoire et al. \(1999\)](#) proposed a two-time-scale turbulence model by partitioning the turbulent kinetic energy spectrum into two regions, using the filtering process within the Favre averaging framework. The equations for the first region are the spectral flux and the dissipation rate, and the short time scale is closed along the same line as in a previously described $K-\varepsilon$ model. There is an energy transfer between these two spectral regions and the modeling equations are restricted to the large Reynolds numbers limit.

[Souffland et al. \(2002\)](#) applied the same methodology to compute the Rayleigh–Taylor configuration and three RMI shock tube experiments (CEA, VNIIEF and Caltech) experiments. The time evolution of the mixing layer width was reproduced reasonably well, except for the Caltech experiment. Also, the agreement on turbulence levels between the calculation results and CEA experimental data was only qualitative. Nevertheless, this study showed that two-time-scale turbulence models give extra information compared with a classical $K-\varepsilon$ model, in configurations where the turbulence energy spectrum is often far away from equilibrium. Yet, some of the well-known limitations of the $K-\varepsilon$ model, such as handling the anisotropy, still remain in the model that makes use of the turbulent viscosity concept.

A transport mix model has been developed ([Zhou et al., 2002](#)) based on a single velocity framework because of the desire to preserve a relatively quick turnaround time for ICF calculations and to permit relatively easy implementation in the code structure. This is an attempt to recover the physics of multi-fluid based turbulence models, but using a considerably simpler system based on a single velocity framework. A two-scale model, in the spirit of [Hanjalić et al. \(1980\)](#) and [Schiestel \(1987\)](#), has been developed for mix calculations (see also [Zhou et al., 2003c](#)). More specifically, this model partitions the turbulent mix induced by RTI and RMI into two distinct regions identified by B (generalized buoyancy–drag model) description and T (turbulence model description), respectively. The model treats the dynamics of interpenetration between the heavy and light fluids in the B region using a buoyancy–drag model and an energy equation for the buoyancy–drag description. The interfacial region, B , also provides the energy source to the turbulence region, T (modeled with a $K-\varepsilon$ equations). A summary version of the equations is given in Table I of [Zhou et al. \(2003b\)](#). Because it uses the buoyancy–drag model in the B region, this model is not restricted to fully turbulent regimes and can treat inhomogeneous, anisotropic flows.

This two-scale model was validated against a constant acceleration experiment conducted by [Kucherenko et al. \(1991\)](#), the impulsive acceleration experiment of [Dimonte and Schneider \(1996, 2000\)](#) and a RMI reshock experiment conducted by [Vetter and Sturtevant \(1995\)](#). [Hoffman et al. \(2010\)](#) compared the model prediction with results from high-resolution 2D multimode simulations of a NIF Rev3 CH(Ge) ignition capsule, using the time-varying angle-averaged radial profiles of ion species composition as the calibration reference.

12.5. Three- and four-equation models

12.5.1. Original Besnard, Harlow, Rauenzhan (BHR) model

Like many standard turbulence transport models, the BHR model was based on the decomposition of the fluid variables into a mean component and a fluctuating part, from which statistical correlations were then formed. A standard Favre average ([Favre, 1965](#); [Bilger, 1975](#)) was used given the desired application to variable density flows. [Besnard et al. \(1992\)](#) recognized that many applications of interest are time-unsteady flows involving two or more materials. They realized that the Reynolds stress models must consistently include evolution equations for all relevant second-order correlations, in order to describe flows of this nature adequately ([Besnard et al., 1987](#)).

The evolution equations are given after closure approximations for the important fields of the original BHR model ([Besnard et al., 1992](#)). These fields are the Reynolds stress, turbulence length scale, mass flux, and density-specific volume correlation. The quantity of the mass flux, a_i , is defined as

$$a_i = \frac{\overline{\rho' u'_i}}{\overline{\rho}} = -\overline{u''_i} \quad (12.5a)$$

and the density self correlation (or density-specific-volume), b , is given by

$$b = -\overline{\rho' \left(\frac{1}{\rho}\right)'} \quad (12.5b)$$

[Besnard et al. \(1989\)](#) stressed that the unique features of BHR are that, unlike other transport models, it is not restricted to fully turbulent regimes. The very choice of retaining second-order correlations such as the turbulent mass flux and the density variance not only gives the model the ability to describe the two-field, non-turbulent interpenetration of the different materials, but also to account for the different phases of the instability development.

[Valerio et al. \(1999\)](#) also pointed out that the originality of this treatment is that it includes equations for all the second-order correlations that can be formed from the fluctuations of velocity and density, computed either with higher-order correlation evolution equations or algebraic closures. These closure choices result in different versions of the BHR models.

12.5.2. BHR-CEA, BHR1, K-L-a

[Besnard et al. \(1989\)](#) and [Valerio et al. \(1999\)](#) described their implementation of the BHR model at CEA. The reduced model equations used the turbulent kinetic energy K , the turbulent mass flux a , the correlation of the density fluctuation, and the dissipation correlation. The model results for the mixing rates and intensities compare favorably with a 2D, second-order Eulerian code with a mixed-cell treatment, EAD ([Besnard et al., 1989](#)).

[Valerio et al. \(1999\)](#) further calibrated this model with data from the shock tube experiments of [Andronov et al. \(1976\)](#) and [Brouillette and Sturtevant \(1993\)](#). With the same set of model constants, the authors presented the comparison between calculated and experimental measured ([Jourdan et al., 1997](#)) time evolution of the turbulent mixing zone widths, obtained in the heavy/light (CO_2/He), close densities (CO_2/Ar), and light/heavy (CO_2/Kr) gas combinations, respectively. Different gas pairs with both various Atwood and incident shock wave Mach numbers were considered, in order to delineate the influence of these parameters.

The so-called BHR1 model has been implemented in a LANL RAGE hydrocode ([Gittings et al., 2008](#)) and consists of dynamic equations for the turbulent kinetic energy K , the length scale L , and the turbulent mass flux a (Eq. (12.5a)). It should be stressed that with the exception of [Denissen et al. \(2012\)](#), “ S ” has been used by LANL authors to denote the length scale for all of the different BHR versions. In any case, the BHR1 model may be considered a variable-density extension of the more traditional two-equation models, coupled with a modeling methodology suitable for variable-density flows ([Banerjee et al., 2010a](#)). The density-specific volume correlation, b , is coupled to the principal driving term in the mass flux equation and is approximated by a two-fluid algebraic expression. The results of the BHR1 model have been compared to a variety of turbulence experiments and numerical simulations of turbulent flows, that include low speed shear layer flows, reshock experiments, RTI flows over a wide range of Atwood numbers, and moderate Atwood number DNS of RTI flows ([Banerjee et al., 2010a](#)).

Essentially, a $K-L-a$ model could be obtained from the original BHR formulation if one foregoes the evolution equations for R_{ij} and b . Of course, such three equation models can also be constructed from the opposite direction by adding a dynamic equation for the mass flux, a , to a standard $K-L$ model (for example [Dimonte and Tipton, 2006](#)). The equation for the mass flux, a_i , is given by ([Morgan and Wickett, 2015](#))

$$\bar{\rho} \frac{D a_j}{D t} = C_B^2 b \frac{\partial \bar{p}}{\partial x_j} - C_a \bar{\rho} a_j \frac{(2K)^{1/2}}{L} + \tau_{ij} \frac{\partial \bar{\rho}}{\partial x_i} + \frac{\partial}{\partial x_i} \left(\frac{\mu_t}{N_a} \frac{\partial a_j}{\partial x_i} \right) \quad (12.6)$$

where b is closed in terms of component partial densities and volume fractions, C_a , C_B , and N_a are undetermined model constants which will be set through similarity analysis (along with other $K-L$ model coefficients in [Table 12.1](#)). [Morgan and Wickett \(2015\)](#) applied a $K-L-a$ model to several one-dimensional test problems and reported favorable comparisons with shock tube data up to $A = 0.67$ and $Mach = 1.98$, demonstrating model flexibility at least comparable to the standard $K-L$ model.

Recently, [Wang et al. \(2015b\)](#) used a time-dependent radiation hydrodynamics simulation code, KULL ([Rathkopf et al., 2000](#)), to perform two- and three-dimensional numerical simulations of the recent NIF counter-propagating shear flow experiments ([Doss et al., 2015](#)). The experiments provided the data to calibrate the initial conditions of a $K-L-a$ model, and the numerical model was used to investigate the geometry effects at late times. The initial condition for the length scale L_0 of the model was determined so that the evolution of the mixing layer width obtained from the simulations would agree with that measured from the experiments.

With the BHR1 model implementation, the dynamic equation for the density self-correlation, b , is approximated by an analytic expression. [Stalsberg-Zarling and Gore \(2011\)](#) discussed in detail the challenges caused by this simplification when applied to homogeneous variable density turbulence. As shown in [Fig. 12.3](#), the BHR1 model failed to capture the correct physics for both the TKE and mass flux. Using BHR1, b remains constant, but the density fluctuations should decrease due to molecular mixing. Here the fluids are always serving as the driving sources for both the K and a equations, preventing the decay of the TKE.

12.5.3. BHR2

It should come as no surprise that the LANL BHR2 formulation now contains a dynamic equation for the density-self correlation, b ([Stalsberg-Zarling and Gore, 2011](#)). As implemented in the RAGE hydrocode, BHR2 transports this correlation along with evolution equations for the species mass fractions, K , L , a , and the usual conservation equations for mass, momentum, and energy. [Fig. 12.4a, b, c](#) shows that the match between the BHR2 model and the DNS is improved significantly for three Atwood numbers (0.05, 0.25, and 0.5).

BHR2 still represents a significant simplification of the original BHR work. In particular, a gradient approximation for the turbulent heat flux is applied and an algebraic closure for the Reynolds stress is given

$$R_{ij} = \frac{2}{3} \bar{\rho} K \delta_{ij} - \frac{2}{3} \frac{C_S}{R} \bar{\rho} \sqrt{KL} \left(\frac{\partial \tilde{u}_i}{\partial x_j} + \frac{\partial \tilde{u}_j}{\partial x_i} - \frac{2}{3} \delta_{ij} \frac{\partial \tilde{u}_n}{\partial x_n} \right) - \frac{C_A}{R} \frac{L}{\sqrt{K}} \left(a_i \frac{\partial \bar{P}}{\partial x_j} + a_j \frac{\partial \bar{P}}{\partial x_i} - \frac{2}{3} \delta_{ij} a_n \frac{\partial \bar{P}}{\partial x_n} \right). \quad (12.7)$$

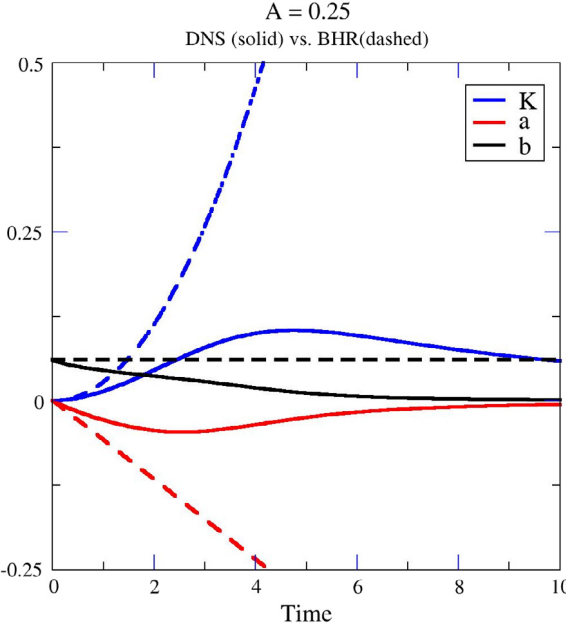


Fig. 12.3. Time evolution of TKE, mass flux, and density self-correlation. Solid curve: DNS of homogeneous variable density turbulence; dashed: BHR1 model calculations.

Source: Fig. 78 of Stalsberg-Zarling and Gore (2011) with permission from Los Alamos National Laboratory.

This Favre averaged Reynolds stress is appropriate for variable density turbulence and the expression \check{R} on the right-hand side of above equation must be evaluated from the velocity gradient as well as other terms (not shown, see Ristorcelli et al., 2005; Stalsberg-Zarling and Gore, 2011). This model now takes into account the principal production terms of TKE in variable-density flows, namely, $\partial P/\partial x_i$.

Yet, Stalsberg-Zarling and Gore (2011) found that the numerical implementation of the term containing C_A leads to instabilities in the results of some flows at very late times. As a result, C_A was set to zero in that study. Of course, the Favre averaged Reynolds stress model reduces to the standard Boussinesq approximation if $C_A = 0$ and $\check{R} = 1$.

Denissen et al. (2012, 2014) implemented and validated the BHR2 model in the arbitrary Lagrangian-Eulerian (ALE) hydrodynamics code FLAG (Waltz and Gianakon, 2012; Denissen et al., 2014; Black et al., 2017). The bulk hydrodynamic equations are the ensemble averaged Euler equations

$$\begin{aligned} \frac{D\bar{\rho}}{Dt} &= -\bar{\rho} \frac{\partial \tilde{u}_j}{\partial x_j} \\ \bar{\rho} \frac{D\tilde{u}_i}{Dt} &= -\frac{\partial}{\partial x_j} \left(\bar{\rho} \delta_{ij} + \overline{\rho u''_i u''_j} \right) + \bar{\rho} g_i \\ \bar{\rho} \frac{D\tilde{e}}{Dt} &= -\bar{p} \frac{\partial \tilde{u}_j}{\partial x_j} - \frac{\partial}{\partial x_j} \left(\overline{\rho e'' u''_j} \right). \end{aligned} \quad (12.8)$$

The BHR2 mix model in Lagrangian form are given by

$$\begin{aligned} \bar{\rho} \frac{DK}{Dt} &= a_j \frac{\partial \bar{p}}{\partial x_j} + \frac{\partial}{\partial x_j} \left(\frac{\mu_t}{\sigma_K} \frac{\partial K}{\partial x_j} \right) - R_{ij} \frac{\partial \tilde{u}_i}{\partial x_j} - \bar{\rho} \frac{K^{3/2}}{L} \\ \bar{\rho} \frac{DL}{Dt} &= \frac{L}{K} \left[\left(\frac{3}{2} - C_4 \right) a_j \frac{\partial \bar{p}}{\partial x_j} - \left(\frac{3}{2} - C_1 \right) R_{ij} \frac{\partial \tilde{u}_i}{\partial x_j} \right] - C_3 \bar{\rho} L \frac{\partial \tilde{u}_j}{\partial x_j} + \frac{\partial}{\partial x_j} \left(\frac{\mu_t}{\sigma_L} \frac{\partial L}{\partial x_j} \right) - \left(\frac{3}{2} - C_2 \right) \bar{\rho} K^{1/2} \\ \bar{\rho} \frac{Da_i}{Dt} &= b \frac{\partial \bar{p}}{\partial x_i} + \bar{\rho} \frac{\partial a_i a_j}{\partial x_j} - \bar{\rho} a_j \frac{\partial (\tilde{u}_i - a_i)}{\partial x_j} - \frac{R_{ij}}{\bar{\rho}} \frac{\partial \bar{\rho}}{\partial x_j} + \frac{\partial}{\partial x_j} \left(\frac{\mu_t}{\sigma_a} \frac{\partial a_i}{\partial x_j} \right) - C_a \bar{\rho} a_i \frac{K^{1/2}}{L} \\ \bar{\rho} \frac{Db}{Dt} &= 2 \bar{\rho} a_j \frac{\partial b}{\partial x_j} - 2(b+1) a_j \frac{\partial \bar{\rho}}{\partial x_j} + \bar{\rho}^2 \frac{\partial}{\partial x_j} \left(\frac{\mu_t}{\bar{\rho}^2 \sigma_b} \frac{\partial b}{\partial x_j} \right) - C_b \bar{\rho} \frac{K^{1/2}}{L} b \end{aligned} \quad (12.9)$$

The coefficients in the model are set from canonical test cases (Banerjee et al., 2010a; Stalsberg-Zarling and Gore, 2011). The default model coefficients that are not set to unity are summarized in Table 12.2.

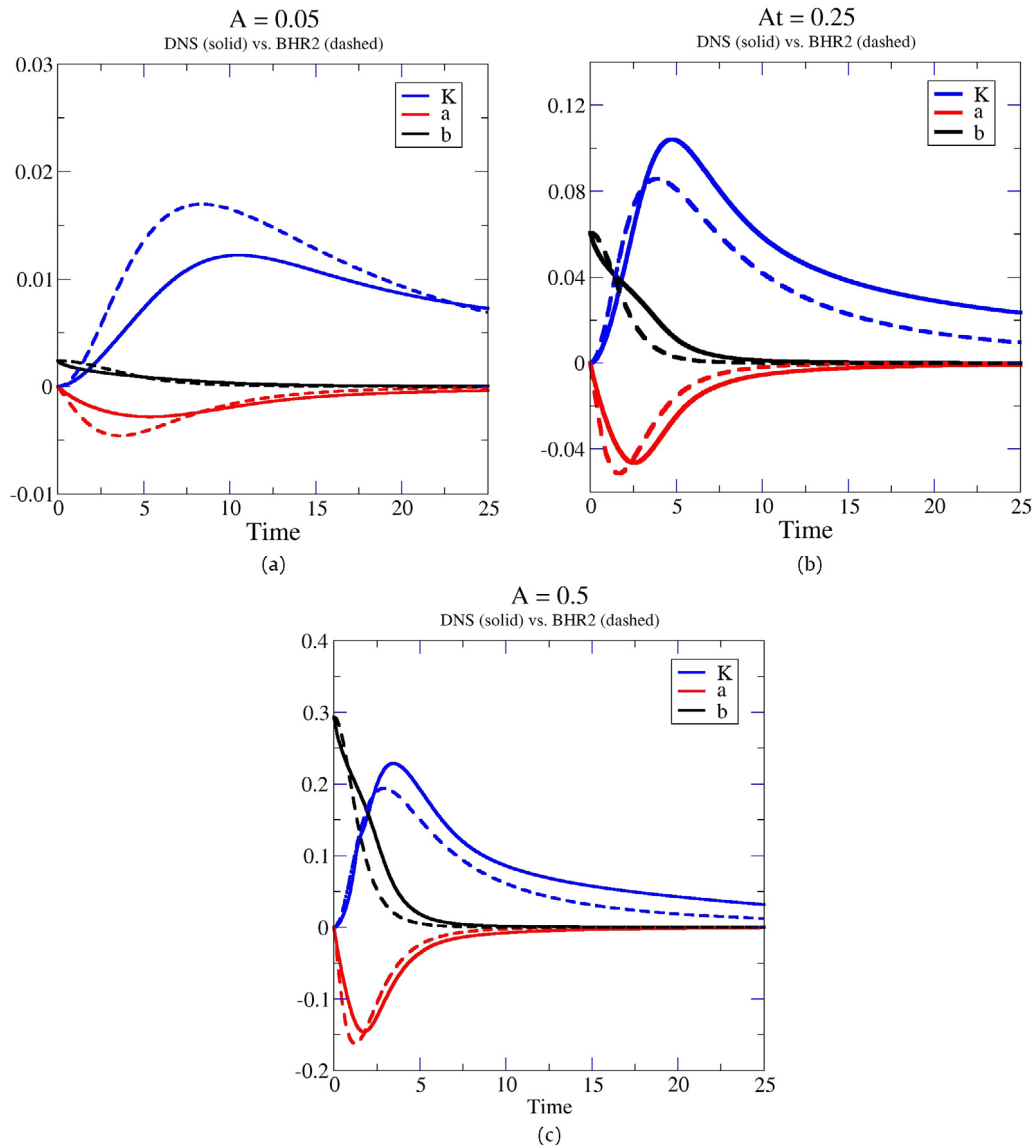


Fig. 12.4. a-c Turbulent kinetic energy, mass flux velocity and density-specific volume correlation results for DNS of homogeneous variable-density turbulence with an Atwood number of 0.05 (Fig. 12.4a), 0.25 (Fig. 12.4b), 0.5 (Fig. 12.4c) compared with results using BHR2.
Source: Figs. 79–81 of [Stalsberg-Zarling and Gore \(2011\)](#), with permission from Los Alamos National Laboratory.

Table 12.2
Default parameter values for BHR2 [Denissen et al. \(2014\)](#).

C_μ	C_1	C_2	C_4	C_a	C_b	σ_c	σ_s	σ_b
0.28	1.44	1.92	1.05	6.0	2.5	0.6	0.1	3.0

To provide detailed quantitative data to assist in validating the BHR2 model, [Welser-Sherrill et al. \(2013\)](#) carried out two experiments on the evolution of shear-driven and reshocked mix layers at the OMEGA laser facility. Simulations of both the reshock and shear experiments using the RAGE hydrodynamics code and the BHR2 mix model showed good agreement with the mix evolution seen in the experimental data, giving confidence that the mix model is capable of simulating the behavior of both flows. [Doss et al. \(2013a,b\)](#), [Merritt et al. \(2015\)](#), [Flippo et al. \(2016a,b\)](#) performed additional comparison between the

shear-driven data and the mix model. This agreement was achieved with BHR2 with standard parameter settings, without tuning of the model constants.²⁶

BHR2 was also evaluated using the data from the AWE “Tilted-Rig” experiments (Smeeton and Youngs, 1987; Youngs, 1989)²⁷. This experiment consists of a tank filled with light fluid above heavy, and then “tilted” on one side of the apparatus. The tilt gives rise to an “angled interface” in relation to an acceleration history due to rockets attached at the top of the tank. The significance of this test problem is that the “Tilted-Rig” is a unique two-dimensional RT mixing experiment that has experimental data, DNS data from Livescu and Wei using the CFDNS code (Livescu et al., 2010, 2011), and ILES and DNS results of Youngs (2017). The TKE, mixedness, and density-self correlations obtained from the DNS are shown in Fig. 12.5 (Andrews et al., 2014).

Denissen et al. (2014) showed that the BHR2 model could efficiently predict a variety of “Tilted-Rig” turbulence quantities, including mixing width, TKE, and mass-flux, which are consistent with more computationally expensive ILES models. Moreover, the model is capable of capturing several distinctive features of the tilted rocket rig, including the distributions of the TKE and mass-flux.

Waltz and Gianakon (2012) compared performance of the BHR2 and $K-L$ models implemented in the FLAG hydrocode. For spherical, radiatively driven ICF capsules, the additional fidelity of the BHR model does not appear to provide any advantage over the $K-L$ model for this class of idealized RT simulation. In another study, Morgan et al. (2017) extracted turbulence kinetic energy, mass-flux velocity, and density-specific-volume correlation profiles from the LES of a low Atwood number RT mixing layer in the self-similar regime and compared them with results obtained using the $K-L-a$ and BHR2 models. It was found that while both RANS models predicted similar linear mass fraction profiles, the $K-L-a$ results appear to agree better with LES for these measurements than do the BHR2 results.

Haines et al. (2013b) performed 3D ILES simulations of the Welser-Sherrill et al. reshock experiment to test the performance of two-dimensional RANS simulations. This work took advantage of a previous 3D ILES simulation (Haines et al., 2013a) of the inverse chevron shock tube laboratory experiment (Holder and Barton, 2004), where an initialization scheme was validated and BHR2 was benchmarked by comparing moments extracted from averaged ILES 3D data and those predicted directly by 2D mix model. The ILES results showed that after first reshock the computed Reynolds stresses in the direction of the shock become anisotropic and remain anisotropic even after the second reshock, an observation that BHR2 failed to capture.

12.6. Reynolds stress models

Reynolds stress models (RSM) trace their roots to the classical work by Chou (1940, 1945), Rotta (1951a, b) and Launder et al. (1975). Andronov et al. (1982) applied such a model to various shock tube experiments and reported that the model simulated the mixing zone thickening satisfactorily.

From the $K-L$, $K-\varepsilon$, BHR1, and BHR2 models, the predictions are all isotropic when the interface is away from the shock. Yet, this result is not supported by the CEA shock tube experiment described in Poggi et al. (1998) and Poggi (1997). More specifically, the measurements of instantaneous velocities were carried out to measure the components of the Reynolds stress tensor through Laser Doppler Anemometry (LDA). The experimental data clearly illustrates the anisotropy of the Reynolds stress tensor.

12.6.1. Reynolds stress and ε model by Grégoire, Souffland, and Gauthier

Grégoire et al. (2005) developed their second-order turbulence model, GSG, relying heavily on the RMI experimental data. The GSG model, which consists of the Reynolds stress and dissipation rate equations, is actually rather similar to the classical work by Hanjalić and Launder (1972).

Supplemented by a dissipation rate equation, the GSG governing equations²⁸ consist of the Reynolds stresses $\tilde{R}_{ij} = \rho u_i'' u_j'' / \bar{\rho}$, mass flux $\bar{u}_i'' = -\rho' \bar{u}'_i / \bar{\rho}$, density variance $\bar{\rho}^2$,

$$\begin{aligned} \bar{\rho} \frac{D\tilde{R}_{ij}}{Dt} &= p_{ij}^R + p_{Hij}^R + \Phi_{ij}^R + \mathcal{D}_{ij}^R + \mathcal{E}_{ij}^R \\ \bar{\rho} \frac{Du_i''}{Dt} &= p_i^u + p_{Hi}^u + \Phi_i^u + \mathcal{D}_i^u + \mathcal{E}_i^u \\ \frac{D\rho^2}{Dt} &= p^\rho + p_H^\rho + \mathcal{D}^\rho + \mathcal{E}^\rho \end{aligned} \quad (12.10)$$

where the production, redistribution, diffusion and dissipation terms in the equations can be found in Table 12.3. Here, the material derivative D/Dt is built with the mean velocity. For the sake of brevity, the GSG model coefficients will not be reproduced here (see Table 2 of Grégoire et al., 2005). Note also the typos in the definition of the mass flux and the transport equation for Reynolds stresses in Grégoire et al. (2005) have been corrected above.

²⁶ See Section 15 for more detailed discussion.

²⁷ There are related tilted-interface experiments at Imperial College (Andrews and Spalding, 1990) and at Cambridge University (Holford et al., 2003).

²⁸ Grégoire et al. (2005) used \bar{u}_i'' to denote the mass flux, while other authors used $a_i = \rho' \bar{u}'_i / \bar{\rho} = -\bar{u}_i''$ (see Eq. (12.5a)).

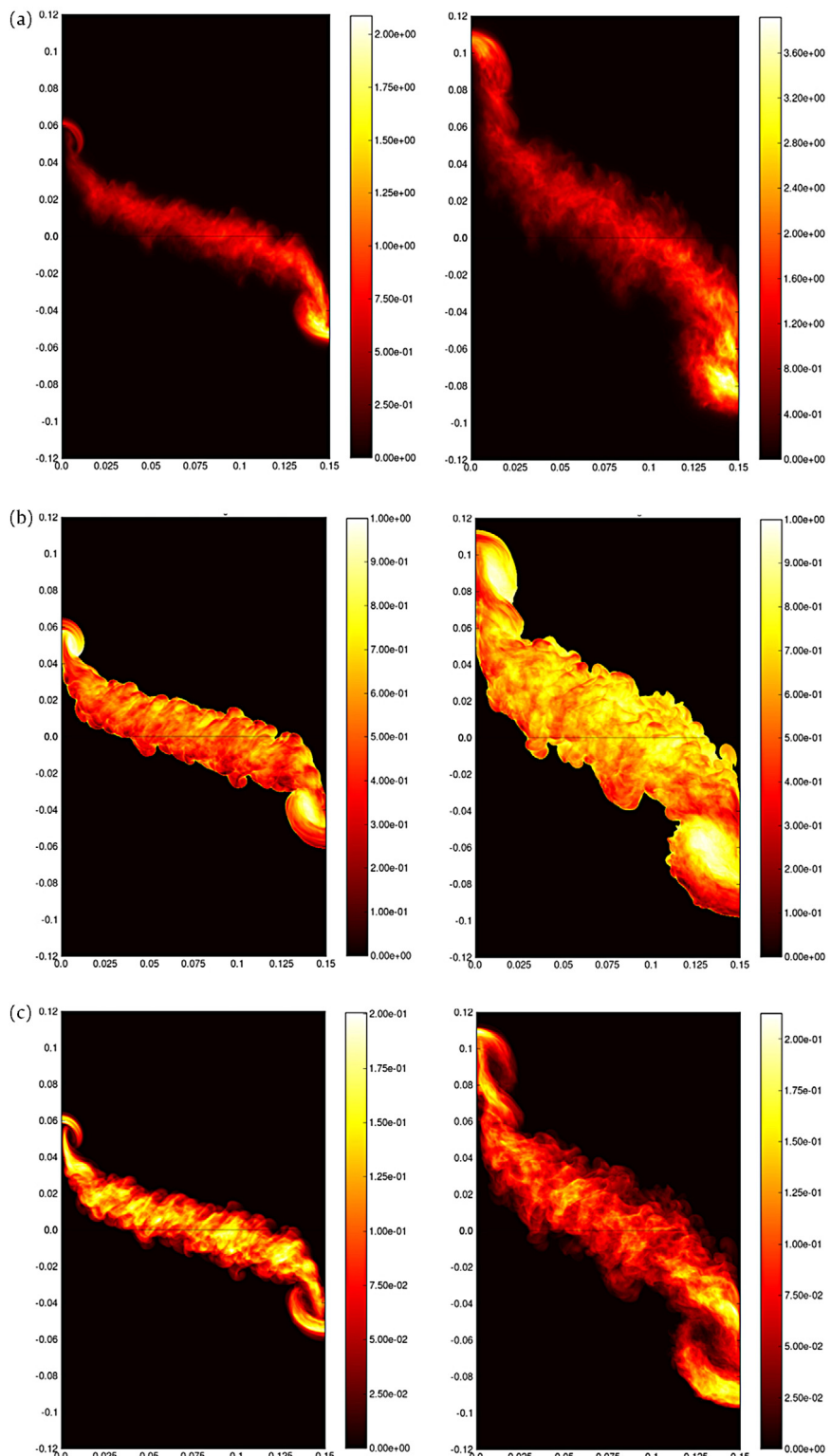


Fig. 12.5. Direct numerical simulations shown for the scaled time = 1.256 (left) and 1.741 (right). (a) the turbulent kinetic energy, (b) molecular mix parameter, and (c) density-specific volume correlation.

Source: Figs. 22–24 of Andrews et al. (2014), ASME J. Fluids Eng. with permission.

Table 12.3

Production, redistribution, diffusion and dissipation terms in the equations for Reynolds stresses, mass flux, density variance. The notation # stands for R , u , and ρ , respectively.

Source: From Table 1 of Grégoire et al. (2005).

\tilde{R}_{ij}	$\overline{u''_i}$	$\overline{\rho'^2}$
$p^# - \bar{\rho} \tilde{R}_{ik} \frac{\partial \bar{u}_j}{\partial x_k} - \bar{\rho} \tilde{R}_{jk} \frac{\partial \bar{u}_i}{\partial x_k}$	$-\bar{\rho} \overline{u_j''} \frac{\partial \bar{u}_i}{\partial x_j}$	$-2\bar{\rho} \overline{u_i''} \frac{\partial \bar{u}_i}{\partial x_i}$
$\tilde{p}_H^# - \overline{u_i''} \frac{\partial \bar{p}}{\partial x_j} - \overline{u_j''} \frac{\partial \bar{p}}{\partial x_i}$	$\tilde{R}_{ij} \frac{\partial \bar{p}}{\partial x_j} - \frac{\bar{\rho}'^2}{\bar{\rho}^2} \frac{\partial \bar{p}}{\partial x_i}$	$2\bar{\rho} \overline{u_i''} \frac{\partial \bar{p}}{\partial x_i}$
$\Phi^# P' \frac{\partial u_i''}{\partial x_j} + P' \frac{\partial u_j''}{\partial x_i}$	$-P' \frac{\partial}{\partial x_i} \frac{\bar{\rho}'}{\bar{\rho}}$	
$\mathfrak{D}^# - \frac{\partial}{\partial x_k} \bar{\rho} u_i'' u_j'' u_k'' - \frac{\partial}{\partial x_k} \left(\bar{P}' u_i'' \delta_{jk} + \bar{P}' u_j'' \delta_{ik} \right) + \frac{\partial}{\partial x_k} \left(\overline{u_i'' \sigma_{jk}} + \overline{u_j'' \sigma_{ik}} \right)$	$\bar{P} \frac{\partial}{\partial x_j} \frac{\bar{\rho}' u_i'' u_j''}{\bar{\rho}} + \frac{\partial}{\partial x_j} \frac{\bar{\rho}'}{\bar{\rho}} P' \delta_{ij} - \frac{\partial}{\partial x_j} \frac{\bar{\rho}'}{\bar{\rho}} \sigma_{ij}$	$-\frac{\partial \bar{\rho}'^2 u_i''}{\partial x_i}$
$\mathfrak{E}^# - \bar{\rho} \left(\frac{\sigma_{ik}}{\bar{\rho}} \frac{\partial u_i''}{\partial x_k} + \frac{\sigma_{jk}}{\bar{\rho}} \frac{\partial u_j''}{\partial x_k} \right)$	$\bar{\rho} u_i'' \frac{\partial u_j''}{\partial x_j} - \frac{\bar{\rho}'^2}{\bar{\rho}^2} \frac{\partial \bar{p}'}{\partial x_i} + \sigma_{ij} \frac{\partial}{\partial x_j} \frac{\bar{\rho}'}{\bar{\rho}} + \frac{\bar{\rho}'^2}{\bar{\rho}^2} \frac{\partial \sigma_{ij}}{\partial x_j}$	$-2\bar{\rho} \bar{\rho}' \frac{\partial u_i''}{\partial x_i} - \overline{\rho'^2} \frac{\partial u_i''}{\partial x_i}$

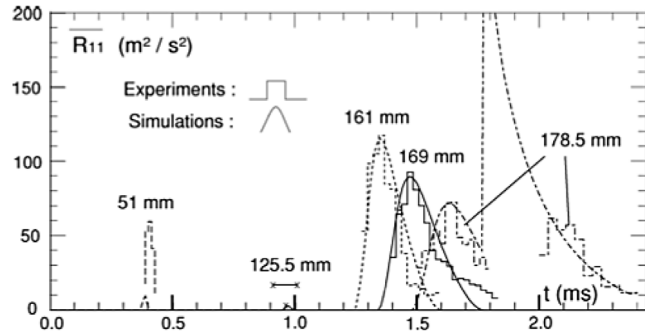


Fig. 12.6a. CEA shock tube experiment: R_{11} at the measurement locations 51 (—) 125.5 (x-x), 161 (---), 169 (—) and 178.5 (---) mm above the initial location of the interface. Broken lines stand for the experimental data while curves are GSG model calculation results.

Source: Figure 4 of Grégoire et al. (2005), *J. Turbulence*, with permission.

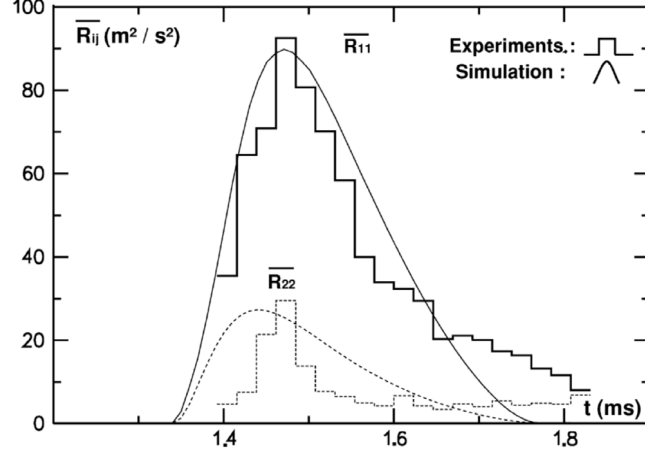


Fig. 12.6b. CEA shock tube experiment. The Reynolds stress components at the abscissa 169 mm above the initial location of the interface. Broken lines stand for the experimental data while curves are GSG model calculation results.

Source: Figure 5 of Grégoire et al. (2005), *J. Turbulence*, with permission.

The shock tube RMI data of Poggi et al. (1998) provide an opportunity to compare and contrast the performance of GSG (Figs. 12.6a and 12.6b). Overall, the agreement between the GSG prediction and the data is reasonable. The two components of the Reynolds stress tensor also compare reasonably well with the data, although the model predictions in the transverse direction are somewhat broader than the data.

12.6.2. GSG-R, GSGf, and GSG+ models

Some additional refinements were made to the GSG model. Griffond et al. (2010, 2014) pointed out that the model should be able to predict the turbulent quantities downstream from a shock front crossing a homogeneous turbulent mixture.²⁹ The focus here was on fitting the GSG to match the linear interaction analysis (LIA). With some approximations, LIA and RSM results were shown to be described by transfer matrices connecting upstream and downstream turbulent fields (Griffond and Soulard, 2012). Then, the compatibility of the RSM with LIA required that both matrices coincide for all shock Mach numbers and polytropic indices. Furthermore, PDF models (Pope, 1994) are used in order to derive consistent RSMs ensuring realizability conditions.³⁰ This improved version of the GSG model has been named GSG-R.

Souffland et al. (2014) noted that the models were generally derived from quasi-equilibrium weakly anisotropic assumptions, which are not met during shock crossing. The authors paid special attentions to the numerical difficulties encountered with the first gradient assumption, extensively used to close the turbulent moments although strictly valid only when a quasi-equilibrium hypothesis is satisfied. The flux limitation method (FLM) was proposed to improve the model. The further improved model is called GSG+ and its version fitted to LIA is referred to as GSGf (see Appendix B of Griffond and Soulard (2014) for detail). The focus of these efforts is again directed to ensure that the GSG+ and GSGf models are realizable.

Gréa et al. (2016b) showed that the GSG+ model performed very well at short time as it adjusted to a rapid acceleration from an isotropic state. However, the final capture of the transients was a bit disappointing as there was a clear underestimation of the kinetic energy production compared to the EDQNM model.

Finally, Soulard et al. (2012) derived a pseudo-compressible approximation and illustrated its implications to the second-order one-point turbulence models relevant for turbulent mixing flows. They found that the approximation led to a direct closure of the turbulent transport term appearing in the mean energy equation and allowed one to specify unambiguously some production terms appearing in the evolution equations of the density variance and density flux of these models.

12.6.3. BHR3

To account for anisotropies in turbulent energy, Schwarzkopf et al. (2011) computed the components of the Reynolds stress directly using their transport equations. This also allowed an anisotropic form of the turbulent diffusion terms to be included in constitutive models. The turbulence closures used were an extension of those proposed by Besnard et al. (1992), which included closures for the turbulence mass flux and density-specific-volume covariant. The key differences with GSG are that BHR uses the length scale equation instead of the dissipation rate equation.

The experimental and DNS data of Banerjee et al. (2010b) and Livescu et al. (2010), among others, were used during the development of the model. The model with the calibrated constants was then applied to RMI flows. Schwarzkopf et al. (2011) highlighted the importance of using the density-self correlation for variable density turbulent flows, instead of the density variance, which is appropriate only in the Boussinesq limit. Because of its importance, the density-self correlation was obtained from both the simulations and experiments and was even the subject of a dedicated experimental study (Tomkins et al., 2013). The measurements of the velocity-density correlation can be found, for example, in Ramaprabhu and Andrews (2003).

The BHR3 model takes the following form,

$$\begin{aligned} \frac{\partial(\bar{\rho}\tilde{R}_{ij})}{\partial t} + (\bar{\rho}\tilde{u}_k\tilde{R}_{ij})_{,k} &= \underbrace{[a_i\bar{P}_{,j} + a_j\bar{P}_{,i}] - \bar{\rho}[\tilde{R}_{ik}\tilde{u}_{j,k} + \tilde{R}_{jk}\tilde{u}_{i,k}]}_{\text{Production}} \\ &\quad + \underbrace{C_r\left(\frac{L}{\sqrt{K}}\bar{\rho}\tilde{R}_{kn}\tilde{R}_{ij,n}\right)_{,k}}_{\text{Diffusion}} - \underbrace{C_{r3}\bar{\rho}\frac{\sqrt{K}}{L}\left(\tilde{R}_{ij} - \frac{1}{3}\tilde{R}_{kk}\delta_{ij}\right)}_{\text{Return to isotropy}} \\ &\quad - \underbrace{C_{r1}[a_i\bar{P}_{,j} + a_j\bar{P}_{,i}] + C_{r2}\bar{\rho}[\tilde{R}_{ik}\tilde{u}_{j,k} + \tilde{R}_{jk}\tilde{u}_{i,k}]}_{\text{Rapid Distortion}} \\ &\quad - \underbrace{C_{r2}\frac{2}{3}\bar{\rho}\tilde{R}_{mk}\tilde{u}_{m,k}\delta_{ij} + C_{r1}\frac{2}{3}a_k\bar{P}_{,k}\delta_{ij}}_{\text{Rapid Distortion}} - \underbrace{\bar{\rho}\frac{2}{3}\frac{K^{3/2}}{L}\delta_{ij}}_{\text{Dissipation}} \\ \frac{\partial(\bar{\rho}L)}{\partial t} + (\bar{\rho}\tilde{u}_jL)_j &= -\frac{L}{K}\left(\frac{3}{2} - C_1\right)\bar{\rho}\tilde{R}_{ij}\tilde{u}_{i,j} + \frac{L}{K}\left(\frac{3}{2} - C_3\right)a_j\bar{P}_{,j} - \left(\frac{3}{2} - C_2\right)\bar{\rho}\sqrt{K} + \underbrace{C_s\left(\frac{L}{\sqrt{K}}\bar{\rho}\tilde{R}_{kn}L_{,n}\right)_{,k}}_{\text{Net Production}} \\ &\quad + \underbrace{\bar{\rho}\tilde{u}_jL}_{\text{Diffusion}} \end{aligned}$$

²⁹ In a related work, Vedula and Sinha (2017) considered Reynolds stress models applied to canonical shock-turbulence interaction.

³⁰ A Reynolds stress model (RSM) is called realizable if, for any realizable initial state, the RSM maintains realizability of the states throughout the time evolution (Schumann, 1977; Lumley, 1979, 1983; Speziale, 1991; Wilcox, 1998).

Table 12.4

BHR2 and BHR3 coefficients summarized in Haines et al. (2013a) or Grinstein (2017) for single phase, single and multi-component flows. For discussion of choice of coefficients can be found in Schwarzkopf et al. (2011) for BHR3 and in Stalsberg-Zarling and Gore (2011) and Banerjee et al. (2010a) for BHR2.

	C_{r1}	C_{r2}	C_{r3}	C_r	C_a	C_{a1}	C_b	C_{b1}	C_c	C_s	C_1	C_2	C_3	C_{ARS}	C_μ
BHR3	0.3	0.6	1.8	0.42	0.3	3.2	0.3	2.0	0.56	4.2	1.2	1.92	1.2	0.28	
BHR2				0.42	0.42	6.0	0.14	0.45	0.7	4.2	1.44	1.92	1.05	0.5	0.28

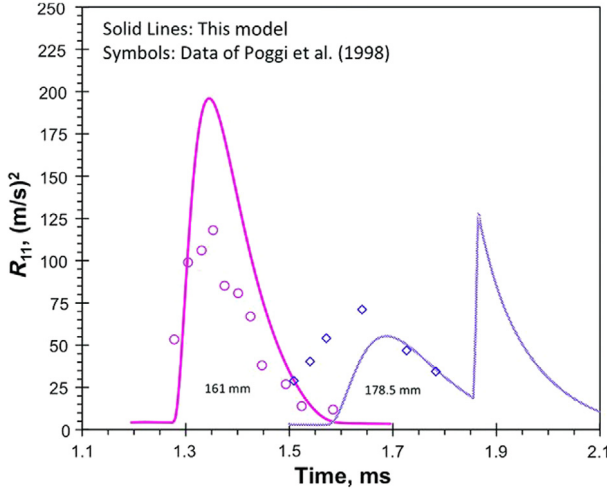


Fig. 12.7a. Second-moment model compared to axial Reynolds stress data from the CEA shock tube experiment. Source: Fig. 16 of Schwarzkopf et al. (2011), with permission from *J. Turbulence*.

$$\begin{aligned} \frac{\partial(\bar{\rho}a_i)}{\partial t} + (\bar{\rho}\tilde{u}_k a_i)_k &= \underbrace{b\bar{P}_{,i} - \tilde{R}_{ik}\bar{\rho}_{,k} - \bar{\rho}a_k\bar{u}_{i,k}}_{\text{Net Production}} + \underbrace{\bar{\rho}(a_k a_i)_{,k}}_{\text{Redistribution}} + \underbrace{\bar{\rho}C_a\left(\frac{L}{\sqrt{K}}\tilde{R}_{kn}a_{i,n}\right)_{,k}}_{\text{Diffusion}} - \underbrace{C_{a1}\bar{\rho}\frac{\sqrt{K}}{L}a_i}_{\text{Destruction}} \\ \frac{\partial(\bar{\rho}b)}{\partial t} + (\bar{\rho}b\tilde{u}_k)_{,k} &= \underbrace{-2(b+1)a_k\bar{\rho}_{,k}}_{\text{Production}} + \underbrace{2\bar{\rho}a_k b_{,k}}_{\text{Redistribution}} + \underbrace{\bar{\rho}^2 C_b\left(\frac{L}{\bar{\rho}\sqrt{K}}\tilde{R}_{mn}b_{,n}\right)_{,m}}_{\text{Diffusion}} - \underbrace{C_{b1}\bar{\rho}\frac{\sqrt{K}}{L}b}_{\text{Destruction}} \end{aligned} \quad (12.11)$$

where $C_X, X = r, r1, r2, r3, s, 1, 2, 3, k, a, a1, b, b1$, are model coefficients (Schwarzkopf et al., 2011).

Schwarzkopf et al. (2011) compared the prediction of values of R_{11} from BHR3 to those from Poggi et al. (1998). The decay region after the first shock, but before reshock, is between the positions 161 mm and 178.5 mm beyond the initial interface. The spike in R_{11} , between 1.85 and 1.9 ms (at 178.5 mm), is due to the second reshock. Overall the model compares reasonably well with the experimental data.

As mentioned previously, one of the key findings from Poggi et al. (1998) was that the Reynolds stress is anisotropic at 169 mm. Figs. 12.7a and 12.7b show that BHR3 is capable of capturing the anisotropy of the flow. While the transverse component from the model is substantially higher than the data, Schwarzkopf et al. (2011) noted that the differences are within the measurement noise.

Using ILES as a benchmark, Haines et al. (2013a) compared the performance between BHR2 and BHR3. The standard constants of BHR2 and BHR3 models are listed in Table 12.4. Anisotropy of the flow is shown in Fig. 12.8a by inspecting Lumley's anisotropy tensor b_{ij} . For the inverse chevron shock tube laboratory experiment (Holder and Barton, 2004; Hahn et al., 2011) used for the simulation, first reshock occurs at $t \sim 1.7$ ms and the second reshock at ~ 2.25 ms. Recall that $b_{ii} = -1/3$ and $2/3$ correspond respectively to having either none or all of the TKE. One can see that BHR3 improves over BHR2 by predicting the anisotropy quite reasonably compared to ILES after the first reshock, but the disagreement increases after the second reshock.

Grinstein (2017) used ILES to simulate the inverse chevron AWE shock tube experiments (Holder and Barton, 2004; Hahn et al., 2011) and planar shock experiments (Poggi et al., 1998) to highlight some unsatisfactory aspects of the current unsteady RANS (URANS) paradigm for IC-dependent non-equilibrium flows in shock driven turbulence. Apart from the known issue that this turbulence modeling was based on equilibrium turbulence assumptions, a major issue is the *ad hoc* (as opposed to physics based) choices for initialization – e.g., initial turbulent length scale, specific TKE values, and start time in BHR.

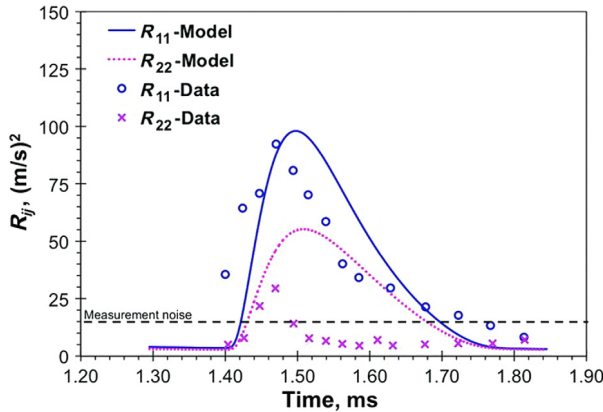


Fig. 12.7b. Comparison of the Reynolds stress components to the experimental data of CEA shock tube experiment. Measurement position is 169 mm beyond the initial interface.

Source: Fig. 17 of [Schwarzkopf et al. \(2011\)](#), with permission from *J. Turbulence*.

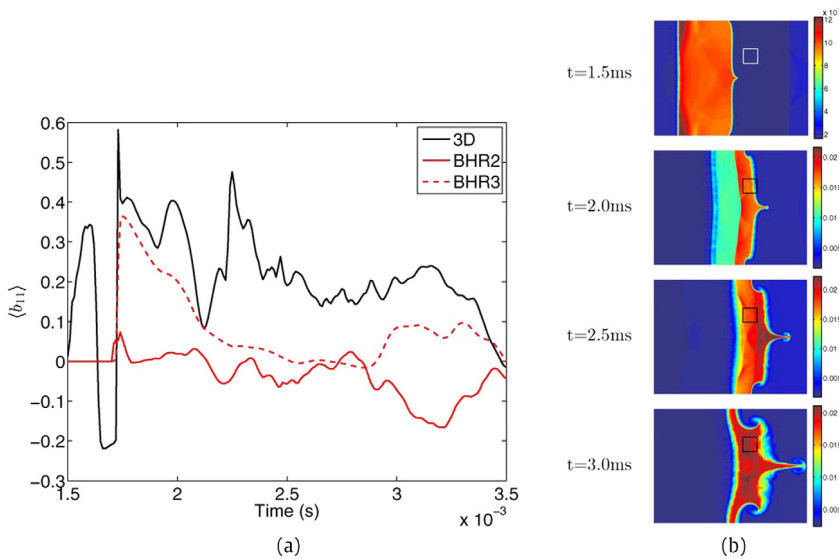


Fig. 12.8a. (a) Anisotropy component in the direction of the shock ($\langle b_{11} \rangle$) as a function of time; at each time, b_{11} is spatially averaged over the box indicated in (b). $\langle b_{11} \rangle$ is based on z-averaged ILES, BHR2 using an algebraic Reynolds stress, or BHR3 using a transported Reynolds stress model.

Source: Fig. 10 of [Haines et al. \(2013a\)](#), with permission from *J. Turbulence*.

Grinstein also demonstrated the differences between the results from the 3D and 2D BHR3 models. [Fig. 12.8b](#) shows the detailed planar distributions of the mass density for the inverse chevron case. At early times, the 2D and 3D BHR visualizations are comparable, but the 3D mixing layers clearly exhibit smaller structures hinting at a transitional flow cascade. For later times, the 3D BHR visualizations suggest smoothed 3D ILES distributions while late-time mixing over-predictions are indicated in the 2D case.

12.6.4. BHR two-length scale model (TLSM)

[Schwarzkopf et al. \(2016\)](#) demonstrated that both the BHR2 ([Stalsberg-Zarling and Gore, 2011](#)) and BHR3 ([Schwarzkopf et al., 2011](#)) missed the DNS results of a homogeneous RT instability flow at $A = 0.25$ ([Fig. 12.9](#)). The authors found that for both models, the turbulent kinetic energy is off primarily due to (i) using the wrong length scale for turbulence dissipation, and (ii) over predicting the production of the mean mass-weighted velocity fluctuation. Indeed, for this case, the turbulence growth and decay are associated with a strong variation of the turbulence production (P) over dissipation (ε) ratio ([Fig. 12.10](#), from Fig. 6 of [Schwarzkopf et al., 2016](#)). These discrepancies were tracked down to the assumption of high Reynolds number turbulence, where destruction terms can be approximated as simple decay models and the dissipation equation is a scaled version of the kinetic energy (an assumption that is valid when P/ε is quasi-constant).

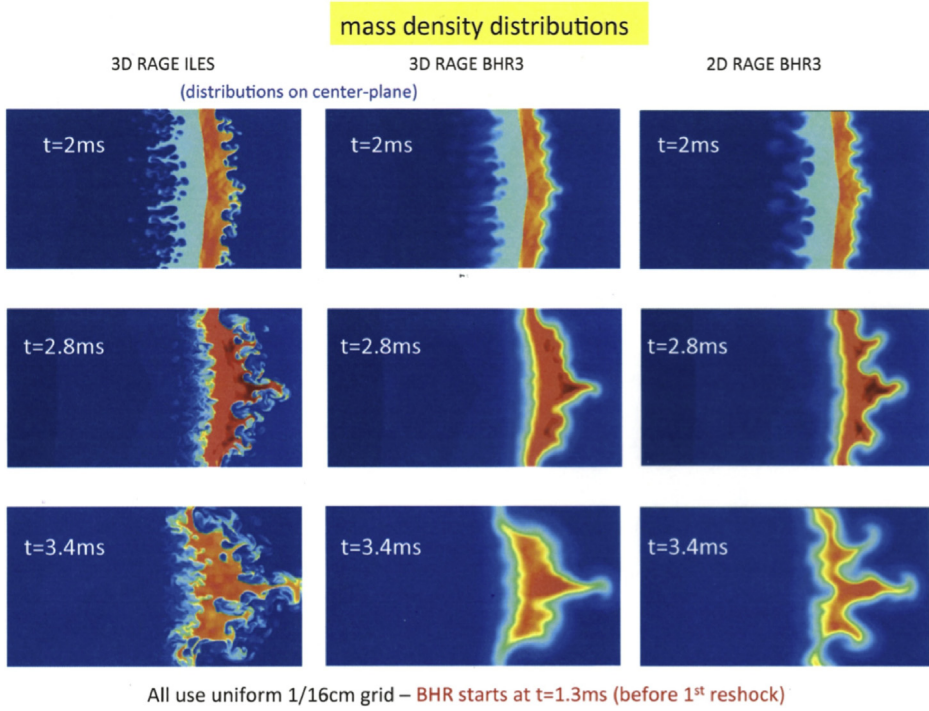


Fig. 12.8b. ILES and 2D/3D BHR3 mass-density distributions.
Source: Fig. 6 of Grinstein, Computers and Fluids, 2017.

The fix has been consistent throughout the BHR Two-length scale model (TLSM) – its main idea is that of two independently evolved length scales – there are no changes once coefficients are set.³¹ The BHR TLSM model (Schwarzkopf et al., 2016) reads,

$$\begin{aligned} \frac{\partial (\bar{\rho}L_T)}{\partial t} + (\bar{\rho}\tilde{u}_j L_T)_j &= -\underbrace{\frac{L_T}{K} \left(\frac{3}{2} - C_1 \right) \bar{\rho} \tilde{R}_{ij} \tilde{u}_{i,j}}_{\text{Net Production}} + \underbrace{\frac{L_T}{K} \left(\frac{3}{2} - C_4 \right) a_j \bar{P}_j - \left(\frac{3}{2} - C_2 \right) \bar{\rho} \sqrt{K}}_{\text{Transport}} + \underbrace{\frac{C_\mu}{\sigma_s} (\bar{\rho} L_T \sqrt{K} L_{T,j})_j}_{\text{Transport}} \\ \frac{\partial (\bar{\rho}L_D)}{\partial t} + (\bar{\rho}\tilde{u}_j L_D)_j &= -\underbrace{\frac{L_D}{K} \left(\frac{3}{2} - C_{1v} \right) \bar{\rho} \tilde{R}_{ij} \tilde{u}_{i,j}}_{\text{Net Production}} + \underbrace{\frac{L_D}{K} \left(\frac{3}{2} - C_{4v} \right) a_j \bar{P}_j - \left(\frac{3}{2} - C_{2v} \right) \bar{\rho} \sqrt{K}}_{\text{Net Production}} \\ &\quad + \underbrace{\frac{C_\mu}{\sigma_{2s}} (\bar{\rho} L_T \sqrt{K} L_{D,j})_j}_{\text{Transport}} \end{aligned} \quad (12.12)$$

where L_T is the turbulent transport length scale and L_D is the turbulent decay length scale.

The new coefficients for Eq. (12.12) have been calibrated based on several fundamental flows and are given in Table 1 of Schwarzkopf et al. (2016) (not shown).

The two-scale concept, of course, is consistent with previous suggestions described in Section 12.4 (Grégoire et al., 1999; Souffland et al., 2002; Zhou et al., 2002, 2003c). It should be noted, however, the two-scale length scales equations in TLSM model are part of the Reynolds stress transport equations.

In order to assess the capability of the calibrated BHR TLSM model, Schwarzkopf et al. (2016) have applied it to two interesting flows that contain similar physics, namely, variable density shear driven turbulence and RMI driven turbulence. The comparisons of the Reynolds stresses and the mean mass-weighted velocity fluctuations between the model and DNS are reasonable in the first test case (shown in Fig. 12.11a and 12.11b, respectively). For the RMI flows, the authors restricted their comparison with the simulations to the mix width of the Vetter and Sturtevant (1995) reshock experiments.

³¹ R.A. Gore, private communication (2016).

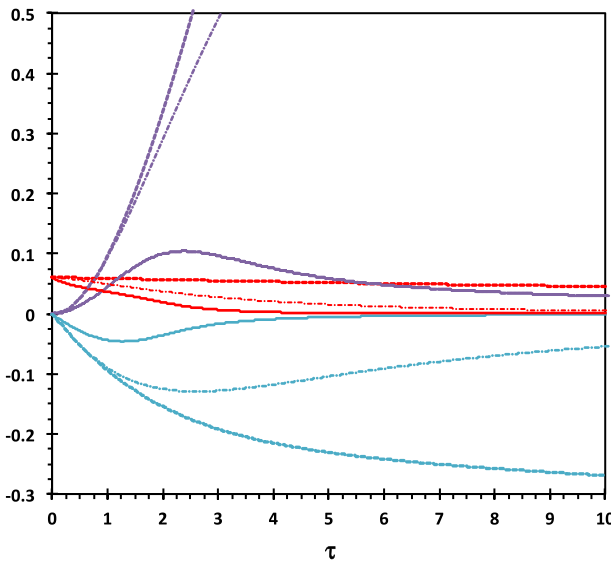


Fig. 12.9. A comparison of single time scale turbulence models with DNS for a homogeneous RT instability flow, $At = 0.25$ and τ is normalized time scale. TKE = purple, b = red, a = cyan; solid lines – DNS, dashed lines – BHR2 model of Stalsberg-Zarling and Gore (2011), dash-dot lines – BHR3 model of Schwarzkopf et al. (2011).

Source: Fig. 2 of Schwarzkopf et al. (2016), *Flow, Turbulence, and Combustion*, with permission.

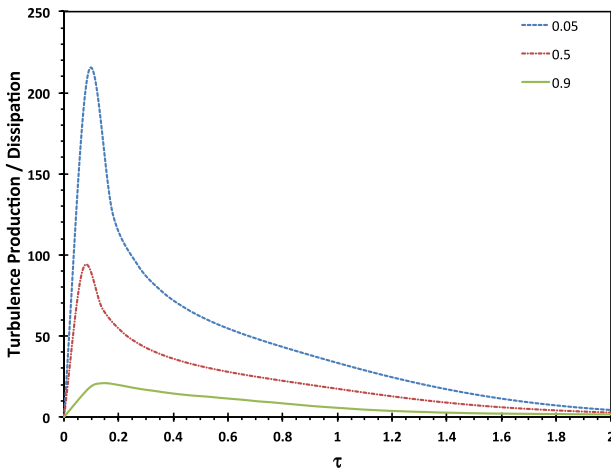


Fig. 12.10. DNS production/dissipation ratio in HRT at different Atwood numbers, showing large values attained during the growth stage.
Source: Fig. 6 of Schwarzkopf et al. (2016), *Flow, Turbulence, and Combustion*, with permission.

12.6.5. Nikiforov model

Nikiforov (1993) developed an advanced model involving equations for all second-order correlations of interest and compared the results with the experimental data in both planar and cylindrical geometries. The most detailed reference in English on the Russian modeling literature is provided in the Los Alamos report written by Andronov et al. (1995).³²

12.7. Multi-fluids

The multifluid based turbulence model, theoretically speaking, could be the most complete and accurate. This model is simply the partial differential equation (PDE) extension of the buoyancy-drag models discussed at length in an earlier section. This type of model, however, could also be demanding in both the implementation and computational cost. Youngs (1989, 1994, 1995) developed such a model. Processes such as differential acceleration by shock or pressure gradient, drag,

³² This report also describes the experimental work at VNIIEF and the Lagrangian-Eulerian methods implanted within the EGAK code.

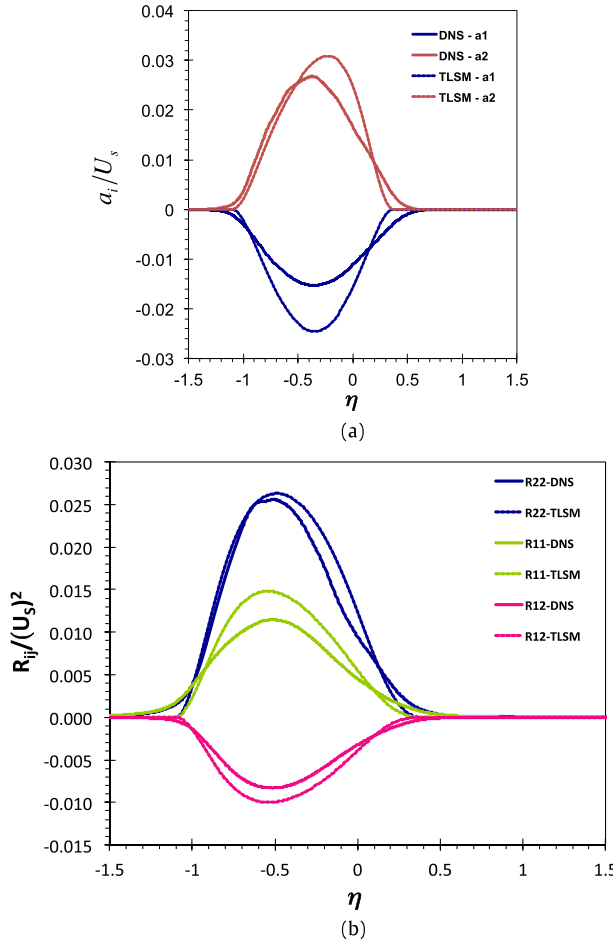


Fig. 12.11. (a) the dimensionless mean mass-weighted velocity fluctuation and (b) the Favre averaged Reynolds stress across the variable density shear layer, $A=0.75$ (solid lines – DNS, dashed lines – TLSM).

Source: Fig. 21 of Schwarzkopf et al. (2016), *Flow, Turbulence, and Combustion*, with permission.

and added mass, could be modeled in a physically plausible and consistent way (Kokkinakis et al., 2015). For a RT unstable mixing layer, Freed et al. (1991) obtained good analytic approximations to the volume fraction and velocity profiles using an extension of Youngs' 1989 treatment.

Youngs' model 1994, in which there was no mass transfer between the fluids, takes the following form,

mass transport

$$\frac{\partial}{\partial t} (\rho_r f_r) + \frac{\partial}{\partial x_j} (\rho_r f_r u_{rj}) = 0;$$

momentum transport:

$$\frac{\partial}{\partial t} (\rho_r f_r u_{ri}) + \frac{\partial}{\partial x_j} (\rho_r f_r u_{rj} u_{ri}) = -f_r \frac{\partial p}{\partial x_i} - m_r \frac{\partial R_{ij}}{\partial x_j} + \sum_s (D_{rsi} + M_{rsi}) + \rho_r f_r g_i;$$

internal energy transport:

$$\frac{\partial}{\partial t} (\rho_r f_r e_r) + \frac{\partial}{\partial x_j} (\rho_r f_r u_{rj}) = -h_r p_r \frac{\partial \bar{u}_j}{\partial x_j} + \frac{\partial}{\partial x_j} \left(\rho_r f_r D \frac{\partial e_r}{\partial x_j} \right) + \varepsilon$$

turbulence kinetic energy:

$$\frac{\partial}{\partial t} (\rho K) + \frac{\partial}{\partial x_j} (\rho K \tilde{u}_j) = \frac{\partial}{\partial x_j} \left(\rho D_K \frac{\partial K}{\partial x_j} \right) + \check{S}_K - \varepsilon;$$

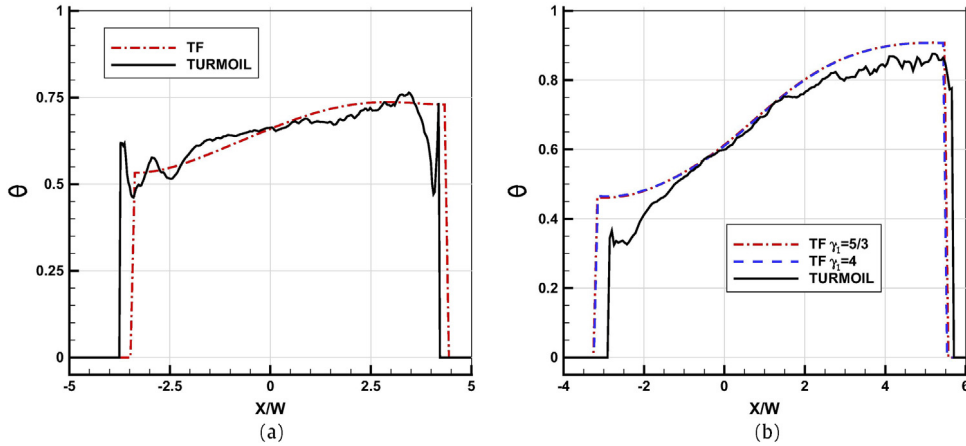


Fig. 12.12. Molecular mixing parameter for density ratios 3 (a) and 20 (b) over 1; comparison of two-fluid model with ILES (TURMOIL). Source: Fig. 19 of Kokkinakis et al. (2015), International Journal of Heat and Fluid Flow.

length scale:

$$\frac{\partial L}{\partial t} + u_{lj} \frac{\partial L}{\partial x_j} = \frac{\partial}{\partial x_j} \left(D_L \frac{\partial L}{\partial x_j} \right) + \check{S}_L + e_L L, \quad (12.13)$$

where D is the turbulent diffusion coefficient, and \check{S}_K and \check{S}_L are the source terms. D_{rsi} denotes the drag force on fluid r due to fluids s ,

$$D_{rsi} = -c_1 \frac{\rho_{rs} f_r f_s}{L} W (u_{ri} - u_{si} - w_{ri} + w_{si}),$$

$$\rho_{rs} = (f_r \rho_r + f_s \rho_s) / (f_r + f_s),$$

$$W = |\mathbf{u}_r - \mathbf{u}_s + \mathbf{w}_r - \mathbf{w}_s|, \quad w_{ri} = -\frac{D}{f_r \rho_r} \frac{\partial}{\partial x_i} (f_r \rho_r),$$

where c_1 is the drag coefficient. The added mass effect for fluid r due to fluid s is

$$M_{rsi} = -c_a \rho_{rs} f_r f_s \left\{ \frac{D_r u_{ri}}{Dt} - \frac{D_s u_{si}}{Dt} \right\}.$$

The coefficient c_a is chosen to be 0.5, the value for a solid sphere of fluid r surrounded by fluid s .

The notation used is as follows (Youngs, 1994):

f_r = fraction by volume of fluid r ;

ρ_r = density of fluid r ;

ρ = $\sum_r f_r \rho_r$, mean fluid density;

$m_r = \frac{f_r \rho_r}{\rho}$, fraction by mass of fluid r ;

e_r = internal energy of fluid r ;

p_r = pressure of fluid r ;

u_{ri} = i -th component of the velocity of fluid r (mass averaged);

$\tilde{u}_i = \sum_r m_i u_{ri}$, mass weighted mean velocity;

\bar{u}_i = volume weighted mean velocity. Note also that h_r depends on the relative compressibility of fluid r . In the internal energy equation, the work done in compressing fluid r is $-h_r p_r \operatorname{div} \bar{u}$. The reader is referred to Youngs (1994) for further detail.

In Youngs (1995), mass transfer between the initial fluids was included, which of course increased the complexity of the model. Kokkinakis et al. (2015) pointed out that a key advantage of the multifluid model over the two-equation model is that the multifluid model can represent the degree of molecular mixing in a direct way. Fig. 12.12 compared the two-fluid model with ILES (with TURMOIL code) on the molecular mixing parameter for density ratios 3 (a) and 20 (b) over 1.

Brown et al. (2014) discussed the implementation of Youngs' dedicated mix model (1994, 1995) within a two-dimensional finite-element host hydrocode. Here, an issue was addressed that is not only relevant to Youngs' multifluid model, but also to other mix schemes if the code uses the following two general phases. First of all, a "Lagrangian" phase, in which the equations of fluid flow are solved in a Lagrangian reference frame (the model mesh moves wholly with the fluid). Secondly, an optional "mesh movement" (or "remapping" phase) in which the mesh is decoupled from the fluid and relaxed (or repositioned) into

a smoother form; the underlying fluid solution is then reconstituted onto the new mesh. As noted by Brown et al. (2014), this remapping may be done to improve mesh quality, or to maintain the simulation on a fixed (Eulerian) mesh. For such schemes to be self-consistent, the mixing should be dominated by the mass introduced by the dedicated mixing model, with minimal contribution from the numerical methods of the host code.

The Youngs' model (1989, 1994, 1995) was constructed without the usual closure process of fluctuating quantities generally used for RANS models. Llor provided a statistical derivation of the two-fluid model (Llor, 2005) and compared a modified $K-\varepsilon$ model and Youngs' two-fluid formalism (Llor, 2003). Another turbulent two-field concept was proposed for modeling RT, RM, and KH mixing layers (Llor and Bailly, 2003). Equations are used for K and ε for each fluid, in contrast to the Youngs model which uses K and L for the mixture as a whole.

Cranfill (1991) found that it is possible to develop a multifluid model based on the decomposition of the fluid properties (Besnard and Harlow, 1988) into mean and fluctuating components from the Navier–Stokes equations. His innovation was to divide the turbulent contributions to the bulk fluid into ordered convective and disordered diffusive parts (Cranfill, 1992). In other words, the instability induced flows are now characterized by the coexistence of deterministic large-scale and disordered small-scale flow (Rightley et al., 1999). The ordered contributions are obtained from the average drift motions produced by a set of multifluid interpenetration equations. The disordered parts are simply given by a set of single-fluid turbulence equations ($K-L$ equations).

In both the Cranfill (1992) and Youngs (1994) models, the significantly increased number of required constants necessary for the multifluid model equations demand careful calibrations against appropriate experimental data or numerical simulations (Drew, 1983; Drew and Passman, 1999; Ishii and Hibiki, 2010). Glimm et al. (1998, 1999) performed single-phase averages of the Euler equations over an infinite ensemble of microscopic flow realizations. The boundary conditions of the model are given by equations of motion for the edges of the mixing layer (Cheng et al., 1999; Cheng et al. 2002c). The incompressible self-similar solutions for the edge velocities of the mixing layers are also invoked to close the interfacial quantities. For additional work on the approach taken by Glimm and co-workers, the reader is referred to Bo et al. (2008), Chen et al. (1996), Cheng et al. (2005, 2008) and Jin (2017) and references therein.

Scannapieco and Cheng (2002) rigorously derived a set of multifluid moment equations from the collisional Boltzmann equation (Holt and Haskell, 1965) in a self-consistent manner. The authors utilized a unique approach that result in only requiring a closure (with a single free parameter) for the drag term. This parameter can then be determined from experimental data. This phenomenological quantity, i.e., the collisional frequency, characterizes the physical system and describes the unresolved physics in the model at an atomic level. The species couple to each other through phenomenological momentum and energy exchange terms.

In the absence of external forces, the Scannapieco and Cheng model equations reduce to the Cranfill (1992) mix model if the disordered Reynolds stress is ignored. Also, according to Cheng and Scannapieco (2005), a buoyancy–drag equation for describing the motion of the edges of a mixing layer driven by RT or RM instabilities can be derived from this multifluid interpenetration mix model.

For the Scannapieco and Cheng model, implemented in a LANL code, the implicit assumption is made that subgrid scale perturbation growth, represented by a single free parameter, has become so nonlinear that the flow is independent of unmodeled initial perturbations (Wilson et al., 2003, 2004, 2011). Materials are also treated as atomically mixed within a computational cell. The model attempts to mimic the averaged effect of turbulent mix, whereby interpenetration is enhanced through turbulent convection of material (Christensen et al., 2004). Wilson et al. (2008) applied the model to the mix between the ablator and fuel of the ICF capsules, but with different values of its mix parameters.

13. Coupled fields and multiple instabilities

The stabilizing mechanisms for the incompressible case, viscosity, surface tension, and diffuse interface were considered in Part I. Many additional physics and external factors could enhance or most likely suppress the RTI or RMI. Some recent examples are those by Alexeev and Oron (2007), Amiroudine et al. (2005), Bakhsh and Samtaney (2017), Bond et al. (2017), Das and Kaw (2014), Garai et al. (2015), Gol'Berg and Velikovich (1993), Zhigalin et al. (2015), Jiang et al. (2017), Otani et al. (2007), Piriz et al. (2011), Poehlmann et al. (2013) and Sen and Store (1997). Also, shear (Hameiri, 1979; Hassam, 1992; Mikhailenko et al., 2002; Theofanous, 2011; Theofanous and Li, 2008; Theofanous et al., 2004, 2012; Jalaal and Mehravar, 2014; Meng and Colonius, 2018) and electric field (Mohamed and El Shehawey, 1983; Barannyk et al., 2012; Cimpeanu et al., 2014; Tofighi et al., 2016; Yang, Li, and Xu, 2017) have been studied for control and suppression of the RTI. Moreover, in viscoelastic fluids, the addition of polymers³³ could also modify the properties of the RTI flows in both large and small scales (Boffetta et al., 2010, 2011). The competition between the growth of the instabilities and one of these external factors that are attempting to suppress them could occur in many applications.

³³ Polymers are very large molecules (macromolecules) that are comprised or built up of smaller units or monomers. The arrangements of these units, the various types of chains that can be synthesized and the shapes that these chains can bend themselves into, result in a class of materials that are characterized by an enormous and intriguing range of properties (Painter and Coleman, 1997).

13.1. Compressibility

A number of publications have considered the effect of compressibility, such as Plesset and Hsieh (1964), Mitchner and Landshoff (1964), Plesset and Prosperetti (1982), Mikaelian (1994a), Mathews and Blumenthal (1974), Baker (1983), Fraley (1986), Glimm et al. (1990), Yang et al. (1994), Wouchuk and Nishihara (1996), Piriz (2001), George and Glimm (2005) and Le Creurer and Gauthier (2008). Taking compressibility into account, Vandervoort (1961) developed a variational approach to study the RTI eigenvalue problem for two fluids of uniform densities separated by a common boundary. The resulting growth rate would reduce to the classical one under the limit of the infinite sound speed. It should be noted, however, that Plesset and Prosperetti (1982) pointed out an inconsistency in Vandervoort's paper.

Bhatia (1974) applied this variational approach for the problem of the RTI of a hydromagnetic plasma of varying density to investigate the influence of the simultaneous presence of the effects of compressibility and viscosity. The influence of compressibility is found to be destabilizing. Refining the classic linear model of Layzer (1955), Margolin and Reisner (2017) created an early-time model of the RMI that takes account of compressibility and viscous effects. The description of the very earliest stage of phase inversion provided a justification for the more ad hoc modifications of the initial conditions suggested by Richtmyer (1960), Meyer and Blewett (1972) and Butler et al. (2012).

Guo and Tice (2011) studied the equations obtained from linearizing the compressible Navier–Stokes equations around a steady-state profile of a RTI. The authors developed a general method of studying a family of modified variational problems in order to produce modes with maximal growth. Using these growing modes, they constructed smooth (when restricted to each fluid domain) solutions to the linear equations that grow exponentially in time in Sobolev spaces and proved an estimate for arbitrary solutions to the linearized equations in terms of the fastest possible growth rate for the growing modes.

In the linear regime, Livescu (2004) analyzed the linearized Navier–Stokes equations to reconcile the stabilizing and destabilizing effects of compressibility reported in the literature. In previous publications, Bernstein and Book (1978), Vandervoort (1961), Scannapieco (1981), Newcomb (1983) and Yang and Zhang (1993) determined that compressibility has a destabilizing effect and it accelerates the RTI growth, but Blake (1972), Sharp (1984) and Li (1993) reached opposite conclusion. Mitra et al. (2016) extended the mathematical model formulated by Bernstein and Book and concluded that both compressibility and viscosity suppress the RT instability growth.³⁴ Also, Baker (1983) found both stabilizing and destabilizing effects of compressibility in the linear regime, and other papers illustrated (Plesset and Hsieh, 1964; Baker, 1983) that the compressibility effect depends on the ratio between the sound velocities of two fluids. Livescu (2004) concluded that the compressibility could be characterized by two parameters, the specific heats and speed of sound, with opposing influence on the instability growth. He also found the results remain valid in the presence of surface tension or for viscous fluids.

Ribeyre et al. (2004) also tackled the same issue, but stressed that it is important to compare the characteristics that are comparable in two different systems. In order to examine the compressibility effect on the RTI, one should compare the two superimposed fluids from one system to another with the same density profiles and, consequently, the same masses.³⁵ This work was perceived as a criticism of Livescu (2004), although that paper was not referenced. This and several other contentious matters resulted in an extensive back and forth discussion (Livescu, 2005a; Ribeyre et al., 2005; Livescu, 2005b). In a related article, He et al. (2008) repeated some of this analysis, but with the initial condition of Chandrasekhar (1961). They obtained similar conclusions regarding the compressibility effects on the growth rates offered by Livescu (2004), but disagreed with the conclusions given in that work.

Xue and Ye (2010) utilized a variational principle to solve the eigenvalue problem of RTI for fluids with fixed density profile. In particular, they argued that the influence of compressibility alone could be hidden by the mass variation (Ribeyre et al., 2005) in Livescu's conclusion (2004). For an inviscid compressible fluid with exponentially variable density profile, the authors found that compressibility has a destabilizing effect independently of decreasing specific heat ratio or decreasing pressure on the interface.

Compressibility can cause a phenomenon dubbed "freeze-out" by Mikaelian (1994a) where perturbations "freeze" and do not grow after the passage of a shock. This happens for specific choices of the densities and compressibilities of the fluids and has been studied primarily in the linear regime. There is no experimental confirmation but freeze-out has been confirmed theoretically (Yang et al., 1994; Wouchuk and Nishihara, 2004) and continues to be studied (Cobos Campos and Wouchuk, 2016).

Cobos Campos and Wouchuk (2014) attempted to obtain accurate analytical estimates of the asymptotic velocities in a RM-like environment for a single shock moving into one fluid. To simplify the matter, they considered two idealized cases with a single fluid: a corrugated rigid piston and a corrugated free surface. Building on this work, the authors further evaluated asymptotic normal and tangential velocity perturbations in the linear stage of RMI for the case of a reflected shock. Taking into account the whole perturbation history between the transmitted and reflected fronts, Cobos Campos and Wouchuk (2016) derived both the explicit and exact analytical expansions of the asymptotic normal velocity from the conservation equations. The theoretical results were subsequently compared with the experimental results of Vandenboomgaerde et al. (2014) and Motl et al. (2009).³⁶

³⁴ However with viscosity there is no cut-off as opposed to the surface tension effect.

³⁵ It appears that this point is relevant only for confined geometries.

³⁶ Note that Stanic et al. (2013) performed Arbitrary Lagrange Eulerian and Smoothed Particle Hydrodynamics numerical simulations, showing agreement with the experimental results of Motl et al. (2009).

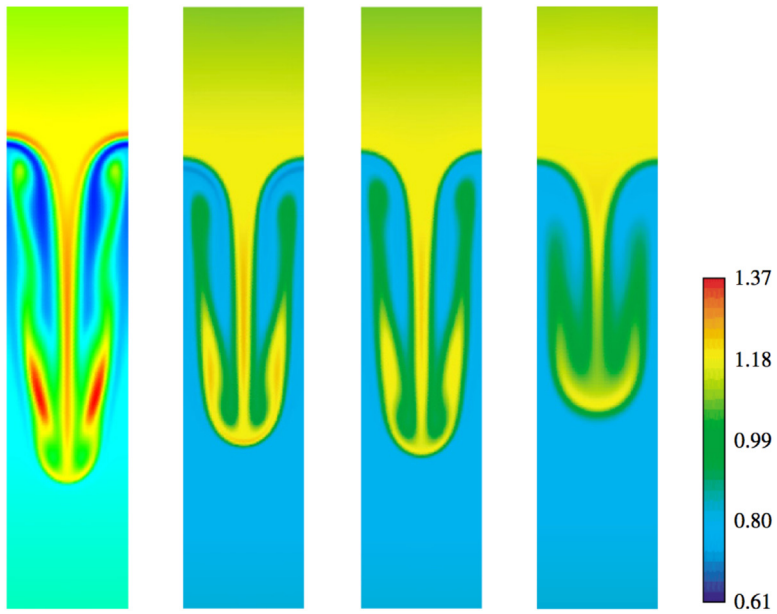


Fig. 13.1. Density vs. time, for four couples of different compressibilities (5;5/3), (5/3;5/3), (5;5) and (5/3;5).
Source: Fig. 8 of [Lafay et al. \(2007\)](#), *Europhysics Letters* with permission.

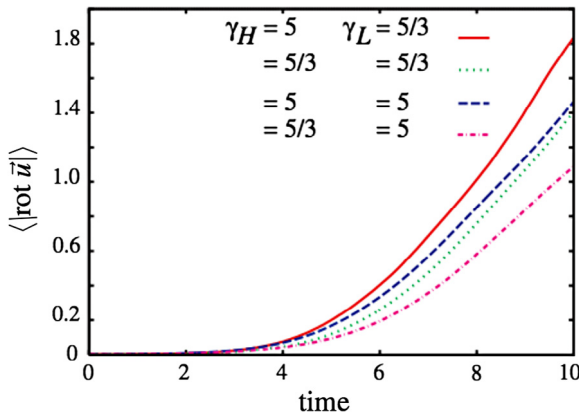


Fig. 13.2. Mean value of vorticity vs. time, for four couples of different compressibility (5;5/3), (5/3;5/3), (5;5) and (5/3;5).
Source: Fig. 9b of [Lafay et al. \(2007\)](#), *Europhysics Letters* with permission.

In the nonlinear regime, [Gupta et al. \(2009\)](#) relaxed the restriction of constant density in RMI and RTI. The system these authors obtained is described by the compressibility dependent temporal evolution of the bubble or spike structures (essentially, the tip of the bubble/spike) of the two fluid interfaces. Reducing to the case of constant density, this set of equations is consistent with the phenomenological buoyancy–drag model equation.

[Lafay et al. \(2007\)](#) solved the linear RT problem for two miscible compressible viscous fluids for the first time and reported that the flow is destabilized with increased values of the compressibility parameters, γ_H and γ_L (Fig. 13.1). These conclusions were found to usually hold in the nonlinear single-mode regime using 2D numerical simulations. The only exception is when the values of the compressibility are equal. In this case linear and nonlinear growth rates exhibit opposite trends (see the vorticity plot, Fig. 13.2).

[Reckinger et al. \(2016\)](#) carried out direct numerical simulations of two-dimensional single-mode RTI to extreme late-times for a number of Mach and Atwood numbers. Confirming a prediction from linear stability analysis ([Livescu, 2004](#)), the flow compressibility acts to reduce the growth of RTI for various Mach values for Atwood number $A = 0.1$ (Fig. 13.3). The authors suggested that for compressible flow, the perturbation might spread slower with a finite sound velocity than that for incompressible case, which results in the energy accumulation near the interface. In further studies, [Wieland et al. \(2017\)](#) have looked in more detail at the compressibility effects at low A and found the effects are qualitatively similar in 2D

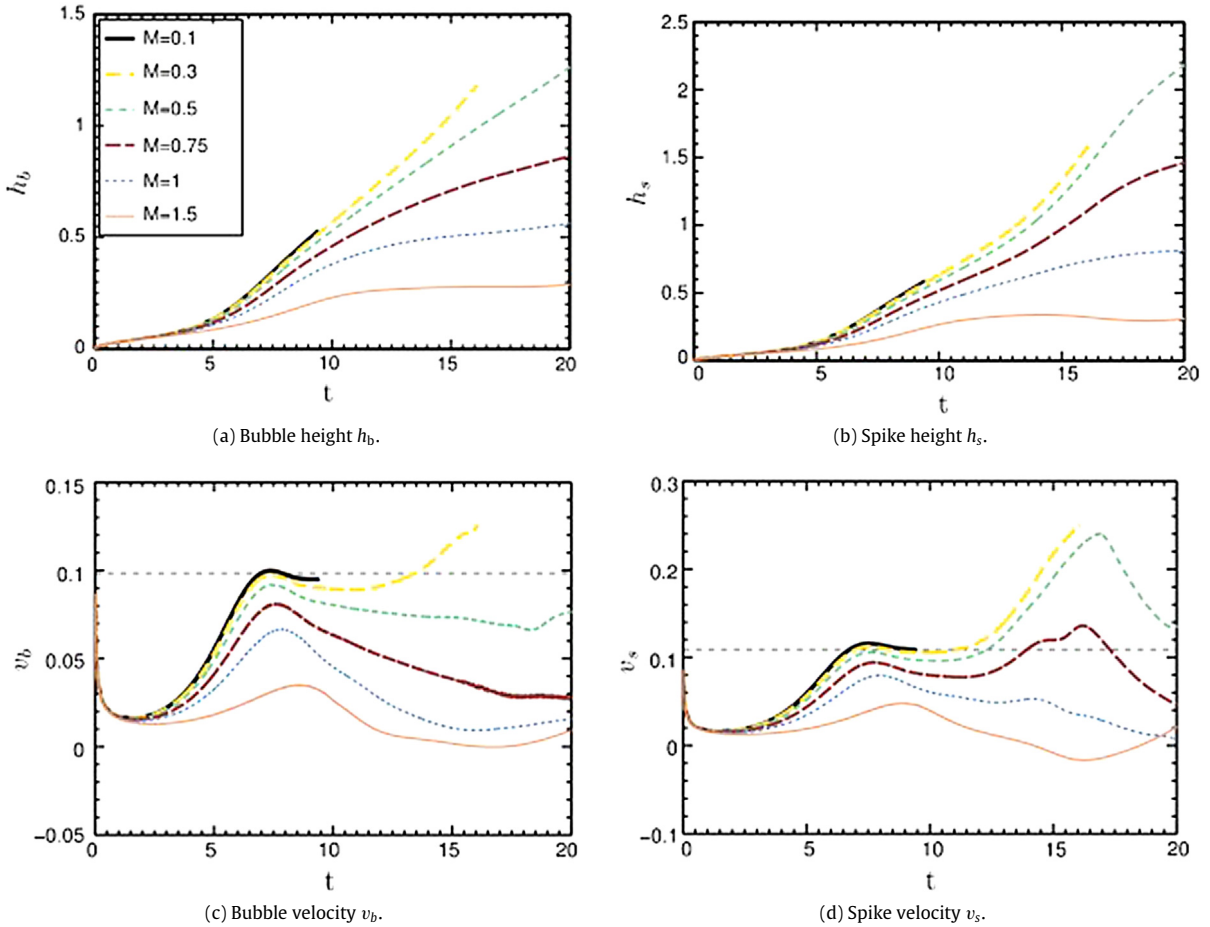


Fig. 13.3. Bubble height (h_b), spike height (h_s), bubble velocity, and spike velocity are shown for various *Mach number* (denoted as M by the authors) values for Atwood number $A = 0.1$.

Source: Figure 16 of Reckinger et al. (2016). *J. Computational Phys.*

and 3D. As the Atwood number is increased, however, the authors observed a decrease in the intensity of the suppression, such that they were not able to make a conclusive statement about the $A = 0.3$ case (Fig. 13.4a, b). For larger molar mass difference, i.e. $A > 0.3$, a reversal in the compressibility/stratification effects was observed on the single-mode RTI growth (Fig. 13.4c,d illustrates the $A = 0.7$ case as an example). However, the computational requirements are much stricter at higher A due to the increased range of dynamical scales. Thus, it is prudent that Reckinger et al. (2016) and Wieland et al. (2017) did not make any conclusive statements about the higher A cases in the papers. Clearly, it is desirable to carry out other computational or experimental studies that can validate or invalidate these observations in this regime.

Using numerical simulations, Gao et al. (2016) also showed that the influence of compressibility on the RMI might be Atwood number dependent. While the effect of compressibility is small in the later stages for most situations, considerable ramification has been found for an extremely high Atwood number case ($A \sim 0.9$) i.e., larger than 10%.

The effect of compressibility on the growth rate of the RTI in the presence of surface tension was investigated, but now with a horizontal layer sheet embedded in two semi-infinite layers (Hoshoudy, 2007). The dispersion relation that determines the growth rate was solved numerically for different values of compressibility, pressure at the two interfaces, and thickness of the intermediate layer. Each interface, either the lower or the upper one, depends on the variables at this interface as well as the thickness of the intermediate layer. The growth rate decreases as compressibility increases, yet the compressibility has no role at high wave number values in the absence of surface tension. In addition, the dispersion relation that determines the growth rate is found as a function of the pressure at the two interfaces, the thickness of the intermediate layer, and the specific internal energy.

However, Livescu (2008) argued that there are several major errors in Hoshoudy's paper, which invalid the results. Regarding this controversial issue, Gauthier and Le Creurer (2010) stated diplomatically "An attempt at solving the three-layer configuration (Hoshoudy, 2007) has to be confirmed (Livescu, 2008)".

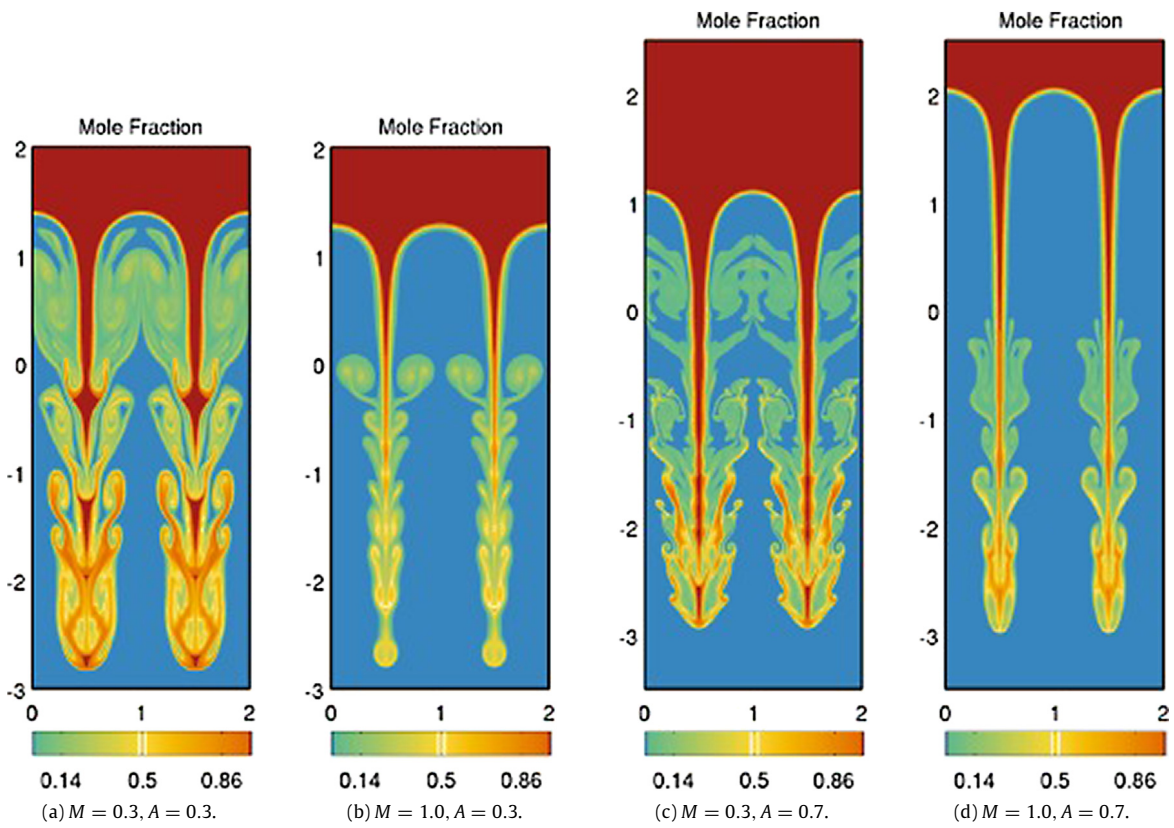


Fig. 13.4. Mole fraction during late-time RTI growth for a wide range of flow compressibility (Mach number, denoted as M by the authors) and variable density (A) effects. The solutions for all of the cases remain symmetric well into late times. (a) $M = 0.3, A = 0.3$ (b) $M = 1.0, A = 0.3$ (c) $M = 0.3, A = 0.7$ (d) $M = 1.0, A = 0.7$.

Source: Fig. 15 of Reckinger et al. (2016), *J. Computational Phys.*

Scagliarini et al. (2010) considered the continuum thermohydrodynamical limit of a formulation of lattice kinetic equations for thermal compressible flows (Sbragaglia et al., 2009; Biferale et al., 2010, 2011). The authors used this method to study Rayleigh–Taylor instability for compressible stratified flows and determined the growth of the mixing layer at changing Atwood numbers up to $A = 0.4$. Lai et al. (2016) also applied a discrete Boltzmann model and found compressibility delays the initial stage of RTI and accelerates the later stage.

Mellado et al. (2005) turned their attention to RT turbulence with miscible fluids in an unbounded domain. Compressibility effects were studied in LES by decomposing the density fluctuation into an entropic part, due to variation of composition, and an acoustic part, due to intrinsic compressibility. This latter was found to be less than 10% of the total density fluctuation, indicating that the intrinsic compressibility effects are indeed small. Consequently, key features such as the quadratic time evolution of the mixing depth, the anisotropy of the Reynolds stresses, and the value of the mixing parameters compare well with those observed in the incompressible cases reported in the literature.

Mellado et al. (2005) also found that compressibility imposes a negative buoyancy–frequency and thus unstable stratification, which results in the increase of the density fluctuations. The increase in the effective Atwood number due to this buoyancy–compressibility coupling is of the order of 20%.

In a limiting case where the computational domain was extended significantly, Olson and Cook (2007) reported that strong compressibility effects could be observed outside the mixing layer. This process was driven, in part, by expansion of the bubbles of light fluid as they rise in altitude. Their LES suggested that the rising bubbles of light fluid act like pistons, compressing the heavy fluid ahead of the fronts and generating shocklets. These shocklets coalesce in multidimensional fashion into a strong normal shock, which increases in strength as it propagates upwards (Fig. 13.5).

From the full compressible Navier–Stokes system, Schneider and Gauthier (2015) derived the Boussinesq approximation as one of three zero- and low-Mach number models. Gauthier (2017) also considered the anisotropy of the compressible

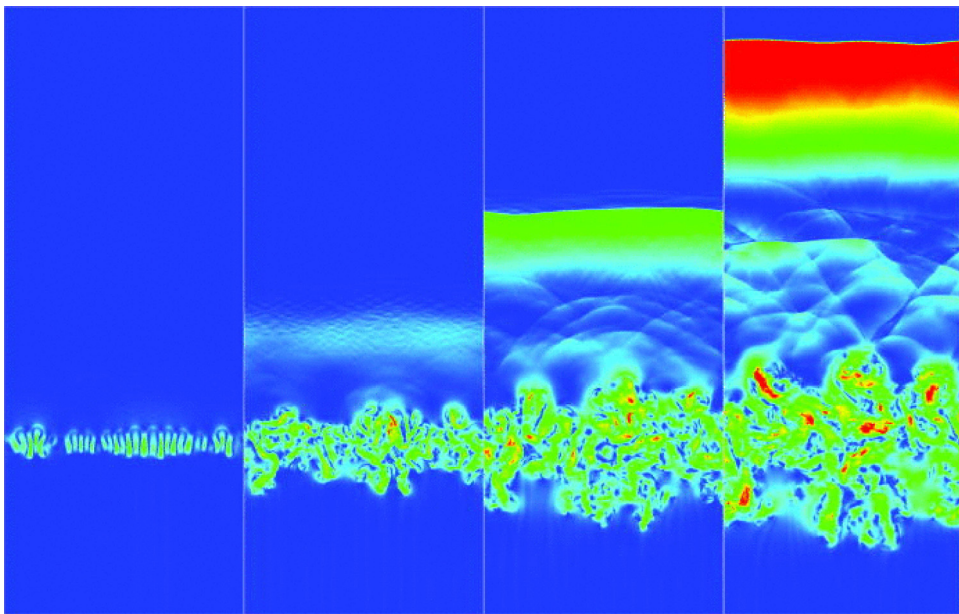


Fig. 13.5. Local Mach number from a 512×2048 point simulation of compressible R-T instability. The upper fluid is xenon and the lower fluid is neon. The RGB color map ranges from 0 (blue) to 1 (red). The snapshots show a 12.8×32.6 km portion of the 12.8×51.2 km flow domain. Simulation times from left to right are: $t = 25, 50, 75$, and 100 s.

Source: Fig. 1 of Olson and Cook (2007), *Phys. Fluids*, with the permission of AIP Publishing.

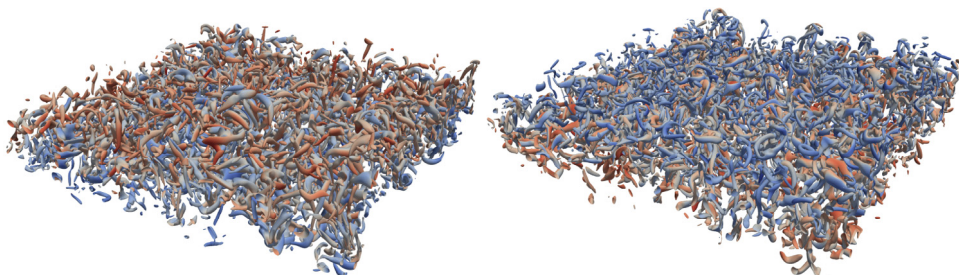


Fig. 13.6. Simulation CG: Q-criterion isosurfaces with $Q = 10$ colored by the concentration (heavy fluid in red and light fluid in blue). Left: top view, right: bottom view. Time at which the vorticity is at a maximum.

Source: Fig. 23 of Schneider and Gauthier (2016b), *Fluid Dyn. Res.* with permission.

miscible Newtonian fluids using large-scale spectral numerical simulations.³⁷ For the Boussinesq simulations, the intermediate scales are close to isotropy, while at the Kolmogorov scale, the energy in the vertical direction is around twice the energy in one horizontal direction (not shown). There is a similar result from the Reynolds stress anisotropy tensor (Figure 8 of Schneider and Gauthier, 2016a), but this an averaged value on all scales. The same qualitative conclusions are found for the compressible case.

Fig. 13.6 shows RTI flow visualizations of two (so called Q-criterion) isosurfaces of the compressible simulation ($Re = 6 \times 10^4$) taken at the time of the maximum vorticity (Schneider and Gauthier, 2016b). Here, the quantity $Q = (u_{i,i}^2 - u_{i,j}u_{j,i})/2$ refers to the second invariant of the velocity gradient tensor (Jeong and Hussain, 1995; Dubief and Delcayre, 2000). Positive values of Q correspond to vortices, while negative values are associated with shear. It illustrated an intricate set of vortices

³⁷ The so-called “indicator for velocity anisotropy” (Chung and Pullin, 2010) also provides some interesting insight into the development of the flow fields.

stirring the heavy and light fluids. The visualization indicated that the mixing layers generated between two stably stratified equilibrium states are strongly homogeneous. Also, the acceleration acts as a restoring force.³⁸

[Lezzi and Prosperetti \(1989\)](#) reminded us that compressibility can have a different origin, a point that was further enforced by [Lafay et al. \(2007\)](#). In an acceleration field, the variable density of the fluid results in stratification to the density gradient length scales for the heavy and light fluids, respectively. Alternatively, the effect of the equation of state (EOS) also led to compressibility and for a perfect gas EOS, it is governed by the adiabatic indexes. [Lafay et al. \(2007\)](#) attributed the old and new disagreements in the community to an imprecise utilization of the word “compressible” without distinguishing its meanings. [Gauthier and Le Creurer \(2010\)](#) offered an updated table, where the compressible RTI problems were carefully classified into isothermal and isentropic cases, as well as a general case, which incorporates both situations. The reader is referred to that work for details.

For compressible RT simulations at an interface between two fluids, there is a key point to make concerning how the stratification is set up either side of the interface. Hydrostatic equilibrium is of course assumed: $\frac{\partial p}{\partial x_3} = -\rho g$. The flow within each fluid is neutrally stable if entropy is constant either side of the interface. This was used by [Youngs \(1994\)](#) to minimize the effect of compressibility and so give the best approximation to incompressible mixing. If constant density is assumed on either side of the interface then the flow within each fluid is unstable. If constant temperature is assumed within each fluid then the flow within each fluid is stabilized. It is well known in atmospheric physics, [Turner \(1973\)](#), that an isentropic atmosphere is neutrally stable. Some RANS models use a correction to allow for this, for example [Andronov et al. \(1979\)](#) uses a turbulence kinetic energy source term

$$\propto -\frac{\nabla p}{\rho^2} \left(\nabla \rho - \frac{\nabla p}{c^2} \right).$$

[Morán-López and Schilling \(2013, 2014\)](#) also recognized the importance of modeling the source term using the mean entropy gradient.

13.2. Stratification

For increasing values of stratification, [Lafay et al. \(2007\)](#) demonstrated that the RTI flow is stabilized (see Fig. 13.7a). Here the stratification parameter is attached to the hydrostatic equilibrium, defined by the acceleration, width of the box, temperature, and molar weight. The stabilization corresponds to the reduction of the vorticity (Fig. 13.7b).

Hence, [Gauthier \(2013\)](#) argued that the influence of the stratification could be classified into various stages. When the instability develops and transition occurs, this regime does not seem to be affected by stratification and the flow behaves essentially as a classical Rayleigh–Taylor regime. In the second step, the mixing layer starts to smooth the density jump and an effective Atwood number, based on the mean density profile, decreases.

As expected, stratification first annihilates turbulence production by smoothing the initial density jump. The baroclinic source term in the vorticity equation and turbulence production also begin to decrease. As a result, the mixing layer thickness saturates. The larger the stratification, the sooner the flow saturates.

Motivated by ICF applications, Mikaelian generalized the results of the classical RT instability to a system of an arbitrary number N of stratified fluids ([Mikaelian, 1982, 1983](#)). Subsequently, he derived the corresponding equations for the RM instability ([Mikaelian, 1985](#)). These problems were addressed by solving Chandrasekhar's incompressible eigenvalue problems based on variational principles. He illustrated the cases of $N = 2$ (classical results) and $N = 3$ by examples patterned after ICF implosions. For other work with the same methodology, see for example, [Mikaelian and Lindl \(1984\)](#), [Mikaelian \(1986\)](#) and [Munro \(1988\)](#).

For the geophysical flows, [Jacobs and Dalziel \(2005\)](#) recognized that the instability will often develop as the result of breaking internal gravity waves, giving initial conditions characterized by both shear and complex stratifications that contain both stable and unstable portions. To recreate these two portions in a laboratory setting, a third layer was introduced to the problem. The apparatus uses the novel barrier design described in [Dalziel et al. \(1999\)](#), which minimizes the disturbance produced by the removal of the barrier. Here, the upper interface is statically unstable (i.e. $\rho_1 > \rho_2$) and the lower interface is statically stable with $\rho_2 < \rho_3$. In these experiments, the Atwood number ratio, introduced for the three layer experiments, $B = A_{13}/A_{12} \approx \{(\rho_1 - \rho_3)/(\rho_1 - \rho_2)\}$, varied from –1 to 0.75 (see Fig. 13.8). The choices of the densities were limited to the Boussinesq limit where the density differences are small compared to the densities themselves.

Clearly, three configurations are possible here. When the density of the bottom layer is decreased below that of the top layer, the erosion increases as expected. In this situation, the turbulent mixing region at late times is found to grow similarly to that of single-interface Rayleigh–Taylor instability. When the top- and bottom-layer densities are the same, the erosion of the bottom-layer fluid by the turbulence generated by the upper unstable interface is found to be small owing to the fact that this interface is always stably stratified. Finally, when the density of the bottom layer is increased above that of the top layer, the degree of erosion is further decreased.

In a related configuration, [Cheng et al. \(2014b\)](#) studied the growth of the RTI interfaces formed by two semi-infinitely distributed fluids and one middle fluid layer. The authors also found that the instability growth rate depends on the density

³⁸ If a blob of fluid escapes the mixing layer moving upward or downward, it would be surrounded either by lighter fluid or by heavier fluid, respectively ([Schneider and Gauthier, 2016b](#)).

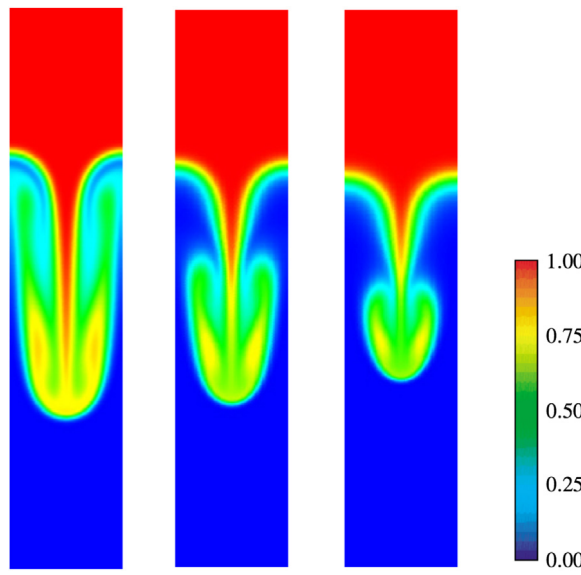


Fig. 13.7a. Stratification effects: concentration fields at time $t = 10$ for three values of the stratification parameter $Sr = 0.05$, $Sr = 0.50$ and $Sr = 1.00$ (from left to right). The Reynolds number is $Re = 1000$.

Source: Fig. 7 of [Lafay et al. \(2007\)](#), *Europhysics Letters* with permission.

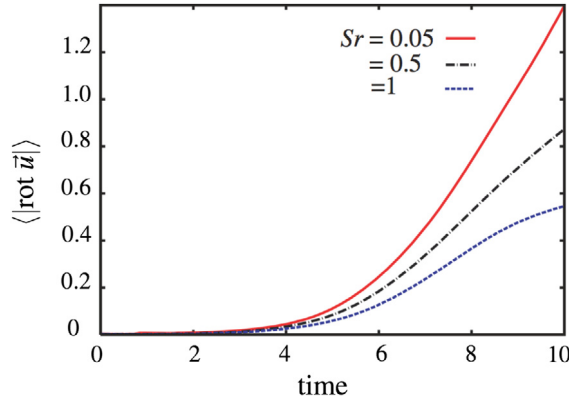


Fig. 13.7b. The stratification effects. Mean value of vorticity vs. time, for three values of the stratification parameter ($Sr = 0.05$, 0.50 and 1.00).

Source: Fig. 9a of [Lafay et al. \(2007\)](#), *Europhysics Letters* with permission.

and thickness of the interlayer. When the thickness of the interlayer was large enough, greater than 0.6 times the wavelength of the perturbation, then the coupling influence was weak on the growth rate of the interfaces. However, the strong coupling effect resulted in a complicated growth rate in other situations. This problem was studied by [Mikaelian \(1982\)](#) who gave the linear growth rates for arbitrary densities and showed that growth is minimized if the density ρ_2 of the middle fluid was the geometric mean of the other two: $\rho_2 = \sqrt{\rho_1 \rho_3}$. Using normal mode analysis, [Parhi and Nath \(1991\)](#) obtained an analytical criterion for RTI of three-layer fluids. More recently, [Youngs \(2017\)](#) presented DNS results (Fig. 13.9a) for one of the cases for which ILES results were given ([Youngs, 2009](#)). DNS is able to assess the influence of viscosity at moderate Reynolds number and at Schmidt number $Sc \sim 1$. The ILES appears to give an adequate approximation to the high-Re behavior (Fig. 13.9b). The overall progress of the mixing process, as indicated for the volume fraction distributions, is very similar for the ILES and the highest resolution DNS.

[Lawrie and Dalziel \(2011a\)](#) and [Davies Wykes and Dalziel \(2014\)](#) investigated the mixing efficiency of stratification in confined RTI for a variety of initial density profiles (Fig. 13.10). Sketch (a) is the classical case of RTI where a layer of dense fluid is above a layer of light fluid. Lawrie and Dalziel presented a series of experiments where a RT unstable interface was confined between two stable linear density profiles (Sketch of (c)). They found that the mixing efficiency for this configuration was higher than that of the simple two-layer case, RTI. The follow-up work by [Lawrie and Dalziel \(2011b\)](#) was still confined to stable linear density stratification, but now in a tank with a high-aspect-ratio equal to 40.

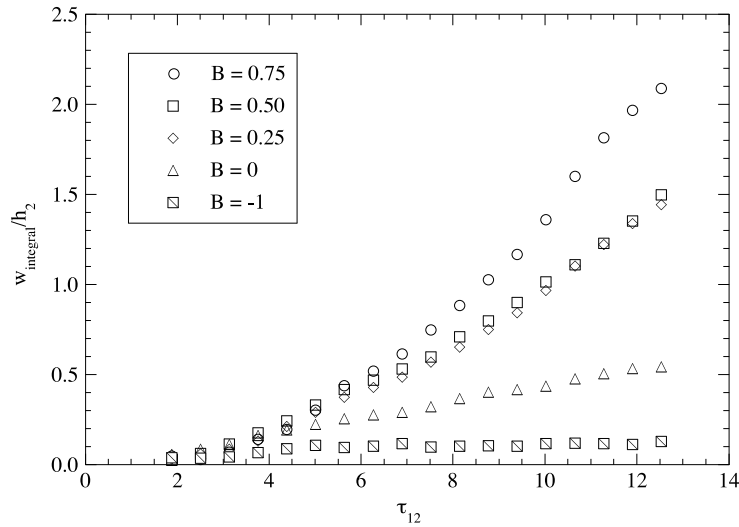


Fig. 13.8. The mixed width, normalized by the width of the middle layer, vs. time. The Atwood ratio is varied from -1 to 0.75 .
Source: Fig. 18 of Jacobs and Dalziel (2005), *J. Fluid Mech.* with permission.

In the stratified case, Davies Wykes and Dalziel (2014) showed that the initial behavior of the instability is similar to the classical case. The development of the instability, when it is confined by stratification, is shown in the shadowgraph images of Fig. 13.11 (Fig. 6 of Davies Wykes and Dalziel, 2014). This experiment had an initially quadratic density profile with a density gradient that increased away from the unstable interface (Sketch of (b)).

To investigate the effect of Atwood number on mixing efficiency, Davies Wykes and Dalziel (2014) carried out a set of 26 experiments with linear profiles and Atwood number varying from 4×10^{-3} to 7×10^{-2} . As shown in Fig. 13.12, the mixing efficiency of these experiments was always at least 95% of the perfect mixing efficiency, 0.75 ± 0.002 , which was calculated from the measured initial density profile of each experiment.

Subsequent theoretical work has investigated the application of concepts from statistical mechanics to these stratified flows (Venaille et al., 2017; Williams, 2017). Venaille et al. extending their previous work on two-dimensional turbulence, apply a maximum entropy production principle to find that at sufficiently large Richardson number, there will be equipartition between potential and kinetic energy. Williams maximizes a configurational entropy functional to derive an analytic form for the density profile which the mixing layer relaxes to at late time. Together, these approaches suggest potential routes forward in deriving models for more general turbulent flows. Williams also discussed 3D simulations related to the stratifications illustrated in Fig. 13.10.

Before closing this subsection, a historical remark on the finite thickness layers is appropriate here. Taylor (1950) did consider a layer of finite thickness at $A = 1$ in his classic paper. There is also an early AWE paper by Hunt (1961a).

13.3. Rotation

The influence of rotation on the RTI was first studied by Hide (1956a, b) for a viscous incompressible fluid, which rotates uniformly at an axis making an angle with the vertical direction. In his classical monograph, Chandrasekhar (1961) showed that rotation could reduce the growth of RTI. To bring out the essential elements of the problem, he took the axis of rotation along the vertical direction and neglected the viscous effect. For RTI in the presence of rotation, Chakraborty and Chandra (1976) added a layer of transition of finite thickness in which density increases exponentially with distance in the vertical direction. Later, Chakraborty (1979) found the upper bound of the maximum growth rate of instability, and thus illustrated that the growth rate of instability is finite in a stratified fluid of any continuous density distribution.

Coriolis and centrifugal forces are found in the stellar and planetary as well as engineering systems (Zhou, 1995) and play a role in governing many phenomena including RTI. Khater and Obied Allah (1984) studied the effect of rotation at an accelerating compressible, perfectly conducting, stratified plane layer.³⁹ Dávalos-Orozco and Aguilar-Rosas (1989a) inspected the effect of a general rotation field on the RTI of a continuously stratified fluid and clearly demonstrated the important contribution of the horizontal component of rotation on the stability in different directions of propagation. Dávalos-Orozco and Aguilar-Rosas (1989b) considered the system subject to a continuously stratified background, under a general rotation field and a stratified horizontal magnetic field (see also Dávalos-Orozco, 1996). More recently,

³⁹ Aluie and Kurien (2011) observed forward cascade of both global invariants, the potential enstrophy and energy, in rotating stratified Boussinesq flows. This showed a clear departure of these flows from two-dimensional turbulence.

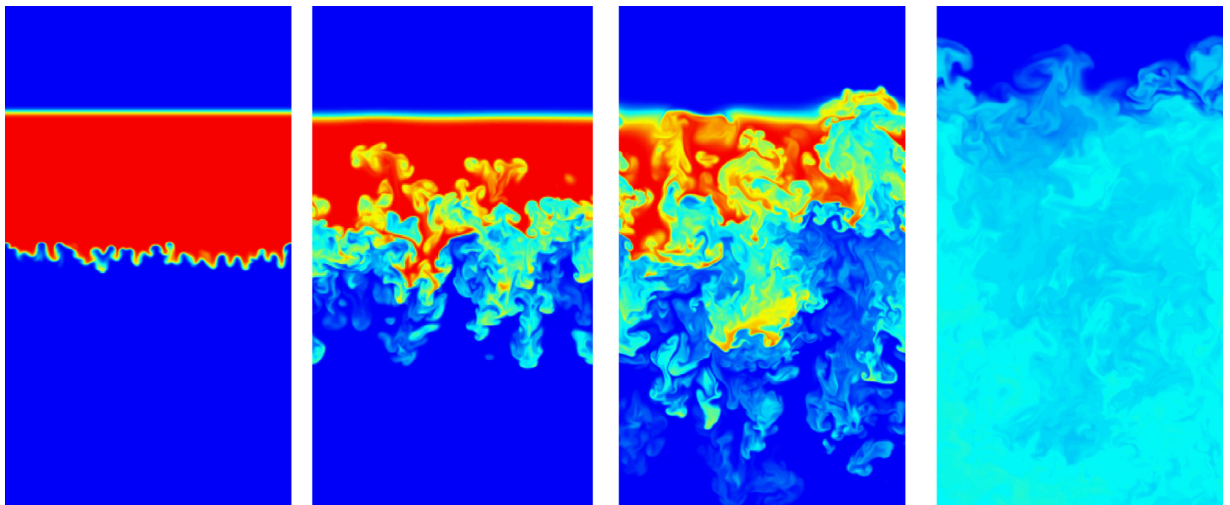


Fig. 13.9a. Dense fluid volume fraction (plane sections) for DNS, $2048 \times 1024 \times 1024$ meshes, $Re = 3400$. Scaled time = 1, 2.5, 4, and 10.
Source: Fig. 6 of Youngs (2017), *Physica Scripta*. ©Crown Owned Copyright. Reproduced with permission.

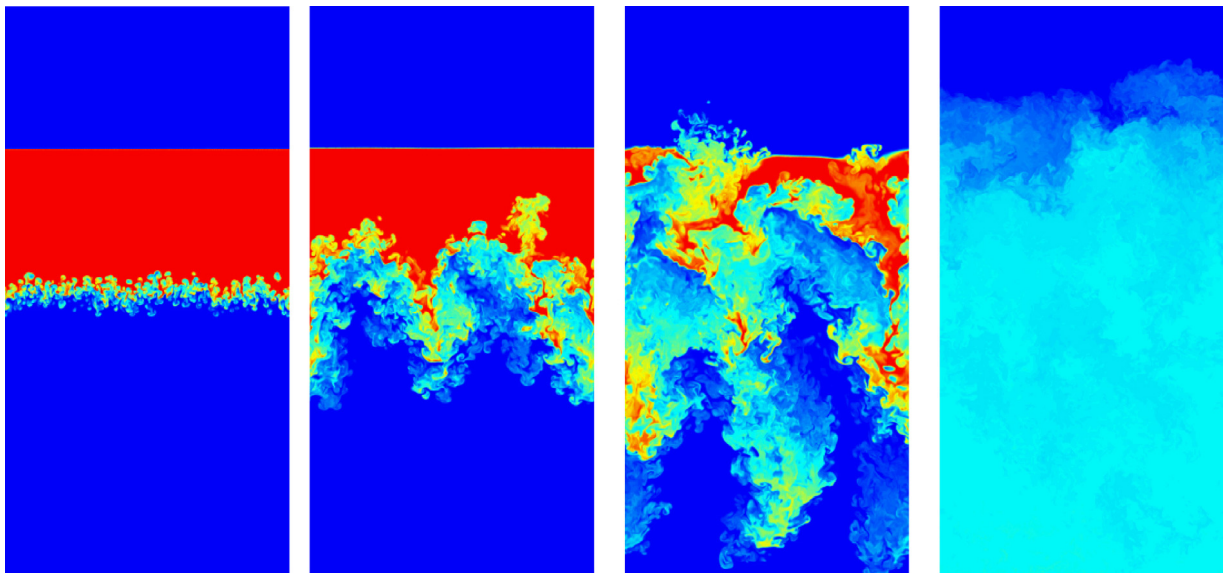


Fig. 13.9b. Dense fluid volume fraction (plane sections) for ILES, $1024 \times 512 \times 512$ meshes. Scaled time = 1, 2.5, 4, and 10.
Source: Fig. 5 of Youngs (2017), *Physica Scripta*. ©Crown Owned Copyright. Reproduced with permission.

Ma et al. (2006) studied the behavior of the Rayleigh–Taylor mode in a dusty plasma with rotational and shear flows, while Prajapati (2016) considered the RTI in non-uniform magnetized rotating strongly coupled viscoelastic fluid. For compressible rotating RTI flows, Duan et al. (2015) applied a general method of studying a family of modified variational problems (Guo and Tice, 2011) and illustrated that rotation diminishes the growth of instability.

To isolate the effect of rotation on the RTI growth, Carnevale et al. (2002) performed a series of numerical simulations of low Atwood number flow (the Boussinesq approximation). The rotation axis is parallel to the acceleration and the flow was in a regime where mass diffusion is comparable to momentum diffusion (Schmidt number $Sc \sim O(1)$). For cases with random initial perturbations, the RTI can be delayed and its growth rate diminished by rotation (Fig. 13.13). Interestingly, the effects of rotation occur even in the earliest phase of the instability that is even before the establishment of a mixing zone. This suggests that it would be possible to understand the effect of rotation, at least in the early phases, in terms of bubble formation. The retarding role that rotation plays was analyzed in the early formation of the vortex ring. Further, bubble formation is completely suppressed for high enough rotation rate (measured with a non-dimensional parameter, the Rossby number, which is inversely proportional to the rotation rate). Boffetta et al. (2016) performed direct numerical

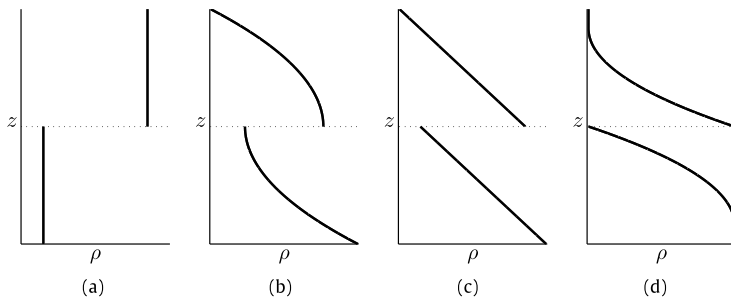


Fig. 13.10. Sketch of (a) the classical case of RTI (a layer of dense fluid above a layer of light fluid) and (b-d) the initial density stratifications used in experiments. The two quadratic profiles (b, d) differ by having a density gradient that either increases [(b); $d^2\rho/d|x_3|^2 > 0$] or decreases [(d); $d^2\rho/d|x_3|^2 < 0$] away from the unstable interface.

Source: Fig. 1 of Davies Wykes and Dalziel (2014), *J. Fluid Mech.* ©Crown Owned Copyright, reproduced with permission.

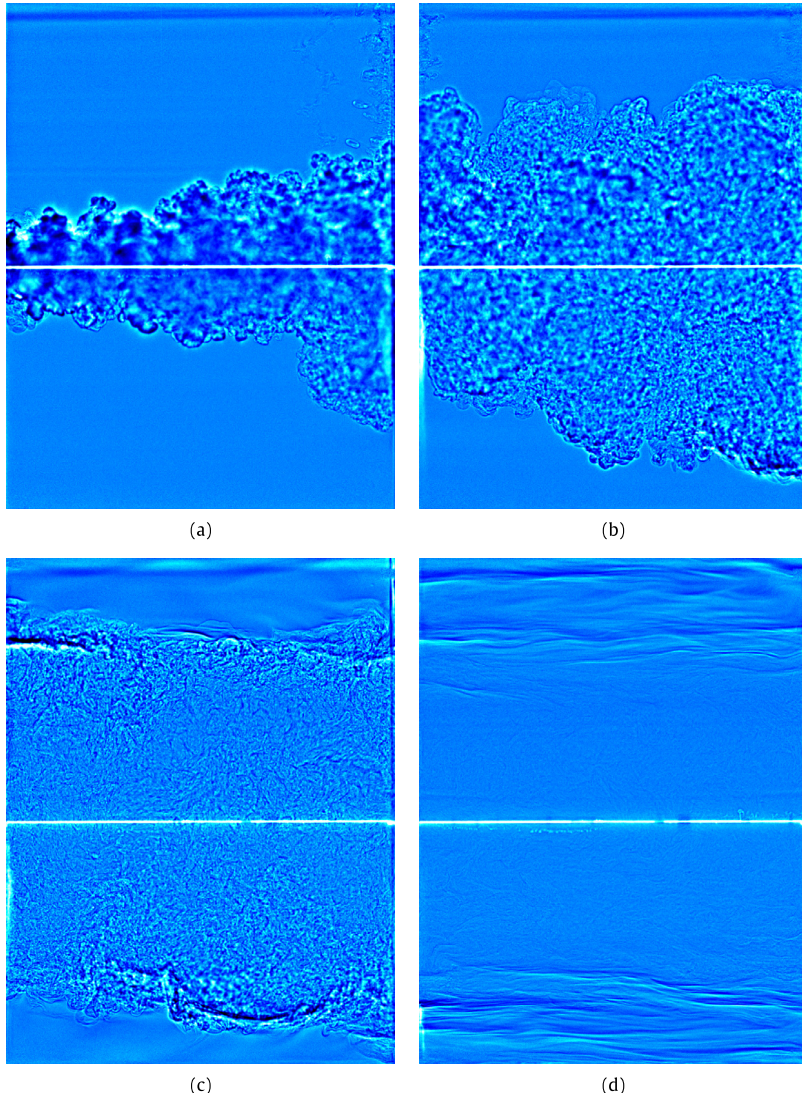


Fig. 13.11. Shadowgraph images showing the development of the instability for $A_0 = 9 \times 10^{-3}$ versus the non-dimensional time, τ . (a) $\tau = 3.3$, a mixing region develops at the unstable interface; (b) $\tau = 6.6$, stable stratification slows the growth of the mixing region; (c) $\tau = 13.3$, turbulent mixing continues but there is no further growth of the mixing region; (d) $\tau = 53.2$, motion has died away in the horizontal white line through the center of each image is the original location of the barrier.

Source: Fig. 6 of Davies Wykes and Dalziel (2014), *J. Fluid Mech.* ©Crown Owned Copyright, reproduced with permission.

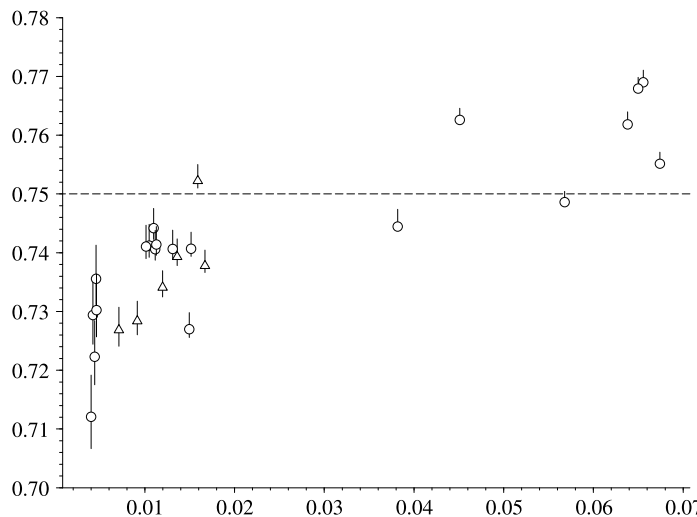


Fig. 13.12. Mixing efficiency of experiments with linear stratification in the upper and lower layers. Dashed line shows perfect mixing efficiency, which for all experiments was 0.75 ± 0.002 . All experiments had a mixing efficiency of at least 95% of the perfect mixing efficiency.
Source: Fig. 11 of Davies Wykes and Dalziel (2014), J. Fluid Mech. ©Crown Owned Copyright, reproduced with permission.

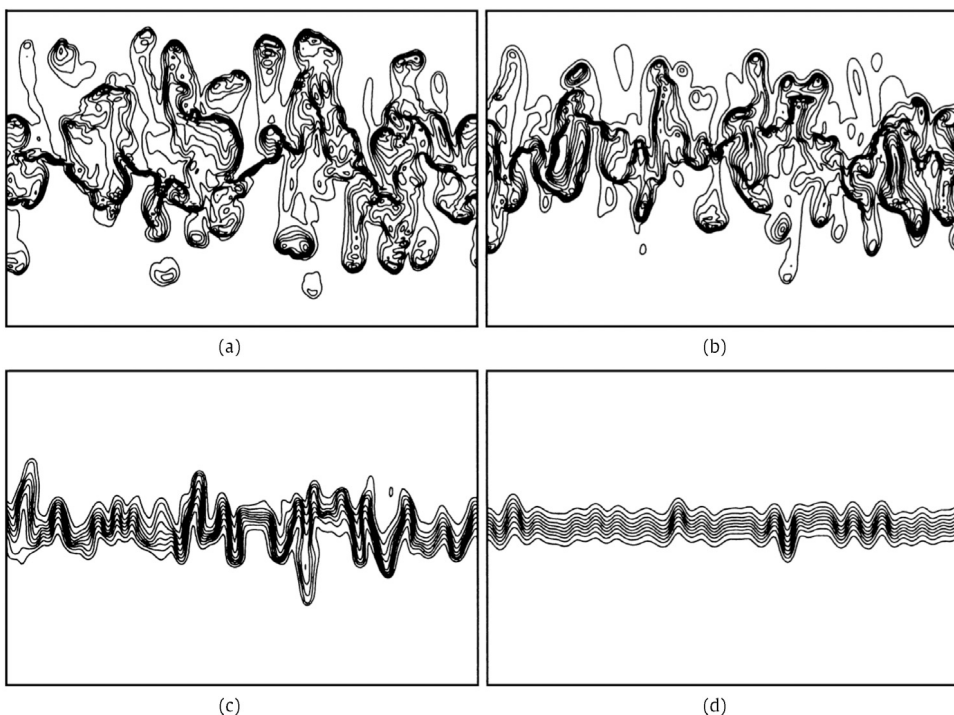


Fig. 13.13. Contour plots of the scaled density θ in a vertical cross-section (y, z -plane) at time $t = 5$. The contour increment is $\Delta\theta = 0.1$. Both the vertical axis z and the horizontal axis y range from -1 to 1 (images have been cropped in the vertical direction). (a) $Ro = \infty$, (b) $Ro = 1/4$, (c) $Ro = 1/8$, (d) $Ro = 1/12$.

Source: Fig. 1 of Carnevale et al. (2002), J. Fluid Mech.

simulations within the Boussinesq approximation and reported that rotation reduces the efficiency of the conversion of the available potential energy into large-scale kinetic energy, and relatively more energy is dissipated at small scales. The rotation reduced the temporal growth of the mixing layer with respect to the case without rotation and the intensity of turbulent velocity fluctuations (Figs. 13.14a and 13.14b).

Baldwin et al. (2015) performed a set of experiments with rotation of a liquid system ($Sc \sim 10^4$) about an axis parallel to the direction of acceleration (Fig. 1 of Baldwin et al., 2015, not shown). Fig. 13.15 (Fig. 7 of Baldwin et al., 2015) shows

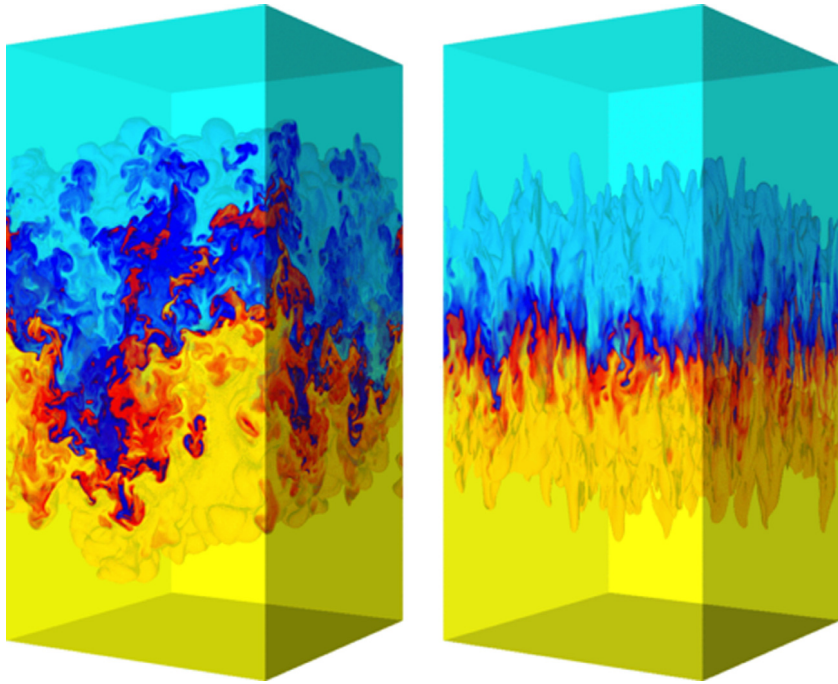


Fig. 13.14a. Snapshots of the temperature field at time $t = 5.2\tau$ for two simulations with $\Omega\tau = 0$ (left) and $\Omega\tau = 10$ (right) starting from the same initial conditions. Yellow (blue) represents hot (cold), light (heavy) fluid.

Source: Fig. 1 of Boffetta et al. (2016), *Phys. Rev. Fluids* with permission.

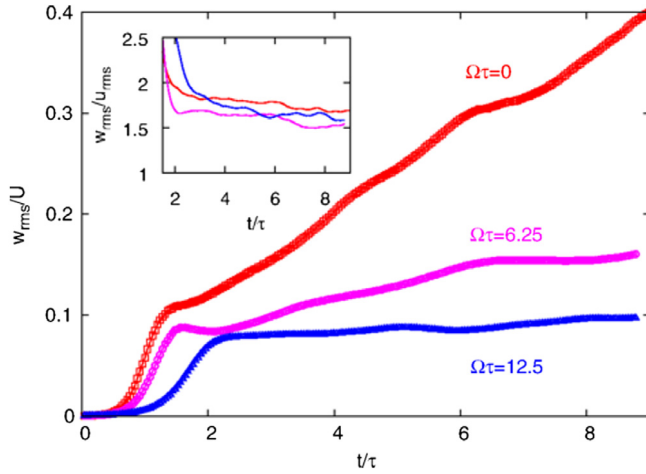


Fig. 13.14b. Vertical velocity fluctuations w_{rms} in the mixing layer as a function of time for three different rotations, $\Omega\tau = 0$ (red squares), $\Omega\tau = 6.25$ (pink circles), and $\Omega\tau = 12.5$ (blue triangles). Inset: ratio of vertical to horizontal velocity fluctuations as a function of time, for the same values of rotation.

Source: Fig. 2 of Boffetta et al. (2016), *Phys. Rev. Fluids* with permission.

the dominant initial radial wavelength, λ , as a function of the rotation rate, Ω . The bars on each data point indicate the minimum and maximum value of λ measured over the first 2 s after onset of RTI. The rotation caused a decrease in λ from 16 ± 2 mm at 1 rad s^{-1} , to approximately 6 mm at 4 rad s^{-1} . (Below 1 rad s^{-1} , the length scale was too large to resolve with the autocorrelation function. Above 4 rad s^{-1} , increasing rotation rate had little effect on λ .) Hence, both the numerical results and the experimental data demonstrated that rotation slows the growth of the RT instability.

In a comprehensive work, Scase et al. (2017a) showed that the effect of the rotation could be seen to restrict the size of the vortices that form and inhibit the bulk vertical transport of fluid (Fig. 13.16). A result of this is that axisymmetric instabilities in cylindrical geometries may be completely stabilized above a critical rotation rate that they derived. The observations from

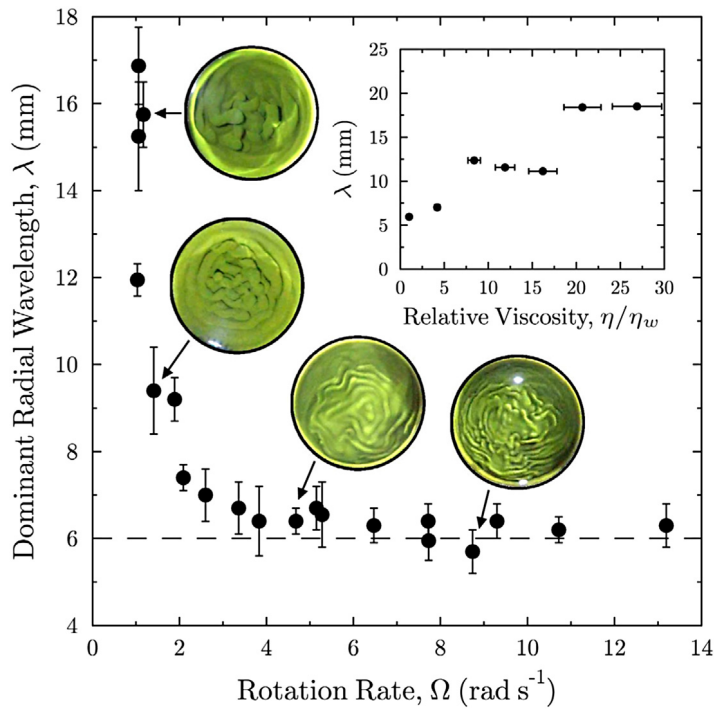


Fig. 13.15. Plot of the dominant initial radial wavelength λ as a function of rotation rate. Dashed line: approximate lower wavelength limit observed, $\lambda \approx 6$ mm Inset shows the effect of viscosity (in units of the viscosity of water, η_w) on λ , for $\Omega = 7.8$ rad s⁻¹.
Source: Fig. 7 of Baldwin et al. (2015), Sci. Rep. with permission.

the experiments are broadly in line with their theoretical predictions, specifically that by rotating the system the growth of large wave modes is inhibited and the growth rate of the instability is suppressed (see e.g., Scase et al., 2016). Also, the authors derived the dispersion relation for rotating RTI. The theoretically predicted growth rates compare well with the observations, provided that the dominant wavelength of instability is obtained from experiment⁴⁰.

Tao et al. (2013) studied analytically the nonlinear regime of the RTI of rotating inviscid fluids where the rotation axis is instead perpendicular to the direction of acceleration. For this situation akin to a fluid–fluid centrifuge, the growth of the RTI can be retarded by the rotation at arbitrary Atwood numbers.

13.4. Magnetic field

The magnetic Rayleigh–Taylor instability has further complication due to the presence of a magnetic field throughout both media and is responsible for several observed astrophysical phenomenon (Parker, 1966; Jun et al., 1995; Kulkarni and Romanova, 2008; Shin et al., 2008; Favier et al., 2012; Contopoulos et al., 2016; Hillier, 2016; Gold et al., 2017; Jiang and Jiang, 2017), the solid media (Sun and Piriz, 2014), Z-pinch (Shumlak and Roderick, 1998; Qiu et al., 2003) and ICF (Nishiguchi, 2002; Haines, 1997; Fryxell et al., 2010; Srinivasan et al. 2012; Srinivasan and Tang, 2012, 2013; Velikovich et al., 1996) applications. For the RMI induced by the ionized heavy gas cloud eruption (Zhuang et al., 2013), Lin et al. (2017) determined that magnetic fields can suppress the formation of spike and bubble structures induced by the eruption in both cylindrical and spherical cases.

Chandrasekhar (1961) studied magnetic RTI fluids that are incompressible, stratified, inviscid, and have zero resistivity. He showed that the linear growth rate of the RTI with constant acceleration is mitigated at high-wave numbers in the presence of a magnetic field. In case the magnetic field is parallel to the surface of separation, Chandrasekhar (1961) also found that according to linear theory there exists no effect of the magnetic field on the instability if the latter is perpendicular to the wave vector (see also Gupta et al., 2010; Khan et al., 2011).

⁴⁰ As articulated by Scase et al. (2017a), the rotating RTI system under investigation undergoes two competing effects. The first one is between the destabilizing effect of the denser fluid overlying the lighter fluid that generates an overturning motion at the interface and the stabilizing effect of the rotation that is organizing the flow into vertical structures and preventing the layers passing each other. The second one is between rotation suppressing the larger structures and viscosity suppressing the smaller structures, leading to an observed instability structure that depends on both the rotation rate and the fluid viscosity.

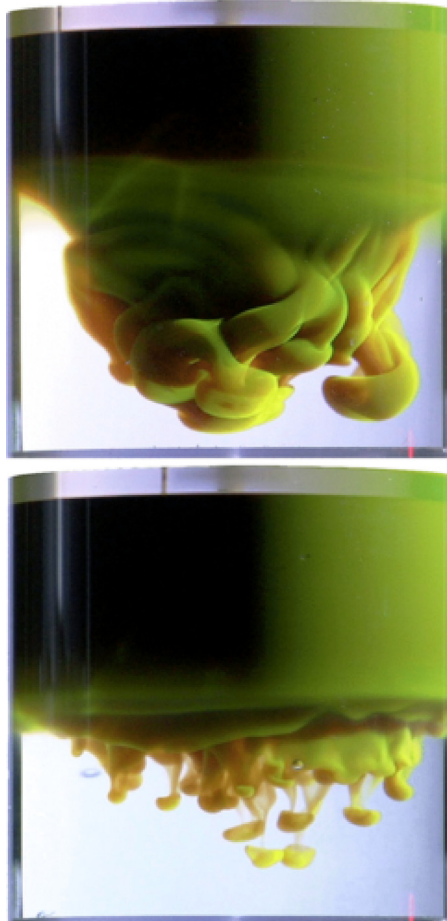


Fig. 13.16. The top image, taken from the authors' experiments, is of a magnetically induced RTI developing in a nonrotating system. The instability develops in time, forming large vortices that transport the green fluid downward. The bottom image is of the same fluids, but here the system is rotating. Rotation can be seen to restrict the size of the vortices that form and inhibit the bulk vertical transport of fluid. The times shown are 1.92 and 3.52 s after initiation in the top and bottom images, respectively. The experiments are described in Baldwin et al. (2015) and Scase et al. (2017b). The tank diameter is 90 mm and the rotation rate in the bottom image was 2.52 rad s^{-1} .

Source: Fig. 1 of Scase et al. (2017a), *Phys. Rev. Fluids* with permission.

Pacitto et al. (2000) perform RTI experiment for different values of the magnetic field. Near the onset of the instability, the authors measured the wavelength and the growth rate of the observed fingers. The observed growth rates for the various wavelengths induced by the perturbations were found to lie between the theoretical values calculated for the minimum and maximum magnetization values (see Chambers and Forbes, 2011 for a discussion on comparing the experimental results with the linear theory). Rannacher and Engel (2007) also carried out the RTI experiments of a magnetic fluid superimposed on a nonmagnetic liquid of lower density, but now with the help of a spatially homogeneous magnetic field rotating in the plane of the undisturbed interface. For various angular frequencies of the rotation rate, they found that if the magnetic field amplitudes get larger than a threshold value, parametric excitation due to the time-dependent magnetic field gives rise to new instabilities at higher wavenumbers.

Stone and Gardiner (2007a) investigated the idealized case of two inviscid, perfectly conducting fluids of constant density separated by a contact discontinuity perpendicular to the effective gravity g , with a uniform magnetic field parallel to the interface. To facilitate comparison with previous experimental and computational studies of the RTI, a relatively modest difference in density between the fluids was chosen ($A = 0.5$). Fig. 13.17 (Fig. 5 of Stone and Gardiner, 2007a) is a comparison of the three-dimensional structure using vertical slices of the density at the edges of the computational domain, as well as a horizontal slice at the midplane $z = 0$. The hydrodynamic calculation can be compared directly to the results for a weak and a strong magnetic field. At late times, even a weak field has strongly affected the structure, and for a strong field, these structures are unlike any of the bubbles seen in the hydrodynamic RTI.

For the weak case, the bubbles have become long columns, which have extended far above the midplane. These structures show no anisotropy and there continues to be little mixing between the fluids. At late times in the strong field case, the

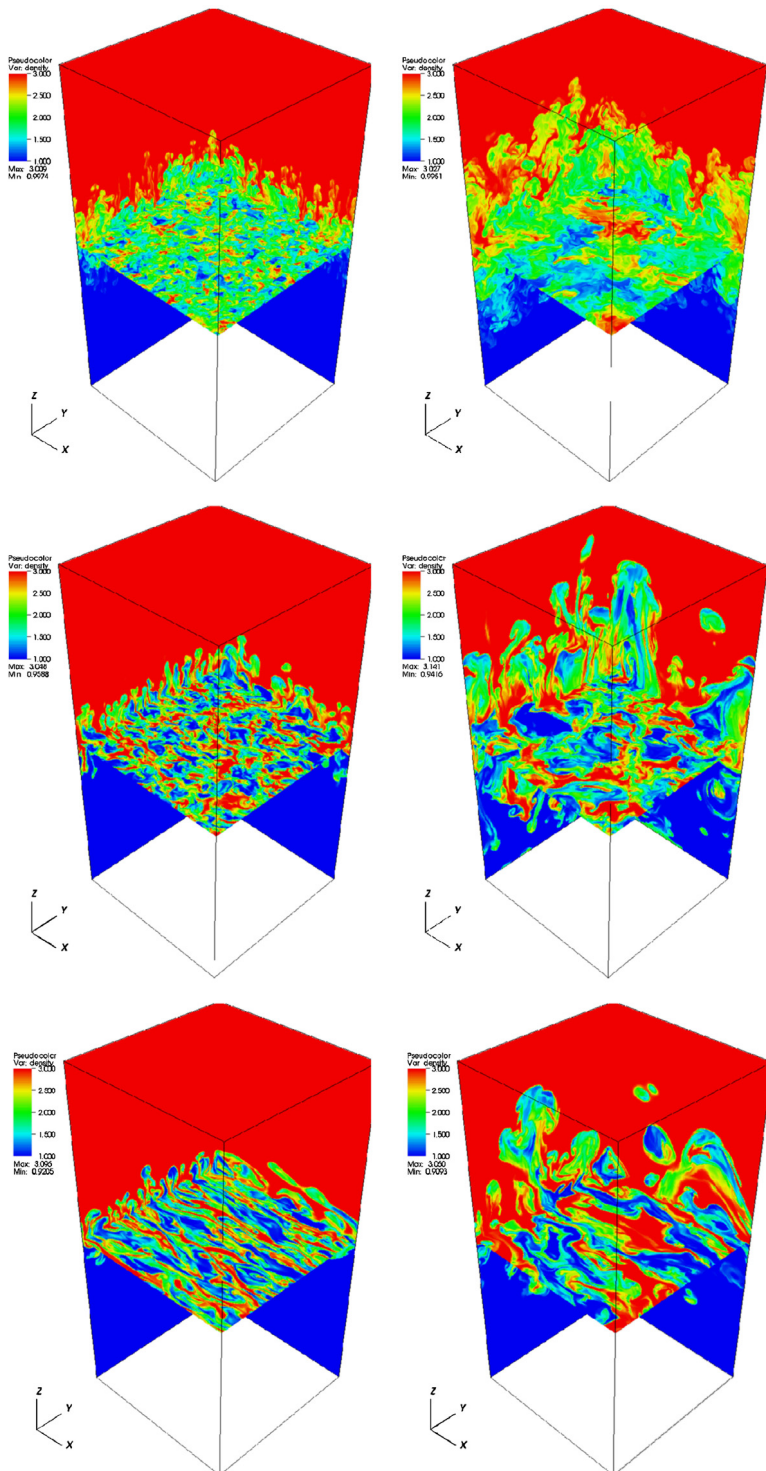


Fig. 13.17. Slices of the density at $t/t_s = 29.6$ (left panels) and $t/t_s = 60.0$ (right panels) in runs RH (top, hydrodynamic), R2 (middle, weak field), and R6 (bottom, strong field). Note the decrease in mixing in the MHD RTI (as evidenced by reduced volume at intermediate densities, i.e. gray regions), and the elongation of structures along the magnetic field (x -axis) in the strong field case.

Source: Fig. 5. Stone and Gardiner, *Phys. Fluids*, 2007a, with the permission of AIP Publishing.

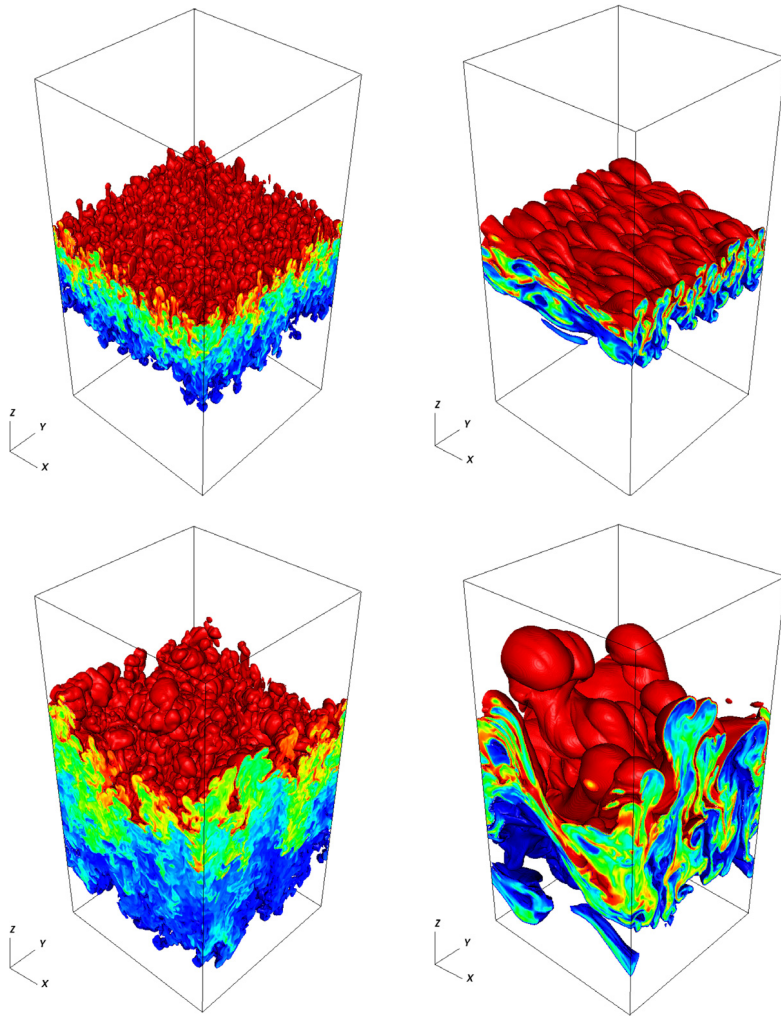


Fig. 13.18. Isosurfaces of the density at 9.9 and 1.1 at normalized times 20 and 40. Left panels: pure hydro; Right panel: uniform magnetic field applied. Source: Fig. 1 of [Stone and Gardiner, *Astrophys. J.*, \(2007b\)](#) with permission.

dominant structures are smooth and highly anisotropic. Nevertheless, it is not possible to suppress fully the RTI in all directions through the use of a background magnetic field alone.

For a density ratio more relevant to astrophysical applications ($A = 9/11$), [Stone and Gardiner \(2007b\)](#) compared the results in the uniformly strongly magnetized simulation run with those of a hydro-dynamical calculation (Fig. 13.18) (Fig. 1 of [Stone and Gardiner, 2007b](#)). The early non-linear phase of the magnetic RTI shows the strongly anisotropic structure of modes. Perpendicular to the field, interchange modes grow fastest at short wavelength, whereas along the field short wavelengths are suppressed. As a result, the interface develops a filamentary structure that is strongly reminiscent of the structure reported by [Isobe et al. \(2005, 2006\)](#) in simulations of flux tubes emerging from the solar photosphere (see also [Kim et al., 1998](#)). This produces large-scale smooth bubbles. Slices along the edges of the domain reveal far less mixing than in the hydrodynamic case ([Stone and Gardiner, 2007b](#)).

Taking the nonlinear effects into account, [Gupta et al. \(2010\)](#) studied the time development of the nonlinear interfacial structure caused by RT instability in the presence of a magnetic field parallel to the surface of separation of the two fluids. The wave vector is assumed to lie in the same plane and perpendicular to the magnetic field. Thus, the RT instability driving pressure difference is modified by the inclusion of the magnetic pressure difference. As a result, the growth rate may be enhanced or depressed according to whether the extra contribution is either positive or negative. Such nonlinear effects, of course, disappear in the linear approximation.

Through the analysis of both the fluid and magnetic vorticities and stream functions, [Chambers and Forbes \(2011\)](#) computed the growth of the interface in the nonlinear regime. It demonstrated how different initial conditions give rise to outcomes that are very different in terms of the geometry of the interface between the two fluids (see also, [Forbes, 2009](#)).

Of particular interest, they considered the cases with strong and weak magnetic fields as well as the cases with magnetic fields oriented at different angles relative to the interface of the two fluids.

In a more complex situation, Liberatore and Bouquet (2008) investigated the magnetic Rayleigh–Taylor instability (MRTI) in the case of compressible plasmas. The work detailed the influence of both the magnetic field and the compressibility of the material on the growth rate of the Rayleigh–Taylor instability, compared to the classical growth rate derived for incompressible fluids. Within the framework of the ideal magnetohydrodynamics (MHD) theory, the analytical linear models indicate that stratification weakens the MRTI while compressibility has a destabilizing effect. The magnetic field enhances these phenomena (see a follow up work by Liberatore et al., 2009). Díaz et al. (2014) investigated the effects of considering partially ionized plasma in the MHD RTI, while Hoshoudy (2011) considered the effect of quantum mechanism on RTI of stratified viscous plasmas layer in the presence of a vertical magnetic field. Zhang et al. (2005) studied a flow where a sharp interface exists and the shear flows and magnetic field are both not perpendicular to the wave vector. It is shown that the magnetic stabilization is balanced by the destabilizing effect of shear flow.

RMI has been found in applications involved with ionized fluids and therefore could be affected by magnetic fields. In ideal MHD, Samtaney (2003) inspected the behavior of an impulsively accelerated perturbed interface separating incompressible conducting fluids of different densities, in the presence of a magnetic field that is parallel to the acceleration. Using numerical simulations, he showed that the growth of the RMI is suppressed in the presence of a magnetic field. Wheatley et al. (2005a) illustrated the suppression of the instability by changes in the shock refraction process at contact discontinuity with the application of a magnetic field. As a result, these changes prevent the deposition of circulation on the contact discontinuity.

Wheatley et al. (2005b) analytically solved the appropriate linearized initial value MHD problem. In this model, the initial growth rate of the interface is unaffected by the presence of a magnetic field. The growth rate then decays resulting in an asymptotic constant value of the interface amplitude. The difference between the initial and final interface amplitudes is inversely proportional to the magnetic field magnitude. Thus the instability of the interface is suppressed by the presence of the magnetic field. In a follow up work, Wheatley et al. (2009) compared the model predictions to results obtained from numerical simulation of impulse driven linearized, shock driven linearized, and nonlinear compressible MHD. For weak shocks, small initial perturbation amplitudes, and weak magnetic fields, the model collapses simulation results well. When these conditions are not met, the linear model may give a rough estimate of the interface behavior, but it is not quantitatively accurate.

In the case when the magnetic field is parallel to the interface and there is no mean shear,⁴¹ Cao et al. (2008) found that the instability is suppressed by a different physics, a Lorentz force that opposes the perturbation of the interface. Wheatley et al. (2009) remarked that the instability may not be suppressed by transport of vorticity, since a jump in tangential velocity across the interface is allowed, which allowed most of the vorticity generated by the shock refraction process to remain on the interface. However, Wheatley et al. (2014) found that such a field causes vorticity to be carried parallel and antiparallel to the interface, causing in turn an oscillating behavior of the interface through their mutual interference, effectively suppressing the instability. In a related study, Cao et al. (2009) considered RMI of a stratified fluid in transverse magnetic field, extending the previous publications of Mikaelian (1985, 1989) where the magnetic field was not considered.

Khan et al. (2011) extended the work of Gupta et al. (2010) to consider the temporal development of the nonlinear interfacial structure caused by RM and RT instability in the presence of a magnetic field parallel to the surface of separation and perpendicular to the acceleration of the two fluids. While no effect of the magnetic field is found in the linear approximation, again in the nonlinear regime, the effect of a magnetic field is predominant. The nonlinear growth rate may be enhanced or depressed depending on whether the magnetic pressure contribution is positive or negative.

Based on an analogy between the Rayleigh and the Schrödinger equations (Mikaelian, 1996b; Tavakoli et al., 1999),⁴² Tavakoli et al. (2000) generalized the “equivalent potential” to include the uniform magnetic field for an arbitrary density profile. In presence of a uniform magnetic field for a smoothly varying density profile in a limit of small Atwood numbers, it was found that the spectrum of unstable modes is two-side-bounded and the external magnetic field stabilizes some or all modes.

For astrophysical plasmas, it is also known that strong magnetic fields may lead to various quantum effects being important (Harding and Lai, 2006; Modestov et al., 2009). When the de Broglie wavelength of the charge carriers becomes equal to or greater than the dimension of the quantum plasma system, the quantum effects become important in the behavior of the charged plasma particles (Manfredi, 2005; Haas, 2005; Ali et al., 2007; Bret, 2007; Lundin et al., 2007). Bychkov et al. (2008) illustrated that quantum effects in the form of the Bohm-de Broglie dispersion reduce the RT instability. The instability is stabilized completely at sufficiently short wavelength, the quantum cutoff. Cao et al. (2008) also showed that the magnetic field has a stabilizing effect on RT instability similar to the behavior in classical plasmas and the quantum effects also suppress RT instability with the appropriate physical quantities. Similarly, Wang et al. (2012a) illustrated how the RTI can be completely quenched by magnetic field stabilization and/or quantum effect stabilization in proper circumstances resulting in a cutoff wavelength.

To take advantage of the stabilizing effect of magnetic fields, incorporation of strong magnetic fields in ICF implosions has been suggested, and work along these lines is continuing – see Perkins et al. (2013, 2017). Here, simulations indicate that imposed magnetic fields of tens of Tesla that increase to greater than 10 kT (100 MGauss) under implosion compression

⁴¹ The effect of shear flows on fluid stability is quite complicated. Some arguments are that shear flow suppresses turbulence (see Terry, 2000).

⁴² See also, Jia et al. (2012).

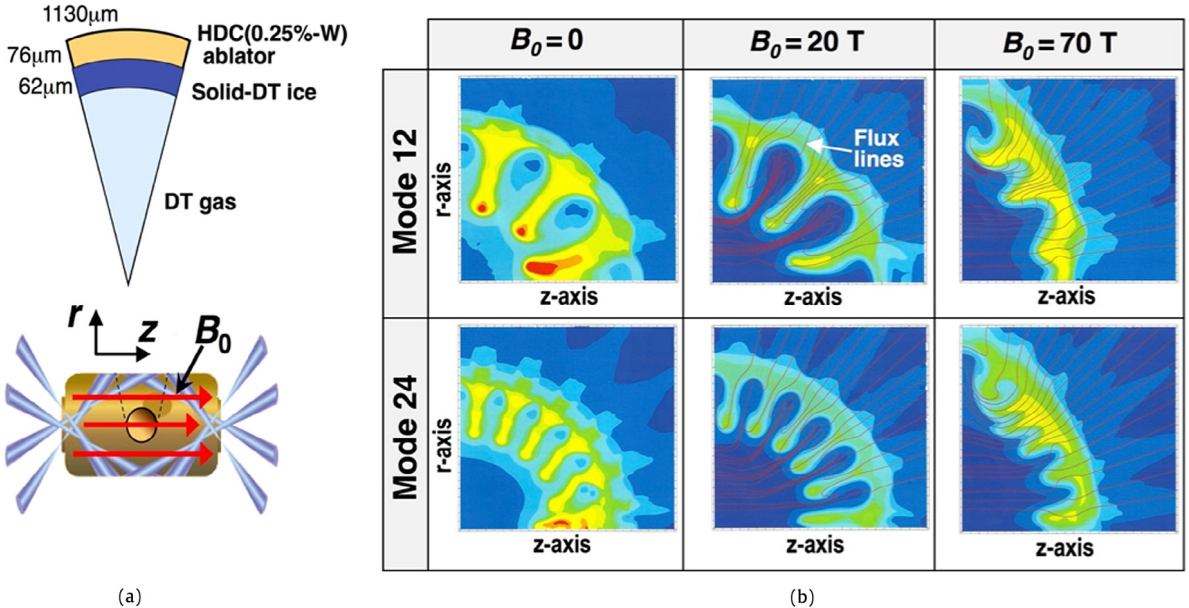


Fig. 13.19. (a) Standard NIF indirect-drive ignition capsule with 62 μm -thick cryogenic solid-DT fuel layer and 76 μm -thick high-density-carbon (diamond) ablator (b) Density contours at stagnation in the r - z plane (relative scale) under the initial application of single-mode perturbations to the capsule inner DT-ice surface with large initial amplitudes of 5 μm for imposed fields of $B_0 = 0, 20$ and 70 T.

Source: Fig. 6 of Perkins et al. (2017), *Phys. Plasma* with permission.

may relax the conditions required for ignition and propagating burn in ICF targets. This may allow the attainment of ignition, or at least significant fusion energy yields, in presently-performing ICF targets on the NIF that today are sub-marginal for thermonuclear burn through adverse hydrodynamic conditions at stagnation. Results of detailed two-dimensional (2D) radiation-hydrodynamic-burn simulations applied to NIF capsule implosions with low-mode shape perturbations and residual kinetic energy loss indicate that such compressed fields may increase the probability for ignition through range reduction of fusion alpha particles, suppression of electron heat conduction and potential stabilization of higher-mode RTI. Regarding the latter RTI stabilization, Fig. 13.19 taken from Perkins et al. (2017) shows the effect of applying two single-mode initial perturbations of mode number $2\pi/\lambda = 12$ and 24 but of large initial 5 μm amplitude to the inner DT-ice surface of the standard NIF capsule shown Fig. 13.19a. The plots in Fig. 13.19b show shell density contours at stagnation for three initial imposed axial fields of 0, 20T and 70T. In the case of the magnetized implosions, the flux lines are frozen into the shell and the initial fields B_0 compress to high values at stagnation scaling as the square of the convergence ratio (CR), i.e. $B_z \sim B_0 CR^2$, where $CR \sim 32$. For shorter wavelength RT modes to grow during late time capsule deceleration, they would have to force a sharp curvature in their entrained flux. This requires increased field line bending energy and thus will be stabilizing to such interchange-like modes. In Fig. 13.19b, the frozen-in field lines are evident for the magnetized cases as is the significant damping of the non-linear RT growth compared with the zero-field case. These are relatively low-mode numbers so increased stabilization might be expected for higher modes due to increased bending energy required. Of course, these 2D simulations require shell perturbations to be axisymmetric. Thus, 3D simulations are needed to fully quantify the extent to which compressed fields might suppress higher-mode RT growth.

13.5. Multiple hydro instabilities

13.5.1. RTI and RMI

Since the earliest efforts, the necessity and advantage of treating the Rayleigh–Taylor and Richtmyer–Meshkov instabilities in a similar fashion has been recognized. Building on the original linear stability theory for constant acceleration Taylor (1950) and Richtmyer (1960) proposed similar analysis of RM instability a decade later in which he modeled the shock interaction with an interface as the impulsive (a Dirac delta function) acceleration of two incompressible fluids. Many examples that multiple hydro instabilities must be considered together can be found in Part I, Section 1.

As mentioned in subsection 6.4 (Part I), a phenomenological treatment was proposed which takes into account the influences of the RTI and RMI time scales. The resulting spectral law varies between “ $-7/4$ ” (RTI driven turbulent flow) or “ $-3/2$ ” spectrum (RMI driven turbulent flow). For a situation when both instabilities must be considered simultaneously, the slope of the energy spectrum is dictated by a controlling parameter, which indicates the extended range of influences exerted by the external time scales in wave number space as well as the ratio between the values of the RTI and RMI time scales (Zhou, 2001).

Table 13.1

Relevant properties for the third gas (C).
Source: Table 1 of [Henry de Frahan et al. \(2015\)](#).

Case	Gas A	Gas B	ρ_c [kg/m ³]	γ_c
Nominal	Air	SF ₆		
1	Air	SF ₆	0.178	5/3
2	Air	SF ₆	10	5/3

Such an approach could be helpful in understanding the interrelation between these two fundamental instabilities. Using a multifunctional shock tube at the Institute of Technical Physics ([Kucherenko et al., 2003a](#)), [Kucherenko et al. \(2010\)](#) studied statistical and spectral characteristics of the turbulent mixing zone formed under the consecutive actions of the Richtmyer–Meshkov and Rayleigh–Taylor instability obtained for some time instants by the laser sheet technique ([Landeg et al., 1993](#); [Houas et al., 1999](#)).⁴³ [Di Stefano et al. \(2017\)](#) carried out a laser experiment designed to observe coupled RM and RT growth and illustrate an analysis technique to extract quantitative information from measurements of coherent multimode surfaces. A paper by [Zhang et al. \(2006\)](#) addresses the question of how a mixing layer induced by a RT instability interacts with shock waves, using a numerical simulation of two-dimensional compressible Navier–Stokes equations with a high-order weighted essentially nonoscillatory finite difference shock capturing scheme. It was observed that shock waves could speed up the transition to turbulence for the RT interface significantly. Stronger shocks are more effective in this speed-up process. Recently, these numerical simulation results have been used to compare with the experimental data of laser-induced 3D RMI and RTI on metal target in the semi-confined configuration regarding the deformation of the mushroom-shape spikes, symmetry breakup, and other issues ([Lugomer, 2017](#)).

Using the discontinuous Galerkin method, [Henry de Frahan et al. \(2015\)](#) solved the two-dimensional multifluid Euler equations to investigate the interaction of a shock wave with successive perturbed interfaces, and specifically Richtmyer–Meshkov (due to shocks) and Rayleigh–Taylor (due to rarefactions) growth. At each interface, the incoming shock generates reflected and transmitted shocks and rarefactions, which further interact with the interfaces. The single-mode RMI experiments with just two layers, Air and SF₆ ([Collins and Jacobs, 2002](#)) were used to validate the numerical method (the nominal case). Fig. 13.20 shows the results for the enstrophy and TKE with a third gas region added (see detail in Table 13.1 for the relevant properties for the regions). If the third gas is lighter than the second (namely, helium), the reflected rarefaction at the second interface amplifies the growth at the first interface. If the third gas is heavier, however, the reflected shock decreases the growth and tends to reverse the Richtmyer–Meshkov instability as the thickness of the second gas is increased.

In Part I, the discussion of the single mode RMI ([Collins and Jacobs \(2002\)](#)) was limited to the relatively early time of this experiment prior to the arrival of the RMI reshock. Fig. 13.21 exhibit the density fields of the simulation of the Collins and Jacobs experiment for the late-times. As described in [Schilling et al. \(2007\)](#), the densities develop small-scale structures inside the rollup at 6 ms, which forms because of the secondary vorticity deposition from the interface rollup. Reshock is a refraction from a heavier gas (SF₆) into a lighter gas (air and acetone mixture), resulting in a transmitted shock that enters the air (acetone) and a reflected rarefaction that returns into the SF₆. The details of the rollup in the density fields, vorticity, and baroclinic vorticity production are shown in Fig. 13.22, indicating the arrival of the reflected shock at 6.38 ms, the shock refraction and the transmitted shock in air (acetone), the reflected rarefaction returning into the SF₆ at 6.48 and 6.58 ms. The inversion process when the bubble transforms into a spike and vice versa at 6.58, 6.68, and 6.78 ms, and the formation of additional small rollups and complex disordered structures at 7 and 7.18 ms. The detailed wave structure can be illustrated (Fig. 13.23) using simulated density Schlieren fields, which visualize density gradients associated with the waves and fine-scale mixing structures.

[Schilling and Latini \(2010\)](#) also investigated the flow morphology, and amplification effects of reshock using the evolution of the turbulent kinetic energy and turbulent enstrophy spectra. Fig. 13.24a, b, c shows the mass fraction isosurface, enstrophy, and the density cross section from the multi-mode, multiple reshocked RMI simulation with the air and SF₆ system of [Vetter and Sturtevant \(1995\)](#). Fig. 13.25a also illustrates the corresponding baroclinic production of the enstrophy. Following the passage of the incident shock, spikes and bubbles form at $t = 0.25$ ms. The spikes begin to roll-up, which can barely be seen through $t = 3$ ms. Reshock occurs at $t \approx 3.25$ ms and the mixing layer is compressed. At $t \approx 5$ ms, the reflected rarefaction wave induced by the refraction of the shock at the interface, interacts with the evolving interface. Following reshock, the instability develops complex structure and the enstrophy field transforms from elongated tubular structures into short, disordered tubular structures with random orientations. The arrival of the reflected rarefaction represents the last important wave-interface interaction. Consequently, the flow nearly becomes a purely decaying flow after $t = 6$ ms. Also, displayed in Fig. 13.25 is the buoyancy- and shear-production of the turbulent kinetic energy transport equation.

⁴³ [Kucherenko et al. \(1997a, 2003b\)](#) used X-ray radiography to measure the mixing layer widths. [Kucherenko et al. \(2003c\)](#) also obtained the distribution of fluid fragment sizes within an immiscible, RTI mixing zone. However, [Kucherenko et al. \(2010\)](#) reported that a jump in density was found at the boundary between the heavy gas and the mixing zone, which contradicted the integral measurements of the density distributions of fluids with different densities in by the X-ray technique ([Kucherenko et al., 1991](#)). As a result, a careful calibration of the measurement technique must be performed.

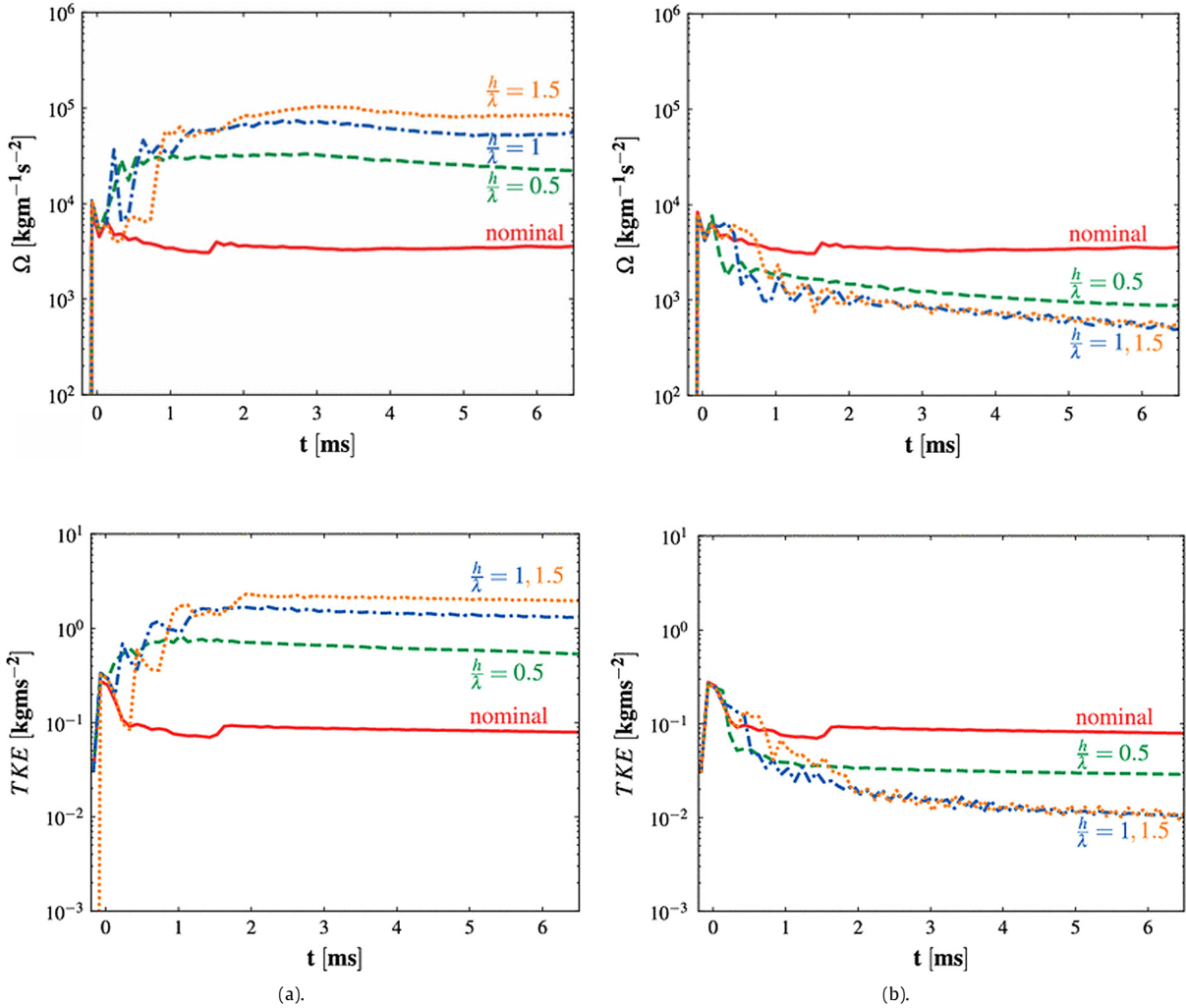


Fig. 13.20. Enstrophy (top) and Turbulent kinetic energy (bottom) versus time for the baseline problem for different thicknesses of gas B. (a) Light third gas. (b) Heavy third gas.

Source: Figs. 14 and 15 of Henry de Frahan et al. (2015), Shock Waves with permission.

Wang et al. (2015c) carried out a comparative analysis of RMI large-eddy simulations with three subgrid scale (SGS) models. The performance of the dynamic Smagorinsky (Germano et al., 1991), Vreman (2004) and the stretched-vortex models (Misra and Pullin, 1997; Kosovic et al., 2002; Pullin, 2000) were evaluated against the experimental data of Leinov et al. (2009). While the mixed zone width computed with these SGS models are comparable, the decay factors of turbulent kinetic energy have been shown to differ significantly, with the relative error up to about 50%. The paper found that the dynamic Smagorinsky model and stretched-vortex model can predict the energy backscatter (see Leith, 1990; Zhou, 1991). Also, the stretched-vortex model was found extremely time-consuming. Recently, Wang et al. (2017) simulated the dynamical behavior of the RMI induced flow under multiple shock interactions using LES with Vreman's subgrid model. The computational model is based on the RMI shock tube experiments that use the SF_6/air fluid system ($A = 0.67$) and with a Mach 1.2 initial shock (Erez et al., 2000). For the time-dependent mixing zone width, the authors have an alternative fit to their numerical simulations although the curves generated under multiple shocks (their Fig. 4, not shown) appear to be combinations of functions linear in time and t^θ .

13.5.2. RTI and/or RMI with KHI

The Kelvin–Helmholtz (KHI) instability is induced from an unstable perturbed interface between fluids subject to a parallel shear flow and is one of the classical problems in fluid dynamics (Kelvin, 1871; von Helmholtz, 1868). The development of KHI instabilities (KHI) often constitutes the critical step towards the onset of turbulent mixing observed both in the atmosphere and in oceans (Peltier and Caulfield, 2003; Woods, 1968). The traditional (Brown and Roshko, 1974; Ho and Huerre, 1984)

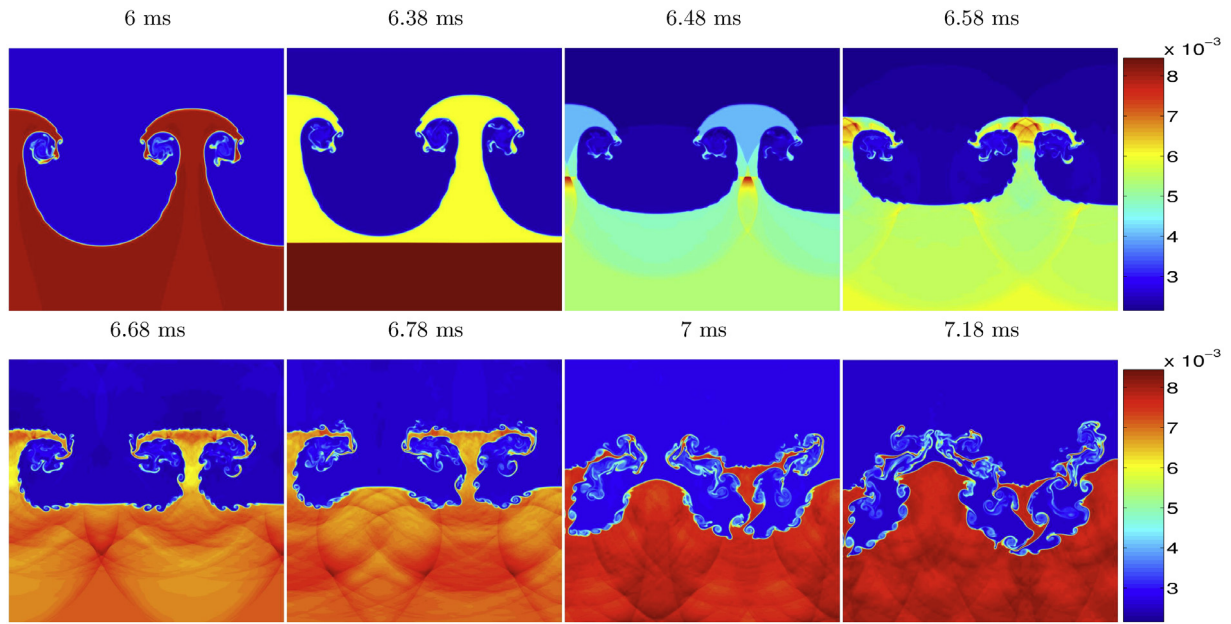


Fig. 13.21. The density fields (air/acetone on top and SF₆ at bottom) of the single mode RMI in units of g/cm³ at 6, 6.38, 6.48, 6.58, 6.68, 6.78, 7, and 7.18 ms.

Source: Fig. 1 of Schilling et al. (2007), *Phys. Rev. E* with permission.

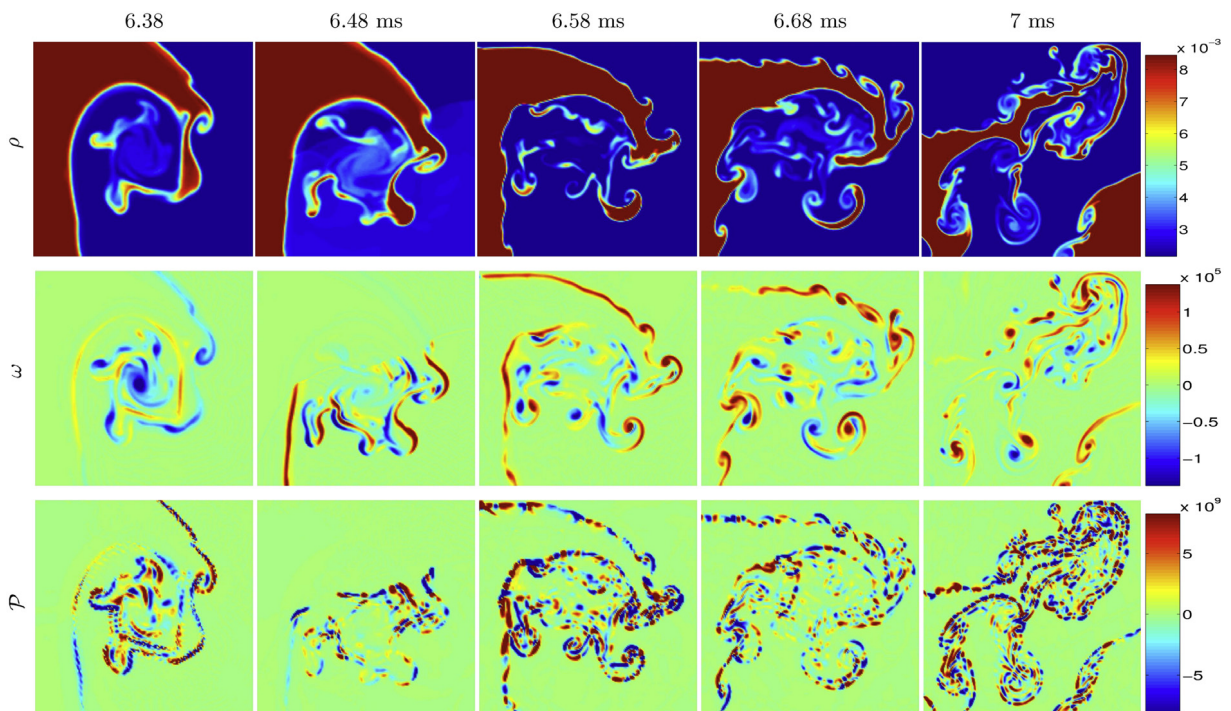


Fig. 13.22. Details of the rollup of the single mode RMI in the density, vorticity, and baroclinic vorticity production fields at 6.38, 6.48, 6.58, 6.68, and 7 ms.

Source: Fig. 5 of Schilling et al. (2007), *Phys. Rev. E* with permission.

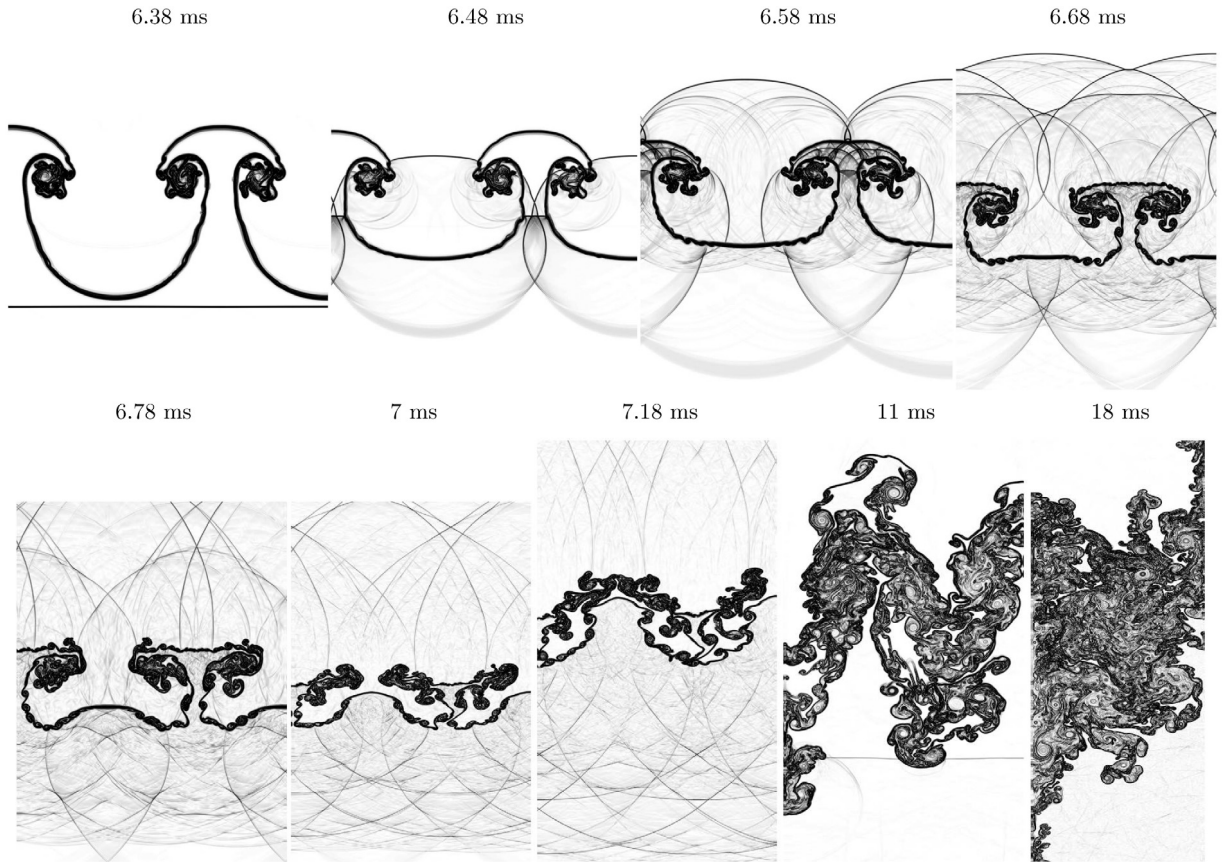


Fig. 13.23. Simulated density Schlieren fields of the single mode RMI at various times.
Source: Fig. 6 of [Schilling et al. \(2007\)](#), *Phys. Rev. E* with permission.

and counter-flowing ([Papamoschou, 1995](#); [Alvi et al., 1996](#); [Strykowski et al., 1996](#)) shear flow laboratory experiments have been performed in the liquid or gas phase. Furthermore, coupled shear and buoyancy driven mixing has found applications in discharges into rivers ([Imberger and Hamblin, 1982](#)), oceans and atmosphere environment ([Browand and Winant, 1973](#); [Turner, 1973](#); [Werne and Fritts, 1999](#); [Kelley et al., 2005](#)), and chemical reactions ([Nagata and Komori, 2000](#)).

As mentioned already, understanding the dynamics of the KH instability is important not only for its own sake, but also in the study of other hydrodynamic instabilities that one confronts in inertial confinement fusion (ICF) research. A shock oblique to an interface generates both RMI and KHI. [Pullin \(1982\)](#) performed an early study the nonlinear growth of finite-amplitude normal modes for both KHI and RTI. Coherent interfacial motion could be followed well into the nonlinear regime for both the KH and RT modes, with the inclusion of an interfacial tension term in the circulation equation. An analytic expression for the growth rate of perturbations in the linear regime when all three (RTI, RMI, KHI) instabilities are present was given by [Mikaelian \(1994b\)](#). Recently, [Vadivukkarasan and Panchagnula \(2017\)](#) considered the three-dimensional destabilization characteristics of an annular liquid sheet when subjected to the combined action of RTI and KHI instability mechanisms. Indeed, the KHI is the reason for the evolution of the mushroom structures during the RT and RM nonlinear process ([Yabe et al., 1991](#); [Zabusky, 1999](#)), and it plays a critical role for the time-dependent transition to turbulence ([Zhou, 2007](#); [Zhou et al., 2003a,b](#)) of flows driven by RT and RM instabilities.

The KHI linear instability growth is well established ([Chandrasekhar, 1961](#), [Drazin and Reid, 1981](#)), but its late-time dynamics is still an area of active research. [Wang et al. \(2009a\)](#) suggested a weakly nonlinear model for the KHI in 2D incompressible fluids. For a single-mode perturbation, the mode coupling will generate higher harmonics and the authors considered the second- and third-harmonic generation effects and the nonlinear correction to the exponential growth of the fundamental modulation. A resonance in the mode-coupling process was found important in supporting the evolution of the instability in the weakly nonlinear regime of KHI.

[Sohn et al. \(2010\)](#) carried out long-time computations for the nonlinear evolution of an interface subject to a parallel shear flow. The vortex sheet in density-stratified fluids is calculated by using the point vortex method. The numerical results indicate that the KHI produces a secondary instability at a late time, distorting the internal rollup, and eventually develops to a disordered structure.

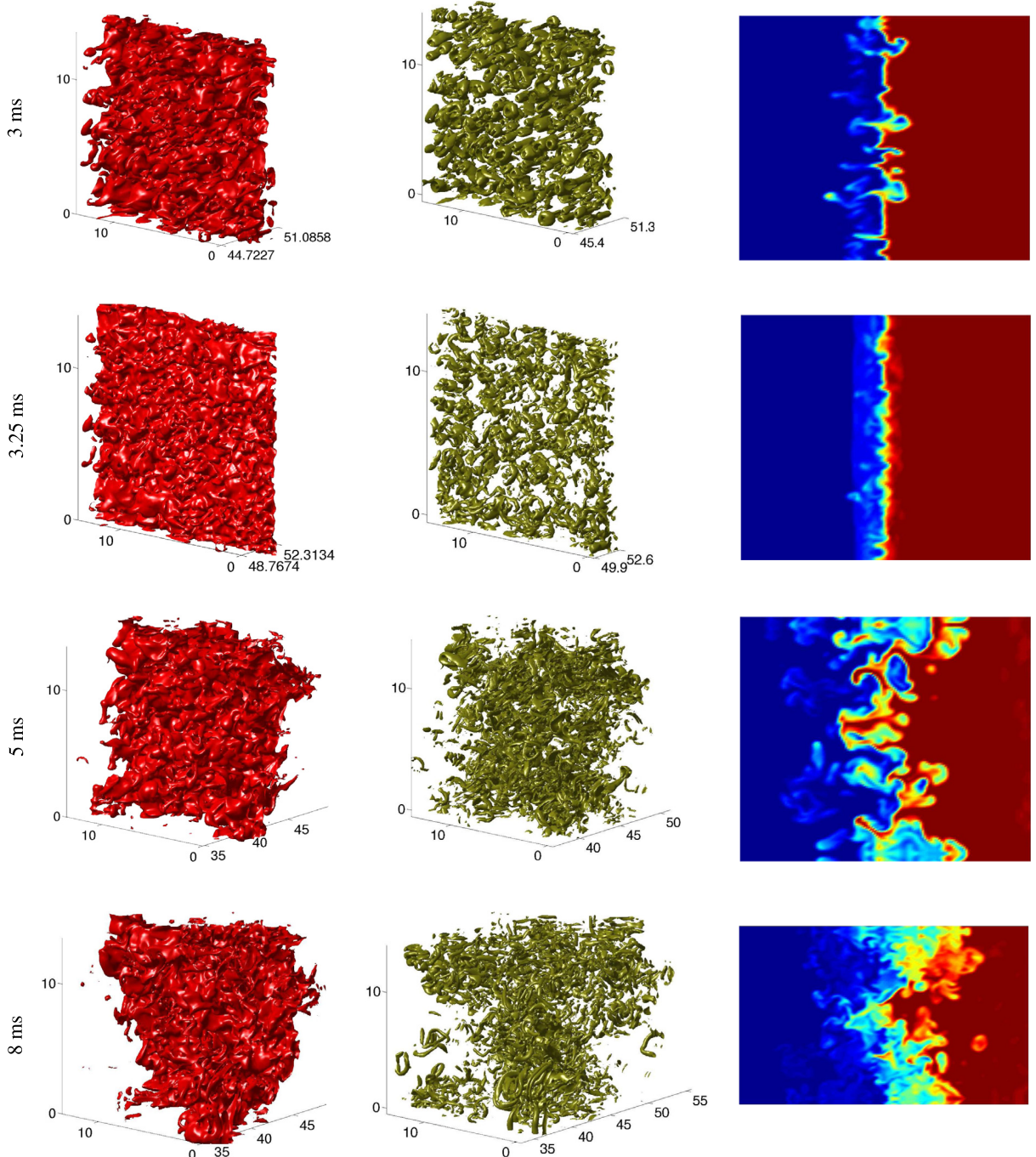


Fig. 13.24. Visualization of the mass fraction isosurface (left column), enstrophy isosurface (middle column), and density (x, z)-cross-section (right column), where blue represents air and red represents SF₆ at 3, 3.25, 5, and 8 ms. The height of each density cross-section is 27 cm.
Source: Fig. 8 of Schilling and Latini (2010), *Acta Mathematica Scientia* with permission.

Rikanati et al. (2003) introduced a large-scale statistical model (Alon et al., 1993, 1994, 1995; Oron et al., 1998) for the KH instability in the incompressible limit. The model is based on a characterization of the single vortex behavior and of the two eddy pairing process, achieved using an extended vortex-line model similar to that already used in Corcos and Sherman (1976) for the single mode case and in Rikanati et al. (1998) for the RM instability. The scaling laws and the statistical characteristics of the incompressible KHI are obtained for any density ratio. The mixing layer growth was shown to be in very good agreement with the linear spatial growth measured experimentally by Brown and Roshko.

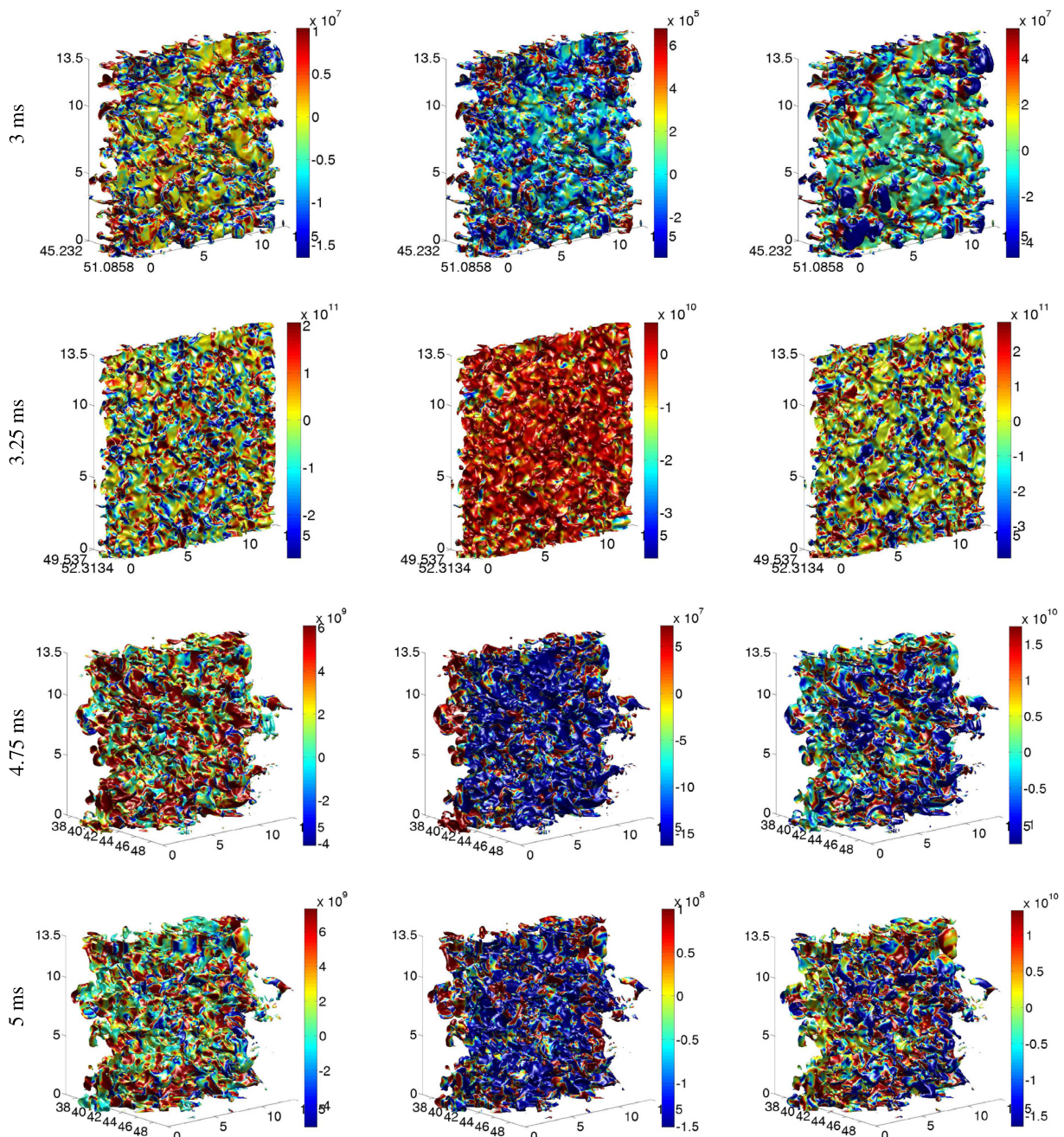


Fig. 13.25. The baroclinic production of enstrophy (left column), buoyancy production of kinetic energy (middle column), and shear production of kinetic energy (right column) of multi-mode RMI visualized on the mass fraction isosurface $m_{SF6} = 1/2$ before reshock (3 ms), after reshock (3.25 ms), at 4.75 ms, and at 5 ms (corresponding to the arrival of the reflected rarefaction at the interface).

Source: Fig. 13 of Schilling and Latini (2010), *Acta Mathematica Scientia* with permission.

Using Layzer's model, Mandal et al. (2011) studied the nonlinear evolution of two fluid interfacial structures such as bubbles and spikes arising due to the combined action of RTI and KHI. They found that the growth rate of the RT instability-induced nonlinear interfacial structures is further enhanced due to KH instability.

Within a linear growth regime, Ye et al. (2011) evaluated analytically the competition between the RTI and KHI in the condition of arbitrary density ratio and continuous density and velocity profiles. It is determined that the competition

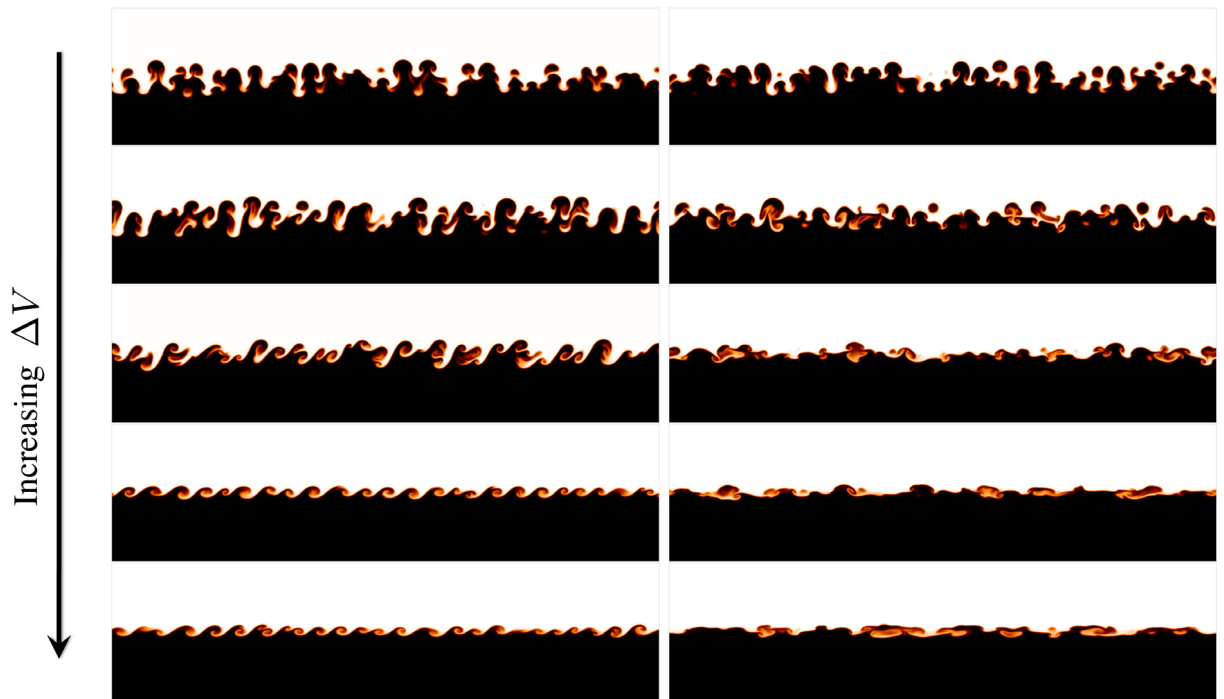


Fig. 13.26. Density contours of cases with increasing amounts of shear, [1, 0.71, 0.45, 0.28, 0.15], (top to bottom) at the time of peak mixing rate in the x (left) and y direction (right). Note that the middle row is near the optimum amount of shear [0.45].
Source: Fig. 14. of Olson et al. (2011), *Phys. Fluids*, with the permission of AIP Publishing.

depends on the Froude and Atwood numbers, and the thicknesses of the density transition layer and the velocity shear layer.

Banerjee et al. (2012) studied the development of the interfacial structures like bubbles of the RT/KHI or RMI/KHI viscous fluids analytically and numerically. It is found that the growth and normal velocity of the structures are dependent on the relative velocity shear and the coefficient of kinematic viscosity. For instance, the growth rate and the bubble growth are decreased significantly for fluids of higher viscosity coefficient with small velocity shear difference.

To build an intuition for the effect of a dominant initial single mode on the KHI, it is helpful to recall some experimental observations performed on the OMEGA-60 laser facility (Di Stefano et al., 2014). The target was designed and machined to have a multimode initial perturbation, but the radiographs show that the initial seed perturbations in the experiment have a multimode spectrum with a dominant single-mode of 16 μm wavelength. The late-time measured mixed width has surpassed 100 μm , an order of magnitude larger than what one would expect from the saturated value from single-mode-dominated KHI flows. In an interesting work, Shimony et al. (2016) inspected the vortex dynamics of such experimental initial spectrum, using both numerical simulations and a statistical model. They concluded that the KHI evolution in the experiment is dominated by multimode, vortex-merger dynamics, overcoming the dominant initial mode.

In the early nonlinear regime, Olson et al. (2011) observed that addition of a small amounts of shear, in fact, decrease the growth rate and changes the structure of the instability such that less energy is channeled into vertical mixing. At the point of minimum peak mixing rate, the structure has changed to largely resemble a pure KH instability (Fig. 13.26). Continued increase of the shear increases the amount of energy available and therefore the mixing rate once again is enhanced.

Akula et al. (2013, 2017), carried out an experimental investigation of coupled Kelvin-Helmholtz and Rayleigh-Taylor instability (KHRT) in the multi-layer gas tunnel facility (Fig. 13.27), an improved version of the two-layer gas tunnel used by Banerjee and Andrews (2006). Here, one needed to modify the classical RTI scaling, $h_b = \alpha A g t^2$, as initially the growth is driven by the KHI. The authors suggested that the mixed width for the KHRT case could be obtained⁴⁴

$$h = 2\beta_{kh} \Delta U t + 2\alpha_{khrt} A g t^2, \quad t > t_{tr} \quad (13.1)$$

⁴⁴ For several KHRT flows, Akula et al. (2013) documented the experimental values of the RTI growth parameter, α , evaluated directly from the expressions. $h_b = \alpha A g t^2$ and $dh/dt = 2\alpha g t$. However, these results are not expected to be realistic.

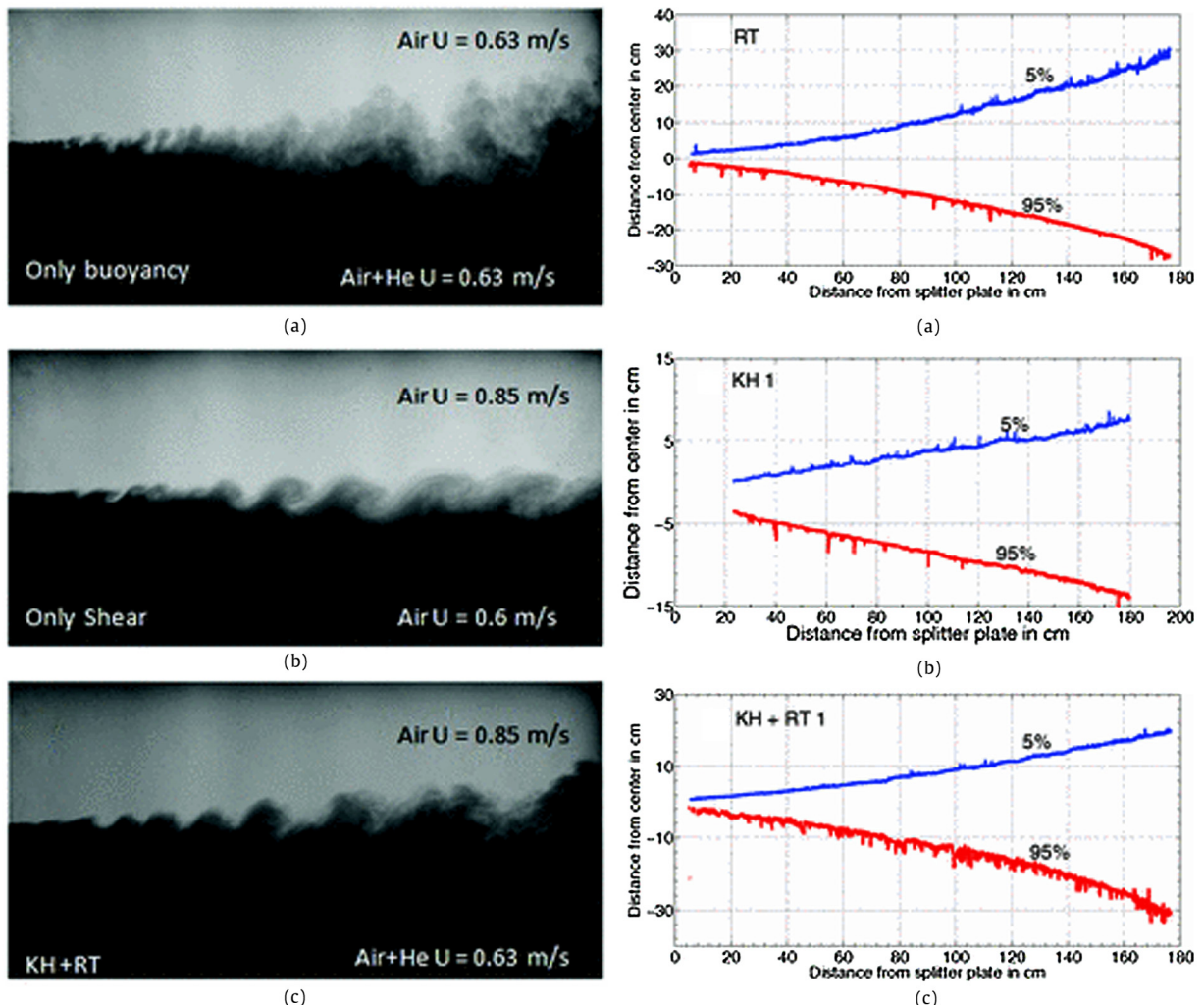


Fig. 13.27. Sample images taken for the flow with (a) only buoyancy, (b) only shear, and (c) combined buoyancy and shear at Atwood ~ 0.032 and corresponding volume fraction contours of bottom stream fluid (0.05 and 0.95) (ensemble average of 200 images taken over 200 s).
Source: Fig. 3 of Akula et al. (2013), *Physical Review E*, with permission.

Here, ΔU denotes the difference between the top and bottom stream velocities. Experimentally, the streamwise location at which the plot of the mixing width gradient shifts from a constant value to linear growth is identified as the transition location, x_{tr} , with corresponding transition time, t_{tr} . The coefficients α_{khrt} and β_{kh} can also be obtained by differentiating Eq. (13.1),

$$dh/dt = 2\beta_{kh}\Delta U + 4\alpha_{khrt}Agt, \quad t > t_{tr}. \quad (13.2)$$

The constant β_{kh} for KHRT cases is obtained from corresponding shear only case without buoyancy.

After substituting the value of β_{kh} into Eq. (13.1), the values of α_{khrt} have been calculated from measured data using the virtual origin (VO) method (Snider and Andrews, 1994) as well as the method of Ristorcelli and Clark (2004) (RC). When the flow has the comparable amount of shear and buoyancy dominance, α_{khrt} is less than the measured α value of pure RTI, 0.074 (Akula et al., 2013). When additional KHRT cases ($A = 0.035$ –0.159) are considered, the α_{khrt} value can be found in a narrow range of ~ 0.064 –0.082 (Akula, 2014)⁴⁵. It is interesting that this range of α_{khrt} is quite consistent with that typically measured for pure RTI flows.

Akula et al. (2017) have attempted to quantify the switch from KH to RT dynamics in an unstably stratified free shear flow using a transitional Richardson number whose magnitude closely resembled critical Richardson number after which

⁴⁵ Note that there is slight uncertainty due to difference between VO and RC methods.

turbulence decays in case of stably stratified free shear flow. This observation suggests a universal behavior of stable/unstable stratification in affecting free shear flows. Additionally, the authors also report and discuss myriad of turbulence statistics for unstably stratified free shear flows.

14. Converging geometries

14.1. Order of increasing convergence effects

When the perturbed interface undergoes geometrical convergence or compression, such as in the situation of an interface embedded in a collapsing sphere or cylinder, the perturbation growth is modified. The famous Bell–Plesset (BP) effects occur with radially accelerated compressible fluids (Bell, 1951; Plesset, 1954). Also, Penney and Price (1942) showed that the surface of an underwater explosion bubble is similarly unstable.⁴⁶

It was remarkable that Penney and Price (1942) derived the Bell–Plesset model for $A = 1$ several years before the G.I. Taylor paper. Unfortunately, their British Report SW-27 has become somewhat obscure soon after it was discussed in Cole's book (1948) and Birkhoff's (1955) Los Alamos report.

The RTI evolves in planar, cylindrical, and spherical geometries as

$$\frac{d^2a}{dt^2} - gkAa = 0, \quad (14.1)$$

$$\frac{d^2a}{dt^2} + 2\frac{\dot{\mathcal{R}}}{\mathcal{R}}\frac{da}{dt} - (nA - 1)\frac{\ddot{\mathcal{R}}}{\mathcal{R}}a = 0, \quad (14.2)$$

$$\frac{d^2a}{dt^2} + 3\frac{\dot{\mathcal{R}}}{\mathcal{R}}\frac{da}{dt} - nA(n)\frac{\ddot{\mathcal{R}}}{\mathcal{R}}a = 0, \quad (14.3)$$

where

$$nA(n) = \frac{n(n-1)\rho_2 - (n+1)(n+2)\rho_1}{n\rho_2 + (n+1)\rho_1} = \frac{2n(n+1)A}{2n+1-A} - 2. \quad (14.4)$$

Here, $a(t)$ is the amplitude of sinusoidal perturbations of wavelength $\lambda = 2\pi/k$ between fluids of densities ρ_1 and ρ_2 , A is the Atwood number and n is the mode number of the perturbation. Also, \mathcal{R} is the cylindrical radius between fluids 1 and 2 in Eq. (14.2) and the spherical radius between fluids 1 and 2 in Eq. (14.3), respectively. These equations, collected neatly in Mikaelian (1990c, 1990d, 2005b), are developed by the classical work of Rayleigh, Taylor, Bell, and Plesset and listed in order of increasing convergence effects. Mikaelian pointed out that this is reflected in the increase of the coefficient factor from 2 to 3 in the second term as one goes from cylindrical geometry to the more convergent spherical one. He noted that the quintessential convergence effect occurs in the case $A = 0$, i.e., $\rho_1 = \rho_2$: The two fluids are identical and there is no growth in planar geometry (first equation above), but in cylindrical or spherical geometries, second and third equations above, there is growth from pure geometry. In the planar geometry, the above equations reduce to Eq. (14.1).

Mikaelian (2005b) presented a linearized analysis for different geometries, and performed 2D numerical simulation of the gelatin-ring experiments, which was a case of concentric shells of fluid undergoing implosion or explosion (Weir et al., 1998). He also suggested an incompressible model, unverified so far, for turbulent mixing widths in cylindrical and spherical geometries.

There were some early papers on perturbations on spherical interfaces. Hunt (1961b) and Elliott (1965a) obtained analytic solutions for the case $\dot{\mathcal{R}} = -k\mathcal{R}^{-a}$. Elliott (1965b) also carried out Lagrangian simulations of perturbation growth in spherically converging flow. For RT and RM instabilities and mixing in stratified spherical shells, Mikaelian (1990a, b) extended Plesset's (1954) analysis to include an arbitrary number of incompressible shells. Revisiting the dispersion relation for the RTI growth rate, he confirmed the soundness of Plesset's result and pointed out its difference from that of Binnie (1953) (Mikaelian, 1987).⁴⁷ For the more complex matter of viscous fluids in planar geometry, some well-known classical work included Bellman and Pennington (1954), Hide (1955) and Reid (1961),⁴⁸ among others. The effect of viscosity on perturbation growth at a spherical interface was considered by Ceschia and Nabergoj (1978), Prosperetti and Seminara (1978), Hao and Prosperetti (1999). The latter paper notes the relevance to sonoluminescence (mentioned in Section 1). More recently, Mikaelian (2016) investigated three successively simpler dispersion relations for the spherical viscous problem. He found that the simplest form, an *ansatz*, is recommended based on a detailed comparison with the exact results of Chandrasekhar (1955) as well as that of Terrones and Carrara (2015). To further distinguish the Bell–Plesset and RTI effects,

⁴⁶ Lord Penney was a professor of mathematical physics at the Imperial College. During World War II, he led the United Kingdom delegation to the Manhattan Project and then went on to become the first director of Atomic Weapon Research Establishment, United Kingdom. The author would like to thank Prof. D.L. Youngs for bringing this reference to his attention.

⁴⁷ Mikaelian (1987) also noted that an expression derived recently by Gupta and Lawande (1986a) for the growth rate of the RTI in spherical geometry is identical to that of Binnie (1953), a result that was subsequently shown to be in error by Plesset (1954). While agreeing with Mikaelian that Plesset's equation contains additional information, Gupta and Lawande (1986a) stated that their formulation does allow an easy generalization towards an analysis of the instability in the multilayered shell targets (Gupta and Lawande, 1986b).

⁴⁸ Note that Reid's work pointed out an error in Hide's derivation.

[Terrones and Carrara \(2015\)](#) studied the RT instability problem for incompressible fluids at a perturbed spherical interface and thus completely decoupled BP effects from the effects of convergence.

An important distinction between the works of [Binnie \(1953\)](#), [Chandrasekhar \(1955\)](#), [Gupta and Lawande \(1986a, b\)](#), [Terrones and Carrara \(2015\)](#) on the one hand and the works of [Bell \(1951\)](#) and [Plesset \(1954\)](#) on the other is that the former papers deal with the stability of a static interface under a gravitational force, and hence the radius is constant, while the latter papers treat the dynamic problem of a moving interface in which $\mathcal{R} = \mathcal{R}(t)$, in other words, the spherical analog of the two problems treated in planar geometry⁴⁹ by Lord Rayleigh (static interface in a gravitational field) and subsequently by G. I. Taylor (accelerating interface). While Rayleigh's and Taylor's results are identical in planar geometry, in spherical geometry there are differences between the two approaches and these are generally known as "Bell-Plesset effects".

Plesset considered two incompressible fluids at any value of A . Bell considered the case $A = 1$ but did allow for compressibility under the assumption that compression was uniform. [Epstein \(2004\)](#) extended Bell's work to two uniformly compressing fluids, being compressed at the same rate. He used a renormalization procedure of the perturbation amplitudes and distinguished pure RTI behavior from BP growth in the case of identically compressible, homogeneous fluids. Epstein reasoned that the BP effects are not a distinct instability from that of RT, but rather affect and modify the RT growth rates. For the linearized perturbation equations, a change of variable and rearrangement in terms of the "mass amplitude" of interface perturbations led to the segregation of the driving terms that are proportional to the RT growth rates.

[Lombardini and Pullin \(2009\)](#) follow on the Epstein paper and extended the theory to two uniformly compressing fluids but the rates could be different for each fluid. More specifically, the authors derived an expression for the asymptotic RMI growth rate for a three-dimensional combination of azimuthal and axial perturbations as a function of the Atwood ratio, the axial and azimuthal wave numbers, the initial radial position and perturbation amplitude of the interface, and the interface velocity gain due to the shock interaction. From the linearized theory, Lombardini and Pullin extended the analytical work by [Mikaelian \(1990c, 2005b\)](#) and obtained a unified expression for the impulsive asymptotic growth rate in plane, cylindrical, and spherical geometries. This expression is especially helpful as it clearly delineates the effects of perturbation growth due to both geometry and baroclinic vorticity deposition.

[Velikovich and Schmit \(2015\)](#) noted that the BP analysis typically focuses on a single accelerated surface or an embedded material interface and should be generalized for the ICF implosion case when the development of the acceleration phase RTI at the outer surface of the imploding shell ends and the deceleration-phase RTI growth localized at its inner surface begins. The authors derived small-amplitude perturbation equations for finite-thickness spherical and cylindrical shells. In the limit of the shell thickness being small compared to its inner and outer radii, Velikovich and Schmit obtained the thin-shell perturbation equations that generalized those of [Harris \(1962\)](#), [Ott \(1972\)](#), [Colombant et al. \(1984\)](#), [Manheimer et al. \(1984\)](#), [Bud'ko et al. \(1989, 1990\)](#), and [Ryutov and Dorf \(2014\)](#). These equations fully incorporate the relevant BP effects, making them possible to follow the perturbation evolution through its acceleration and deceleration phase.

[Joggerst et al. \(2014\)](#) compared different codes on the evolution of RT and RM instabilities arising from perturbations in 2D cylindrical and spherical implosions. Four different compressible, Eulerian codes used were FLASH ([Dubey et al., 2009](#); [Calder et al., 2002](#); [Fryxell et al., 2000](#)), CASTRO ([Almgren et al., 2010](#); [Joggerst et al., 2010](#)), RAGE ([Gittings et al., 2008](#)), and PPM ([Woodward et al. 2010](#); [Ramaprabhu et al., 2012](#)). The first code employed polar grid geometry, while the other three codes employed Cartesian grid geometry. The authors noted that they differ in the details of the discretization schemes, shock-capturing methods, limiters, and steepeners, the treatment of materials in mixed cells, and their support for different coordinate systems. Nevertheless, the bubble and spike amplitudes agree between the simulations performed on Cartesian and spherical coordinate grids, in both cylindrical and spherical geometry.

For the cylindrical simulations, [Fig. 14.1](#) shows the snapshots of fluid density near maximum compression, for FLASH (top row), PPM (middle row) and RAGE (bottom row). In terms of bubble and spike amplitudes, the small differences between Cartesian codes are actually bigger than the differences between Cartesian and polar-coordinate codes.

For the spherical simulations, [Fig. 14.2](#) shows the snapshots of fluid density in the spherical simulations, after maximum compression, for FLASH (top row), CASTRO (middle row) and RAGE (bottom row). The amplitude of perturbation growth is essentially the same between the three codes for both the low- and high-mode perturbations ([Joggerst et al., 2014](#)).

[Bakhsh et al. \(2016\)](#) computationally investigated the cylindrical converging RMI in a magnetic radial field using a linearized model, for a combination of azimuthal and axial perturbations, seeing again suppression of the instability due to MHD transport of vorticity away from the interface. In converging flows with applied fields that are not spherically symmetric, [Mostert et al. \(2015\)](#) performed simulations of nonlinear ideal MHD, finding that the instability remains suppressed by the transport of vorticity by MHD waves roughly along magnetic field lines as described by the previous studies for both cylindrical and spherical settings. They noted however that the geometry of the applied magnetic field will influence the kind and extent of suppression nonuniformly across the interface.

Furthermore, [Mostert et al. \(2014\)](#) found that the application of a magnetic field affects the dynamics of converging flows in MHD, so that the cylindrical or spherical symmetry of the flow may be lost depending on the particular applied field configuration. Moreover, [Pullin et al. \(2014\)](#) found using the technique of geometrical shock dynamics in MHD that in cylindrically converging flows, an azimuthal field generated by a line current on the axis of implosion compromises the ability of the converging shock to compress the flow; the shock pressure ratio in fact approaches unity on convergence instead of exhibiting singular growth. This effect can be mitigated by tuning the line current in time in a manner which again promotes

⁴⁹ See Section 1, Part I, [Zhou, 2017](#).

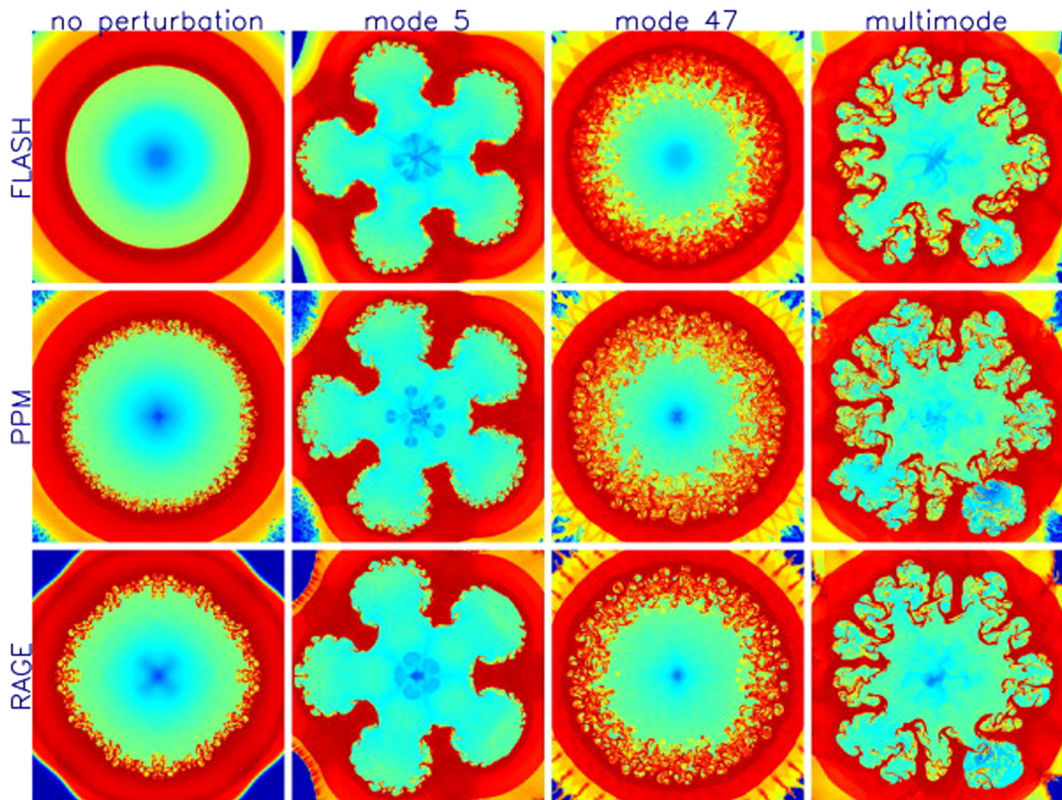


Fig. 14.1. Snapshots of fluid density in the cylindrical calculations at 2.5 s, near maximum compression, for FLASH (top row), PPM (middle row) and RAGE (bottom row). The inner cylindrical interface is preserved for the FLASH simulation (which uses a cylindrical mesh), but small perturbations seeded by the Cartesian grid have grown in the PPM and RAGE calculations, as expected. The simulations for which perturbations were imposed appear similar between codes overall, with differences for a particular perturbation varying more greatly between Cartesian codes (PPM and RAGE) than between the Cartesian codes and the simulations performed on a cylindrical mesh (FLASH).

Source: Fig. 5 of [Joggerst et al. \(2014\)](#), *J. Computational Physics*.

a singular shock collapse in this sense ([Mostert et al., 2016](#)). Finally, [Mostert et al. \(2017\)](#) developed a formulation of two-dimensional geometrical shock dynamics ([Chisnell, 1957](#); [Whitham, 1974](#)) for fast shocks in ideal MHD. This model was applied to a cylindrically symmetric converging MHD shock in the presence of a non-uniform upstream field at an oblique angle and produced satisfactory comparison with results from numerical solutions of the full MHD equations.

14.2. Cylindrical geometry

For RTI, the direction of acceleration has a significant influence in the cylindrical cases. [Yu and Livescu \(2008\)](#) found that the RTI grows faster in the 3D cylindrical case than the Cartesian case in the convergent (gravity acting inward) configuration but slower in the divergent (gravity acting outward) configuration.

In a series of papers, [Guo et al. \(2014\)](#), [Liu et al. \(2014a, b, c, 2015a\)](#), [Wang et al. \(2013a, 2015a\)](#) have looked at various aspects of weakly nonlinear or nonlinear incompressible RTI growth at cylindrically convergent interfaces. Seeking a spectral solution to the non-linear system of three transport equations for density, vorticity, and magnetic vorticity (current), [Chambers and Forbes \(2012\)](#) considered the mechanisms of the surface roll-ups of the cylindrical RTI ([Forbes, 2011](#)) subject to a magnetic field.

For Richtmyer–Meshkov instability, Matsuoka and Nishihara studied analytically the motion of the fluid interface with cylindrical geometry, with the Bernoulli equation and the kinematic boundary conditions as the governing equations, and performed the weakly nonlinear analysis up to the third order. The analytical growth rates agree well with the numerical vortex sheet calculations until the neighborhood of the break down of numerical computations ([Matsuoka and Nishihara, 2006a,b](#)). In the RMI weakly nonlinear regime, [Liu et al. \(2012b\)](#) found that the interface expression consists of two parts: the result in the planar system and that from the cylindrical effects. Based on both a technique of Padé approximation and an approach of perturbation expansion directly on the perturbed interface rather than the unperturbed interface, [Liu et al. \(2014b\)](#) obtained a nonlinear model which is in good agreement with previous simulations of Matsuoka and Nishihara. [Matsuoka \(2010\)](#) further suggested that the renormalization group (RG, see [Zhou, 2010](#) for a review) might be employed in the cylindrical case to obtain a better approximation than the calculations by the weakly nonlinear analysis ([Matsuoka and Nishihara, 2006b](#)).

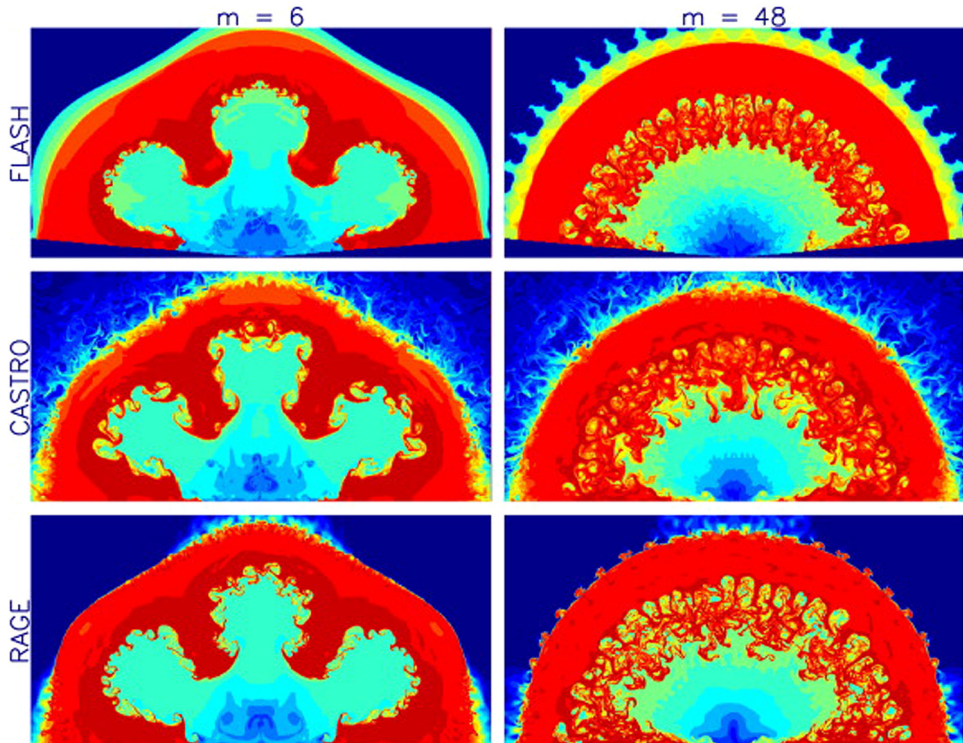


Fig. 14.2. Snapshots of fluid density at 2.5 s in the spherical simulations, after maximum compression, for FLASH (top row), CASTRO (middle row) and RAGE (bottom row). The growth of higher-mode instabilities in the low-mode perturbation simulations (left panel) differs between the Cartesian codes RAGE and CASTRO, with CASTRO calculations showing more dramatic growth of secondary perturbations and a spectrum tilted towards lower mode numbers than RAGE.

Source: Fig. 10 of [Joggerst et al. \(2014\)](#), *J. Computational Physics*.

Zhang and Graham (1998) presented a comprehensive study of single mode RM instability in cylindrical geometry. The growth rate of the fingers at an unstable material interface in the nonlinear regime is one of the most important physical quantities (Graham and Zhang, 2000). The authors carefully considered four classes of RM unstable interfacial fluid mixing systems in curved geometry: a shock wave exploding (imploding) from light fluid to heavy; a shock exploding (imploding) from heavy fluid to light fluid. The presence of the reshock, which is unavoidable for the cylindrical geometry, significantly complicated the dynamics of the RMI. Motivated by experimental studies of the RM unstable interface driven by strong shocks (Mach >20) on the Nova laser (Dimonte and Schneider, 1996), Zhang and Graham (1997) derived the scaling laws for RM unstable interface driven by strong shocks on the overall growth rate, the amplitudes, and the shape of the unstable interface. Numerical simulations confirmed these scaling laws are indeed satisfied once the Mach number is larger than 10. It is significant that the authors believe that these useful relationships should hold in spherical geometry as well (Zhang and Graham, 1997; Graham and Zhang, 2000).

Yong et al. (2016) introduced a multi-material arbitrary Lagrangian and Eulerian method for the hydrodynamic radiative multi-group diffusion model in 2D cylindrical coordinates. This code was used to study the influence of the cylindrical hohlraum's length on the capsule symmetry and inspect a series of experiments carried out on the ShengGuang-II and ShengGuang-III prototype laser facilities in China. Suponitsky et al. (2014) studied numerically the RMI in the extreme regime of Atwood number $A = -1$ with a liquid as one of the working fluids. The motivation of the authors was to estimate the minimum smoothness required to achieve efficient compression of the gas cavity.

In a laboratory setting, Weir et al. (1998) measured RT growth in a 2D cylindrically convergent geometry by imploding gelatin cylinders with high-pressure gases. Here, the experiment features both the precise control of initial perturbations and high-resolution images of the RT and feedthrough growth. Holder et al. (2003b) described a high-convergence experiment on the AWE convergent shock tube and comparison with the 3D TURMOIL simulations. In an annular coaxial vertical diaphragmless shock tube, Hosseini and Takayama (2005a, b) were able to observe the instability and mixing that occurred at the interface.

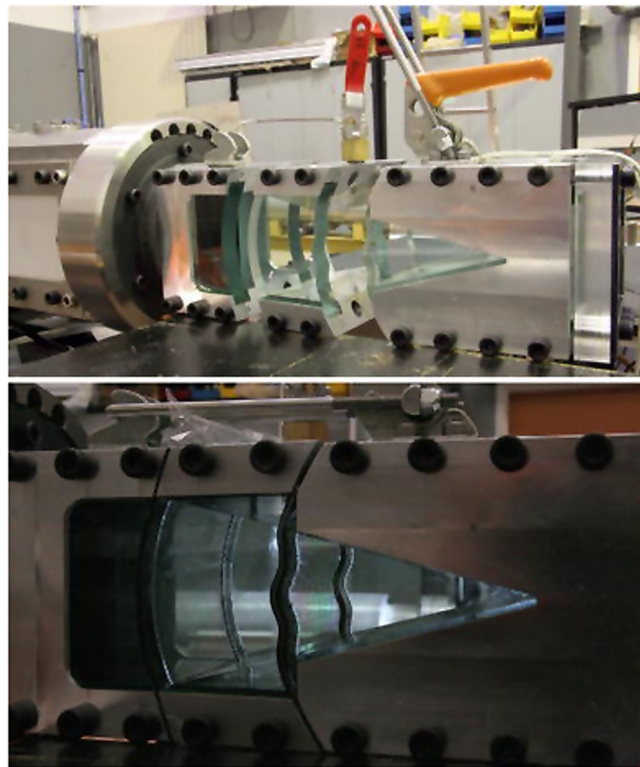


Fig. 14.3. Views of the convergent experimental chamber.

Source: Fig. 2 of Biamino et al. (2015), from *Exp. Fluids* with permission.

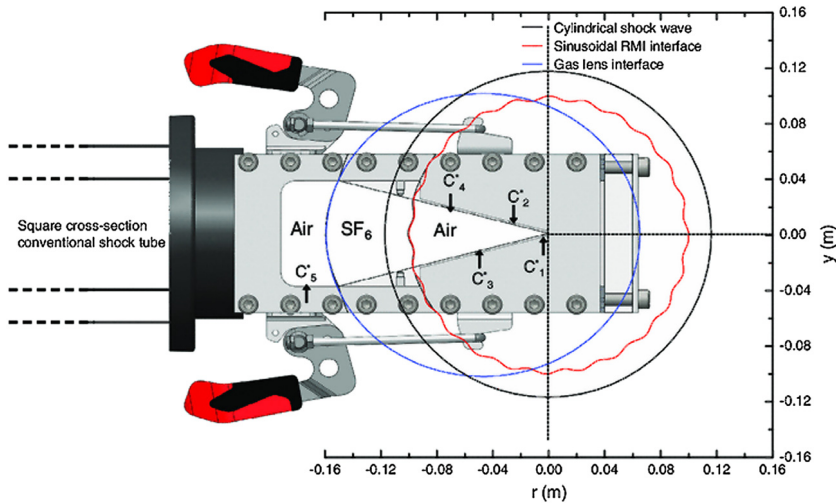


Fig. 14.4. Details of the experimental device added to the T80 shock tube; C'_1 to C'_5 are the locations of the five pressure transducers placed in the converging section. The blue and red lines show the curves of the gas lens and the perturbed interfaces.

Source: Fig. 1 of Biamino et al. (2015), from *Exp. Fluids* with permission.

From a theoretical perspective, Dimotakis and Samtaney (2006) developed a gas lensing technique that can smoothly focus a plane shock into a segment of a circular cylinder in two-dimensional wedge geometry.⁵⁰ Vandenboomgaerde and Aymard (2011), generalized this method by proposing to use a suitable interface between two gases.

⁵⁰ In a related work, Bond et al. (2009) investigated the behavior of an initially planar shock wave propagating into a linearly convergent wedge experimentally and numerically. See also, Chisnell (1957) and Payne (1957).

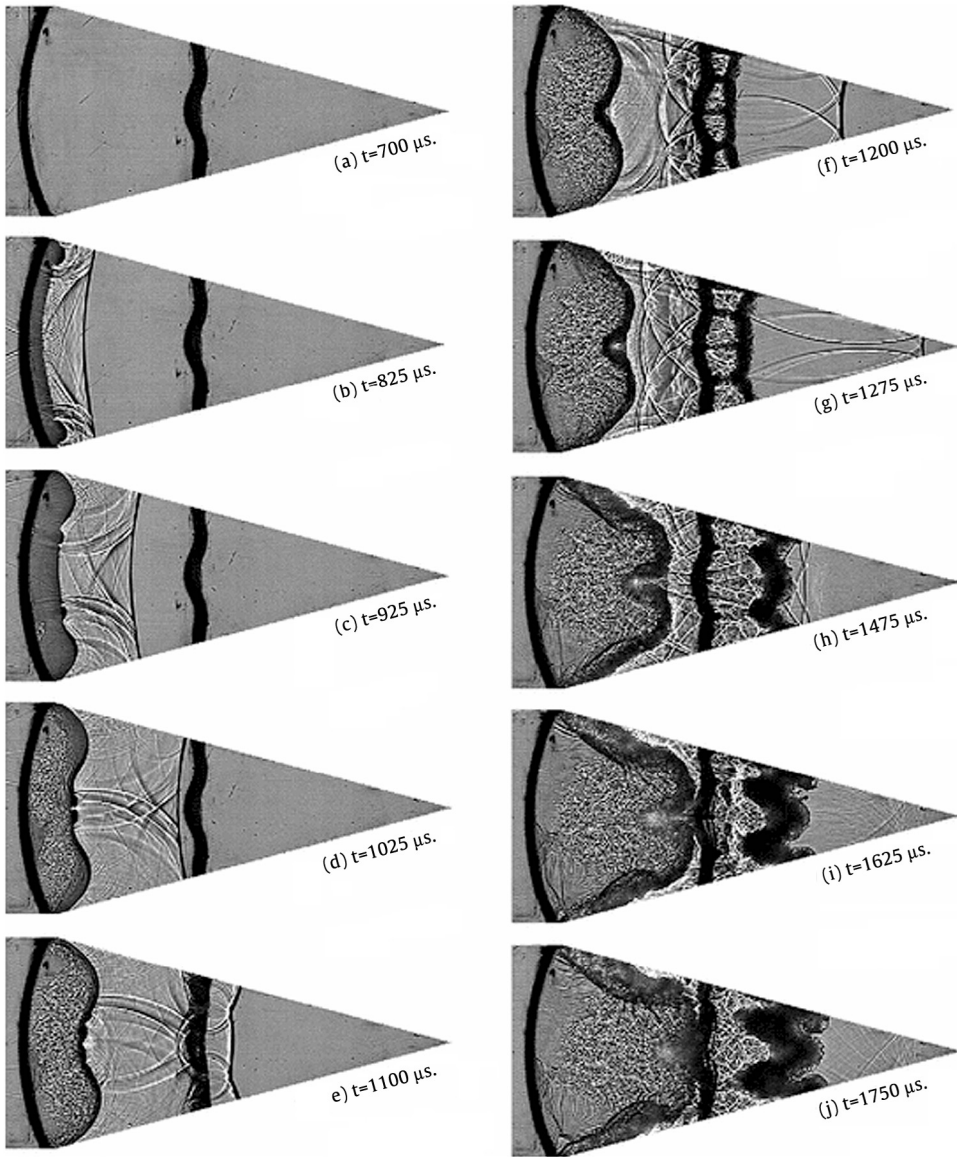


Fig. 14.5. Schlieren pictures (from run T80#923) showing the evolution of the converging Richtmyer–Meshkov instability issued from a $M_{is} = 1.15$ plane shock wave going out from a conventional shock tube and refracted through an air/SF₆ gas lens.
Source: Fig. 3 of Biamino et al. (2015), from *Exp. Fluids* with permission.

In order to experimentally check the feasibility of this approach, Biamino et al. (2014) implemented the gas lens technique on the T80 conventional shock tube of IUSTI (Jourdan et al., 2004; Houas et al., 2003, 2012). For the convergent experimental chamber shown in Figs. 14.3 and 14.4, the flow field generated by a planar shock wave ($Mach = 1.15$ in air) propagating through the three zones (air/SF₆/air) is shown in Fig. 14.5. As demonstrated in detail in Biamino et al. (2015), the planar shock wave is visible at $t = 700 \mu s$ (frame a) on the left side in contact with the gas lens. When the incident shock wave collides with the air/SF₆ interface, it bifurcates into a transmitted converging cylindrical shock wave which moves from left to right in the central zone filled with the dense fluid (from $t = 700$ to $1,025 \mu s$), and a reflected expanding wave. The converging shock wave impacts the sinusoidally perturbed SF₆/air interface near $t = 1,050 \mu s$, and the subsequent pictures (from $t = 1100$ to $1475 \mu s$) show the different stages of the converging RMI.

Luo et al. (2014, 2015), Zhai et al. (2010, 2012, 2017), Wang et al. (2015d), Yang, Zhu, and Yang, 2017, Ding et al. (2017), and Liang et al. (2017) also designed a shock tube facility for generating a cylindrical converging shock wave based on the shock dynamics theory. A specific wall profile is designed for the test section of the shock tube to transform a planar shock

into a cylindrical one. Using this cylindrical converging shock tube, Si et al. (2014a, b, 2015) considered two types of interface, i.e., gas bubble and gas cylinder, and investigated the evolution of such interfaces accelerated by the converging shock and the reflected shock formed from the center of convergence.

HEDP cylindrical implosion experiments (Hsing and Hoffman, 1997; Hsing et al., 1997; Tubbs et al. 1999; Barnes et al., 2002; Lanier et al., 2003) have inspected the compression and convergence effects, both as effects modifying perturbation growth and as the cause of perturbation growth. These experiments have been interpreted in terms of the simplest solutions of constant mass amplitude. Other interesting papers relevant to strongly shocked cylindrically convergent implosions include Marinak et al. (2001), Parker et al. (2004), Fincke et al. (2004, 2005), Perez et al. (2009), and Ramis (2013). Some relevant numerical simulations can be found in López Ortega et al. (2015), Tian et al. (2006), Zheng et al. (2008) and Azarova (2015). The work by López Ortega et al. is especially interesting as the authors studied RMI flows for elastic-plastic solids in both planar and converging geometries using an Eulerian framework (López Ortega et al., 2010, 2014a,b, 2015).

14.3. Spherical geometry

Ramshaw and Amendt (2003) determined the effects of slow compression by the application of linear stability analysis to a slight generalization of the conventional potential flow theory, using the analyses which have been previously reported for accelerated shear layers in planar geometry (Ramshaw, 2000) and for accelerated interfaces in spherical geometry (Amendt et al., 2003). The work by Amendt (2006) focused on the effects of contiguous density gradients at an accelerating spherical surface. As an analogous one for his unstable planar fluid interface representation (Ramshaw, 1998), Ramshaw (1999) proposed a linear and nonlinear model in spherical geometry. This model is based on a heuristic expression for the kinetic energy of the system of a linearly perturbed interface, but with a dynamically renormalized effective wavelength.

Built on Layzer's (1955) theory, Goncharov and Li (2005) studied the effects of both the spherical convergence and temporal density variation on the nonlinear bubble evolution of single-mode, classical RTI. Clark and Tabak (2005a) also obtained a generalization of the Layzer (1955) nonlinear bubble rise rate for a self-similar spherically converging flow of the type studied by Kidder (1976). Clark and Tabak (2005b) further extended the model to the case of bubble growth during the deceleration phase of a spherical implosion and to the growth of spikes during both the acceleration and deceleration phases. When compared with planar results, the authors found differences in the nonlinear growth rates for both bubbles and spikes. Here, the model is limited in assuming a self-similar background implosion history as well as only addressing growth from a single-mode perturbation of already nonlinearly large amplitude. Clark and Tabak (2006) remedied these limitations and found that convergence in the nonlinear regime is not substantially modified from the multimode predictions of Haan's original model (See also related papers by Liu et al., 2015b, 2017; Zhang et al., 2017).

Youngs and Williams (2008) performed accurate 3D TURMOIL hydrocode numerical mixing simulations in a simple spherical implosion, a simplified version of an inertial confinement fusion implosion. It was found that the code has good low Mach number behavior, a key requirement for calculation of turbulent flow, and the kinetic energy dissipation could be accurately quantified. Recently, several quantities of interest, including the turbulent kinetic energy, components of the anisotropy tensor, density self-correlation, and atomic mixing, have been described in a recent publication (Boureima et al., 2017). Results are presented from 3D numerical simulations performed using the FLASH code, while the underlying problem description is adopted from Youngs and Williams. Focusing on the linear growth rate and nonlinear bubble-spoke structures, Sakagami and Nishihara (1990) studied 3D RTI of the pusher-fuel contact interface in a spherical system in detail. Shortly afterwards, Town and Bell (1991) published a similar paper on 3D simulations. There was an earlier UK paper (Henshaw et al., 1987) -2D simulation of the ablation front in spherical geometry.

Dutta et al. (2004) conducted numerical simulations of RMI in spherical geometry for axisymmetric flow. The Front tracking algorithm based simulations were used to illustrate some scaling invariance with respect to shock Mach number for fluid mixing statistics.

Lombardini et al. (2014a) performed large-eddy simulations of turbulent mixing at a perturbed, spherical interface that is subsequently impacted by a spherically imploding shock wave. Fig. 14.6 shows the temporal evolution of the isosurfaces of the heavy-fluid mass fraction. The authors also obtained a significant number of turbulence statistics, which offers better understanding of physics and provides data for engineering modeling (Lombardini et al., 2014b). For instance, the mixedness and effective Atwood number measurement are obtained for the air to SF₆ and SF₆ to air configurations (Fig. 14.7).

Given that many numerical studies of supernova dynamics are still carried out in 1D, Duffell (2016) presented a method for approximating the multidimensional effects of RTI as a modification of the one-dimensional spherical hydro equations. Following Gull (1973) and Shakura and Sunyaev (1973), an additional scalar quantity, representing the magnitude of turbulent RT fluctuations, is evolved along with the usual hydro variables.

Many HEDP experiments have been performed in spherical geometry and published by Henshaw et al. (1987), Cherfils et al. (1999), Glendinning et al. (2000), Robey et al. (2001), Drake et al. (2002), Smalyuk et al. (2002, 2009), Srebro et al. (2003), Terrones and Carrara (2015), Olson and Leeper (2013), Olson et al. (2016), and Haines et al. (2017).

15. Astrophysical fluid dynamics and high energy density physics experiments

Ablative and other hydrodynamic instabilities have been the subject of study in astrophysics for a long period. The Rayleigh-Taylor (RT) instability, the Richtmyer-Meshkov (RM) instability, and the Kelvin-Helmholtz (KH) instability play

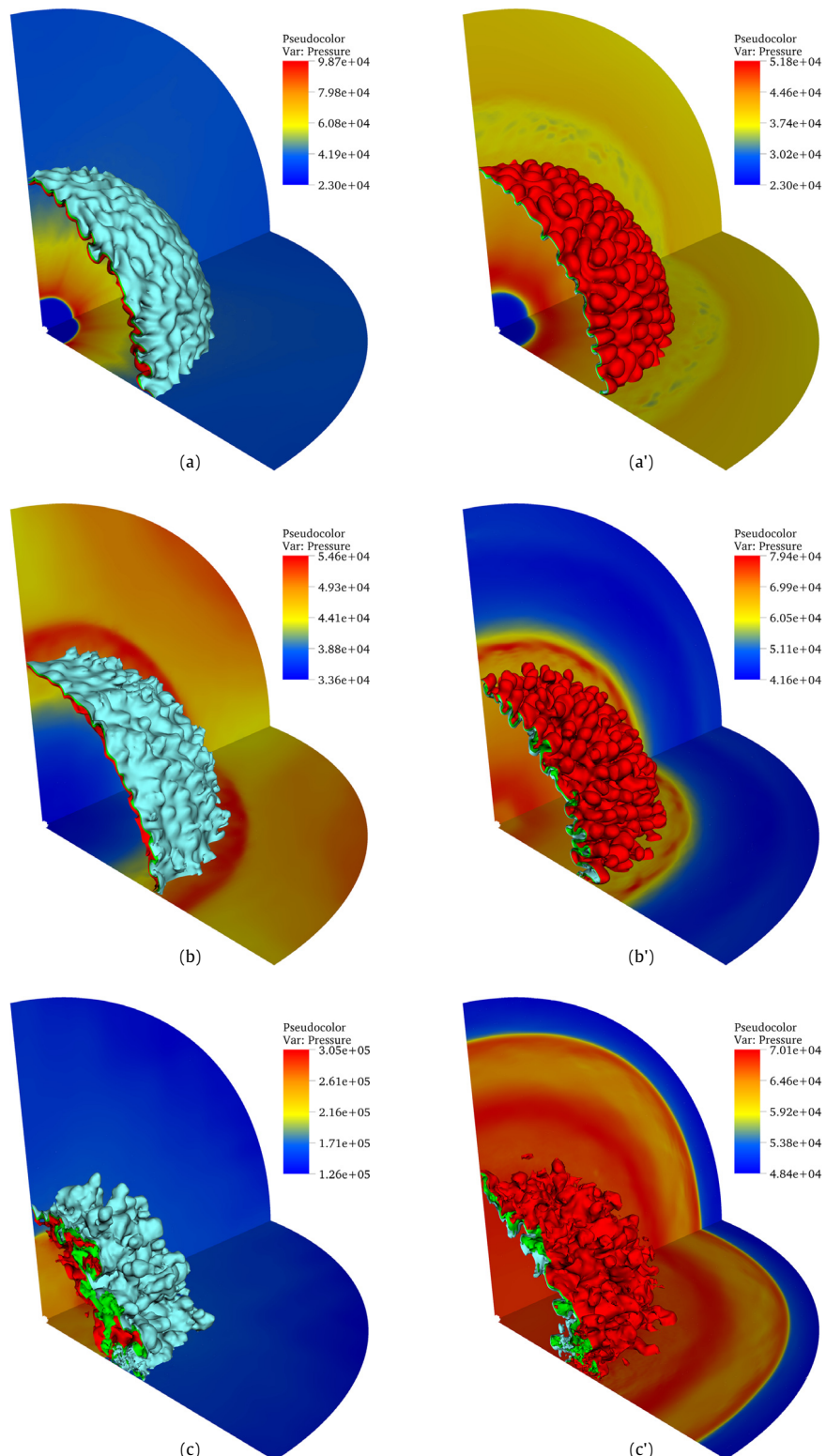


Fig. 14.6. Isosurfaces of the heavy-fluid mass fraction (cyan blue for 25%, green for 50% and red for 75%) and contours of pressure, at three different times: (a) or (a') $t \approx t_{\text{Res1}}/2$; (b) or (b') $1.5 t_{\text{Res1}}$; (c) or (c') $3 t_{\text{Res1}}$. Cases air \rightarrow SF₆ (a, b, c) and SF₆ \rightarrow air (a', b', c').
Source: Fig. 5 of Lombardini et al. (2014a), *J. Fluid Mech.* with permission.

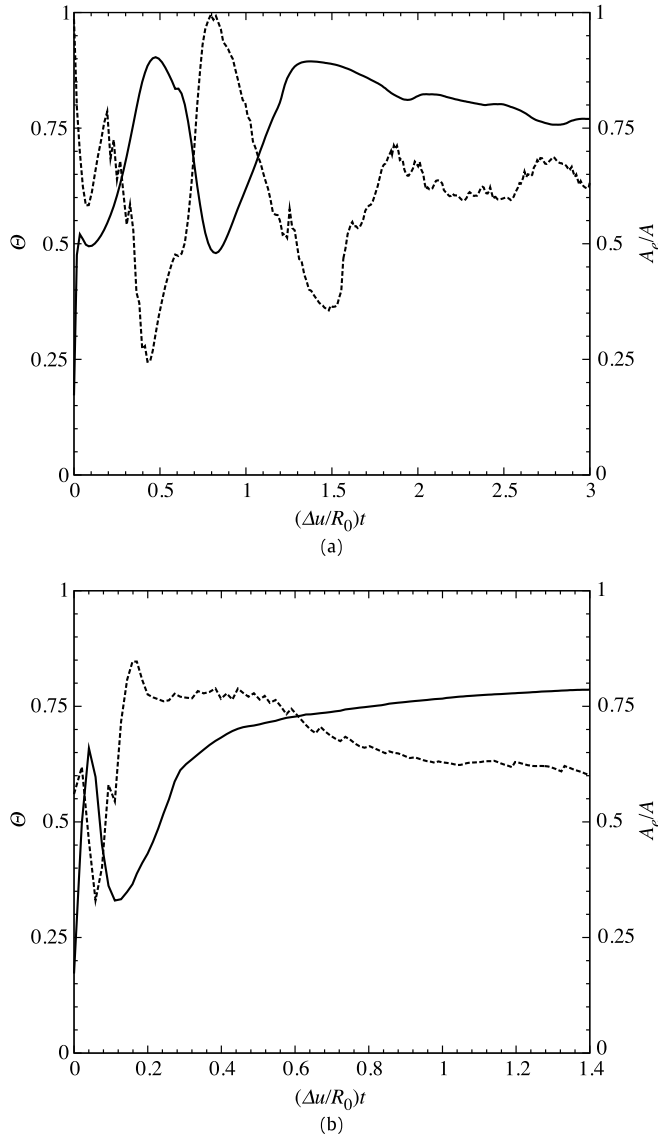


Fig. 14.7. The mixedness parameter (solid line) and effective Atwood number ratio (dashed line) versus t : (a) air to SF_6 and (b) SF_6 to air.
Source: Fig. 2 of Lombardini et al. (2014b), *J. Fluid Mech.* with permission.

a major role in three different classes of astrophysical problems. For the problem of shock-induced star formation (or equivalently, jet/shock cloud interactions), Fragile et al. (2004) simulated the propagation of shocks generated by radio jets through an inhomogeneous, clumpy medium. The interaction triggers gravitational collapse in overdense regions and leads to star formation (Begelman and Cioffi, 1989; De Young, 1989; Rees, 1989). The nature of the collapse (and, therefore, of the star formation) is affected strongly by both KH and RT instabilities, as they both act on a comparable time scale to the cloud compression in the presence of magnetic fields (Fragile et al., 2005). Also, the galactic center has a complicated thermal and density structure (Yuan et al., 2003), and any gas cloud (or star) moving through it is subject to KH, ram pressure, and RT breakup processes, in addition to tidal disruption resulting from close interactions with the supermassive black hole at the center of our Galaxy. The time scale for RT and KH can be significantly shorter than orbital timescales and comparable to the tidal stretching time scale (Anninos et al., 2012). Instabilities are thus important physical processes to include in modeling the interaction of clouds/stars in the vicinity of the galactic center and for predicting accurate radiation emissions from these sorts of encounters. Another place where RT/RM instabilities likely play a role is in the uniform mixing of radioactive nuclides in the pre-solar nebula (Gritschneider et al., 2012).

The origin of Elephant Trunk Nebula-like structures observed in photoionized nebulae is a subject of enduring controversy: are they the result of instability at the surface of the nebula (Spitzer, 1954; Frieman, 1954) or of pre-existing density

structures advected into the photoionized core of a nebula as its pressure drives it out into the surrounding medium (Kahn, 1958)? They are also potentially important as sites where massive star formation may lead to the compression and collapse of material to form many additional low-mass stars in its environment (as reviewed by Bisbas, 2016).

We must first briefly discuss the nature of astrophysical ablation (for a more complete description, see, for instance, the review by Henney, 2007). In so-called HII regions, the intense ultraviolet emission from a hot star heats and ionizes the material which surrounds it, from an equilibrium state with a temperature controlled by molecular emission at a temperature of order 100 K to an equilibrium state controlled by the excitation of atoms and ions at a temperature of order 10⁴ K. The resulting increase in pressure in the ionized gas drives a shock into the surrounding cold medium.

The size of the ionized region is controlled by recombination, with what may be a very sharp discontinuity separating the ionized gas from a dense shell of swept-up neutral material which surrounds it. As the shell expands, for a fixed rate of ionizing illumination, the mass of the ionized region increases, and so mass is advected across the surface. The stability of the surface is controlled not only by the barotropic generation of vorticity, as in classical RTI, but also by the rate at which material is advected across the front and the impact of structures downstream of the ionized surface on the illumination of the front. The classical Takabe formula (Takabe et al., 1985, 1988) models the effect of advection in suppressing surface instability but does not treat the illumination effects. The effects of the changes in illumination intensity with the aspect angle of the surface on the flux advected into the region were first considered by Vandervoort (1962), who demonstrated that the ionization fronts were unstable even in absence of acceleration. Subsequent work has considered the effect that recombination in the ionized material flowing from the surface has on this mass flux in a steady-flow frame (Axford, 1964; Sysoev, 1997; Williams, 2002) and of the acceleration of the interface and the effect of magnetic fields (Kim and Kim, 2014; Ricotti, 2014). The ablation of the surface material tends to suppress barotropic instabilities but can lead to the growth of overstable surface modes for unaccelerated interfaces, particularly where these are oblique to the source of illumination.⁵¹ If the supersonically expanding ionization front sweeps over any form of density inhomogeneity, this can have a major effect on the transition process. The effect of any density increase will be to increase the recombination rate, reducing the intensity of illumination to the material behind it. This will slow the expansion of the ionization front, leading to earlier transition. The most important effect, however, can be at the edges of a shadow, where the gradient in the ionization front surface reduces the propagation parallel to its normal. This geometric effect can bring forward the transition to shock formation dramatically, seeding long-lived structures in the flow (Williams, 1999). The sharp edges of these structures can also lead to narrow ‘daggers’ of ionizing illumination breaking through the swept-up shell and penetrating deeply into the surrounding neutral material (Garcia-Segura and Franco, 1996; Williams, 1999; Whalen and Norman, 2008).

Porth et al. (2013, 2014a) inspected the development of Rayleigh–Taylor (RT) filaments in axisymmetric simulations of pulsar wind nebulae (PWN). In this case, the impact of a magnetic field on the development of RTI in the Crab Nebula is likely to be rather minimal, which is consistent with the observations (Porth et al., 2014b). Porth et al. (2014b) showed the logarithmic densities of the entire nebula and filaments at t=1060 yr (Fig. 15.1), where visual inspection illustrates that at higher resolution the size of eddies reaching the RT interface is reduced via development of the turbulent cascade. Yet, the growing power on small scales with numerical resolution can be interpreted as a result of weaker damping of small-scale RT perturbations by numerical viscosity. Indeed, for lower temporal or spatial resolution, truncation errors affect the simulation results and can be of similar magnitude as physical effects (Schraner et al., 2015).

Reynolds et al. (2005) argued that viscous transport may have a significant effect on RTI on the scale of galaxy clusters. Specifically, they considered the buoyant evolution of AGN-blown cavities in the intracluster medium (ICM). In this case, the initially static bubble starts accelerating due to buoyancy. The RT instabilities induce circulatory motions within the bubbles, which then induce ‘secondary’ KH instabilities along the contact discontinuity between the low-density bubble and ambient ICM. The authors found their models of bubble evolution in modestly viscous ICMs can reproduce both the morphology and inferred flow patterns seen around the best-studied of the ghost ICM cavities, the north-west cavity in Perseus-A. Specifically, they present a numerical investigation of the buoyant evolution of AGN-blown cavities in the intracluster medium (ICM) with non-negligible shear viscosity.

The relevant coefficient of viscosity is given by Braginskii (1958, 1965) for a single ion species in the absence of magnetic fields,

$$\mu_i = 0.96 n_i T_i \tau_i, \quad \tau_i = 3m_i^{1/2} T_i^{3/2} / 4\pi^{1/2} n_i Z^4 e^4 \ln \Lambda, \quad (15.1)$$

$$\mu_e = (0.73 \rightarrow 1.81) n_e T_e \tau_e, \quad (Z = 1 \rightarrow \infty), \quad \tau_e = 3m_e^{1/2} T_e^{3/2} / 4(2\pi)^{1/2} n_i Z^2 e^4 \ln \Lambda. \quad (15.2)$$

Here the subscription denotes the ions (*i*) and electrons (*e*), *n* is the number of particles of a given species per unit volume, *m* is the per-particle mass, *T* is the temperature of the plasma measured in Kelvin, *Z* is the charge, and $\ln \Lambda$ is the Coulomb

⁵¹ One case for which shadowing effects can result in very strong instability is where the intensity of the incident radiation has increased suddenly. In numerical studies of the development of HII regions, the illumination from the central massive star is often assumed to switch on instantaneously. This may seem rather artificial, but the large ratio in dimension between the illuminating source, with a radius of order 10¹¹ cm, and the surrounding nebula, with radius of order 10¹⁸ cm, means that dynamical changes close to the source may well appear close to instantaneous. The effect of this is that ionization fronts may on occasion move supersonically. The transition between super-sonic and sub-sonic motion of the front has properties somewhat analogous to those of the deflagration to detonation transition. In particular, ionization fronts expand supersonically until their speed reduces to roughly twice the sound speed in the ionized gas, at which stage the front stalls. A leading shock then separates from the ionization front, and between them, a growing shell of swept up neutral material.

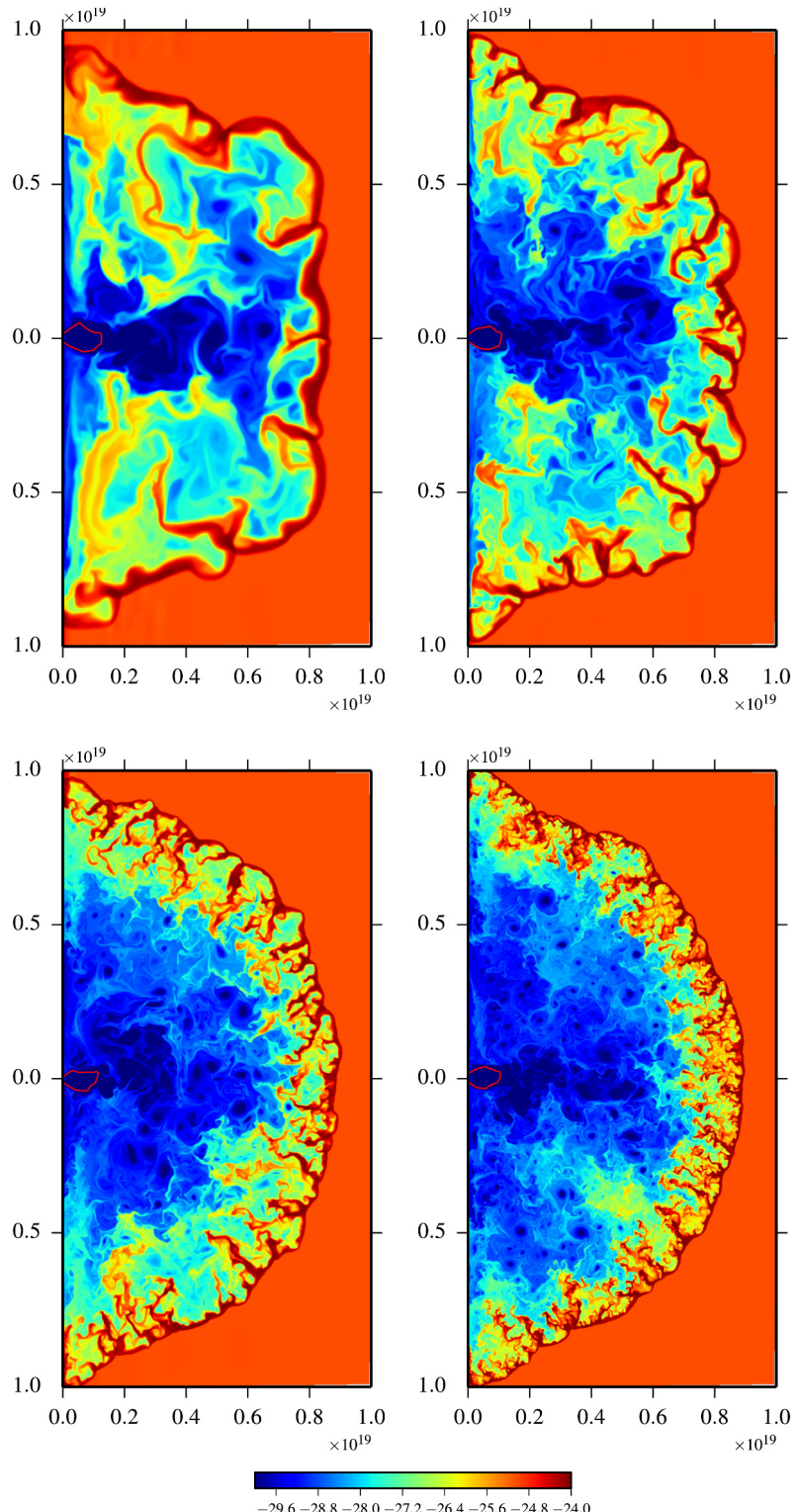


Fig. 15.1. Logarithmic densities showing the entire nebula and filaments at $t \approx 1060$ yr with increasing resolution. The models shown here are A0 (topleft), A1 (top right), A2 (bottom left) and A3 (bottom right). Each subsequent model has twice the resolution of the previous one. The PWN termination shock is outlined as a red contour.

Source: Porth et al. (2014b), *Monthly Notices of the Royal Astronomical Soc.*, with permission.

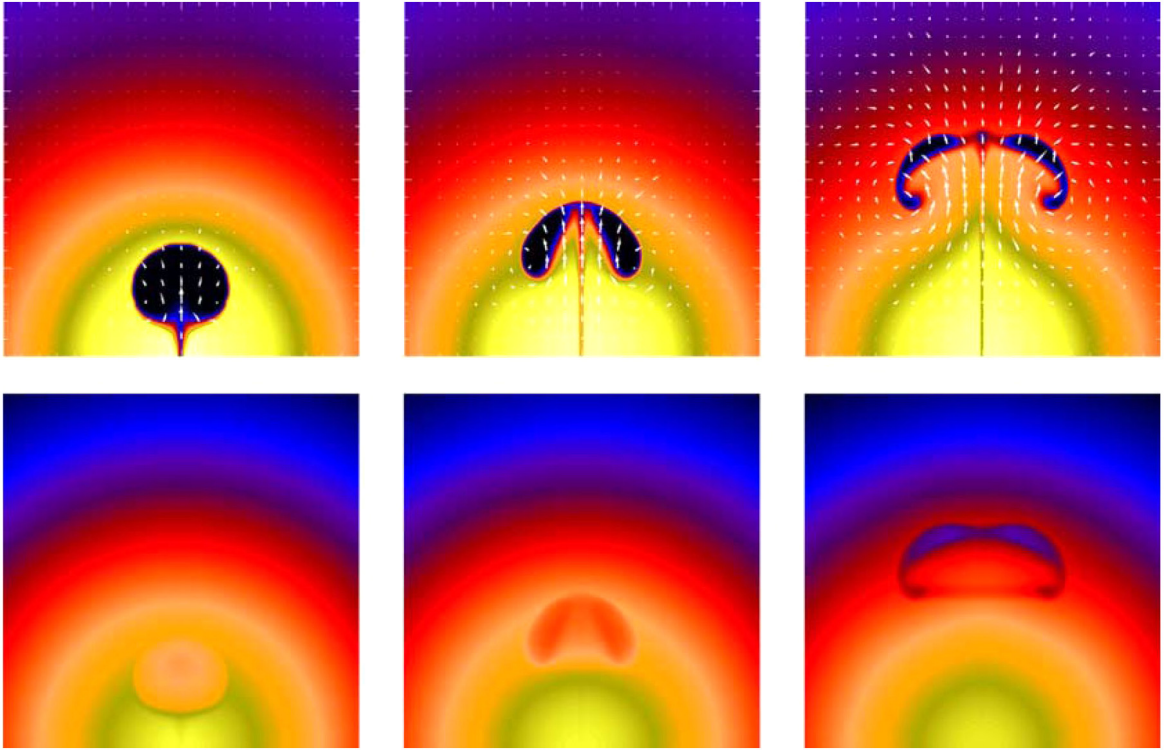


Fig. 15.2. Mid-plane density slices (upper panels) and simulated X-ray surface brightness maps (lower-panels) for the $Re = 250$ case (Run 3) shown at three times: $t = 1$ (left panels), $t = 2$ (middle panels) and $t = 4$ (right panels). Arrows indicating fluid velocity have been superposed on the density slices. Note how the viscosity stabilizes the bubble, allowing a flattened but intact buoyant ‘cap’ to form. Both the X-ray surface brightness and Ha-inferred velocity field around the ghost cavity of Perseus-A can be qualitatively reproduced by this model.

Source: Fig. 3 of Reynolds et al. (2005), *Monthly Notices of the Royal Astronomical Soc.* with permission.

logarithm proportional to the collision integral (Spitzer, 1962). The electron viscosity coefficients have been determined for $Z=1$ (Braginskii, 1965) and $Z \rightarrow \infty$ (Whitney, 1999; Simakov and Molvig, 2014). The electron viscosity is dominant at high Z ,

$$\frac{\mu_e}{\mu_i} \sim Z \frac{\tau_e}{\tau_i} \sim \left(\frac{m_e}{m_i} \right)^{1/2} Z^3. \quad (15.3)$$

These formulae, updated from those found in the popular NRL Formulary (Huba, 2004), indicate there is an ion mass and charge dependency applicable to high-temperature, low-density plasma states, where the ionic coupling is small (Baus and Hansen, 1980; Ichimaru et al., 1987). The plasma coupling parameter

$$\Gamma_i = Z^2 e^2 / k_B T_i a_i, \quad a_i = (3/4\pi n_i)^{1/3}, \quad (15.4)$$

is the ratio of the energy due to Coulomb forces with respect to the thermal energy.

Reynolds et al. (2005) noted that the principal effect of viscosity is to stabilize the bubble against both RT and KH instabilities, thereby allowing it to remain intact as it floats upwards in the ICM atmosphere. On the one hand, the flattening of such bubbles as they rise provides a natural explanation for the elongated morphology of the north-west cavity in Perseus-A (Fig. 15.2). On the other hand, the authors found that these KH instabilities are primarily responsible for shredding the bubble within 2–3 dynamical times (i.e., ~ 5 sound crossing times of the bubble; top panels of Fig. 15.3) for the inviscid case. Due to the shredding of the bubble, one never observes a detached and flattened but otherwise intact structure such as we appear to see in the ghost cavity of Perseus-A (see bottom panels of Fig. 15.3).

The viscosity of liquid iron under high pressure is important for modeling planetary bodies such as the physical conditions of the Earth's core (de Wijs et al., 1998; Alfè et al., 2000; Rutter et al., 2002). As stressed by Clérouin et al. (1998), the problem of estimating the viscosity of a dense plasma mixture is a crucial issue for predicting turbulent mixing occurring during the compression of a laser fusion pellet (Galmiche and Gauthier, 1996) or in astrophysical mixing of heavier core elements outward into the low-density envelope. The classical transport theories described in Chapman and Cowling (1939) and Spitzer (1962) must be extended to plasma transport of a dense plasma mixture. Note that while most of the attention

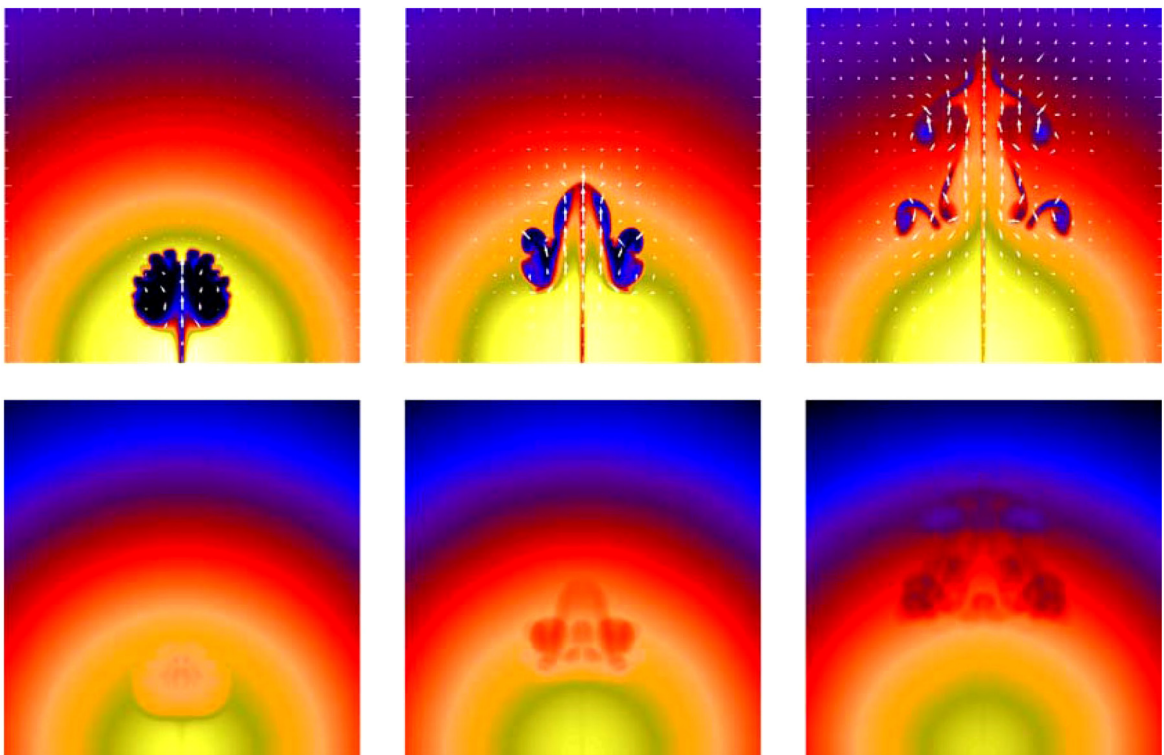


Fig. 15.3. Mid-plane density slices (upper panels) and simulated X-ray surface brightness maps (lower-panels) for the inviscid control case (Run 1) shown at three times: $t = 1$ (left panels), $t = 2$ (middle panels) and $t = 4$ (right panels). Arrows indicating fluid velocity have been superposed on the density slices. Note how the bubble is rapidly destroyed by the combined action of RT and KH instabilities. At no time would one observe a flattened, detached ghost cavity as we see in Perseus-A.

Source: Fig. 2 of Reynolds et al. (2005), *Monthly Notices of the Royal Astronomical Soc.* with permission.

here has been paid to the viscosity, the electron conductivity (Lee and More, 1984) and diffusion (Paquette et al., 1986) coefficients are also important for dense plasma.

Plasma viscosity increases in both the high- and low-temperature limits (Dufrèche and Clérouin, 2000; Saigo and Hamaguchi, 2002). Murillo (2008) advanced a practical method of computing the viscosity based on mapping the system of interest onto the Yukawa model; he compared the model with quantum molecular dynamics results for compressed iron, relevant to the Earth's core, to the experimental data for many liquid metals, and to simulation results for dense deuterium relevant to inertial confinement fusion experiments.

An improved shear viscosity formulation for asymmetric plasma mixtures at thermodynamic conditions relevant to astrophysical and inertial confinement fusion plasmas has been achieved largely with assistance from large-scale molecular dynamics (MD) calculations.⁵² Recently, Haxhimali et al. (2015) proposed a simple hybrid model that interpolates between the strong and weak coupling limits, with Murillo's Yukawa viscosity model and classical transport theory, respectively. In the latter, the collision integrals in the 1st approximation of Chapman and Cowling's formulation are tabulated by Paquette et al. (1986) or Stanton and Murillo (2016) for static screened Coulomb (Yukawa) potentials with weak to moderate coupling. Higher level approximations for classical transport theory formulated by Simakov and Molvig (2016a, b) are only valid in the weakly coupled (Lorentz) limit. Ticknor et al. (2016) have developed similar hybridizations for viscosity and diffusivity in asymmetric binary plasma mixtures using one-component plasma (OCP) models and classical transport theory. Over a wide range of thermodynamic conditions, these hybrid models compare reasonably well with MD simulation results.

In spherical geometry, Weber et al. (2014b, 2015) and Clark et al. (2015) carried out three dimensional simulations including radiation and viscosity all of which act to suppress but not eliminate the RT instability. Weber et al. (2014b) presented large-eddy simulations with the high-order Eulerian code Miranda (Cook and Cabot, 2004) linked from simulations with the ALE code HYDRA (Marinak et al., 1996, 1998). Fig. 15.4 (reproduced from Fig. 4 of Weber et al., 2014b) illustrated that the plasma viscosity from this Yukawa system, along with the low plasma coupling parameter correction (Braginskii,

⁵² There are many molecular dynamics schemes. For detail, the reader is referred to the references cited in Murillo (2008), Haxhimali et al. (2015), Ticknor et al. (2016) and White et al. (2017).

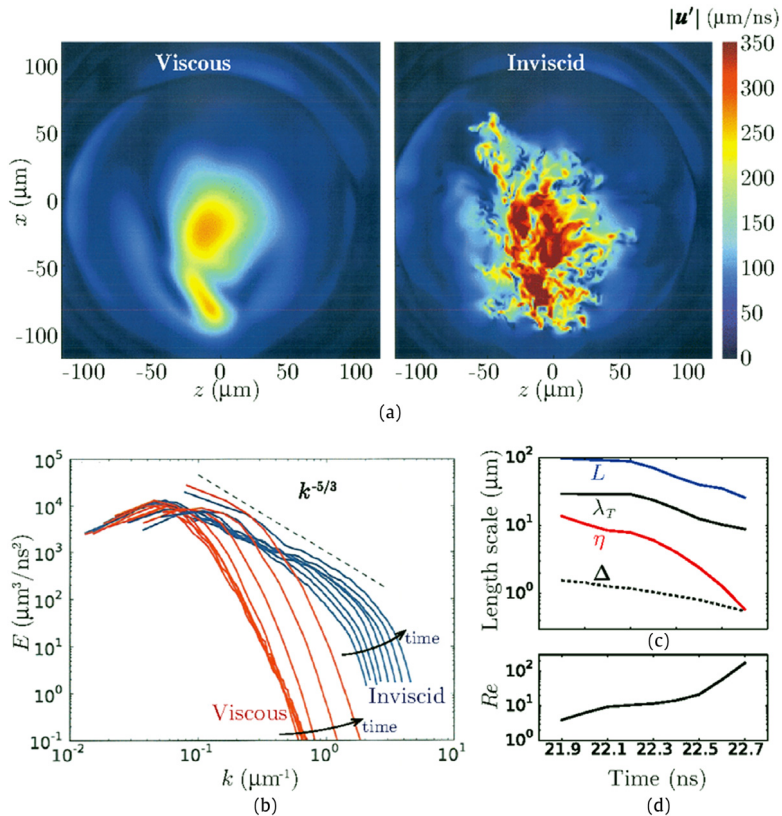


Fig. 15.4. Viscous effects on the fluctuating velocity. (a) Fluctuating velocity magnitude at 22.21 ns with (left) and without (right) viscosity. (b) Kinetic energy spectra in the hot spot from the viscous and inviscid simulations from 21.9 to 22.6 ns. (c) Turbulent length scales and (d) Reynolds number from the hot spot.

Source: Fig. 4 of Weber et al. (2014b), *Phys. Rev. E* with permission.

1965), play a role in smoothing small scale fluctuations in a 2D ICF fuel region Eulerian simulations.⁵³ Applying a normal mode analysis, Gerashchenko and Livescu (2016) studied the viscous effects on the compressible RTI in the presence of a background temperature gradient. Using a set of parameters taken from Weber et al., the authors also illustrated the importance of inclusion of viscosity, which can significantly dampen the growth rates starting from small wave numbers.

For mode scale lengths and conditions relevant in ICF, Haines et al. (2014) used the RAGE 2D hydrodynamics code (Gittings et al., 2008; Baltrusaitis et al., 1996) to arrive at a similar conclusion. Vold et al. (2015) studied the effect of plasma ion viscosity on ICF implosions using a one-dimensional, three-temperature, Lagrangian hydrodynamics model that also includes a treatment of fuel-plastic mass mixing by plasma transport. While yield and time-integrated burn-weighted temperature show less sensitivity to viscosity, it demonstrated a significant influence of the viscosity on timing in 1D implosions, particularly at first shock convergence and burn conditions. More recently, Vold et al. (2017) found that the viscosity and mass diffusion have increased significance as scale lengths decrease in an ICF relevant KH instability mix layer.⁵⁴

Strong stabilized RTI due to material strength at high pressure may provide a means of controlling the mixing in ICF (Barnes et al., 1974, 1980; Swegle and Robinson, 1989; Robinson and Swegle, 1989; Dimonte, 1999; Colvin et al., 2003; Piriz et al., 2005; Remington et al., 2015). There are several other references on strength effects for RMI – e.g. Piriz et al. (2008, 2009), Dimonte et al. (2011). There are also a few Russian publications – see, for example, Bakhrakh et al. (1997). A laser-driven platform at the OMEGA laser has been developed to explore the strength of iron at high pressures and strain rates (Huntington et al., 2017a). This laser-driven platform produces pressure greater than 1 Mbar on a thin Fe disk with a sinusoidal ripple pattern imposed on its face. These ripples seed the RTI, the growth of which is suppressed by the material strength of the

⁵³ Given the non-negligible increase in computational cost when viscosity is included, Clark et al. (2016) performed simulations without viscosity, but noted a small decrease in simulation fidelity.

⁵⁴ Vold et al. (2016) noted that plasma viscosity reduces the need for artificial viscosity to maintain numerical stability in the Lagrangian formulation and argued that artificial viscosity may provide an unphysical stability in implosion simulations. The authors also cautioned that high resolution simulations or a more Lagrangian-like treatment of species interfaces may be required to distinguish plasma transport and numerical diffusion in a Eulerian computation of complex and dynamically evolving mix regions (Vold et al., 2017).

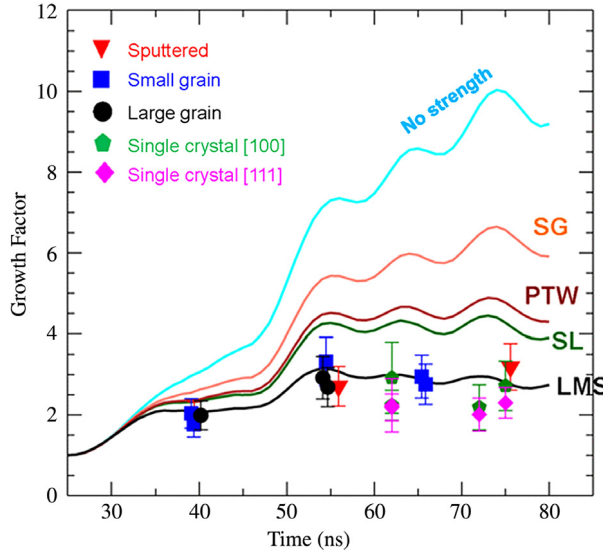


Fig. 15.5. Measured GF (points) compared with 2D simulations by using different flow stress models referenced in the text (curves). Source: Fig. 5, Park et al. (2015), Phys. Rev. Lett., with permission.

sample. Park et al. (2010a, b) performed a number of experiments on metals to infer the flow stress at pressures of ~ 100 GPa on the Omega Laser. At the National Ignition Facility (NIF) (Hurricane and Herrmann, 2017; Hogan et al., 2001; Miller et al., 2004a,b; Moses and Wuest, 2003; Moses et al., 2009), Park et al. (2015) obtained experimental results with more than 30 laser shots in a new regime of high pressures and strain rates and measured the ripple growth experimentally by face on, in-flight, point projection radiography using a 22 keV X-ray pulse (Park et al., 2008). The authors showed that the measured growth factor⁵⁵ GF, as a function of the delay times and compared the NIF data with the simulations results of ARES hydrodynamic code (Darlington et al., 2001) with various constitutive models of flow stress (Fig. 15.5). The predictions of the Livermore multiscale strength (LMS) model (Barton et al., 2011; Barton and Rhee, 2013) agree with the experimental data well, but the models of Steinberg–Guinan (SG) (Steinberg et al., 1980), Steinberg–Lund (SL) (Steinberg and Lund, 1989) and Preston–Tonks–Wallace (PTW) (Preston et al., 2003) underpredict the Ta flow stress at these strain rates and pressures. Clearly, the high-pressure material strength significantly reduces the RTI growth.

The potential stabilization of RT instabilities by ablation in ICF was already recognized in an early landmark article by Nuckolls et al. (1972). Indeed, the imploding capsule experiences two phases of RT instability (Lindl and Mead, 1975; Lindl, 1995; Tabak et al., 1990; Takabe et al., 1983; Verdon et al., 1982). The ablation front is unstable during the acceleration phase and the pusher-fuel interface becomes unstable during deceleration and stagnation. Strong perturbation growth can lead to spikes of the capsule wall material protruding into the fuel, which can severely degrade capsule performance (Betti et al., 1996, 1998, 2001; Bodner, 1974; Kull, 1991; Lindl, 1998; Marinak et al., 1996; Sanz, 1994; Huntington et al., 2011; Piriz, 2001; Piriz et al., 1997). Indeed, the linear growth of the ablative RTI (ARTI), described in the linear theory known as Takabe's formula and modified Takabe's formula (Takabe et al., 1985, 1988; Takabe, 2004; Atzeni and Meyer-ter-Vehn, 2004), is very well understood with excellent agreement between experiment and simulation for planar geometry (Kilkenny et al., 1994).

It should be noted that the two effects have been modeled (Lindl et al., 2004; Betti et al., 1998; Hurricane et al., 2014a,b), in Takabe formula,

$$\gamma_{A-RTI} = \tilde{\alpha}_2(F_r, \zeta_h) \sqrt{\frac{kg}{1 + kL_0}} - \tilde{\beta}_2(F_r, \zeta_h) kV_a \quad (15.5)$$

ablation velocity V_a and density gradient smoothing L_0 (see also, LeLevier et al., 1955, part I). Specifically, k is the perturbation wavenumber, g is the ablator acceleration, L_0 is the density gradient scale length of the ablation front, $\tilde{\alpha}_2$ and $\tilde{\beta}_2$ are parameters of order unity whose exact values depend on the Froude number, $F_r = V_a^2/(gL_0)$, and a heat conduction scale-length parameter, ζ_h . Early simulations offered evidence on ablative stabilization at the short wavelength (Gardner et al., 1991; Tabak et al., 1990), see also, (Dahlburg et al., 1993, 1995). Later, Sanz et al. (2002) considered weakly nonlinear regime of RTI with ablation effect from the Spitzer–Harm electron thermal conduction. Some of these weakly nonlinear results were discussed and later confirmed in Garnier et al. (2003). As stressed by Sanz et al. (2004), the highly nonlinear single mode and

⁵⁵ The growth factor is the ratio of the final ripple amplitude in areal density, to the initial ripple amplitude, as determined from radiography using the procedure detailed in Park et al. (2010a, b).

multimode evolution can only be studied with a full nonlinear model such as the one presented by the authors. Such a model was derived from first principles and closed with an approximation similar to the closure of the linear sharp boundary model (Piriz et al., 1997). Also, Garnier and Masse (2005) considered constant thermal conductivity on both sides of the ablation front. Epperlein and Short (1991) and Wang et al. (2010b, c) have also considered the nonlinear development of the ARTI. Yan et al. (2016) studied both numerically and analytically the detailed nonlinear evolution of the single-mode ARTI in three dimensions.

The experimental studies on the Nova laser illustrated the differences between the classical and ablative RTI (Remington et al., 1991; Budil et al., 1996, 2001; Glendinning et al., 1997, 2000). Glendinning and co-workers, for instance, found that the measured growth rate of laser ARTI with preheating is about 50% of the classic result, which is also obtained from the simulations when the electron thermal conductivity is enhanced at a lower temperature and higher density (Ye et al., 2002). On the OMEGA Laser System, Sadot et al. (2005) reported the first experimental observation showing the self-similar behavior of the bubble size and amplitude distributions under ablative conditions. From theoretical and numerical work (Masse, 2007) and experimental measurements on the Omega laser (Huser et al., 2011), it has been shown that the stabilizing term of the ARTI growth rate is due to transverse diffusion. Namely, increasing transverse diffusion using an anisotropic structure could reduce the ARTI. Also, Wang et al. (2012b) found that preheating plays an essential role in the formation of the jet-like spikes. Wang et al. (2009c) also analyzed the ablative effect on the Kelvin–Helmholtz instability using numerical simulation. Moreover, Casner et al. (2014) carried out experimental studies on the ablative RMI growth from laser imprinted perturbations, contrary to the previous measurements of RM oscillations induced by pre-imposed modulations (Aglitskiy et al., 2002).

Casner et al. (2014) reviewed results acquired in planar experiments performed on the OMEGA laser facility on the modeling and mitigation of hydrodynamic instabilities at the ablation front. There are efforts to extend the ablative RTI models from linear into nonlinear regime on the NIF platform (Casner et al., 2012, 2013, 2016).

For the adiabat shaping technique, a strong initial shock by a high intensity pulse is launched, resulting in enhanced shock preheat (see for instance, Masse, 2007). Experimental studies (Glendinning et al., 1997; Shigemori et al., 1997) found that preheat could reduce the density gradient at the ablation front, and as a result, would greatly reduce the RTI growth. With preheat effects incorporated, Fan and Luo (2008), Fan et al. (2009) and Wang et al. (2013b) studied the nonlinear regime of single mode ARTI. Also, Ye et al. (2011) reported that their 2D numerical simulations suggested two regimes of ARTI nonlinear evolution in the presence of preheating.

Cryogenic indirect-drive implosions on the National Ignition Facility illustrated that the ARTI is a driver of the hot spot mix. The shell instability is also the main candidate for performance degradation in low-adiabat direct drive cryogenic implosions (Goncharov et al., 2014; Casner et al., 2014) as well as nominal point design implosion during the National Ignition Campaign (Edwards et al., 2013). This motivates the switch to a lower compression, higher adiabat implosion NIF design (Fig. 15.6). Dittrich et al. (2014), Hurricane et al. (2014a) and Park et al. (2014) pointed out a key to achieving the fusion fuel gains exceeding unity by lowering ablation Rayleigh–Taylor instability growth compared to the National Ignition Campaign (NIC) point design capsule. As shown in Fig. 15.6c, while the main drives are rather similar, the ‘high-foot’ implosion method launched a stronger first shock and earlier main drive. While the “low foot” design strived to maximize the compression by minimizing the adiabat, the high foot has a higher fuel adiabat that limits both fuel compression and theoretical capsule yield. On account of its better stability, high foot implosions driven with more peak laser power showed a monotonic increase in performance as the shell implosion velocity increased up to the maximum laser power achievable on NIF; this monotonic power scaling was not seen with the more unstable low foot.

Several factors contributed to suppression of the instability with the ‘high-foot’ implosion method. The essential stability benefits can be understood from examining Eq. (15.5), an expression for the linear growth rate of the ablation-driven Rayleigh–Taylor instability (Lindl et al., 2004; Betti et al., 1998). First, the stability is enhanced (higher ablation velocity, V_a , which scales as $T_{\text{rad}}^{10/9}$, where T_{rad} is the hohlraum radiation temperature) during the shock passage because of the higher temperature (Hurricane et al., 2014b). Second, the convergence is lower with this design (Plessset, 1954; Goncharov et al., 2000). Finally, the length scale for the density gradient, L_0 , is increased, which in turn, led to a reduced RTI growth rate (Munro, 1988; Lindl, 1998; Atzeni and Meyer-ter-Vehn, 2004). As an illustration of the relative stability of the low and high foot pulse shapes, Dittrich et al. (2014) simulated implosions with various DT fuel adiabats from 1.4 (representative of low foot implosions) to 2.4 (representative of high foot implosions) and with artificially increased capsule surface roughness (4×). The results are shown in Fig. 15.7. While the low adiabat low foot implosion appears to break up with this enhanced surface roughness, the higher adiabat high foot implosions remain intact, although they, of course, do not reach as high a fuel compression as the low foot. This tradeoff between stability and compression was appreciated well before high foot experiments began on NIF (Goldstein, 2012).

The purpose of so-called adiabat shaping is to use a stronger first shock, reducing hydrodynamic instability growth in the ablator. Casey et al. (2014) and Raman et al. (2014) further elucidated the value of mitigating instability growth in NIF ignition experiments, reporting that a 350 TW high-adiabat (high-foot) NIF drive stabilizes hydrodynamic instability when compared to a similar power low-adiabat (low-foot) drive. By raising the foot of the radiation drive, the high-foot drive reduced instability growth by shifting the region of positive growth to a lower mode number, increasing the ablator density scale length, increasing the ablation velocity, and decreasing the in-flight aspect ratio.⁵⁶

⁵⁶ Several related works also considered the hydrodynamic instabilities related to the “high-foot” and “low-foot” drives at the NIF (He et al., 2016; Wang et al., 2016a,b).

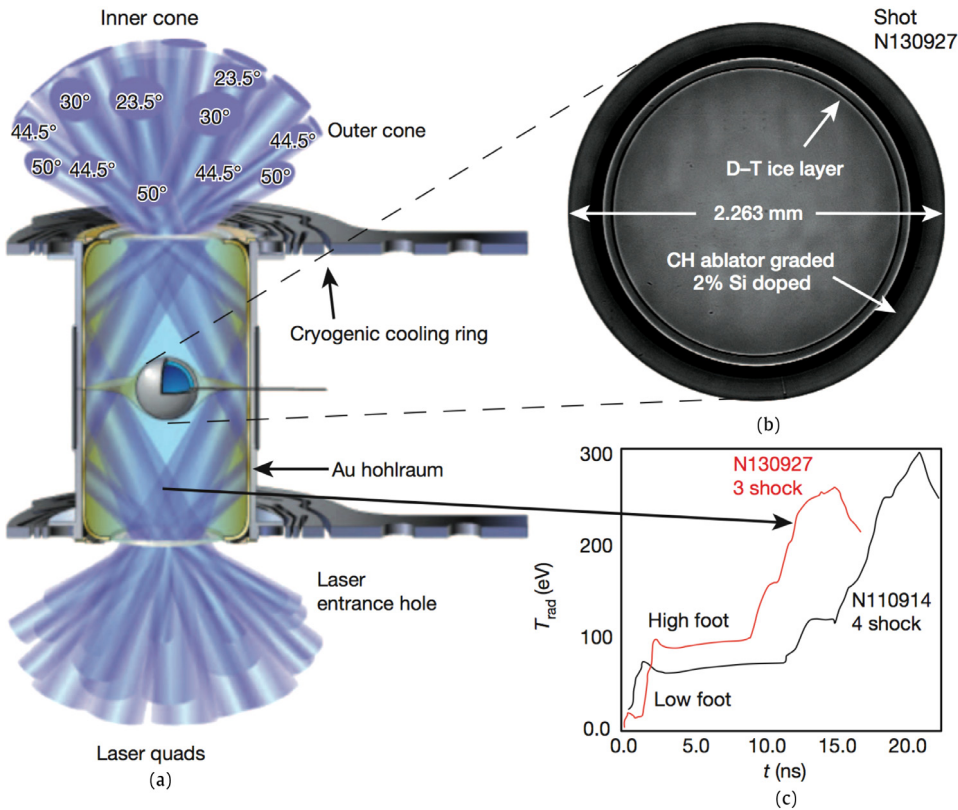


Fig. 15.6. Indirectly driven, inertially confined fusion target for NIF. (a) Schematic NIF ignition target showing a cut-away of the gold hohlraum and plastic capsule with representative laser bundles incident on the inside surface of the hohlraum. (b) X-ray image of the actual capsule for N130927 with D-T fuel layer and surrounding CH (carbon-hydrogen) plastic ablator. (c) X-ray radiation drive temperature versus time for the NIC low-foot implosion and the post-NIC high-foot implosion.

Source: Fig. 1 of Hurricane et al. (2014a), *Nature* with permission.

Clark et al. (2014) systematically scanned the utilization of the multipliers on the X-ray flux during the “picket” and “trough”, the two distinguishing parts of the foot of the X-ray pulse shape. Using a pulse shape with similar picket intensity to the high-foot drive and similar trough intensity to the low-foot drive, stabilization similar to the high-foot drive was achieved (MacPhee et al., 2015). Peterson et al. (2015), on the other hand, advanced the 3-shock drives (similar to high-foot) to keep the same low RMI and RTI growth as the high foot, while reducing the DT fuel adiabat, allowing higher fuel compression. Smalyuk et al. (2015) found that the fuel areal density was improved by ~25% with a new adiabat-shaped drive compared to similar “high-foot” drive (~1.0 g/cm²). The total neutron yield of ~3.8 × 10¹⁵ was improved by more than 4 times, compared to “low-foot” implosions driven at the same compression and implosion. See Clark et al. (2016, 2017) and Robey et al. (2016) for a recent discussion on these issues.

Smalyuk et al. (2017) compared measured Fourier spectra of the 3-D amplitude modulations for high-foot and low-foot drives at the NIF to nonlinear saturation level calculated using Haan's (1989) model. Whereas the amplitudes with the high-foot drive are below the Haan's nonlinear saturation level, the spectral peak with the low-foot drive is near the saturation level with higher modes located above the saturation level. This indicates that nonlinear effects have slowed down the RTI growth of the low-foot perturbations at the time of measurements. By comparing the ratio of the measured X-ray continuum brightness to the neutron yield, Ma et al. (2017) quantified the role of hot spot mix in the high-foot and low-foot implosions on the NIF. The authors found that high-foot implosions showed less susceptibility to mix and allowed velocities of > 380 km/s to be demonstrated. Mix, however, was determined as the principal source of performance variability for the low-foot implosions.

In addition to the pursuit of the energy gain with the ICF, high energy density physics facilities have provided the platforms to study the physics of hydrodynamic instabilities at high temperature and pressure regimes (Remington et al., 2000, 2006; Drake, 2006; Aglitskiy et al., 2010). Hansom et al. (1990) describes one of the earliest laser-driven instability experiments on the AWE HELEN laser. Experiments on the NOVA laser developed the technique of laser-driven instability studies for both RTI (Glendinning et al., 1992; Remington et al., 1994, 1995; Edwards et al., 2000), and RMI (Dimonte and Remington, 1993; Peyser et al., 1995; Dimonte and Schneider, 1996; Dimonte et al., 1996; Farley et al., 1999). Experiments were also developed during this period with the expressed goal of performing experiments at astrophysically relevant conditions using the laser

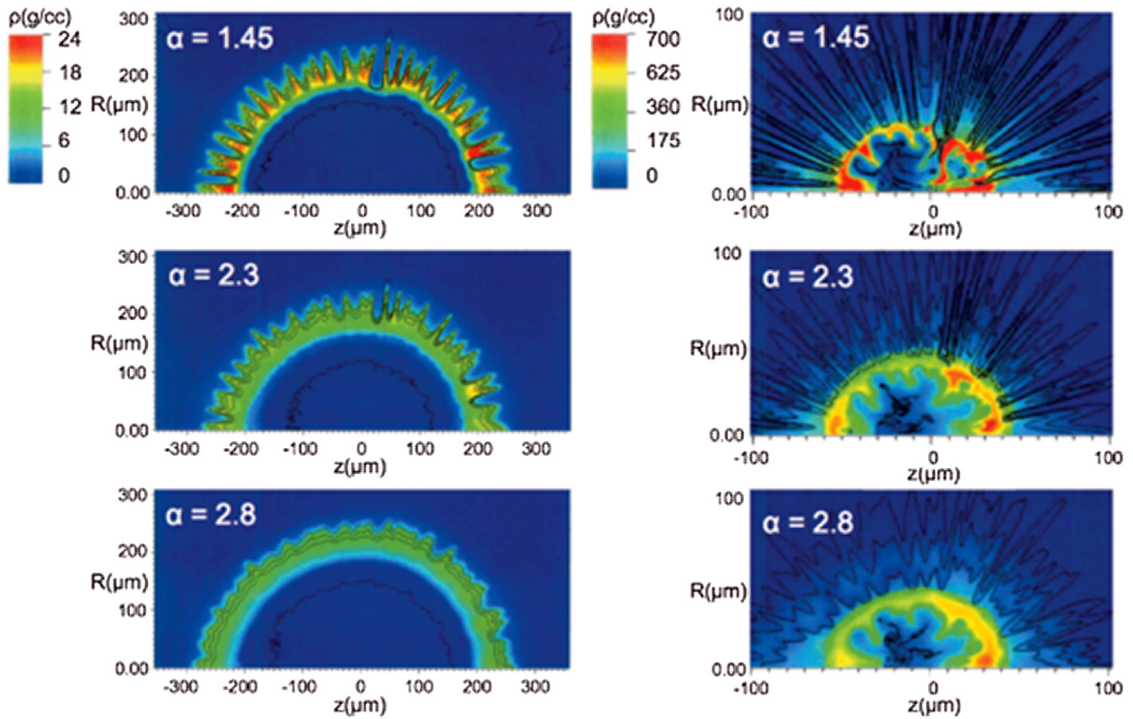


Fig. 15.7. Two-dimensional multimode (up to mode 100) simulations with a spectrum of imposed surface roughness ($4 \times$ nominal) show, in density, the expected instability growth on the capsule. From top to bottom, implosions with $\alpha = 1.45$ (low foot), $\alpha = 2.3$ (high foot), and $\alpha = 2.8$ (high foot) are shown at $R \sim 200 \mu\text{m}$ (left column) and $R \sim 50 \mu\text{m}$ (right column).

Source: Fig. 6 of [Dittrich et al. \(2014\)](#), *Phys. Rev. Lett.* with permission.

drive ([Kane et al., 1997, 1999](#); [Remington et al., 1997](#)). This work continued, and was expanded upon, using the OMEGA laser (see [Boehly et al., 1997](#) for details of the laser facility). New diagnostics and an accommodating laser configuration allowed for improved measurements at embedded interfaces, and carefully scaled experiments were performed to investigate the instability growth at the interfaces in exploding supernovae and jets (see [Drake et al., 2004, 2005, 2009](#); [Kuranz et al., 2007, 2010](#); [Ryutov et al., 1999](#); [Robey et al., 2001](#); [Foster et al., 2005](#); [Rosen et al., 2005](#); [Hartigan et al., 2009](#); [Swisher et al., 2015](#)) Growth at the laser-irradiated surface, seeded by modulations in the laser, were also explored by [Knauer et al. \(2000\)](#) and [Smalyuk et al. \(2006, 2008\)](#). Conceptual designs for both RMI and RTI experiments have been presented by [Grosskopf et al. \(2009, 2013\)](#), [Huntington et al. \(2011\)](#), [Malamud et al. \(2013, 2014b\)](#), and [Flaig et al. \(2014\)](#) and these experiments are currently in progress or preparation on the OMEGA and NIF lasers.

Experimentally, evidence of nonlinear bubble merger growth was seen in the work of [Smalyuk et al. \(2005\)](#). Here, the nonlinear saturation velocities are measured on the OMEGA laser and are found to be in excellent agreement with [Haan's](#) model ([1989](#)). The measured growth of long-wavelength modes is consistent with enhanced, nonlinear, long-wavelength generation in ablative driven targets. In contrast to previous direct drive RTI experiments, the ablation velocity and density gradient scale length are significantly increased with NIF indirect drive leading to cutoff wavelengths large enough, (about 25 microns) to be observable ([Casner et al., 2016](#)). The NIF measurements ([Martinez et al., 2015](#)) of the modulation optical density performed by X-ray radiography illustrated the transition from weakly nonlinear RTI regime to a highly nonlinear, bubble-merger one, beyond the [Haan \(1989\)](#) saturation level. The multi-mode modulation amplitudes evolve towards the longer wavelengths ([Figs. 15.8 and 15.9](#)), but show insensitivity to the initial conditions, a result that differs from a number of other studies.

Based on their experimental study on the OMEGA laser, [Di Stefano et al. \(2015a\)](#) described in detail their first observation of a purely RM system in which the dynamics were well-resolved from the linear phase to multiple later nonlinear phases. At these later times, the two initially-present perturbation modes first interact to produce new modes, ending the linear phase earlier than would be expected from any one of those individual modes in isolation, and subsequently enter into competition with each other, resulting in the reabsorption of higher-frequency modes into the lower-frequency ones (See [Figs. 15.10 and 15.11](#), reproduced from Figs. 2 and 6 of [Di Stefano et al., 2015b](#)). This is accomplished using a technique employing a long driving laser pulse to create a strong, unvarying shock (Mach number ~ 8).

[Kuramitsu et al. \(2012, 2016\)](#) presented the experimental results of a turbulent electric field driven by the Kelvin-Helmholtz instability in collisionless counterstreaming plasmas produced with a high-power laser, LULI2000 at the École Polytechnique in France. [Vandenboomgaerde et al. \(2016\)](#) performed high resolution simulations to model NIF experiments

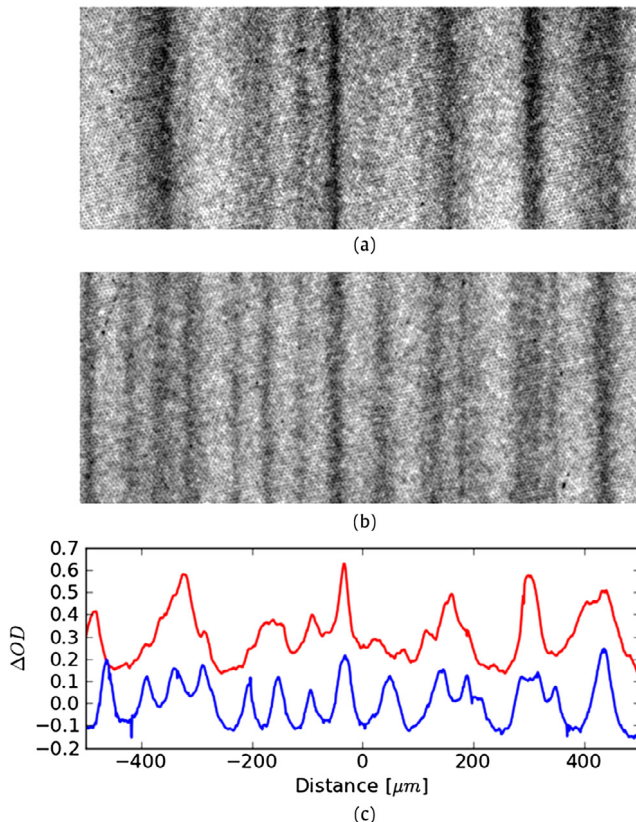


Fig. 15.8. (a) Processed data images at 15.5 ns for an iodine doped CH foil with an initial rms amplitude of $2.8 \mu\text{m}$ where black represents an increase in the optical density (OD). (b) Data with an initial rms amplitude of $0.5 \mu\text{m}$. (c) Lineouts from (a) (red) and (b) (blue). The red plot was shifted by $0.3\Delta OD$ for clarity.

Source: Fig. 2 of Martinez et al. (2015), *Phys. Rev. Lett.* with permission.

and demonstrated how shear flows appear at the surface of the gold bubble ablated from a hohlraum wall, and produce the growth of KHI. Using the OMEGA-EP facility (Maywar et al., 2008), Wan et al. (2015, 2017) reported their observations of the evolution of single-mode modulations under the influence of the Kelvin–Helmholtz instability in a supersonic flow. In the OMEGA experiments in Harding et al. (2009), Hurricane et al. (2009, 2011, 2012), Smalyuk et al. (2013), laser-driven shock waves propagated through low-density plastic foam placed on top of a higher-density plastic foil. Behind the shock front, lower-density foam plasma flowed over the higher-density plastic plasma. The interface between the foam and plastic was KH unstable.

Other OMEGA experiments were carried out using geometries with thin layers separating regions of flow, in which the flows enter the apparatus from opposite directions (Welser-Sherrill et al., 2013; Doss et al., 2013a,b; Haines et al., 2013c,d; Loomis et al., 2014; Merritt et al., 2015; Merritt and Doss, 2016). This geometry was used to further increase the speed difference across the fluid interface. The designs of these laser experiments were based on traditional (Brown and Roshko, 1974; Ho and Huerre, 1984) and counterflowing (Alvi et al., 1996; Papamoschou, 1995; Strykowski et al., 1996) shear flow laboratory experiments performed in the liquid or gas phase. The directly-laser-driven counter-propagating OMEGA platform was then developed to be flexible enough to allow the investigation of different flow conditions and physics package geometries, without reconfiguring the drive lasers or diagnostics. Indeed, the reshock and shear experiments have been carried out using the same basic shock tube setup (Welser-Sherrill et al., 2013).

As shown in Fig. 15.12, this LANL experimental platform at OMEGA (Welser-Sherrill et al., 2013) has been scaled up to the NIF with an indirectly-driven shock tube (Doss et al., 2015; Flippo et al., 2016b). The extended shock tube length, coupled with the available stronger drive and advanced diagnostic capabilities⁵⁷ created a high-energy-density hydrodynamics platform of unprecedented scale (Fig. 15.13). The counterpropagating shear experiment was again fielded to maximize the

⁵⁷ As an example, Flippo et al. (2014) developed a very large area (7.5 mm^2) laser-driven X-ray backlighter [termed the Big Area BackLighter (BABL)] for the NIF. For the purpose of the shear experiments on NIF, the authors showed that the backlighter exceeds the design specifications. The reader is referred to Doss et al. (2016b) for the most current platform development and specification information, along with Flippo et al. (2016a) from the same conference proceedings on the long BABL backlighter pulses.

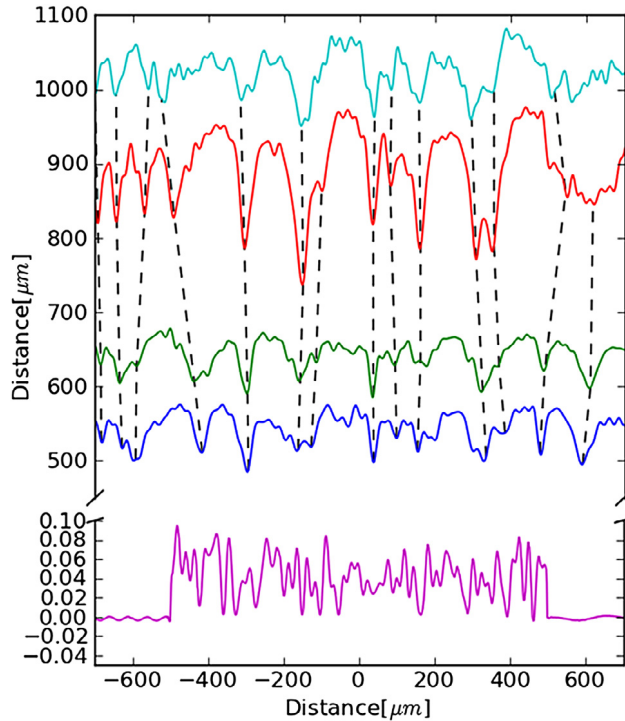


Fig. 15.9. 2D modulation evolution showing the interface position at 14.5 ns (blue), 15.5 ns (green), 17.7 ns (red), and 18.7 ns (cyan). Dashed lines highlight the position of the spikes as a function of time. Initial modulations are shown in the lower panel (magenta).
Source: Fig. 5 of Martinez et al. (2015), *Phys. Rev. Lett.* with permission.

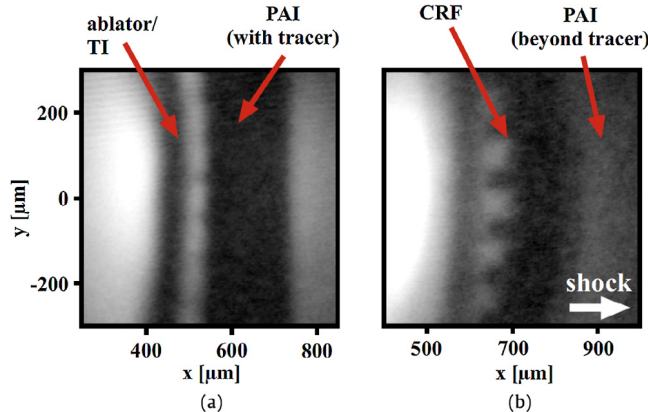


Fig. 15.10. (a) Experimental radiograph, taken at 20 ns; (b) experimental radiograph, taken at 35 ns. The RM growth of the interface structure during the elapsed time is evident from the two frames. [experiment's physics assembly: The first layer, a 125-μm-thick polycarbonate film (the ablator), is pressed against a second film functioning as a thermal insulator (TI), made of 150-μm thick bromine-doped plastic ($C_{50}H_{48}Br_2$). Both layers are of density 1.2 g/cm³. Next, a 200-μm-thick layer of carbonized resorcinol formaldehyde (CRF, of density 0.4 g/cm³) foam is pressed against the TI, and a block of polyamide-imide (PAI, $C_{22}H_{14}O_4N_2$) plastic, of density 1.4 g/cm³, is pressed against the CRF. This block features a 200-μm wide tracer layer of iodine-doped plastic ($C_{50}H_{47}I_3$) at its center, extending 300 μm down the system's axis].
Source: Fig. 2 of Di Stefano et al. 2015b, *High Energy Density Physics*.

driving time of the hydrodynamic system. Using data obtained from a recent NIF experiment, Doss et al. (2016a) reported the appearance of the coherent structures similar to those in the traditional mixing layer experiments.

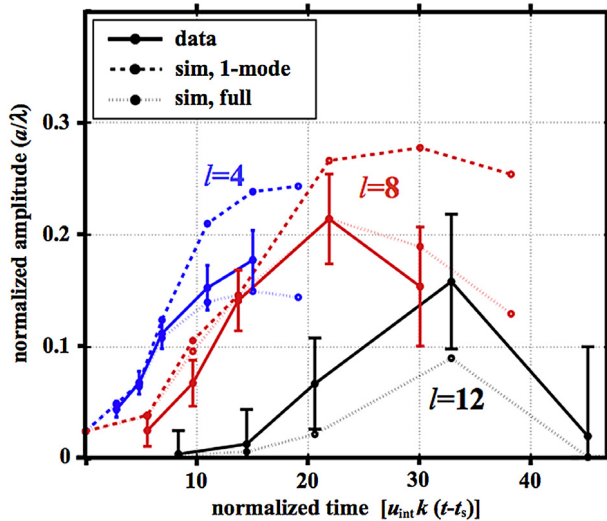


Fig. 15.11. Time evolution of the two fundamental RM modes ($l = 4, 8$) and their lowest coupled harmonic ($l = 12$), as measured using Fourier techniques. The solid lines correspond to the experimental radiographs, the finely-dotted lines to the full experimental simulation, and the heavily-dotted lines to the single-mode simulations. The five data points for each mode correspond to images taken at 20, 22.5, 25, 30, and 35 ns in real time, respectively. Note that the time scale used is normalized to the standard, circular wavenumber k .

Source: Fig. 6 of Di Stefano et al. 2015b, *High Energy Density Physics*.

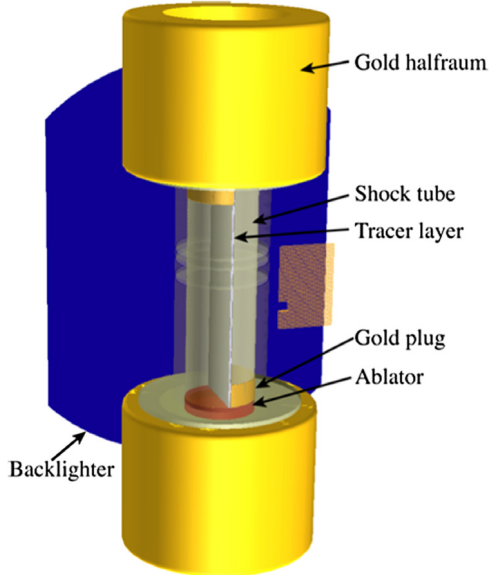


Fig. 15.12. A VISRAD (<http://www.prism-cs.com/Software/VisRad/VisRad.htm>, Prism Computational Sciences, Inc.) rendering of the target, displaying (gray) the shock tube with enclosed metal plate with (yellow) gold plugs embedded on both end and a gold fiducial grid off to the right side. The gold hohlraums on the top and the bottom provide indirect shock drive to the tube by driving the (brown) plastic ablator layer, and the backlighter (blue) is used to diagnose the experiment.

Source: Fig. 2 of Doss et al. (2015), *Phys. Plasma*, with the permission of AIP Publishing.

This is an excellent opportunity to stress that HEDP offers a unique advantage in addressing the mix issue as the surface perturbations of the target could be fabricated on the solid materials to a high precision with excellent repeatability.⁵⁸ As discussed in preceding sections, whether the initial condition still influences the late-time behavior of the flows induced by

⁵⁸ Recently, Merritt et al. (2017) demonstrated the repeatability of the instability growth in the counter-propagating shear experiment at the OMEGA laser facility.

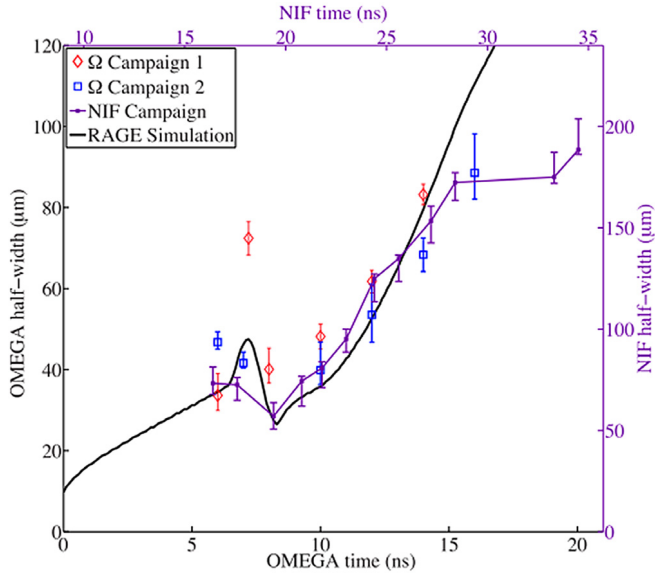


Fig. 15.13. Layer widths as a function of time at OMEGA and NIF. Left and bottom axes refer to widths and times of data from OMEGA, right and top axes show widths and times taken at NIF. The scaling between the two axes is such that the hydrodynamics are equivalent until the longer drive on NIF allows it to extend past the limits of the OMEGA experiment.

Source: Fig. 9 of Doss et al. (2015), *Phys. Plasma*, with the permission of AIP Publishing.

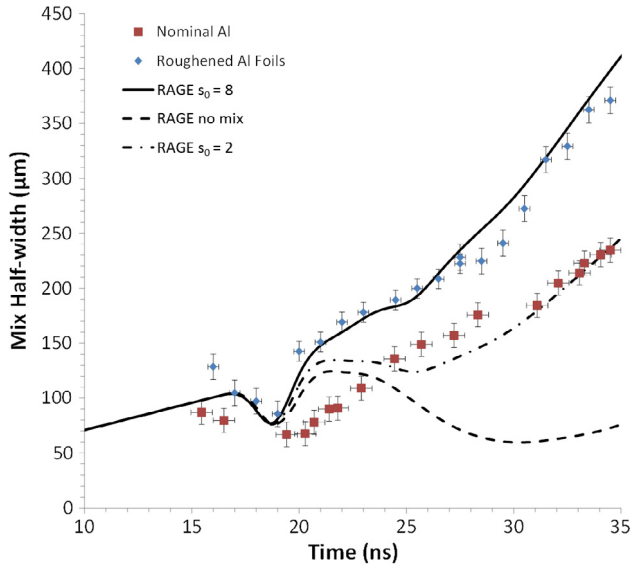


Fig. 15.14. Experimental data plotted with simulation results. Red squares are the nominally smooth Al data, blue diamonds are the roughened Al data. Solid black line is from the simulation with the BHR model turned on with the initial length scale $L_0 = 8$, dot-dashed line is BHR model with $L_0 = 2$, and the dashed line is the same simulation without BHR active.

Source: Fig. 4 of Flippo et al. (2016b), *Phys. Rev. Lett.* with permission.

hydrodynamic instabilities is an important subject.⁵⁹ At the OMEGA Laser Facility, Merritt et al. (2015) performed a series of counter-propagating shear experiments varying two initial types of scale lengths in the experiment: the thickness and surface roughness of a tracer layer at the shear interface. The authors found that decreasing the layer thickness and increasing the surface roughness both have the ability to increase the relative mixing in the system. Recently Flippo et al. (2016b)

⁵⁹ As noted by Di Stefano et al. (2012), experiments are usually designed such that the instability physics occurs in isolation. Yet, secondary processes will eventually develop within the experimental system and affect the physics. Di Stefano et al. studied the conditions under which a system can begin to exhibit such behavior and, in this context, consider data from an OMEGA laser experiment exploring Rayleigh–Taylor hydrodynamic instability.

showed the ability to control the morphology of those structures and the mixing rate of the shear layer. This was done by changing the initial surface roughness from 0.3 to 5 μm rms, while keeping everything else in the experiment the same. The experiment revealed significant changes in the growth rate of the Al tracer layer and the coherent structures, which gave way quickly to an almost homogeneous mix layer. Using the RAGE hydrocode and the BHR turbulent mix model, they were able to model the system in 2D and by only changing the initial scale length in the BHR model (called L_0 , see Section 12) by a factor of 4 they were able to match the nominally smooth aluminum case (see Fig. 15.14 dot-dashed line) and the roughed aluminum case (see Fig. 15.14 solid line). When RAGE was run without the turbulent mix model, the hydrodynamics could not capture the behavior of the system (see Fig. 15.14 dashed line). This appears to be the first time a hydrocode has been used to match two sets of data from the same experiment with just a simple change in the initialization of the turbulence model.

With this optimized NIF platform, Nagel et al. (2017) and Huntington et al. (in preparation) reported single- and reshocked RMI measurements. They obtained late-time mixing layer evolution for both the single- and multi-modes RMI flows using X-ray area backlit imaging. For the reshocked case, the shocks are driven from opposite sides of the tube and the strength of the reshock could be easily adjusted. This work considered whether the growth rate of the mixed width becomes universal and investigated a possible loss of memory of initial conditions.

The resulting datasets from HEDP experiments could be very helpful in developing mix models in a high-temperature, high-pressure environment. The shear flow results, for instance, have been used (Welser-Sherrill et al., 2013; Doss et al., 2013a,b; Merritt et al., 2015; Flippo et al., 2016b) to verify the parameters of the BHR turbulence model (Besnard et al., 1992) as implemented in the Los Alamos National Laboratory (LANL) Eulerian code, RAGE (Gittings et al., 2008), to provide the validation data for development of new techniques in large-eddy-simulations (Zhou et al., 2014), and to study the physics of thermal-turbulence coupling (Doss et al., 2013b). The NIF experiments (Doss et al., 2015; Flippo et al., 2016b) also provided the data to calibrate the initial condition of a $K-L-a$ Reynolds Averaging Navier-Stokes (RANS) model, and the numerical model was subsequently used to investigate the geometry effects at late times (Wang et al., 2015b). Undoubtedly, the advent of high-power lasers facilities such as the National Ignition Facility (NIF), and Laser Megajoule (LMJ) (Andre, 1999; Tassart, 2004; Fleurot et al. 2005; Bourgade et al., 2008; Casner et al., 2015a), in the near future opens a new era (Casner et al., 2015a)⁶⁰.

16. Conclusion

The goal of this review is to analyze the Rayleigh-Taylor instability, single-and reshocked Richtmyer-Meshkov instability induced flows within a unified framework. The linear and nonlinear theories of the mixing layer evolutions induced by RT and RM instabilities have been developed and compared with experimental data for early times. A significant complication is that the subject matter is amenable only to very limited treatment by statistical closure theories at the late-time. Several linearized schemes have been adopted from turbulence and aeroacoustic analyses (Ribner, 1953, 1985; Kovasznay, 1953; Batchelor and Proudman, 1954; Townsend, 1976; Hunt and Carruthers, 1990). The statistical approaches (Kraichnan, 1959; Leslie, 1973; Orszag, 1970, 1977; Lesieur, 1990; Sagaut and Cambon, 2008; Zhou et al., 2004; Zhou, 2010) are simply too cumbersome for flows subject to strong external agencies, such as shocks, and accelerations. Nevertheless, researchers made progress in this direction, for instance, for the unconfined homogeneous turbulence with a destabilizing background density gradient in the Boussinesq approximation.

Laboratory experiments have provided some of the most crucial knowledge of the flows. For Rayleigh-Taylor instability, these results included, but are not limited to the measurements obtained at the Rocket-Rig (Atomic Weapons Establishment, United Kingdom), Russian Federal Nuclear Center, Academician E.I. Zababakhin, All-Russian Research Institute of Technical Physics (Chelyabinsk, Russia), the water and gas channel experiments at Texas A&M University, and the sliding barrier experiment in Cambridge University. For Richtmyer-Meshkov instability, the data have been obtained at the Russian Federal Nuclear Center-All-Russian Research Institute of Experimental Physics (RFNC-VNIIEF, Sarov, Russia), California Institute of Technology, Commissariat à l'Energie Atomique, France, Institut Universitaire des Systèmes Thermiques Industriels (IUSTI), Université de Provence,⁶¹ Marseille, France, University of Wisconsin, Los Alamos National Laboratory, Ben-Gurion University, Israel, and more recently, University of Science and Technology of China. The apparatuses developed at University of Arizona and the Linear Electric Motor (LEM) of Lawrence Livermore National Laboratory have been used for both the RTI and RMI experiments. LEM deserves particular mention for pioneering experiments with variable accelerations, in addition to standard ones with a constant (RTI) or impulsive (RMI) acceleration.

At the same time, advances in laboratory scale experimental techniques such as the use of modern high energy intensive pulsed laser beams have achieved capabilities which can produce energy densities in submillimeter-scale volumes that otherwise are only manifest in actual astrophysical events. Beam target materials, pulse duration, energetic drive, etc. can be reproducibly prepared for generating conditions closely simulating scaled features of astrophysical events. These techniques are presently recreating aspects of astrophysical phenomena in the laboratory. This is tantamount to creation

⁶⁰ Casner et al. (2015b) noted, for example, the concept of multi-barrel hohlraum will be implemented on NIF in the near-term for Eagle nebula experiments (Kane et al., 2005; Mizuta et al., 2007; Ryutov et al., 2007).

⁶¹ Recently, Université de Provence has merged with the Paul Cézanne University and University of the Mediterranean to become Aix-Marseille University.

of experimental testbeds where theory and modeling can be quantitatively tested against astrophysical observations (so called *laboratory astrophysics*) (Remington et al., 2000, 2006; Drake, 1999, 2006, 2009; Azechi et al., 2000; Robey et al., 2001; Casner et al., 2015a). In a laboratory setting, the initial conditions, diagnostic techniques, and energetic laser drives can be carefully controlled. It is anticipated that the powerful laser facilities such as the National Ignition Facility (NIF) and French Laser Mégajoule (LMJ) will provide continued opportunities for conducting much more advanced research in laboratory astrophysics.

High resolution direct numerical simulation (DNS) or large-eddy simulation (LES) of turbulence allows direct measurements of the individual terms of the Navier–Stokes equation, and is now a well-established adjunct to experiments for testing various theoretical predictions. The benefit of a DNS is that the calculation faithfully resolved all the scales that can be handled by the computational resource allocated to the researcher. It should be stressed, however, that the Reynolds numbers of the flows for the problems of interest are extremely high and still beyond the current capabilities of the supercomputers. Fortunately, the problem of the turbulent flow mixing at very high Reynolds number has been tackled successfully using large-eddy simulation methods (LES). In LES, the large scales of the flow field are resolved, while the unresolvable scales are represented by the subgrid models or by numerical methods in an implicit fashion (implicit LES or ILES). An estimation of the effective viscosity in ILES is an active research area.

Due to the time consuming nature of fully three-dimensional (3D) simulations of the hydrodynamic instabilities induced flows, it is desirable to run computations in two-dimensional (2D) where possible. As pointed out by Boffetta and Ecke (2012), large-scale motions in the atmosphere and oceans are described, to first approximation, as 2D turbulent fluids owing to the large aspect ratio (the ratio of lateral to vertical length scales) of these systems. However, the physics of two-dimensional turbulence is dramatically different from its 3D counterpart (Lee, 1951; Hammer et al., 2010; Müller, 2015), as is very well summarized in the review by Kraichnan and Montgomery (1980), Lesieur (1990) and Tabeling (2002). Hence, it is important to assess how to transfer the knowledge gained from a series of 2D simulations through to its corresponding 3D case.

Well-controlled laboratory and numerical data, therefore, formed the foundation for our understanding of the physics of the flows due to hydrodynamic instability. While the flow fields are obviously inhomogeneous, the measurements in terms of the component kinetic energy ratios and Lumley tensor suggested the anisotropy as well. The energy transfer analysis, constructed with databases from numerical simulations, provided the detailed information on the input, nonlinear transfer, and dissipation process. The mixed zones have been characterized in terms of the mixed width and mixedness. Moreover, a recent suggestion to use mixed mass as a more direct marker of the mixing process is advanced.

We have provided a detailed discussion of the late-time self-similar scaling for the RT and RM growth factors, α and θ . These parameters are influenced by the initial conditions. It should be noted that some recent Reynolds-averaging-Navier–Stokes (RANS) models set their coefficients based on a self-similar analysis. In some cases, RT and RM instabilities induced flows can transition to turbulence. Both the spatial and temporal criteria to achieve the transition to turbulence have been presented.

Yet, the mix models are remaining the only efficient way to carry out practical engineering calculations. Over the years, mix models of various complexities and capabilities have been proposed. The simulation and experimental data, such as well-known reshock data of Vetter and Sturtevant (1995), have been used routinely for validating these models. With advanced diagnostic tools, the laboratory facilities at several universities and national laboratories are proving increasingly accurate data for calibrating the free parameters of the empirical models.

In summary, it is fair to say that significant advancement has been made in understanding the physics of flow fields induced by Rayleigh–Taylor and Richtmyer–Meshkov instabilities. As documented in this review, major progress has been made with many ingenious analytical treatments. However, it is clear that much of our understanding would not have been possible without the sophisticated laboratory and high-energy-density-physics experimental work carried out over the past two decades. In the meantime, intensive numerical simulations performed on the state-of-art supercomputers offered the insightful statistics and structures of the flows. These efforts have largely been driven by the desire to generate data at high Reynolds numbers. The resulting databases might soon be in a position to provide much required information to understand the physics and develop mix models. Indeed, while the Reynolds number in supernovae appears out of reach at 10^{10} (Ryutov et al., 1999), accurate and time dependent three-dimensional computations or measurements of the large scales may be all that is needed from an application perspective (Zhou, 2007).

The author would like to register two remarks. First, as this review covers a significant body of work, there is always a chance to misconstrue the contents of the articles cited. Therefore, this review attempts to follow the text, meaning, and intent of the researchers as much as possible. This is appropriate as the focus is on the mosaic constructed from many contributions. Second, while the best efforts were made to incorporate major contributions to this vast field, but it would be virtually impossible to give a complete account on all present investigations, which was noted by H.J. Kull already in his *Physics Reports* review article published 1991. Hence, for that reason, references in this review are by no means exhaustive. I apologize in advance to those whose work may not be cited appropriately and would appreciate very much for the readers or authors to bring these omissions to my attention (yezhou@llnl.gov).

Acknowledgments

The author is deeply indebted to Prof. D.L. Youngs (Atomic Weapons Establishment, United Kingdom, now with University of Strathclyde), Dr. K.O. Mikaelian, Dr. M.G. Mustafa, and Dr. O. Schilling (Lawrence Livermore National Laboratory), Dr.

T.T. Clark (Los Alamos National Laboratory, now with University of New Mexico), Dr. R.J.R. Williams (Atomic Weapons Establishment, United Kingdom), and Dr. R. Rubinstein (NASA Langley Research Center) for their careful review and insightful suggestions. He is extremely grateful to Drs. W.H. Cabot, D.S. Clark, S.G. Glendinning, M. Ulitsky, and Q. Zhang for their fruitful discussions and detailed feedback. He acknowledges many stimulating discussions over the years with Drs. M.J. Andrews, A. Banerjee, R. Bonazza, A.C. Buckingham, A.W. Cook, S.B. Dalziel, G. Dimonte, P.E. Dimotakis, R.P. Drake, D. Drikakis, S. Gauthier, F.F. Grinstein, S.W. Haan, O.A. Hurricane, J.W. Jacobs, C.E. Leith, D. Livescu, D.I. Meiron, E.E. Meshkov, K.P. Prestridge, P. Ramaprabhu, B.A. Remington, H.F. Robey, D.D. Ryutov, C.-W. Shu, B. Thornber, L. Welser-Sherrill, and G.B. Zimmerman. The author also thanks the valuable comments and assistances by Drs. P. Anninos, C. Batha, G.C. Burton, P. Carlès, G. Carnevale, R. Cohen, M. Davies Wykes, T.R. Dittrich, F.W. Doss, D. Eliason, K.A. Flippo, R.A. Gore, J. Griffond, C.M. Huntington, B.I. Jun, V.V. Krivets, A.L. Kuhl, A. Lawrie, E. Leinov, M. Lombardini, S. Lugomer, S.A. McLaren, W.D. Mostert, S.D. Murray, S.R. Nagel, B.J. Olson, C. Pantano, L. J. Perkins, K.S. Raman, D. Ranjan, S. Reckinger, M.M. Scase, J.D. Schwarzkopf, M.A.R. Skinner, K.L. Stalsberg-Zarling, C. Tomkins, P. Wang, and C. Weber. Finally, the author is appreciative of Prof. D. Jewitt for providing his original photograph. This work was performed under the auspices of the Lawrence Livermore National Security, LLC under Contract No. DE-AC52-07NA27344.

References

- Aglitskiy, Y., Velikovich, A.L., Karasik, M., Serlin, V., Pawley, C.J., Schmitt, A.J., Obenschain, S.P., Mostovych, A.N., Gardner, J.H., Metzler, N., 2002. Direct observation of mass oscillations due to ablative Richtmyer–Meshkov instability and feedout in planar plastic targets. *Phys. Plasmas* 9, 2264.
- Aglitskiy, Y., Velikovich, A.L., Karasik, M., Metzler, N., Zalesak, S.T., Schmitt, A.J., Phillips, L., Gardner, J.H., Serlin, V., Weaver, J.L., Obenschain, S.P., 2010. Basic hydrodynamics of Richtmyer–Meshkov-type growth and oscillations in the inertial confinement fusion-relevant conditions. *Philos. Trans. R. Soc. Lond. Ser. A* 368, 1739.
- Akula, B., 2014. Experimental Investigation of Buoyancy Driven Mixing with and Without Shear at Different Atwood Numbers (Ph.D. thesis), Texas A&M University.
- Akula, B., Ranjan, D., 2016. Dynamics of buoyancy-driven flows at moderately high Atwood numbers. *J. Fluid Mech.* 795, 313.
- Akula, B., Andrews, M.J., Ranjan, D., 2013. Effect of shear on Rayleigh–Taylor mixing at small Atwood number. *Phys. Rev. E* 87, 033013.
- Akula, B., Suchandrea, P., Mikhæil, M., Ranjan, D., 2017. Dynamics of unstably stratified free shear flows: An experimental investigation of coupled Kelvin–Helmholtz and Rayleigh–Taylor instability. *J. Fluid Mech.* 816, 619.
- Alexeev, A., Oron, A., 2007. Suppression of the Rayleigh–Taylor instability of thin liquid films by the Marangoni effect. *Phys. Fluids* 19, 082101.
- Alfè, D., Kresse, G., Gillan, M.J., 2000. Structure and dynamics of liquid iron under Earth's core conditions. *Phys. Rev. B* 61, 132.
- Ali, S., Moslem, W.M., Shukla, P.K., Schlickeiser, R., 2007. Linear and nonlinear ion-acoustic waves in an unmagnetized electron-positron-ion quantum plasma. *Phys. Plasmas* 14, 082307.
- Almgren, A.S., Beckner, V.E., Bell, J.B., Day, M.S., Howell, L.H., Joggerst, C.C., Lijewski, M.J., Nonaka, A., Singer, M., Zingale, M., 2010. CASTRO: a new compressible astrophysical solver. I. Hydrodynamics and self-gravity. *Astrophys. J.* 715, 1221.
- Alon, U., Shvarts, D., Mukamel, D., 1993. Scale invariant regime in Rayleigh–Taylor bubble-front dynamics. *Phys. Rev. E* 48, 1008.
- Alon, U., Hecht, J., Mukamel, D., Shvarts, D., 1994. Scale invariant mixing rates of hydrodynamically unstable interfaces. *Phys. Rev. Lett.* 72, 2867.
- Alon, U., Hecht, J., Ofer, D., Shvarts, D., 1995. Power laws and similarity of Rayleigh–Taylor and Richtmyer–Meshkov mixing fronts at all density ratios. *Phys. Rev. Lett.* 74, 534.
- Aluie, H., Kurien, S., 2011. Joint downscale fluxes of energy and potential enstrophy in rotating stratified Boussinesq flows. *Europhys. Lett.* 96, 44006.
- Alvi, F.S., Krothapalli, A., Washington, D., 1996. Experimental study of a compressible countercurrent turbulent shear layer. *AIAA J.* 34, 728.
- Amendt, P., 2006. Bell-Plesset effects for an accelerating interface with contiguous density gradients. *Phys. Plasmas* 13, 042702.
- Amendt, P., Colvin, J.D., Ramshaw, J.D., Robey, H.F., Landen, O.L., 2003. Modified Bell-Plesset effect with compressibility: Application to double-shell ignition target designs. *Plasma* 10, 820.
- Amiroudine, S., Boutrouf, K., Zappoli, B., 2005. The stability analysis of two layers in a supercritical pure fluid: Rayleigh–Taylor-like instabilities. *Phys. Fluids* 17, 054102.
- Andre, M.L., 1999. The French Megaloue Laser project (LMJ). *Fusion Eng. Des.* 44, 43.
- Andrews, M.J., 1995. Accurate computation of convective transport in transient two-phase flow. *Internat. J. Numer. Methods Fluids* 21, 205.
- Andrews, M.J., Dalziel, S.B., 2010. Small Atwood number Rayleigh–Taylor experiments. *Phil. Trans. R. Soc. A* 368, 1663.
- Andrews, M.J., Spalding, D.B., 1990. A simple experiment to investigate two-dimensional mixing by Rayleigh–Taylor instability. *Phys. Fluids A* 2, 922.
- Andrews, M.J., Youngs, D.L., Livescu, D., Wei, T., 2014. Computational studies of two-dimensional Rayleigh–Taylor driven mixing for a tilted-rig. *ASME J. Fluids Eng.* 136, 091212.
- Andronov, V.A., Bakhrakh, S.M., Meshkov, E.E., Mokhov, V.N., Nikiforov, V.V., Pevnitskii, A.V., Tolshmyakov, A.I., 1976. Turbulent mixing at contact surface accelerated by shock waves. *Sov. Phys.–JETP* 44, 424.
- Andronov, V.A., Bakhrakh, S.M., Mokhov, V.N., Nikiforov, V.V., Pevnitskii, A.V., 1979. Effect of turbulent mixing on the compression of laser targets. *Sov. Phys. JETP Lett.* 29, 56.
- Andronov, V.A., Bakhrakh, S.M., Meshkov, E.E., Nikiforov, V.V., Pevnitskii, A.V., Tolshmyakov, A.I., 1982. An experimental investigation and numerical modeling of turbulent mixing in one-dimensional flows. *Sov. Phys. Dokl.* 27, 393.
- Andronov, V.A., Zhidov, I.G., Meshkov, E.E., Nevmerzhitskii, N.V., Nikiforov, V.V., Razin, A.N., Rogatchev, V.G., Tolshmyakov, A.I., Yanilkin, Y.V., 1995. Computational and Experimental Studies of Hydrodynamic Instabilities and Turbulent Mixing (Review of VNIIEF Efforts) (no. LA-12896). Los Alamos National Lab., NM (United States).
- Anninos, P., Fragile, P.C., Wilson, J., Murray, S.D., 2012. Three-dimensional moving-mesh simulations of galactic center cloud G2. *Astrophys. J.* 759, 132.
- Asida, S.M., Livne, E., Stein, J., Metzker, L., 2005. 3D simulations of Rayleigh–Taylor using "Vulcan3D". *Astrophys. Space Sci.* 298, 363.
- Aslangil, D., Banerjee, A., Lawrie, A.G.W., 2016. Numerical investigation of initial condition effects on Rayleigh–Taylor instability with acceleration reversals. *Phys. Rev. E* 94, 053114.
- Atzeni, S., Meyer-ter-Vehn, J., 2004. The Physics of Inertial Fusion. Oxford University Press, Oxford, UK.
- Axford, W.I., 1964. The stability of ionization fronts. *Astrophys. J.* 140, 112.
- Azarova, O.A., 2015. Generation of Richtmyer–Meshkov and secondary instabilities during the interaction of an energy release with a cylinder shock layer. *Aerosp. Sci. Technol.* 42, 376.
- Azechi, H., Shigemori, K., Nakai, M., Miyanaga, N., Takabe, H., 2000. Formation of initial perturbation of Rayleigh–Taylor instability in supernovae and laser-irradiated targets – is there any similarity?. *Astrophys. J. Suppl. Ser.* 127, 219.

- Bai, J.S., Zou, L.Y., Wang, T., Liu, K., Huang, W.B., Liu, J.H., Li, P., Tan, D.W., Liu, C.L., 2010. Experimental and numerical study shock-accelerated elliptic heavy gas cylinders. *Phys. Rev. E* 82, 056318.
- Baker, L., 1983. Compressible Rayleigh–Taylor instability. *Phys. Fluids* 26, 950.
- Baker, L., Freeman, J.R., 1981. Heuristic model of the nonlinear Rayleigh–Taylor instability. *J. Appl. Phys.* 52, 655.
- Bakhrakh, S.M., Klopov, B.A., Meshkov, E.E., Tolshmyakov, A.I., Yanilkin, Y.V., 1995. Development of perturbations of a shock-accelerated interface between two gases. *J. Appl. Mech. Tech. Phys.* 36, 341.
- Bakhrakh, S.M., Drennov, O.B., Kovalev, N.P., Lebedev, A.I., Meshkov, E.E., Mikhailov, A.L., Nevmerzhitsky, N.V., Nizovtsev, P.N., Rayevsky, V.A., Simonov, G.P., Solovyev, V.P., Zhidov, I.G., 1997. Hydrodynamic Instability in Strong Media. No. UCRL-CR-126710. Lawrence Livermore National Lab., CA (United States). Russian Federal Nuclear Center (Russian Federation).
- Bakhsh, A., Gao, S., Samtaney, R., Wheatley, V., 2016. Linear simulations of the cylindrical Richtmyer–Meshkov instability in magnetohydrodynamics. *Phys. Fluids* 28, 034106.
- Bakhsh, A., Samtaney, R., 2017. Linear analysis of converging Richtmyer–Meshkov instability in the presence of an azimuthal magnetic field. *ASME. J. Fluids Eng.* <http://dx.doi.org/10.1115/1.4038487>.
- Balakumar, B.J., Orlicz, G.C., Tomkins, C.D., Prestridge, K.P., 2008a. Dependence of growth patterns and mixing width on initial conditions in Richtmyer–Meshkov unstable fluid layers. *Phys. Scr.* 132, 014013.
- Balakumar, B.J., Orlicz, G.C., Tomkins, C.D., Prestridge, K.P., 2008b. Simultaneous particle-image velocimetry–planar laser-induced fluorescence measurements of Richtmyer–Meshkov instability growth in a gas curtain with and without reshock. *Phys. Fluids* 20, 124103.
- Balakumar, B.J., Orlicz, G.C., Ristorcelli, J.R., Balasubramanian, S., Prestridge, K.P., Tomkins, C.D., 2012. Turbulent mixing in a Richtmyer–Meshkov fluid layer after reshock: velocity and density statistics. *J. Fluid Mech.* 696, 67.
- Balasubramanian, S., Orlicz, G.C., Prestridge, K.P., Balakumar, B.J., 2012. Experimental study of initial condition dependence on Richtmyer–Meshkov instability in the presence of reshock. *Phys. Fluids* 24, 034103.
- Balasubramanian, S., Orlicz, G.C., Prestridge, K.P., 2013. Experimental study of initial condition dependence on turbulent mixing in shock-accelerated Richtmyer–Meshkov fluid layers. *J. Turbulence* 14, 170.
- Baldwin, K.A., Scase, M.M., Hill, R.J.A., 2015. The Inhibition of the Rayleigh–Taylor Instability by Rotation. *Sci. Rep.* 5, 11706 Corrigendum: The Inhibition of the Rayleigh–Taylor Instability by Rotation, *Sci. Rep.* 6 (2016) 26574.
- Balsara, D., Shu, C.-W., 2000. Monotonicity preserving weighted essentially non-oscillatory schemes with increasingly high order of accuracy. *J. Comput. Phys.* 160, 405.
- Baltrusaitis, R.M., Gittings, M.L., Weaver, R.P., Benjamin, R.F., Budzinski, J.M., 1996. Simulation of shock-generated instabilities. *Phys. Fluids* 8, 2471.
- Banerjee, A., Andrews, M.J., 2006. Statistically steady measurements of Rayleigh–Taylor mixing in a gas channel. *Phys. Fluids* 18, 035107.
- Banerjee, A., Andrews, M.J., 2009. 3-D Simulations to investigate initial condition effects on the growth of Rayleigh–Taylor mixing. *Int. J. Heat Mass Transfer* 52, 3906.
- Banerjee, A., Mutnuri, L.A.R., 2012. Passive and reactive scalar measurements in a transient high-Schmidt-number Rayleigh–Taylor mixing layer. *Exp. Fluids* 53, 717.
- Banerjee, A., Gore, R.A., Andrews, M.J., 2010a. Development and validation of a turbulent-mix model for variable-density and compressible flows. *Phys. Rev. E* 82, 046309.
- Banerjee, A., Kraft, W.N., Andrews, M.J., 2010b. Detailed measurements of a statistical steady Rayleigh–Taylor mixing layer from small to high Atwood numbers. *J. Fluids Mech.* 659, 127.
- Banerjee, R., Mandal, L., Khan, M., Gupta, M.R., 2012. Effect of viscosity and shear flow on the nonlinear two fluid interfacial structures. *Phys. Plasmas* 19, 122105.
- Barannyk, L.L., Papageorgiou, D.T., Petropoulos, P.G., 2012. Suppression of Rayleigh–Taylor instability using electric fields. *Math. Comput. Simulation* 82, 1008.
- Barenblatt, G.I., 1983. Self-similar turbulence propagation from an instantaneous plane source. In: Barenblatt, G.I., Looss, G., Joseph, D.D. (Eds.), *Nonlinear Dynamics and Turbulence*. Pitman Publishing, London.
- Barmparousis, C., Drikakis, D., 2017. Multi-dimensional quantification of uncertainty and application to a turbulent mixing model. *Internat. J. Numer. Methods Fluids* 85, 385.
- Barnes, C.W., Batha, S.H., Dunne, A.M., Magelssen, G.R., Rothman, S., Day, R.D., Elliott, N.E., Haynes, D.A., Holmes, R.L., Scott, J.M., Tubbs, D.L., Youngs, D.L., Boehly, T.R., Jaanimagi, P., 2002. Observation of mix in a compressible plasma in a convergent cylindrical geometry. *Phys. Plasmas* 9, 4431.
- Barnes, J.F., Blewett, P.J., McQueen, R.G., Meyer, K.A., Venable, D., 1974. Taylor instability in solids. *J. Appl. Phys.* 45, 727.
- Barnes, J.F., Janney, D.H., London, R.K., Meyer, K.A., Sharp, D.H., 1980. Further experimentation on Taylor instability in solid. *J. Appl. Phys.* 51, 4678.
- Barton, N.R., Rhee, M., 2013. A multiscale strength model for tantalum over an extended range of strain rates. *J. Appl. Phys.* 114, 123507.
- Barton, N.R., Bernier, J.V., Becker, R., Arsenlis, A., Cavallo, R., Marian, J., Rhee, M., Park, H.-S., Remington, B.A., Olson, R.T., 2011. A multiscale strength model for extreme loading conditions. *J. Appl. Phys.* 109, 073501.
- Bashurov, V.V., Bondarenko, Yu A., Gubkov, E.V., Dudin, V.I., Meshkov, E.E., Poduvalov, A.N., Shanin, A.A., et al., 1997. Experimental and numerical evolution studies for 2D perturbations of the interface accelerated by shock waves. *Laser Part. Beams* 15, 101.
- Batchelor, G.K., 1953. *The Theory of Homogeneous Turbulence*. Cambridge University Press, Cambridge, UK.
- Batchelor, G.K., 1969. Computation of the energy spectrum in homogeneous two-dimensional turbulence. *Phys. Fluids* 12, II–233.
- Batchelor, G.K., Proudman, I., 1954. The effect of rapid distortion of a fluid in turbulent motion. *Q. J. Mech. Appl. Math.* 7, 83.
- Bates, K.R., Nikiforakis, N., Holder, D., 2007. Richtmyer–Meshkov instability induced by the interaction of a shock wave with a rectangular block of SF₆. *Phys. Fluids* 19, 036101.
- Baus, M., Hansen, J.P., 1980. Statistical mechanics of simple Coulomb system. *Phys. Rep.* 59, 1.
- Begelman, M.C., Cioffi, D.F., 1989. Overpressured cocoons in extragalactic radio sources. *Astrophys. J.* 345, L21.
- Belen'kii, S.Z., Fradkin, E.S., 1965. Theory of turbulent mixing. *Tr. Fiz. Inst. Akad. Nauk SSSR* 29, 207.
- Bell, G.I., 1951. Taylor Instability on Cylinders and Spheres in the Small Amplitude Approximation, Los Alamos National Laboratory, Report LA-1321.
- Bell, J.H., Mehta, R.D., 1990. Development of a two-stream mixing layer from tripped and untripped boundary layers. *AIAA J.* 28, 2034.
- Bellman, R., Pennington, R.H., 1954. Effect of surface tension and viscosity on Taylor instability. *Q. Appl. Math.* 12, 151.
- Bernstein, I.B., Book, D.L., 1983. Effect of compressibility on the Rayleigh–Taylor instability. *Phys. Fluids* 26, 453.
- Besnard, D., Harlow, F.H., 1988. Turbulence in multiphase flow. *Int. J. Multiph. Flow* 14, 679.
- Besnard, D., Harlow, F.H., Rauenzahn, R.M., 1987. Conservation and Transport Properties of Turbulence with Large-Density Variations, Los Alamos National Laboratory Report LA-10911-MS.
- Besnard, D., Haas, J.F., Rauenzahn, R.M., 1989. Statistical modeling of shock-interface interaction. *Physica D* 37, 227.
- Besnard, D., Harlow, F.H., Rauenzahn, R.M., Zemach, C., 1992. Turbulence Transport Equations for Variable-Density Turbulence and their Relationship to Two-Field Models, Los Alamos National Laboratory Report LA-12303-MS.
- Bethe, H.A., 1990. Supernova mechanisms. *Rev. Modern Phys.* 62, 801.
- Betti, R., Hurricane, O.A., 2016. Inertial-confinement fusion with lasers. *Nat. Phys.* 12, 435.

- Betti, R., Goncharov, V.N., McCrory, R.L., Sorotkin, P., Verdon, C.P., 1996. Self-consistent stability analysis of ablation fronts in inertial confinement fusion. *Phys. Plasmas* 3, 2122.
- Betti, R., Goncharov, V.N., McCrory, R.L., Verdon, C.P., 1998. Growth rates of the ablative Rayleigh–Taylor instability in inertial confinement fusion. *Phys. Plasmas* 5, 1446.
- Betti, R., Umansky, M., Lobatchev, V., Goncharov, V.N., McCrory, R.L., 2001. Hot-spot dynamics and deceleration-phase Rayleigh–Taylor instability of imploding inertial confinement fusion capsules. *Phys. Plasmas* 8, 5257.
- Bhatia, P.K., 1974. Rayleigh–Taylor instability of a viscous compressible plasma of variable density. *Astrophys. Space Sci.* 26, 319.
- Biamino, L., Mariani, C., Jourdan, G., Houas, L., Vandenboomgaerde, M., Souffland, D., 2014. Planar shock focusing through perfect gas lens: First experimental demonstration. *ASME J. Fluids Eng.* 136, 091204.
- Biamino, L., Jourdan, G., Mariani, C., Houas, L., Vandenboomgaerde, M., Souffland, D., 2015. On the possibility of studying the converging Richtmyer–Meshkov instability in a conventional shock tube. *Exp. Fluids* 56, 26.
- Biferale, L., Procaccia, I., 2005. Anisotropy in turbulent flows and in turbulent transport. *Phys. Rep.* 414, 43.
- Biferale, L., Mantovani, F., Sbragaglia, M., Scagliarini, A., Toschi, F., Tripiccione, R., 2010. High resolution numerical study of Rayleigh–Taylor turbulence using a thermal lattice Boltzmann scheme. *Phys. Fluids* 22, 115112.
- Biferale, L., Mantovani, F., Sbragaglia, M., Scagliarini, A., Toschi, F., Tripiccione, R., 2011. Reactive Rayleigh–Taylor systems: Front propagation and non-stationarity. *Europhys. Lett.* 94, 54004.
- Bilger, R.W., 1975. A note on favre averaging in variable density flows. *Combust. Sci. Technol.* 11, 215.
- Binnie, A.M., 1953. The stability of the surface of a cavitation bubble. *Math. Proc. Camb. Phil. Soc.* 49, 151.
- Birkhoff, G., 1955. Taylor Instability and Laminar Mixing, University of California Report No. LA-1862.
- Bisbas, T.G., 2016. Triggered star formation. In: *The Interstellar Medium, Expanding Nebulae and Triggered Star Formation*. Springer International Publishing, pp. 35–50.
- Black, W.J., Denissen, N., McFarland, J.A., 2017. Evaporation effects in shock driven multiphase instabilities. *ASME J. Fluids Eng.* 139, 071204.
- Blake, G.M., 1972. Fluid dynamic stability of double radio sources. *Mon. Not. R. Astron. Soc.* 156, 67.
- Bo, W., Jin, H., Kim, D., Liu, X., Lee, H., Pesteau, N., Yu, Y., Glimm, J., Grove, J.W., 2008. Comparison and validation of multi phase closure models. *Comput. Math. Appl.* 56, 1291.
- Bodner, S.E., 1974. Rayleigh–Taylor instability and laser-pellet fusion. *Phys. Rev. Lett.* 33, 761.
- Boehly, T.R., Craxton, R.S., Hinterman, T.H., Kelly, J.H., Kessler, T.J., Kumpan, S.A., Letzring, S.A., Marshall, F.J., McCrory, R.L., Morse, S.F.B., Seka, W., Sowes, J.M., Verdon, C.P., 1997. Initial performance results of the OMEGA laser system. *Opt. Commun.* 133, 495.
- Boffetta, G., 2007. Energy and enstrophy fluxes in the double cascade of two-dimensional turbulence. *J. Fluid Mech.* 589, 253.
- Boffetta, G., Ecke, R., 2012. Two-dimensional turbulence. *Annu. Rev. Fluid Mech.* 44, 427.
- Boffetta, G., Mazzino, A., Musacchio, S., Vozella, L., 2009. Kolmogorov scaling and intermittency in Rayleigh–Taylor turbulence. *Phys. Rev. E* 79, 065301.
- Boffetta, G., Mazzino, A., Musacchio, S., Vozella, L., 2010. Rayleigh–Taylor instability in a viscoelastic binary fluid. *J. Fluid Mech.* 643, 127.
- Boffetta, G., Mazzino, A., Musacchio, S., 2011. Effects of polymer additives on Rayleigh–Taylor turbulence. *Phys. Rev. E* 83, 056318.
- Boffetta, G., De Lillo, F., Mazzino, A., Musacchio, S., 2012. Bolgiano scale in confined Rayleigh–Taylor turbulence. *J. Fluid Mech.* 690, 426.
- Boffetta, G., Mazzino, A., Musacchio, S., 2016. Rotating Rayleigh–Taylor turbulence. *Phys. Rev. Fluids* 1, 054405.
- Bolgiano, R., 1959. Turbulent spectra in a stably stratified atmosphere. *J. Geophys. Res.* 64, 2226.
- Bonazza, R., Sturtevant, B., 1996. X-ray measurements of growth rates at a gas interface accelerated by shock waves. *Phys. Fluids* 8, 2496.
- Bond, C., Hill, D.J., Dimotakis, P.E., 2009. Shock focusing in a planar convergent geometry: experiment and simulation. *J. Fluid Mech.* 641, 297.
- Bond, D., Wheatley, V., Samtaney, R., Pullin, D.I., 2017. Richtmyer–Meshkov instability of a thermal interface in a two-fluid plasma. *J. Fluid Mech.* 833, 332.
- Boris, J., Grinstein, F., Oran, E., Kolbe, R., 1992. New insights into large eddy simulation. *Fluid Dyn. Res.* 10, 199.
- Bouquet, S., Feix, M.R., Leach, P.G.L., 1991. Properties of second-order ordinary differential equations invariant under time translation and self-similar transformation. *J. Math. Phys.* 32, 1480.
- Bouquet, S., Gandeboeuf, P., Pailhories, P., 2007. Analytical study of the buoyancy-drag equation. *Math. Methods Appl. Sci.* 30, 2027.
- Boureima, I., Ramaprabhu, P., Attal, N., 2017. Properties of the turbulent mixing layer in a spherical implosion. *ASME J. Fluids Eng.* <http://dx.doi.org/10.1115/1.4038401>.
- Bourgade, J.L., Marmoret, R., Darbon, S., Rosch, R., Troussel, P., Villette, B., Glebov, V., et al., 2008. Diagnostics hardening for harsh environment in Laser Mégajoule. *Rev. Sci. Instrum.* 79, 10F301.
- Boussinesq, V.J., 1877. *Essai sur la théorie des eaux courantes*. Mem. Présentés par Divers Savants à L'Académie des Sciences, Paris 23, 1.
- Bouzgarrou, G., 2014. Analyse d'un mélange gazeux issu d'une instabilité de Richtmyer–Meshkov (Ph.D. thesis), Univ. de Toulouse, France.
- Bouzgarrou, G., Bury, Y., Jamme, S., Joly, L., Haas, J.-F., 2014. Laser doppler velocimetry measurements in turbulent gaseous mixing induced by the Richtmyer–Meshkov instability: Statistical convergence issues and turbulence quantification. *ASME J. Fluids Eng.* 136, 091209.
- Braginskii, S.I., 1958. Transport phenomena in a completely ionized two-temperature plasma. *Sov. Phys. JETP* 6, 358.
- Braginskii, S.I., 1965. In: Leontovich, M.A. (Ed.), *Review of Plasma Physics*, vol. 1. Consultants Bureau, New York, p. 205.
- Bret, A., 2007. Filamentation instability in a quantum plasma. *Phys. Plasmas* 14, 084503.
- Brouillette, M., 2002. The Richtmyer–Meshkov instability. *Annu. Rev. Fluid Mech.* 34, 445.
- Brouillette, M., Bonazza, R., 1999. Experiments on the Richtmyer–Meshkov instability: wall effects and wave phenomena. *Phys. Fluids* 11, 1127.
- Brouillette, M., Sturtevant, B., 1989. Growth induced by multiple shock waves normally incident on plane gaseous interfaces. *Physica D* 37, 248.
- Brouillette, M., Sturtevant, B., 1993. Experiments on the Richtmyer–Meshkov instability: small-scale perturbations on a plane interface. *Phys. Fluids A* 5, 916.
- Brouillette, M., Sturtevant, B., 1994. Experiments on the Richtmyer–Meshkov instability: single-scale perturbations on a continuous interface. *J. Fluid Mech.* 263, 271.
- Browand, F.K., Winant, C.D., 1973. Laboratory observations of shear-layer instability in a stratified fluid. *Bound.-Layer Meteorol.* 5, 67.
- Brown, G.L., Roshko, A., 1974. On density effects and large structure in turbulent mixing layers. *J. Fluid Mech.* 64, 775.
- Brown, M.A., Batha, C.A., Williams, R.J.R., 2014. Statistics for assessing mixing in a finite element hydrocode. *ASME J. Fluids Eng.* 136, 091103.
- Brüggen, M., Scannapieco, E., Heinz, S., 2009. Evolution of X-ray cavities. *Mon. Not. R. Astron. Soc.* 395, 2210.
- Budil, K.S., Remington, B.A., Peyser, T.A., Mikaelian, K.O., Miller, P.L., Woolsey, N.C., Wood-Vasey, W.M., Rubenchik, A.M., 1996. Experimental comparison of classical versus ablative Rayleigh–Taylor instability. *Phys. Rev. Lett.* 76, 4536.
- Budil, K.S., Lasinski, B., Edwards, M.J., Wan, A.S., Remington, B.A., Weber, S.V., Glendinning, S.G., Suter, L., Stry, P.E., 2001. The ablation-front Rayleigh–Taylor dispersion curve in indirect drive. *Phys. Plasmas* 8, 2344.
- Bud'ko, A.B., Velikovich, A.L., Kleev, A.I., Liberman, M.A., Felber, F.S., 1989. Theory of the dynamic stability of plasma systems. *Sov. Phys.-JETP* 68, 279.

- Bud'ko, A.B., Liberman, M.A., Velikovich, A.L., Felber, F.S., 1990. Suppression of Rayleigh–Taylor and bulk convective instabilities in imploding plasma liners and pinches. *Phys. Fluids* B 1159.
- Budzinski, J.M., Benjamin, R.F., Jacobs, J.W., 1994. Influence of initial conditions on the flow patterns of a shock-accelerated thin fluid layer. *Phys. Fluids* 6, 3510.
- Burlot, A., Gréa, B.-J., Godefert, F.S., Cambon, C., Griffond, J., 2015. Spectral modelling of high Reynolds number unstably stratified homogeneous turbulence. *J. Fluid Mech.* 765, 17.
- Burton, G.C., 2008. The nonlinear large-eddy simulation method (nLES) applied to $Sc \approx 1$ and $Sc \gg 1$ passive-scalar mixing. *Phys. Fluids* 20, 035103.
- Burton, G.C., 2011. Study of ultrahigh Atwood-number Rayleigh–Taylor mixing dynamics using the nonlinear large-eddy simulation method. *Phys. Fluids* 23, 045106.
- Buttler, W.T., Oró, D.M., Preston, D.L., Mikaelian, K.O., Cherne, F.J., Hixson, R.S., Mariam, F.G., Morris, C., Stone, J.B., Terrones, G., Tupa, D., 2012. Unstable Richtmyer–Meshkov growth of solid and liquid metal in vacuum. *J. Fluid Mech.* 703, 60.
- Bychkov, V., Marklund, M., Modestov, M., 2008. The Rayleigh–Taylor instability and internal waves in quantum plasmas. *Phys. Lett. A* 372, 3042.
- Cabot, W., 2006. Comparison of two- and three-dimensional simulations of miscible Rayleigh–Taylor instability. *Phys. Fluids* 18, 045101.
- Cabot, W., Cook, A.W., 2006. Reynolds number effects on the Rayleigh–Taylor instability with possible implications for type-Ia supernovae. *Nat. Phys.* 2, 562.
- Cabot, W., Zhou, Y., 2013. Statistical measurements of scaling and anisotropy of turbulent flows induced by Rayleigh–Taylor instability. *Phys. Fluids* 25, 015107.
- Calder, A.C., Fryxell, B., Plewa, T., Rosner, R., Dursi, L.J., Weirs, V.G., Dupont, T., Robey, H.F., Kane, J.O., Remington, B.A., Drake, R.P., Dimonte, G., Zingale, M., Timmes, F.X., Olson, K., Ricker, P., MacNeice, P., Tufo, H.M., 2002. On validating an astrophysical simulation code. *Astrophys. J. Suppl. Ser.* 143, 201.
- Cao, J.T., Wu, Z.W., Ren, H.J., Li, D., 2008. Effects of shear flow and transverse magnetic field on Richtmyer–Meshkov instability. *Phys. Plasmas* 15, 042102.
- Cao, J.T., Li, D., Wu, Z.W., 2009. Richtmyer–Meshkov instability of a stratified fluid in transverse magnetic field. *Phys. Plasmas* 16, 062103.
- Cao, Y.G., Chow, W.K., 2005. A theoretical analysis on Rayleigh–Taylor and Richtmyer–Meshkov mixing. *J. Phys. A* 38, 6613.
- Cao, Y.G., Chow, W.K., Fong, N.K., 2011. Solutions to buoyancy-drag equation for dynamical evolution of Rayleigh–Taylor and Richtmyer–Meshkov instabilities. *Commun. Theor. Phys.* 56, 751.
- Carnevale, G., Orlandi, P., Zhou, Y., Kloosterziel, R., 2002. Rotation suppression of Rayleigh–Taylor instability. *J. Fluid Mech.* 457, 181.
- Casey, D.T., Smalyuk, V.A., Raman, K.S., Peterson, J.L., Berzak Hopkins, L., Callahan, D.A., Clark, D.S., Dewald, E.L., Dittrich, T.R., Haan, S.W., Hinkel, D.E., Hoover, D., Hurricane, O.A., Kroll, J.J., Landen, O.L., Moore, A.S., Nikroo, A., Park, H.-S., Remington, B.A., Robey, H.F., Rygg, J.R., Salmonson, J.D., Tommasini, R., Widmann, K., 2014. Reduced instability growth with high-adiabat high-foot implosions at the National Ignition Facility. *Phys. Rev. E* 90, 011102(R).
- Casner, A., Smalyuk, V.A., Masse, L., Igumenshchev, I., Liberatore, S., Jacquet, L., Chicanne, C., et al., 2012. Designs for highly nonlinear ablative Rayleigh–Taylor experiments on the National Ignition Facility. *Phys. Plasmas* 19, 082708.
- Casner, A., Smalyuk, V., Masse, L., Moore, A., Delorme, B., Martinez, D., Igumenshev, I., Jacquet, L., Liberatore, S., Seugling, R., Chicane, C., 2013. Design and implementation plan for indirect-drive highly nonlinear ablative Rayleigh–Taylor instability experiments on the National Ignition Facility. *High Energy Density Phys.* 9, 32.
- Casner, A., Masse, L., Delorme, B., Martinez, D., Huser, G., Galmiche, D., Liberatore, S., et al., 2014. Progress in indirect and direct-drive planar experiments on hydrodynamic instabilities at the ablation front. *Phys. Plasmas* 21, 122702.
- Casner, A., Caillaud, T., Darbon, S., Duval, A., Thfouin, I., Jadaud, J.P., LeBreton, J.P., Reverdin, C., Rosse, B., Rosch, R., Blanchot, N., Villette, B., Wrobel, R., Miquel, J.L., 2015a. 2014. LMJ/PETAL laser facility: Overview and opportunities for laboratory astrophysics. *High Energy Density Phys.* 17, 2.
- Casner, A., Martinez, D., Smalyuk, V., Masse, L., Kane, J.O., Villette, B., Faraut, J., et al., 2015b. Long duration X-ray drive hydrodynamics experiments relevant for laboratory astrophysics. *High Energy Density Phys.* 17, 146.
- Casner, A., Liberatore, S., Masse, L., Martinez, D., Haan, S.W., Kane, J., Moore, A.S., et al., 2016. Experimental evidence of a bubble-merger regime for the Rayleigh–Taylor Instability at the ablation front. *J. Phys. Conf. Ser.* 717, 012010.
- Celani, A., Mazzino, A., Vozella, L., 2006. Rayleigh–Taylor turbulence in two dimensions. *Phys. Rev. Lett.* 96, 134504.
- Ceschia, M., Nabergoj, R., 1978. On the motion of a nearly spherical bubble in a viscous liquid. *Phys. Fluids* 21, 140.
- Chakraborty, B.B., 1979. A note on Rayleigh–Taylor instability in the presence of rotation. *ZAMM Z. Angew. Math. Mech.* 59, 651.
- Chakraborty, B.B., Chandra, J., 1976. Rayleigh–Taylor instability in the presence of rotation. *Phys. Fluids* 19, 1851.
- Chambers, K., Forbes, L.K., 2011. The magnetic Rayleigh–Taylor instability for inviscid and viscous fluids. *Phys. Plasmas* 18, 052101.
- Chambers, K., Forbes, L.K., 2012. The cylindrical magnetic Rayleigh–Taylor instability for viscous fluids. *Phys. Plasmas* 19, 102111.
- Chandrasekhar, S., 1955. The character of the equilibrium of an incompressible fluid sphere of variable density and viscosity subject to radial acceleration. *Quart. J. Mech. Appl. Math.* 8, 1.
- Chandrasekhar, S., 1961. *Hydrodynamic and Hydromagnetic Stability*. Oxford Univ. Press, Oxford, UK.
- Chapman, S., Cowling, T., 1939. *The Mathematical Theory of Non-Uniform Gases: An Account of the Kinetic Theory of Viscosity, Thermal Conduction and Diffusion in Gases*. Cambridge Mathematical Library (Cambridge University Press), Cambridge.
- Charakhch'yan, A.A., 2000. Richtmyer–Meshkov instability of an interface between two media due to passage of two successive shocks. *J. Appl. Mech. Tech. Phys.* 41, 23.
- Charakhch'yan, A.A., 2001. Reshocking at the non-linear stage of Richtmyer–Meshkov instability. *Plasma Phys. Control. Fusion* 43, 1169.
- Chen, C.-J., Jaw, S.-Y., 1998. Fundamentals of Turbulence Modeling. In: *Combustion: An International Series*, Taylor & Francis, London.
- Chen, S., Doolen, G.D., 1998. Lattice Boltzmann method for fluid flows. *Annu. Rev. Fluid. Mech.* 30, 329.
- Chen, Y., Glimm, J., Sharp, D.H., Zhang, Q., 1996. A two-phase flow model of the Rayleigh–Taylor mixing zone. *Phys. Fluids* 8, 816.
- Cheng, B., Scannapieco, A.J., 2005. Buoyancy-drag mix model obtained by multifluid interpenetration equations. *Phys. Rev. E* 72, 046310.
- Cheng, B., Glimm, J., Saltz, D., Sharp, D.H., 1999. Boundary conditions for a two pressure two phase flow model. *Physica D* 133, 84.
- Cheng, B., Glimm, J., Sharp, D.H., 2000. Density dependence of Rayleigh–Taylor and Richtmyer–Meshkov mixing fronts. *Phys. Lett. A* 268 (2000), 366.
- Cheng, B., Glimm, J., Sharp, D.H., 2002a. Dynamical evolution of Rayleigh–Taylor and Richtmyer–Meshkov mixing fronts. *Phys. Rev. E* 66, 036312.
- Cheng, B., Glimm, J., Sharp, D.H., 2002b. A multi-temperature multiphase flow model. *ZAMM Z. Angew. Math. Phys.* 53, 211.
- Cheng, B., Glimm, J., Sharp, D.H., 2002c. A three-dimensional renormalization group bubble merger model for Rayleigh–Taylor mixing. *Chaos* 12, 267.
- Cheng, B., Glimm, J., Sharp, D.H., Yu, Y., 2005. A multiphase flow model for the unstable mixing of incompressible layered materials. *Phys. Fluids* 17, 087102.
- Cheng, B., Glimm, J., Sharp, D.H., Yu, Y., 2008. A multiphase flow model for the layered incompressible materials. *Phys. Scr. T* 132, 014016.
- Cheng, B., Kwan, T.J.T., Wang, Y.-M., Batha, S.H., 2013. Scaling laws for ignition at the National Ignition Facility from first principles. *Phys. Rev. E* 88, 041101.
- Cheng, B., Kwan, T.J.T., Wang, Y.-M., Batha, S.H., 2014a. On thermonuclear ignition criterion at the National Ignition Facility. *Phys. Plasmas* 21, 102707.
- Cheng, B., Kwan, T.J.T., Wang, Y.M., Yi, S.A., Batha, S.H., Wysocki, F.J., 2016. Effects of preheat and mix on the fuel adiabat of an imploding capsule. *Phys. Plasmas* 23, 120702.
- Cheng, T., Liu, S.-G., Liu, X.-Y., Hao, N., Teng, A.-P., Li, Y.-J., 2014b. Effects of density and thickness of interlayer on RT instability of interfaces. *Commun. Theor. Phys.* 61, 649.
- Cherfils, C., Glendinning, S.G., Galmiche, D., Remington, B.A., Richard, A.L., Haan, S., Wallace, R., Dague, N., Kalantar, D.H., 1999. Convergent Rayleigh–Taylor experiments on the Nova laser. *Phys. Rev. Lett.* 83, 5507.

- Chiravalle, V.P., 2006. The k-L turbulence model for describing buoyancy-driven fluid instabilities. *Laser Part. Beams* 24, 381.
- Chisnell, R.F., 1957. The motion of a shock wave in a channel, with applications to cylindrical and spherical shock waves. *J. Fluid Mech.* 2, 286.
- Chou, P.Y., 1940. On an extension of Reynolds' method of finding apparent stress and the nature of turbulence. *Chin. J. Phys.* 4, 1.
- Chou, P.Y., 1945. On velocity correlations and the solutions of the equations of turbulent fluctuation. *Q. Appl. Math.* 11, 38.
- Christensen, C.R., Wilson, D.C., Barnes, C.W., Grim, G.P., Morgan, G.L., Wilke, M.D., 2004. The influence of asymmetry on mix in direct-drive inertial confinement fusion experiments. *Phys. Plasmas* 11, 2771.
- Chung, D., Pullin, D.I., 2010. Direct numerical simulation and large-eddy simulation of stationary buoyancy-driven turbulence. *J. Fluid Mech.* 643, 279.
- Cimpeanu, R., Papageorgiou, D.T., Petropoulos, P.G., 2014. On the control and suppression of the Rayleigh–Taylor instability using electric fields. *Phys. Fluids* 26, 022105.
- Clark, D.S., Tabak, M., 2005a. Nonlinear Rayleigh–Taylor growth in convergent geometry. *Phys. Rev. E* 71, 055302(R).
- Clark, D.S., Tabak, M., 2005b. Acceleration- and deceleration-phase nonlinear Rayleigh–Taylor growth at spherical interfaces. *Phys. Rev. E* 72, 056308.
- Clark, D.S., Tabak, M., 2006. Linear and nonlinear Rayleigh–Taylor growth at strongly convergent spherical interfaces. *Phys. Fluids* 18, 064106.
- Clark, D.S., Milovich, J.L., Hinkel, D.E., Salmonson, J.D., Peterson, J.L., Berzak Hopkins, L.F., Eder, D.C., et al., 2014. A survey of pulse shape options for a revised plastic ablator ignition design. *Phys. Plasmas* 21, 112705.
- Clark, D.S., Marinak, M.M., Weber, C.R., Eder, D.C., Haan, S.W., Hammel, B.A., Hinkel, D.E., et al., 2015. Radiation hydrodynamics modeling of the highest compression inertial confinement fusion ignition experiment from the National Ignition Campaign. *Phys. Plasmas* 22, 022703.
- Clark, D.S., Weber, C.R., Milovich, J.L., Salmonson, J.D., Kritcher, A.L., Haan, S.W., Hammel, B.A., et al., 2016. Three-dimensional simulations of low foot and high foot implosion experiments on the National Ignition Facility. *Phys. Plasmas* 23, 056302.
- Clark, D.S., Kritcher, A.L., Milovich, J.L., Salmonson, J.D., Weber, C.R., Haan, S.W., Hammel, B.A., et al., 2017. Capsule modeling of high foot implosion experiments on the National Ignition Facility. *Plasma Phys. Control. Fusion* 59, 055006.
- Clark, T.T., 2003. A numerical study of the statistics of a 2D Rayleigh–Taylor mixing layer. *Phys. Fluids* 15, 2413.
- Clark, T.T., Zhou, Y., 2003. Self-similarity of two flows induced by instabilities. *Phys. Rev. E* 68, 066305.
- Clark, T.T., Zhou, Y., 2006. Growth rate exponents of Richtmyer–Meshkov mixing layers. *ASME J. Appl. Mech.* 73, 461.
- Clérouin, J.G., Cherfils, M.H., Zérah, G., 1998. The viscosity of dense plasmas mixtures. *Europhys. Lett.* 42, 37.
- Clift, R., Grace, J.R., Weber, M.E., 1978. *Bubbles, Drops and Particles*. Academic, New York.
- Cobos Campos, F., Wouchuk, J.G., 2014. Analytical asymptotic velocities in linear Richtmyer–Meshkov-like flows. *Phys. Rev. E* 90, 053007.
- Cobos Campos, F., Wouchuk, J.G., 2016. Analytical scalings of the linear Richtmyer–Meshkov instability when a shock is reflected. *Phys. Rev. E* 93, 053111.
- Cohen, R.H., Dannevik, W.P., Dimits, A.M., Eliason, D.E., Mirin, A.A., Zhou, Y., Porter, D.H., Woodward, P.R., 2002. Three-dimensional simulation of a Richtmyer–Meshkov instability with a two-scale initial perturbation. *Phys. Fluids* 14, 3692.
- Cole, R.H., 1948. *Underwater Explosions*. Princeton University Press, Princeton, New Jersey.
- Collins, B.D., Jacobs, J.W., 2002. PLIF flow visualization and measurements of the Richtmyer–Meshkov instability of an air/SF₆ interface. *J. Fluid Mech.* 464, 113.
- Colombant, D., Manheimer, W., Ott, E., 1984. Three-dimensional, nonlinear evolution of the Rayleigh–Taylor instability of a thin layer. *Phys. Rev. Lett.* 53, 446.
- Colvin, J.D., Legrand, M., Remington, B.A., Schurtz, G., Weber, S.V., 2003. A model for instability growth in accelerated solid metals. *J. Appl. Phys.* 93, 5287.
- Contopoulos, I., Kazanas, D., Papadopoulos, D.B., 2016. The magnetic Rayleigh–Taylor instability in astrophysical discs. *Mon. Not. R. Astron. Soc.* 462, 565.
- Cook, A.W., 2009. Enthalpy diffusion in multicomponent flows. *Phys. Fluids* 21, 055109.
- Cook, A.W., Cabot, W.H., 2004. A high-wavenumber viscosity for high-resolution numerical methods. *J. Comput. Phys.* 195, 594.
- Cook, A.W., Dimotakis, P.E., 2001. Transition stages of Rayleigh–Taylor instability between miscible fluids. *J. Fluid Mech.* 443, 69.
- Cook, A.W., Zhou, Y., 2002. Energy transfer in Rayleigh–Taylor instability. *Phys. Rev. E* 66, 026312.
- Cook, A.W., Cabot, W., Miller, P.L., 2004. The mixing transition in Rayleigh–Taylor instability. *J. Fluids Mech.* 511, 333.
- Corcos, G.M., Sherman, F.S., 1976. Vorticity concentration and the dynamics of unstable free shear layers. *J. Fluid Mech.* 73, 241.
- Couch, S.M., Ott, C.D., 2015. The role of turbulence in neutrino-driven core-collapse supernova explosions. *Astrophys. J.* 799, 5.
- Cranfill, C.W., 1991. A Multifluid Turbulent-Mix Model. Technical Report LA-UR-91-0403. Los Alamos National Lab.
- Cranfill, C.W., 1992. A New Multifluid Turbulent-Mixing Model. Technical Report LA-UR-92-2484. Los Alamos National Lab.
- Dahlburg, J.P., Gardner, J.H., Doolen, G.D., Haan, S.W., 1993. The effect of shape in the three-dimensional ablative Rayleigh–Taylor instability. I. Single-mode perturbations. *Phys. Fluids* B 5, 571.
- Dahlburg, J.P., Fyfe, D.E., Gardner, J.H., Haan, S.W., Bodner, S.E., Doolen, G.D., 1995. Three dimensional multimode simulations of the ablative Rayleigh–Taylor instability. *Phys. Plasmas* 2, 2453.
- Dalziel, S.B., Linden, P.F., Youngs, D.L., 1999. Self-similarity and internal structure of turbulence induced by Rayleigh–Taylor instability. *J. Fluid Mech.* 399, 1.
- Dankwerts, P.V., 1952. The definition and measurement of some characteristics of mixtures. *Appl. Sci. Res. Sect. A* 3, 279.
- Darlington, R.M., McAbee, T.L., Rodrigue, G., 2001. A study of ALE simulations of Rayleigh–Taylor instability. *Comput. Phys. Comm.* 135, 58.
- Das, A., Kaw, P., 2014. Suppression of Rayleigh Taylor instability in strongly coupled plasmas. *Phys. Plasmas* 21, 062102.
- da Silva, C.B., Dos Reis, R.J.N., Pereira, J.C.F., 2011. The intense vorticity structures near the turbulent/non-turbulent interface in a jet. *J. Fluid Mech.* 685, 165.
- Dávalos-Orozco, L.A., 1996. Rayleigh–Taylor stability of a two-fluid system under a general rotation field. *Dyn. Atmos. Oceans* 23, 247.
- Dávalos-Orozco, L.A., Aguilar-Rosas, J.E., 1989a. Rayleigh–Taylor instability of a continuously stratified fluid under a general rotation field. *Phys. Fluids A* 1, 1192.
- Dávalos-Orozco, L.A., Aguilar-Rosas, J.E., 1989b. Rayleigh–Taylor instability of a continuously stratified magneto-fluid under a general rotation field. *Phys. Fluids A* 1, 1600.
- Davies Wykes, M.S., Dalziel, S.B., 2014. Efficient mixing in stratified flows: experimental study of a Rayleigh–Taylor unstable interface within an otherwise stable stratification. *J. Fluid Mech.* 756, 1027.
- Dell, Z., Stellingwerf, R.F., Abarzhi, S.I., 2015. Effect of initial perturbation amplitude on Richtmyer–Meshkov flows induced by strong shocks. *Phys. Plasmas* 22, 092711.
- Denissen, N.A., Fung, J., Reisner, J.M., Andrews, M.J., 2012. Implementation and Validation of the BHR Turbulence Model in the FLAG Hydrocode, Los Alamos National Lab Report, LA-UR-12-24386.
- Denissen, N.A., Rollin, B., Reisner, J.M., Andrews, M.J., 2014. The tilted rocket rig: A Rayleigh–Taylor test case for RANS models. *ASME J. Fluids Eng.* 136, 091301.
- de Wijs, G.A., Kresse, G., Vočadlo, L., Dobson, D., Alfè, Dario, Gillan, M.J., Price, G.D., 1998. The viscosity of liquid iron at the physical conditions of the Earth's core. *Nature* 392, 805.
- De Young, D.S., 1989. Star formation in radio galaxies at large redshift. *Astrophys. J.* 342, L59.
- Díaz, A.J., Khomenko, E., Collados, M., 2014. Rayleigh–Taylor instability in partially ionized compressible plasmas: One fluid approach. *Astron. Astrophys.* 564, A97.
- Dimonte, G., 1999. Nonlinear evolution of the Rayleigh–Taylor and Richtmyer–Meshkov instabilities. *Phys. Plasmas* 2009.

- Dimonte, G., 2000. Spanwise homogeneous buoyancy-drag model for Rayleigh–Taylor mixing and experimental verification. *Phys. Plasmas* 7, 2255.
- Dimonte, G., 2004. Dependence of turbulent Rayleigh–Taylor instability on initial perturbations. *Phys. Rev. E* 69, 056305.
- Dimonte, G., Ramaprabhu, P., 2010. Simulations and model of the nonlinear Richtmyer–Meshkov instability. *Phys. Fluids* 22, 014104.
- Dimonte, G., Remington, B., 1993. Richtmyer–Meshkov experiments on the Nova laser at high compression. *Phys. Rev. Lett.* 70, 1806.
- Dimonte, G., Schneider, M., 1996. Turbulent Rayleigh–Taylor instability experiments with variable acceleration. *Phys. Rev. E* 54, 3740.
- Dimonte, G., Schneider, M., 2000. Density ratio dependence of Rayleigh–Taylor mixing for sustained and impulsive acceleration histories. *Phys. Fluids* 12, 304.
- Dimonte, G., Tipton, R., 2006. K-L turbulence model for the self-similar growth of the Rayleigh–Taylor and Richtmyer–Meshkov instabilities. *Phys. Fluids* 18, 085101.
- Dimonte, G., Frerking, C.E., Schneider, M., Remington, B.A., 1996. Richtmyer–Meshkov instability with strong radiatively driven shocks. *Phys. Plasmas* 3, 614.
- Dimonte, G., Youngs, D.L., Dimits, A., Weber, S., Marinak, M., Wunsch, S., Garasi, C., Robinson, A., Andrews, M.J., Ramaprabhu, P., Calder, A.C., Fryxell, B., Biello, J., Dursi, L., MacNeice, P., Olson, K., Ricker, P., Rosner, R., Timmes, F., Tufo, H., Young, Y.-N., Zingale, M., 2004. A comparative study of the turbulent Rayleigh–Taylor instability using high-resolution three-dimensional numerical simulations: The Alpha-Group collaboration. *Phys. Fluids* 16, 1668.
- Dimonte, G., Ramaprabhu, P., Andrews, M.J., 2007. Rayleigh–Taylor instability with complex acceleration history. *Phys. Rev. E* 76, 046313.
- Dimonte, G., Terrones, G., Cherne, F.J., Germann, T.C., Dupont, V., Kadau, K., Buttler, W.T., Oro, D.M., Morris, C., Preston, D.L., 2011. Use of the Richtmyer–Meshkov instability to infer yield stress at high-energy densities. *Phys. Rev. Lett.* 107, 264502.
- Dimotakis, P.E., 2000. The mixing transition in turbulent flows. *J. Fluid Mech.* 409, 69.
- Dimotakis, P.E., Samtaney, R., 2006. Planar shock cylindrical focusing by a perfect-gas lens. *Phys. Fluids* 18, 031705.
- Ding, J., Si, T., Yang, J., Lu, X., Zhai, Z., Luo, X., 2017. Measurement of a Richtmyer–Meshkov instability at an air-SF₆ interface in a semiannular shock tube. *Phys. Rev. Lett.* 119, 014501.
- Di Stefano, C.A., Kuranz, C.C., Keiter, P.A., Klein, S.R., Marion, D.C., Drake, R.P., 2012. Late-time breakup of laser-driven hydrodynamics experiments. *High Energy Density Phys.* 360.
- Di Stefano, C.A., Malamud, G., Henry de Frahan, M.T., Kuranz, C.C., Shimony, A., Klein, S.R., Drake, R.P., Johnsen, E., Shvarts, D., Smalyuk, V.A., Martinez, D., 2014. Observation and modeling of mixing-layer development in high-energy-density blast-wave-driven shear flow. *Phys. Plasmas* 21, 056306.
- Di Stefano, C.A., Malamud, G., Kuranz, C.C., Klein, S.R., Stoeckl, C., Drake, R.P., 2015a. Richtmyer–Meshkov evolution under steady shock conditions in the high-energy-density regime. *Appl. Phys. Lett.* 106, 114103.
- Di Stefano, C.A., Malamud, G., Kuranz, C.C., Klein, S.R., Drake, R.P., 2015b. Measurement of Richtmyer–Meshkov mode coupling under steady shock conditions and at high energy density. *High Energy Density Phys.* 17, 263.
- Di Stefano, C.A., Rasmus, A.M., Doss, F.W., Flippo, K.A., Hager, J.D., Kline, J.L., Bradley, P.A., 2017. Multimode instability evolution driven by strong, high-energy-density shocks in a rarefaction-reflected geometry. *Phys. Plasmas* 24, 052101.
- Dittrich, T.R., Hurricane, O.A., Callahan, D.A., Dewald, E.L., Döppner, T., Hinkel, D.E., Berzak Hopkins, L.F., Le Pape, S., Ma, T., Milovich, J.L., Moreno, J.C., Patel, P.K., Park, H.-S., Remington, B.A., Salmonson, J.D., Kline, J.L., 2014. Design of a high-foot/high-adiabat ICF capsule for the National Ignition Facility. *Phys. Rev. Lett.* 112, 055002.
- Domaradzki, J.A., Rogallo, R.S., 1990. Local energy transfer and non-local interactions in homogeneous, isotropic turbulence. *Phys. Fluids A* 2, 413.
- Doss, F.W., Loomis, E.N., Welser-Sherrill, L., Fincke, J.R., Flippo, K.A., Keiter, P.A., 2013a. Instability, mixing, and transition to turbulence in a laser-driven counterflowing shear experiment. *Phys. Plasmas* 20, 012707.
- Doss, F.W., Fincke, J.R., Loomis, E.N., Welser-Sherrill, L., Flippo, K.A., 2013b. The high-energy-density counterpropagating shear experiment and turbulent self-heating. *Phys. Plasmas* 20, 122704.
- Doss, F.W., Kline, J.L., Flippo, K.A., Perry, T.S., DeVolder, B.G., Tregillis, I., Loomis, E.N., Merritt, E.C., Murphy, T.J., Welser-Sherrill, L., Fincke, J.R., 2015. The shock/shear platform for planar radiation-hydrodynamics experiments on the National Ignition Facility. *Phys. Plasmas* 22, 056303.
- Doss, F.W., Flippo, K.A., Merritt, E.C., 2016a. Observation and analysis of emergent coherent structures in a high-energy-density shock-driven planar mixing layer experiment. *Phys. Rev. E* 94, 023101.
- Doss, F.W., Flippo, K.A., Capelli, D., Cardenas, T., DeVolder, B., Kline, J., Kot, L., et al., 2016b. Increasing shot and data collection rates of the Shock/Shear experiment at the National Ignition Facility. *J. Phys. Conf. Ser.* 717, 012059.
- Drake, R.P., 1999. Laboratory experiments to simulate the hydrodynamics of supernova remnants and supernovae. *J. Geophys. Res.* 104, 14505.
- Drake, R.P., 2005. Hydrodynamic instabilities in astrophysics and in laboratory high-energy-density systems. *Plasma Phys. Control. Fusion* 47, B419.
- Drake, R.P., 2006. High Energy Density Physics: Fundamentals, Inertial Fusion, and Experimental Astrophysics. Springer, Berlin.
- Drake, R.P., 2009. Perspectives on high-energy-density physics. *Phys. Plasmas* 16, 055501.
- Drake, R.P., 2012. Spike penetration in blast-wave-driven instabilities. *Astrophys. J.* 744, 184.
- Drake, R.P., Robey, H.F., Hurricane, O.A., Zhang, Y., Remington, B.A., Knauer, J., Glimm, J., et al., 2002. Experiments to produce a hydrodynamically unstable, spherically diverging system of relevance to instabilities in supernovae. *Astrophys. J.* 564, 896.
- Drake, R.P., Leibrandt, D.R., Harding, E.C., Kuranz, C.C., Blackburn, M.A., Robey, H.F., Remington, B.A., et al., 2004. Nonlinear mixing behavior of the three-dimensional Rayleigh–Taylor instability at a decelerating interface. *Phys. Plasmas* 11, 2829.
- Drake, R.P., Kuranz, C.C., Miles, A.R., Muthsam, H.J., Plewa, T., 2009. Stellar explosions, instabilities, and turbulence. *Phys. Plasmas* 16, 041004.
- Drazin, P.G., Reid, W.H., 1981. *Hydrodynamic Stability*. Cambridge Univ. Press, Cambridge, UK.
- Drew, D.A., 1983. Mathematical modeling of two-phase flow. *Annu. Rev. Fluid Mech.* 15, 261.
- Drew, D.A., Passman, S., 1999. *Theory of Multicomponent Fluids*. In: *Applied Mathematical Sciences*, Springer-Verlag, New York.
- Drikakis, D., 2003. Advances in turbulent flow computations using high-resolution methods. *Prog. Aerosp. Sci.* 39, 405.
- Drikakis, D., Grinstein, F., Youngs, D., 2005. On the computation of instabilities and symmetry-breaking in fluid mechanics. *Prog. Aerosp. Sci.* 41, 609.
- Drikakis, D., Tsangaris, S., 1993. On the solution of the compressible Navier–Stokes equations using improved flux vector splitting methods. *Appl. Math. Model.* 17, 282.
- Duan, R., Jiang, F., Yin, J., 2015. Rayleigh–Taylor instability for compressible rotating flows. *Acta Math. Sin.* 35B, 1359.
- Dubey, A., Reid, L.B., Weide, K., Antypas, K., Ganapathy, M.K., Riley, K., Sheeler, D., Siegal, A., 2009. Extensible component based architecture for FLASH, a massively parallel, multiphysics simulation code, arXiv e-prints, arXiv:0903.4875.
- Dubief, Y., Delcayre, F., 2000. On coherent-vortex identification in turbulence. *J. Turbul.* 11, 1.
- Duff, R.E., Harlow, F.H., Hirt, C.W., 1962. Effects of diffusion on interface instability between gases. *Phys. Fluids* 5, 417.
- Duffell, P.C., 2016. A one-dimensional model for Rayleigh–Taylor instability in supernova remnants. *Astrophys. J.* 821, 76.
- Dufrèche, J.-F., Clérouin, J., 2000. Viscosity coefficient of dense fluid hydrogen. *J. Phys. IV (France)* 10, 303.
- Durbin, P.A., 1996. On the k-3 stagnation point anomaly. *Int. J. Heat Fluid Flow* 17, 89.
- Durbin, P.A., Petterson Reif, B.A., 2001. *Statistical Theory and Modeling for Turbulent Flows*. Wiley, New York.
- Dutta, S., Glimm, J., Grove, J.W., Sharp, D.H., Zhang, Y., 2004. Spherical Richtmyer–Meshkov instability for axisymmetric flow. *Math. Comput. Simulation* 65, 417.

- Edwards, M.J., Glendinning, S.G., Suter, L.J., Remington, B.A., Landen, O., Turner, R.E., Shepard, T.J., et al., 2000. Turbulent hydrodynamics experiments using a new plasma piston. *Phys. Plasmas* 7, 2099.
- Edwards, M.J., Patel, P.K., Lindl, J.D., Atherton, L.J., Glenzer, S.H., Haan, S.W., Kilkenny, J.D., Landen, O.L., Moses, E.I., Nikroo, A., Petrasso, R., Sangster, T.C., Springer, P.T., Batha, S., Benedetti, R., Bernstein, L., Betti, R., Bleuel, D.L., Boehly, T.R., Bradley, D.K., Caggiano, J.A., Callahan, D.A., Celliers, P.M., Cerjan, C.J., Chen, K.C., Clark, D.S., Collins, G.W., Dewald, E.L., Divol, L., Dixit, S., Doeppner, T., Edgell, D.H., Fair, J.E., Farrell, M., Fortner, R.J., Frenje, J., Gatu Johnson, M.G., Giraldez, E., Glebov, V.Yu., Grim, G., Hammel, B.A., Hamza, A.V., Harding, D.R., Hatchett, S.P., Hein, N., Herrmann, H.W., Hicks, D., Hinkel, D.E., Hoppe, M., Hsing, W.W., Izumi, N., Jacoby, B., Jones, O.S., Kalantar, D., Kauffman, R., Kline, J.L., Knauer, J.P., Koch, J.A., Kozioziemski, B.J., Kyrala, G., LaFortune, K.N., Le Pape, S., Leeper, R.J., Lerche, R., Ma, T., MacGowan, B.J., MacKinnon, A.J., Macphee, A., Mapoles, E.R., Marinak, M.M., Mauldin, M., McKenty, P.W., Meezan, M., Michel, P.A., Milovich, J., Moody, J.D., Moran, M., Munro, D.H., Olson, C.L., Opachich, K., Pak, A.E., Parham, T., Park, H.-S., Ralph, J.E., Regan, S.P., Remington, B., Rinderknecht, H., Robey, H.F., Rosen, M., Ross, S., Salmonson, J.D., Sater, J., Schneider, D.H., Sé, F.H., Sepke, S.M., Shaughnessy, D.A., Smalyuk, V.A., Spears, B.K., Stoeckl, C., Stoeffl, W., Suter, L., Thomas, C.A., Tommasini, R., Town, R.P., Weber, S.V., Wegner, P.J., Widman, K., Wilke, M., Wilson, D.C., Yeamans, C.B., Zylstra, A., 2013. Progress towards ignition on the National Ignition Facility. *Phys. Plasmas* 20, 070501.
- Elliott, L.A., 1965a. Perturbations on fluid surfaces. *Proc. R. Soc. Lond. Ser. A Math. Phys. Eng. Sci.* 284, 397.
- Elliott, L.A., 1965b. Calculation of the growth of interface instabilities by a Lagrangian mesh method. In: Proc. of 4th Symp. (Intern.) on Detonation, White Oak, USA.
- Epperlein, E.M., Short, R.W., 1991. A practical nonlocal model for electron heat transport in laser plasmas. *Phys. Fluids B* 3, 3092.
- Epstein, R., 2004. On the Bell-Plesset effects: The effects of uniform compression and geometrical convergence on the classical Rayleigh-Taylor instability. *Phys. Plasmas* 11, 5114.
- Erez, L., Sadot, O., Oron, D., Erez, G., Levin, L.A., Shvarts, D., Ben-Dor, G., 2000. Study of the membrane effect on turbulent mixing measurements in shock tubes. *Shock Waves* 10, 241.
- Fan, M.-R., Zhai, Z.-G., Shi, T., Luo, X.-S., Zou, L.-Y., Tan, D.-W., 2012. Numerical study on the evolution of the shock-accelerated SF₆ interface: Influence of the interface shape. *Sci. China-Phys. Mech. Astron.* 55, 284.
- Fan, Z.F., Luo, J.S., 2008. Weak nonlinearity of ablative Rayleigh-Taylor instability. *Chin. Phys. Lett.* 25, 624.
- Fan, Z.F., Luo, J.S., Ye, W.H., 2009. Weakly nonlinear ablative Rayleigh-Taylor instability at preheated ablation front. *Phys. Plasmas* 16, 102104.
- Farley, D.R., Peyser, T.A., Logory, L.M., Murray, S.D., Burke, E.W., 1999. High Mach number mix instability experiments of an unstable density interface using a single-mode, nonlinear initial perturbation. *Phys. Plasmas* 6, 4304.
- Favier, B., Jouve, L., Edmunds, W., Silvers, L.J., Proctor, M.R.E., 2012. How can large-scale twisted magnetic structures naturally emerge from buoyancy instabilities? *Mon. Not. R. Astron. Soc.* 426, 3349.
- Favre, A., 1965. Equations des gaz turbulents compressibles, I Formes générales. *J. Mec.* 4, 361.
- Fincke, J.R., Lanier, N.E., Batha, S.H., Hueckstaedt, R.M., Magelssen, G.R., Rothman, S.D., Parker, K.W., Horsfield, C.J., 2004. Postponement of saturation of the Richtmyer-Meshkov instability in a convergent geometry. *Phys. Rev. Lett.* 93, 115003.
- Fincke, J.R., Lanier, N.E., Batha, S.H., Hueckstaedt, R.M., Magelssen, G.R., Rothman, S.D., Parker, K.W., Horsfield, C.J., 2005. Effect of convergence on growth of the Richtmyer-Meshkov instability. *Laser Part. Beams* 23, 21.
- Flaig, M., Plewa, T., Keiter, P.A., Drake, R.P., Grosskopf, M., Kuranz, C., Park, H.-S., 2014. Design of a supernova-relevant Rayleigh-Taylor experiment on the National Ignition Facility. I. Planar target design and diagnostics. *High Energy Density Phys.* 12, 35.
- Fleurot, N., Cavaller, C., Bourgade, J.L., 2005. The Laser Megajoule (LMJ) Project dedicated to inertial confinement fusion: Development and construction status. *Fusion Eng. Des.* 74, 147.
- Flippo, K.A., Kline, J.L., Doss, F.W., Loomis, E.N., Emerich, M., Devolder, B., Murphy, T.J., et al., 2014. Development of a Big Area BackLighter for high energy density experiments. *Rev. Sci. Instrum.* 85, 093501.
- Flippo, K.A., Doss, F.W., Devolder, B., Fincke, J.R., Loomis, E.N., Kline, J.L., Welser-Sherrill, L., 2016a. Investigating turbulent mix in HEDLP experiments. *J. Phys. Conf. Ser.* 688, 012018.
- Flippo, K.A., Doss, F.W., Kline, J.L., Merritt, E.C., Capelli, D., Cardenas, T., DeVolder, B., Fierro, F., Huntington, C.M., Kot, L., Loomis, E.N., McLaren, S.A., Murphy, T.J., Nagel, S.R., Perry, T.S., Randolph, R.B., Rivera, G., Schmidt, D.W., 2016b. Late-time mixing sensitivity to initial broadband surface roughness in high-energy-density shear layers. *Phys. Rev. Lett.* 117, 225001.
- Forbes, L.K., 2009. The Rayleigh-Taylor instability for inviscid and viscous fluids. *J. Eng. Math.* 65, 273.
- Forbes, L.K., 2011. A cylindrical Rayleigh-Taylor instability: radial outflow from pipes or stars. *J. Eng. Math.* 70, 205.
- Foster, J.M., Wilde, B.H., Rosen, P.A., Williams, R.J.R., Blue, B.E., Coker, R.F., Drake, R.P., Frank, A., Keiter, P.A., Khokhlov, A.M., Knauer, J.P., 2005. High-energy-density laboratory astrophysics studies of jets and bow shocks. *Astrophys. J. Lett.* 634 (2005), L77.
- Fragile, P.C., Murray, S.D., Anninos, P., Van Breugel, W., 2004. Radiative shock-induced collapse of intergalactic clouds. *Astrophys. J.* 604, 74.
- Fragile, P.C., Anninos, P., Gustafson, K., Murray, S.D., 2005. Magnetohydrodynamic simulations of shock interactions with radiative clouds. *Astrophys. J.* 619, 327.
- Fraleigh, G., 1986. Rayleigh-Taylor stability for a normal shock wave-density discontinuity interaction. *Phys. Fluids* 29, 376.
- Freed, N., Ofer, D., Shvarts, D., Orszag, S.A., 1991. Two-phase flow analysis of self-similar turbulent mixing by Rayleigh-Taylor instability. *Phys. Fluids A* 3, 912.
- Frieman, E.A., 1954. On elephant-trunk structures in the region of O associations. *Astrophys. J.* 120, 18.
- Frisch, U., 1995. Turbulence: The Legacy of A.N. Kolmogorov. Cambridge University Press, Cambridge.
- Fryxell, B., Olson, K., Ricker, P., Timmes, F.X., Zingale, M., Lamb, D.Q., MacNeice, P., Rosner, R., Truran, J.W., Tufo, H., 2000. FLASH: An adaptive mesh hydrodynamics code for modeling astrophysical thermonuclear flashes. *Astrophys. J. Suppl. Ser.* 131, 273.
- Fryxell, B., Kuranz, C.C., Drake, R.P., Grosskopf, M.J., Budde, A., Plewa, T., Hearn, N., Hansen, J.F., Miles, A.R., Miles, A.R., Knauer, J., 2010. The possible effects of magnetic fields on laser experiments of Rayleigh-Taylor instabilities. *High Energy Density Phys.* 6, 162.
- Gallis, M.A., Koehler, T.P., Torczynski, J.R., Plimpton, S.J., 2015. Direct simulation Monte Carlo investigation of the Richtmyer-Meshkov instability. *Phys. Fluids* 27, 084105.
- Galmiche, D., Gauthier, S., 1996. On the Reynolds number in laser experiments. *Japan. J. Appl. Phys.* 35, 4516.
- Gao, F.-J., Zhang, Y.-S., He, Z.-W., Tian, B.-L., 2016. Formula for growth rate of mixing width applied to Richtmyer-Meshkov instability. *Phys. Fluids* 28, 114101.
- Garai, S., Banerjee, D., Janaki, M.S., Chakrabarti, N., 2015. Stabilization of Rayleigh-Taylor instability in a non-Newtonian incompressible complex plasma. *Phys. Plasmas* 22, 033702.
- Garcia-Segura, G., Franco, J., 1996. From ultracompact to extended HII regions. *Astrophys. J.* 469, 171.
- Gardner, J.H., Bodner, S.E., Dahlburg, J.P., 1991. Numerical simulation of ablative Rayleigh-Taylor instability. *Phys. Fluids B* 3, 1070.
- Garnier, J., Masse, L., 2005. Statistical approach of weakly nonlinear ablative Rayleigh-Taylor instability. *Phys. Plasmas* 12, 062707.
- Garnier, J., Raviart, P.-A., Cherfils-Clérouin, C., Masse, L., 2003. Weakly nonlinear theory for the ablative Rayleigh-Taylor instability. *Phys. Rev. Lett.* 90, 185003.
- Gauthier, S., 2013. Compressibility effects in Rayleigh-Taylor flows: influence of the stratification. *Phys. Scr. T* 155, 014012.
- Gauthier, S., 2017. Compressible Rayleigh-Taylor turbulent mixing layer between Newtonian miscible fluids. *J. Fluid Mech.* 830, 211.

- Gauthier, S., Bonnet, M., 1990. A $K-\varepsilon$ model for turbulent mixing in shock-tube flows induced by Rayleigh–Taylor instability. *Phys. Fluids A* 2, 1685.
- Gauthier, S., Le Creurer, B., 2010. Compressibility effects in Rayleigh–Taylor instability induced flows. *Phil. Trans. R. Soc. A* 368, 1681.
- George, E., Glimm, J., 2005. Self-similarity of Rayleigh–Taylor mixing rates. *Phys. Fluids* 17, 054101.
- Gerashchenko, S., Livescu, D., 2016. Viscous effects on the Rayleigh–Taylor instability with background temperature gradient. *Phys. Plasmas* 23, 072121.
- Germano, M., Piomelli, U., Moin, P., Cabot, W.H., 1991. A dynamic subgrid-scale eddy viscosity model. *Phys. Fluids A* 1760.
- Ghanem, R.G., 1999a. Ingredients for a general purpose stochastic finite elements implementation. *Comput. Methods Appl. Mech. Engrg.* 168, 19.
- Ghanem, R.G., 1999b. Stochastic finite elements for heterogeneous media with multiple random nonGaussian properties. *ASCE J. Eng. Mech.* 125, 26.
- Ghanem, R.G., Spanos, P., 1991. Stochastic Finite Elements: A Spectral Approach. Springer-Verlag, NY.
- Gittings, M., Weaver, R., Clover, M., Betlach, T., Byrne, N., Coker, R., Dendy, E., Hueckstaedt, R., New, K., Oakes, W.R., Ranta, D., Stefan, R., 2008. The RAGE radiation-hydrodynamic code. *Comput. Sci. Discov.* 1, 015005.
- Glendinning, S.G., Weber, S.V., Bell, P., DaSilva, L.B., Dixit, S.N., Henesian, M.A., Kania, D.R., Kilkenny, J.D., Powell, H.T., Wallace, R.J., Wegner, P.J., Knauer, J.P., Verdon, C.P., 1992. Laser-driven planar Rayleigh–Taylor instability experiments. *Phys. Rev. Lett.* 69, 1201.
- Glendinning, S.G., Dixit, S.N., Hammel, B.A., Kalantar, D.H., Key, M.H., Kilkenny, J.D., Knauer, J.P., Pennington, D.M., Remington, B.A., Wallace, R.J., Weber, S.V., 1997. Measurement of a dispersion curve for linear-regime Rayleigh–Taylor growth rates in laser-driven planar targets. *Phys. Rev. Lett.* 78, 3318.
- Glendinning, S.G., Colvin, J., Haan, S., Kalantar, D.H., Landen, O.L., Marinak, M.M., Remington, B.A., Wallace, R., Cherfils, C., Dague, N., Divol, L., Galmiche, D., Richard, A.L., 2000. Ablation front Rayleigh–Taylor growth experiments in spherically convergent geometry. *Phys. Plasmas* 7, 2033.
- Glendinning, S.G., Bolstad, J., Braun, D.G., Edwards, M.J., Hsing, W.W., Lasinski, B.F., Louis, H., Miles, A., Moreno, J., Peyster, T.A., Remington, B.A., Robey, H.F., Turano, E.J., Verdon, C.P., Zhou, Y., 2003. Effect of shock proximity on Richtmyer–Meshkov growth. *Phys. Plasmas* 10, 1931.
- Glimm, J., Li, X.L., Menikoff, R., Sharp, D.H., Zhang, Q., 1990. A numerical study of bubble interactions in Rayleigh–Taylor instability for compressible fluids. *Phys. Fluids A* 2, 2046.
- Glimm, J., Saltz, D., Sharp, D.H., 1998. Statistical evolution of chaotic fluid mixing. *Phys. Rev. Lett.* 80, 712.
- Glimm, J., Saltz, D., Sharp, D.H., 1999. Two phase modeling of a fluid mixing layer. *J. Fluid Mech.* 378, 119.
- Glimm, J., Sharp, D.H., Kaman, T., Lim, H., 2013. New directions for Rayleigh–Taylor mixing. *Philos. Trans. R. Soc. Lond. Ser. A Math. Phys. Eng. Sci.* 371, 20120183.
- Gol'berg, S.M., Velikovich, A.L., 1993. Suppression of Rayleigh–Taylor instability by the snowplow mechanism. *Phys. Fluids B* 5, 1164.
- Gold, R., McKinney, J.C., Johnson, M.D., Doeleman, S.S., 2017. Probing the magnetic field structure in on black hole horizon scales with polarized radiative transfer simulations. *Astrophys. J.* 837, 180.
- Goldstein, W.H., 2012. Science of Fusion Ignition on NIF. Lawrence Livermore National Laboratory Report No. LLNL-TR-570412.
- Goncharov, V.N., 2002. Analytical model of nonlinear-single-mode, classical Rayleigh–Taylor instability at arbitrary Atwood numbers. *Phys. Rev. Lett.* 88, 134502.
- Goncharov, V.N., Li, D., 2005. Effects of temporal density variation and convergent geometry on nonlinear bubble evolution in classical Rayleigh–Taylor instability. *Phys. Rev. E* 71, 046305.
- Goncharov, V.N., McKenty, P., Skupsky, S., Betti, R., McCrory, R.L., Cherfils-Clérouin, C., 2000. Modeling hydrodynamic instabilities in inertial confinement fusion targets. *Phys. Plasmas* 7, 5118.
- Goncharov, V.N., Sangster, T.C., Betti, R., Boehly, T.R., Bonino, M.J., Collins, T.J.B., Craxton, R.S., et al., 2014. Improving the hot-spot pressure and demonstrating ignition hydrodynamic equivalence in cryogenic deuterium–tritium implosions on OMEGA. *Phys. Plasmas* 21, 056315.
- Gowardhan, A.A., Grinstein, F.F., 2011. Numerical simulation of Richtmyer–Meshkov instabilities in shocked gas curtains. *J. Turbulence* 12, N43.
- Gowardhan, A.A., Ristorcelli, J.R., Grinstein, F.F., 2011. The bipolar behavior of the Richtmyer–Meshkov instability. *Phys. Fluids* 23, 071701.
- Graham, M.J., Zhang, Q., 2000. Numerical simulations of deep nonlinear Richtmyer–Meshkov instability. *Astrophys. J. Suppl. Ser.* 127, 339.
- Gréa, B.-J., 2013. The rapid acceleration model and the growth rate of a turbulent mixing zone induced by Rayleigh–Taylor instability. *Phys. Fluids* 25, 015118.
- Gréa, B.-J., 2015. The dynamics of the $K-\varepsilon$ model toward its self-similar Rayleigh–Taylor solution. *J. Turbulence* 16, 184.
- Gréa, B.-J., Griffond, J., Godeferd, F., 2014. Strain and stratification effects on the rapid acceleration of a turbulent mixing zone. *ASME J. Fluids Eng.* 136, 091203.
- Gréa, B.-J., Burlot, A., Godeferd, F., Griffond, J., Soulard, O., Cambon, C., 2016a. Dynamics and structure of unstably stratified homogeneous turbulence. *J. Turbul.* 17, 651.
- Gréa, B.-J., Burlot, A., Griffond, J., Llor, A., 2016b. Challenging mix models on transients to self-similarity of unstably stratified homogeneous turbulence. *ASME J. Fluids Eng.* 071204.
- Grégoire, O., Souffland, D., Gauthier, S., Schiestel, R., 1999. A two-time-scale turbulence model for compressible flows: Turbulence dominated by mean deformation interaction. *Phys. Fluids* 11, 3793.
- Grégoire, O., Souffland, D., Gauthier, S., 2005. A second-order turbulence model for gaseous mixtures induced by Richtmyer–Meshkov instability. *J. Turbulence* 6, N29.
- Griffond, J., 2005. Linear interaction analysis applied to a mixture of two perfect gases. *Phys. Fluids* 17, 086101.
- Griffond, J., 2006. Linear interaction analysis for Richtmyer–Meshkov instability at low Atwood number. *Phys. Fluids* 18, 054106.
- Griffond, J., Soulard, O., 2012. Evolution of axisymmetric weakly turbulent mixtures interacting with shock of rarefaction waves. *Phys. Fluids* 24, 115108.
- Griffond, J., Soulard, O., 2014. Evaluation of augmented RSM for interaction of homogeneous turbulent mixture with shock and rarefaction waves. *J. Turbulence* 15, 569.
- Griffond, J., Soulard, O., Souffland, D., 2010. A turbulent mixing Reynolds stress model fitted to match linear interaction analysis predictions. *Phys. Scr. T* 142, 014059.
- Griffond, J., Gréa, B.-J., Soulard, O., 2014. Unstably stratified homogeneous turbulence as a tool for turbulent mixing modeling. *ASME J. Fluids Eng.* 136, 091201.
- Griffond, J., Gréa, B.-J., Soulard, O., 2015. Numerical investigation of self-similar unstably stratified homogeneous turbulence. *J. Turbul.* 16, 167.
- Griffond, J., Haas, J.-F., Souffland, D., Bouzgarrou, G., Bury, Y., Jamme, S., 2017. Experimental and numerical investigation of the growth of an air/SF₆ turbulent mixing zone in a shock tube. *ASME J. Fluids Eng.* 139, 091205.
- Grinstein, F.F., 2017. On simulations of shock driven turbulent material mixing. *Comput. & Fluids* 151, 58.
- Grinstein, F.F., Margolin, L.G., Rider, W.G. (Eds.), 2007. Implicit Large Eddy Simulation: Computing Turbulent Flow Dynamics. Cambridge University Press, New York, 2nd printing.
- Grinstein, F.F., Gowandhan, A.A., Wachtor, A.J., 2011. Simulations of Richtmyer–Meshkov instabilities in planar shock-tube experiments. *Phys. Fluids* 23, 034106.
- Grinstein, F.F., Gowandhan, A.A., Ristorcelli, J.R., 2013. Implicit large eddy simulation of shock-driven material mixing. *Philos. Trans. R. Soc. Lond. Ser. A* 371, 20120217.
- Gritschneider, M., Lin, D.N.C., Murray, S.D., Yin, Q.-Z., Gong, M.-N., 2012. The supernova triggered formation and enrichment of our solar system. *Astrophys. J.* 745, 22.

- Grosskopf, M.J., Drake, R.P., Kuranz, C.C., Miles, A.R., Hansen, J.F., Plewa, T., Hearn, N., Arnett, D., Wheeler, J.C., 2009. Modeling of multi-interface, diverging, hydrodynamic experiments for the National Ignition Facility. *Astrophys. Space Sci.* 322, 57.
- Grosskopf, M.J., Drake, R.P., Miles, A.R., Plewa, T., Kuranz, C.C., 2013. Modeling of aspheric, diverging hydrodynamic instability experiments on the National Ignition Facility. *High Energy Density Phys.* 9, 439.
- Grove, J.W., Holmes, R., Sharp, D.H., Yang, Y., Zhang, Q., 1993. Quantitative theory of Richtmyer–Meshkov instability. *Phys. Rev. Lett.* 71, 3473.
- Gull, S.F., 1973. A numerical model of the structure and evolution of young supernova remnants. *Mon. Not. R. Astron. Soc.* 161, 47.
- Guo, H.Y., Yu, X.J., Wang, L.F., Ye, W.H., Wu, J.F., Li, Y.J., 2014. On the second harmonic generation through Bell–Plesset effects in cylindrical geometry. *Chin. Phys. Lett.* 31, 044702.
- Guo, Y., Tice, I., 2011. Linear Rayleigh–Taylor instability for viscous compressible fluids. *SIAM J. Math. Anal.* 42, 1688.
- Gupta, M.R., Roy, S., Khan, M., Pant, H.C., Sarkar, S., Srivastava, M.K., 2009. Effect of compressibility on the Rayleigh–Taylor and Richtmyer–Meshkov instability induced nonlinear structure at two fluid interface. *Phys. Plasmas* 16, 032303.
- Gupta, M.R., Mandal, L., Roy, S., Khan, M., 2010. Effect of magnetic field on temporal development of Rayleigh–Taylor instability induced interfacial nonlinear structure. *Phys. Plasmas* 17, 012306.
- Gupta, N.K., Lawande, S.V., 1986a. Rayleigh–Taylor instability in spherical geometry. *Phys. Rev. A* 33, 2813.
- Gupta, N.K., Lawande, S.V., 1986b. Rayleigh–Taylor instability in multi-structured spherical targets. *Plasma Phys. Control. Fusion* 28, 925.
- Haan, S.W., 1989. Onset of nonlinear saturation for Rayleigh–Taylor growth in the presence of a full spectrum of modes. *Phys. Rev. A* 39, 5812.
- Haan, S.W., 1991. Weakly nonlinear hydrodynamic instabilities in inertial fusion. *Phys. Fluids B* 3, 2349.
- Haas, F., 2005. A magnetohydrodynamic model for quantum plasma. *Phys. Plasmas* 12, 062117.
- Hahn, M., Drakakis, D., Youngs, D.L., Williams, R.J.R., 2011. Richtmyer–Meshkov turbulent mixing arising from an inclined material interface with realistic surface perturbations and reshocked flow. *Phys. Fluids* 23, 046101.
- Haines, B.M., Grinstein, F.F., Schwarzkopf, J.D., 2013a. Reynolds-averaged Navier–Stokes initialization and benchmarking in shock-driven turbulent mixing. *J. Turbulence* 14, 46.
- Haines, B.M., Grinstein, F.F., Welser-Sherrill, L., Fincke, J.R., 2013b. Simulation of material mixing in laser–driven shear experiments. *Phys. Plasmas* 20, 022309.
- Haines, B.M., Grinstein, F.F., Welser-Sherrill, L., et al., 2013c. Analysis of the effects of energy deposition on shock-driven turbulent mixing. *Phys. Plasmas* 20, 072306.
- Haines, B.M., Grinstein, F.F., Welser-Sherrill, L., 2013d. Simulation ensemble for a laser–driven shear experiment. *Phys. Plasmas* 20, 092301.
- Haines, B.M., Vold, E.L., Molvig, K., Aldrich, C., Rauenzahn, R., 2014. The effects of plasma diffusion and viscosity on turbulent instability growth. *Phys. Plasmas* 21, 092306.
- Haines, B.M., Yi, S.A., Olson, R.E., Khan, S.F., Kyrala, G.A., Zylstra, A.B., Bradley, P.A., Peterson, R.R., Kline, J.L., Leeper, R.J., Shah, R.C., 2017. The effects of convergence ratio on the implosion behavior of DT layered inertial confinement fusion capsules. *Phys. Plasmas* 24, 072709.
- Haines, M.G., 1997. Saturation mechanisms for the generated magnetic field in nonuniform laser-matter irradiation. *Phys. Rev. Lett.* 78, 254.
- Hameiri, E., 1979. Shear stabilization of Rayleigh–Taylor modes. *Phys. Fluids* 22, 89.
- Hammer, J.H., Tabak, M.M., Wilks, S.C., Lindl, J.D., Bailey, D.S., Rambo, P.W., Toor, A., Zimmerman, G.B., Porter Jr., J.J., 1999. High yield inertial confinement fusion target design for a Z-pinch-driven hohlraum. *Phys. Plasmas* 6, 2129.
- Hammer, N.J., Janka, H.-Th., Müller, E., 2010. Three-dimensional simulations of mixing instability in supernova explosion. *Astrophys. J.* 714, 1371.
- Hanjalić, K., 1994. Advanced turbulence closure models: a view of current status and future prospects. *Int. J. Heat Fluid Flow* 15, 178.
- Hanjalić, K., Launder, B.E., 1972. A Reynolds stress model of turbulence and its application to the thin shear flows. *J. Fluid Mech.* 52, 609.
- Hanjalić, K., Launder, B.E., Schiestel, R., 1980. Multiple-time-scale concept in turbulent transport modelling. In: Bradbury, J.S. (Ed.), *Turbulent Shear Flows*, Vol. 2. Springer, Berlin, p. 36.
- Hansom, J.C., Rosen, P.A., Goldsack, T.J., Oades, K., Fieldhouse, P., Cowperthwaite, N., Youngs, D.L., Mawhinney, N., Baxter, A.J., 1990. Radiation driven planar foil instability and mix experiments at the AWE HELEN laser. *Laser Part. Beams* 8, 51.
- Hao, Y., Prosperetti, A., 1999. The dynamics of vapor bubbles in acoustic pressure fields. *Phys. Fluids* 11, 2008.
- Harding, A.K., Lai, D., 2006. Physics of strongly magnetized neutron stars. *Rep. Progr. Phys.* 69, 2631.
- Harding, E.C., Hansen, J.F., Hurricane, O.A., Drake, R.P., Robey, H.F., Kuranz, C.C., Remington, B.A., Bono, M.J., Grosskopf, M.J., Gillespie, R.S., 2009. Observation of a Kelvin–Helmholtz instability in a high-energy-density plasma on the Omega laser. *Phys. Rev. Lett.* 103, 045005.
- Harlow, F.H., 2004. Fluid dynamics in group T-3 Los Alamos national laboratory:(LA-UR-03-3852). *J. Comput. Phys.* 195, 414.
- Harlow, F.H., Nakayama, P.I., 1967. Turbulence transport equations. *Phys. Fluids* 10, 2323.
- Harlow, F.H., Nakayama, P.I., 1968. Transport of Turbulence Energy Decay Rate, No. LA-3854. Los Alamos Scientific Lab, New Mexico.
- Harris, E.G., 1962. Rayleigh–Taylor instabilities of a collapsing cylindrical shell in a magnetic field. *Phys. Fluids* 5, 1057.
- Hartigan, P., Foster, J.M., Wilde, B.H., Coker, R.F., Rosen, P.A., Hansen, J.F., Blue, B.E., Williams, R.J.R., Carver, R., Frank, A., 2009. Laboratory experiments, numerical simulations, and astronomical observations of deflected supersonic jets: Application to HH 110. *Astrophys. J.* 705, 1073.
- Hassam, A.B., 1992. Nonlinear stabilization of the Rayleigh–Taylor instability by external velocity shear. *Phys. Fluids B* 4, 485.
- Haxhimali, T., Rudd, R.E., Cabot, W.H., Graziani, F.R., 2015. Shear viscosity for dense plasmas by equilibrium molecular dynamics in asymmetric Yukawa ionic mixtures. *Phys. Rev. E* 92, 053110.
- He, X., Zhang, R., Chen, S., Doolen, G.D., 1999a. On the three-dimensional Rayleigh–Taylor instability. *Phys. Fluids* 11, 1143.
- He, X., Chen, S., Zhang, R., 1999b. A lattice Boltzmann scheme for incompressible multiphase flow and its application in simulation of Rayleigh–Taylor instability. *J. Comput. Phys.* 152, 642.
- He, X.T., Li, J.W., Fan, Z.F., Wang, L.F., Liu, J., Lan, K., Wu, J.F., Ye, W.H., 2016. A hybrid-drive nonisobaric-ignition scheme for inertial confinement fusion. *Phys. Plasmas* 23, 082706.
- He, Y., Hu, X.-W., Jiang, Z.-H., 2008. Compressibility effects on the Rayleigh–Taylor instability growth rates. *Chin. Phys. Lett.* 25, 1015.
- Hecht, J., Ofer, D., Alon, U., Shvarts, D., Orszag, S., McCrory, R., 1995. Three-dimensional simulations and analysis of the nonlinear stage of the Rayleigh–Taylor instability. *Laser Part. Beams* 13, 423.
- von Helmholz, H., 1868. On discontinuous movements of fluids. *Phil. Mag.* 36, 337.
- Henney, W.J., 2007. How to move ionized gas: an introduction to the dynamics of HII regions. In: Hartquist, T.W., Pittard, J.M., Falle, S.A.E.G. (Eds.), *Diffuse Matter from Star Forming Regions to Active Galaxies*. Springer, Netherlands, pp. 103–127.
- Henry de Frahan, M.T., Movahed, P., Johnsen, E., 2015. Numerical simulations of a shock interacting with successive interfaces using the discontinuous Galerkin method: the multilayered Richtmyer–Meshkov and Rayleigh–Taylor instabilities. *Shock Waves* 25, 329.
- Henshaw, M.J.deC., Pert, G.J., Youngs, D.L., 1987. Non-linear Rayleigh–Taylor instability in (spherical) laser accelerated targets. *Plasma Phys. Control. Fusion* 29, 405.
- Hide, R., 1955. The character of the equilibrium of an incompressible heavy viscous fluid of variable density: An approximate theory. *Proc. Cambridge Philos. Soc.* 51, 179.
- Hide, R., 1956a. The character of the equilibrium of a heavy, viscous, incompressible, rotating fluid of variable density. I. General theory. *Q. J. Mech. Appl. Math.* 9, 22.

- Hide, R., 1956b. The character of the equilibrium of a heavy, viscous, incompressible rotating fluid of variable density. II. Two special cases. *Q. J. Mech. Appl. Math.* 9, 35.
- Hill, D.J., Pantano, C., Pullin, D.I., 2006. Large-eddy simulation and multiscale modelling of a Richtmyer-Meshkov instability with reshock. *J. Fluid Mech.* 557, 29.
- Hillier, A.S., 2016. On the nature of the magnetic Rayleigh-Taylor instability in astrophysical plasma: the case of uniform magnetic field strength. *Mon. Not. R. Astron. Soc.* 462, 2256.
- Ho, C.-M., Huerre, P., 1984. Perturbed free shear layers. *Annu. Rev. Fluid Mech.* 16, 365.
- Hoffman, N.M., Hammel, B.A., Schilling, O., 2010. Calibrating mix models for NIF tuning. *J. Phys. Conf. Ser.* 244, 022011.
- Hogan, W.J., Moses, E.I., Warner, B.E., Sorem, M.S., Soures, J.M., 2001. The National Ignition Facility. *Nucl. Fusion* 41, 567.
- Holder, D.A., Barton, C.J., Shock tube Richtmyer-Meshkov experiments: Inverse chevron and half height. In: Proceedings of the Ninth International Workshop on the Physics of Compressible Turbulent Mixing, 2004.
- Holder, D.A., Smith, A.V., Barton, C.J., Youngs, D.L., 2003a. Shock-tube experiments on Richtmyer-Meshkov instability growth using an enlarged double-bump perturbation. *Laser Part. Beams* 21, 411.
- Holder, D.A., Smith, A.V., Barton, C.J., Youngs, D.L., 2003b. Mix experiments using a two-dimensional convergent shock-tube. *Laser Part. Beams* 21, 403.
- Holford, J.M., Dalziel, S.B., Youngs, D.L., 2003. Rayleigh-Taylor instability at a tilted interface in laboratory experiments and numerical simulations. *Laser Part. Beams* 21, 419.
- Holt, E.H., Haskell, R.E., 1965. Foundations of Plasma Dynamics. Macmillan, New York.
- Hoshoudy, G.A., 2007. Compressible effects on the Rayleigh-Taylor instability of three layers. *Phys. Fluids* 19, 096103.
- Hoshoudy, G.A., 2011. Rayleigh-Taylor instability in quantum magnetized viscous plasma. *Plasma Phys. Rep.* 37, 775.
- Hosseini, S.R.R., Takayama, K., 2005a. Experimental study of Richtmyer-Meshkov instability induced by cylindrical shock waves. *Phys. Fluids* 17, 084101.
- Hosseini, S.H.R., Takayama, K., 2005b. Implosion of a spherical shock wave reflected from a spherical wall. *J. Fluid Mech.* 530, 223.
- Houas, L., Biamino, L., Mariani, C., Igra, O., Jourdan, G., Massol, A., 2012. The effects that changes in the diaphragm aperture have on the resulting shock tube flow. *Shock Waves* 22, 287.
- Houas, L., Chemouni, I., 1996. Experimental investigation of Richtmyer-Meshkov instability in shock tube. *Phys. Fluids* 8, 614.
- Houas, L., Jourdan, G., Schwaeberlé, L., Carrey, R., Diaz, F., 2003. A new large cross-section shock tube for studies of turbulent mixing induced by interfacial hydrodynamic instability. *Shock Waves* 12, 431.
- Houas, L., Meshkov, E.E., Jourdan, G., 1999. Overview of diagnostic methods used in shocktube investigations of mixing induced by Richtmyer-Meshkov instability. *Shock Waves* 9, 249.
- Hsing, W.W., Hoffman, N.M., 1997. Measurement of feedthrough and instability growth in radiation-driven cylindrical implosions. *Phys. Rev. Lett.* 78, 3876.
- Hsing, W.W., Barnes, C.W., Beck, J.B., Hoffman, N.M., Galmiche, D., Richard, A., Edwards, J., Graham, P., Rothman, S., Thomas, B., 1997. Rayleigh-Taylor instability evolution in ablative driven cylindrical implosions. *Phys. Plasmas* 4, 1832.
- Huba, J.D., 2004. NRL: Plasma Formulary. No. NRL/PU/6790-04-477. Naval Research Lab, Beam Physics Branch, Washington DC.
- Hunt, J., Carruthers, D., 1990. Rapid distortion theory and the problems of turbulence. *J. Fluids Mech.* 202, 233.
- Hunt, J.N., 1961a. Taylor instability in a thin fluid layer. *Appl. Sci. Res.* 10, 45.
- Hunt, J.N., 1961b. Instability in a spherical fluid shell. *Appl. Sci. Res.* 10, 59.
- Huntington, C.M., Kuranz, C.C., Drake, R.P., Miles, A.R., Prisbrey, S.T., Park, H.-S., Robey, H.F., Remington, B.A., 2011. Design of experiments to observe radiation stabilized Rayleigh-Taylor instability growth at an embedded decelerating interface. *Phys. Plasmas* 18, 112703.
- Huntington, C.M., Belfof, J.L., Blobaum, K.J.M., Cavallo, R.M., Kostinski, N.B., Maddox, B.R., Park, H.-S., et al., 2017a. Investigating iron material strength up to 1 Mbar using Rayleigh-Taylor growth measurements. *AIP Conf. Proc.* 1793, 110007.
- Huntington, C.M., Nagel, S.R., Bender, J., Raman, K.S., Baumann, T., McLaren, S.A., Prisbrey, S., Zhou, Y., (2017b). Measurement of the full mix hydrodynamic mix width at a planar unstable interface (in preparation).
- Hurricane, O.A., Hansen, J.F., Robey, H.F., Remington, B.A., Bono, M.J., Harding, E.C., Drake, R.P., Kuranz, C.C., 2009. A high energy density shock driven Kelvin-Helmholtz shear layer experiment. *Phys. Plasmas* 16, 056305.
- Hurricane, O.A., Hansen, J.F., Harding, E.C., Smalyuk, V.A., Remington, B.A., Langstaff, G., Park, H.-S., Robey, H.F., Kuranz, C.C., Grosskopf, M.J., Gillespie, R.S., 2011. Blast-wave driven Kelvin-Helmholtz shear layers in a laser driven high-energy-density plasma. *Astrophys. Space Sci.* 336, 139.
- Hurricane, O.A., Herrmann, M.C., 2017. High-energy-density physics at the National Ignition Facility. *Annu. Rev. Nucl. Part. Sci.* 67, 213.
- Hurricane, O.A., Smalyuk, V.A., Raman, K., Schilling, O., Hansen, J.F., Langstaff, G., Martinez, D., Park, H.-S., Remington, B.A., Robey, H.F., Greenough, J.A., Wallace, R., Di Stefano, C.A., Drake, R.P., Marion, D., Krauland, C.M., Kuranz, C.C., 2012. Validation of a turbulent Kelvin-Helmholtz shear layer model using a high-energy-density OMEGA laser experiment. *Phys. Rev. Lett.* 109, 15.
- Hurricane, O.A., Callahan, D.A., Casey, D.T., Celliers, P.M., Cerjan, C., Dewald, E.L., Dittrich, T.R., Doppner, T., Hinkel, D.E., Berzak Hopkins, L.F., Kline, J.L., Le Pape, S., Ma, T., MacPhee, A.G., Milovich, J.L., Pak, A., Park, H.-S., Patel, P.K., Remington, B.A., Salmonson, J.D., Springer, P.T., Tommasini, R., 2014a. Fuel gain exceeding unity in an inertially confined fusion implosion. *Nature* 506, 343.
- Hurricane, O.A., Callahan, D.A., Casey, D.T., Dewald, E.L., Dittrich, T.R., Döppner, T., Garcia, M.A. Barrios, et al., 2014b. The high-foot implosion campaign on the National Ignition Facility. *Phys. Plasmas* 21, 056314.
- Huser, G., Casner, A., Masse, L., Liberatore, S., Galmiche, D., Jacquet, L., Theobald, M., 2011. Reduced ablative Rayleigh-Taylor growth measurements in indirectly driven laminated foils. *Phys. Plasmas* 18, 012706.
- Ibragimov, N.H., 1999. Elementary Lie Group Analysis and Ordinary Differential Equations. Wiley, New York.
- Ichimaru, S., Iyetomi, H., Tanaka, S., 1987. Statistical physics of dense plasma: thermodynamics, transport coefficients and dynamical correlations. *Phys. Rep.* 149, 91.
- Imberger, J., Hamblin, P.F., 1982. Dynamics of lakes, reservoirs, and cooling ponds. *Annu. Rev. Fluid Mech.* 14, 153.
- Inogamov, N.A., 1978. Turbulent stage of the Rayleigh-Taylor instability. *Sov. Tech. Phys. Lett.* 4, 299.
- Ishii, M., Hibiki, T., 2010. Thermo-Fluid Dynamic Theory of Two-Phase Flow. Springer, New York.
- Isobe, H., Miyagoshi, T., Shibata, K., Yokoyama, T., 2005. Filamentary structure on the sun from the magnetic Rayleigh-Taylor instability. *Nature* 434, 478.
- Isobe, H., Miyagoshi, T., Shibata, K., Yokoyama, T., 2006. Three-dimensional simulation of solar emerging flux using the earth simulator I. Magnetic Rayleigh-Taylor instability at the top of the emerging flux as the origin of filamentary structure. *Pub. Astron. Soc. Japan* 58, 423.
- Jacobs, J.W., 1993. The dynamics of shock accelerated light and heavy gas cylinders. *Phys. Fluids A* 5, 2239.
- Jacobs, J.W., Dalziel, S.B., 2005. Rayleigh-Taylor instability in complex stratifications. *J. Fluid Mech.* 542, 251.
- Jacobs, J.W., Krivets, V.V., 2005. Experiments on the late-time development of single-mode Richtmyer-Meshkov instability. *Phys. Fluids* 17, 034105.
- Jacobs, J.W., Klein, D.L., Jenkins, D.G., Benjamin, R.F., 1993. Instability growth patterns of a shock-accelerated thin fluid layer. *Phys. Rev. Lett.* 70, 583.
- Jacobs, J.W., Jenkins, D.G., Klein, D.L., Benjamin, R.F., 1995. Nonlinear growth of the shock-accelerated instability of a thin fluid layer. *J. Fluid Mech.* 295, 23.
- Jacobs, J.W., Krivets, V.V., Tsiklashvili, V., Likhachev, O.A., 2013. Experiments on the Richtmyer-Meshkov instability with an imposed random initial perturbation. *Shock Waves* 23, 407.
- Jalaal, M., Mehravar, K., 2014. Transient growth of droplet instabilities in a stream. *Phys. Fluids* 26, 012101.

- Janka, H-Th., Langanke, K., Marek, A., Martínez-Pinedo, G., Müller, B., 2007. Theory of core-collapse supernovae. *Phys. Rep.* 442, 38.
- Jeong, J., Hussain, F., 1995. On the identification of a vortex. *J. Fluid Mech.* 285, 69.
- Jia, S., Haataja, M., Fleischer, J.W., 2012. Rayleigh–Taylor instability in nonlinear Schrödinger flow. *New J. Phys.* 14, 075009.
- Jiang, F., Jiang, S., 2017. Rayleigh–Taylor and Parker instabilities in MHD fluids. *Sci. Sin. Math.* 47, 1.
- Jiang, F., Jiang, S., Wu, G.-C., 2017. On stabilizing effect of elasticity in the Rayleigh–Taylor problem of stratified viscoelastic fluids. *J. Funct. Anal.* 272, 3763.
- Jiang, G.-S., Shu, C.-W., 1996. Efficient implementation of weighted ENO schemes. *J. Comput. Phys.* 126, 202.
- Jin, H., 2017. Verification of compressible closure models for turbulent multifluid mixing. *Acta Math. Appl. Sin. Engl. Ser.* 33, 157.
- Jin, H., Liu, X.F., Lu, T., Cheng, B., Glimm, J., Sharp, D.H., 2005. Rayleigh–Taylor mixing rates for compressible flow. *Phys. Fluids* 17, 024104.
- Joggerst, C.C., Almgren, A., Woosley, S.E., 2010. Three-dimensional simulations of Rayleigh–Taylor mixing in core-collapse supernovae. *Astrophys. J.* 723, 353.
- Joggerst, C.C., Nelson, A., Woodward, P., Lovekin, C., Masser, T., Fryer, C.L., Ramaprabhu, P., Francois, M., Rockefeller, G., 2014. Cross-code comparisons of mixing during the implosion of dense cylindrical and spherical shell. *J. Comput. Phys.* 275, 154.
- Johnson, B., Schilling, O., 2011a. Reynolds-averaged Navier–Stokes model predictions of linear instability. I: Buoyancy- and shear-driven flows. *J. Turbul.* 12, 36.
- Johnson, B., Schilling, O., 2011b. Reynolds-averaged Navier–Stokes model predictions of linear instability. II: Shock-driven flows. *J. Turbul.* 12, N37.
- Jones, M.A., Jacobs, J.W., 1997. A membraneless experiment for the study of Richtmyer–Meshkov instability of a shock-accelerated gas interface. *Phys. Fluids* 9, 3078.
- Jones, W.P., Launder, B., 1972. The prediction of laminarization with a two-equation model of turbulence. *Int. J. Heat Mass Transfer* 15, 301.
- Jourdan, G., Houas, L., 1996. Experimental investigation of Richtmyer–Meshkov instability before and after reflected shock compression. *Phys. Fluids* 8, 1353.
- Jourdan, G., Houas, L., Haas, J.-F., Ben-Dor, G., 1997. Thickness and volume measurements of a Richtmyer–Meshkov instability induced mixing zone in a square shock tube. *J. Fluid Mech.* 349, 67.
- Jourdan, G., Houas, L., Schwaderlé, L., Layes, G., Carrey, R., Diaz, F., 2004. A new variable inclination shock tube for multiple investigations. *Shock Waves* 13, 501.
- Jun, B.I., Norman, M.L., Stone, J.M., 1995. A numerical study of Rayleigh–Taylor instability in magnetic fluids. *Astrophys. J.* 453, 332.
- Kahn, F.D., 1958. On the stability of ionization fronts. *Rev. Modern Phys.* 30, 1058.
- Kane, J., Arnett, D., Remington, B.A., Glendinning, S.G., Bazan, G., Drake, R.P., Fryxell, B.A., Teyssier, R., Moore, K., 1999. Scaling supernova hydrodynamics to the laboratory. *Phys. Plasmas* 6, 2065.
- Kane, J., Arnett, D., Remington, B.A., Glendinning, S.G., Castor, J., Wallace, R., Rubenchik, A., Fryxell, B.A., 1997. Supernova-relevant hydrodynamic instability experiments on the Nova laser. *Astrophys. J. Lett.* 478, L75.
- Kane, J.O., Mizuta, A., Pound, M.W., Remington, B.A., Ryutov, D.D., 2005. Molecular clouds: observation to experiment. *Astrophys. Space Sci.* 298, 261.
- Kelley, M.C., Chen, C.Y., Beland, R.R., Woodman, R., Chau, J.L., Werne, J., 2005. Persistence of a Kelvin–Helmholtz instability complex in the upper troposphere. *J. Geophys. Res.* 110, D14106.
- Kelvin, Lord, 1871. Hydrokinetic solutions and observations. *Phil. Mag.* 42, 362.
- Khan, M., Mandal, L., Banerjee, R., Roy, S., Gupta, M.R., 2011. Development of Richtmyer–Meshkov and Rayleigh–Taylor instability in the presence of magnetic field. *Nucl. Instrum. Methods Phys. Res. A* 653, 2.
- Khater, A.H., Obied Allah, M.H., 1984. Effects of rotation on Rayleigh–Taylor instabilities of an accelerating, compressible, perfectly conducting plane layer. *Astrophys. Space Sci.* 106, 245.
- Kidder, R.E., 1976. Laser-driven compression of hollow shells: power requirements and stability limitations. *Nucl. Fusion* 16, 3.
- Kilkenny, J.D., Glendinning, S.G., Haan, S.W., Hammel, B.A., Lindl, J.D., Munro, D., Remington, B.A., Weber, S.V., Knauer, J.P., Verdon, C.P., 1994. A review of the ablative stabilization of the Rayleigh–Taylor instability in regimes relevant to inertial confinement fusion. *Phys. Plasmas* 1, 1379.
- Kim, J., Hong, S.S., Ryu, D., Jones, T.W., 1998. Three-dimensional evolution of the Parker instability under a uniform gravity. *Astrophys. J.* 506, L139.
- Kim, J.G., Kim, W.T., 2014. Instability of magnetized ionization fronts surrounding HII regions. *Astrophys. J.* 797, 135.
- Knauer, J.P., Betti, R., Bradley, D.K., Boehly, T.R., Collins, T.J.B., Goncharov, V.N., McKenty, P.W., et al., 2000. Single-mode Rayleigh–Taylor growth-rate measurements on the Omega laser system. *Phys. Plasmas* 7, 338.
- Kokkinakis, I.W., Drikakis, D., Youngs, D.L., Williams, R.J.R., 2015. Two-equation and multi-fluid turbulence models for Rayleigh–Taylor mixing. *Int. J. Heat Fluid Flow* 56, 233.
- Kolmogorov, A.N., 1941. The local structure of turbulence in incompressible viscous fluid for very large Reynolds number. *Dokl. Akad. Nauk SSSR* 30, 301.
- Kosovic, B., Pullin, D.I., Samtaney, R., 2002. Subgrid-scale modeling for large-eddy simulations of compressible turbulence. *Phys. Fluids* 14, 1511.
- Kovasznay, L.S.G., 1953. Turbulence in supersonic flow. *J. Aeronaut. Sci.* 20, 657.
- Kraft, W., Banerjee, A., Andrews, M.J., 2009. On hot-wire diagnostics in Rayleigh–Taylor mixing layers. *Exp. Fluids* 47, 49.
- Kraichnan, R.H., 1959. Structure of isotropic turbulence at very large Reynolds number. *J. Fluid Mech.* 5, 497.
- Kraichnan, R.H., 1967. Inertial ranges in two dimensional turbulence. *Phys. Fluids* 10, 1417.
- Kraichnan, R.H., 1971. Inertial-range transfer in two-and three-dimensional turbulence. *J. Fluid Mech.* 47, 525.
- Kraichnan, R., Montgomery, D., 1980. Two-dimensional turbulence. *Rep. Progr. Phys.* 43, 547.
- Krivets, V., Ferguson, K., Jacobs, J.W., 2017. Richtmyer–Meshkov instability shock tube experiments with mixing measurements. In: Ben-Dor, G., Igra, O., Sadot, O. (Eds.), Proc. 30th International Symposium on Shock Waves. II. Springer, NY, p. 1121.
- Kucherenko, Yu.A., Shibarshov, L.I., Chitaikin, V.I., Balabin, S.I., Pylaev, A.P., 1991. Experimental study of the gravitational turbulent mixing self-similar mode. In: Dautray, R. (Ed.), Proceedings of the Third International Workshop on Physics Compressible Turbulent Mixing. Commissariat Energie Atomique, Cesta, France, p. 427.
- Kucherenko, Yu., Neuvazhayev, V.E., Pylaev, A.P., 1993. Behavior of gravitational turbulent mixing region under conditions leading to separation. In: Linden, P.F., Youngs, D.L., Dalziel, S.B. (Eds.), Proceedings of the 4th International Workshop on the Physics of Compressible Turbulent Mixing. Cambridge University Press, Cambridge, England, p. 70.
- Kucherenko, Yu., Balabin, S.I., Cherret, R., Haas, J.F., 1997a. Experimental investigation into inertial properties of Rayleigh–Taylor turbulence. *Laser Part. Beams* 15, 25.
- Kucherenko, Yu., Balabin, S.I., Ardashova, R.I., Kozelkov, O.E., Romanov, I.A., Cherret, R., Haas, J.F., 1997b. Determination of space and time distributions of the average density of substance in the turbulized mixture region at the stage of separation. In: Jourdan, G., Houas, L. (Eds.), Proceedings of the 6th International Workshop on the Physics of Compressible Turbulent Mixing. Provence University Press, Marseille, France, p. 258.
- Kucherenko, Yu.A., Shestachenko, O.E., Balabin, S.I., Pylaev, A.P., 2003a. RFNC VNIIITF multifunctional shock tube for investigating the evolution of instabilities in non-stationary gas dynamic flows. *Laser Part. Beams* 21, 381.
- Kucherenko, Yu.A., Balabin, S.I., Ardashova, R.I., Kozelkov, O.E., Dulov, A.V., Romanov, I.A., 2003b. Experimental study of the influence of the stabilizing properties of transitional layers on the turbulent mixing evolution. *Laser Part. Beams* 21, 369.

- Kucherenko, Yu.A., Pylaev, A.P., Murzakov, V.D., Belomestnii, A.V., Popov, V.N., Tyaktev, A.A., 2003c. Experimental study into the Rayleigh–Taylor turbulent mixing zone heterogeneous structure. *Laser Part. Beams* 21, 375.
- Kucherenko, Yu.A., Pavlenko, A.V., Shestachenko, O.E., Balabin, S.I., Pylaev, A.P., Tyaktev, A.A., 2010. Measurement of spectral characteristics of the turbulent mixing zone. *J. Appl. Mech. Tech. Phys.* 51, 299.
- Kuchibhatla, S., Ranjan, D., 2013. Effect of initial conditions on Rayleigh–Taylor mixing: modal interaction. *Phys. Scr. T* 155, 014057.
- Kuchugov, P., Rozanov, V.B., Zmitrenko, N.V., 2014. The differences in the development of Rayleigh–Taylor instability in 2D and 3D geometries. *Plasma Phys. Rep.* 40, 451.
- Kulkarni, A.K., Romanova, M.M., 2008. Accretion to magnetized stars through the Rayleigh–Taylor instability: global 3D simulations. *Mon. Not. R. Astron. Soc.* 386, 673.
- Kull, H.J., 1991. Theory of the Rayleigh–Taylor instability. *Phys. Rep.* 206, 197.
- Kumar, S., Orlicz, G., Goodenough, C., Prestridge, K., Vorobieff, P., Benjamin, R., 2005. Stretching of material lines in shock-accelerated gaseous flows. *Phys. Fluids* 17, 082107.
- Kuramitsu, Y., Mizuta, A., Sakawa, Y., Tanji, H., Ide, T., Sano, T., Koenig, M., Ravasio, A., Pelka, A., Takabe, H., Gregory, C.D., 2016. Time evolution of Kelvin–Helmholtz vortices associated with collisionless shocks in laser-produced plasmas. *Astrophys. J.* 828, 93.
- Kuramitsu, Y., Sakawa, Y., Dono, S., Gregory, C.D., Pikuz, S.A., Loupias, B., Koenig, M., Waugh, J.N., Woolsey, N., Morita, T., Moritaka, T., 2012. Kelvin–Helmholtz turbulence associated with collisionless shocks in laser produced plasmas. *Phys. Rev. Lett.* 108, 195004.
- Kuranz, C.C., Drake, R.P., Donajkowski, T.L., Dannenberg, K.K., Grosskopf, M., Kremer, D.J., Krauland, C., Marion, D.C., Robey, H.F., Remington, B.A., Hansen, J.F., Blue, B.E., Knauer, J., Plewa, T., Hearn, N., 2007. Assessing mix layer amplitude in 3D decelerating interface experiments. *Astrophys. Space Sci.* 307, 115.
- Kuranz, C.C., Drake, R.P., Harding, E.C., Grosskopf, M.J., Robey, H.F., Remington, B.A., Edwards, M.J., Miles, A.R., Perry, T.S., Plewa, T., Hearn, N.C., Knauer, J.P., Arnett, D., Leibrandt, D.R., 2009. Two-dimensional blast-wave-driven Rayleigh–Taylor instability: experiment and simulation. *Astrophys. J.* 696, 749.
- Kuranz, C.C., Drake, R.P., Grosskopf, M.J., Fryxell, B., Budde, A., Hansen, J.F., Miles, A.R., Plewa, T., Hearn, N.C., Knauer, J.P., 2010. Spike morphology in blast-wave-driven instability experiments. *Phys. Plasmas* 17, 052709.
- Lafay, M.-A., Le Creurer, B., Gauthier, S., 2007. Compressibility effects on the Rayleigh–Taylor instability between miscible fluids. *Europhys. Lett.* 79, 64002.
- Lai, H., Xu, A., Zhang, G., Gan, Y., Ying, Y., Succi, S., 2016. Non-equilibrium thermo-hydrodynamic effects on the Rayleigh–Taylor instability in compressible flows. *Phys. Rev. E* 94, 023106.
- Lamb, H., 1932. *Hydrodynamics*. Dover, New York.
- Landau, L.D., Lifshitz, E.M., 1987. *Fluid Mechanics*. Pergamon, Oxford.
- Landeg, D., Philpott, M., Smith, I., Smith, A., 1993. The laser sheet as a quantitative diagnostic in shock tube experiments. In: Proc. 4th Intl Workshop on the Physics of Compressible Turbulent Mixing, Cambridge, UK, p. 230.
- Lanier, N.E., Barnes, C.W., Batha, S.H., Day, R.D., Magelssen, G.R., Scott, J.M., Dunne, A.M., Parker, K.W., Rothman, S.D., 2003. Multimode seeded Richtmyer–Meshkov mixing in a convergent, compressible, miscible plasma system. *Phys. Plasmas* 10, 1616.
- Latini, M., Schilling, O., Don, W.S., 2007a. High-resolution simulations and modeling of reshocked single-mode Richtmyer–Meshkov instability: comparison to experimental data an to amplitude growth model predictions. *Phys. Fluids* 19, 024104.
- Latini, M., Schilling, O., Don, W.S., 2007b. Effects of WENO flux reconstruction order and spatial resolution on reshocked two-dimensional Richtmyer–Meshkov instability. *J. Comput. Phys.* 221, 805.
- Launder, B.E., 2015. First steps in modelling turbulence and its origins: a commentary on Reynolds (1895) 'On the dynamical theory of incompressible viscous fluids and the determination of the criterion'. *Phil. Trans. R. Soc. A* 373, 20140231.
- Launder, B.E., Spalding, D.B., 1974. The numerical computation of turbulent flows. *Comput. Methods Appl. Mech. Engrg.* 3, 269.
- Launder, B.E., Reece, G.J., Rodi, W., 1975. Progress in the development of a Reynolds-stress turbulence closure. *J. Fluid Mech.* 68, 537.
- Lawrie, A.G.W., Dalziel, S.B., 2011a. Turbulent diffusion in tall tubes. I. Models for Rayleigh–Taylor instability. *Phys. Fluids* 23, 085109.
- Lawrie, A.G.W., Dalziel, S.B., 2011b. Turbulent diffusion in tall tubes. II. Confinement by stratification. *Phys. Fluids* 23, 085110.
- Layzer, D., 1955. On the instability of superposed fluids in a gravitational field. *Astrophys. J.* 122, 1.
- Leach, P.G.L., Feix, M.R., Bouquet, S., 1988. Analysis and solutions of a nonlinear second-order differential equation through rescaling and through a dynamical point of view. *J. Math. Phys.* 29, 2563.
- Le Creurer, B., Gauthier, S., 2008. A return toward equilibrium in a two-dimensional Rayleigh–Taylor flows instability for compressible miscible fluids. *Theor. Comput. Fluid Dyn.* 22, 125.
- Lee, H., Jin, H., Yu, Y., Glimm, J., 2008. On validation of turbulent mixing simulations for Rayleigh–Taylor instability. *Phys. Fluids* 20, 012102.
- Lee, T.D., 1951. Difference between turbulence in a two-dimensional fluid and in a three-dimensional fluid. *J. Appl. Phys.* 22, 524.
- Lee, Y.T., More, R.M., 1984. An electron conductivity model for dense plasma. *Phys. Fluids* 27, 1273.
- Leinov, E., Sadot, O., Formoza, A., Malamud, G., Elbaz, Y., Levin, L.A., Ben-Dor, G., Shvarts, D., 2008. Investigation of the Richtmyer–Meshkov instability under re-shock conditions. *Phys. Scr. T* 132, 014014.
- Leinov, E., Malamud, G., Elbaz, Y., Levin, L.A., Ben-Dor, G., Shvarts, D., Sadot, O., 2009. Experimental and numerical investigation of the Richtmyer–Meshkov instability under re-shock conditions. *J. Fluid Mech.* 626, 449.
- Leith, C.E., 1968. Diffusion approximation for two-dimensional turbulence. *Phys. Fluids* 11, 671.
- Leith, C.E., 1986. Development of a Two-Equation Turbulent Mix Model. UCRL-96036; CONF-8611116-4. Lawrence Livermore National Lab., CA.
- Leith, C.E., 1990. Stochastic backscatter in a subgrid-scale model: plane shear mixing layer. *Phys. Fluids A* 2, 297.
- Leith, C.E., Margolin, L.G., 1990. Turbulence Modeling in the SHALE Code. UCRL-ID-103271. Lawrence Livermore National Lab. CA.
- LeLievre, R., Lasher, G.J., Bjorklund, F., 1955. Effect of a Density Gradient on Taylor Instability (No. UCRL-4459). Radiation Lab. Univ. of Calif., Livermore.
- Lesieur, M., 1990. *Turbulence in Fluids*. Kluwer, Dordrecht.
- Leslie, D.C., 1973. *Developments in the Theory of Turbulence*. Clarendon, Oxford, UK.
- Lezzi, A.M., Prosperetti, A., 1989. Rayleigh–Taylor instability for adiabatically stratified fluids. *Phys. Fluids A* 1, 1784.
- Li, J.-T., Sun, Y.-T., Pan, J.-H., Ren, Y.-X., 2016. Instability and turbulent mixing of shocked "V" shaped interface. *Acta Phys. Sin.* 65, 245202.
- Li, P., Bai, J.-S., Wang, T., Zou, L.-Y., 2010. Large eddy simulation of a shocked gas cylinder instability induced turbulence. *Sci. China Phys. Mech. Astron.* 53, 262.
- Li, X.L., 1993. Study of three dimensional Rayleigh–Taylor Instability in compressible fluids through level set method and parallel computation. *Phys. Fluids A* 5, 1904.
- Li, Y., Umemura, A., 2014. Mechanism of the large surface deformation caused by Rayleigh–Taylor instability at large Atwood number. *J. Appl. Math. Phys.* 2, 971.
- Liang, Y., Ding, J., Zhai, Z., Si, T., Luo, X., 2017. Interaction of cylindrically converging diffracted shock with uniform interface. *Phys. Fluids* 29, 086101.
- Liberatore, S., Bouquet, S., 2008. Analytical modeling of magnetic Rayleigh–Taylor instabilities in compressible fluids. *Phys. Fluids* 20, 116101.
- Liberatore, S., Jaouen, S., Tabakhoff, E., Canaud, B., 2009. Compressible magnetic Rayleigh–Taylor instability in stratified plasmas: Comparison of analytical and numerical results in the linear regime. *Phys. Plasmas* 16, 044502.
- Lighthill, M.J., 1986. *An Informal Introduction to Theoretical Fluid Mechanics*. Oxford University Press, Oxford.

- Lim, H., Iwerks, J., Glimm, J., Sharp, D.H., 2010. Nonideal Rayleigh–Taylor mixing. *Proc. Nat. Acad. Sci.* 107, 12786.
- Lin, Z.-Y., Zhang, H.-H., Chen, Z.-H., Liu, Y., Hong, Y.-J., 2017. The influence of magnetic field on the physical explosion of a heavy gas cloud. *Int. J. Comput. Fluid Dyn.* 31, 21.
- Linden, P.F., Redondo, J.M., 1991. Molecular mixing in Rayleigh–Taylor instability. Part I: Global mixing. *Phys. Fluids A* 3, 1269.
- Linden, P.F., Redondo, J.M., Youngs, D.L., 1994. Molecular mixing in Rayleigh–Taylor instability. *J. Fluid Mech.* 265, 97.
- Lindl, J.D., 1995. Development of the indirectdrive approach to inertial confinement fusion and the target physics basis for ignition and gain. *Phys. Plasmas* 2, 3933.
- Lindl, J.D., 1998. *Inertial Confinement Fusion*. Springer.
- Lindl, J.D., Mead, W.C., 1975. Two-dimensional simulation of fluid instability in laser-fusion pellets. *Phys. Rev. Lett.* 34, 1273.
- Lindl, J.D., Amendt, P., Berger, R.L., Glendinning, S.G., Glenzer, S.H., Haan, S.W., Kauffman, R.L., Landen, O.L., Suter, L.J., 2004. The physics basis for ignition using indirect-drive targets on the National Ignition Facility. *Phys. Plasmas* 11, 339.
- Liu, H., Xiao, Z.-L., 2016. Scale-to-scale energy transfer in mixing flow induced by the Richtmyer–Meshkov instability. *Phys. Rev. E* 93, 053112.
- Liu, J.H., Tan, D.W., Bai, J.S., Wang, W.B., Zou, L.Y., Zhang, X., 2012a. Experimental study of Richtmyer–Meshkov instability in nonuniform flow by shock tube. *J. Exp. Mech.* 27, 160.
- Liu, W.H., He, X.T., Yu, C.P., 2012b. Cylindrical effects on Richtmyer–Meshkov instability for arbitrary Atwood numbers in weakly nonlinear regime. *Phys. Plasmas* 19, 072108.
- Liu, W.H., Yu, C.P., Ye, W.H., Wang, L.F., 2014a. Nonlinear saturation amplitude of cylindrical Rayleigh–Taylor instability. *Chin. Phys. B* 23, 094502.
- Liu, W.H., Yu, C.P., Ye, W.H., Wang, L.F., He, X.T., 2014b. Nonlinear theory of classical cylindrical Richtmyer–Meshkov instability for arbitrary Atwood numbers. *Phys. Plasmas* 21, 062119.
- Liu, W.H., Yu, C.P., Li, X.L., 2014c. Effects of initial radius of the interface and Atwood number on nonlinear saturation amplitudes in cylindrical Rayleigh–Taylor instability. *Phys. Plasmas* 21, 112103.
- Liu, W.H., Ma, W.F., Wang, X.L., 2015a. Cylindrical effects in weakly nonlinear Rayleigh–Taylor instability. *Chin. Phys. B* 24, 015202.
- Liu, W.H., Chen, Y.L., Yu, C.P., Li, X.L., 2015b. Harmonic growth of spherical Rayleigh–Taylor instability in weakly nonlinear regime. *Phys. Plasmas* 22, 112112.
- Liu, W.H., Yu, C.P., Jiang, H.B., Li, X.L., 2017. Bell-Plessent effect on harmonic evolution of spherical Rayleigh–Taylor instability in weakly nonlinear scheme for arbitrary Atwood numbers. *Phys. Plasmas* 24, 022102.
- Liu, X., George, E., Bo, W., Glimm, J., 2006. Turbulent mixing with physical mass diffusion. *Phys. Rev. E* 73, 056301.
- Livescu, D., 2004. Compressible effects on the Rayleigh–Taylor instability growth between immiscible fluids. *Phys. Fluids* 16, 118.
- Livescu, D., 2005a. Comment on ‘Compressible Rayleigh–Taylor instabilities in supernova remnants’. *Phys. Fluids* 17, 069101.
- Livescu, D., 2005b. Reply to “Response to ‘Comment on ‘Compressible Rayleigh–Taylor instabilities in supernova remnants’” [Phys. Fluids 17, 069102 (2005)]. *Phys. Fluids* 17, 089101.
- Livescu, D., 2008. Comment on “Compressibility effects on the Rayleigh–Taylor instability of three layers” [Phys. Fluids 19, 096103 (2007)]. *Phys. Fluids* 20, 029103.
- Livescu, D., 2013. Numerical simulations of two-fluid turbulent mixing at large density ratios and applications to the Rayleigh–Taylor instability. *Philos. Trans. R. Soc.* 371, 20120185.
- Livescu, D., Wei, T., Direct numerical simulations of Rayleigh–Taylor instability with gravity reversal. In: Seventh International Conference on Computational Fluid Dynamics, ICCFD7, Big Island, Hawaii, July 9–13, 2012.
- Livescu, D., Ristorcelli, J.R., Gore, R.A., Dean, S.H., Cabot, W.H., Cook, A.W., 2009. High Reynolds number Rayleigh–Taylor turbulence. *J. Turbulence* 10, N13.
- Livescu, D., Ristorcelli, J.R., Petersen, M.R., Gore, R.A., 2010. New phenomena in variable-density Rayleigh–Taylor turbulence. *Phys. Scr. T* 142, 014015.
- Livescu, D., Wei, T., Petersen, M.R., 2011. Direct numerical simulations of Rayleigh–Taylor instability. *J. Phys. Conf. Ser.* 318, 082007.
- Llor, A., 2003. Bulk turbulent transport and structure in Rayleigh–Taylor, Richtmyer–Meshkov, and variable acceleration instabilities. *Laser Part. Beams* 21, 305.
- Llor, A., 2005. Statistical hydrodynamic models for developed mixing instability flows. In: *Lecture Notes in Physics*, vol. 681, Springer, Berlin, Germany.
- Llor, A., Bailly, P., 2003. A new turbulent two-field concept for modeling Rayleigh–Taylor, Richtmyer–Meshkov, and Kelvin–Helmholtz mixing layers. *Laser Part. Beams* 21, 311.
- Lombardini, M., Pullin, D.I., 2009. Small-amplitude perturbations in the three-dimensional cylindrical Richtmyer–Meshkov instability. *Phys. Fluids* 21, 114103.
- Lombardini, M., Hill, D.J., Pullin, D.I., Meiron, D.I., 2011. Atwood ratio dependence of Richtmyer–Meshkov flows under reshock conditions using large-eddy simulations. *J. Fluid Mech.* 670, 439.
- Lombardini, M., Pullin, D.I., Meiron, D.I., 2012. Transition to turbulence in shock-driven mixing: a Mach number study. *J. Fluid Mech.* 690, 203.
- Lombardini, M., Pullin, D.I., Meiron, D.I., 2014a. Turbulent mixing driven by spherical implosions. Part 1. Flow description and mixing-layer growth. *J. Fluid Mech.* 748, 85.
- Lombardini, M., Pullin, D.I., Meiron, D.I., 2014b. Turbulent mixing driven by spherical implosions. Part 2. Turbulence statistics. *J. Fluid Mech.* 748, 113.
- Loomis, E., Doss, F., Flippo, K., Fincke, J., 2014. Measurements of continuous mix evolution in a high energy density shear flow. *Phys. Plasmas* 21, 044508.
- López Ortega, A., Hill, D.J., Pullin, D.I., Meiron, D.I., 2010. Linearized Richtmyer–Meshkov flow analysis for impulsively accelerated incompressible solids. *Phys. Rev. E* 81, 066305.
- López Ortega, A., Lombardini, M., Pullin, D.I., Meiron, D.I., 2014a. Numerical simulations of the Richtmyer–Meshkov instability in solid–vacuum interfaces using calibrated plasticity laws. *Phys. Rev. E* 89, 033018.
- López Ortega, A., Lombardini, M., Pullin, D.I., Meiron, D.I., 2014b. Numerical simulation of elastic–plastic solid mechanics using an Eulerian stretch tensor approach and LLRD Riemann solver. *J. Comput. Phys.* 257, 414.
- López Ortega, A., Lombardini, M., Barton, P.T., Pullin, D.I., Meiron, D.I., 2015. Richtmyer–Meshkov instability for elastic–plastic solids in converging geometries. *J. Mech. Phys. Solids* 76, 291.
- Lugomer, S., 2017. Laser generated Richtmyer–Meshkov and Rayleigh–Taylor instabilities and nonlinear wave-vortex paradigm in turbulent mixing. II Near-central region of Gaussian spot. *Laser Part. Beams* 35, 210.
- Lumley, J.L., 1979. Computational modeling of turbulent flows. *Adv. Appl. Mech.* 18, 123.
- Lumley, J.L., 1983. Turbulence modeling. *ASME J. Appl. Mech.* 50, 1097.
- Lumley, J.L., Newman, G.R., 1977. The return to isotropy of homogeneous turbulence. *J. Fluid Mech.* 82, 161.
- Lundin, J., Zamanian, J., Marklund, M., Brodin, G., 2007. Short wavelength electromagnetic propagation in magnetized quantum plasmas. *Phys. Plasmas* 14, 062112.
- Luo, X., Si, T., Yang, J., Zhai, Z., 2014. A cylindrical converging shock tube for shock-interface studies. *Rev. Sci. Instrum.* 85, 015107.
- Luo, X., Ding, J., Wang, M., Zhai, Z., Si, T., 2015. A semi-annular shock tube for studying cylindrically converging Richtmyer–Meshkov instability. *Phys. Fluids* 27, 091702.
- Luo, X., Dong, P., Si, T., Zhai, Z., 2016. The Richtmyer–Meshkov instability of a ‘V’ shaped air/SF₆ interface. *J. Fluid Mech.* 802, 186.
- Ma, J., Chen, Y.-H., Gan, B.-X., Yu, M.Y., 2006. Behavior of the Rayleigh–Taylor mode in a dusty plasma with rotational and shear flows. *Planet. Space Sci.* 54, 719.

- Ma, T., Patel, P.K., Izumi, N., Springer, P.T., Key, M.H., Atherton, L.J., Benedetti, L.R., Bradley, D.K., Callahan, D.A., Celliers, P.M., Cerjan, C.J., Clark, D.S., Dewald, E.L., Dixit, S.N., Doppner, T., Edgell, D.H., Epstein, R., Glenn, S., Grim, G., Haan, S.W., Hammel, B.A., Hicks, D., Hsing, W.W., Jones, O.S., Khan, S.F., Kilkenny, J.D., Kline, J.L., Kyrala, G.A., Landen, O.L., Le Pape, S., MacGowan, B.J., Mackinnon, A.J., MacPhee, A.G., Meezan, N.B., Moody, J.D., Pak, A., Parham, T., Park, H.-S., Ralph, J.E., Regan, S.P., Remington, B.A., Robey, H.F., Ross, J.S., Spears, B.K., Smalyuk, V., Suter, L.J., Tommasini, R., Town, R.P., Weber, S.V., Lindl, J.D., Edwards, M.J., Glenzer, S.H., Moses, E.I., 2013. Onset of hydrodynamic mix in high-velocity highly compressed inertial confinement fusion implosions. *Phys. Rev. Lett.* 111, 085004.
- Ma, T., Patel, P.K., Izumi, N., Springer, P.T., Key, M.H., Atherton, L.J., Barrios, M.A., et al., 2017. The role of hot spot mix in the low-foot and high-foot implosions on the NIF. *Phys. Plasmas* 24, 056311.
- MacPhee, A.G., Peterson, J.L., Casey, D.T., Clark, D.S., Haan, S.W., Jones, O.S., Landen, O.L., Milovich, J.L., Robey, H.F., Smalyuk, V.A., 2015. Stabilization of high-compression, indirect-drive inertial confinement fusion implosions using a 4-shock adiabat-shaped drive. *Phys. Plasmas* 22, 080702.
- Malamud, G., Di Stefano, C.A., Elbaz, Y., Huntington, C.M., Kuranz, C.C., Keiter, P.A., Drake, R.P., 2013. A design of a two-dimensional, multimode RM experiment on OMEGA-EP. *High Energy Density Phys.* 9, 122.
- Malamud, G., Leinov, E., Sadot, O., Elbaz, Y., Ben-Dor, G., Shvarts, D., 2014a. Reshocked Richtmyer-Meshkov instability: numerical study and modeling of random multi-mode experiments. *Phys. Fluids* 26, 084107.
- Malamud, G., Grosskopf, M.J., Drake, R.P., 2014b. Conceptual design of a Rayleigh-Taylor experiment to study bubble merger in two dimensions on NIF. *High Energy Density Phys.* 11, 17.
- Mandal, L., Roy, S., Banerjee, R., Khan, M., Gupta, M.R., 2011. Evolution of nonlinear interfacial structure induced by combined effect of Rayleigh-Taylor and Kelvin-Helmholtz instability. *Nucl. Instrum. Methods Phys. Res. A* 653, 103.
- Manfredi, G., 2005. How to model quantum plasma. *Fields Inst. Commun.* 46, 263.
- Manheimer, W., Colombant, D., Ott, E., 1984. Three-dimensional, nonlinear evolution of the Rayleigh-Taylor instability of a thin layer. *Phys. Fluids* 27, 2164.
- Margolin, L.G., Reisner, J.M., 2017. Fully compressible solutions for early stage Richtmyer-Meshkov instability. *Comput. & Fluids* 151, 46.
- Marinak, M.M., Tipton, R.E., Landen, O.L., Murphy, T.J., Amendt, P., Haan, S.W., Hatchet, S.P., Keane, C.J., Mceahern, R., Wallace, R., 1996. Three-dimensional simulations of Nova high growth factor capsule implosion experiments. *Phys. Plasmas* 3, 2070.
- Marinak, M.M., Glendinning, S.G., Wallace, R.J., Remington, B.A., Budil, K.S., Haan, S.W., Tipton, R.E., Kilkenny, J.D., 1998. Nonlinear Rayleigh-Taylor evolution of a three-dimensional multimode perturbation. *Phys. Rev. Lett.* 80, 4426.
- Marinak, M.M., Kerbel, G.D., Gentile, N.A., Jones, O., Munro, D., Pollaine, S., Dittrich, T.R., Haan, S.W., 2001. Three-dimensional HYDRA simulations of National Ignition Facility targets. *Phys. Plasmas* 8, 2275.
- Marocchino, A., Atzeni, S., Schiavi, A., 2010. Numerical study of the ablative Richtmyer-Meshkov instability of laser-irradiated deuterium and deuterium-tritium targets. *Phys. Plasmas* 17, 112703.
- Martinez, D.A., Smalyuk, V.A., Kane, J.O., Casner, A., Liberatore, S., Masse, L.P., 2015. Evidence for a bubble-competition regime in indirectly driven ablative Rayleigh-Taylor instability experiments on the NIF. *Phys. Rev. Lett.* 114, 215004.
- Masse, L., 2007. Stabilizing effect of anisotropic thermal diffusion on the ablative Rayleigh-Taylor instability. *Phys. Rev. Lett.* 98, 245001.
- Mathews, W.G., Blumenthal, G.R., 1974. Rayleigh-Taylor stability of compressible and incompressible radiation-supported surfaces and slabs. *Astrophys. J.* 214, 10.
- Mathieu, J., Scott, J., 2000. An Introduction to Turbulent Flow. Cambridge University Press.
- Matsuoka, C., 2010. Renormalization group approach to interfacial motion in incompressible Richtmyer-Meshkov instability. *Phys. Rev. E* 82, 036320.
- Matsuoka, C., Nishihara, K., 2006a. Fully nonlinear evolution of a cylindrical vortex sheet in incompressible Richtmyer-Meshkov instability. *Phys. Rev. E* 73, 055304(R).
- Matsuoka, C., Nishihara, K., 2006b. Analytical and numerical study on a vortex sheet in incompressible Richtmyer-Meshkov instability in cylindrical geometry. *Phys. Rev. E* 74, 066303.
- Maywar, D.N., Kelly, J.H., Waxer, L.J., Morse, S.F.B., Begishev, I.A., Bromage, J., Dorror, C., et al., 2008. OMEGA EP high-energy petawatt laser: progress and prospects. *J. Phys. Conf. Ser.* 112, 032007.
- McFarland, J.A., Greenough, J.A., Ranjan, D., 2011. Computational parametric study of a Richtmyer-Meshkov instability for an inclined interface. *Phys. Rev. E* 84, 026303.
- McFarland, J.A., Greenough, J.A., Ranjan, D., 2013. Investigation of the initial perturbation amplitude for the inclined interface Richtmyer-Meshkov instability. *Phys. Scr. T* 155, 014014.
- McFarland, J.A., Reilly, D., Creel, S., McDonald, C., Finn, T., Ranjan, D., 2014a. Experimental investigation of the inclined interface Richtmyer-Meshkov instability before and after reshock. *Exp. Fluids* 55, 1640.
- McFarland, J.A., Greenough, J.A., Ranjan, D., 2014b. Simulations and analysis of the reshocked inclined interface Richtmyer-Meshkov instability for linear and nonlinear interface perturbations. *ASME J. Fluids Eng.* 136, 071203.
- Mellado, J.P., Sarkar, S., Zhou, Y., 2005. Large-eddy simulation of Rayleigh-Taylor turbulence with compressible miscible fluids. *Phys. Fluids* 17, 076101.
- Mellor, G.L., Herring, H.J., 1973. A survey of mean turbulent field closure models. *AIAA J.* 11, 590.
- Mellor, G.L., Yamada, T., 1982. Development of a turbulence closure model for geophysical fluid problems. *Rev. Geophys. Space Phys.* 20, 851.
- Melvin, J., Lim, H., Rana, V., Cheng, B., Glimm, J., Sharp, D.H., Wilson, D.C., 2015. Sensitivity of inertial confinement fusion hot spot properties to the deuterium-tritium fuel adiabat. *Phys. Plasmas* 22, 022708.
- Meng, J.C., Colonius, T., 2018. Numerical simulation of the aerobreakup of a water droplet. *J. Fluid Mech.* 835, 1108.
- Merritt, E.C., Doss, F.W., 2016. Wavelet analysis methods for radiography of multidimensional growth of planar mixing layers. *Rev. Sci. Instrum.* 87, 075103.
- Merritt, E.C., Doss, F.W., Loomis, E.N., Flippo, K.A., Kline, J.L., 2015. Modifying mixing and instability growth through the adjustment of initial conditions in a high-energy-density counter-propagating shear experiment on OMEGA. *Phys. Plasmas* 22, 062306.
- Merritt, E.C., Doss, F.W., Di Stefano, C.A., Flippo, K.A., Rasmus, A.M., Schmidt, D.W., 2017. Demonstration of repeatability in a high-energy-density planar shear mixing layer experiment. *High Energy Density Phys.* 23, 90.
- Meshkov, E.E., 1969. Instability of the interface of two gases accelerated by a shock wave. *Sov. Fluid Dyn.* 4, 101.
- Meyer, K.A., Blewett, P.J., 1972. Numerical investigation of the stability of a shock accelerated interface between two fluids. *Phys. Fluids* 15, 753.
- Mikaelian, K.O., 1982. Normal modes and symmetries of the Rayleigh-Taylor instability in stratified fluids. *Phys. Rev. Lett.* 48, 1365.
- Mikaelian, K.O., 1983. Time evolution of density perturbations in accelerating stratified fluids. *Phys. Rev. A* 28, 1637.
- Mikaelian, K.O., 1985. Richtmyer-Meshkov instabilities in stratified fluids. *Phys. Rev. A* 31, 410.
- Mikaelian, K.O., 1986. Approximate treatment of density gradients in Rayleigh-Taylor instabilities. *Phys. Rev. A* 33, 1216.
- Mikaelian, K.O., 1987. Comment on "Rayleigh-Taylor instability in spherical geometry". *Phys. Rev. A* 36, 411.
- Mikaelian, K.O., 1989. Turbulent mixing generated by Rayleigh-Taylor and Richtmyer-Meshkov instabilities. *Physica D* 36, 343.
- Mikaelian, K.O., 1990a. Rayleigh-Taylor and Richtmyer-Meshkov instabilities in multilayer fluids with surface tension. *Phys. Rev. A* 42, 7211.
- Mikaelian, K.O., 1990b. Turbulent energy at accelerating and shocked interfaces. *Phys. Fluids A* 2, 592.
- Mikaelian, K.O., 1990c. Rayleigh-Taylor and Richtmyer-Meshkov instabilities and mixing in stratified spherical shells. *Phys. Rev. A* 42, 3400.
- Mikaelian, K.O., 1990d. Stability and mix in spherical geometry. *Phys. Rev. Lett.* 65, 992.

- Mikaelian, K.O., 1991. Density gradient stabilization of the Richtmyer–Meshkov instability. *Phys. Fluids A* 3, 2638.
- Mikaelian, K.O., 1994a. Freeze-out and the effect of compressibility in the Richtmyer–Meshkov instability. *Phys. Fluids* 6, 356.
- Mikaelian, K.O., 1994b. Oblique shocks and the combined Rayleigh–Taylor, Kelvin–Helmholtz, and Richtmyer–Meshkov instabilities. *Phys. Fluids* 6, 1943.
- Mikaelian, K.O., 1996a. Numerical simulations of Richtmyer–Meshkov instabilities in finite-thickness fluids layers. *Phys. Fluids* 8, 1269.
- Mikaelian, K.O., 1996b. Connection between the Rayleigh and the Schrödinger equations. *Phys. Rev. E* 53, 3551.
- Mikaelian, K.O., 2005a. Richtmyer–Meshkov instability of arbitrary shapes. *Phys. Fluids* 17, 034101.
- Mikaelian, K.O., 2005b. Rayleigh–Taylor and Richtmyer–Meshkov instabilities and mixing in stratified cylindrical shells. *Phys. Fluids* 17, 094105.
- Mikaelian, K.O., 2011. Extended model for Richtmyer–Meshkov mix. *Physica D* 240, 935.
- Mikaelian, K.O., 2014. Boussinesq approximation for Rayleigh–Taylor and Richtmyer–Meshkov instabilities. *Phys. Fluids* 26, 054103.
- Mikaelian, K.O., 2015. Testing an analytic model for Richtmyer–Meshkov turbulent mixing widths. *Shock Waves* 25, 35.
- Mikaelian, K.O., 2016. Viscous Rayleigh–Taylor instability in spherical geometry. *Phys. Rev. E* 93, 023104.
- Mikaelian, K.O., Lindl, J.D., 1984. Density gradients to reduce fluid instabilities in multishell inertial-confinement-fusion targets. *Phys. Rev. A* 29, 290.
- Mikhailenko, V.S., Mikhailenko, V.V., Weiland, J., 2002. Rayleigh–Taylor instability in plasma with shear flow. *Phys. Plasmas* 9, 2891.
- Miles, A.R., Edwards, M.J., Greenough, J.A., 2004a. Effect of initial conditions on two-dimensional Rayleigh–Taylor instability and transition to turbulence in planar blast-wave-driven systems. *Phys. Plasmas* 11, 5278.
- Miles, A.R., Braun, D.G., Edwards, M.J., Robey, H.F., Drake, R.P., Leibrandt, D.R., 2004b. Numerical simulation of supernova-relevant laser-driven hydro experiments on OMEGA. *Phys. Plasmas* 11, 3631.
- Miller, G.H., Moses, E.I., Wuest, C.R., 2004a. The National Ignition Facility. *Opt. Eng.* 43, 2841.
- Miller, G.H., Moses, E.I., Wuest, C.R., 2004b. The National Ignition Facility: enabling fusion ignition for the 21st century. *Nucl. Fusion* 44, S228.
- Milovich, J.L., Amendt, P., Marinak, M., Robey, H., 2004. Multimode short-wavelength perturbation growth studies for the National Ignition Facility double-shell ignition target designs. *Phys. Plasmas* 11, 1552.
- Misra, A., Pullin, D.I., 1997. A vortex-based model for large-eddy simulation. *Phys. Fluids* 9, 2443.
- Mitchner, M., Landshoff, R.K.M., 1964. Rayleigh–Taylor instability for compressible fluids. *Phys. Fluids* 7, 862.
- Mitra, A., Roychoudhury, R., Khan, M., 2016. Stabilization of Rayleigh–Taylor instability in the presence of viscosity and compressibility: A critical analysis. *Phys. Plasmas* 23, 024503.
- Mizuta, A., Kane, J., Pound, M.W., Remington, B., Ryutov, D., Takabe, H., 2007. Nonlinear dynamics of ionization fronts in HII regions. *Astrophys. Space Sci.* 307, 183.
- Modestov, M., Bychkov, V., Marklund, M., 2009. The Rayleigh–Taylor instability in quantum magnetized plasma with para- and ferromagnetic properties. *Phys. Plasmas* 16, 032106.
- Mohamed, A.A., El Shehawey, E.F., 1983. Nonlinear electrohydrodynamic Rayleigh–Taylor instability. Part 1. A perpendicular field in the absence of surface charges. *J. Fluid Mech.* 129, 473.
- Morán-López, J.T., Schilling, O., 2013. Multi-component Reynolds-averaged Navier–Stokes simulations of reshocked Richtmyer–Meshkov instability induced mixing. *High Energy Density Phys.* 9, 112.
- Morán-López, J.T., Schilling, O., 2014. Multi-component Reynolds-averaged Navier–Stokes simulations of Richtmyer–Meshkov instability and mixing induced by reshock at different times. *Shock Waves* 24, 325.
- Morgan, B.E., Greenough, J.A., 2016. Large-eddy and unsteady RANS simulations of a shock-accelerated heavy gas cylinder. *Shock Waves* 26, 355.
- Morgan, B.E., Wickett, M.E., 2015. Three-equation model for the self-similar growth of Rayleigh–Taylor and Richtmyer–Meshkov instabilities. *Phys. Rev. E* 91, 043002.
- Morgan, B.E., Olson, B.J., White, J.E., McFarland, J.A., 2017. Self-similarity of a Rayleigh–Taylor mixing layer at low Atwood number with a multimode initial perturbation. *J. Turbulence* 18, 973.
- Moses, E.I., Boyd, R.N., Remington, B.A., Keane, C.J., Al-Ayat, R., 2009. The National Ignition Facility: ushering in a new age for high energy density science. *Phys. Plasmas* 16, 041006.
- Moses, E.I., Wuest, C.R., 2003. The National Ignition Facility: status and plans for laser fusion and high-energy-density experimental studies. *Fusion Sci. Technol.* 43, 420.
- Mostert, W., Wheatley, V., Samtaney, R., Pullin, D.I., 2014. Effects of seed magnetic fields on magnetohydrodynamic implosion structure and dynamics. *Phys. Fluids* 26, 126102.
- Mostert, W., Wheatley, V., Samtaney, R., Pullin, D.I., 2015. Effects of magnetic fields on magnetohydrodynamic cylindrical and spherical Richtmyer–Meshkov instability. *Phys. Fluids* 27, 104102.
- Mostert, W., Pullin, D.I., Samtaney, R., Wheatley, V., 2016. Converging cylindrical magnetohydrodynamic shock collapse onto a power-law-varying line current. *J. Fluid Mech.* 793, 414.
- Mostert, W., Pullin, D.I., Samtaney, R., Wheatley, V., 2017. Geometrical shock dynamics for magnetohydrodynamic fast shocks. *J. Fluid Mech.* 811, R2.
- Motl, B., Oakley, J., Ranjan, D., Weber, C., Anderson, M., Bonazza, R., 2009. Experimental validation of a Richtmyer–Meshkov scaling law over large density ratio and shock strength ranges. *Phys. Fluids* 21, 126102.
- Mueschke, N.J., Schilling, O., 2009a. Investigation of Rayleigh–Taylor turbulence and mixing using direct numerical simulations with experimentally measured initial conditions. I. Comparison to experimental data. *Phys. Fluids* 21, 014106.
- Mueschke, N.J., Schilling, O., 2009b. Investigation of Rayleigh–Taylor turbulence and mixing using direct numerical simulation with experimentally measured initial conditions. II. Dynamics of transitional flow and mixing statistics. *Phys. Fluids* 21, 014107.
- Mueschke, N.J., Andrews, M.J., Schilling, O., 2006. Experimental characterization of initial conditions and spatio-temporal evolution of a small-Atwood-number Rayleigh–Taylor mixing layer. *J. Fluid Mech.* 567, 27.
- Mueschke, N.J., Andrews, M.J., Youngs, D.L., Schilling, O., 2009. Measurements of molecular mixing in a high-schmidt-number Rayleigh–Taylor mixing layer. *J. Fluid* 632, 17.
- Mügler, C., Gauthier, S., 2000. Two-dimensional Navier–Stokes simulations of gaseous mixtures induced by Richtmyer–Meshkov instability. *Phys. Fluids* 12, 1783.
- Müller, B., 2015. The dynamics of neutrino-driven supernova explosions after shock revival in 2D and 3D. *Mon. Not. R. Astron. Soc.* 453, 287.
- Munro, D.H., 1988. Analytical solution for Rayleigh–Taylor growth rate in smooth density gradients. *Phys. Rev. A* 38, 1433.
- Murillo, M.S., 2008. Viscosity estimates of liquid metals and warm dense matter using the Yukawa reference system. *High Energy Density Phys.* 4, 49.
- Nagata, K., Komori, S., 2000. The effects of unstable stratification and mean shear on the chemical reaction in grid turbulence. *J. Fluid Mech.* 408, 39.
- Nagel, S.R., Raman, K.S., Huntington, C.M., MacLaren, S.A., Wang, P., Barrios, M.A., Baumann, T., Bender, J.D., Benedetti, L.R., Doane, D.M., Felker, S., Fitzsimmons, P., Flippo, K.A., Holder, J.P., Kaczala, D.N., Perry, T.S., Seugling, R.M., Savage, L., Zhou, Y., 2017. A platform for studying the Rayleigh–Taylor and Richtmyer–Meshkov instabilities in a planar geometry at high energy density at the National Ignition Facility. *Phys. Plasmas* 24, 072704.
- Nelson, N.J., Grinstein, F.F., 2015. Effects of initial condition spectral content on shock-driven turbulent mixing. *Phys. Rev. E* 92, 013014.
- Neuvazhaev, V.E., 1994. Turbulent mixing, induced by the Richtmyer–Meshkov instability. *Shock Waves* 3, 263.
- Neuvazhaev, V.E., Yakovlev, V.G., 1976a. Turbulent mixing of an interface in a numerical gasdynamic calculation. *Zh. Vychisl. Mat. Fiz.* 16, 154.
- Neuvazhaev, V.E., Yakovlev, V.G., 1976b. Theory of turbulent mixing at the interface of fluids in a gravity field. *J. Appl. Mech. Tech. Phys.* 17, 513.

- Neuvazhaev, V.E., Parshukov, I.É., Pervinenko, N.V., Ponomarev, A.V., 2004. analysis of experiments on determining the turbulent mixing constant on the basis of two-dimensional calculations. *J. Appl. Mech. Tech. Phys.* 45, 656.
- Nevmerzhitskiy, N.V., 2013. Some peculiarities of turbulent mixing growth and perturbations at hydrodynamic instabilities. *Phil. Trans. R. Soc. A* 371, 20120291.
- Nevmerzhitskiy, N.V., Sotskov, E.A., Sen'kovskiy, E.D., Krivonos, O.L., Polovnikov, A.A., Levkina, E.V., Frolov, S.V., Abakumov, S.A., Marmyshev, V.V., 2014. Study of the Reynolds number effect on the progress of instability transition into the turbulent stage. *ASME J. Fluids Eng.* 136, 091207.
- Newcomb, W.A., 1983. Compressibility effect on instability growth. *Phys. Fluids* 26, 3246.
- Ng, H.D., Abderrahmane, H.A., Bates, K.R., Nikiforakis, N., 2011. The growth of fractal dimension of an interface evolution from the interaction of a shock wave with a rectangular block of SF₆. *Commun. Nonlinear Sci. Numer. Simul.* 16, 4158.
- Niederhaus, C.E., Jacobs, J.W., 2003. Experimental study of the Richtmyer–Meshkov instability of incompressible fluids. *J. Fluid Mech.* 485, 243.
- Nikiforov, V.V., Calculation of gravitational turbulent mixing in non-automodel flows, in: P.F. Linden, D.L. Youngs and S.B. Dalziel (Eds.), Proc. of the 4th International Workshop on the Physics of Compressible Turbulent Mixing, Cambridge, England, 1993.
- Nikiforov, V.V., Andronov, V.A., Razin, A.N., Trutnev, Yu. A., 1995. Development of a turbulent mixing zone driven by a shock wave. *Sov. Phys. Dokl.* 40, 333.
- Nishiguchi, A., 2002. Effects of self-generated magnetic field on the Rayleigh–Taylor instability. *Japan. J. Appl. Phys.* 41, 326.
- Nuckolls, J., Wood, L., Thiessen, A., Zimmerman, G., 1972. Laser compression of matter to super-high density: Thermonuclear (CTR) applications. *Nature* 239, 139.
- Ofer, O., Alon, U., Shvarts, D., McCrory, R.L., Verdon, C.P., 1996. Modal model for the nonlinear multimode Rayleigh–Taylor instability. *Phys. Plasmas* 3, 3073.
- Oggian, T., Drikakis, D., Youngs, D.L., Williams, R.J.R., 2014. A hybrid compressible–incompressible CFD method for Richtmyer–Meshkov mixing. *ASME J. Fluids Eng.* 136, 091210.
- Oggian, T., Drikakis, D., Youngs, D.L., Williams, R.J.R., 2015. Computing multi-mode shock-induced compressible turbulent mixing at late times. *J. Fluid Mech.* 779, 411.
- Ohkitani, K., Kida, S., 1992. Triad interactions in a forced turbulence. *Phys. Fluids A* 4, 794.
- Olson, B.J., Cook, A.W., 2007. Rayleigh–Taylor shock wave. *Phys. Fluids* 19, 128108.
- Olson, B.J., Greenough, J.A., 2014. Comparison of two- and three-dimensional simulations of miscible Richtmyer–Meshkov instability with multimode initial conditions. *Phys. Fluids* 26, 101702.
- Olson, B.J., Larsson, J., Lele, S.K., Cook, A.W., 2011. Nonlinear effects in the combined Rayleigh–Taylor/Kelvin–Helmholtz instability. *Phys. Fluids* 23, 114107.
- Olson, D.H., Jacobs, J.W., 2009. Experimental study of Rayleigh–Taylor instability with complex initial perturbation. *Phys. Fluids* 21, 034103.
- Olson, R.E., Leeper, R.J., 2013. Alternative hot spot formation techniques using liquid deuterium-tritium layer inertial confinement fusion capsules. *Phys. Plasmas* 20, 092705.
- Olson, R.E., Leeper, R.J., Kline, R.J., Zylstra, A.B., Yi, S.A., Biener, J., Braun, T., Kozioziemski, B.J., Sater, J.D., Bradley, P.A., Peterson, R.R., 2016. First liquid layer inertial confinement fusion implosions at the National Ignition Facility. *Phys. Rev. Lett.* 117, 245001.
- Olver, P.J., 1993. Applications of Lie Groups to Differential Equations. Springer, Berlin.
- Orlicz, G.C., Balakumar, B.J., Tomkins, C.D., Prestridge, K.P., 2009. A Mach number study of the Richtmyer–Meshkov instability in a varicose, heavy-gas curtain. *Phys. Fluids* 21, 064102.
- Orlicz, G.C., Balakumar, B.J., Prestridge, K.P., 2013. Incident shock Mach number effects on Richtmyer–Meshkov mixing in a heavy gas layer. *Phys. Fluids* 25, 114101.
- Orlicz, G.C., Balasubramanian, S., Vorobieff, P., Prestridge, K.P., 2015a. Mixing transition in a shocked variable-density flow. *Phys. Fluids* 27, 114102.
- Orlicz, G.C., Balasubramanian, S., Prestridge, K.P., 2015b. Investigation of Mach number dependence on the Richtmyer–Meshkov mixing transition for a shocked heavy-gas curtain. In: Bonazzza, R., Ranjan, D. (Eds.), 29th International Symposium on Shock Waves, Vol. 2. Springer, NY, p. 1101.
- Oron, D., Alon, U., Shvarts, D., 1998. Scaling laws of the Rayleigh–Taylor ablation front mixing zone evolution in inertial confinement fusion. *Phys. Plasmas* 5, 1467.
- Oron, D., Arazi, L., Kartoon, D., Rikanati, A., Alon, A., Shvarts, D., 2001. Dimensionality dependence of Rayleigh–Taylor and Richtmyer–Meshkov instability late time scaling laws. *Phys. Plasmas* 8, 2883.
- Orszag, S.A., 1970. Analytical theories of turbulence. *J. Fluid Mech.* 41, 363.
- Orszag, S.A., 1977. In: Balian, R., Peube, J.L. (Eds.), Fluid Dynamics: Les Houches. Gordon & Breach, NY.
- Otani, K., Shigemori, K., Sakaiya, T., Fujioka, S., Sunahara, A., Nakai, M., Shiraga, H., Azechi, H., Mima, K., 2007. Reduction of the Rayleigh–Taylor instability growth with cocktail color irradiation. *Phys. Plasmas* 14, 122702.
- Ott, E., 1972. Nonlinear evolution of the Rayleigh–Taylor instability of a thin layer. *Phys. Rev. Lett.* 29, 1429.
- Pacitto, G., Flament, C., Bacri, J.-C., Widom, M., 2000. Rayleigh–Taylor instability with magnetic fluids: Experiment and theory. *Phys. Rev. E* 62, 7941.
- Painter, P.C., Coleman, M.M., 1997. Fundamentals of Polymer Science: An Introductory Text. Technomic Pub. Co., Lancaster, Pa.
- Palekar, A., Vorobieff, P., Truman, C.R., 2007. Two dimensional simulation of Richtmyer–Meshkov instability. *Progr. Comput. Fluid Dyn.* 7, 427.
- Pandian, A., Stellingwerf, R.F., Abarzhi, S.I., 2017. Effect of a relative phase of waves constituting the initial perturbation and the wave interference on the dynamics of strong-shock-driven Richtmyer–Meshkov flows. *Phys. Rev. Fluids* 2, 073903.
- Papamoschou, D., 1995. Evidence of shocklets in a counterflow supersonic shear layer. *Phys. Fluids* 7, 233.
- Paquette, C., Pelletier, C., Fontaine, G., Michaud, G., 1986. Diffusion coefficients for stellar plasma. *Astrophys. J. Suppl. Ser.* 61, 177.
- Parhi, S., Nath, G., 1991. A sufficient criterion for Rayleigh–Taylor instability of incompressible viscous three-layer flow. *Internat. J. Engrg. Sci.* 29, 1439.
- Park, H.-S., Lorenz, K.T., Cavallo, R.M., Pollaine, S.M., Prisbrey, S.T., Rudd, R.E., Becker, R.C., Bernier, J.V., Remington, B.A., 2010a. Viscous Rayleigh–Taylor instability experiments at high pressure and strain rate. *Phys. Rev. Lett.* 104, 135504.
- Park, H.-S., Remington, B.A., Becker, R.C., Bernier, J.V., Cavallo, R.M., Lorenz, K.T., Pollaine, S.M., Prisbrey, S.T., Rudd, R.E., Barton, N.R., 2010b. Strong stabilization of the Rayleigh–Taylor instability by material strength at megabar pressures. *Phys. Plasmas* 17, 056314.
- Park, H.-S., Maddox, B.R., Giraldez, E., Hatchett, S.P., Hudson, L.T., Izumi, N., Key, M.H., Le Pape, S., MacKinnon, A.J., MacPhee, A.G., Patel, P.K., 2008. High-resolution 17–75 keV backlitters for high energy density experiments. *Phys. Plasmas* 15, 072705.
- Park, H.-S., Hurricane, O.A., Callahan, D.A., Casey, D.T., Dewald, E.L., Dittrich, T.R., Döppner, T., Hinkel, D.E., Berzak Hopkins, L.F., Le Pape, S., Ma, T., Patel, P.K., Remington, B.A., Robey, H.F., Salmonson, J.D., Kline, J.L., 2014. High-adiabat, high-foot, inertial confinement fusion implosion experiments on the National Ignition Facility. *Phys. Rev. Lett.* 112, 055001.
- Park, H.-S., Rudd, R.E., Cavallo, R.M., Barton, N.R., Arsenlis, A., Belof, J.L., Blobaum, K.J.M., El-dasher, B.S., Florando, J.N., Huntington, C.M., Maddox, B.R., May, M.J., Plechaty, C., Prisbrey, S.T., Remington, B.A., Wallace, R.J., Wehrenberg, C.E., Wilson, M.J., Comley, A.J., Giraldez, E., Nikroo, A., Farrell, M., Randall, G., Gray III, G.T., 2015. Grain-size-independent plastic flow at ultrahigh pressures and strain rates. *Phys. Rev. Lett.* 114, 065502.
- Parker, E.N., 1966. The dynamical state of the interstellar gas and field. *Astrophys. J.* 245, 811.
- Parker, K., Horsfield, C.J., Rothman, S.D., Batha, S.H., Balkey, M.M., Delamater, N.D., Fincke, J.R., Hueckstaedt, R.M., Lanier, N.E., Magelssen, G.R., 2004. Observation and simulation of plasma mix after reshock in a convergent geometry. *Phys. Plasmas* 11, 2696.
- Payne, R.B., 1957. A numerical method for a converging cylindrical shock. *J. Fluid Mech.* 2, 185.
- Peltier, W.R., Caulfield, C.R., 2003. Mixing efficiency in stratified shear flows. *Annu. Rev. Fluid Mech.* 35, 135.

- Penney, W.G., Price, A.T., 1942. On the changing form of a nearly spherical submarine bubble, British Report SW-27. In: Hartmann, G.K., Hill, E.G. (Eds.), Underwater Explosion Research, Vol. II. Office of Naval Research, Washington, DC, p. 145.
- Perez, F., Koenig, M., Batani, D., Baton, S.D., Beg, F.N., Benedetti, C., Brambrink, E., Chawla, S., Dorchies, F., Fournier, C., Galimberti, M., Gizzi, L.A., Heathcote, R., Higginson, D.P., Hulin, S., Jafer, R., Koester, P., Labate, L., Lancaster, K., MacKinnon, A.J., McPhee, A.G., Nazarov, W., Nicolai, P., Pasley, J., Ravasio, A., Richecca, M., Santos, J.J., Sgattoni, A., Spindloe, C., Vauzour, B., Volpe, L., 2009. Fast-electron transport in cylindrically laser-compressed matter. *Plasma Phys. Control. Fusion* 51, 124035.
- Perkins, L.J., Logan, B.G., Zimmerman, G.B., Werner, C.J., 2013. Two-dimensional simulations of thermonuclear burn in ignition-scale inertial confinement fusion targets under compressed axial magnetic fields. *Phys. Plasmas* 20, 072708.
- Perkins, L.J., Ho, D.D.-M., Logan, B.G., Zimmerman, G.B., Rhodes, M.A., Strozzi, D.J., Blackfield, D.T., Hawkins, S.A., 2017. The potential of imposed magnetic fields for enhancing ignition probability and fusion energy yield in indirect-drive inertial confinement fusion. *Phys. Plasmas* 24, 062708.
- Peterson, J.L., Hopkins, L.F.B., Jones, O.S., Clark, D.S., 2015. Differential ablator-fuel adiabat tuning in indirect-drive implosions. *Phys. Rev. E* 91, 031101.
- Peyser, T.A., Miller, P.L., Stry, P.E., Budil, K.S., Burke, E.W., Wojtowicz, D.A., Griswold, D.L., Hammel, B.A., Phillion, D.W., 1995. Measurement of radiation-driven shock-induced mixing from nonlinear initial perturbations. *Phys. Rev. Lett.* 75, 2332.
- Pham, T., Meiron, D.I., 1993. A numerical study of Richtmyer-Meshkov instability in continuously stratified fluids. *Phys. Fluids A* 5, 344.
- Picone, J.M., Boris, J.P., 1998. Vorticity generation by shock propagation through bubbles in a gas. *J. Fluid Mech.* 189, 23.
- Piriz, A.R., 2001. Compressibility effects on the Rayleigh-Taylor instability of an ablation front. *Phys. Plasmas* 8, 5268.
- Piriz, A.R., Sanz, J., Ibañez, L.F., 1997. Rayleigh-Taylor instability of steady ablation fronts: the discontinuity model revisited. *Phys. Plasmas* 4, 1117.
- Piriz, A.R., López Cela, J.J., Cortazar, O.D., Tahir, N.A., Hoffmann, D.H.H., 2005. Rayleigh-Taylor instability in elastic solids. *Phys. Rev. E* 72, 056313.
- Piriz, A.R., López Cela, J.J., Tahir, N.A., Hoffmann, D.H.H., 2008. Richtmyer-Meshkov instability in elastic-plastic media. *Phys. Rev. E* 78, 056401.
- Piriz, A.R., Lopez Cela, J.J., Tahir, N.A., 2009. Richtmyer-Meshkov instability as a tool for evaluating material strength under extreme conditions. *Nucl. Instrum. Methods Phys. Res. A* 606, 139.
- Piriz, A.R., Piriz, S.A., Tahir, N.A., 2011. Dynamic stabilization of classical Rayleigh-Taylor instability. *Phys. Plasmas* 18, 092705.
- Plesset, M.S., 1954. On the stability of fluid flows with spherical symmetry. *J. Appl. Phys.* 25, 96.
- Plesset, M.S., Hsieh, D., 1964. General analysis of the stability of superposed fluids. *Phys. Fluids* 7, 1099.
- Plesset, M.S., Prosperetti, A., 1982. Reply to comments on "General analysis of the stability of superposed fluids". *Phys. Fluids* 25, 911.
- Poehlmann, A., Richter, R., Rehberg, I., 2013. Unraveling the Rayleigh-Taylor instability by stabilization. *J. Fluid Mech.* 732, R3.
- Poggi, F., 1997. Analyze Par Vélocimétrie D'Un Mélange Gazeux Crée Par Instabilité De Richtmyer-Meshkov (Ph.D. thesis), Université de Poitiers, Poitiers, France.
- Poggi, F., Thorembey, M.-H., Rodriguez, G., 1998. Velocity measurements in turbulent gaseous mixture induced by Richtmyer-Meshkov instability. *Phys. Fluids* 10, 2698.
- Pope, S.B., 1994. On the relationship between stochastic lagrangian models of turbulence and second-moment closures. *Phys. Fluids* 6, 973.
- Pope, S.B., 2000. Turbulent Flows. Cambridge University Press, Cambridge UK.
- Poroseva, S., Colmenares Fernandez, J.D., Murman, S., 2016. On the accuracy of RANS simulations with DNS data. *Phys. Fluids* 28, 115102.
- Porth, O., Komissarov, S.S., Keppens, R., 2013. Solution to the sigma problem of pulsar wind nebulae. *Mon. Not. R. Astron. Soc.* 431, L48.
- Porth, O., Komissarov, S.S., Keppens, R., 2014a. Three-dimensional magnetohydrodynamic simulations of the Crab Nebula. *Mon. Not. R. Astron. Soc.* 438, 278.
- Porth, O., Komissarov, S.S., Keppens, R., 2014b. Rayleigh-Taylor instability in magnetohydrodynamic simulations of the Crab Nebula. *Mon. Not. R. Astron. Soc.* 443, 547.
- Poujade, O., Peybernes, M., 2010. Growth rate of Rayleigh-Taylor turbulent mixing layers from first principles. *Phys. Rev. E* 81, 016316.
- Prajapati, R.P., 2016. Rayleigh-Taylor instability in non-uniform magnetized rotating strongly coupled viscoelastic fluid. *Phys. Plasmas* 23, 022106.
- Preston, D.L., Tonks, D.L., Wallace, D.C., 2003. Model of plastic deformation for extreme loading conditions. *J. Appl. Phys.* 93, 211.
- Prestridge, K., Orlicz, G., Balasubramanian, S., Balakumar, B.J., 2013. Experiments on the Richtmyer-Meshkov instability. *Phil. Trans. R. Soc. A* 371, 20120165.
- Prosperetti, A., Seminara, G., 1978. Linear stability of a growing or collapsing bubble in a slightly viscous liquid. *Phys. Fluids* 21 (1978), 1465.
- Pullin, D.I., 1982. Numerical studies of surface-tension effects in nonlinear Kelvin-Helmholtz and Rayleigh-Taylor instability. *J. Fluid Mech.* 119, 507.
- Pullin, D.I., 2000. A vortex-based model for the subgrid flux of a passive scalar. *Phys. Fluids* 12, 2311.
- Pullin, D.I., Mostert, W., Wheatley, V., Samtaney, R., 2014. Converging cylindrical shocks in ideal magnetohydrodynamics. *Phys. Fluids* 26, 097103.
- Qiu, X.M., Huang, L., Jian, G.D., 2003. Synergistic mitigation of the Rayleigh-Taylor instability in Z-pinch implosions by sheared axial flow and finite Larmor radius effect. *Phys. Plasmas* 10, 2956.
- Raman, K.S., Smalyuk, V.A., Casey, D.T., Haan, S.W., Hoover, D.E., Hurricane, O.A., Kroll, J.J., Nikroo, A., Peterson, J.L., Remington, B.A., Robey, H.F., Clark, D.S., Hammel, B.A., Landen, O.L., Marinak, M.M., Munro, D.H., Peterson, K.J., Salmonson, J., 2014. An in-flight radiography platform to measure hydrodynamic instability growth in inertial confinement fusion capsules at the National Ignition Facility. *Phys. Plasmas* 21, 072710.
- Ramaprabhu, P., Andrews, M.J., 2003. Simultaneous measurements of velocity and density in buoyancy-driven mixing. *Exp. Fluids* 34, 98.
- Ramaprabhu, P., Andrews, M.J., 2004a. Experimental investigation of Rayleigh-Taylor mixing at small Atwood number. *J. Fluid Mech.* 502, 233.
- Ramaprabhu, P., Andrews, M.J., 2004b. On the initialization of Rayleigh-Taylor simulations. *Phys. Fluids* 16, L59.
- Ramaprabhu, P., Dimonte, G., Andrews, M.J., 2005. A numerical study of the influence of initial perturbations on the turbulent Rayleigh-Taylor instability. *J. Fluid Mech.* 536, 285.
- Ramaprabhu, P., Dimonte, G., Woodward, P., Fryer, C., Rockefeller, G., Muthuraman, K., Lin, P.H., Jayaraj, J., 2012. The late-time dynamics of the single-mode Rayleigh-Taylor instability. *Phys. Fluids* 24, 074107.
- Ramaprabhu, P., Karkhanis, V., Lawrie, A.G.W., 2013. The Rayleigh-Taylor Instability driven by an accel-decel-accel profile. *Phys. Fluids* 25, 115104.
- Ramaprabhu, P., Karkhanis, V., Banerjee, R., Varshochi, H., Khan, M., Lawrie, A.G.W., 2016. Evolution of the single-mode Rayleigh-Taylor instability under the influence of time-dependent accelerations. *Phys. Rev. E* 93, 013118.
- Ramis, R., 2013. Hydrodynamic analysis of laser-driven cylindrical implosions. *Phys. Plasmas* 20, 082705.
- Ramshaw, J.D., 1998. Simple model for linear and nonlinear mixing at unstable fluid interfaces with variable acceleration. *Phys. Rev. E* 58, 5834.
- Ramshaw, J.D., 1999. Simple model for linear and nonlinear mixing at unstable fluid interfaces in spherical geometry. *Phys. Rev. E* 60, 1775.
- Ramshaw, J.D., 2000. Effect of slow compression on the linear stability of an accelerated shear layer. *Phys. Rev. E* 61, 1486; *Phys. Rev. E* 64, 069904 (Erratum).
- Ramshaw, J.D., Amendt, P., 2003. Linearized stability analysis of accelerated planar and spherical fluid interfaces with slow compression. *Phys. Rev. E* 67, 056304.
- Rana, V., Lim, H., Melvin, J., Glimm, J., Cheng, B., Sharp, D.H., 2017. Mixing with applications to inertial-confinement-fusion implosions. *Phys. Rev. E* 95, 013203.
- Ranjan, D., Oakley, J., Bonazza, R., 2011. Shock-bubble interactions. *Annu. Rev. Fluid Mech.* 43, 117.
- Rannacher, D., Engel, A., 2007. Suppressing the Rayleigh-Taylor instability with a rotating magnetic field. *Phys. Rev. E* 75, 016311.
- Rathkopf, J.A., Miller, D.S., Owen, J.M., Stuart, L.M., Zika, M.R., Eltgroth, P.G., Madsen, N.K., McCandless, K.P., Nowak, P.F., Nemanic, M.K., Gentile, N.A., Keen, N.D., Palmer, T.S., 2000. Proceedings of the PHYSOR: ANS International Topical Meeting on Physics and Mathematics and Computation Into the Next

- Millennium. American Nuclear Society. Also available as Technical Report UCRL-JC-137053, Lawrence Livermore National Laboratories, Livermore, CA, February.
- Rayleigh, Lord, 1883. Investigation of the character of the equilibrium of an incompressible heavy fluid of variable density. *Proc. London Math. Soc.* 14, 170.
- Read, K.I., 1984. Experimental investigation of turbulent mixing by Rayleigh–Taylor instability. *Physica D* 12, 45.
- Reckinger, S.J., Livescu, D., Vasilyev, O.V., 2016. Comprehensive numerical methodology for direct numerical simulations of compressible Rayleigh–Taylor instability. *J. Comput. Phys.* 313, 181.
- Rees, M.J., 1989. The radio/optical alignment of high-z radio galaxies: triggering of star formation in radio lobes. *Mon. Not. R. Astron. Soc.* 239, 1P.
- Reese, D., Oakley, J., Navarro-Nunez, A., Rothamer, D., Weber, C., Bonazza, R., 2014. Simultaneous concentration and velocity field measurements in a shock-accelerated mixing layer. *Exp. Fluids* 55, 1.
- Reid, W.H., 1961. The effect of surface tension and viscosity on the stability of two superposed fluids. *Proc. Camb. Philos. Soc.* 57, 415.
- Reilly, D., McFarland, J., Mohaghfar, M., Ranjan, D., 2015. The effects of initial conditions and circulation deposition on the inclined-interface reshocked Richtmyer–Meshkov instability. *Exp. Fluids* 56, 168.
- Remington, B.A., Haan, S.W., Glendinning, S.G., Kilkenny, J.D., Munro, D.H., Wallace, R.J., 1991. Large growth Rayleigh–Taylor experiments using shaped laser pulses. *Phys. Rev. Lett.* 67, 3259.
- Remington, B.A., Weber, S.V., Marinak, M.M., Haar, S.W., Kilkenny, J.D., Wallace, R., Dimonte, G., 1994. Multimode Rayleigh–Taylor experiments on Nova. *Phys. Rev. Lett.* 73, 545.
- Remington, B.A., Weber, S.V., Marinak, M.M., Haan, S.W., Kilkenny, J.D., Wallace, R.J., Dimonte, G., 1995. Single-mode and multimode Rayleigh–Taylor experiments on Nova. *Phys. Plasmas* 2, 241.
- Remington, B.A., Kane, J., Drake, R.P., Glendinning, S.G., Estabrook, K., London, R., Castor, J., et al., 1997. Supernova hydrodynamics experiments on the Nova laser. *Phys. Plasmas* 4, 1994.
- Remington, B.A., Drake, R.P., Ryutov, D.D., 2000. A review of astrophysics experiments on intense lasers. *Phys. Plasmas* 7, 1641.
- Remington, B.A., Drake, R.P., Ryutov, D.D., 2006. Experimental astrophysics with high power lasers and Z pinches. *Rev. Modern Phys.* 78, 755.
- Remington, B.A., Rudd, R.E., Wark, J.S., 2015. From microjoules to megajoules and kilobars to gigabars: Probing matter at extreme states of deformation. *Phys. Plasmas* 22, 090501.
- Reynolds, C.S., McKernan, B., Fabian, A.C., Stone, J.M., Vernaleo, J.C., 2005. Buoyant radio lobes in a viscous intracluster medium. *Mon. Not. R. Astron. Soc.* 357, 242.
- Reynolds, O., 1895. On the dynamical theory of incompressible viscous fluids and the determination of the criterion. *Philos. Trans. R. Soc. Lond. Ser. A* 186, 123.
- Ribeyre, X., Tikhonchuk, V.T., Bouquet, S., 2004. Compressible Rayleigh–Taylor instabilities in supernova remnants. *Phys. Fluids* 16, 4661.
- Ribeyre, X., Tikhonchuk, V.T., Bouquet, S., 2005. Response to ‘Comment on “Compressible Rayleigh–Taylor instabilities in supernova remnants”’. *Phys. Fluids* 17, 069102.
- Ribner, H.S., 1953. Convection of a Pattern of Vorticity Through a Shock Wave, Technical Report TN 2864, NACA, January.
- Ribner, H.S., 1985. Cylindrical sound wave generated by shock-vortex interaction. *AIAA J.* 23, 1708.
- Richtmyer, R.D., 1960. Taylor instability in shock acceleration of compressible fluids. *Comm. Pure Appl. Math.* 13, 297.
- Ricotti, M., 2014. Rayleigh–Taylor instability at ionization fronts: perturbation analysis. *Mon. Not. R. Astron. Soc.* 437, 371.
- Rightley, P.M., Vorobieff, R., Benjamin, R.F., 1997. Evolution of a shock-accelerated thin fluid layer. *Phys. Fluids* 9, 1770.
- Rightley, P.M., Vorobieff, R., Martin, R., Benjamin, R.F., 1999. Experimental observations of the mixing transition in a shock-accelerated gas curtain. *Phys. Fluids* 11, 186.
- Rikanati, A., Alon, U., Shvarts, D., 1998. Vortex model for the nonlinear evolution of the multimode Richtmyer–Meshkov instability at low Atwood numbers. *Phys. Rev. E* 58, 7410.
- Rikanati, A., Alon, U., Shvarts, D., 2003. Vortex-merger statistical-mechanics model for the late time self-similar evolution of the Kelvin–Helmholtz instability. *Phys. Fluids* 15, 3776.
- Ristorcelli, J.R., Clark, T.T., 2004. Rayleigh–Taylor turbulence: self-similar analysis and direct numerical simulations. *J. Fluid Mech.* 507, 213.
- Ristorcelli, J.R., Hjelm, N., 2005. An Eddy Viscosity Expression for Favre Averaged Reynolds Stresses in Variable Density Turbulence, Tech. Rep. LA-UR-05-5837. Los Alamos National Laboratory, Los Alamos, NM.
- Ristorcelli, J.R., Hjelm, N., 2010. Initial moments and parameterizing transition for Rayleigh–Taylor unstable stochastic interfaces. *J. Turb.* 11, N46.
- Ristorcelli, J.R., Gowardhan, A.A., Grinstein, F.F., 2013. Two classes of Richtmyer–Meshkov instabilities: a detailed statistical look. *Phys. Fluids* 25, 044106.
- Robey, H.F., Kane, J.O., Remington, B.A., Drake, R.P., Hurricane, O.A., Louis, H., Wallace, R.J., Knauer, J., Keiter, P., Arnett, D., Ryutov, D.D., 2001. An experimental testbed for the study of hydrodynamic issues in supernovae. *Phys. Plasmas* 8, 2446.
- Robey, H.F., Smalyuk, V.A., Milovich, J.L., Döppner, T., Casey, D.T., Baker, K.L., Peterson, J.L., et al., 2016. Performance of indirectly driven capsule implosions on the National Ignition Facility using adiabat-shaping. *Phys. Plasmas* 23, 056303.
- Robinson, A.C., Swegle, J.W., 1989. Acceleration instability in elastic–plastic solids. II. Analytical techniques. *J. Appl. Phys.* 66, 2859.
- Rollin, B., Andrews, M.J., 2013. On generating initial conditions for turbulence models: the case of Rayleigh–Taylor instability turbulent mixing. *J. Turbul.* 14, 77.
- Rosen, P.A., Wilde, B.H., Williams, R.J.R., Foster, J.M., Keiter, P.A., Coker, R.F., Perry, T.S., Taylor, M.J., Khokhlov, A.M., Drake, R.P., Bennett, G.R., 2005. Recent experimental results and modelling of high-Mach-number jets and the transition to turbulence. *Astrophys. Space Sci.* 298, 121.
- Rotta, J.C., 1951a. Statistische theorie nichthomogene turbulenz, 1. *Z. Phys.* 129, 547.
- Rotta, J.C., 1951b. Statistische theorie nichthomogener turbulenz, 2. *Z. Phys.* 131, 51.
- Rozanov, V.B., Kuchugov, P.A., Zmitrenko, N.V., Yanilkin, Yu. V., 2015. Effect of initial conditions on the development of Rayleigh–Taylor instability. *J. Russian Laser Res.* 36, 139.
- Rutter, M.D., Secco, R.A., Liu, H.-J., Uchida, T., Rivers, M.L., Sutton, S.R., Wang, Y.-B., 2002. Viscosity of liquid Fe at high pressure. *Phys. Rev. B* 66, 060102.
- Ryutov, D.D., Dorf, M.A., 2014. Evolution of helical perturbations in a thin-shell model of an imploding liner. *Phys. Plasmas* 21, 112704.
- Ryutov, D.D., Drake, R.P., Kane, J., Liang, E., Remington, B.A., Wood-Vasey, W.M., 1999. Similarity criteria for the laboratory simulation of supernova hydrodynamics. *Astrophys. J.* 518, 821.
- Ryutov, D.D., Kane, J.O., Mizuta, A.M., Pound, W., Remington, B.A., 2007. Phenomenological theory of the photo evaporation front instability. *Astrophys. Space Sci.* 307, 173.
- Sadot, O., Smalyuk, V.A., Delettrez, J.A., Meyerhofer, D.D., Sangster, T.C., Betti, R., Goncharov, V.N., Shvarts, D., 2005. Observation of self-similar behavior of the 3D, nonlinear Rayleigh–Taylor instability. *Phys. Rev. Lett.* 95, 265001.
- Saffman, P.G., Meiron, D.I., 1989. Kinetic energy generated by the incompressible Richtmyer–Meshkov instability in a continuously stratified fluid. *Phys. Fluids A* 1, 1767.
- Sagaut, P., Cambon, C., 2008. Homogeneous Turbulence Dynamics. Cambridge University Press.
- Saigo, T., Hamaguchi, S., 2002. Shear viscosity of strongly coupled Yukawa systems. *Phys. Plasmas* 9, 1210.
- Sakagami, H., Nishihara, K., 1990. Three-dimensional Rayleigh–Taylor instability of spherical system. *Phys. Rev. Lett.* 65, 432.
- Samtaney, R., 2003. Suppression of the Richtmyer–Meshkov instability in the presence of a magnetic field. *Phys. Fluids* 15, L53.

- Samtaney, R., Zabusky, N.J., 1993. On shock polar analysis and analytical expressions for vorticity deposition in shock-accelerated density-stratified interfaces. *Phys. Fluids A* 5, 1285.
- Samtaney, R., Zabusky, N.J., 1994. Circulation deposition on shock-accelerated planar and curved density-stratified interfaces: Models and scaling laws. *J. Fluid Mech.* 269, 45.
- Samtaney, R., Zabusky, N.J., 2000. Shock interactions with heavy gaseous elliptic cylinders: Two leeward-side shock competition modes and a heuristic model for interfacial circulation deposition at early times. *Phys. Fluids* 12, 707.
- Sanz, J., 1994. Self-consistent analytical model of the Rayleigh–Taylor instability in inertial confinement fusion. *Phys. Rev. Lett.* 73, 2700.
- Sanz, J., Ramirez, J., Ramis, R., Betti, R., Town, R.P.J., 2002. Nonlinear theory of the ablative Rayleigh–Taylor instability. *Phys. Rev. Lett.* 89, 195002.
- Sanz, J., Betti, R., Ramis, R., Ramírez, J., 2004. Nonlinear theory of the ablative Rayleigh–Taylor instability. *Plasma Phys. Control. Fusion* 46, B367.
- Sbragaglia, M., Benzi, R., Biferale, L., Chen, H., Shan, X., Succi, S., 2009. Lattice Boltzmann method with self-consistent thermo-hydrodynamic equilibria. *J. Fluid Mech.* 628, 299.
- Scagliarini, A., Biferale, L., Sbragaglia, M., Sugiyama, K., Toschi, F., 2010. Lattice Boltzmann methods for thermal flows: Continuum limit and applications to compressible Rayleigh–Taylor systems. *Phys. Fluids* 22, 055101.
- Scannapieco, A.J., 1981. Atmospheric type modes in laser fusion targets. *Phys. Fluids* 24, 1699.
- Scannapieco, A.J., Cheng, B., 2002. A multifluid interpenetration mix model. *Phys. Lett. A* 299, 49.
- Scannapieco, E., Brüggen, M., 2008. Subgrid modeling of AGN-driven turbulence in galaxy clusters. *Astrophys. J.* 686, 927.
- Scase, M.M., Baldwin, K.A., Hill, R.J.A., 2016. The Rotating Rayleigh–Taylor instability. arXiv preprint [arXiv:1603.00675](https://arxiv.org/abs/1603.00675).
- Scase, M.M., Baldwin, K.A., Hill, R.J.A., 2017a. The Rotating Rayleigh–Taylor Instability. *Phys. Rev. Fluids* 2, 024801.
- Scase, M.M., Baldwin, K.A., Hill, R.J.A., 2017b. Magnetically-induced rotating Rayleigh–Taylor instability. *J. Visualized Exp.* 121, 55088.
- Schiestel, R., 1987. Multiple-time-scale modeling of turbulent flows in one-point closures. *Phys. Fluids* 30, 722.
- Schilling, O., Latini, M., 2010. High-order WENO simulations of three-dimensional reshocked Richtmyer–Meshkov instability to late times: dynamics, dependence on initial conditions, and comparison to experimental data. *Acta Math. Sci. Ser. B* 30, 595.
- Schilling, O., Mueschke, N.J., 2010. Analysis of turbulent transport and mixing in transitional Rayleigh–Taylor unstable flow using direct numerical simulation data. *Phys. Fluids* 22, 105102.
- Schilling, O., Zhou, Y., 2002. Analysis of spectral eddy viscosity and backscatter in incompressible, isotropic turbulence using statistical closure theory. *Phys. Fluids* 14, 1244.
- Schilling, O., Latini, M., Don, W.S., 2007. Physics of reshock and mixing in single-mode Richtmyer–Meshkov instability. *Phys. Rev. E* 76, 026319; *Phys. Rev. E* 85, 2012. 049904 (Erratum).
- Schneider, N., Gauthier, S., 2015. Asymptotic analysis of Rayleigh–Taylor flow for Newtonian miscible fluids. *J. Eng. Math.* 92, 55.
- Schneider, N., Gauthier, S., 2016a. Vorticity and mixing in Rayleigh–Taylor Boussinesq turbulence. *J. Fluid Mech.* 802, 395.
- Schneider, N., Gauthier, S., 2016b. Visualization of Rayleigh–Taylor flows from Boussinesq approximation to fully compressible Navier–Stokes model. *Fluid Dyn. Res.* 48, 015504.
- Schranner, F.S., Domaradzki, J.A., Hickel, S., Adams, N.A., 2015. Assessing the numerical dissipation rate and viscosity in numerical simulations of fluid flows. *Comput. & Fluids* 114, 84.
- Schulz, J.C., Gottiparthi, K.C., Menon, S., 2013. Richtmyer–Meshkov instability in dilute gas-particle mixtures with re-shock. *Phys. Fluids* 25, 114105.
- Schumann, U., 1977. Realizability of Reynolds-stress turbulence models. *Phys. Fluids* 20, 721.
- Schwarzkopf, J.D., Livescu, D., Gore, R.A., Rauenzahn, R.M., Ristorcelli, J.R., 2011. Application of a second-moment closure model to mixing processes involving multicomponent miscible fluids. *J. Turbul.* 12, N49.
- Schwarzkopf, J.D., Livescu, D., Baltzer, J.R., Gore, R.A., Ristorcelli, J.R., 2016. A two-length scale turbulence model for single-phase multi-fluid mixing. *Flow Turbul. Combust.* 96, 1.
- Sen, S., Store, R.G., 1997. Suppression of Rayleigh–Taylor instability by flow curvature. *Phys. Plasmas* 4, 3731.
- Shakura, N.I., Sunyaev, R.A., 1973. Black holes in binary systems. Observational Appearance. *Astron. Astrophys.* 24, 337.
- Shankar, S.K., Lele, S.K., 2014. Numerical investigation of turbulence in reshocked Richtmyer–Meshkov unstable curtain of dense gas. *Shock Waves* 24, 79.
- Shankar, S., Kawai, S., Lele, S., 2011. Two-dimensional viscous flow simulation of a shock accelerated heavy gas cylinder. *Phys. Fluids* 23, 024102.
- Sharp, D.H., 1984. An overview of Rayleigh–Taylor instability. *Physica D* 12, 3.
- Sharp, D.H., Wheeler, J.A., 1961. Late stage of Rayleigh–Taylor instability, Institute for Defense Analysis, Report AD-A009 943 (Distributed by National Technical Information Service, U. S. Department of Commerce).
- Shi, H.-H., Zhang, G., Du, K., Jia, H.-X., 2009. Experimental study on the mechanism of the Richtmyer–Meshkov instability at a gas-liquid interface. *J. Hydrodynamics* 21, 423.
- Shigemori, K., Azechi, H., Nakai, M., Honda, M., Meguro, K., Miyanaga, N., Takabe, H., Mima, K., 1997. Measurements of Rayleigh–Taylor growth rate of planar targets irradiated directly by partially coherent light. *Phys. Rev. Lett.* 78, 250.
- Shih, T.H., Liou, W.W., Shabbir, A., Yang, Z., Zhu, J., 1995. A new $k - \varepsilon$ eddy viscosity model for high Reynolds number turbulent flows. *Comput. Fluids* 24, 227.
- Shimony, A., Malamud, G., Shvarts, D., 2017. Density ratio and entrainment effects on asymptotic Rayleigh–Taylor instability. *ASME. J. Fluids Eng.* <http://dx.doi.org/10.1115/1.4038400>.
- Shimony, A., Shvarts, D., Malamud, G., Di Stefano, C.A., Kuranz, C.C., Drake, R.P., 2016. The effect of a dominant initial single mode on the Kelvin–Helmholtz instability evolution: New insights on previous experimental results. *ASME J. Fluids Eng.* 138, 070902.
- Shin, M.-S., Stone, J.M., Snyder, G.F., 2008. The magnetohydrodynamics of shock-cloud interaction in three dimensions. *Astrophys. J.* 680, 336.
- Shu, C.-W., 1999. High order ENO and WENO schemes for computational fluid dynamics. In: Barth, T.J., Deconinck, H. (Eds.), *High-Order Methods for Computational Physics*. Springer-Verlag, New York, p. 439.
- Shu, C.-W., Osher, S., 1988. Efficient implementation of essentially non-oscillatory shock-capturing schemes. *J. Comput. Phys.* 77, 439.
- Shumlak, U., Roderick, N.F., 1998. Mitigation of the Rayleigh–Taylor instability by shear axial flows. *Phys. Plasmas* 5, 2384.
- Shvarts, D., Sadot, O., Oron, D., Rikanati, A., Alon, U., 2000. Shock-induced instability of interfaces. In: Ben-Dor, G., Igra, O., Elperin, T. (Eds.), *HandBook of Shock Waves*, Vol. 2. Academic, San Diego, p. 489.
- Si, T., Zhai, Z., Luo, X., 2014a. Experimental study of Richtmyer–Meshkov instability in a cylindrical converging shock tube. *Laser Part. Beams* 32, 343.
- Si, T., Zhai, Z., Luo, X., Yang, J., 2014b. Experimental study on a heavy-gas cylinder accelerated by cylindrical converging shock waves. *Shock Waves* 24, 3.
- Si, T., Long, T., Zhai, Z., Luo, X., 2015. Experimental investigation of cylindrical converging shock waves interacting with a polygonal heavy gas cylinder. *J. Fluid Mech.* 784, 225.
- Simakov, A.N., Molvig, K., 2014. Electron transport in a collisional plasma with multiple ion species. *Phys. Plasmas* 21, 024503.
- Simakov, A.N., Molvig, K., 2016a. Hydrodynamic description of an unmagnetized plasma with multiple ion species. I. General formulation. *Phys. Plasmas* 23, 032115.
- Simakov, A.N., Molvig, K., 2016b. Hydrodynamic description of an unmagnetized plasma with multiple ion species. II. Two and three ion species plasmas. *Phys. Plasmas* 23, 032116.

- Sinha, K., Mahesh, K., Candler, G.V., 2003. Modeling shock unsteadiness in shock/turbulence interaction. *Phys. Fluids* 15, 2290.
- Smalyuk, V.A., Delettrez, J.A., Goncharov, V.N., Marshall, F.J., Meyerhofer, D.D., Regan, S.P., Sangster, T.C., Town, R.P.J., Yaakobi, B., 2002. Rayleigh–Taylor instability in the deceleration phase of spherical implosion experiments. *Phys. Plasmas* 9, 2738.
- Smalyuk, V.A., Sadot, O., Delettrez, J.A., Meyerhofer, D.D., Regan, S.P., Sangster, T.C., 2005. Fourier-space nonlinear Rayleigh–Taylor growth measurements of 3D laser-imprinted modulations in planar targets. *Phys. Rev. Lett.* 95, 215001.
- Smalyuk, V.A., Sadot, O., Betti, R., Goncharov, V.N., Delettrez, J.A., Meyerhofer, D.D., Regan, S.P., Sangster, T.C., Shvarts, D., 2006. Rayleigh–Taylor growth measurements of three-dimensional modulations in a nonlinear regime. *Phys. Plasmas* 13, 056312.
- Smalyuk, V.A., Hu, S.X., Goncharov, V.N., Meyerhofer, D.D., Sangster, T.C., Stoeckl, C., Yaakobi, B., 2008. Systematic study of Rayleigh–Taylor growth in directly driven plastic targets in a laser-intensity range from $\sim 2 \times 10^{14}$ to $\sim 1.5 \times 10^{15} \text{ W/cm}^2$. *Phys. Plasmas* 15, 082703.
- Smalyuk, V.A., Hu, S.X., Hager, J.D., Delettrez, J.A., Meyerhofer, D.D., Sangster, T.C., Shvarts, D., 2009. Rayleigh–Taylor growth measurements in the acceleration phase of spherical implosions on OMEGA. *Phys. Rev. Lett.* 103, 105001.
- Smalyuk, V.A., Hansen, J.F., Hurricane, O.A., Langstaff, G., Martinez, D., Park, H.-S., Raman, K., Remington, B.A., Robey, H.F., Schilling, O., Wallace, R., Elbaz, Y., Shimony, A., Shvarts, D., Di Stefano, C., Drake, R.P., Marion, D., Krauland, C.M., Kuranz, C.C., 2012. Experimental observations of turbulent mixing due to Kelvin–Helmholtz instability on the OMEGA laser facility. *Phys. Plasmas* 19, 092702.
- Smalyuk, V.A., Hurricane, O.A., Hansen, J.F., Langstaff, G., Martinez, D., Park, H.-S., Raman, K., Remington, B.A., Robey, H.F., Schilling, O., Wallace, R., Elbaz, Y., Shimony, A., Shvarts, D., Di Stefano, C., Drake, R.P., Marion, D., Krauland, C.M., Kuranz, C.C., 2013. Measurements of turbulent mixing due to Kelvin–Helmholtz instability in high-energy-density plasmas. *High Energy Density Phys.* 9, 47.
- Smalyuk, V.A., Tipton, R.E., Pino, J.E., Casey, D.T., Grim, G.P., Remington, B.A., Rowley, D.P., Weber, S.V., Barrios, M., Benedetti, L.R., Bleuel, D.L., Bradley, D.K., Caggiano, J.A., Callahan, D.A., Cerjan, C.J., Clark, D.S., Edgell, D.H., Edwards, M.J., Frenje, J.A., Gatou-Johnson, M., Glebov, V.Y., Glenn, S., Haan, S.W., Hamza, A., Hatarik, R., Hsing, W.W., Izumi, N., Khan, S., Kilkenney, J.D., Kline, J., Knauer, J., Landen, O.L., Ma, T., McNaney, J.M., Mintz, M., Moore, A., Nikroo, A., Pak, A., Parham, T., Petrasso, R., Sayre, D.B., Schneider, M.B., Tommasini, R., Town, R.P., Widmann, K., Wilson, C., Yeamans, C.B., 2014. Measurements of an ablator-gas atomic mix in indirectly driven implosions at the National Ignition Facility. *Phys. Rev. Lett.* 112, 025002.
- Smalyuk, V.A., Robey, H.F., Döppner, T., Jones, O.S., Milovich, J.L., Bachmann, B., Baker, K.L., et al., 2015. First results of radiation-driven, layered deuterium–tritium implosions with a 3-shock adiabat-shaped drive at the National Ignition Facility. *Phys. Plasmas* 22, 080703.
- Smalyuk, V.A., Weber, C.R., Robey, H.F., Casey, D.T., Chen, K.-C., Clark, D.S., Farrell, M., Felker, S., Field, J.E., Haan, S.W., Hammel, B.A., Hamza, A.V., Hoover, D., Kroll, J.J., Landen, O.L., MacPhee, A.G., Martinez, D., Nikroo, A., Rice, N., 2017. Hydrodynamic instability growth of three-dimensional modulations in radiation-driven implosions with “low-foot” and “high-foot” drives at the National Ignition Facility. *Phys. Plasmas* 24, 042706.
- Smarr, L., 2009. Progenitors of core-collapse supernovae. *Annu. Rev. Astron. Astrophys.* 47, 63.
- Smeeton, V.S., Youngs, D.L., 1987. Experimental investigation of turbulent mixing by Rayleigh–Taylor instability, III, AWE report N.O 35/87.
- Smith, A.V., Holder, D.A., Barton, C.J., Morris, A.V., Youngs, D.L., 2001. Shock tube experiments on Richtmyer–Meshkov instability across a chevron profiled interface. In: Proceedings of the Eighth International Workshop on the Physics of Compressible Turbulent Mixing.
- Snider, D.M., Andrews, M.J., 1994. Rayleigh–Taylor and shear driven with an unstable thermal stratification. *Phys. Fluids* 6, 3324.
- Sohn, S.-I., Yoon, D., Hwang, W., 2010. Long-time simulations of the Kelvin–Helmholtz instability using an adaptive vortex method. *Phys. Rev. E* 82, 046711.
- Souffland, D., Grégoire, O., Gauthier, S., Schiestel, R., 2002. A two-time-scale model for turbulent mixing flows induced by Rayleigh–Taylor and Richtmyer–Meshkov instabilities. *Flow. Turbul. Combust.* 69, 123.
- Souffland, D., Soulard, O., Griffond, J., 2014. Modeling of Reynolds stress models for diffusion fluxes inside shock waves. *ASME J. Fluids Eng.* 136, 091102.
- Soulard, O., Griffond, J., 2012. Inertial range anisotropy in Rayleigh–Taylor turbulence. *Phys. Fluids* 24, 025101.
- Soulard, O., Griffond, J., Souffland, D., 2012. Pseudocompressible approximation and statistical turbulence modeling: Application to shock tube flows. *Phys. Rev. E* 85, 026307.
- Soulard, O., Griffond, J., Gréa, B.-J., 2014. Large-scale analysis of self-similar unstably stratified homogeneous turbulence. *Phys. Fluids* 26, 015110.
- Soulard, O., Griffond, J., Gréa, B.-J., 2015. Large-scale analysis of unconfined self-similar Rayleigh–Taylor turbulence. *Phys. Fluids* 27, 095103.
- Soulard, O., Griffond, J., Gréa, B.-J., 2016. Influence of the mixing parameter on the second order moments of velocity and concentration in Rayleigh–Taylor turbulence. *Phys. Fluids* 28, 065107.
- Speziale, C.G., 1987. On nonlinear $K-L$ and $K-\epsilon$ models of turbulence. *J. Fluid Mech.* 178, 459.
- Speziale, C.G., 1991. Analytical methods for the development of Reynolds stress closures in turbulence. *Annu. Rev. Fluid Mech.* 23, 107.
- Speziale, C.G., Mac Giolla Mhuiris, N., 1989. On the prediction of equilibrium states in homogeneous turbulence. *J. Fluid Mech.* 209, 591.
- Spitzer Jr., L., 1954. Behavior of matter in space. *Astrophys. J.* 120, 1.
- Spitzer, L., 1962. Physics of Fully Ionized Gases. Interscience Publishers, Geneva.
- Srebro, Y., Elbaz, Y., Sadot, O., Arazi, L., Shvarts, D., 2003. A general buoyancy–drag model for the evolution of the Rayleigh–Taylor and Richtmyer–Meshkov instabilities. *Laser Part. Beams* 21, 347.
- Srinivasan, B., Tang, X.-Z., 2012. Mechanism for magnetic field generation and growth in Rayleigh–Taylor unstable two-fluid plasmas. *Phys. Plasmas* 19, 082703.
- Srinivasan, B., Tang, X.-Z., 2013. The mitigating effect of magnetic fields on Rayleigh–Taylor unstable inertial confinement fusion plasmas. *Phys. Plasmas* 20, 056307.
- Srinivasan, B., Dimonte, G., Tang, X.-Z., 2012. Magnetic field generation in Rayleigh–Taylor unstable inertial confinement fusion plasmas. *Phys. Rev. Lett.* 108, 165002.
- Stalsberg-Zarling, K., Gore, R., 2011. The BHR2 Turbulence Model: Incompressible Isotropic Decay, Rayleigh–Taylor, Kelvin–Helmholtz and Homogeneous Variable-Density Turbulence, Los Alamos National Lab report LA-UR-11-04773.
- Stanic, M., McFarland, J., Stellingwerf, R.F., Cassibry, J.T., Ranjan, D., Bonazza, R., Greenough, J.A., Abarzhi, S.I., 2013. Non-uniform volumetric structures in Richtmyer–Meshkov flows. *Phys. Fluids* 25, 106107.
- Stanton, L.G., Murillo, M.S., 2016. Ionic transport in high-energy-density matter. *Phys. Rev. E* 93, 043203.
- Steinberg, D.J., Lund, C.M., 1989. A constitutive model for strain rates from 10^{-4} to 10^6 s^{-1} . *J. Appl. Phys.* 65, 1528.
- Steinberg, D.J., Cochran, S.G., Guinan, M.W., 1980. A constitutive model for metals applicable at high-strain rate. *J. Appl. Phys.* 51, 1498.
- Stone, J.M., Gardiner, T., 2007a. Nonlinear evolution of the magnetohydrodynamic Rayleigh–Taylor instability. *Phys. Fluids* 19, 094104.
- Stone, J.M., Gardiner, T., 2007b. The magnetic Rayleigh–Taylor instability in three dimensions. *Astrophys. J.* 671, 1726.
- Strykowski, P.J., Krothapalli, A., Jendoubi, S., 1996. The effect of counterflow on the development of compressible shear layers. *J. Fluid Mech.* 308, 63.
- Subramaniam, A., Ghaisas, N., Lele, S., 2017. High-order Eulerian simulations of multi-material elastic-plastic flow. *ASME J. Fluids Eng.* <http://dx.doi.org/10.1115/1.4038399>.
- Sun, Y.B., Piriz, A.R., 2014. Magneto-Rayleigh–Taylor instability in solid media. *Phys. Plasmas* 21, 072708.
- Suponitsky, V., Froese, A., Barsky, S., 2014. Richtmyer–Meshkov instability of a liquid–gas interface driven by a cylindrical imploding pressure wave. *Comput. & Fluids* 89, 1.
- Swegle, J.W., Robinson, A.C., 1989. Acceleration instability in elastic–plastic solids. I. Numerical simulations of plate acceleration. *J. Appl. Phys.* 66, 2838.
- Swisher, N.C., Kuranz, C.C., Arnett, D., Hurricane, O., Remington, B.A., Robey, H.F., Abarzhi, S.I., 2015. Rayleigh–Taylor mixing in supernova experiments. *Phys. Plasmas* 22, 102707.

- Sysoev, N.E., 1997. Long-wave instability of an ionization front. *Astron. Lett.* 23, 409.
- Tabak, M., Munro, D.H., Lindl, J.D., 1990. Hydrodynamic stability and the direct drive approach to laser fusion. *Phys. Fluids B* 2, 1007.
- Tabeling, P., 2002. Two-dimensional turbulence: a physicist approach. *Phys. Rep.* 362.
- Takabe, H., 2004. A historical perspective of developments in hydrodynamic instabilities, integrated codes and laboratory astrophysics. *Nucl. Fusion* 44, S149.
- Takabe, H., Montierth, L., Morse, R.L., 1983. Self-consistent eigenvalue analysis of Rayleigh–Taylor instability in an ablating plasma. *Phys. Fluids* 26, 2299.
- Takabe, H., Mima, K., Montierth, L., Morse, R.L., 1985. Self-consistent growth rate of the Rayleigh–Taylor instability in an ablatively accelerating plasma. *Phys. Fluids* 28, 3676.
- Takabe, H., Yamanaka, M., Mima, K., Yamanaka, C., Azechi, H., Miyanaga, N., Nakatsuka, M., Jitsuno, T., Norimatsu, T., Takagi, M., Nishimura, H., Nakai, M., Yabe, T., Sasaki, T., Yoshida, K., Kato, Y., Izawa, Y., Yamanaka, T., Nakai, S., 1988. Scalings of implosion experiments for high neutron yield. *Phys. Fluids* 31, 2884.
- Tao, J.J., He, X.T., Ye, W.H., Busse, F.H., 2013. Nonlinear Rayleigh–Taylor instability of rotating inviscid fluids. *Phys. Rev. E* 87, 013001.
- Tassart, J., 2004. Overview of inertial fusion and high-intensity laser plasma research in Europe. *Nucl. Fusion* 44, S134.
- Tavakoli, A., Tskhakaya, D.D., Tsintsadze, N.L., 1999. Rayleigh–Taylor instability in the presence of a density transition layer. *Phys. Lett. A* 256, 212.
- Tavakoli, A., Hadzievski, L., Tskhakaya, D.D., 2000. Rayleigh–Taylor instability of magnetized density transition layer. *Phys. Plasmas* 7, 89.
- Taylor, G.I., 1950. The instability of liquid surfaces when accelerated in a direction perpendicular to their plane. *Proc. R. Soc. Lond. Ser. A Math. Phys. Eng. Sci.* 201, 192.
- Tennekes, H., Lumley, J.L., 1972. First Course in Turbulence. MIT Press, Cambridge, MA.
- Terrones, G., Carrara, M.D., 2015. Rayleigh–Taylor instability at spherical interfaces between viscous fluids: fluid/vacuum interface. *Phys. Fluids* 27, 054105.
- Terry, P.W., 2000. Suppression of turbulence and transport by sheared flow. *Rev. Modern Phys.* 72, 109.
- Theofanous, T.G., 2011. Aerobreakup of Newtonian and viscoelastic liquids. *Annu. Rev. Fluid Mech.* 43, 661.
- Theofanous, T.G., Li, G.J., 2008. On the physics of aerobreakup. *Phys. Fluids* 20, 052103.
- Theofanous, T.G., Li, G.J., Dinh, T.N., 2004. Aerobreakup in rarefied supersonic gas flows. *ASME J. Fluid Eng.* 126, 516.
- Theofanous, T.G., Mitkin, V.V., Ng, C.L., Chang, C.H., Deng, X., Sushchikh, S., 2012. The physics of aerobreakup. Part II: Viscous liquids. *Phys. Fluids* 24, 022104.
- Thornber, B., 2016. Impact of domain size and statistical errors in simulations of homogeneous decaying turbulence and the Richtmyer–Meshkov instability. *Phys. Fluids* 28, 045106.
- Thornber, B., Zhou, Y., 2015. Numerical simulations of the two-dimensional multimode Richtmyer–Meshkov instability. *Phys. Plasmas* 22, 032309.
- Thornber, B., Mosedale, A., Drikakis, D., Youngs, D.L., Williams, R.J.R., 2008. An improved reconstruction method for compressible flows with low Mach number features. *J. Comput. Phys.* 227, 4873.
- Thornber, B., Drikakis, D., Youngs, D.L., Williams, R.J.R., 2010. The influence of initial conditions on turbulent mixing due to Richtmyer–Meshkov instability. *J. Fluid Mech.* 654, 99.
- Thornber, B., Drikakis, D., Youngs, D.L., Williams, R.J.R., 2011. Growth of a Richtmyer–Meshkov turbulent layer after reshock. *Phys. Fluids* 23, 095107.
- Thornber, B., Drikakis, D., Youngs, D.L., Williams, R.J.R., 2012. Physics of the single-shocked and reshocked Richtmyer–Meshkov instability. *J. Turbul.* 13, N10.
- Tian, B.-L., Fu, D.-X., Ma, Y.-W., 2006. Numerical investigation of Richtmyer–Meshkov instability driven by cylindrical shocks. *Acta Mech. Sinica* 22, 9.
- Ticknor, C., Kress, J.D., Collins, L.A., Clérouin, J., Arnault, P., Decoster, A., 2016. Transport properties of an asymmetric mixture in the dense plasma regime. *Phys. Rev. E* 93, 063208.
- Tipton, R.E., 1999. A phenomenological k-L mix model for NIF targets in 1, 2 and 3 dimensions. In: Proc. 7th International Workshop on the Physics of Compressible Turbulent Mixing, Sarov, Russia: RFNC-VNIIEF.
- Tofiqhi, N., Ozbulut, M., Feng, J.J., Yildiz, M., 2016. The effect of normal electric field on the evolution of immiscible Rayleigh–Taylor instability. *Theor. Comput. Fluid Dyn.* 30, 469.
- Tomkins, C., Kumar, S., Orlicz, G., Prestridge, K., 2008. An experimental investigation of mixing mechanisms in shock-accelerated flow. *J. Fluid Mech.* 611, 131.
- Tomkins, C., Balakumar, B.J., Orlicz, G., Prestridge, K., Ristorcelli, J.R., 2013. Evolution of the density self-correlation in developing Richtmyer–Meshkov turbulence. *J. Fluid Mech.* 735, 288.
- Town, R.J., Bell, A.R., 1991. Three-dimensional simulations of the implosion of inertial confinement fusion targets. *Phys. Rev. Lett.* 67, 1863.
- Townsend, A.A., 1976. Structure of Turbulent Shear Flow. Cambridge Univ. Press, Cambridge, UK.
- Tritschler, V.K., Avdonin, A., Hickel, S., Hu, X.Y., Adam, N.A., 2014a. Quantification of initial-data uncertainty on a shock-accelerated gas cylinder. *Phys. Fluids* 26, 026101.
- Tritschler, V.K., Olson, B.J., Lele, S.K., Hickel, S., Hu, X.Y., Adam, N.A., 2014b. On the Richtmyer–Meshkov instability evolving from a deterministic multimode planar interface. *J. Fluid Mech.* 755, 429.
- Tritschler, V.K., Zubel, M., Hickel, S., Adams, N.A., 2014c. Evolution of length scales and statistics of Richtmyer–Meshkov instability from direct numerical simulations. *Phys. Rev. E* 90, 063001.
- Tryggvason, G., Unverdi, S.O., 1990. Computations of three-dimensional Rayleigh–Taylor instability. *Phys. Fluids A* 2, 656.
- Tubbs, D.L., Barnes, C.W., Beck, J.B., Hoffmann, N.M., Oertel, J.A., Watt, R.G., Boehly, T., Bradley, D., Jaanimagi, P., Knauer, J., 1999. Cylindrical implosion experiments using laser direct drive. *Phys. Plasmas* 6, 2095.
- Turner, J.S., 1973. Buoyancy Effects in Fluids. Cambridge Univ. Press, London.
- Ukai, S., Balakrishnan, K., Menon, S., 2010. On Richtmyer–Meshkov instability in dilute gas-particle mixtures. *Phys. Fluids* 22, 104103.
- Ukai, S., Balakrishnan, K., Menon, S., 2011. Growth rate predictions of single- and multi-mode Richtmyer–Meshkov instability with reshock. *Shock Waves* 21, 533.
- Vadivukkarasan, M., Panchagnula, M.V., 2017. Combined Rayleigh–Taylor and Kelvin–Helmholtz instabilities on an annular liquid sheet. *J. Fluid Mech.* 812, 152.
- Valerio, E., Jourdan, G., Houas, L., Zeitoun, D., Besnard, D.C., 1999. Modeling of Richtmyer–Meshkov instability-induced turbulent mixing in shock-tube experiments. *Phys. Fluids* 11, 214.
- Vandenboomgaerde, M., Aymard, C., 2011. Analytical theory for planar shock focusing through perfect gas lens and shock tube experiment designs. *Phys. Fluids* 23, 016101.
- Vandenboomgaerde, M., Souffland, D., Mariani, C., Biamino, L., Jourdan, G., Houas, L., 2014. An experimental and numerical investigation of the dependency on the initial conditions of the Richtmyer–Meshkov instability. *Phys. Fluids* 26, 024109.
- Vandenboomgaerde, M., Bonneville, M., Gauthier, P., 2016. The Kelvin–Helmholtz instability in National Ignition Facility hohlraums as a source of gold–gas mixing. *Phys. Plasmas* 23, 052704.
- Vandervoort, P.O., 1961. The character of the equilibrium of a compressible, inviscid fluid of varying density. *Astrophys. J.* 134, 699.
- Vandervoort, P.O., 1962. On the stability of ionization fronts. *Astrophys. J.* 135, 212.
- Velikovich, A.L., Schmit, P.F., 2015. Bell-Plesset effects in Rayleigh–Taylor instability of finite-thickness spherical and cylindrical shells. *Phys. Plasmas* 22, 122711.

- Velikovich, A.L., Cochran, F.L., Davis, J., 1996. Suppression of Rayleigh–Taylor instability in Z-pinch loads with tailored density profiles. *Phys. Rev. Lett.* 77, 853.
- Vemula, J.B., Sinha, K., 2017. Reynolds stress models applied to canonical shock-turbulence interaction. *J. Turbul.* 18, 653.
- Venaille, A., Gostiaux, L., Sommeria, J., 2017. A statistical mechanics approach to mixing in stratified fluids. *J. Fluid Mech.* 810, 554.
- Verdon, C.P., McCrory, R.L., Morse, R.L., Baker, G.R., Meiron, D.I., Orszag, S.A., 1982. Nonlinear effects of multifrequency hydrodynamic instabilities on ablatively accelerated thin shells. *Phys. Fluids* 25, 1653.
- Vetter, M., Sturtevant, B., 1995. Experiments on the Richtmyer–Meshkov instability of an air/SF₆ interface. *Shock Waves* 4, 247.
- Vladimirova, N., Chertkov, M., 2009. Self-similarity and universality in Rayleigh–Taylor, Boussinesq turbulence. *Phys. Fluids* 21, 015102.
- Vold, E.L., Joglekar, A.S., Ortega, M.I., Moll, R., Fenn, D., Molvig, K., 2015. Plasma viscosity with mass transport in spherical inertial confinement fusion implosion simulations. *Phys. Plasmas* 22, 112708.
- Vold, E.L., Joglekar, A., Ortega, M., Moll, R., Fenn, D., Molvig, K., 2016. Plasma and artificial viscosity in spherical ICF implosion simulations. *J. Phys. Conf. Ser.* 717, 012056.
- Vold, E.L., Rauenzahn, R.M., Aldrich, C.H., Molvig, K., Simakov, A.N., Haines, B.M., 2017. Plasma transport in an Eulerian AMR code. *Phys. Plasmas* 24, 042702.
- Vorobieff, P., Rightley, P.M., Benjamin, R.F., 1998. Power-law spectra of incipient gas-curtain turbulence. *Phys. Rev. Lett.* 81, 2240.
- Vorobieff, P., Mohamed, N.G., Tomkins, C., Goodenough, C., Marr-Lyon, M., Benjamin, R.F., 2003. Scaling evolution in shock-induced transition to turbulence. *Phys. Rev. E* 68, 065301.
- Vreman, A.M., 2004. An eddy-viscosity subgrid-scale model for turbulent shear flow: Algebraic theory and applications. *Phys. Fluids* 16, 3670.
- Waddell, J.T., Niederhaus, C.E., Jacobs, J.W., 2001. Experimental study of Rayleigh–Taylor instability: Low Atwood number liquid systems with single-mode initial perturbations. *Phys. Fluids* 13, 1263.
- Waltz, J., Gianakon, T.A., 2012. A comparison of mix models for the Rayleigh–Taylor instability. *Computer Phys. Commun.* 183, 70.
- Wan, W.C., Malamud, G., Shimony, A., Di Stefano, C.A., Trantham, M.R., Klein, S.R., Shvarts, D., Kuranz, C.C., Drake, R.P., 2015. Observation of single mode, Kelvin–Helmholtz instability in a supersonic flow. *Phys. Rev. Lett.* 115, 145001.
- Wan, W.C., Malamud, G., Shimony, A., Di Stefano, C.A., Trantham, M.R., Klein, S.R., Soltis, J.D., Shvarts, D., Drake, R.P., Kuranz, C.C., 2017. Impact of ablator thickness and laser drive duration on a platform for supersonic, shockwave-driven hydrodynamic instability experiments. *High Energy Density Physics* 22, 6.
- Wan, X., Karniadakis, G.E., 2006. Multi-element generalized polynomial chaos for arbitrary probability measures. *SIAM J. Sci. Comput.* 28, 901.
- Wang, L.F., Ye, W.H., Fan, Z.F., Li, Y.J., He, X.T., Yu, M.Y., 2009a. Weakly nonlinear analysis on the Kelvin–Helmholtz instability. *Europhys. Lett.* 86, 15002.
- Wang, L.F., Ye, W.H., Li, Y.J., 2009c. Numerical investigation on the ablative Kelvin–Helmholtz instability. *Europhys. Lett.* 87, 54005.
- Wang, L.F., Ye, W.H., Fan, Z.F., Li, Y.J., 2010b. Nonlinear saturation amplitude in the Rayleigh–Taylor instability at arbitrary Atwood numbers with continuous profiles. *Europhys. Lett.* 90, 15001.
- Wang, L.F., Ye, W.H., Sheng, Z.M., Don, W.-S., Li, Y.J., He, X.T., 2010c. Preheating ablation effects on the Rayleigh–Taylor instability in the weakly nonlinear regime. *Phys. Plasmas* 17, 122706.
- Wang, L.F., Yang, B.L., Ye, W.H., He, X.T., 2012a. Stabilization of the Rayleigh–Taylor instability in quantum magnetized plasma. *Phys. Plasmas* 19, 072704.
- Wang, L.F., Ye, W.H., He, X.T., Zhang, W.Y., Sheng, Z.M., Yu, M.Y., 2012b. Formation of jet-like spikes from the ablative Rayleigh–Taylor instability. *Phys. Plasmas* 19, 100701.
- Wang, L.F., Wu, J.F., Ye, W.H., Zhang, W.Y., He, X.T., 2013a. Weakly nonlinear incompressible Rayleigh–Taylor instability growth at cylindrically convergent interfaces. *Phys. Plasmas* 20, 042708.
- Wang, L.F., Ye, W.H., Zhang, W.Y., He, X.T., 2013b. Numerical investigation of nonlinear ablative single-mode Rayleigh–Taylor instability in the presence of preheating. *Phys. Scr. T* 155, 014018.
- Wang, L.F., Wu, J.F., Guo, H.Y., Ye, W.H., Liu, J., Zhang, W.Y., He, X.T., 2015a. Weakly nonlinear Bell-Plesset effects for a uniformly converging cylinder. *Phys. Plasmas* 22, 082702.
- Wang, L.F., Ye, W.H., Wu, J.F., Liu, J., Zhang, W.Y., He, X.T., 2016a. A scheme for reducing deceleration-phase Rayleigh–Taylor growth in inertial confinement fusion implosions. *Phys. Plasmas* 23, 052713.
- Wang, L.F., Ye, W.H., Wu, J.F., Liu, J., Zhang, W.Y., He, X.T., 2016b. Main drive optimization of a high-foot pulse shape in inertial confinement fusion implosions. *Phys. Plasmas* 23, 122702.
- Wang, P., Zhou, Y., MacLaren, S.A., Huntington, C.M., Raman, K.S., Doss, F.W., Flippo, K.A., 2015b. Three- and two-dimensional simulations of counter-propagating shear experiments at high energy densities at the National Ignition Facility. *Phys. Plasmas* 22, 112701.
- Wang, T., Bai, J.S., Li, P., Zhong, M., 2009. The numerical study of shock-induced hydrodynamic instability and mixing. *Chin. Phys. B* 18, 1127.
- Wang, T., Bai, J.S., Li, P., Liu, K., 2010. Large-eddy simulations of the Richtmyer–Meshkov instability of rectangular interfaces accelerated by shock waves. *Sci. China Phys. Mech. Astron.* 53, 905.
- Wang, T., Liu, J.-H., Bai, J.-S., Jiang, Y., Li, P., Liu, K., 2012. Experimental and numerical investigation of inclined air/SF₆ interface instability under shock wave. *Appl. Math. Mech.* 33, 37.
- Wang, T., Tao, G., Bai, J.-S., Li, P., Wang, B., 2015c. Numerical comparative analysis of Richtmyer–Meshkov instability simulated by different SGS. *Can. J. Phys.* 93, 519.
- Wang, T., Tao, G., Bai, J.-S., Li, P., Wang, B., Du, L., Xiao, J.-X., 2017. The dynamical behavior of the Richtmyer–Meshkov instability-induced turbulent mixing under multiple shock interactions. *Can. J. Phys.* 95, 671.
- Wang, X., Yang, D., Wu, J., Luo, X., 2015d. Interaction of a weak shock wave with a discontinuous heavy-gas cylinder. *Phys. Fluids* 27, 064104.
- Weber, C.R., Motl, B., Oakley, J.G., Anderson, M., Bonazza, R., 2009. Richtmyer–Meshkov parameter study. *Fusion Sci. Tech.* 56, 460.
- Weber, C.R., Haehn, N.S., Oakley, J.G., Rothamer, D.A., Bonazza, R., 2012a. Turbulent measurements in the Richtmyer–Meshkov instability. *Phys. Fluids* 24, 074105.
- Weber, C.R., Haehn, N.S., Oakley, J.G., Anderson, M., Bonazza, R., 2012b. Richtmyer–Meshkov instability on a low Atwood number interface after reshock. *Shock Waves* 22, 317.
- Weber, C.R., Haehn, N.S., Oakley, J.G., Rothamer, D.A., Bonazza, R., 2014a. An experimental investigation of the turbulent mixing transition in the Richtmyer–Meshkov instability. *J. Fluid Mech.* 748, 457.
- Weber, C.R., Clark, D.S., Cook, A.W., Busby, L.E., Robey, H.F., 2014b. Inhibition of turbulence in inertial-confinement-fusion hot spots by viscous dissipation. *Phys. Rev. E* 89, 053106.
- Weber, C.R., Clark, D.S., Cook, A.W., Eder, D.C., Haan, S.W., Hammel, B.A., Hinkel, D.E., Jones, O.S., Marinak, M.M., Milovich, J.L., Patel, P.K., Robey, H.F., Salmonson, J.D., Sepke, S.M., Thomas, C.A., 2015. Three-dimensional hydrodynamics of the deceleration stage in inertial confinement fusion. *Phys. Plasmas* 22, 032702.
- Wei, Y.-K., Dou, H.-S., Qian, Y.-H., Wang, Z.-D., 2017. A novel two-dimensional coupled lattice Boltzmann model for incompressible flow in application of turbulence Rayleigh–Taylor instability. *Comput. & Fluids* 156, 97.
- Weir, S.T., Chandler, E.A., Goodwin, B.T., 1998. Rayleigh–Taylor instability experiments examining feedthrough growth in an incompressible, convergent geometry. *Phys. Rev. Lett.* 80, 3763.

- Welser-Sherrill, L., Fincke, J., Doss, F., Loomis, E., Flippo, K., Offermann, D., Keiter, P., Haines, B., Grinstein, F., 2013. Two laser-driven mix experiments to study reshock and shear. *High Energy Density Phys.* 9, 496.
- Werne, J., Fritts, D.C., 1999. Stratified shear turbulence: Evolution and statistics. *Geophys. Res. Lett.* 26, 439.
- Whalen, D.J., Norman, M.L., 2008. Three-dimensional dynamical instabilities in Galactic ionization fronts. *Astrophys. J.* 672, 287.
- Wheatley, V., Pullin, D.I., Samtaney, R., 2005a. Regular shock refraction at an oblique planar density interface in magnetohydrodynamics. *J. Fluid Mech.* 522, 179.
- Wheatley, V., Pullin, D.I., Samtaney, R., 2005b. Stability of an impulsively accelerated density interface in magnetohydrodynamics. *Phys. Rev. Lett.* 95, 125002.
- Wheatley, V., Pullin, D.I., Samtaney, R., 2009. The Richtmyer–Meshkov instability in magnetohydrodynamics. *Phys. Fluids* 21, 082102.
- Wheatley, V., Pullin, D.I., Samtaney, R., Gehre, R.M., 2014. The transverse Richtmyer–Meshkov instability in magnetohydrodynamics. *Phys. Fluids* 26, 016102.
- White, A.J., Collins, L.A., Kress, J.D., Ticknor, C., Clérouin, J., Arnault, P., Desbiens, N., 2017. Correlation and transport properties for mixtures at constant pressure and temperature. *Phys. Rev. E* 95, 063202.
- Whitham, G.B., 1974. *Linear and Nonlinear Waves*. Wiley, NY.
- Whitney, K.G., 1999. K. G. Momentum and heat conduction in highly ionizable plasmas. *Phys. Plasmas* 6, 816.
- Wieland, S., Reckinger, S., Hamlington, P., Livescu, D., 2017. Effects of background stratification on the compressible Rayleigh–Taylor instability. In: 47th AIAA Fluid Dynamics Conference. Denver, CO.
- Wiener, N., 1938. The homogeneous chaos. *Amer. J. Math.* 60, 897.
- Wilcox, D.C., 1998. *Turbulence Modeling for CFD*. DCW Industries, Inc, La, Canada, CA.
- Williams, R.J.R., 1999. Shadowing instabilities of ionization fronts. *Mon. Not. R. Astron. Soc.* 310, 789.
- Williams, R.J.R., 2002. On the instability of D-type ionization fronts. *Mon. Not. R. Astron. Soc.* 331, 693.
- Williams, R.J.R., 2017. Rayleigh–Taylor mixing between density stratified layers. *J. Fluid Mech.* 810, 584.
- Wilson, D.C., Scannapieco, A.J., Cranfill, C.W., Clover, M.R., Hoffman, N.M., Collins, J., 2003. Degradation of radiatively driven inertial confinement fusion capsule implosions by multifluid interpenetration mixing. *Phys. Plasmas* 10, 4427.
- Wilson, D.C., Cranfill, C.W., Christensen, C., Forster, R.A., Peterson, R.R., Hoffman, N.M., Pollak, G.D., Li, C.K., Seguin, F.H., Frenje, J.A., Petrasso, R.D., McKenty, P.W., Marshall, F.J., Glebov, V.Y., Stoeckl, C., Schmid, G.J., Izumi, N., Amendt, P., 2004. Multifluid interpenetration mixing in directly driven inertial confinement fusion capsule implosions. *Phys. Plasmas* 11, 2723.
- Wilson, D.C., Bradley, P.A., Cerjan, C.J., Salmonson, J.D., Spears, B.K., Hatchet II, S.P., Herrmann, H.W., Glebov, V. Yu., 2008. Diagnosing ignition with DT reaction history. *Rev. Sci. Instrum.* 79, 10E525.
- Wilson, D.C., Ebey, P.S., Sangster, T.C., Shmayda, W.T., Glebov, V. Yu., Lerche, R.A., 2011. Atomic mix in directly driven inertial confinement implosions. *Phys. Plasmas* 18, 112707.
- Wilson, P.N., Andrews, M.J., 2002. Spectral measurements of Rayleigh–Taylor mixing at small Atwood number. *Phys. Fluids* 14, 938.
- Wilson, P., Andrews, M., Harlow, F., 1999. Spectral nonequilibrium in a turbulent mixing layer. *Phys. Fluids* 11, 2425.
- Wolfshtein, M., 1970. Length-scale-of-turbulence equation. *Isr. J. Technol.* 8, 87.
- Woods, J.D., 1968. Wave-induced shear instability in the summer thermocline. *J. Fluid Mech.* 32, 791.
- Woodward, P.R., Porter, D.H., Dai, W., Fuchs, T., Nowatzki, A., Knox, M., Dimonte, G., Herwig, F., Fryer, C., 2010. The piecewise-parabolic Boltzmann advection scheme (PPB) applied to multifluid hydrodynamics. Los Alamos Report No. LAUR-10-01823.
- Wouchuk, J.G., Nishihara, K., 1996. Linear perturbation growth at a shocked interface. *Phys. Plasmas* 3, 3761.
- Wouchuk, J.G., Nishihara, K., 2004. Normal velocity freeze-out of the Richtmyer–Meshkov instability when a shock is reflected. *Phys. Rev. E* 70, 026305.
- Xiao, J.-X., Bai, J.-S., Wang, T., 2016. Numerical study of initial perturbation effects on Richtmyer–Meshkov instability in nonuniform flows. *Phys. Rev. E* 94, 013112.
- Xiu, D., Karniadakis, G.E., 2003. Modeling uncertainty in flow simulations via generalized polynomial chaos. *J. Comput. Phys.* 187, 137.
- Xue, C., Ye, W., 2010. Destabilizing effect of compressibility on Rayleigh–Taylor instability for fluids with fixed density profile. *Phys. Plasmas* 17, 042705.
- Yabe, T., Hoshino, H., Tsuchiya, T., 1991. Two- and three-dimensional behavior of Rayleigh–Taylor and Kelvin–Helmholtz instabilities. *Phys. Rev. A* 44, 2756.
- Yan, R., Betti, R., Sanz, J., Aluie, H., Liu, B., Frank, A., 2016. Three-dimensional single-mode nonlinear ablative Rayleigh–Taylor instability. *Phys. Plasmas* 23, 022701.
- Yang, J., Kubota, T., Zukoski, E.E., 1994. A model for characterization of a vortex pair formed by shock passage over a light-gas inhomogeneity. *J. Fluid Mech.* 258, 217.
- Yang, J.-T., Zhu, Y.-J., Yang, J.-M., 2017. Self-ignition induced by cylindrically imploding shock adapting to a convergent channel. *Phys. Fluids* 29, 031702.
- Yang, M., Wang, L.L., Zhang, S.D., 2011. Numerical simulation of turbulent mixing induced by Rayleigh–Taylor instability. *Engrg. Mech.* 28, 236.
- Yang, Q.-Z., Li, B.Q., Xu, F., 2017. Electrohydrodynamic Rayleigh–Taylor instability in leaky dielectric fluids. *Int. J. Heat Mass Transfer* 109, 690.
- Yang, Y., Zhang, Q., 1993. General properties of a multilayer stratified fluids system. *Phys. Fluids A* 5, 1167.
- Yang, Y., Zhang, Q., Sharp, D.H., 1994. Small amplitude theory of Richtmyer–Meshkov instability. *Phys. Fluids* 6, 1856.
- Yanilkin, Yu. V., Nikiforov, V.V., Bondarenko, Yu A., Gubkov, E.V., Zharova, G.V., Statsenko, V.P., Tarasov, V.I., 1995. Two-parameter model and method for computations of turbulent mixing in 2D compressible flows. In: 5rd International Workshop on the Physics of Compressible Turbulent Mixing, Stony Brook, USA.
- Ye, W.H., Zhang, W., He, X.T., 2002. Stabilization of ablative Rayleigh–Taylor instability due to change of the Atwood number. *Phys. Rev. E* 65, 057401.
- Ye, W.H., Wang, L.F., Xue, C., Fan, Z.F., He, X.T., 2011. Competitions between Rayleigh–Taylor instability and Kelvin–Helmholtz instability with continuous density and velocity profiles. *Phys. Plasma* 18, 022704.
- Yeung, P.K., Brasseur, J.G., 1991. The response of isotropic turbulence to isotropic and anisotropic forcing at large scales. *Phys. Fluids A* 3, 884.
- Yong, H., Zhai, C.L., Jiang, S., Song, P., Dai, Z.S., Gu, J.F., 2016. Numerical simulations of instabilities in the implosion process of inertial confined fusion in 2D cylindrical coordinates. *Sci. China-Phys. Mech. Astron.* 59, 614704.
- Young, Y.-N., Tufo, H., Dubey, A., Rosner, R., 2001. On the miscible Rayleigh–Taylor instability: Two and three dimensions. *J. Fluid Mech.* 447, 377.
- Youngs, D.L., 1982. Time-dependent multimaterial flow with large fluid distortion. *Numer. Methods Fluid Dyn.* 24, 273.
- Youngs, D.L., 1989. Modeling turbulent mixing by Rayleigh–Taylor instability. *Physica D* 37, 270.
- Youngs, D.L., 1991. Three-dimensional numerical simulation of turbulent mixing by Rayleigh–Taylor instability. *Phys. Fluids A* 3, 1312.
- Youngs, D.L., 1992. Experimental investigation of turbulent mixing by Rayleigh–Taylor instability. In: Dannevik, W.P., Buckingham, A.C., Leith, C.E. (Eds.), *Advances in Compressible Turbulent Mixing*. Proceeding of the 1st International Workshop on the Physics of Compressible Turbulent Mixing, Princeton Univ., p. 607.
- Youngs, D.L., 1994. Numerical simulation of mixing by Rayleigh–Taylor and Richtmyer–Meshkov instabilities. *Laser Part. Beams* 12, 725.
- Youngs, D.L., 1995. Representation of the molecular mixing process in a two-phase flow turbulent mixing model. In: Proceeding of the 5th International Workshop on the Physics of Compressible Turbulent Mixing, World Scientific, p. 83.
- Youngs, D.L., 1997. Variable acceleration Rayleigh–Taylor mixing Jourdan G, Houas L. In: *Proceedings of the 6th International Workshop on the Physics of Compressible Turbulent Mixing*. Provence University Press, Marseille, France, p. 534.
- Youngs, D.L., 2003. Application of MILES to Rayleigh–Taylor and Richtmeyer–Meshkov mixing. AIAA paper 2003-4102.

- Youngs, D.L., 2004. Effect of initial conditions on self-similar turbulent mixing. In: Proceedings of the International Workshop on the Physics of Compressible Turbulent Mixing, p. 9. Available online at: <http://www.iwpcrm.org/>.
- Youngs, D.L., 2007. In: Grinstein, F.F., Margolin, L.G., Rider, W.J. (Eds.), *Implicit Large Eddy Simulation: Computing Turbulent Fluid Dynamics*. Cambridge University Press, Cambridge, pp. 392–412.
- Youngs, D.L., 2009. Application of monotone integrated large eddy simulation to Rayleigh–Taylor mixing. *Phil. Trans. R. Soc. A* 367, 2971.
- Youngs, D.L., 2013. The density ratio dependence of self-similar Rayleigh–Taylor mixing. *Phil. Trans. R. Soc. A* 371, 20120173.
- Youngs, D.L., 2017. Rayleigh–Taylor mixing: direct numerical simulation and implicit large eddy simulation. *Phys. Scr.* 92, 074006.
- Youngs, D.L., Williams, R.J.R., 2008. Turbulent mixing in spherical implosions. *Internat. J. Numer. Methods Fluids* 56, 1597.
- Yu, H., Livescu, D., 2008. Rayleigh–Taylor instability in cylindrical geometry with compressible fluids. *Phys. Fluids* 20, 104103.
- Yuan, F., Quataert, E., Narayan, R., 2003. Nonthermal electrons in radiatively inefficient accretion flow models of Sagittarius A. *Astrophys. J.* 598, 301.
- Zabusky, N.J., 1999. Vortex Paradigm for accelerated inhomogeneous flows: Visiometrics for the Rayleigh–Taylor and Richtmyer–Meshkov environments. *Annu. Rev. Fluid Mech.* 31, 495.
- Zaitsev, S.V., Lazareva, E.V., Chernukha, V.V., Belyaev, V.M., 1985. An experimental investigation and numerical modeling of turbulent mixing in one-dimensional flows. *Sov. Phys. Dokl.* 30, 579.
- Zhai, Z., Liu, C., Qin, F., Yang, J., Luo, X., 2010. Generation of cylindrical converging shock waves based on shock dynamics theory. *Phys. Fluids* 22, 041701.
- Zhai, Z., Si, T., Luo, X., Yang, J., Liu, C., Tan, D., Zou, L., 2012. Parametric study of cylindrical converging shock waves generated based on shock dynamics theory. *Phys. Fluids* 24, 026101.
- Zhai, Z., Dong, P., Si, T., Luo, X., 2016. The Richtmyer–Meshkov instability of a “V” shaped air/helium interface subjected to a weak shock. *Phys. Fluids* 28, 082104.
- Zhai, Z., Li, W., Si, T., Luo, X., Yang, J., Lu, X., 2017. Refraction of cylindrical converging shock wave at an air/helium gaseous interface. *Phys. Fluids* 29, 016102.
- Zhang, J., Wang, L.F., Ye, W.H., Wu, J.F., Guo, H.Y., Zhang, W.Y., He, X.T., 2017. Weakly nonlinear incompressible Rayleigh–Taylor instability in spherical geometry. *Phys. Plasmas* 24, 062703.
- Zhang, Q., Sohn, S.I., 1996. An analytical nonlinear theory of Richtmyer–Meshkov instability. *Phys. Lett. A* 212, 149.
- Zhang, Q., 1998. Analytical solutions of Layzer-type approach to unstable interfacial fluid mixing. *Phys. Rev. Lett.* 81, 3391.
- Zhang, Q., Graham, M.J., 1997. Scaling laws for unstable interfaces driven by strong shocks in cylindrical geometry. *Phys. Rev. Lett.* 79, 2674.
- Zhang, Q., Graham, M.J., 1998. A numerical study of Richtmyer–Meshkov instability driven by cylindrical shocks. *Phys. Fluids* 10, 974.
- Zhang, W., Wu, Z.-W., Li, D., 2005. Effect of shear flow and magnetic field on the Rayleigh–Taylor instability. *Phys. Plasmas* 12, 042106.
- Zhang, X., Tan, D.-W., 2009. Direct numerical simulation of the Rayleigh–Taylor instability with the spectral element method. *Chin. Phys. Lett.* 26, 084703.
- Zhang, Y.-S., He, Z.-W., Gao, F.-J., Li, X.-L., Tian, B.-L., 2016. Evolution of mixing width induced by general Rayleigh–Taylor instability. *Phys. Rev. E* 93, 063102.
- Zhang, Y.-T., Shu, C.-W., Zhou, Y., 2006. Effects of shock waves on Rayleigh–Taylor instability. *Phys. Plasmas* 13, 062705.
- Zheng, J.G., Lee, T.S., Winoto, S.H., 2008. Numerical simulation of Richtmyer–Meshkov instability driven by imploding shocks. *Math. Comput. Simulation* 79, 749.
- Zhigalin, A.S., Roussikh, A.G., Baksht, R.B., Chaikovsky, S.A., Labetskaya, N.A., Oreshkin, V.I., 2015. Suppression of Rayleigh–Taylor instabilities in Z-pinchers. *Tech. Phys. Lett.* 41, 554.
- Zhou, Q., 2013. Temporal evolution and scaling of mixing in two-dimensional Rayleigh–Taylor turbulence. *Phys. Fluids* 25, 085107.
- Zhou, Y., 1991. Eddy damping backscatter and subgrid stresses in subgrid modeling of turbulence. *Phys. Rev. A* 43, 7049.
- Zhou, Y., 1993a. Degree of locality of energy transfer in the inertial range. *Phys. Fluids A* 5, 1092.
- Zhou, Y., 1993b. Interacting scales and energy transfer in isotropic turbulence. *Phys. Fluids A* 5, 2511.
- Zhou, Y., 1995. A phenomenological treatment of rotating turbulence. *Phys. Fluids* 7, 2092.
- Zhou, Y., 2001. A scaling analysis of turbulent flows driven by Rayleigh–Taylor and Richtmyer–Meshkov instabilities. *Phys. Fluids* 13, 538.
- Zhou, Y., 2007. Unification and extension of the concepts of similarity criteria and mixing transition for studying astrophysics using high energy density laboratory experiments or numerical simulations. *Phys. Plasmas* 14, 082701.
- Zhou, Y., 2010. Renormalization group theory for fluid and plasma turbulence. *Phys. Rep.* 488, 1.
- Zhou, Y., 2017. Rayleigh–Taylor and Richtmyer–Meshkov instability induced flow, turbulence, and mixing. I. *Phys. Rep.* 720–722, 1–136.
- Zhou, Y., Speziale, C.G., 1998. Advances in the fundamental aspects of turbulence: energy transfer, interacting scales, and self-preservation in isotropic decay. *ASME Appl. Mech. Rev.* 51, 267.
- Zhou, Y., Yeung, P.K., Brasseur, J.G., 1996. Scale disparity and spectral transfer in anisotropic numerical turbulence. *Phys. Rev. E* 53, 1261.
- Zhou, Y., Zimmerman, C.B., Burke, E.W., 2002. Formulation of a two-scale transport scheme for the turbulent mix induced by Rayleigh–Taylor and Richtmyer–Meshkov instabilities. *Phys. Rev. E* 65, 056303.
- Zhou, Y., Robey, H.F., Buckingham, A.C., 2003a. Onset of turbulence in accelerated high-Reynolds-number flow. *Phys. Rev. E* 67, 056305.
- Zhou, Y., Remington, B.A., Robey, H.F., Cook, A.W., Glendinning, S.G., Dimits, A., Buckingham, A.C., Zimmerman, G.B., Burke, E.W., Peyser, T.A., Cabot, W., Eliason, D., 2003b. Progress in understanding turbulent mixing induced by Rayleigh–Taylor and Richtmyer–Meshkov instabilities. *Phys. Plasmas* 10, 1883.
- Zhou, Y., Rubinstein, R., Eliason, D., Cabot, W., 2003c. Computing turbulent flows driven by Rayleigh–Taylor and Richtmyer–Meshkov instabilities. *Astron. Astrophys.* 405, 379.
- Zhou, Y., Matthaeus, W.H., Dmitruk, P., 2004. Colloquium: Magnetohydrodynamic turbulence and time scales in astrophysical and space plasma. *Rev. Modern Phys.* 76, 1015.
- Zhou, Y., Buckingham, A.C., Bataille, F., Mathelin, L., 2009. Minimum state for high Reynolds and Pécelt number turbulent flows. *Phys. Lett. A* 373, 2746.
- Zhou, Y., Grinstein, F.F., Wachtor, A.J., Haines, B.M., 2014. Estimating the effective Reynolds number in implicit large eddy simulation. *Phys. Rev. E* 89, 013303.
- Zhou, Y., Cabot, W.H., Thorner, B., 2016. Asymptotic behavior of the mixed mass in Rayleigh–Taylor and Richtmyer–Meshkov instability induced flows. *Phys. Plasmas* 23, 052712.
- Zhuang, Z.-H., Xue, D.-W., Chen, Z.H., Jiang, X.-H., 2013. The eruption of a high-pressure cylindrical heavy gas cloud. *Can. J. Phys.* 91, 850.
- Zingale, M., Woosley, S.E., Rendleman, C.A., Day, M.S., Bell, J.B., 2005. Three-dimensional numerical simulations of Rayleigh–Taylor unstable flames in Type Ia supernovae. *Astrophys. J.* 632, 1021.
- Zou, L.Y., Liu, C.L., Tan, D.W., Huang, W.B., Luo, X., 2010. On interaction of shock wave with elliptic gas cylinders. *J. Visualization* 13, 347.
- Zou, L.Y., Huang, W.B., Liu, C.L., Yu, J., Luo, X.S., 2014. One the evolution of double shock-accelerated elliptic gas cylinders. *ASME J. Fluids Eng.* 136, 091205.
- Zyryanov, K.I., Ruev, G.A., Fedorov, A.V., 2017. Development of Richtmyer–Meshkov instability as a result of the transmission of a shock wave through a cylindrical structure of heavy gas. *J. Eng. Phys. Thermophys.* 90, 430.